REPUBLIQUE DU CAMEROUN
Paix – Travail – Patrie
****
UNIVERSITE DE YAOUNDE I
FACULTE DES SCIENCES
DEPARTEMENT DE SCIENCES DE LA TERRE
****
CENTRE DE RECHERCHE ET DE FORMATION DOCTORALE EN SCIENCES
TECHNOLOGIES ET GEOSCIENCES
LABORATOIRE DE GEOSCIENCES DE FORMATIONS SUPERFICIELLES

REPUBLIC OF CAMEROUN
Peace – Work – Fatherland
****
UNIVERSITY OF YAOUNDE I
FACULTY OF SCIENCE
DEPARTMENT OF EARTH SCIENCES
****
POSTGRADUATE SCHOOL OF SCIENCE, TECHNOLOGIES AND GEOSCIENCES
GEOSCIENCES LABORAT

SEDIMENTOLOGY, MINERALOGY AND GEOCHEMISTRY OF CRETACEOUS-TERTIARY (GORGONILLA, COLOMBIA, AND ZUMAYA, SPAIN) AND PALEOCENE-EOCENE (DOUALA, CAMEROON) TRANSITIONS: implications for paleoenvironmental reconstruction

THÈSE DE DOCTORAT/Ph.D EN SCIENCES DE LA TERRE

Par : **MBABI BITCHONG André**
Master en Sciences de la Terre

Sous la direction de
NGOS III Simon
Professeur, Université de Yaoundé I
ADATTE Thierry
Professeur, Université de Lausanne (Suisse)

Année Académique : 2020

UNIVERSITE DE YAOUNDE I
FACULTE DES SCIENCES
BP 812 Yaoundé
Tél : (+237) 222 23 44 96
Courriel : doyen@facsciences.uy1.cm
CENTRE DE RECHERCHE ET DE FORMATION DOCTORALE SCIENCES TECHNOLOGIES ET GEOSCIENCES

THE UNIVERSITY OF YAOUNDE I
FACULTY OF SCIENCE
PO. Box 812 Yaoundé
Phone: (+237) 222 23 44 96
Email: doyen@facsciences.uy1.cm
POSTGRADUATE SCHOOL IN SCIENCES TECHNOLOGIES AND GEOSCIENCES

DEPARTEMENT DES SCIENCES DE LA TERRE
DEPARTMENT OF EARTH SCIENCES

URFD GEOSCIENCES ET APPLICATIONS
DOCTORAL RESEARCH UNIT FOR GEOSCIENCES AND APPLICATIONS

LABORATOIRE DE GEOSCIENCES DE FORMATIONS SUPERFICIELLES
GEOSCIENCES LABORATORY OF SURFACE FORMATIONS

SEDIMENTOLOGY, MINERALOGY AND GEOCHEMISTRY OF CRETACEOUS-TERTIARY (GORGONILLA, COLOMBIA, AND ZUMAYA, SPAIN) AND PALEOCENE-EOCENE (DOUALA, CAMEROON) TRANSITIONS: implications for paleoenvironmental reconstruction

THÈSE DE DOCTORAT/Ph.D EN SCIENCES DE LA TERRE
Spécialité : Géosciences des Formations Superficielles et Applications
Option : Géologie du Sédimentaire et du Pétrole

Par

MBABI BITCHONG André
Matricule : 03R167
Master en Sciences de la Terre

Soutenue publiquement le 23 décembre 2020 devant le jury composé de

Président : **NDJIGUI Paul-Désiré, Professeur, Université de Yaoundé I**

Rapporteurs : **NGOS III Simon, Professeur, Université de Yaoundé I**
ADATTE Thierry, Professeur, Université de Lausanne (Suisse)

Membres : **KHOZYEM M. Saley Hassan, Professeur, Université d'Aswan (Égypte)**
NZENTI Jean Paul, Professeur, Université de Yaoundé I
BESSONG Moïse, Maître de Recherche, IRGM

UNIVERSITE DE YAOUNDE I
FACULTE DES SCIENCES
BP 812 Yaoundé
Tél : (+237) 222 23 44 96
Courriel : doyen@facsciences.uy1.cm
CENTRE DE RECHERCHE ET DE FORMATION DOCTORALE EN SCIENCES TECHNOLOGIES ET GEOSCIENCES

THE UNIVERSITY OF YAOUNDE I
FACULTY OF SCIENCE
PO. Box 812 Yaoundé
Phone: (+237) 222 23 44 96
Email: doyen@facsciences.uy1.cm
POSTGRADUATE SCHOOL OF SCIENCE, TECHNOLOGIES AND GEOSCIENCES

DEPARTEMENT DES SCIENCES DE LA TERRE
DEPARTMENT OF EARTH SCIENCES

URFD EN GEOSCIENCES ET APPLICATIONS
DOCTORAL RESEARCH UNIT FOR GEOSCIENCES AND APPLICATIONS

ATTESTATION DE CORRECTION DE THÈSE DE DOCTORAT/Ph.D

****

Spécialité : **Géosciences des Formations Superficielles et Applications**
Option : **Géologie du Sédimentaire et du Pétrole**

Nom et prénom du candidat : **MBABI BITCHONG André**
Matricule : **03R167**

Titre de la thèse : « **Sedimentology, mineralogy and geochemistry of Cretaceous-Tertiary (Gorgonilla, Colombia, and Zumaya, Spain) and Paleocene-Eocene (Douala sub-basin, Cameroon) transitions : implications for paleoenvironmental reconstruction** »

Date de soutenance : **Mercredi, le 23 décembre 2020**.

Nous, membres du jury, après avoir lu le document qui nous a été présenté, relevons que le candidat a effectué toutes les corrections, conformément aux observations formulées lors de la soutenance.

En foi de quoi, la présente **Attestation de Correction** lui est établie pour servir et valoir ce que de droit.

25/01/21

Le président du Jury

Ndjigui Paul-Désiré
Professeur

Les Membres

Nzenti Jean Paul
Docteur d'Etat ès-Sciences
Professeur Titulaire Hors Echelle

Dedication

To my father Antoine BITCHONG MBABI.

To my sweetheart Glwadys NGO MANDENG.

To my sons: Mylane Marc-Antoine BITCHONG MBABI and Léandre Ernest NDJEMBE MBABI.

Acknowledgements

Scientific work, and more particularly a doctoral thesis, constitutes a veritable "crystal structure" implemented by its author but whose external contribution is always necessary for its success. This is why, at this moment when I am ending my doctoral research, I would like to think of anyone who have been useful to me in carrying out this important work.

First of all, I would like to express my gratitude to the Department of Earth Sciences, Faculty of Science, University of Yaoundé I, Cameroon for giving me the opportunity to pursue my science career to PhD level.

This work would not have been possible without financial support. I would like to thank the Swiss Government through the Federal Commission for Scholarships for Foreign Students (FCS) for the research grant that I was awarded. My gratitude also goes to ISTE of the University of Lausanne and rectorate of the University of Maroua for having funded different budgetary components related to this doctoral research.

I warmly thank Professor Thierry ADATTE, promoter of this work, who put at my disposal all his skills, experience and services for the success of this work. His involvement at different levels for the smooth running of my stays in Switzerland was very effective. I would also like to thank Professor Simon NGOS III, local promoter, with whom I have benefited from an essential academic supervision since I was recruited as an assistant lecturer at the Faculty of Mines and Petroleum Industries of the University of Maroua. My warm and sincere thanks are also addressed to Professors Karl FÖLLMI of late memory, Paul BILONG and Paul-Désiré NDJIGUI for their permanent encouragement and marks of attention towards me.

My gratitude also goes to Professors Gerta KELLER (Princeton University), Eric FONT (University of Coimbra) and Gilbert-François NGON NGON (University of Douala) for their fruitful collaboration during this doctoral research.

I am very grateful to Doctor Moïse BESSONG for his kind advice and the nice moments during our stay in Lausanne, and for his agreeing to be a member of the jury of my thesis. I appreciate and acknowledge Professors Jean Paul NZENTI and Hassan KHOZYEM for being welling to serve on Jury committee for my PhD thesis.

My sincere thanks go to the main laboratory managers who welcomed me and accepted to carry out the various analyses of my study samples:

- Doctor Jorge E. SPANGENBERG, Organic geochemistry and Stable isotope laboratories;
- Doctor Pierre VONLANTHEN, MEB laboratory.
- Doctor Alexey ULIANOV, LA-ICP-MS laboratory;
- Doctor Martin ROBYR, electron microprobe laboratory;
- Doctor CLAUDIA BAUMGARTNER, Digital Microscopy Laboratory.

My sincere thanks to the various laboratory staffs for their technical support, especially to Jean-Claude LAVANCHY and Fabio CAPPONI for the FRX analyses, Tiffany MONNIER for the mineralogy and sedimentary geochemistry analyses and Laurent NICOD for the thin section preparations.

My Geologist colleagues, Doctor Alicia FANTASIA from the University of Lausanne and Serge Parfait KOA-NA-LEBOGO from the University of Yaoundé 1, find here the expression of my gratitude for having respectively supported and accompanied me on different sites sampling, as well as Doctor Simplice AYAGMA BONOHO for the very good times spent in Switzerland and that we continue to spend in Cameroon..

A thesis work, in addition to being the result of numerous scientific collaborations, is also shaped in a general atmosphere. Thanks to my colleagues from the FMIP (Doctors Daniel Hervé GOUET, Sifeu TAKOUGANG KIGNI, Sylvestre KANOUO and Firmin NTOUALA) and the DST (Doctors Elisé SABABA, Achille ANABA ONANA and Jules MBANGA

NYOBE). Thanks also to all actual or former students of the FMIP who have always encouraged me.

My thanks go of course especially to my sweetheart Glwadys and my dad for their constant support, in all forms whatsoever. Thanks also to all my family who is always there when needed.

I am also thinking of those who would have appreciated seeing this work completed, my mom Céline, and my aunts Marie and Odile.

Finally, I would like to express my gratitude to Jean Jacques NKONDJOCK for his multiform support throughout my doctoral research stays in Lausanne.

Table of contents

Abstract

The Cretaceous–Paleogene and Paleocene-Eocene boundaries (KPB: ~66 Ma and PEB: ~55.8 Ma respectively) were examined respectively at Gorgonilla Island (Colombia, South America) and Zumaya beach (Spain, Western Europe) for KPB and in Douala sub-basin (Cameroon, Central Africa) for PEB in order to evaluate KPB mass extinction and Paleocene-Eocene Thermal Maximum (PETM) signatures and their corollary effects on paleoenvironment and paleoclimate. Based on a multidisciplinary approach integrating detailed lithology, sedimentology, biostratigraphy (planktics, benthics, ostracods and pollens), mineralogy (bulk rock, clay and MEB) and geochemistry (stable isotopes, TOC, mercury, major, trace and rare earth elements), it clearly appears that the Gorgonilla K/Pg section consists of light green calcareous mudstones containing a various microfossil species deposited in bathyal environment between lysocline and CCD, alternating with dark-olive litharenites derived from volcanism processes of the Caribbean Large Igneous Province (CLIP) and which have reached deep sea waters via turbidity currents. Transition between Cretaceous and Paleogene materials is marked by an erosional surface, topped by a 3 cm spherules-rich layer indicating the Chicxulub impact, which triplicates in one edge of outcrop and shows tektites of black to yellow color with various size (0.80–1.50 mm) presenting a normal size-gradation. Five planktic foraminiferal zones including CF3, CF2, CF1, P1a(2) and P1b are highlighted across the section, that indicates missing zones (P0, P1a(1) and lower P1a(2)) testifying of a KPB hiatus, above which another short hiatus is evidenced. Chemical composition dissimilarity (mainly in Co, Cr and Ni) observed between large size and smaller tektites testifies of a tektites reworking during which large spherules are enriched in common shale elements (with a composition very close to that of the matrix), while the smaller ones show a chemical composition close to that of chondrite. No evidence of Deccan volcanism (and/or another distal volcanism episode) in Gorgonilla as well as hydrothermalism. However, hydrothermal plume particles, probably from Caribbean Large Igneous Province (CLIP), and a weak burial diagenesis have impregnated these materials. K/Pg transition is marked by a contrasted climate and strong sea-level variability: the drop in $\delta^{18}O_{carb}$ (~3 ‰) and detrital index (DI) as well as the high CIA values observed just below the KPB are evidence of a hot and humid end-Maastrichtian associated to a relatively low sea-level, in contrast to the first Danian stage.

At Zumaya, apart minor hiatuses just below KPB layer and at the P1a (2)/P1b boundary, results show two majors hiatuses: KTB hiatus of ~225 kyr above K/Pg boundary surface (~66 Ma) with P0 and lower P1a (1) missing, and early Danian hiatus of about 110 kyr at the P1a (1)/P1a (2) boundary (~65,76 Ma) with the lower part of P1a (2) zone missing. CF1 (more Guembelitria cretacea species) and P1a (1) biozones are the scene of maximum stress due to dissolution-acidification processes linked to the main phase of Deccan (~65 Ma). For example, P1a (1) zone is dominated by smallest planktic foraminifera morphologies (38-63µm). K/Pg boundary layer is enriched in calcite synonymous of an ocean acidification, mass extinction and dissolution-recrystallization processes in deeper environment during warm/humid climate (high K/CMIS ratio). The Zumaya KTB interval is also enriched in some trace elements as Ni, Co, V, Cr, Pb, U, Ba and Sr with an indice of cosmic input (high Ni/Co ratio at the KTB-2). Earliest Danian marls are deposited in a shallower environment under a strong detritism

(increased amount in SiO_2, TiO_2, Al_2O_3, MgO, Fe_2O_3 and K_2O, high CIA and DI < 1) which suggests more humid conditions above KTB layer.

For the PETM event, combination of lithology with microfossil assemblage and carbon isotope data suggest the latest Paleocene P5 zone, just below the PETM, and allows to define the Paleocene-Eocene boundary (PEB). A negative carbon-isotope excursion (CIE) is indicated from the uppermost Paleocene deposits (pre-PETM interval) to earliest Eocene sediments (PETM interval), place of minimum values, with a shift in $\delta^{13}C$ of 1,48‰ in Bongue and 2,98‰ in Dibamba. These intervals are affected by widespread acidification, as revealed by carbonate dissolution and microfossil condition (species are dwarfed, broken and thin shelled with holes). Acidification is more severe across the PETM involving the absence of carbonate and rarity of microfauna, where the only identified species (*Igorina broedermanni*) characterizes the early Eocene. Mercury anomalies as well as TOC and sensitive trace elements data suggest volcanic activity linked to intrusive magma of future Cameroon Volcanic Line (CVL), and decreasing productivity prior the PETM. Geochemical and mineralogical results in this section support that, in addition to climate change, other environmental perturbations including increase in productivity and detrital input, and decrease in bottom water oxygenation, occurred during the PETM and post-PETM in the Douala sub-basin.

Furthermore, the materials of the Tondè locality in the Douala sub-basin are paleosols of Pleistocene to Holocene age, resulting from alteration of intermediate rocks, probably from the surrounding basement (gneiss and micaschist), and recycling of pre-existing sandy materials. These paleosols are mainly composed of pyriteous clays (grey and red) and unconsolidated sandstones that developed in a subequatorial to equatorial climate. The pyrite encountered, of euhedral (isolated and clustered crystals) and massive appearance with various morphologies and sizes, is a product of late diagenesis formed by secondary enrichment and coupled with precipitation under more reducing conditions, linked to the fluctuation of the water table.

Keywords: KPB mass extinction, Paleocene-Eocene Thermal Maximum (PETM), Paleosols, Gorgonilla, Zumaya, Douala sub-basin.

Résumé

La limite Crétacé-Paléogène (KPB : ~66 Ma) à Gorgonilla (Colombie, Amérique Latine) et à Zumaya (Espagne, Europe Occidentale) ainsi que celle du Paléocène-Éocène (PEB : ~55,8 Ma) dans le sous-bassin de Douala (Cameroun, Afrique centrale), ont été examinées afin d'évaluer les signatures de l'extinction de masse du KPB et du maximum thermique du Paléocène-Éocène (PETM) et leurs impacts sur le paléoenvironnement et le paléoclimat. Sur la base d'une approche multidisciplinaire intégrant la lithologie détaillée, la sédimentologie, la biostratigraphie (foraminifères planctoniques et benthiques, ostracodes et pollens), la minéralogie (roche totale, argile et MEB) et la géochimie (isotopes stables, COT, mercure, éléments majeurs, traces et terres rares), il apparaît clairement que la section K/Pg de Gorgonilla est constituée de mudstones calcaires vert clair contenant diverses espèces microfossiles déposées dans un environnement bathyal entre la lysocline et la profondeur de compensation de la calcite, alternant avec des litharénites sombres-olives issues des processus volcaniques de la Grande Province Ignée des Caraïbes (CLIP) et qui ont atteint les eaux profondes par le biais des courants de turbidité. La transition entre les matériaux du Crétacé et du Paléogène est marquée par une surface d'érosion, surmontée d'une couche riche en sphérules de 3 cm qui se dissocie en trois sur un bord de l'affleurement et présente des tektites de couleur noire à jaune de taille variable (0,80-1,50 mm) présentant un granoclassement normal. Cinq zones à foraminifères planctoniques, dont CF3, CF2, CF1, P1a(2) et P1b, sont mises en évidence dans la section, ce qui indique des zones manquantes (P0, P1a(1) et P1a(2) inférieur) témoignant d'un hiatus KPB, au-dessus duquel un autre hiatus de faible amplitude est mis en évidence. La dissimilitude de composition chimique (principalement en Co, Cr et Ni) observée entre les tektites de grande taille et les plus petites témoigne d'un remaniement de celle-ci au cours duquel les larges sphérules s'enrichissent en éléments detritiques communs (avec une composition très proche de celle de la matrice), tandis que les plus petites présentent une composition chimique proche de celle de la chondrite. Aucun signe de volcanisme du Deccan (et/ou d'un autre épisode de volcanisme distal) ni de d'hydrothermalisme n'a été mis en évidence à Gorgonilla. Cependant, des particules de panaches hydrothermaux, provenant probablement de la Grande Province Ignée des Caraïbes (CLIP), et une faible diagenèse d'enfouissement ont imprégné ces matériaux. La transition K/Pg est marquée par un climat contrasté et une forte variabilité du niveau de la mer : la baisse de $\delta^{18}O_{carb}$ (~ 3 ‰) et de l'indice du détritisme (DI) ainsi que les valeurs élevées de CIA observées juste en dessous de la KPB sont la preuve d'un Maastrichtien terminal chaud et humide associé à un niveau de la mer relativement bas, et ce contrairement Danien précoce.

A Zumaya, en dehors des hiatus mineurs juste sous la couche KTB et à la limite P1a (2)/P1b, les résultats montrent deux hiatus majeurs : hiatus KPB de~225.000 ans au-dessus de la limite KPB (~66 Ma) avec la zone P0 et la partie inférieure de P1a(1) manquantes, et le hiatus du Danien précoce d'environ 110.000 ans à partir de la limite P1a(1)/P1a(2) (~65,76 Ma), avec la partie inférieure de la zone P1a(2) manquante. Les biozones CF1 (espèce *Guembelitria cretacea* abondante) et P1a(1) sont le théâtre d'un stress maximal dû aux processus de dissolution-acidification liés à la phase principale du Deccan (~65 Ma). Par exemple, la zone P1a(1) est dominée par les plus petites morphologies de foraminifères planctoniques (38-63µm). La couche limite KPB est enrichie en calcite, synonyme des processus d'acidification,

d'extinction de masse et de dissolution-cristallisation dans un environnement marin plus profond, caractérisé par un climat chaud/humide (rapport K/CMIS élevé). La couche KPB de Zumaya est également enrichi en certains éléments traces tels que le Ni, Co, V, Cr, Pb, U, Ba et Sr avec un indice d'apport cosmique (rapport Ni/Co élevé au KTB-2). Les premiers dépôts marneux du Danien se déposent dans un environnement moins profond sous un détritisme relativement élevé (quantité accrue en SiO_2, TiO_2, Al_2O_3, MgO, Fe_2O_3 et K_2O, CIA élevé et DI < 1) ce qui suggère des conditions plus humides au-dessus de la couche de KPB.

En ce qui concerne l'évènement du PETM observé dans le bassin de Douala, la combinaison de la lithologie avec l'assemblage de microfossiles et les données sur les isotopes du carbone suggère la dernière zone P5 du Paléocène, juste en dessous du PETM, et permet de définir la limite Paléocène-Éocène (PEB). Une excursion négative de l'isotope du carbone (CIE) est indiquée depuis les dépôts du Paléocène supérieur (intervalle pré-PETM) jusqu'aux sédiments de l'Éocène le plus ancien (intervalle PETM), lieu des valeurs minimales, avec un décalage des valeurs de $\delta^{13}C$ de 1,48 ‰ à Bongue et 2,98 ‰ à Dibamba. Ces intervalles sont affectés par une acidification généralisée, comme le révèlent la dissolution des carbonates et l'état de microfossiles (les espèces sont nanifiées, brisées et minces avec des trous). L'acidification est plus sévère dans le PETM, impliquant l'absence de carbonate et la rareté de la microfaune, où la seule espèce identifiée (*Igorina broedermanni*) caractérise le début de l'Éocène. Les anomalies de mercure ainsi que les données sur le COT et les éléments traces sensibles suggèrent une activité volcanique liée au magma intrusif de la future ligne volcanique du Cameroun (CVL), et une diminution de la productivité avant le PETM. Les résultats géochimiques et minéralogiques présentés dans cette partie confirment qu'en plus du changement climatique, d'autres perturbations environnementales, notamment une augmentation de la productivité et des apports de détritus, ainsi qu'une diminution de l'oxygénation des eaux de fond, se sont produites pendant le PETM et après le PETM dans le sous-bassin de Douala.

Par ailleurs, les matériaux de la localité de Tondè dans le sous-bassin de Douala sont des paléosols d'âge Pléistocène à Holocène, résultant de l'altération de roches intermédiaires, probablement du socle environnant (gneiss et micaschiste), et du recyclage de matériaux sableux préexistant. Ces paléosols sont principalement constitués d'argiles pyriteuses (grises et rouges) et de grès non consolidés qui se sont mis en place à la faveur d'un climat subéquatorial à équatorial. La pyrite rencontrée, d'aspect automorphe (cristaux isolés et en grappes) et massive avec des morphologies et des tailles diverses, est un produit de la diagenèse tardive formé par un enrichissement secondaire et couplé à des précipitations dans des conditions plus réductrices, liées à la fluctuation de la nappe phréatique.

Mots clés : Extinction massive de KPB, maximum thermique du Paléocène-Eocène (PETM), Paléosols, Gorgonilla, Zumaya, sous-bassin de Douala

List of Tables

List of Figures

CHAPTER I. GENERAL INTRODUCTION

1. OVERVIEW ON KPB MASS EXTINCTION AND PETM

1.1. The Cretaceous-Paleogene boundary (KPB) mass extinction event

The Cretaceous-Paleogene (K/Pg) extinction event is the latest of five major extinction events in the Phanerozoic. It is marked globally by a biotic turnover evidenced in the marine realm by the extinction of ~ 36% of known marine animal genera and ~ 76% of known marine invertebrates (Raup and Sepkoski, 1982; Jablonski, 1994; Rohde and Muller, 2005), including ammonites, marine reptiles and extensive extinction among planktic foraminifera and other micro-organisms (Smit 1999). In the terrestrial realm this is evidenced by the extinction of non-avian dinosaurs and major die-back of other terrestrial fauna (e.g., Sheehan and Fastovsky 1992; Labandeira et al. 2002; Buffetaut 2004) as well as a global turnover of the flora (Sweet et al. 1990; Vajda et al. 2001; Nichols and Johnson 2002; Vajda and McLoughlin 2004, 2005, 2007). Since 1980, theory for the event invokes the Chicxulub asteroid impact (65.8 Ma; Gradstein and Ogg, 2004) as the sole cause of rapid global climatologic and ecologic crisis that occurred at the start of the Cenozoic (e.g., Jablonski and Raup, 1995; Schulte e al., 2010; Renne et al., 2013). However, this theory is controversial by some authors which claimed the possibility that such a colossal impact may have predated the Cretaceous–Paleogene transition (e.g. Keller et al., 2004, 2009, 2010; Archibald et al., 2010; Courtillot and Fluteau, 2010) and then can no longer be considered a direct cause for the mass extinction (Keller et al., 2003a, 2004, 2007).

Based on ^{40}Ar–^{39}Ar dating of tektites and bentonite beds, the KTB mass extinction and the Chicxulub impact were synchronous to within 32 kyr (Renne et al., 2013). Alternatively, the Deccan volcanism phase-2, the world's longest lava flows (Self et al., 2008), has been correlated with the KTB at 65.5 Ma and regarded as responsible for this mass extinction (Keller et al., 2008). A correlative plot of Cretaceous mass extinction intensity versus impact crater size and volcanism events (Fig. 1) shows a potential close association of the Chicxulub impact with the KPB mass extinction (Courtillot, 1999; Wignall, 2001; MacLeod, 2003; Keller, 2005a; White and Saunders, 2005), and a coincidence of the Deccan phase-2 with KPB mass extinction.

Based on five main criteria, the Tunisian El Kef section has been adopted in 1991 by the International Commission on Stratigraphy (ICS) and the International Union of Geological Sciences (IUGS) as "Global Stratotype Section and Point" (GSSP) of the K/Pg boundary. These

criteria, summarized in Keller (2011), are the follows: (1) the major lithological change from carbonate-rich sediments in Late-Maastrichtian to more organic-rich clay layer in Early-Danian, called the "boundary clay", (2) the mass extinction of tropical and subtropical planktic foraminifera and calcareous nannofossils at the end of Cretaceous, (3) the first appearances of Danian species immediately above the extinction horizon, (4) chemical markers such as negative shift (2–3 ‰) in $\delta^{13}C$ values of marine carbonate at the K/T boundary clay, and (5) an iridium anomaly at the KTB with sometimes Ni-rich spinels.

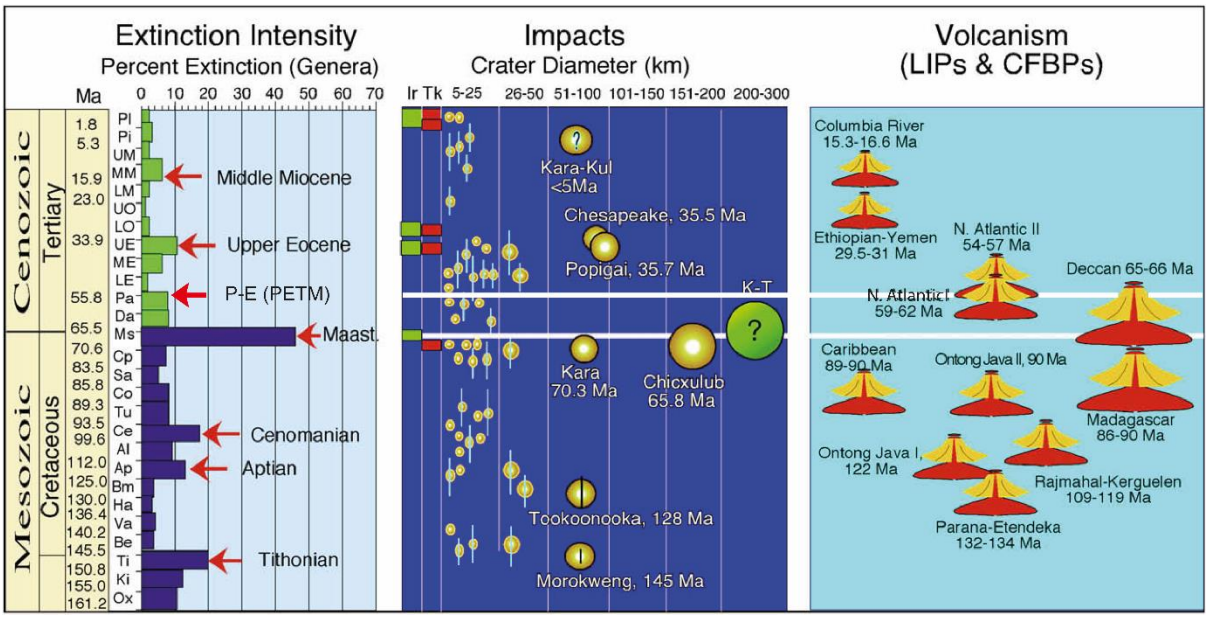

Figure 1. *Mass extinctions, impacts and large igneous provinces during the Cretaceous and Cenozoic (from Keller, 2008). Diversity and extinction data (genera) from Sepkoski (1996, 1997). Time scale after Gradstein and Ogg (2004); impacts from Grieve database and volcanic provinces after Courtillot and Renne (2003). Note that the Chicxulub impact predates the K-Pg boundary by 300 ky and a second larger (>200 km) impact crater is postulated for the K-Pg boundary based on the Ir distribution pattern and mass extinction.*

Because of abnormal concentration of Ir in thin layer commonly associate with the K-Pg mass extinction, Keller (2008) suggests that in addition to the late Maastrichtian Chicxulub impact, another larger impact, with a crater exceeding 200 km in diameter, occurred at the K-Pg boundary (Fig. 3) with more grave biotic consequences.

1.2. The Paleocene-Eocene Thermal Maximum (PETM) event

The Paleogene period displayed was punctuated by a dramatic and short lived (~200 kyr) spike in global temperatures at the Paleocene/Eocene boundary (PEB), ~56 Ma ago (e.g., Kennett and Stott, 1991; Zachos et al., 1993; Westerhold et al., 2009; Cui et al., 2011). Geologic

records from this part of Earth`s history present severe environmental changes linked to carbon cycle perturbations that resulted in the increase or decrease in Earth`s temperature linked to variations between extremes of expansive warmth with ice-free poles to extremes of cold with massive continental ice-sheets and polar ice caps. Such extreme climatic changes are controlled on a global scale by Earth's orbital geometry and/or plate tectonics (Zachos et al., 2001).

The Paleocene-Eocene Thermal Maximum (PETM) formerly called Late Paleocene Thermal Maximum (LPTM), is the latest known oceanic anoxic event (OAE; Jenkyns, 2010) during which global temperatures rose between 5 and 9 °C (e.g., Kennett and Stott, 1991; Zachos et al., 2001; McInerney and Wing, 2011). It is characterized by (i) a short-lived 170-230 kyr long, negative $\delta^{13}C$ excursion of 1 to 8 in marine and terrestrial archives (e.g.,McInerney and Wing, 2011; Murphy et al., 2010; Röhl et al., 2007), (ii) warming of bottom and surface water by several degrees Celsius (e.g.,Kennett and Stott, 1991; Tripati and Elderfield, 2005), (iii) a decrease of $CaCO_3$ in deep-sea sediments related to lysocline shallowing and ocean acidification (e.g., Zachos et al., 2005; Ridgwell and Schmidt, 2010), and (iv) a major extinction of deep-sea benthic foraminifera and a turnover of the calcareous plankton communities (e.g., Kelly et al., 1996; Gibbs et al., 2006; Thomas, 2007; Speijer et al., 2012).

2. PROPOSED SCENARIOS FOR KPB MASS EXTINCTION AND PETM

2.1. KPB mass extinction scenario

Crises that have affected our biosphere (P-T, K-Pg, etc…) are not the result of a single cause. They are the result of an accumulation of short and long-lasting unfavourable causes. At the Cretaceous-Paleogene boundary, Deccan volcanism and bolide impact at Chicxulub, may have equally contributed to the demise of a large number of species at the end of Cretaceous (Prasad and Parmar, 2020). Despite assertions of a consensus (Schulte et al., 2010), there is still vigorous debate over the potential contribution of Deccan Traps volcanism to the end Cretaceous mass extinction (Archibald et al., 2010; Courtillot and Fluteau, 2010; Keller et al., 2010). Tobin et al. (2017) reveal a 3 °C warming over several 100 kyr, sufficient to contribute to the K/Pg mass extinction though "press-pulse" mechanism, in which warming stresses ecosystems, which then respond more catastrophically to the Chicxulub impactor (Arens and West, 2008; Mitchell et al., 2012; Arens et al., 2014).

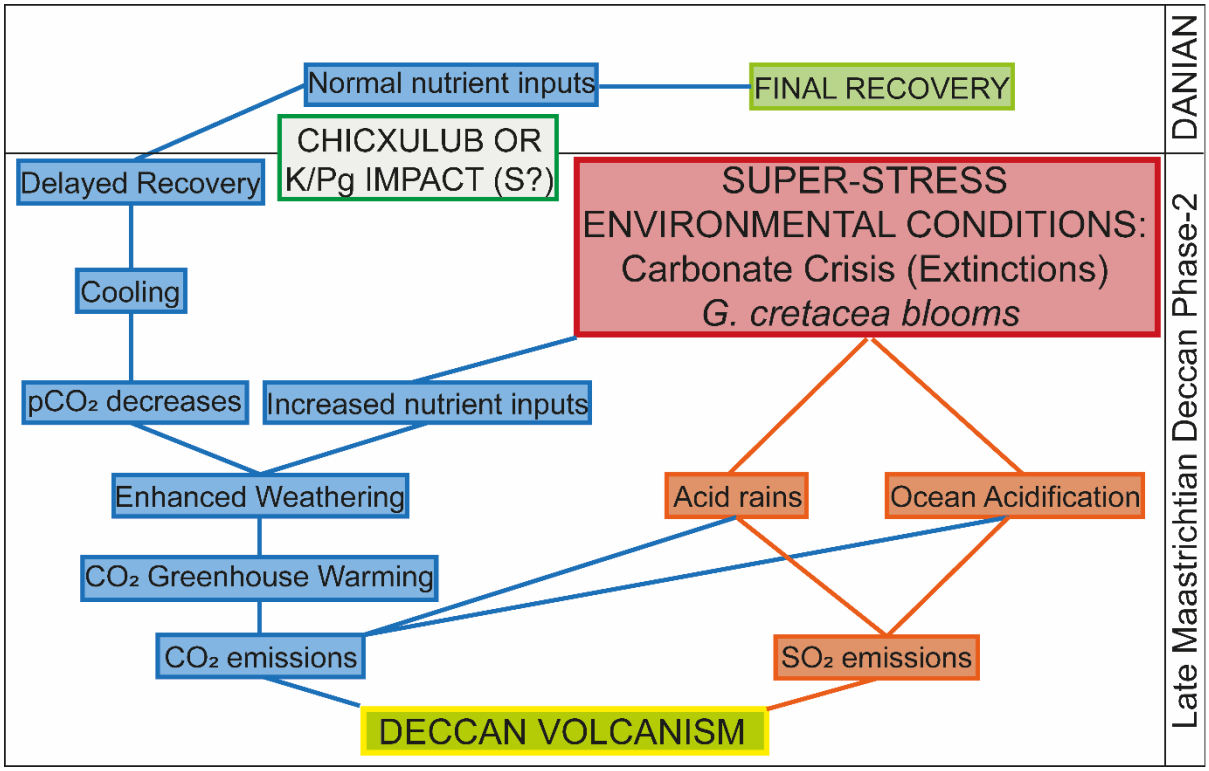

Figure 2. *Model of the possible feedbacks and environmental consequences resulting from the Deccan main phase-2 during the terminal Maastrichtian (from Gertsch et al., 2011) associate with eventual K/Pg impacts.*

Direct effects of Chicxulub impact may be mega tsunamis, generalized wildfires, blast damages, earthquakes (Alvarez et al., 1992; Toon et al., 1997) and subsequently CO_2 and SO_2 emissions, acidification (acid rains) and ozone destruction, darkening and cooling (Bond and Grasby, 2017). This established a prolonged period of stresses (e.g., climatic and eustatic fluctuations, volcanism) that induces gradual changes in biodiversity (Ammonites, planktonic foraminifera, benthic foraminifera dinosaurs, Ostracods).

For the Deccan Traps to have contributed to the extinction, that was probably be possible through a combination of SO_2 driven cooling and/or CO_2 driven warming. Both these factors are capable of biologically problematic climate change. To this effect, both Mussard et al. (2014) and Schmidt et al. (2016) demonstrate that significant cooling events driven by the Deccan Traps are possible. Tobin et al. (2016) demonstrate that CO_2 release is sufficient to drive substantial warming, and that the total amount, pattern, and duration of CO_2 emissions are the most important controls on the rate and magnitude of warming. Given estimates of these values, the Deccan Traps are plausibly large enough to drive the warming observed in paleoclimate proxies, though the match with paleoclimate proxies required increased rates of weathering.

Given the numerous data, in addition to prolonged stresses observed at the K-Pg transition, rapid changes (K/Pg impact, dissociation of methane hydrates, eruptions volcanoes) can cause mass extinctions, thus noticing the notion of conjunction of causes.

2.2. PETM scenario

Substantial data and modelling efforts have explored the shape and magnitude of the $\delta^{13}C$ curve, and the probable CO_2 sources (e.g. Sluijs and Dickens, 2012; Bowen, 2013; Zeebe, 2013). It appears that the strong negative PETM carbon isotope excursion (CIE) indicates that depending on the isotopic composition of the carbon source, 2000 to 12,000 Gt of isotopically light carbon was added to the global carbon cycle within less than 20 kyr (Dickens, 2011).

The isotopically light carbon was primarily injected into the atmosphere as methane and/or carbon dioxide before being progressively absorbed into the deeper levels of the ocean. However, several authors point to the intervention of another greenhouse enhancer, as the large temperature increase observed during the PETM cannot be forced by carbon dioxide alone, although originally in the form of methane (Dickens et al., 1995; Dickens, 2000; Zeebe et al., 2009). This is the increased rate of denitrification with concomitant release of nitrous oxide into the atmosphere (Jenkyns, 2010). Figure 3 proposed by Jenkyns (2010), resumes the processes that generally characterize OAEs.

Five potential carbon sources are summarized by McInerney and Wing (2011). They include:

(1) Methane clathrates: They are icy solids consisting of methane surrounded by water molecules. They are stable in deep-sea sediments, but they can be destabilized by increasing temperature caused by changes in ocean circulation (Dickens et al. 1995, 1997) or by decreasing pressure resulting from slope failure (Katz et al. 1999). This microbial methane has a $\delta^{13}C$ value of ~ -60 (Kvenvolden, 1993).

(2) **Wildfires:** Burning of the extensive peat and coal deposited during the Paleocene ($\delta^{13}C$ of ~ -22) could have resulted from increasing atmospheric O_2, dryer climates, and/or uplift of coal basins (Kurtz et al. 2003). However, no increase in combustion byproducts was observed in cores from either the Atlantic or Pacific (Moore and Kurtz, 2008).

(3) Thermogenic methane: Injection of magma into organic-rich sediments would have caused the explosive release of thermogenic methane ($\delta^{13}C$ of ~ -30) from Cretaceous-

Paleocene mudstones during the emplacement of the North Atlantic Igneous Province (Fig. 1) (Svensen et al. 2004, 2010; Westerhold et al. 2009).

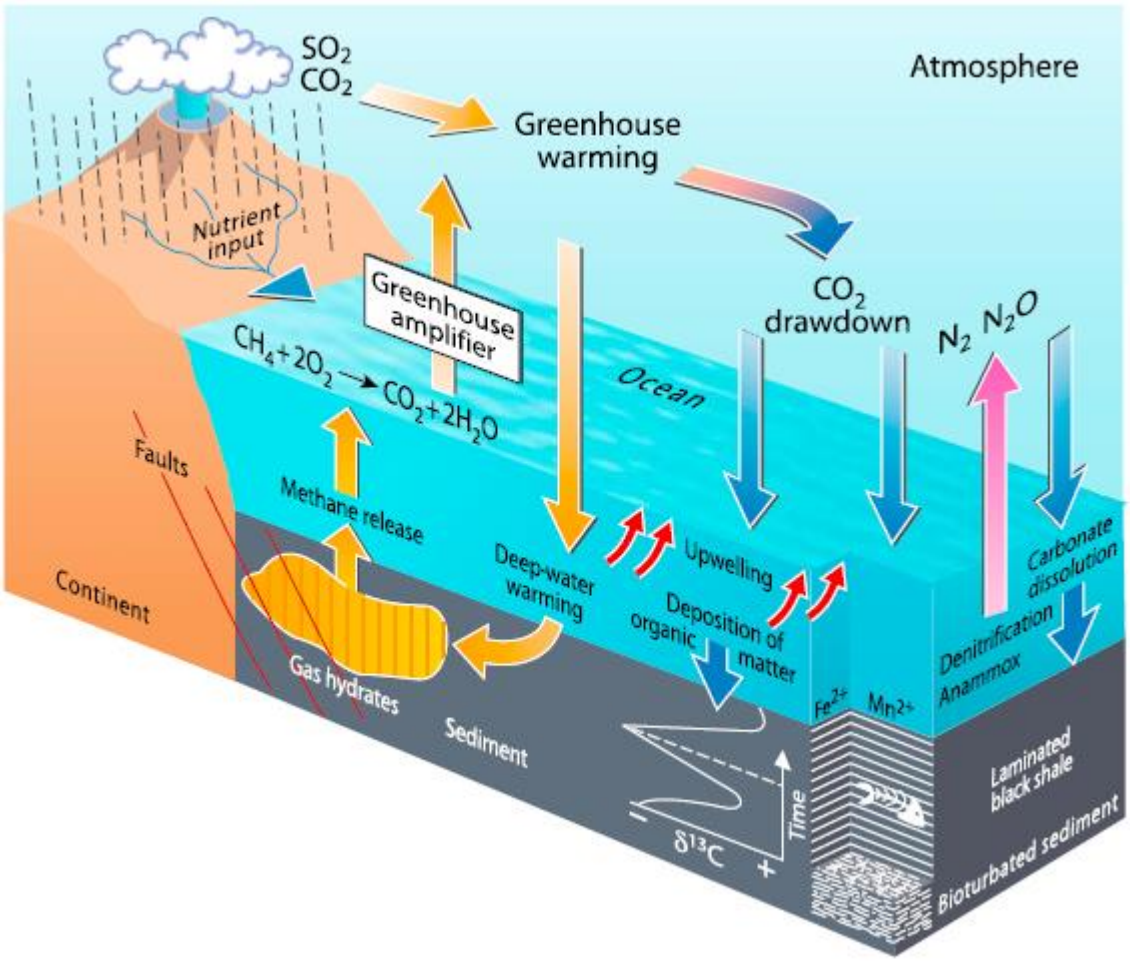

Figure 3*. Model to illustrate the variety of geochemical processes characteristic of OAEs (from Jenkyns, 2010). Volcanism, through the venting of greenhouse gases, initiates global warming; increased acidification of the oceans from dissolution of CO_2 and SO_2 causes increased carbonate dissolution; and methane release from gas hydrates, triggered either by warming of bottom waters and the subjacent sedimentary pile and/or synsedimentary faulting, produces further increase in temperature in seawater and atmosphere. The hydrological cycle accelerates with increased nutrient flux to the oceans; upwelling intensifies, as does organic productivity. As depicted in this early phase of the OAE, oxygen depletion has advanced to a state where denitrification and the anammox process have reduced nitrate and nitrite, such that nitrous oxide (a potent greenhouse gas that would promote further global warming) and elemental dinitrogen are being lost from the ocean. organic-rich sediments change from bioturbated to laminated (rich in fish remains) as the benthos is excluded from the sea bottom by the spread of anoxic conditions. Manganese is fixed as early diagenetic carbonate phases at or just below the seafloor; iron is fixed as pyrite below the seafloor. the carbon isotope profile illustrated shows the effect of a global increase in carbon burial, causing a positive d13c excursion interrupted by a negative excursion produced by the input of isotopically negative methane and its oxidation product carbon dioxide.*

(4) Drying epicontinental seas: Tectonically driven isolation of an epicontinental seaway would have led to rapid (<20 ka) desiccation and oxidation of organic matter ($\delta^{13}C$ of ~ −22) (Higgins and Schrag 2006). Though vast areas of central Asia were covered by shallow seaways in the Paleocene-Eocene, none are known to have dried up coincident with the PETM (Gavrilov et al. 2003).

(5) Permafrost: During the Paleogene, Antarctica did not support a large ice cap and may have stored vast quantities of carbon as permafrost and peat that could have been rapidly thawed and oxidized, releasing carbon ($\delta^{13}C$ of ~ −30) (DeConto et al. 2010).

The main manifestation of PETM, $\delta^{13}C$ record, have generally been used to segment the PETM into three phases (see McInerney and Wing, 2011; Khoyem et al., 2015): (1) rapid 4–20 kyr onset also called pre-PETM, marked by the input of $\delta^{13}C$ depleted carbon resulting in the negative CIE, followed by (2) body of the PETM (70–100 kyr) where $\delta^{13}C$ remains constantly low, and (3) recovery phase of ~ 50 kyr (post-PETM) indicated by a return to pre-event $\delta^{13}C$ values suggests a period of CO_2 drawdown (Lyons et al., 2019).

3. COROLLARY EFFECTS TO KPB MASS EXTINCTION AND PETM EVENTS

The KPB mass extinction and PETM phenomena with one of the main effect of increasing temperature, ~ 3 °C for K/Pg extinction (Tobin, 2017) and ~ 5 to 9 °C for PETM (Kennett and Stott, 1991; Zachos et al., 2001; McInerney and Wing, 2011), very often leads to corollary manifestations that significantly affect marine and continental environments, and whose nature and magnitude are dependent on the causes and their epicentre. These corollary effects, broadly similar, show however some particularities when it comes to the KPB mass extinction or the PETM. Two major manifestations are generally related to both KPB mass extinction and PETM. There are:

(1) A clay-rich layer matched to $\delta^{13}C$ negative shift, deposited just above the KPB and PEB (e.g., Kennett and Stott, 1991; Bralower et al., 1997; Thompson and Schmitz, 1997; McInerney and Wing, 2011; Bowen et al., 2015) in both continental and marine environments.

(2) Injection of toxic gases (CO_2, SO_2, Hg…) into biosphere that leads to an ocean acidification coupled to carbonate dissolution across the KPB (see Punekar et al., 2016; Dameron et al., 2017; Sprain et al., 2019) and the PEB (see Bralower et al., 2014; Khozyem et al., 2015).

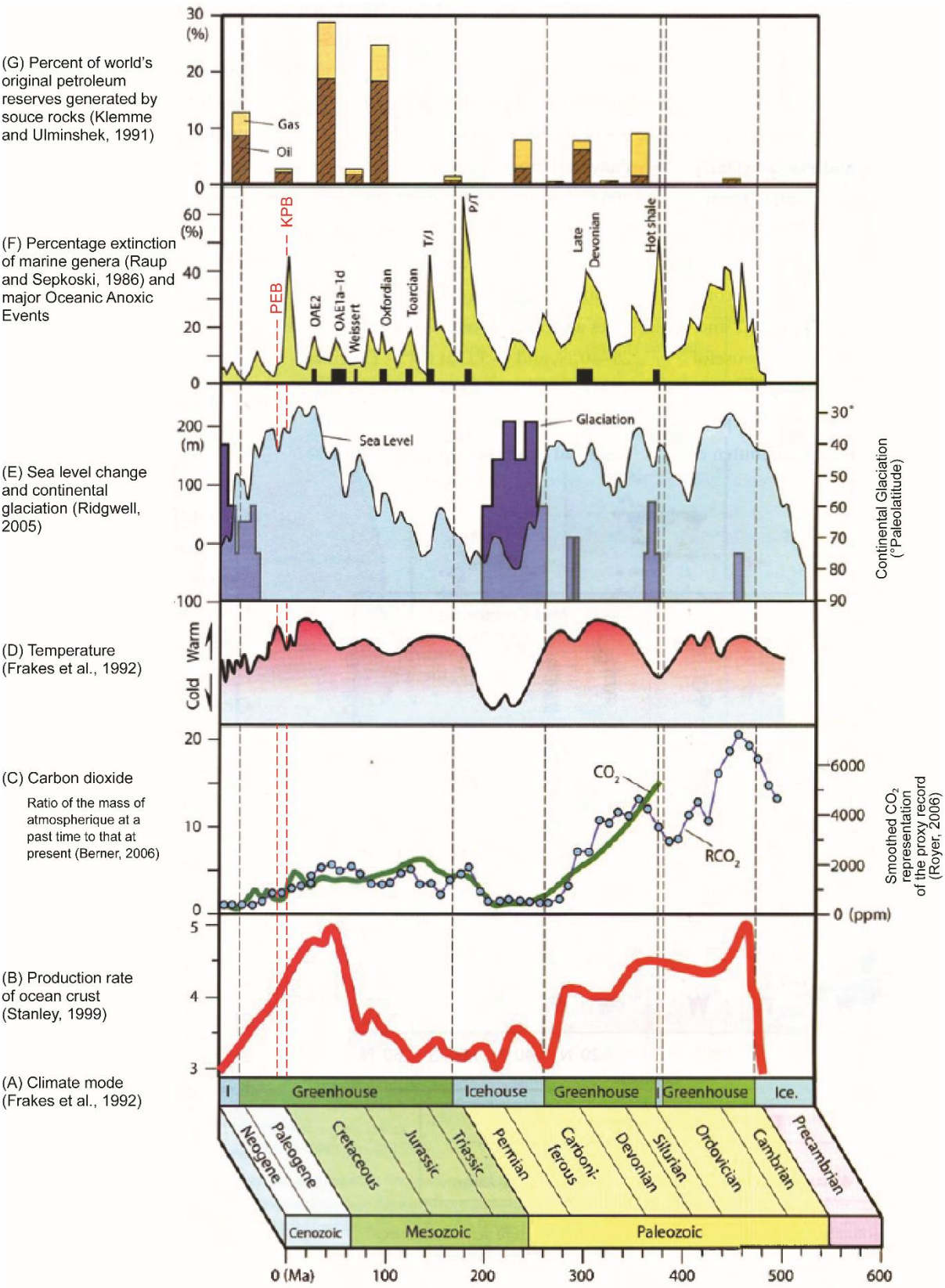

Figure 4. *Compilation showing the changes in climate, and geological and paleontological events through the Phanerozoic (from Takashima et al., 2006).*

In contrast, other specific effects whose some of them are summarized in figure 4, also characterized each event. For the KPB mass extinction event, megatsunamis, generalised

wildfires, blast damages, earthquakes, darkening, gradual cooling massive species extinctions and biotic turnover are the related manifestations (Alvarez et al., 1992; Toon et al., 1997; Keller, 2014; Bond and Grasby, 2017). For the PETM case, a stepped negative carbon isotope excursion that propagated downward from the shallowest levels of the ocean, a positive sulfur isotope shift, an osmium isotope excursion to more radiogenic values, implying elevation of the calcite compensation depth (Speijer and Wagner, 2002; Jenkyns, 2003; Kurtz et al., 2003; Erba, 2004; Cohen et al., 2007; John et al., 2008; Sluijs et al., 2008). Also, a high seasonality in precipitation, enhanced river discharge, associated sedimentary mass movements and an increase of terrestrial input into the oceans (Bowen et al., 2004; Kelly et al., 2005; Pagani et al., 2006; Schmitz and Pujalte, 2007; Sluijs et al., 2007; McInerney and Wing, 2011).

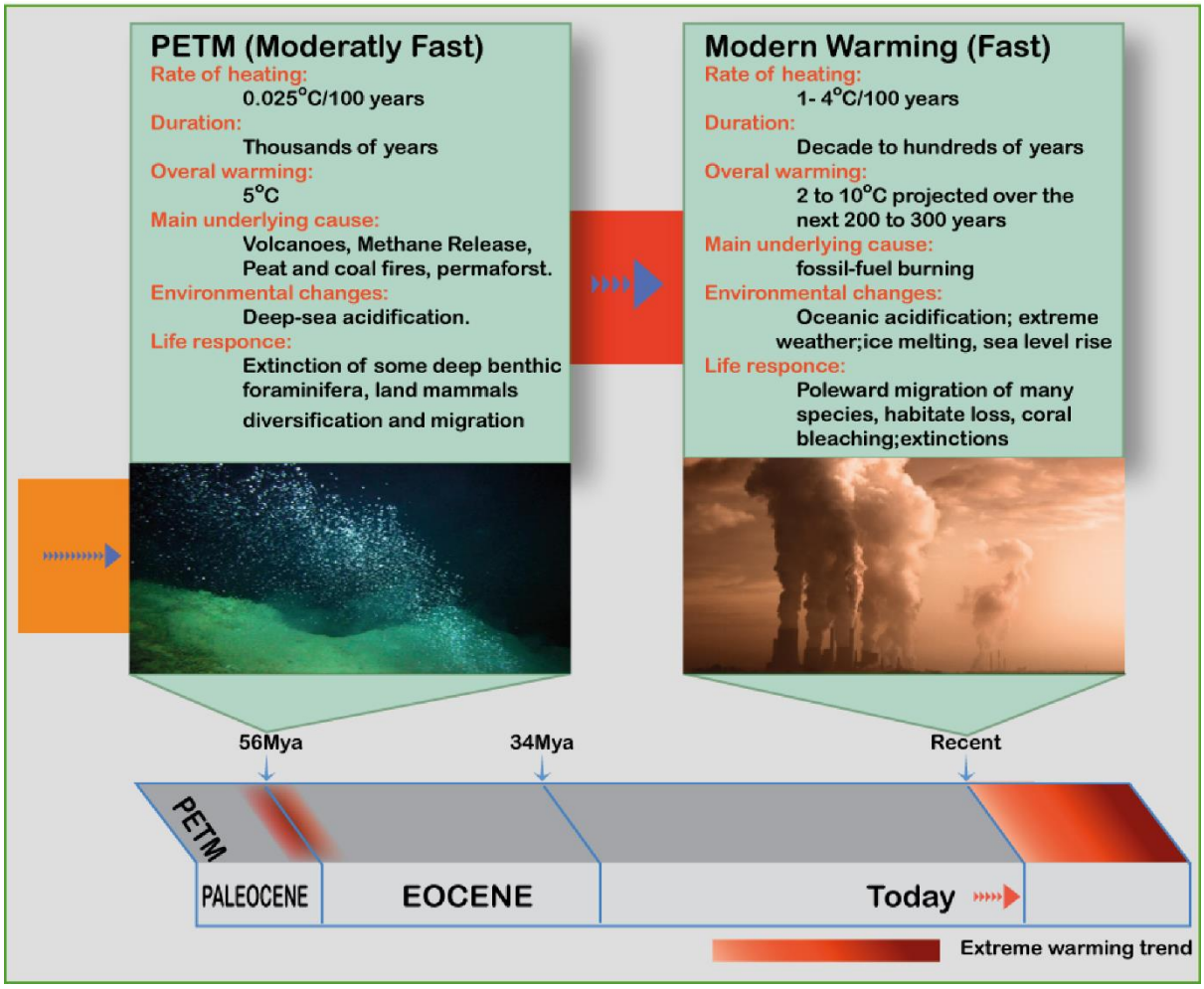

Figure 5. *Comparison between the PETM and the current warming, that reflect the importance of the PETM study, and how it can help to understand the future climatic changes and the effect of the temperature increase on various environments (from Khozyem, 2013).*

4. IMPORTANCE OF KPB MASS EXTINCTION AND PETM STUDIES

Since many years, numerous studies have been worldwide undertaken on oceanic anoxic and major extinction events that impacted the Earth evolution over the geological times. The KPB mass extinction (~ 66 Ma ago) is the latest known major extinction event during which important fauna and flora species, including the well-known dinosaurs and many other microfaunas, disappeared. This mass extinction raises a lot of questions. For example, what would be the causes of such a catastrophe? What is the extent of the damage? Would there have been corollary effects? If so, what were they? Is it possible today to envisage an such event? On the other hand, PETM (~ 55.8 Ma ago), the latest oceanic anoxic event (Jenkyns, 2010), is known today as a rapid warming period (~ 5 to 9 °C) which is mainly attributed to methane degassing from seafloor sediments, linked to the North Atlantic Igneous Province (NAIP) (Keller et al., 2018).

Today, the rapid increase in atmospheric CO_2 and climate warming are magnitude faster than at the KPB or PETM events (Fig. 5). The Knowledge of causes and mechanisms related to these two events (KPB mass extinction and PETM) could help us foresee the climate warming in our near future and design possible ways to mitigate its potentially adverse impact. In addition, there may also be economic repercussions, in particular for hydrocarbons (Fig. 4), due to the high accumulation rate of organic matter.

5. AIMS OF THE PRESENT STUDY

Two sections, well known as KPB mass extinction sections, from Gorgonilla Island in Colombia (South America) and Zumaya in Spain (Western Europe) (Fig. 6A) as well as four sections from Douala sub-basin in Cameroon (Central Africa) (Fig. 6B) were subjected to a careful study in order to highlight climatic and environmental changes that prevailed across K/Pg transition at Gorgonilla and Zumaya, and P/E transition in Douala sub-basin.

The present study was specially focused on the causes of the KPB mass extinctions with, for example, the examination of Chicxulub impact, through spherule-rich layer, as the probable cause of mass extinction at Gorgonilla. Similar approach is used at Zumaya, although there is rather clay-rich layer, and not spherule-rich layer. For the case of Douala sub-basin, the main objective is the detection of PETM signatures and evaluation of the environmental response to this hyperthermal event.

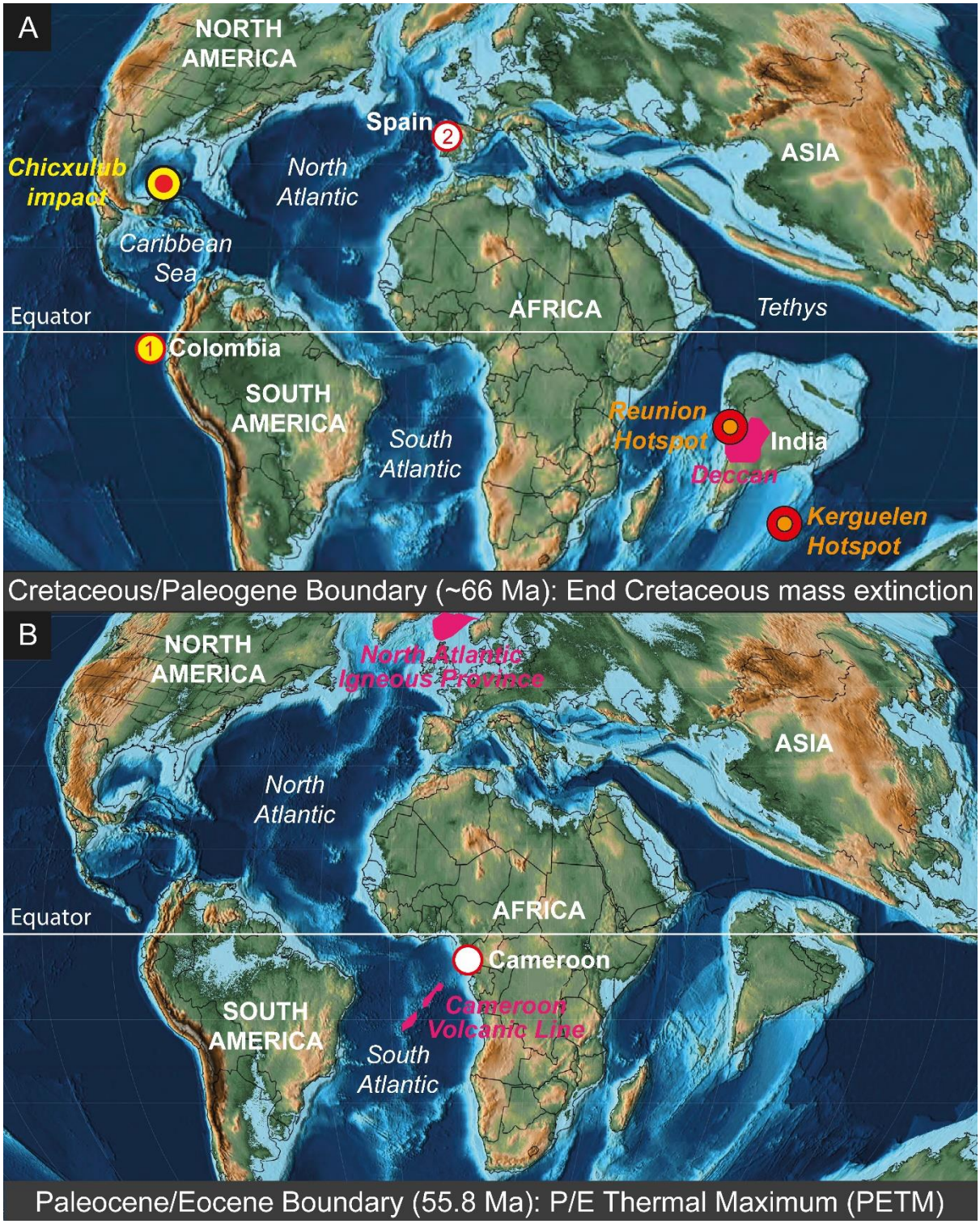

Figure 6. *(A) Paleogeography at the KPB (~66 Ma) and paleolocations of Gorgonilla (1) and Zumaya (2) sections, Reunion and Kerguelen hotspots, Deccan volcanism and Chicxulub impact site. (B) Paleogeography at the PEB (55.8 Ma) and paleolocations of Douala sub-basin, Cameroon Volcanic Line and North Atlantic Igneous Province. Paleomaps are from Scotese (2013, 2014).*

6. MATERIALS AND METHODS

6.1. Sampling and sample preparation

Lots of samples were carefully collected throughout different sites. A total of 147 analyzed samples (including 103 bulk materials as well as 42 tektites and 2 matrixes from spherule-rich layers) are from Gorgonilla section, 113, 30 and 33 bulk sediments are respectively from Zumaya, Bongue and Dibamba sections, and 74 samples (64 bulk materials and 10 pyrite samples) from Tondè area. Detailed description of sections and log reconstruction were done at once.

The collected samples, except pyrite, were subsequently dried in an oven at 45 °C. Then, a part of all samples (included pyrite) is crushed in an agate mortar and 25 g of powder are deducted for a multidisciplinary approach integrating measurements of total organic carbon and mercury contents, carbon and oxygen stable isotopes, bulk mineralogy as well as major, trace and rare earth elements. Remained uncrushed bulk samples were used for the preparations of thin sections and biostratigraphy (benthic, planktic foraminifera and ostracods, palynology) as well as for clay mineralogy, laser ablation inductively coupled plasma mass spectrometry (LA-ICPMS), electron microprobe, scanning electron microscopy (SEM) coupled to energy dispersive X-ray (EDX) analyses.

6.2. Total organic carbon (TOC) contents

Organic matter content was determined using Rock Eval 6 with an IFP160000 as standard following the method described by Behar et al. (2001). Samples were placed in an oven and first heated at 300 °C under an inert atmosphere and then gradually pyrolysed up to 650 °C. After the pyrolysis is completed, the samples are transferred into another oven and gradually heated up to 850 °C in the presence of air. The determined parameters are total organic carbon (TOC), Hydrogen Index (HI as mg HC/g TOC) and Oxygen Index (OI as mg CO_2/g TOC), which permit an overall characterization of the sedimentary organic.

6.3. Mercury (Hg) contents

Hg content was determined on bulk rock powder using the Zeeman R-915F (Lumex, St. Petersburg, Russia), a high-frequency atomic absorption spectrometer specifically designed

for Hg determination with a detection limit of 0.3–3 ppb. Measurements are based on the direct thermal evaporation of Hg from solid samples, without chemical pretreatment. Analyses were conducted on two aliquots. The accuracy was confirmed by the analysis of GSD-11 certified reference materials, from Chinese alluvium (Zintwana et al., 2012) with a Hg content of 72.0 ppb.

6.4. Mineralogy analyses

Bulk rock mineralogical composition was obtained by XRD patterns on 800 mg of random powder samples pressed (20 bars) into a powder holder at the University of Lausanne, using a X-TRA Thermo-ARL Diffractometer based on semi-quantitative method, following the procedure described in Klug and Alexander (1974), Kübler (1987) and Adatte et al. (1996). External standards, with error margins varying between 5 and 10% for the phyllosilicate and 5% for grain minerals, are used.

For the clay mineral fraction, triturated samples are introduced into glass containers with deionized water and then decarbonized by HCl 10% (1.25 N) during 20 minutes, including an ultrasonic disaggregation of 3 minutes for each sample. The insoluble residues are washed by centrifugation and repeated until a neutral solution (pH 7) is obtained. Following the Stockes law, two granulometric fractions (<2 μm and 2–16 μm) are pipetted and deposited on a glass plate. After air-drying, samples are analyzed by XRD. Subsequently, the <2 μm fraction samples are saturated with ethylen-glycol and remeasured in order to check for swelling minerals. This method allows the semi-quantification of the proportion of clay minerals with a precision better than 5%. These analyses were also performed at the University of Lausanne, using a X-TRA Thermo-ARL Diffractometer based on semi-quantitative method, following the procedure described in Klug and Alexander (1974), Kübler (1987) and Adatte et al. (1996).

Thin sections, manufactured in litholamelling unit and scanning electron microscopy coupled to energy dispersive X-ray (SEM-EDX) after gold or carbon coating, are also used at the University of Lausanne to define amount, morphology and microstructure of some minerals and particles (e.g., tektites and pyrite crystals).

6.5. Stable isotopes

Inorganic carbon and oxygen isotope ratios ($\delta^{13}C_{carb}$ and $\delta^{18}O_{carb}$ values) were measured in whole rock samples following the procedure described by Spangenberg and Herlec (2006).

The analyses were performed in aliquots of powdered whole rock samples (variable size depending on the $CaCO_3$ content) using a Thermo Fisher Scientific (Bremen, Germany) Gas Bench II carbonate preparation device connected to a Delta Plus XL isotope ratio mass spectrometer. The CO_2 extraction was done by reaction with anhydrous phosphoric acid at 70 °C. The stable carbon and oxygen isotope ratios are reported in the delta (δ) notation as the per mil (‰) deviation relative to the Vienna Pee Dee belemnite standard (VPDB). The standardization of the $\delta^{13}C_{carb}$ and $\delta^{18}O_{carb}$ values relative to the international VPDB scale was done by calibration of the reference gases and working standards with IAEA standards. Analytical uncertainty (2σ) monitored by replicate analyses of the international calcite standard NBS-19 and the laboratory standard Carrara Marble was not greater than ± 0.05 ‰ for $\delta^{13}C$ and ± 0.1 ‰ for $\delta^{18}O$.

The organic carbon isotope ratio ($\delta^{13}C_{org}$ values in ‰ VPDB) was determined from decarbonated (10% HCl treatment) samples based on continuous flow elemental analyser/isotope ratio mass spectrometry (EA/IRMS), as described previously (Spangenberg et al., 2010). Aliquots of samples were flash-combusted on a Carlo Erba 1108 (Milan, Italy) elemental analyser connected to a Thermo Fisher Scientific Delta V (Bremen, Germany) isotope ratio mass spectrometer that was operated in the continuous helium flow mode via a Conflo III split interface for the determination of the isotopic composition of the produced CO_2. Reproducibility and accuracy are better than ±0.1‰ for $\delta^{13}C_{org}$.

6.6. Major (MEs), trace (TEs) and rare earth elements (REEs)

Major (MEs) and trace (TEs) elements concentration of whole rock samples and matrixes (only MEs) were determinated by X-ray Fluorescence Spectrometry (XRFS) using a PANalytical PW2400 spectrometer at the ISTE of the University of Lausanne based on different standard reference materials (NIM-G, NIM-N, SY-2, JCH-1, BHVO). Major elements were determined on fused lithium tetraborate glass discs after heating to 1050 °C in an oven in order to calculate the loss of ignition (LOI). Pressed discs, obtained after mixing 15% of the powered samples with Mowiol 2%, are used for TE analysis.

MEs of tektites were determined at the ISTE of the University of Lausanne by electron probe microanalyzer (EPMA), using a JEOL JXA-8530F instrument equipped with 5 WDS spectrometers for maximum sensitivity. TEs and REEs of tektites and matrixes from spherules-rich layers were also measured at the University of Lausanne by laser ablation inductively coupled plasma mass spectrometry (LA–ICPMS). A GeoLas 200M 193 nm excimer ablation

system interfaced to an Elan 6100 DRC quadrupole ICPMS was used for the ablation of the spherules (in the thin sections) and lithium tetraborate discs (for the matrix) previously analysed by EPMA and XRF respectively. The relative sensitivity factors were calibrated using a NIST SRM 612 standard representing a soda-lime-silica glass doped with trace elements and calcium contents by XRF were used for internal standardization.

For the pyrite samples, ME, TE and REE analyses were carried out by both inductively coupled plasma mass spectrometry (ICP-MS) and inductively coupled plasma atomic emission spectrometry (ICP-AES) at the Australian Laboratories Services of Vancouver. The accuracies of these analyses were assessed by analyses of standard reference materials, AMIS0085, AMIS0167, OREAS-14P and SY-4 for MEs and, OREAS-104, TRHB et DUP for TEs and REEs.

6.7. Biostratigraphy

Foraminifera (benthic and planktic) and ostracod biostratigraphy was performed at Princeton University, using washed sediment residues (method described in Keller et al., 1995) for clay-rich samples and thin section for more carbonated samples. Quantitative species analysis was based on washed residues of the fine fraction (38-63µm) to evaluate dwarfing, >63µm to assess dominant species components, and the >150µm size fraction was searched for rare large species. Identification of species was based on standard taxonomic concepts (Robaszynski et al., 1983–1984; Nederbragt, 1991; Olsson et al., 1999). All identified specimens were mounted on microslides for a permanent record.

For palynomorphs extraction, samples were treated with HCl, HF and HNO_3 followed by 5% solution of KOH. The sample residue was washed with water through a 15µm screen. The slides were prepared in polyvinyl alcohol and mounted in Canada balsam. A determination of some pollens and spores have been done in Institute of Earth Sciences of Paris (ISTeP), Université Pierre et Marie Curie by Jean-Pierre Suc.

CHAPTER II. SEDIMENTOLOGY, MINERALOGY AND GEOCHEMISTRY OF THE CRETACEOUS-PALEOGENE (K/Pg) TRANSITION FROM GORGONILLA ISLAND (COLUMBIA). EVIDENCE OF TEKTITES REWORKING AT THE CRETACEOUS-PALEOGENE BOUNDARY (KPB)

1. INTRODUCTION

The Cretaceous-Paleogene (K/Pg) transition (~ 66 Ma) is worldwide recognized as a critical period during which an ecosystem crisis occurred, leading to mass extinction and species renewal in both marine and continental environments (Cowie et al., 1989; Keller, 1989, 2011; Barrera and Keller, 1990; Canudo et al., 1991; Keller et al., 1995, 2009; Alegret et al., 2001; Adatte et al., 2002, 2005; Punekar et al., 2016; Dameron et al., 2017; Taylor et al., 2018; Lyson et al., 2019). This event, usually due to a sudden and rapid change in the environmental conditions, is induced, according to many authors, either by the extraterrestrial impact based mainly on Ir-rich layer (Alvarez et al., 1980) which subsequently attributed to the Chicxulub meteorite impact on Yucatan Peninsula through the presence of impact glass spherules ejected near the KPB (see, Hildebrand et al., 1991; Takayama et al., 2000; Keller et al., 2009, 2013; Schulte et al., 2010; Adatte et al., 2011; Mateo et al., 2016), or more recently by the Large Igneous Provinces through major volcanic episodes (e.g., Deccan Traps volcanism) (Kuhnt et al., 2005; Keller et al., 2008; Bond and Wignall, 2014; Courtillot and Fluteau, 2014; Ernst, 2014; Punekar et al., 2014; Courtillot et al., 2015; Keller et al., 2016; Font et al., 2016, 2018; Bond and Grasby, 2017; Ernst and Youbi, 2017), or both combined (Keller et al., 2001; Stüben et al., 2005; Keller et al., 2018). However, theory that links the Chicxulub impact to the KPB mass extinction and its corollary interpretations have remained more controversial, because of the discovery of spherule-rich layers over the world that indicates a pre-KTB age for Chicxulub impact (e.g., Keller et al., 2003, 2004, 2007, 2009, 2013; Keller, 2011), or that rather shows a glass spherules (tektites) reworking during the last Maastrichtian or first Danian stages (Keller et al., 2001, 2009, 2013; Adatte et al., 2011).

The recent investigations on Chicxulub impact spherule-rich layer from the recently discovered K/Pg section on Gorgonilla Island, Colombia, date glass spherules (or tektites) with an absolute age of 66.051 ± 0.031 Ma by the $^{40}Ar/^{39}Ar$ method (Renne et al., 2018). This age, being very close to the known KPB age (66.043 ± 0.011 Ma; Renne et al., 2013), once again raises the controversy. Some authors argue that Gorgonilla spherule-rich layer consists of primary impact deposits (see Bermudez et al., 2016, 2019; Renne et al., 2018) and therefore, the Chicxulub impact would be responsible of mass extinction and corollary events observed on Gorgonilla K/Pg section. Others, however, evoke a reworking of glass spherules and then no link between impact and KPB, but rather a natural coincidence like in another sites.

The present study investigates the climatic and environmental conditions that prevailed during Cretaceous-Paleogene transition, and re-examines deposition process of spherule-rich

layer on Gorgonilla Island. Our investigations use a multi-proxy approach that includes: (1) biostratigraphy and carbon isotopes stratigraphy to provide high-resolution age control and evaluation of the biotic effects; (2) detailed lithology, sedimentology, microfacies analysis, whole rock geochemistry and bulk rock mineralogy to identify environmental changes; (3) clay mineralogy and oxygen isotope to infer diagenetic overprint and paleoclimatic conditions; (4) mercury content analysis to detect any volcanism influence and (5) sharp geochemistry of spherule-rich layer components in order to assess origin and sedimentological processes of matrix and tektites deposition.

2. LOCATION AND GEOLOGICAL FRAMEWORK

The Gorgonilla K/Pg section at 2°56'N, 78°12'W on the beach located on the southwest coast of Gorgonilla Island, about 35 to 50 km in Pacific offshore of western Colombia (Figs. 7A-B). The island is considered with the Gorgona Island, to have been formed in the late Cretaceous (~90 Ma) (Kerr and Tarney, 2005; Storey et al., 1991) in association to the Caribbean Large Igneous Province (CLIP) in an oceanic slab window setting (Serrano et al., 2011). These islands represent the last accreted fragment of the CLIP to northern South America in the Eocene (Kerr and Tarney, 2005; Kennan and Pindell, 2009). Mafic and ultramafic rocks (e.g., basalts, gabbros, peridotites) intercalated by komatiites and pyroclastic deposits outcrop along their coasts (Fig. 7C). Originally, these islands were formed at a paleolatitude of 26°S (Estrada and MacDonald, 1994) and, by the time of the Chicxulub impact, they were located about 2700-3000 km southwest of the impact site (Bermúdez et al., 2016).

3. METHODS

3.1. Sampling and samples preparation

In the studied section, a total of 103 samples were collected from 15.6 m below the KPB to 6.3 m above it, with at least one sample by bed and a high-resolution sampling at the K/Pg transition. The samples were then dried in an oven at 45 °C and 67 samples (including three of four spherule bed samples: GI-40, 41 and 45) selected for thin sections. Afterwards, the sample matrix of two spherule beds (GI-40 and 43) have been able to be dissociated from their tektites and crushed in an agate mortar, as well as the bulk rock of all samples, for various analyses. The remaining uncrushed samples were used for clay mineralogy analysis.

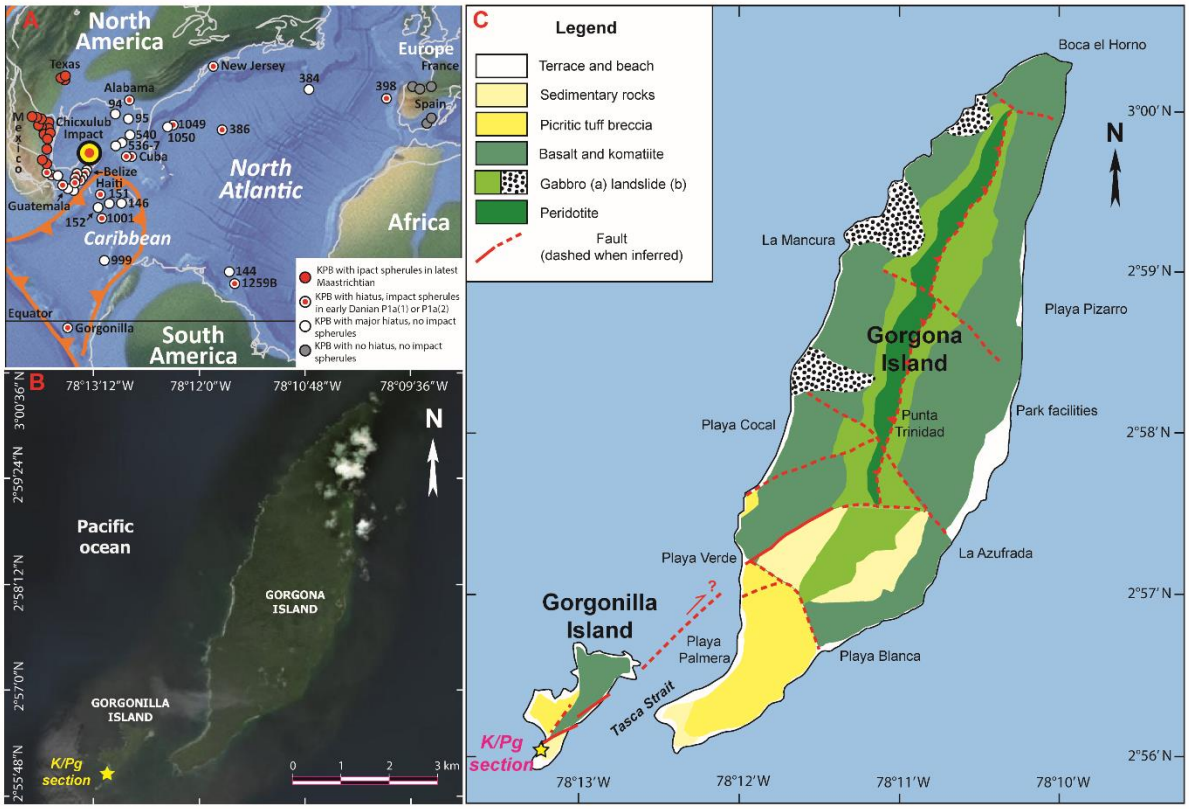

Figure 7*. (A) Cretaceous-Paleogene transition paleogeographic map showing paleolocation of K/Pg sites with presence or not of Chicxulub impact in Caribbean, Mexico, North America, North Atlantic and Western Europe (from Mateo et al., 2019); (B) Location of K/Pg section on Gorgonilla Island (Colombia); (C) Geology of Gorgonilla and Gorgona islands with structural data.*

3.2. Carbon and oxygen stable isotopes

Inorganic carbon and oxygen isotope ratios ($\delta^{13}C_{carb}$ and $\delta^{18}O_{carb}$ values) were measured in whole rock samples following the procedure described by Spangenberg and Herlec (2006). The analyses were performed in aliquots of powdered whole rock samples (variable size depending on the $CaCO_3$ content) using a Thermo Fisher Scientific (Bremen, Germany) Gas Bench II carbonate preparation device connected to a Delta Plus XL isotope ratio mass spectrometer. The CO_2 extraction was done by reaction with anhydrous phosphoric acid at 70 °C. The stable carbon and oxygen isotope ratios are reported in the delta (δ) notation as the per mil (‰) deviation relative to the Vienna Pee Dee belemnite standard (VPDB). The standardization of the $\delta^{13}C_{carb}$ and $\delta^{18}O_{carb}$ values relative to the international VPDB scale was done by calibration of the reference gases and working standards with IAEA standards. Analytical uncertainty (2σ) monitored by replicate analyses of the international calcite standard

NBS-19 and the laboratory standard Carrara Marble was not greater than ± 0.05 ‰ for $\delta^{13}C$ and ± 0.1 ‰ for $\delta^{18}O$.

The bulk rock organic carbon isotope ratio ($\delta^{13}C_{org}$ values in ‰ VPDB) was determined from decarbonated (10% HCl treatment) samples based on continuous flow elemental analyser/isotope ratio mass spectrometry (EA/IRMS), as described previously (Spangenberg et al., 2010). Aliquots of samples were flash-combusted on a Carlo Erba 1108 (Milan, Italy) elemental analyser connected to a Thermo Fisher Scientific Delta V (Bremen, Germany) isotope ratio mass spectrometer that was operated in the continuous helium flow mode via a Conflo III split interface for the determination of the isotopic composition of the produced CO_2. Reproducibility and accuracy are better than ±0.1‰ for $\delta^{13}C_{org}$.

3.3. XRD mineralogy

Mineralogy analyses were performed at the University of Lausanne using a X-TRA Thermo-ARL Diffractometer based on semi-quantitative method, following the procedure described in Klug and Alexander (1974), Kübler (1987) and Adatte et al. (1996). The whole rock mineralogical composition was obtained by XRD patterns on 800 mg of random powder samples pressed (20 bars) into a powder holder. External standards are used with error margins between 5 and 10% for the phyllosilicate and 5% for grain minerals.

For the clay mineral fraction, triturated samples are introduced into glass containers with deionized water and then decarbonized by HCl 10% (1.25 N) during 20 minutes, including an ultrasonic disaggregation of 3 minutes for each sample. The insoluble residues are washed by centrifugation and repeated until a neutral solution (pH 7) is obtained. Following the Stockes law, two granulometric fractions (<2 μm and 2–16 μm) are pipetted and deposited on a glass plate. After air-drying, samples are analyzed by XRD. Subsequently, the <2 μm fraction samples are saturated with ethylen-glycol and remeasured in order to check for swelling minerals. This method allows the semi-quantification of the proportion of clay minerals with a precision higher than 5%.

3.4. Hg analysis

Hg content was determined on bulk rock powder using the Zeeman R-915F (Lumex, St. Petersburg, Russia), a high-frequency atomic absorption spectrometer specifically designed for Hg determination with a detection limit of 0.3–3 ppb. Measurements are based on the direct

thermal evaporation of Hg from solid samples, without chemical pretreatment. Analyses were conducted on two aliquots. The accuracy was confirmed by the analysis of GSD-11 certified reference materials, from Chinese alluvium (Zintwana et al., 2012) with a Hg content of 72.0 ppb.

3.5. Whole rock geochemistry

Bulk geochemistry (major and trace elements) was obtained by X-ray Fluorescence Spectrometry (XRFS) using a PANalytical PW2400 spectrometer at the University of Lausanne based on different standard reference materials (NIM-G, NIM-N, SY-2, BHVO). Major elements (MEs) were determined on fused lithium tetraborate glass discs. Samples were first heated to 1050 °C in an oven in order to determinate the loss of ignition (LOI). Then, 1.2000 ± 0.0002 g of ignited sample was mixed with 6.0000 ± 0.0002 g of lithium tetraborate ($Li_2B_4O_7$) and placed in a Bead machine PerlX'3 at 1250 °C to obtain the fused tablet. The obtained concentrations are given in weight percentages (wt.%). Trace element (TEs) analyses were performed on pressed discs after mixing 15% of the powered samples with Mowiol 2%. The pressed discs were then placed in an oven at 110 °C for at least 6 hours before analysis by XRFS. The trace element concentrations are given in parts per million (ppm).

3.6. Electron microprobe analysis

MEs of selected matrix and tektites were determined at the University of Lausanne respectively by XRFS (described above) and electron probe microanalyzer (EPMA). The last one was performed on the selected tektites from polisher sections using a JEOL JXA-8530F instrument equipped with 5 WDS spectrometers for maximum sensitivity. Tektite trace (TE) and rare earth (REE) element composition as well as that of sample matrix were measured at the University of Lausanne by laser ablation inductively coupled plasma mass spectrometry (LA–ICPMS). A GeoLas 200M 193 nm excimer ablation system interfaced to an Elan 6100 DRC quadrupole ICPMS was used for the ablation of the spherules (in the thin sections) and lithium tetraborate discs (for the matrix) previously analysed by EPMA and XRF respectively. The ablation system was operated at a beam size of 120 mkm, repetition rate of 10 Hz and on-sample energy density of ~10 J/cm2. Helium was used as a carrier gas. The relative sensitivity factors were calibrated using a NIST SRM 612 standard representing a soda-lime-silica glass

doped with trace elements. Calcium contents by XRF were used for internal standardization. Accuracy was typically better than 5%. Detection limits ranged from 0.02 to 0.15 ppm (REE).

3.7. SEM-EDX analyses

Electron backscatter diffraction (EBSD) was performed on the spherules at the University of Lausanne in order to determine real morphologies and microstructures of tektites. After gold-carbon coating of selected spherules, backscatter electron (BSE) images and their corresponding energy dispersive X-ray (EDX) spectroscopic analyses were collected using a Tescan Mira LMU field emission-SEM operated at 20 kV and 30 mm working distance. EDX and EBSD analyses are performed using a Penta-FET 3x detector and a Nordlys S camera, respectively, both being monitored by the AZtec 2.4 software package released by Oxford Instruments.

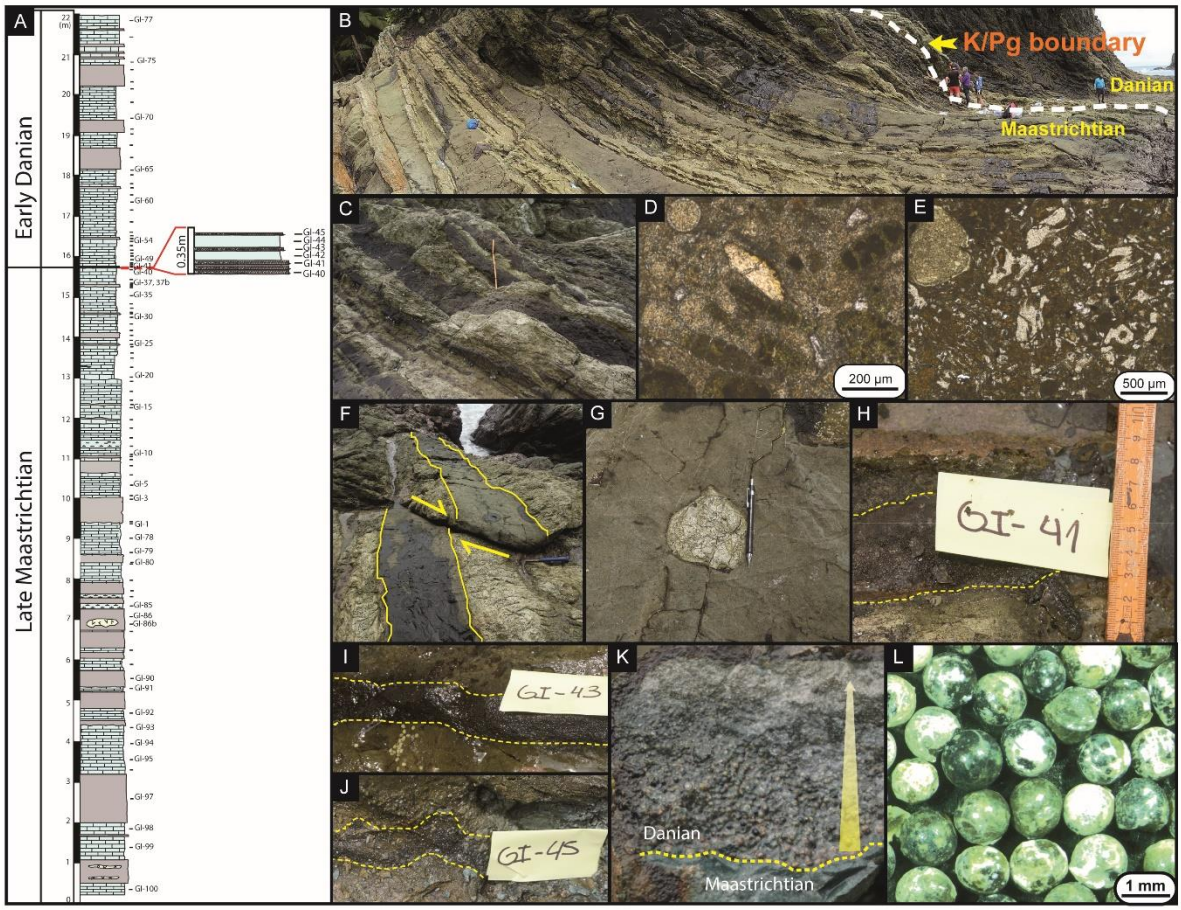

Figure 8. *Lithology encountered in Gorgonilla K/Pg section. (A) K/Pg section log highlighting the tripling of spherule-rich layer; (B) General overview of Gorgonilla KPB section; (C) Alternated light green mudstones with dark turbiditic litharenites across the section; thin sections D (from GI-21 mudstone sample) and E (from GI-62 turbidite sample) respectively*

show some planktic foraminifera microfossils, and lithics and abundant plagioclases. (F) identified microfault; (G) basalt fragment encrusted in turbiditic layer; (H – J) Gorgonilla spherule-rich layers; (K) fresh KPB photograph with erosional surface above which spherule-rich layer presents normal size-gradation of tektites; (L) Tektites from Gorgonilla spherule-rich layer.

3.8. Biostratigraphy

Biostratigraphic analysis based on planktic foraminifera was performed at Princeton University using washed residues and thin sections where the lithology was indurated enough to resist disaggregation. Identification of species was based on standard taxonomic concepts (Robaszynski et al., 1983–1984; Nederbragt, 1991; Olsson et al., 1999). For washed residues, samples were processed in the laboratory following the procedure described in Keller et al. (1996). Samples were soaked overnight in 3% hydrogen peroxide solution to oxidize organic carbon. After disaggregation of sediment particles, samples were washed through 63 μm and 38 μm sieves to obtain clean foraminiferal residues. Washed residues were oven dried at 50 °C. Planktic species analyses were performed on the 38–63 μm and >63 μm size fractions. All specimens were identified and mounted on microslides for a permanent record.

4. LITHOLOGY AND AGE CONSTRAINTS

The Gorgonilla K/Pg section, on about 22 m thick of sampled deposits, consists of an alternation of light green calcareous mudstones and dark olive turbiditic litharenites (Fig. 8A-C). The light green calcareous mudstones (Fig. 8D) are mainly composed by various microfossil assemblages, including abundant radiolarians, benthic and planktic foraminifera, some nannofossil species and sponge spicules (Bermudez et al., 2016; Mateo et al., 2019). This lithology sometimes shows the cracks filled up probably by secondary crystallization of calcite. The nature and species of identified microfossils associated to the absence of bioturbations suggest a pelagic bathyal depositional environment. Dark olive turbiditic litharenites are composed by eroded basaltic lithics (and/or breccia) of various size and a large amount of plagioclases soaked in calcite cement (Fig. 8E, G). Foraminifera, radiolarians and nannofossils are also presents. In the late Maastrichtian, some beds present poorly sorted, structureless sediments above an erosional surface which associate the deposition of these turbidites during

higher dynamic conditions (Mateo et al., 2019). The entire section from late Maastrichtian to early Danian is strongly crossed by minor syn- and post-depositional faults (Fig. 8F).

Late Maastrichtian and early Danian sediments are separated by a 3 cm spherules-rich layer easily recognisable in the outcrop relatively, well cemented and sometimes friable, referring to the Cretaceous/Paleogene boundary (KPB; Fig. 8H). This bed, in triplicate in one edge of outcrop on about 40 cm thick (Figs. 8H – J) because of minor syn- and post-depositional faults, contains abundant glass spherules, microfossils and also lithic elements similar to those of litharenites describe above. All these beds are marked at the base and top by undulations (erosional surfaces) suggesting a relatively high hydrodynamic conditions during their deposition. In addition, a normal size-gradation of sediments observed in these layers (Fig. 8K) can be explain like a deposition by turbidity currents (Reineck and Singh, 1980; Nichols, 2009). Spherules are black to light yellow coloured with various morphologies (including round, oval and more rarely teardrop and dumbbell) and size ranging between 0.80-1.50 mm (Figs. 8L and 9). These spherules are mainly composed by Si, O, Fe, Al, Ca and Mg, and accessorily by Na, K, Cl and Ti (Fig. 9).

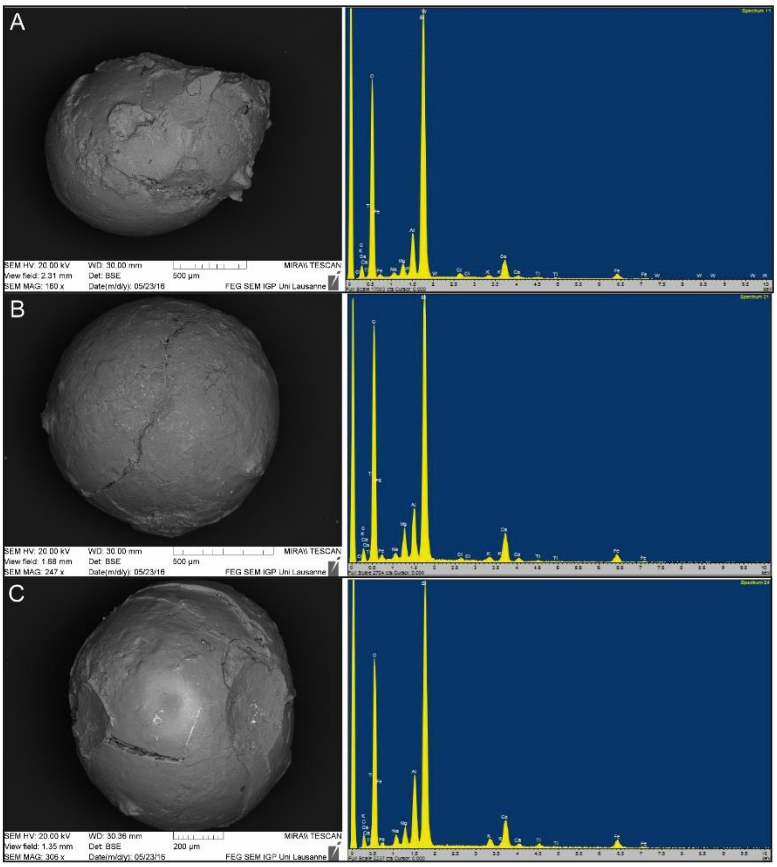

Figure 9. *SEM-EDX micrographs of tektites a, b and c from Gorgonilla spherule-rich layer showing different morphologies, microstructures and preliminary geochemical composition. Note Si, O, Fe, Al, Ca and Mg as main geochemical elements.*

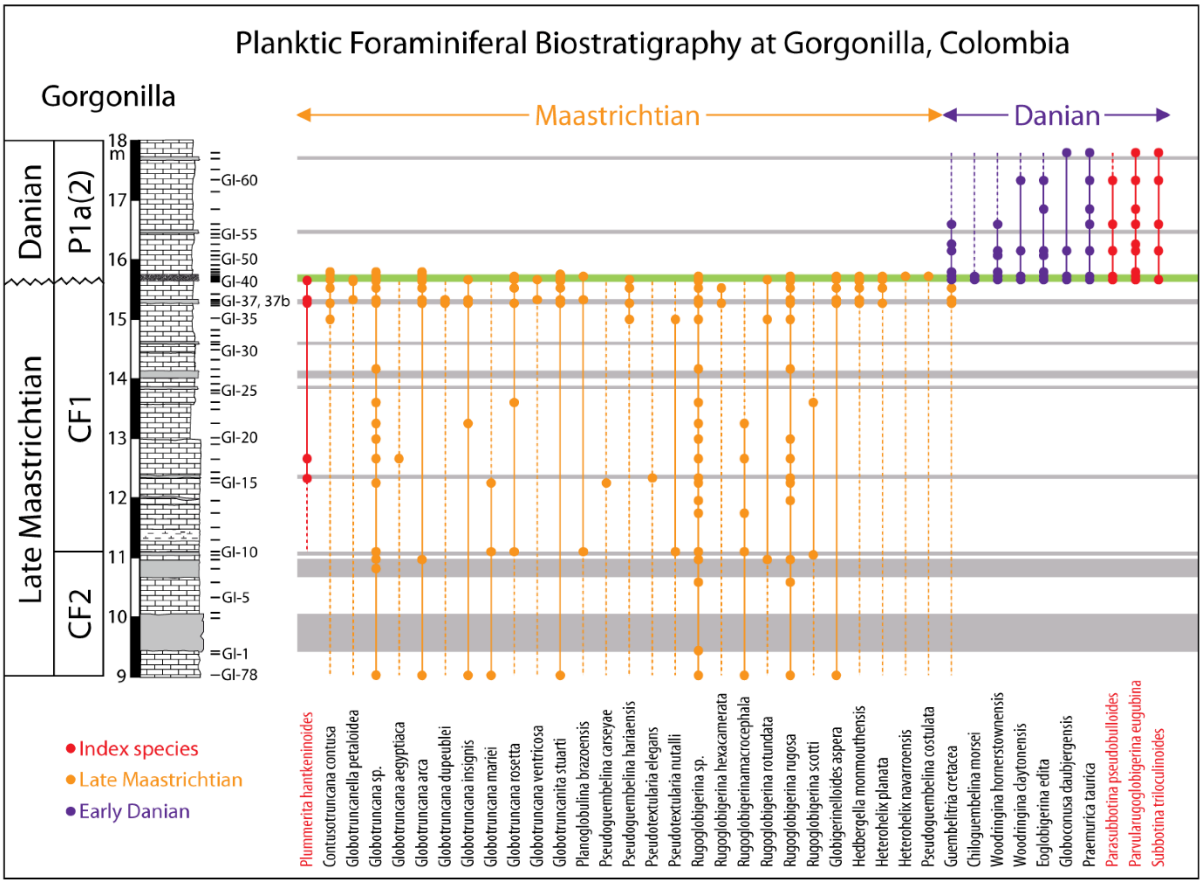

Figure 10. *Planktic foraminiferal biostratigraphy at the Gorgonilla section, Colombia (from Mateo et al., 2019; modified). Grey shaded bands mark turbiditic deposits while green band marks spherule-rich deposits. Only zones CF2 and CF1 for late Maastrichtian and zone P1a(2) for early Danian are reported. Note that major KPB hiatus spans part of zone CF1, zone P0, zone P1a(1), and part of zone P1a(2).*

In this section, the age has been constrained by a planktic foraminiferal (Bermúdez et al., 2016; Renne et al., 2018; Mateo et al., 2019) and radiolarian (Renne et al., 2018; Mateo et al., 2019) biostratigraphy as well as by pollen and spores and $^{40}Ar/^{39}Ar$ dating (Renne et al. 2018). For the planktics, about 9 m (interval 9-18 m; Fig. 10) of sediments were analysed. Biozonation was based on work by Keller and MacLeod (1995), Keller et al. (2002) and Li and Keller (1998) made on several worldwide KPB sections.

Late Maastrichtian planktic zones (CF2 and CF1) are defined by index species. For example, the CF2/CF1 limit, about 4.5 m below the spherule-rich layer, is marked by the first appearance of *Plummerita hantkeninoides* (Fig. 10), species typically indexed to CF1 biozone whose the spaning ends at the KPB (e.g. Keller et al., 2002, 2003; Keller, 2008). These two biozones (CF2 and CF1) also reveal the occurrence of many other species such as globotruncanids, rugoglobigerinids, heterohelicids, hedbergellids and small pseudoguembelinids (Fig. 10), commonly recongnized in the uppermost Maastrichtian.

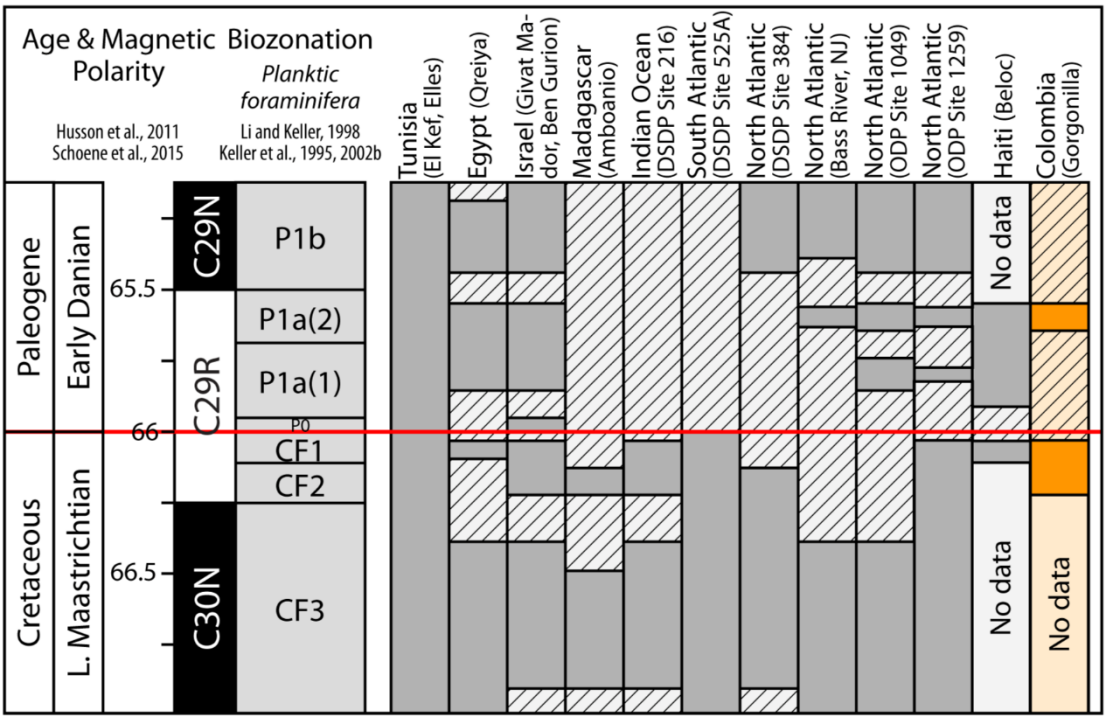

Figure 11. *Overall correlation of hiatuses during the Cretaceous-Paleogene transition reflecting increased climate variability, intensified currents, and erosion on a global scale (from Mateo et al., 2019)*

The K/Pg boundary (KPB) materialized in this section by the spherule-rich layer is characterized by a simultaneous occurrence of latest Maastrichtian (see above) and early Danian planktic species, especially those of P1a(2) subzone (*Parvularugoglobigerina eugubina*, *Parasubbotina pseudobulloides* and *Subbotina triloculinoides*) (Fig. 10). These results suggest the absence of P0 and P1a(1) zones and consequently a hiatus. The hiatus spans over ~250 kyr, from Maastrichtian uppermost CF1 zone to Danian lowest P1a(2) subzone (Fig. 11) (Mateo et al., 2019).

Above the spherule-rich layer, the analysed sediments (~2.3 m thick) are characterized by assemblages of common early Danian planktic species such as *Chiloguembelina midwayensis, C. morsei*, *Eoglobigerina edita, E. eobulloides, Globoconusa daubjergensis*, *Guembelitria cretacea*, *Praemurica taurica*, *Woodringina claytonensis* and *W. hornerstownensis* (see Keller, 1988; Canudo et al., 1991; Keller and Benjamini, 1991; Keller and Abramovich, 2009; Keller et al., 2013; Punekar et al., 2014 ; Mateo et al., 2016). Only P1a(2) index species identified from the spherule-rich layer are still present (Fig.10), thus implying an age of the P1a (2) subzone to these sediments.

5. STABLE ISOTOPES AND MERCURY (Hg) CONTENT

Bulk rock carbon (organic and inorganic) and oxygen isotope values measured on the entire Gorgonilla K/Pg section fluctuate significantly. They globally range from -32.0 ‰ to -19.9 ‰ (with 24.7 ‰ as mean), from -21.5 ‰ to -3.0 ‰ (with a mean of -7.4 ‰) and from -5.5 ‰ to -1.4 ‰ (with -2.6 ‰ as mean value) respectively for organic carbon ($\delta^{13}C_{org}$), inorganic carbon ($\delta^{13}C_{carb}$) and oxygen ($\delta^{18}O$) isotopes (Fig.12; Annex III.3).

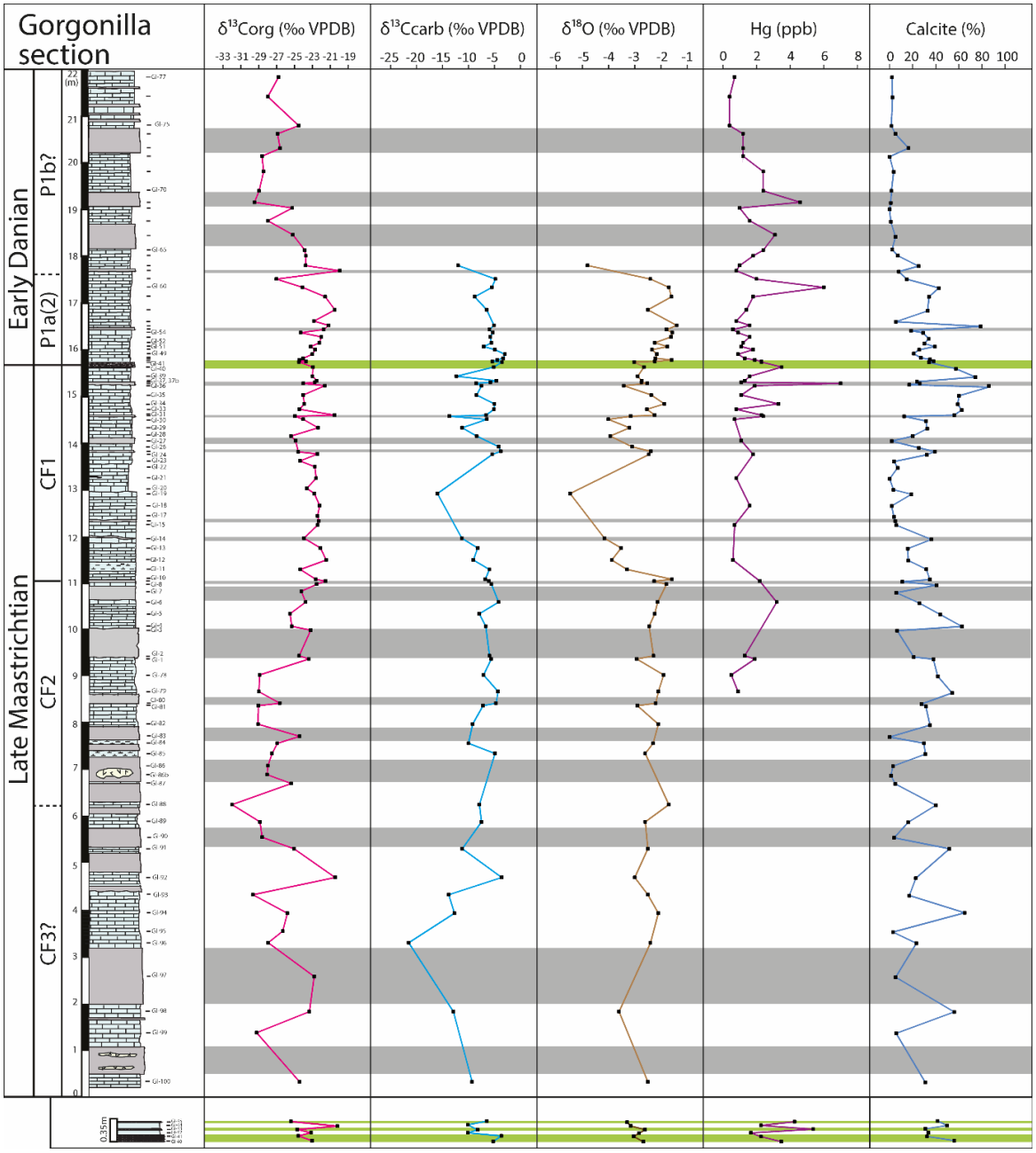

Figure 12. *Stable isotope ($\delta^{13}C_{org}$, $\delta^{13}C_{carb}$ and $\delta^{18}O$), mercury and calcite stratigraphy of Gorgonilla K/Pg transition. The absence of a negative shift in $\delta^{13}c_{org}$ and $\delta^{13}c_{carb}$, of a drop in calcite and a high mercury content usually observed at the Cretaceous-Paleogene transition, supports the KPB hiatus evidenced by biostratigraphy.*

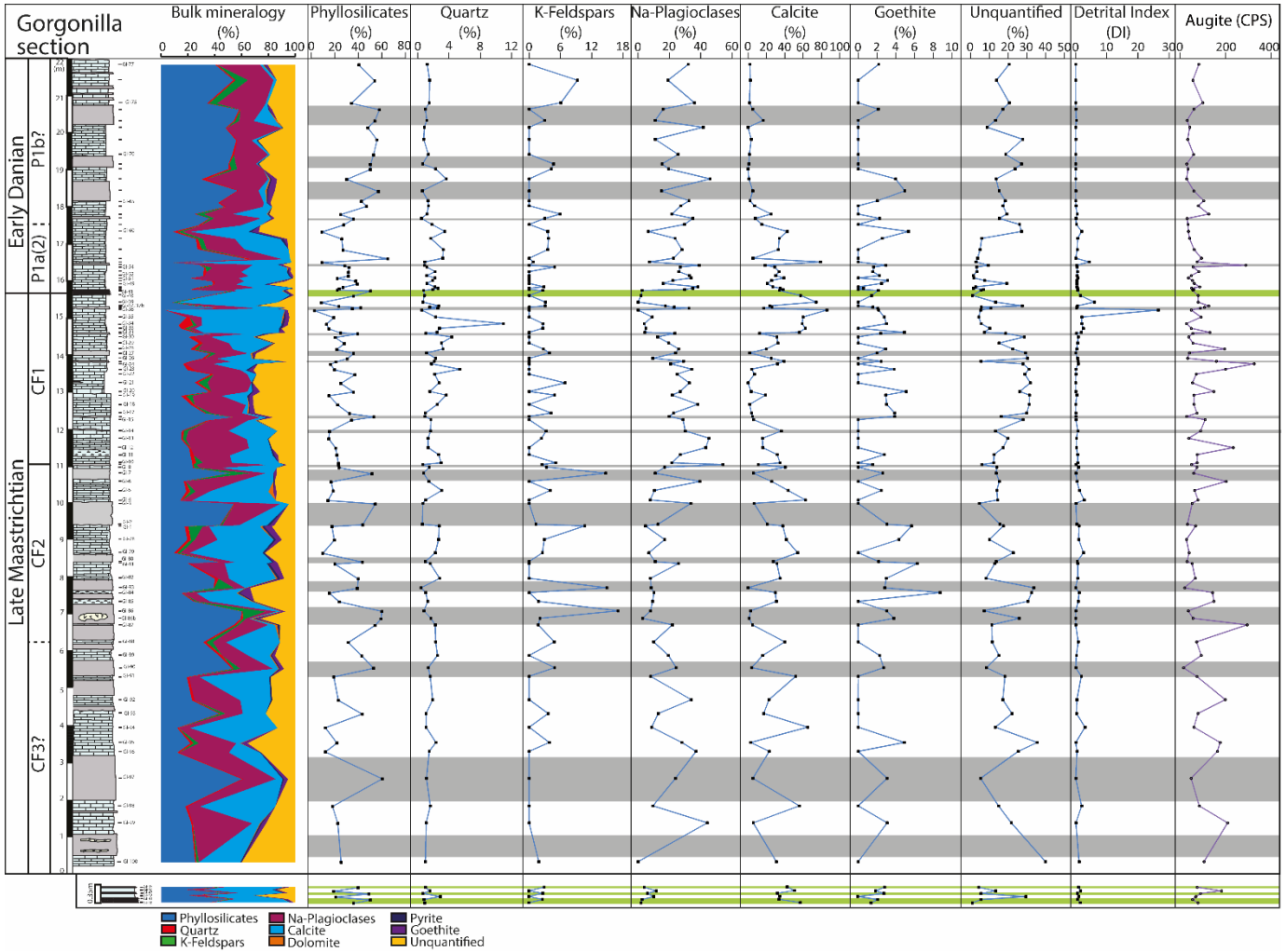

Figure 13. *Bulk mineralogical composition at Gorgonilla K/Pg section. Phyllosilicates, calcite and Na-plagioclases are the main bulk minerals. Note variable distribution of phyllosilicates between Maastrichtian and Danian mudstones, and increasing phyllosilicates at the KPB (green bands), contrary to calcite and Na-plagioclases. Unquantified minerals refer to poorly crystallized quartz (opal) and some ferromagnesian minerals (pyroxenes and amphiboles). Grey shaded bands indicate turbidites.*

From the base of the section, the $\delta^{13}C_{org}$ Maastrichtian values show gradually a negative trend reaching at GI-88, ~9.5 m below KPB, the minimum value (-32.0 ‰). This is in correlation with $\delta^{13}C_{carb}$ and $\delta^{18}O$ which, in contrast, gradually present a positive trend (from -9.3 ‰ to -7.9 ‰ and from -2.5 ‰ to -1.7 ‰ respectively for $\delta^{13}C_{carb}$ and $\delta^{18}O$ values) with a slight inflection at GI-88 for $\delta^{18}O$. These two curves show relatively stable values across the CF2 biozone whereas those of $\delta^{13}C_{org}$ are suddenly increase and reach -21.5 ‰ at the CF2/CF1 boundary (Fig. 12). The top of the CF2 zone (GI-1 to 9) is characterized by relatively high contents in Hg (an average of 2.2 ppb) before to decrease in the lower part of the CF1 zone (GI-12 to 30: 1.0 ppb as average value) where $\delta^{13}C_{carb}$ and $\delta^{18}O$ also decrease whereas $\delta^{13}C_{org}$ increases. The uppermost CF1 zone records intense and large fluctuations of $\delta^{13}C_{org}$ (between -25.0 and -20.5 ‰), $\delta^{13}C_{carb}$ (-13.7 and -4.6 ‰), $\delta^{18}O$ (-3.4 and -1.9 ‰) and Hg (0.8 and 7.0 ppb) (Fig. 12), probably linked to diagenetic overprint and/or volcanism episodes of CLIP and its environmental change effects as it is the case in India (see Punekar et al., 2014a; Keller et al., 2016).

Several works over the world associate a negative shift (2-3 ‰) in $\delta^{13}C_{carb}$ at the KPB (e.g., Keller, 2014; Punekar et al., 2014b, 2016; Mateo et al., 2016) as well as a large positive Hg anomaly (Font et al. 2016, 2018). At Gorgonilla, no significant shift in $\delta^{13}C_{carb}$ and Hg is observed at the KPB but only a slight positive inflection in Hg. These results, coupled to the erosive surface observed in the field, suggest a large hiatus as testified by the biostratigraphy data. Consequently, the upper part of latest Maastrichtian CF1 zone as well as P0, P1a(1) and lower P1a(2) Danian zones are missing (Figs. 10 and 11).

The first 30 cm just above the KPB hiatus are marked by a slight but not significant increase in $\delta^{13}C_{org}$, $\delta^{13}C_{carb}$ and $\delta^{18}O$ while Hg content globally decreases (Fig. 12). Increasing of $\delta^{13}C_{org}$ and $\delta^{18}O$ values continues over the upper part of P1a(2) subzone before a large fluctuation observed from GI-61, ~1.9 m above KPB. The upper part of P1a(2) subzone is also characterized by a gradual decrease in $\delta^{13}C_{carb}$ with a drop, from GI-61, similar to that of $\delta^{18}O$. In addition, a large positive Hg shift is recorded around GI-61. Combination of all these data infers at GI-61 a probable boundary of P1a/P1b biozones (Fig. 12). Similar observations are made in Tunisia (Keller and Lindinger, 1989) and Egypt (Punekar et al., 2014). The probable P1b zone in Gorgonilla section show from the bottom a gradual decrease in $\delta^{13}C_{org}$ towards the top while Hg content considerably increase before returning to P1a/P1b boundary values at the top.

6. BULK AND CLAY MINERALOGY

At Gorgonilla, three types of rock units (pelagic deposits, turbiditic litharenites and spherule-rich layer) have been identified. Each type is related to an origin and specific depositional conditions. Consequently, these materials will therefore have different mineralogical composition (bulk-rock and clay) with, however, specificities related to the corresponding biozones. The bulk-rock mineralogy composition of the entire Gorgonilla section is dominated by phyllosilicates, calcite and Na-plagioclases with accessorily K-felspars, quartz, goethite, pyrite and dolomite (Fig. 13) whereas that of clay mineralogy is mainly consists of zeolite, smectite and illite, with relatively low sporadic pics of chlorite and kaolinite (Fig. 14). The unquantified bulk-rock component corresponds to poorly crystallized minerals (mainly opal with minor pyrite and goethite), pyroxenes (augite) and amphiboles.

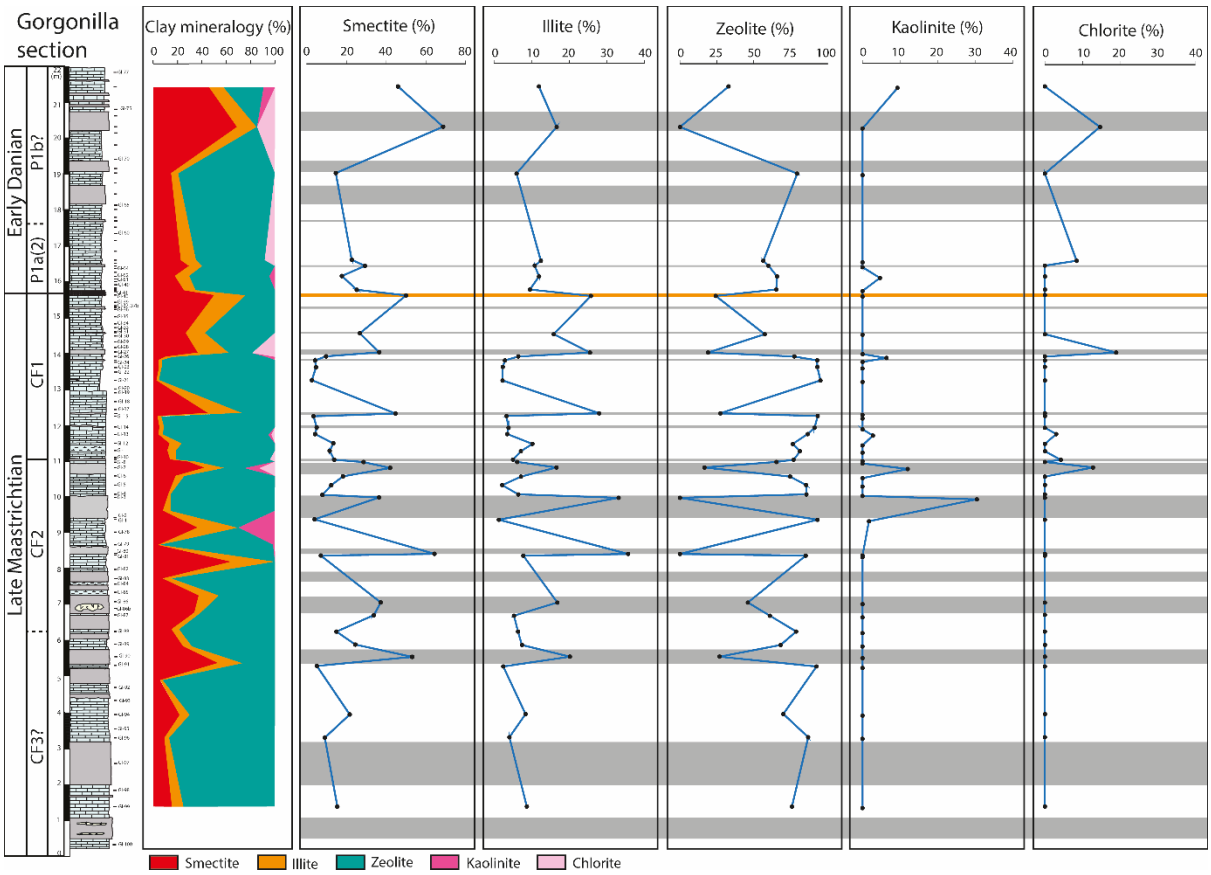

Figure 14. *Relative percent of clay minerals phase at Gorgonilla. Note zeolite increasing and decrease of smectite and illite in mudstone facies, in contrast to turbidite facies. KPB clay minerals percent are similar to that of turbidites.*

Pelagic sediments of probable CF3 zone consist of 29.19 % of calcite, 25.21 % of phyllosilicates, 22.18 % of unquantified minerals and 18.49 % of Na-plagioclases. Quartz, K-feldspars, goethite as well as pyrite and dolomite are, each one, lowly represented (< 2 %).

Only zeolite (71.33 %), smectite (20.51 %) and illite (8.16 %) are present as clay minerals. CF3 zone is followed by CF2 zone with a similar phyllosilicate composition (25.45 %), but a slight increase in calcite (32.18 %) as well as decreasing of Na-plagioclases (16.80 %) and undosed minerals (16.84 %). Minor bulk-rock components are also present (Fig. 13, Annex III.3). Clay minerals composition significantly change in CF2 zone. For example, zeolite content drops considerably reaching the minimum late Maastrichtian zeolite content (58.40 %), whereas smectite (28.00 %) and illite (16.40 %) increase. At CF1 zone, the most important bulk minerals are calcite (29.41 %) followed by phyllosilicates (21.94 %), undosed minerals (20.81 %) and Na-plagioclases (20.61 %) with a clay mineralogical composition very close to that of CF3 (zeolite: 75.59 %; smectite: 14.65 %; illite: 9.76 %). No kaolinite and chlorite are encountered in the late Maastrichtian pelagic deposits.

In contrast, the early Danian pelagic sediments are globally more enriched in phyllosilicates to the detriment of calcite as is the case during the late Maastrichtian (Fig. 13). Na-plagioclases are also more abundant whereas undosed minerals content decrease significantly. However, clay mineralogy, always dominated by zeolite, smectite and illite, remains very close to the late Maastrichtian composition (Fig. 14). In details, the P1a(2) subzone which overlies the spherule-rich layer consists of 27.69 of phyllosilicates, 33.73 % of calcite, 23.50 % of Na-plagioclases and 9.53 % of unquantified minerals with a clay mineral content dominated by the zeolite (64.01 %) and relative proportions of smectite (24.43 %) and illite (11.56 %). In contrast, the pelagic deposits of the Gorgonilla top zone (P1b) are strongly enriched in phyllosilicates (43.66 %) with only 4.20 % for the calcite. Na-plagioclases are also abundant relatively to all other biozones while undosed mineral content (18.44 %) is close to those of late Maastrichtian pelagic sediments. Also, there is a slight change in clay mineral proportions (smectite: 32,63 %; illite: 9.51 %; zeolite: 57.87 %) probably testifying of a change of climatic conditions.

Contrary to pelagic sediments, phyllosilicates are the main bulk mineralogical component of late Maastrichtian turbidites followed by Na-plagioclases, calcite and unquantified minerals (Fig. 13; Annex III.3). Clays are dominated by smectite, illite and zeolite with some pics of kaolinite and chlorite at the top of CF2 and middle CF1 zones. Mineralogical composition of these turbidites remains almost similar during the early Danian.

The most abundant bulk-rock minerals in the spherule-rich layers are phyllosilicates and calcite with respectively 43.80 % and 41.69 % as average values (Fig. 13; Annex III.3). Smectites (50.00 %) are dominant clay minerals in these layers. It is followed by illite (25.77 %) and zeolite (24.23 %). Because of the high phyllosilicates content, the spherule-rich layer

is interpreted as another turbidite deposit, as also indicated by the lithology and biostratigraphy (note only a small percentage of the phyllosilicates corresponds to spherule alteration products). Comparatively to other classic turbidites, the high calcite content in the spherule-rich layers is largely due to infillings of spherule vesicles and shells of planktic foraminifera especially large Cretaceous species reworked and transported downslope by the turbidity current.

7. MAJOR, TRACE AND RARE EARTH ELEMENT GEOCHEMISTRY

7.1. Whole rock geochemistry

Major and trace element abundance from whole rock geochemistry vary significantly relatively to the three main Gorgonilla rock units (pelagic deposits, turbidites and spherules-rich layers) and the age of deposits (late Maastrichtian and early Danian). Major elements (MEs) are mainly linked to variations in clay mineral contents. Because of dual origin of the Gorgonilla deposits (turbidites and pelagic deposits), ME concentrations are simultaneously compared to Lower Continental Crust (LCC) and Post-Archean Australian average Shales (PAAS) reference values (Fig. 15). Trace elements (TEs) are in the first time normalized by the Al-content to avoid carbonate dilution effects (Tribovillard et al., 2006), before the comparison with LCC and PAAS values (Fig. 16). Table 1 presents the average geochemical composition of Gorgonilla rock type units and biozones, as well as reference used values. LCC and PAAS reference values in this study are respectively from Rudnick and Gao (2003) and from Wedepohl et al. (1971, 1991).

Turbidites from the entire section show a relatively uniform geochemical composition, mainly consisting by SiO_2 (50.12 %), CaO (5.92 %), Al_2O_3 (12.28%), Fe_2O_3 (9.10 %), TiO_2 (0.51 %) and K_2O (1.27 %) as major elements with significant Al-normalized trace elements such as V (30.45), Cr (1.53), Co (3.30), Ni (1.67), Cu (2.71), Zn (12.31), Sr (43.73), Zr (10.49) and Ba (88.07). These values are whether very close to their respective LCC values or distant and rather very close to their respective PAAS values (Figs. 15 and 16), thus testified of the mixed origin (volcanic and marine) of the turbidite materials.

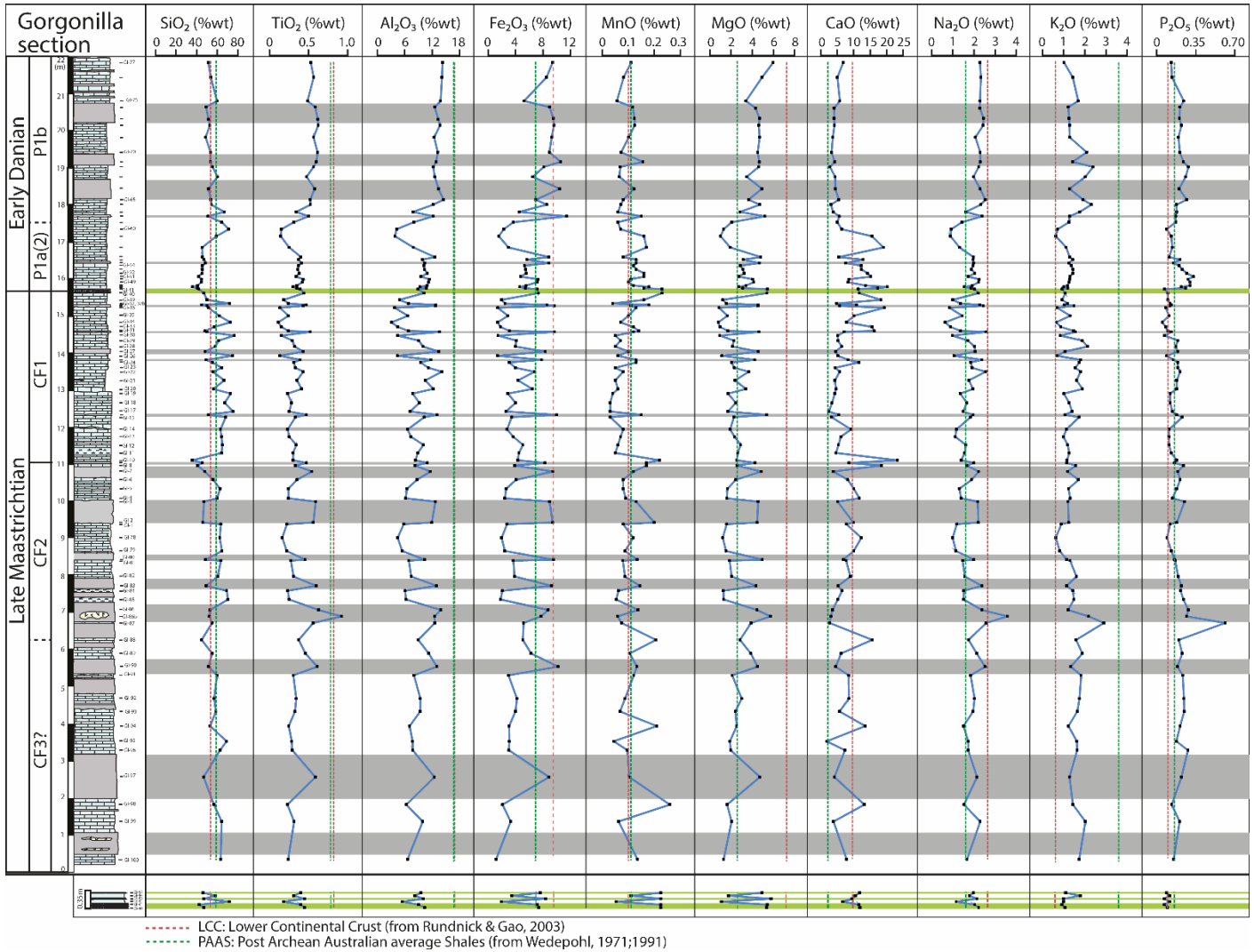

Figure 15. *Whole rock major element composition across the Gorgonilla K/Pg transect. Note enrichment in MnO, MgO and CaO at the KPB. Light green bands refer to spherule-rich layers, and grey shaded bands to turbidites. Red and green dashed lines are respectively LCC (from Rudnick and Gao, 2003) and PAAS (from Wedepohl, 1971; 1991) reference values.*

For the pelagic sediments, abundance in major and trace elements fluctuate significantly across the entire Gorgonilla section. From the bottom to uppermost late Maastrichtian biozones, SiO_2 average content is respectively of 58.60 %, 59.01 % and 62.32 %, very close to the PAAS value (58.90 %). In contrast, the net depletion in Al_2O_3 (CF3: 8.42 %; CF2: 7.72 %; CF1: 7.98 %), Fe_2O_3 (3.48 %; 3.77 %; 3.38 %), TiO_2 (0.31 %; 0.34 %; 0.26 %) and K_2O (1.67 %; 1.44 %; 1.30 %) relative to their respective PAAS values (Al_2O_3: 16.70 %; Fe_2O_3: 6.90 %; TiO_2: 0.78 % and K_2O: 3.60 %) and especially the enrichment in CaO (more than 8.20% per zone) compared to PAAS (2.20%) of these deposits, suggest, correlatively to the mineralogical data, a low detritism and higher sea level. In the same time, some Al-normalized TE such as Cr, Cu, Zn, Sr, Zr and Ba present fluctuating proportions across this lower part of Gorgonilla section. Sc/Al (~3.40), V/Al (~24.00), Co/Al (~2.70), Ni/Al (~1.05), Rb/Al (~4.60) and Sr/Al (~ 62.35) show uniform trends (Fig. 10; Table 1) sometimes very close to LCC (e.g. Sc, V and Rb) and PAAS (e.g., Co) or very depleted relatively to all those reference values (e.g., Ni) (Fig. 16). Although the Cr and Cu Al-normalized slightly increase towards the CF3 zone (average zone values: CF1: 2.94 – CF2: 6.75 – CF3: 5.64 for Cr/Al and CF1: 4.64 – CF2: 5.79 – CF3: 6.51 for Cu/Al), this lower part globally remains depleted in Cr and very close to slightly enriched in Cu relatively to respective LCC (Cr/Al: 24.04; Cu/Al: 2.91) and PAAS (Cr/Al: 10.20; Cu/Al: 5.10) values (Fig. 16). In contrast, Zn/Al, Zr/Al and Ba/Al ratios globally show a slight negative trend from the base to top of this part (CF1: 14.24 – CF2: 14.38 – CF3: 11.81 for Zn/Al, CF1: 11.22 – CF2: 11.46 – CF3: 9.81 for Zr/Al and CF1: 203.30 – CF2: 148.19 – CF3: 125.27 for Ba/Al). However, this part shows a moderate enrichment in Zn and Zr in relation to LCC values (Zn/Al: 8.72 and Zr/Al: 7.60) and rather a depletion in Zr and closeness in Zn relatively to reference PAAS values (Zr/Al: 18.00; Zn/Al: 11.00).

Apart minor inflexions in MnO (0.23 %), CaO (10.97 %) as well as some Al-normalized TE such as Ni (11.80), Zn (25.05) and Co (5.39) which present a slight enrichment relatively to the LCC and PAAS values (Figs. 15 and 16), no remarkable shift testifying a primary Chicxulub impact deposits as described at El Peñon (Mexico) by keller et al. (2009) has been observed in the spherule-rich layers. All other geochemical elements are very close whether to PAAS (e.g. Fe_2O_3, V/Al, Cr/Al and Zr/Al) or LCC values (e.g. CaO, P_2O_5, K_2O, Rb/Al) with sometimes an intermediate composition, thus suggesting mixing sediments (volcanic and pelagic) in the spherule-rich layers similar to turbidites.

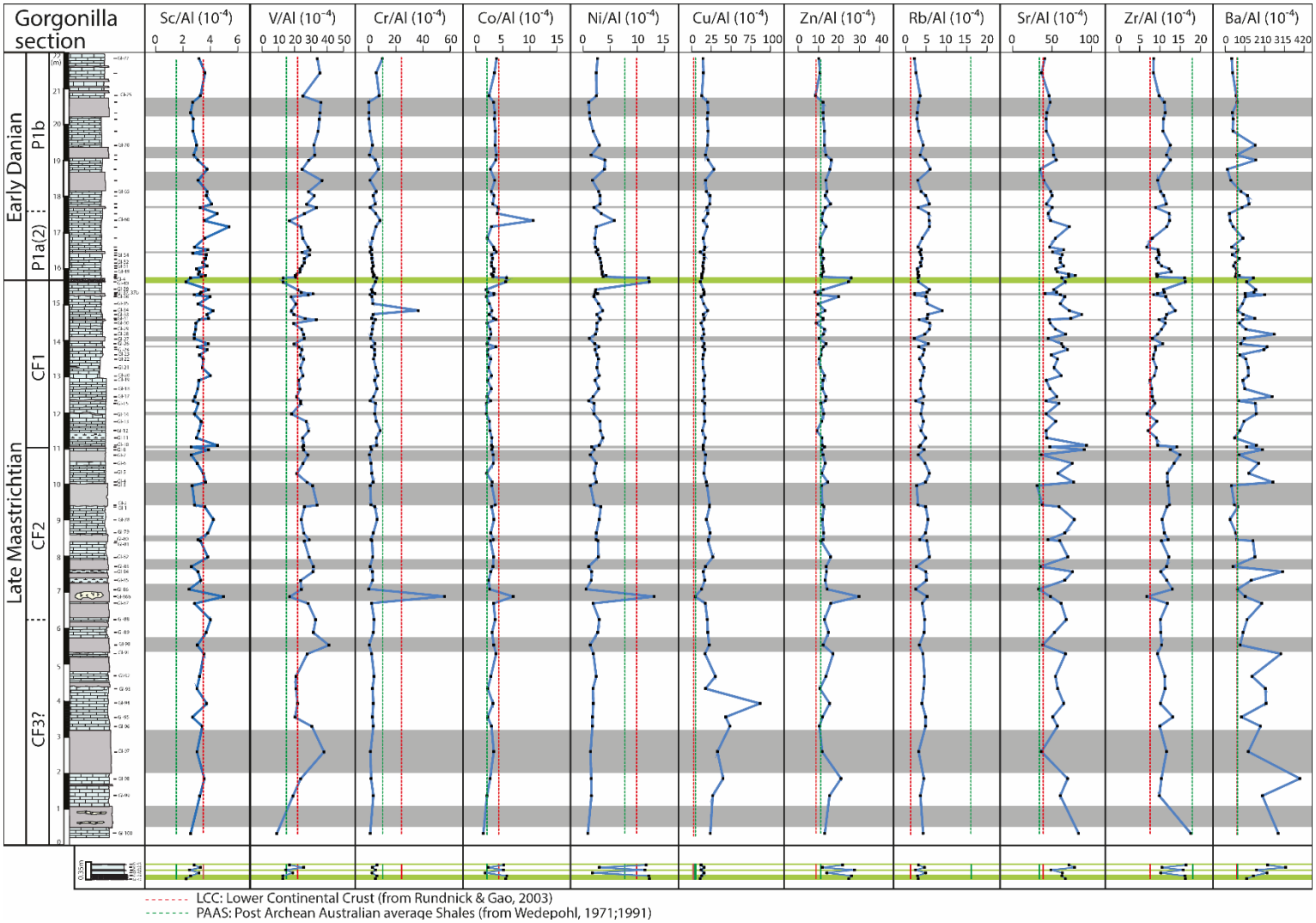

Figure 16. *Al-normalized trace element stratigraphy at Gorgonilla K/Pg section. Co, Ni and Zn are highly mobiles relative to LCC and PAAS at the KPB and in fresh basalt fragment. Light green bands refer to spherule-rich layers, and grey shaded bands to turbidites. Red and green dashed lines are respectively LCC (from Rudnick and Gao, 2003) and PAAS (from Wedepohl, 1971; 1991) reference values.*

Table 1. *Whole rock geochemistry (major and trace elements) of different rock units and zones from Gorgonilla section with PAAS (from Wedepohl et al., 1971, 1991) and LCC (from Rudnick and Gao, 2003) reference values. Avg: average, SD: standard deviation, n: number of samples, lower: mean value of Maastrichtian turbidites and upper: mean values of Danian turbidites.*

	Major elements (ME)											Al-normalized trace elements (TE/Al)										
	SiO_2 (wt.%)	TiO_2 (wt.%)	Al_2O_3 (wt.%)	Fe_2O_3 (wt.%)	MnO (wt.%)	MgO (wt.%)	CaO (wt.%)	Na_2O (wt.%)	K_2O (wt.%)	P_2O_5 (wt.%)	LOI (wt.%)	Sc/Al (10^{-4})	V/Al (10^{-4})	Cr/Al (10^{-4})	Co/Al (10^{-4})	Ni/Al (10^{-4})	Cu/Al (10^{-4})	Zn/Al (10^{-4})	Rb/Al (10^{-4})	Sr/Al (10^{-4})	Zr/Al (10^{-4})	Ba/Al (10^{-4})
Maastrichtian pelagic deposits																						
Avg	60.54	0.29	8.01	3.51	0.09	2.17	8.38	1.62	1.42	0.17	13.18	3.45	23.92	5.35	2.75	2.57	20.38	13.09	4.78	62.17	10.60	149.33
SD	8.80	0.13	2.47	1.59	0.05	0.95	4.92	0.50	0.45	0.08	3.78	0.50	4.20	8.79	0.78	1.63	12.23	3.45	0.91	12.16	1.96	75.53
n	49	49	49	49	49	49	49	49	49	49	49	49	49	49	49	49	49	49	49	49	49	49
CF3	58.60	0.31	8.42	3.48	0.13	2.33	8.38	1.83	1.67	0.21	13.94	3.33	23.50	2.94	2.72	1.90	34.09	14.24	4.41	62.34	11.22	203.30
CF2	59.01	0.34	7.73	3.77	0.09	2.36	8.65	1.70	1.44	0.21	14.18	3.54	25.42	6.75	3.21	3.04	17.73	14.38	4.92	66.63	11.46	148.19
CF1	62.32	0.26	7.98	3.38	0.08	1.98	8.23	1.47	1.30	0.14	12.26	3.45	23.23	5.64	2.50	2.61	15.64	11.81	4.86	59.50	9.81	125.27
Danian pelagic deposits																						
Avg	51.12	0.41	10.86	6.22	0.11	3.51	9.02	1.93	1.43	0.21	14.75	3.52	27.01	4.12	3.49	3.07	17.43	12.29	3.94	53.99	10.39	65.18
SD	8.52	0.13	2.74	2.22	0.04	1.16	5.36	0.42	0.43	0.06	4.91	0.55	4.75	2.32	1.48	0.86	3.87	1.75	1.12	11.53	1.57	38.50
n	26	26	26	26	26	26	26	26	26	26	26	26	26	26	26	26	26	26	26	26	26	26
P1a(2)	49.95	0.32	9.10	4.78	0.12	2.73	11.96	1.70	1.22	0.20	17.43	3.63	24.31	3.55	3.63	3.29	15.61	11.77	3.90	60.80	10.20	53.94
P1b	55.49	0.53	12.82	7.79	0.08	4.31	4.38	2.21	1.74	0.21	10.08	3.36	30.70	4.90	3.29	2.78	19.92	12.99	3.99	44.70	10.66	80.51
Turbidites																						
Avg	50.12	0.51	12.28	9.10	0.13	4.53	5.92	2.22	1.27	0.18	13.49	2.87	30.45	1.53	3.30	1.71	18.04	12.31	2.96	43.73	10.49	88.07
SD	3.64	0.10	1.56	1.63	0.03	0.64	2.08	0.29	0.18	0.04	2.87	0.23	5.64	1.41	0.50	0.69	4.59	1.14	0.46	8.23	1.90	52.19
n	21	21	21	21	21	21	21	21	21	21	21	21	21	21	21	21	21	21	21	21	21	21
lower	49.83	0.50	12.21	8.75	0.13	4.45	6.29	2.19	1.26	0.18	13.96	2.87	29.37	1.87	3.14	1.75	18.12	12.10	2.87	42.36	10.54	100.22
upper	50.86	0.55	12.46	9.96	0.13	4.74	4.99	2.28	1.28	0.20	12.29	2.86	33.16	0.69	3.70	1.62	17.83	12.83	3.17	47.16	10.36	57.70
Spherule-rich layers																						
Avg	45.42	0.42	9.65	7.59	0.23	5.39	10.97	2.08	1.03	0.08	16.96	2.50	14.40	5.56	5.39	11.80	12.42	25.01	2.94	62.28	16.11	163.88
SD	1.99	0.03	0.51	0.45	0.00	0.31	0.98	0.09	0.07	0.01	2.70	0.21	1.66	0.52	0.25	0.35	0.70	2.11	0.29	8.44	0.25	39.85
n	4	4	4	4	4	4	4	4	4	4	4	4	4	4	4	4	4	4	4	4	4	4
Reference values																						
PAAS	58.90	0.78	16.70	6.90	0.11	2.60	2.20	1.60	3.60	0.16	-	1.50	15.00	10.20	2.10	7.70	5.10	11.00	16.00	34.00	18.00	66.00
LCC	53.40	0.82	16.90	9.52	0.10	7.24	9.59	2.65	0.61	0.10	-	3.47	21.91	24.04	4.25	9.84	2.91	8.72	1.23	38.91	7.60	63.06

Above, the early Danian pelagic sediments (P1a(2) and P1b zones) show a net decrease in SiO_2 and Zn/Al, Sr/Al and Ba/Al ratios which are enriched relatively to reference values (Table 1). In contrast, TiO_2, Al_2O_3, Fe_2O_3 and MgO contents as well as V, Co and Ni Al-ratios occur increased in these sediments, although they remain on this side of PAAS and LCC reference values. P1a(2) zone holds the higher CaO (11.96 %) and LOI (17.43 %) contents contrary to P1b in which these contents are the lowest (CaO: 4.38 %; LOI: 10.08 %) (Table 1). Moreover, some significant geochemical elements such as K_2O, Cr/Al and Cu/Al decrease in P1a(2) zone reaching minimum values before increase at P1b (Table 1).

Table 2. *Enrichment factor values for major elements (EF_{ME}) relative to average shale (S) and chondrite (C) of tektites (T) and matrix (M) from spherule-rich layers across the Gorgonilla K/Pg section.*

Sample	Al		Ca		Fe		K		Mg		Mn		Na		Si		Ti	
	S	C	S	C	S	C	S	C	S	C	S	C	S	C	S	C	S	C
GI-40																		
T1	0.90	9.12	2.92	4.95	0.67	0.19	0.41	21.72	0.97	0.15	0.94	0.40	2.43	5.77	1.07	2.77	0.80	8.52
T2	0.75	7.64	9.70	16.43	0.69	0.19	0.14	7.32	1.72	0.27	1.38	0.59	1.04	2.48	0.90	2.32	0.74	7.89
T3	0.91	9.22	3.88	6.57	0.81	0.23	0.36	19.19	1.16	0.18	1.17	0.50	2.18	5.18	1.03	2.67	0.96	10.15
T4	0.87	8.82	4.26	7.22	0.66	0.18	0.37	19.94	0.99	0.16	1.30	0.55	1.98	4.70	1.07	2.77	0.82	8.71
T5	0.86	8.76	3.78	6.40	0.70	0.20	0.36	19.04	1.15	0.18	1.33	0.57	2.63	6.23	1.06	2.75	0.87	9.26
T6	0.90	9.18	3.81	6.45	0.72	0.20	0.38	20.23	1.02	0.16	1.06	0.45	1.97	4.67	1.06	2.75	0.91	9.72
T7	0.66	6.68	8.35	14.14	0.79	0.22	0.28	15.00	1.25	0.20	1.17	0.50	2.23	5.28	0.95	2.45	0.66	7.02
T8	0.59	6.04	5.90	10.01	1.00	0.28	0.23	12.27	1.45	0.23	0.59	0.25	1.94	4.61	1.03	2.67	0.68	7.23
T9	0.69	6.98	5.01	8.50	0.74	0.21	0.44	23.36	1.00	0.16	0.85	0.36	3.06	7.26	1.05	2.72	0.76	8.07
T10	0.91	9.21	3.86	6.55	0.72	0.20	0.38	20.08	1.02	0.16	0.97	0.41	1.92	4.55	1.06	2.75	0.91	9.72
T11	0.61	6.25	5.24	8.88	1.16	0.33	0.26	13.96	1.72	0.27	1.73	0.74	1.91	4.53	1.02	2.63	0.81	8.65
T12	0.72	7.33	6.01	10.18	0.83	0.23	0.34	18.15	1.17	0.18	0.97	0.42	3.27	7.76	0.97	2.52	0.67	7.11
T13	0.78	7.89	4.31	7.30	0.78	0.22	0.32	17.37	1.16	0.18	1.53	0.65	2.31	5.47	1.06	2.74	0.85	9.00
T14	0.54	5.50	7.08	12.00	0.78	0.22	0.22	11.88	1.18	0.19	0.76	0.32	2.68	6.35	1.02	2.63	0.64	6.84
T15	0.59	6.00	5.87	9.94	0.95	0.27	0.47	25.14	1.39	0.22	1.00	0.43	3.49	8.28	0.98	2.54	0.66	6.99
M	0.48	4.84	6.74	11.42	0.85	0.24	0.23	12.06	1.72	0.27	2.35	1.00	1.11	2.63	0.65	1.68	0.45	4.75
GI-41																		
T1	0.93	9.44	3.14	5.31	0.76	0.21	0.45	23.95	0.99	0.16	1.71	0.73	2.43	5.76	1.06	2.75	0.90	9.58
T2	0.91	9.23	2.78	4.71	0.74	0.21	0.46	24.40	0.94	0.15	1.30	0.56	2.34	5.56	1.09	2.82	0.89	9.47
T3	0.92	9.37	5.02	8.50	0.78	0.22	0.34	18.30	1.19	0.19	1.71	0.73	1.85	4.39	1.00	2.59	0.91	9.64
T4(a)	0.92	9.37	2.86	4.84	0.76	0.21	0.42	22.61	0.97	0.15	1.29	0.55	2.25	5.34	1.08	2.80	0.97	10.25
T4(b)	-	-	-	-	-	-	-	-	-	-	-	-	-	-	-	-	-	-
T5	0.93	9.48	3.12	5.28	0.80	0.23	0.41	22.02	1.03	0.16	1.44	0.62	2.43	5.76	1.06	2.74	0.98	10.42
T6	0.88	8.98	4.05	6.86	0.73	0.21	0.40	21.57	1.04	0.17	0.79	0.34	2.08	4.93	1.05	2.72	0.90	9.59
T7(a)	0.91	9.29	2.78	4.71	0.71	0.20	0.44	23.51	0.88	0.14	1.20	0.51	2.23	5.28	1.10	2.83	0.93	9.88
T7(b)	-	-	-	-	-	-	-	-	-	-	-	-	-	-	-	-	-	-
T8	0.81	8.23	5.31	9.00	0.78	0.22	0.19	10.06	1.43	0.23	1.27	0.54	1.48	3.52	1.02	2.64	0.82	8.72
T9	0.64	6.52	5.06	8.57	0.77	0.22	0.29	15.78	1.02	0.16	0.89	0.38	2.63	6.25	1.07	2.76	0.68	7.26
T10	0.65	6.63	5.90	10.01	0.97	0.27	0.16	8.74	1.48	0.23	1.04	0.45	2.09	4.96	1.01	2.60	0.66	7.05
T11	0.81	8.23	4.97	8.43	0.80	0.22	0.23	12.21	1.37	0.22	0.97	0.41	2.48	5.89	1.01	2.61	0.83	8.78
GI-43																		
M	0.49	4.95	4.29	7.27	1.13	0.32	0.21	11.07	2.28	0.36	2.42	1.03	1.10	2.60	0.68	1.76	0.52	5.48
GI-45																		
T3	0.91	9.24	4.09	6.92	0.76	0.21	0.37	19.79	1.05	0.17	1.38	0.59	2.04	4.85	1.04	2.70	0.92	9.76
T4	0.81	8.22	5.63	9.54	0.76	0.21	0.23	12.09	1.24	0.20	1.12	0.48	1.82	4.32	1.02	2.63	0.78	8.30
T6	0.90	9.15	2.59	4.38	0.80	0.22	0.44	23.51	0.95	0.15	1.29	0.55	2.54	6.02	1.09	2.82	0.93	9.92
T7	0.86	8.73	5.01	8.49	0.88	0.25	0.29	15.36	1.30	0.21	1.65	0.71	1.61	3.81	1.01	2.62	0.91	9.70
T8	0.66	6.69	13.15	22.28	0.52	0.15	0.13	6.96	1.32	0.21	1.04	0.44	1.39	3.29	0.82	2.11	0.68	7.26
T9	0.83	8.39	3.35	5.67	0.57	0.16	0.39	20.68	0.77	0.12	0.87	0.37	2.81	6.68	1.12	2.89	0.75	7.99
T10	0.86	8.73	2.42	4.11	0.69	0.19	0.42	22.32	0.81	0.13	0.96	0.41	2.27	5.39	1.13	2.93	0.83	8.85
T11	0.69	7.04	7.00	11.87	0.77	0.22	0.27	14.55	1.40	0.22	1.00	0.43	2.58	6.11	0.98	2.54	0.65	6.92
T12	0.66	6.74	8.39	14.21	0.77	0.22	0.17	8.88	1.22	0.19	0.62	0.26	1.44	3.43	0.97	2.51	0.62	6.55
T13	0.78	7.91	9.78	16.58	0.69	0.20	0.25	13.23	1.28	0.20	1.24	0.53	1.74	4.14	0.88	2.28	0.81	8.55
T14	0.75	7.63	4.85	8.22	0.79	0.22	0.36	19.19	1.17	0.18	0.97	0.41	2.38	5.65	1.05	2.72	0.75	7.96
T15	0.68	6.94	5.04	8.54	0.81	0.23	0.43	22.91	1.20	0.19	1.17	0.50	2.60	6.17	1.05	2.72	0.76	8.03
T16	0.71	7.25	4.74	8.03	0.81	0.23	0.39	21.13	1.21	0.19	1.13	0.48	2.76	6.54	1.05	2.71	0.73	7.76

7.2. Matrix and tektites geochemistry of spherule-rich layers

A total of forty-two tektites (or spherules) and two matrix samples from spherule-rich layer were analysed using methods described in section 2. Fifteen spherules are from GI-40 (Fig. 17A), twelve from GI-41 (Fig. 17B) and sixteen from GI-45 (Fig. 17C). The results of two first analysed tektites (T1 and T2) of sample GI-45 and the last (T12) of GI-41 are wrong and have been excluded. For the matrix, they are respectively from GI-40 and GI-43. Annex III.4 presents geochemical raw data obtained from these analyses. Enrichment factors for ME ($EF_{ME} = X/X_{[PAAS\ or\ Chondrite]}$), TE ($EF_{TE} = [Y/Al]/[Y/Al]_{PAAS}$ or $Y/Y_{Chondrite}$) and REE ($EF_{REE} = [Z/Al]/[Z/Al]_{PAAS}$ or $Z/Z_{Chondrite}$) were calculated using average shale (Wedepohl et al., 1971; 1991) and chondrite (Anders and Grevesse, 1989) values in order to assess the trends of different elements. In these calculation formula, X, Y and Z are respectively specific major, trace and rare earth elements. Figure 18 as well as respectively Tables 2, Annexes III.1 and III.2 show the calculation of major, trace and rare earth element enrichment factors.

Except Ca, Na, Ni, Sc and Sr which are slightly enriched in tektites relative to average shale and K, Cs, Pb, U and Zn which are globally depleted, average EF_{ME} and EF_{TE} of all other elements are generally close to 1 (Fig. 18A and C), which indicates a major and trace element composition of tektite nearly similar to average shales. This suggests an alteration and consequently a reworking of tektites. Also, EFs_{ME} relative to PAAS for matrix samples are close to those of tektite thus suggesting a similar major element composition between tektites and matrix (Fig. 18A). In contrast, TE enrichment factors display distinct composition with important enrichments in Ba, Cu, Mo and Zn (Fig. 18C). In addition, the detailed size tektite analysis (Fig. 17) clearly reveals an enrichment in Co, Cr and Ni of small size tektites relative to average shale (see shaded lines of Annex III.1) while large size tektites are depleted, probably due to large exposed surface to alteration.

Because of their cosmic origin, tektites must normally be enriched in some significant major and trace elements such as Fe, Mg, Co, Cr, Cu, Mn, Ni and Zn. But, major and trace element enrichment factors of tektites relative to Chondrite shows a depletion in these elements and rather an enrichment in Al, K, Na, Ti, Ba, Sr, U and Zr (Fig. 18B and D) which are detrital and/or common shale elements. These enrichment factors, mainly EFs_{TE} except Ba and Mo which are more enriched, are nearly similar to those of matrix samples (Fig. 18D). So, tektites were become poorer in their original elements and have considerably been enriched in detrital and/or common shale elements. In addition, the Ni/Cu ratio from bulk geochemistry of spherule-rich layers which is currently used as an extraterrestrial proxy (see Gertsch et al., 2011

and Munsel et al., 2011), show a low magnitude peak (0.90–1.08; Fig. 19) testifying of a strong dilution between extraterrestrial materials (strongly enriched in Ni) and common marine ones (enriched in Cu). Consequently, these results confirm that tektites and matrix from Grogonilla spherule-rich layers are not primary deposits and then, they were subjected to a reworking as reported by Mateo et al. (2019).

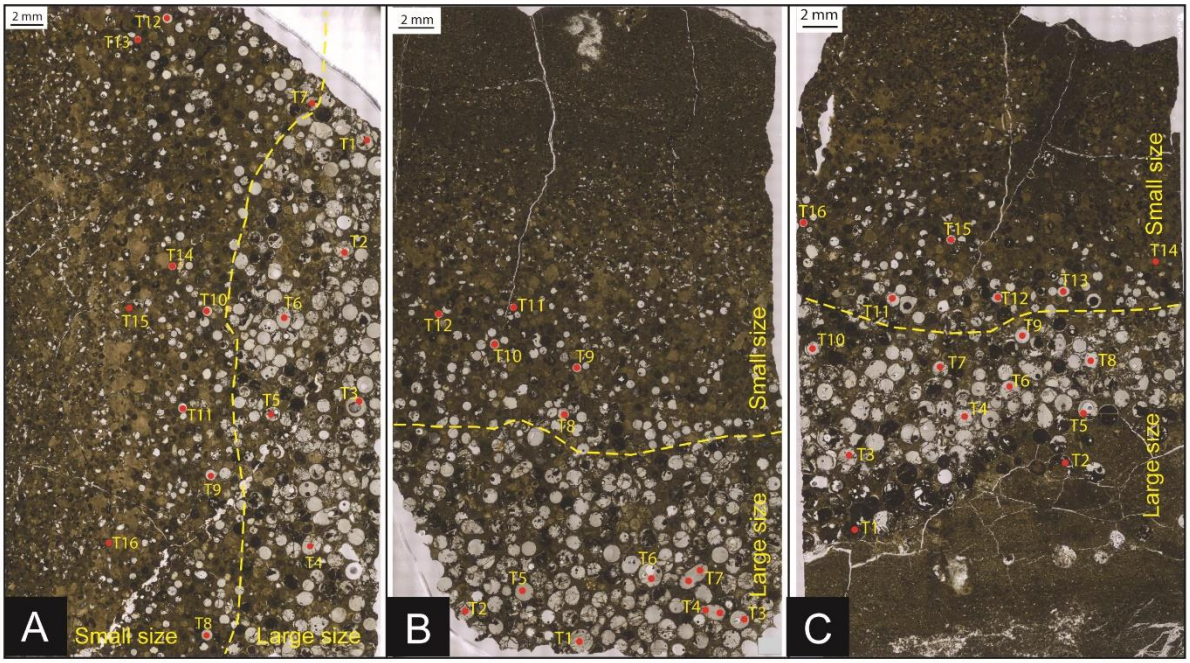

Figure 17. *Thin slide photographs from Gorgonilla spherule-rich layers. Pictures A, B and C are respectively from GI-40, -41 and -45 samples. Note a normal size-gradation of tektites in spherule-rich layers. Red points indicate tektites subject to LA-ICPMS and EPMA analyses. Yellow dashed lines delineate small and large size tektites.*

For the REE, average tektite EFs of thin section samples as well as matrix EFs relatively to average shale are nearly similar for each element (Fig. 18E). This suggests a similar REE composition of tektites and matrix. In addition, excepted Pr which shows a net enrichment relative to PAAS, all other EF values are very close to 1 (Fig. 18E) thus indicating a REE composition of matrix and tektites, very close to that of average shale composition. In contrast, the same EFs relative to Chondrite rather show a high enrichment of all tektite REE (Fig. 18F), which indicates a chemical composition of Gorgonilla reworked tektites very different of primary extraterrestrial tektites.

8. GEOCHEMICAL PROXIES

8.1. Weathering indices

Based on major element concentration, weathering indices such as Chemical Index of Alteration (CIA) from Nesbitt and Young (1982), K_2O-free CIA (CIA-K) also called Chemical Index of Weathering (CIW) from Harnois (1988), and Plagioclase Index of Alteration from Fedo et al. (1995) are commonly used to characterized the extend of weathering in order to infer paleoclimate conditions (Price and Velbel, 2003). Minerals such as illite, montmorillonites and beidellites which are formed under contrasting dry and seasonal climates, show a CIA values range between 75 and 85 whereas kaolinite, mineral of constant humid conditions, presents CIA values very close to 100 (Nesbitt and Young, 1982; Gerstch et al., 2011). Average shale CIA values ranges from 70 to 75 (Nesbitt and Young, 1982).

The weathering indices (CIA, CIA-K and PIA) of Gorgonilla section (Fig. 19) globally presents similar trends. Turbidite CIA values (65-75 %) which correlate with a high amount of smectites and illite, are more different (with positive peaks) of those of the pelagic sediments mainly during the Late Maastrichtian. This suggests different chemical weathering stages between turbidite layers and pelagic sediments during the Late Maastrichtian time. No striking difference has been observed between turbidite and pelagic sediment CIA values during the Danian stage. However, CIA values for the pelagic sediments gradually increase from the base of the section and reach the maximum Maastrichtian value (71.12 %) at sample GI-12, just above of the CF2/CF1 boundary. Across the CF1 zone, chemical weathering intensity sharply decrease towards the top reaching, at about 60 cm below the KPB, the chemical weathering minimum (CIA=58.01 %) of the entire Gorgonilla section, before slightly go back up until the KPB (Fig. 19).

The sudden variation of CIA trends as well as the other weathering indices (CIA-K, PIA; Fig.19) observed between the pelagic sediments of the uppermost CF1 zone and spherule-rich layers, marks the K/Pg transition. This suggests intensification of chemical alteration and consequently, a change of climatic conditions. The intensification of alteration pursues across the earliest Danian sediments before sharply decrease just below the P1a(2)/P1b boundary, following by a gradual recovery towards the top of section (Fig. 19).

8.2. Volcanism proxies

Several proxies, including Na/K, K/(Fe + Mg), Ca/Na, Mg/Na and Hg, are generally used in order to evaluate the detrital and/or volcanism (proximal or distal) influence in sediments and soils (see Dessert et al.,2003; Sageman and Lyons, 2003; Gertsch et al., 2011; Sial et al., 2014, 2016; Font et al. 2016, 2018). Na/K and K/(Fe + Mg) ratios reflect the increase or decrease of siliciclastic flux relative to background volcanic input (Sageman and Lyons, 2003) while a high Hg contents, in the absence of TOC, indicate a distal volcanism influence (Font et al. 2016, 2018).

The two first proxies (Na/K and K/(Fe + Mg)), with their opposite trends, show small pics in all turbidites as well as spherule-rich layers with values range from 1.40 – 2.00 for Na/K and 0.08 – 0.19 for K/(Fe + Mg) implying a volcanic input (Sageman and Lyons, 2003) as described by lithology, whereas mudstones show a more detrital issue. Moreover, Hg contents in Gorgonilla deposits are globally low (< 7 ppb; Fig. 19) relatively to usual volcanic Hg values (see Sial et al., 2013, 2014 and Font et al., 2018). This indicates that no significant volcanic pulses referring to an important volcanism have been recorded in these deposits. In contrast, the basalt weathering proxies such as Ca/Na and Mg/Na, generally used to evaluate geochemical signal of the near-shore basalt erosion (e.g., Dessert et al., 2003), present higher values. However, the opposite trends of these ratios, especially from uppermost Maastrichtian to lowermost Danian, as well as the low PIA values observed in the topmost Maastrichtian (Fig. 19), invalidate the use of these ratios as geochemical proxies in these sediments (Gertsch et al. 2011). Consequently, Gorgonilla was not a drainage domain of basalt weathering (Dessert et al., 2003).

8.3. Hydrothermal activity proxies

The hydrothermal input into sedimentary records is generally evaluated by geochemical methods through some diagnostic trace elements such as Ni, Cu, Cr and Zr (Pierret et al., 2000) and ratios such as Al/(Al + Fe + Mn) and Fe/Ti (Boström et al., 1973; Dias and Barriga, 2006; Pujol et al., 2006; Slack et al., 2009; Gerstsch et al., 2011). At the Gorgonilla KPg section, the geochemical log of Al/(Al +Fe + Mn) ratio (Fig. 19) as well as the Fe/Ti vs. Al/(Al +Fe + Mn) cross-plot (Fig. 20) of all rock unit samples show a relative high Al/(Al +Fe + Mn) ratio values, greater than 0.4 (the minimum value in normal pelagic sediments; Boström et al., 1973). In addition, no dilution or transition has been detected between metalliferous sediments (High

Fe/Ti vs. low Al/(Al +Fe + Mn); Dias and Barriga 2006 and Slack et al., 2009) and pelagic deep-see ones (Fig. 20). All the results clearly indicate that the Gorgonilla KPg section was not affected by hydrothermal activity. However, the abundance of elements typically enriched in hydrothermal plume particles (e.g., Fe, Cu, Zn, V; Cave et al., 2002), mainly observed in turbidites, spherule-rich layers and most Danian pelagic sediments, probably be linked to the influence by fallout from hydrothermal plumes from the nearby hydrothermal fields (Pan et al., 2018) for turbidites and Danian pelagic, and extraterrestrial input through tektites for spherule-rich layers.

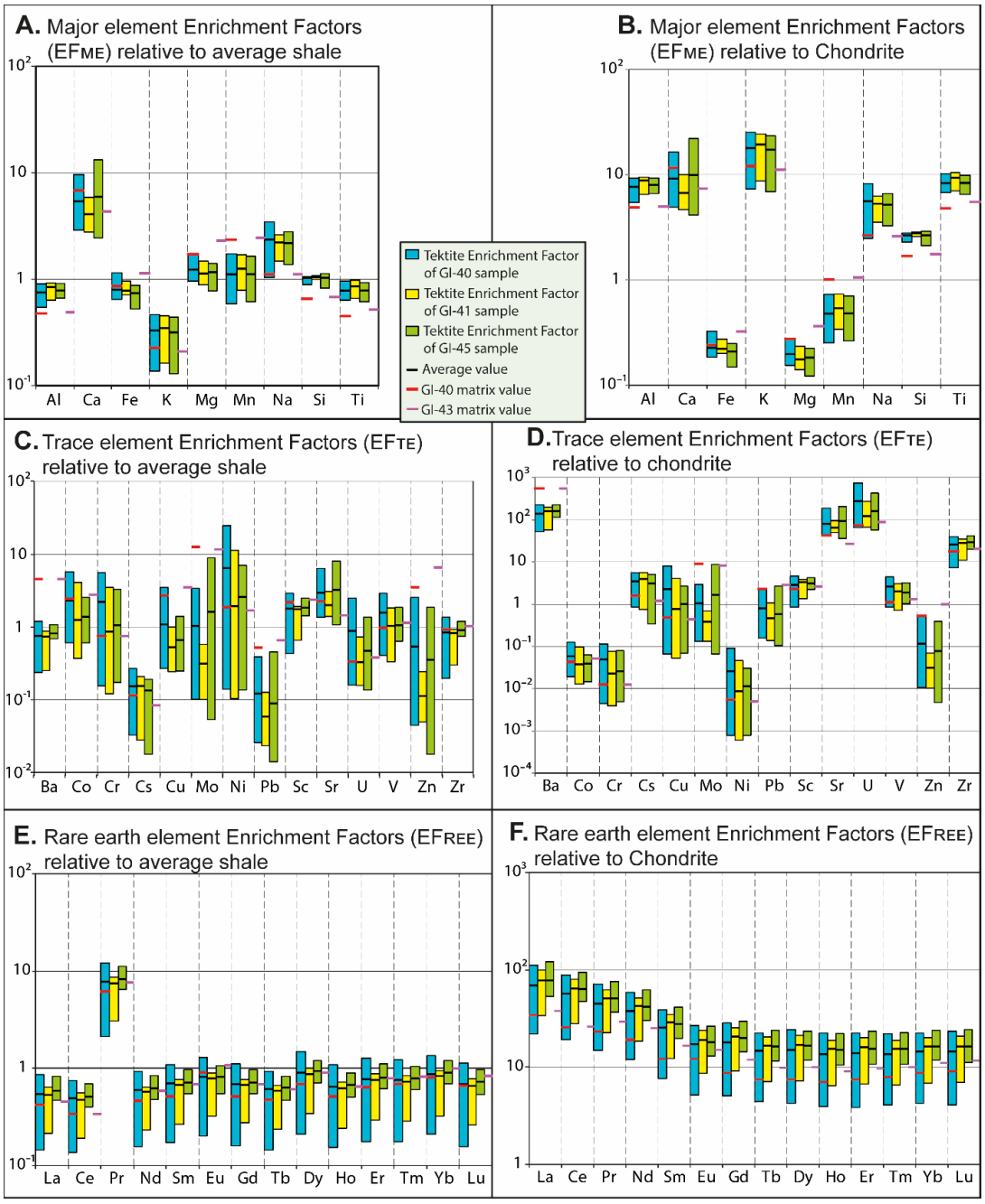

Figure 18. *Calculated enrichment factor (EF) relative to average shale (A, C and E) and to chondrite (B, D and E) for major, trace and rare earth elements measured in tektites and matrix*

from Gorgonilla spherule-rich layers. EF are calculated for tektites from GI-40 (blue boxes), -41 (yellow boxes) and -45 (green boxes) and for matrix from GI-40 (red line) and -43 (purple line). The extend of the boxes corresponds to the range of values (minimum-maximum) and the inner line to their average value.

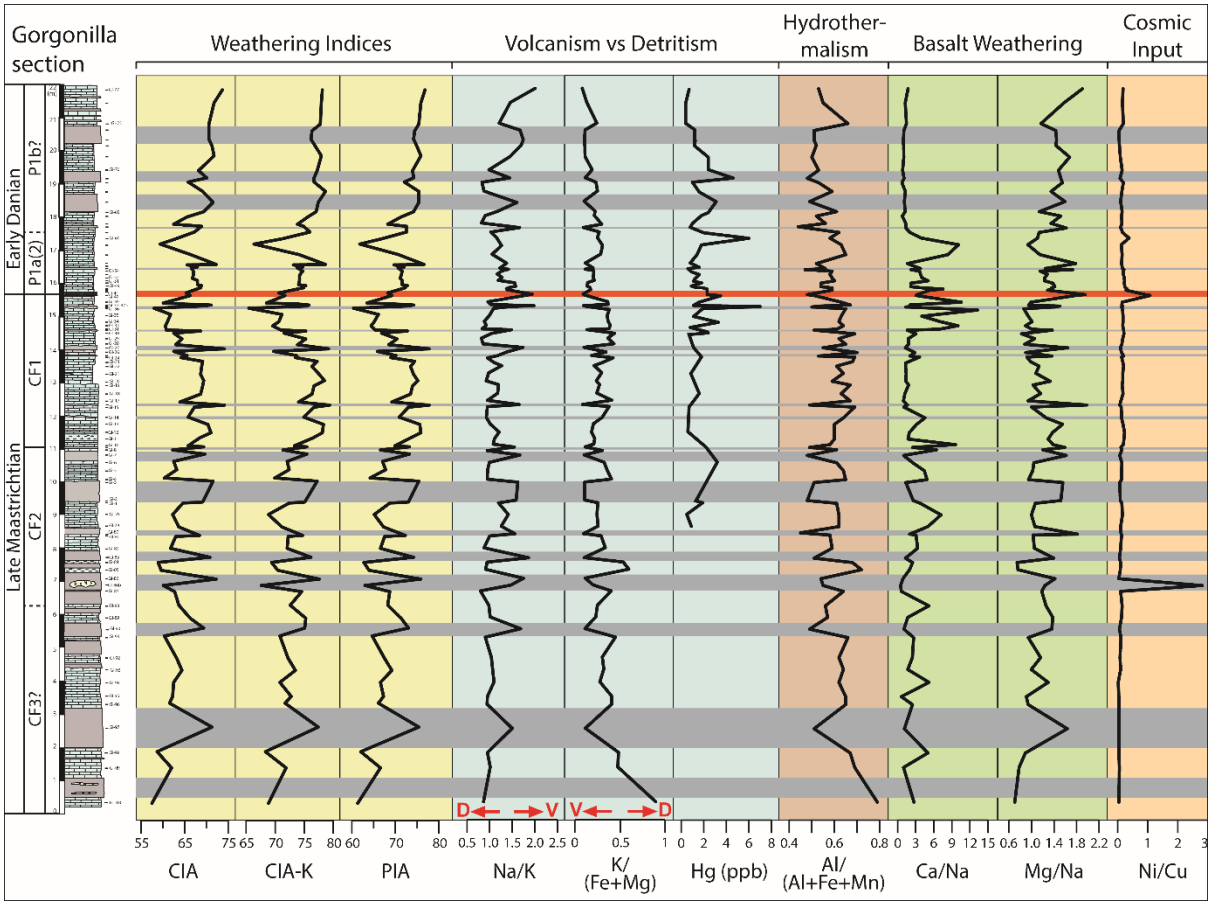

Figure 19. *Summary of all proxies used (weathering, volcanism vs. detritism, basal weathering hydrothermalism, cosmic input) based on major and trace element and mercury geochemistry.*

9. DISCUSSION

9.1. Depositional environment: lithology, microfossils assemblage and trace elements

The lithological features of the entire Gorgonilla KPg section such as the abundance of siliceous microfossils (Radiolarians), presence of typical benthic foraminifera species (e.g., *Nuttallides truempyi*; Mateo et al., 2019), poor preservation of identified planktic foraminifera as well as absence of bioturbations on sedimentary deposits, also reported by other authors (Bermudez et al., 2016, Renne et al., 2018 and Mateo et al., 2019), indicate deposition below

lysocline and probably above calcite compensation depth (CCD), within a pelagic bathyal environment as reported in section 3. This suggests an important height of water column, between 3000 – 4000 m, which is probably relatively stratified due to a more or less intense O_2-depletion with depth. Two elemental ratios from bulk geochemistry, V/Cr and V/(V + Ni), were used as reliable proxies to evaluate bottom water paleo-oxygenation (Hacht and Leventhal,1992; Jones and Manning, 1994) at Gorgonilla. It clearly appears that deposition of all lithological units (except spherule-rich layers) took place under more O_2-depleted (anoxic) conditions (Fig. 21), thus suggesting a strongly stratified water column probably due to his large height. In contrast, during deposition of spherule-rich layers, water column was weakly stratified that allowed a deposition under dysoxic conditions (Fig. 21).

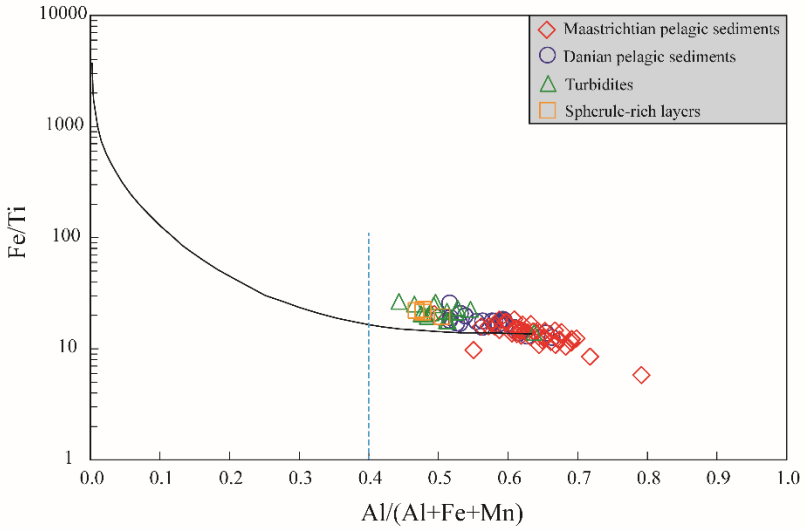

Figure 20. *Crossplot Fe/Ti vs. Al/(Al+Fe+Mn) for whole rock compositions of deposits from Gorgonilla K/Pg transect. Curved line (from Slack et al., 2009) represents the ideal mixing between Al-free hydrothermal sediments and pelagic or terrigenous sediments. Dashed blue line (from Boström et al., 1973) shows the Al/(Al+Fe+Mn) boundary between normal pelagic sediments and samples closer to hydrothermal structures.*

9.2. Diagenesis effect on clay minerals and carbonate stable isotope signatures

Clay minerals compositions are commonly used to detect diagenetic influence in sedimentary deposits through illitization and chloritization processes of smectite (Friedman and O'Neil, 1977; Deconinck and Debrabant, 1985; Chamley, 1989). For the illitization process, progressive appearance, with depth, of illite/smectite mixed-layers (I/S) characterizes burial diagenesis phenomenon in marly interbeds (Šucha et al., 1993; Lanson et al., 2009) while in the limestone beds, this is revealed by a conversion of smectites into chlorites (Deconinck,

1984; Deconinck and Debrabant, 1985; Chamley, 1989). At the Gorgonilla K/Pg section, where materials are mainly consisting by calcareous mudstones interbeded by turbidites (marly beds), no I/S has been detected in the entire section whereas smectites are relatively well represented, which would indicate an absence or a low grade of illitization (Stuben et al., 2002). In addition, the low abundance of chlorite in the upper part of the section (Danian deposits) as well as its virtual absence in the lower part (Maastrichtian sediments) (Fig. 14) is undeniable proof of the non-chloritization of smectites and, therefore, of a weak thermal diagenesis. However, it cannot be excluded that the rather limited influence of diagenesis on Gorgonilla materials, obtained from clay mineral trends, is only the result of paleoenvironmental conditions (Charbonnier et al., 2020).

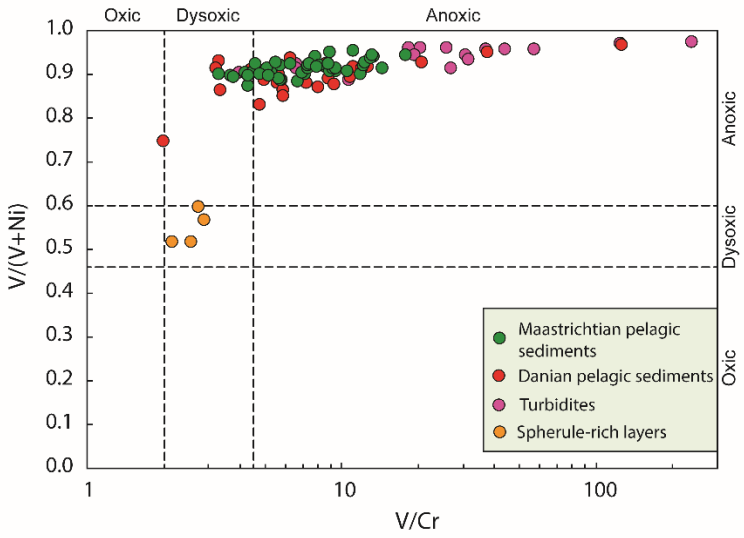

Figure 21. *Trace element cross plot (V/(V+Ni) vs. V/Cr) as redox proxies. Note dysoxic conditions for spherule-rich layers. Ranges for V/Cr and V/(V+Ni) are respectively from Jones and Manning (1994) and Hatch and Leventhal (1992). Green, red, purple and yellow spheres respectively represent Maastrichtian pelagic, Danian pelagic, turbiditic and spherule-rich layers deposits.*

Furthermore, oxygen isotope signal from original sediments is sensitive to prospective fluid-rock interactions as well as neoformation and recrystallization processes of the carbonate phases and therefore, to diagenesis (meteoric and burial) processes (Mitchell et al.,1997; Pearson et al. 2001; Oehlert and Swart, 2014; Swart, 2015; Schobben et al., 2016; Sepulveda et al. 2019; Charbonnier et al., 2020) during which primary oxygen isotopic signal could be resetting with later fluids. Also, the amount of $CaCO_3$ precipitated during these diagenetic processes can induce a significant depletion of primary carbonate isotope ($\delta^{13}C_{carb}$ and $\delta^{18}O_{carb}$) values thus involving strong or weak correlations and covariances respectively between $\delta^{13}C_{carb}$ and $\delta^{18}O_{carb}$, and $\delta^{13}C_{carb}$ and $CaCO_3$ values (Stüben et al., 2003). To this effect, using of cross

plots $\delta^{13}C_{carb}$ vs. $\delta^{18}O_{carb}$ and $\delta^{13}C_{carb}$ vs. $CaCO_3$ is required (e.g., Knauth and Kennedy, 2009; Oehlert and Swart, 2014; Schobben et al., 2016; Rodriguez-Cuicas et al., 2019; Sepulveda et al. 2019). For the case of Gorgonilla KPg section, the crossing of whole rock stable isotopes ($\delta^{13}C_{carb}$ and $\delta^{18}O_{carb}$) were made separately for Maastrichtian, KPg boundary and Danian sediments (Fig. 16). Globally, it clearly appears a weak correlation between $\delta^{13}C_{carb}$ and $\delta^{18}O_{carb}$ values for Maastrichtian ($R^2 \sim 0.10$), KPg boundary ($R^2 \sim 0.11$) and Danian ($R^2 \sim 0.37$) deposits (Fig. 6a) testifying of a weak or lack of burial diagenesis as suggested by the clay mineral assemblage, but rather a strong influence of meteoric diagenesis (Oehlert and Swart, 2014). In addition, there is no significant negative or positive covariance between $\delta^{13}C_{carb}$ signal and $CaCO_3$ content (Fig. 16b; $R^2 \sim 0.0$ for Maastrichtian; $R^2 \sim 0.05$ for KPg boundary; $R^2 \sim 0.0$ for Danian) as it would be expected from strong burial signal (Frank et al., 1999). However, the low correlation observed between $\delta^{13}C_{carb}$ and $\delta^{18}O_{carb}$ for Maastrichtian and spherule-rich layers sediments ($R^2 \sim 0.10$ and 0.11 respectively; Fig. 22a), which suddenly increases in Danian deposits ($R^2 \sim 0.37$; Fig. 16b), coincides with a relative abundance of chlorite during Danian time (Fig. 14). This could be explained by a relatively intense burial diagenesis influence in Danian sediments comparatively to Maastrichtian sediments as well as KPg boundary deposits.

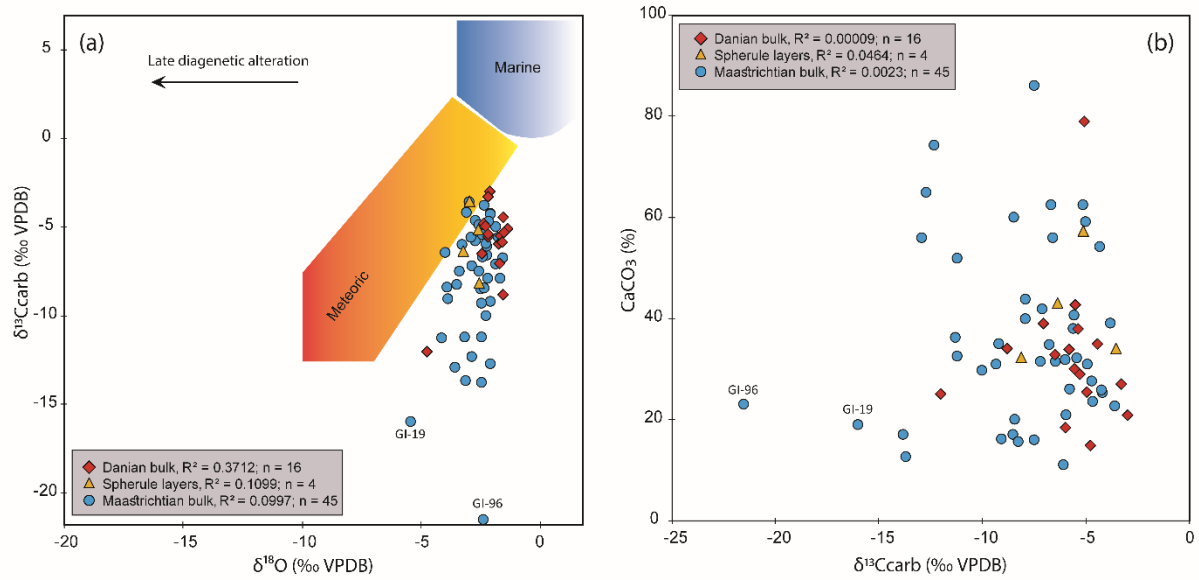

Figure 22. *Cross plots (a) $\delta^{13}C_{carb}$ vs. $\delta^{18}O$ and (b) $CaCO_3$ vs. $\delta^{13}C_{carb}$ for diagenetic overprint at Gorgonilla. Note a more meteoritic diagenesis signal and a weak correlation between $CaCO_3$ and $\delta^{13}C_{carb}$. Blue spheres, red diamonds and yellow triangles are respectively from Maastrichtian, Danian and spherule-rich layer bulk samples.*

9.3. Mineralogy, stable isotopes and CIA as climate and sea-level proxies

Several K/Pg sections from deep-water environments are recently worldwide well documented (e.g., Mateo et al., 2016; Punekar et al., 2016; Sanders et al., 2019). In these environments, changes in the weathering and erosion at the continental areas and related detrital inputs during deposition are inferred using siliciclastic proxies such as Ti/Al ratio and CIA index (Nesbitt and Young, 1982, 1989; Schlanger, 1988; Stuben et al., 2002; Rodriguez-Cuisas et al., 2019). Moreover, in the absence of any or low diagenetic influence, the quality of clay and bulk minerals assemblage as well as the whole-rock stable oxygen isotope signal also reflect climatic conditions that prevailed over the time (Chamley, 1989; Keller and Lindinger, 1989; Thiry, 2000; Adatte et al., 2002; Deconinck et al., 2003; Nascimento-Silva et al. 2011; Punekar et al., 2016). Higher values in detrital proxies coupled to decreasing $\delta^{18}O$, $CaCO_3$ content and DI values, could be interpreted as: (1) heavier rainfall and enhanced continental weathering and runoff, thus increasing of more humid conditions, as (2) lowered carbonate production in surface water, as (3) flooded period, and/or as (4) falling sea-level following marine regression (Adatte et al., 2002; Stüben et al., 2003; Nascimento-Silva et al., 2011; Rodriguez-Cuisas et al., 2019; Sepulveda et al., 2019; Charbonnier et al., 2020; Schöllorn et al., 2020).

At Gorgonilla, spontaneous fluctuations (positive or negative) in the trends of detrital proxies (including CIA, Ti/Al and DI; Fig. 23), corresponding to turbidite layers as well as a basalt fragment (sample GI-86b), are observed and correlated with an increase in the amount of smectite (Fig. 14) probably due to the abundance of volcanic components. These different fluctuations cannot be integrated as they would certainly produce misinterpretations of paleoclimate. From the bottom to top of CF3 zone, gradually increasing $\delta^{18}O_{carb}$ and Ti/Al values, and relatively high CIA combined to increased $CaCO_3$ content and DI (Fig. 23), indicate climate cooling, moderate continental weathering and runoff, and a slight rise sea-level. This zone seems to be a transition between warm episode (probably below) and cold climate. Similar climatic observations were made by Keller (2001) and Stüben et al. (2003) for the nearly time interval. In contrast, high and constant $\delta^{18}O_{carb}$ values associated to relatively low CIA values, to a gradual decrease of Ti/Al ratio and to increased CI and $CaCO_3$ content suggest, across the CF2 zone, a cold climatic episode, a low continental chemical weathering and probably a rising sea-level (Fig. 23). Although most of the $\delta^{13}C_{org}$ negative shifts are associated to substantial mortality increase and dissolution rate of organic carbon, they could also be, however, related

to glacial events (Nascimento-Silva et al., 2011) especially when they are not significant. This would be the case of CF2 zone from the Gorgonilla uppermost Maastrichtian.

Above, the two thirds of CF1 zone from the CF1/CF2 boundary are marked by a strong $\delta^{18}O_{carb}$ negative excursion which coincides with low $CaCO_3$ content and DI index (Fig. 23), thus suggesting that a large amount of fresh water inputs reaching deep-sea water, warm climate and a relatively low sea-level (Schöllorn et al., 2020). In addition, intense continental chemical weathering and runoff materialized by high CIA as well as continuous decrease but following by increasing in Ti/Al ratio values, testify, for this part of CF1 zone, of more warm/humid climatic conditions coupled to falling sea-level. Also, relatively high $\delta^{13}C_{org}$ values compared to previous zone, probably indicate a bloom interval of faunal species (Nascimento-Silva et al., 2011). At the uppermost CF1 zone prior the KPB, the numerous fluctuations but relatively high in $\delta^{18}O_{carb}$, $\delta^{13}C_{org}$ and Ti/Al ratio observed in this period as well as a lowered CIA, a higher calcium carbonate content and a relatively higher abundance in smectite (Figs. 14, 23), characterize a gradual cooling but dry episode (climatic transitional zone) leading up to the KPB and coupled to a rising sea-level. Contrary to many other worldwide K/Pg transitions where the topmost Maastrichtian is marked by a cold climate, the uppermost Maastrichtian in Gorgonilla section rather reveals transition climatic conditions, from warm/humid to progressive cooling but dry conditions. This suggests a missing part of CF1 zone, also reported by Mateo et al. (2019), where the colder climatic conditions would be reached. Moreover, the erosional surface observed at the base of spherule-rich layer (Fig. 8K), the mixed late Maastrichtian and early Danian microfossils species in pherule-rich layers (Mateo et al., 2019) and correlatively, the sudden variation in sea-level curve indicating falling (Fig. 23) also agree with this hypothesis. According to Mateo et al. (2019), this hiatus pursues during early Danian by truncating the entire P0 and P1a(1) zones as well as a part of P1a(2) zone.

The KPB and overlying sediments (lower half of P1a(2)) present colder climatic conditions inferred by relatively high $\delta^{18}O_{carb}$, DI and $CaCO_3$ values. However, the high chemical index of alteration, increase $\delta^{13}C_{org}$ and Ti/Al values and the relatively low sea-level which abruptly increases at the end of this episode, suggest a strong mixing waters and increased carbon flux due to erosion (Stüben et al., 2003) and associated to a waning turbidity current and settling of turbidite material (Mateo et al. 2019) in first. This is probably followed by deposition of tiny materials in suspension, all in relatively cold climate. This could further explain the presence in these deposits of both Maastrichtian and Danian microfossils as reported by Bermudez et al. (2016) and Mateo et al. (2019). The upper half P1a(2) zone, with

important fluctuations in $\delta^{18}O_{carb}$ and $\delta^{13}C_{org}$ and relatively high content in calcium carbonate, indicates a transition towards the more warm/humid conditions. But the rapid change in sea-level (falling) observed at the beginning of this transition presumes a possible short hiatus.

The upper part of the section corresponding to zone P1b (C29N) has rather atypical parameters. A negative shift in $\delta^{13}C_{org}$ (~ 9 ‰) coincides with a drop in $\delta^{18}O_{carb}$ (~ 3 ‰) and $\delta^{13}C_{carb}$ values at the P1a/P1b boundary (Figs. 12 and 23), which would suggest, if the drop in $\delta^{18}O_{carb}$ and $\delta^{13}C_{carb}$ continued over the entire P1b zone, a strong accumulation of organic matter probably due to mass extinction. The relatively high mercury concentrations observed during this period, which commonly originate from organic matter, would also support this hypothesis. But no organic matter abundance has been detected in these materials, that suggests mercury origin other than organic matter. This mercury as well as other acid gases were probably injected into the atmosphere by a distal volcanism (e.g., the surrounding CLIP), which are subsequently fixed by the ocean waters and would have contributed to a considerable reduction in carbonate contents by dissolution as shown by figure 12. Moreover, intense continental weathering and runoff materialized by the maximum CIA and Ti/Al values as well as the lowered calcium carbonate contents, observed during this period, suggest a warm/humid climate coupled to falling sea-level.

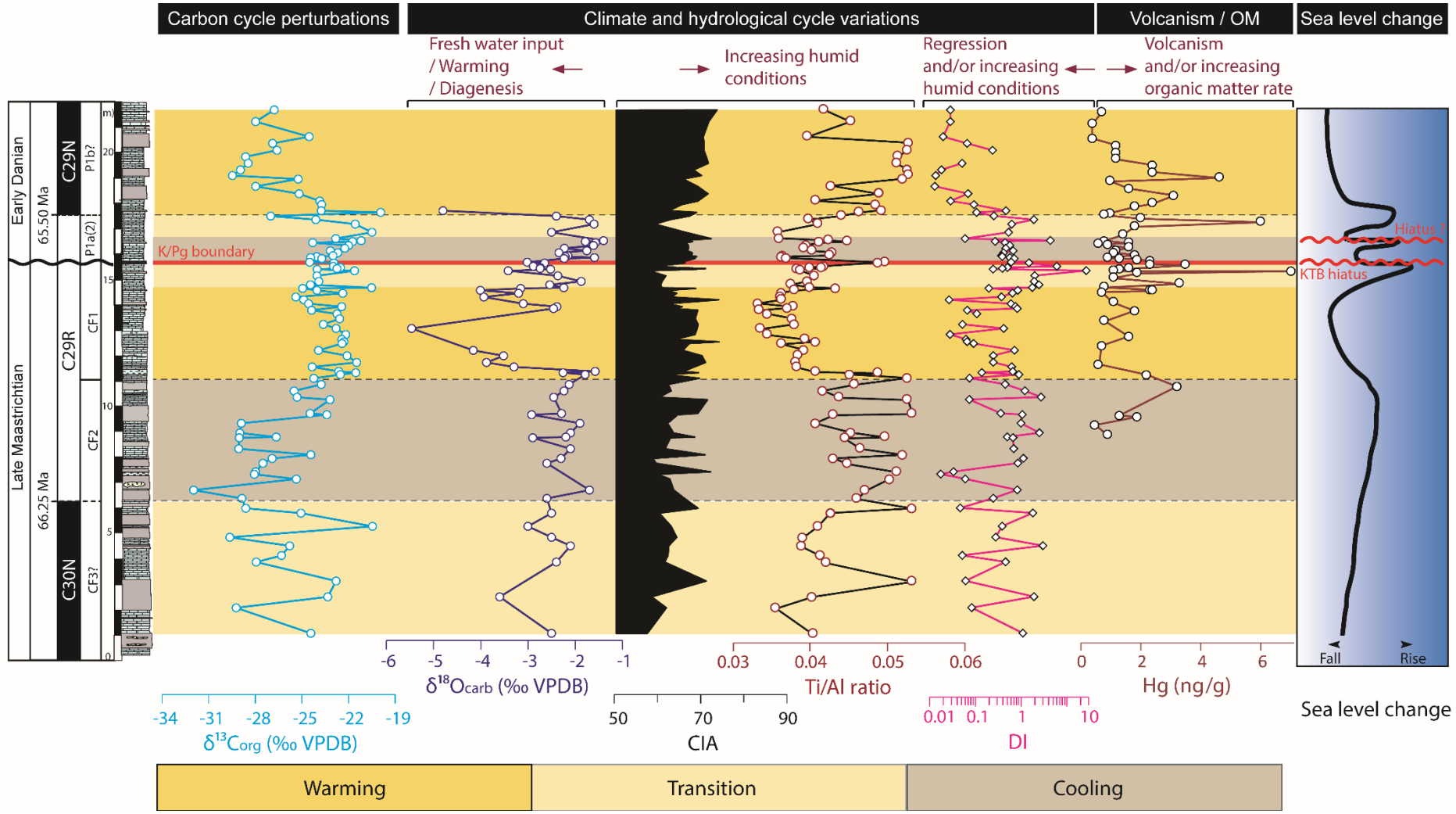

Figure 23. *Proxies of climate and the hydrological cycle compared to the carbon-isotope record, volcanism signal and sea-level change along the Gorgonilla K/Pg section*

10. CONCLUSIONS

The present study conducted on 144 samples (bulk, tektites and matrix samples) from Gorgonilla Cretaceous-Paleogene transition (Colombia) leads the following main conclusions:

i. Lithologically, materials mainly consist of light green calcareous mudstones containing a various microfossil species (including abundant radiolarians, benthic and planktic foraminifera, a few nannofossil species and sponge spicules) deposited in bathyal environment between lysocline and CCD. They alternate with dark-olive litharenites composed by eroded basaltic lithics (and/or breccia) and a large amount of plagioclases, which probably result from volcanism processes of the CLIP and reach deep sea water via turbidity currents. The KPB is materialized by a 3 cm spherules-rich layer which triplicates in one edge of outcrop due to minor syn- and post-depositional faults, and shows an erosional surface at the base. Spherules are black to light yellow with various sizes ranging from 0.80 to 1.50 mm, normally size-graded and soaked in calcareous matrix containing lithic fragments.

ii. Based on planktic biostratigraphy, carbon isotopes and carbonate production rate, five planktic biozones including CF3, CF2, CF1, P1a(2) and P1b, are highlighted as well as two hiatus, including the major KPB hiatus which is materialized by the missing of top part of zone CF1, zone P0, zone P1a(1) and lower part of zone P1a(2), and a short hiatus globally correlated by a sudden change in carbonate production rate.

iii. Tektites with a large exposure surface (large size) show a depletion in common cosmic elements and rather an enrichment in detrital elements (with a chemical composition very close to that of matrices), contrary to smaller tektites. This, combined to normal size-gradation of tektites as well as mixing Danian and Maastrichtian fossils in spherule-rich layers, suggests that a long and intense reworking of tektites preceded their deposition.

iv. No Deccan volcanism (and/or another intense distal volcanism) and hydrothermalism influences have been evidenced in Gorgonilla materials. However, hydrothermal plume particles, probably from Caribbean Large Igneous Province volcanic processes, would have impregnated Gorgonilla materials through fallout from the nearby hydrothermal fields.

v. These materials have undergone a weak thermal diagenesis that is relatively variable in Maastrichtian and Danian sediments, as evidenced by the clay mineral assemblage as well as carbonate stable isotope data.

vi. Climate is globally contrasted, passing from cooler conditions associated to a rising sea level in the first Late Maastrichtian sediments to more warm/humid conditions coupled to a falling sea level at the top of Maastrichtian and Danian periods. However, the K/Pg transition is marked by short transition and cold periods, each associated with a sudden rise in sea level and then, abruptly interrupted by a hiatus.

CHAPTER III. SEDIMENTOLOGY, MINERALOGY AND GEOCHEMISTRY OF CRETACEOUS-TERTIARY TRANSITION OF ZUMAYA SECTION, BASQUE BASIN (SPAIN): NEW INSIGHTS ON PALEOENVIRONMENT AND PALEOCLIMATE

1. INTRODUCTION

The Cretaceous-Tertiary (K/T) transitions were studied worldwide in order to understand conditions that prevailed during Late-Maastrichtian to Early-Paleocene period, and to reconstruct paleoenvironments and paleoclimates (Keller, 1993; 2008; Adatte et al., 1996; 2002; Keller et al., 1998; 2007; 2008; 2013; 2016; Kuhnt et al., 2005; Stüben et al., 2005; Ogorelec et al., 2007; Gertsch et al., 2011; Shrivastava et al., 2013; Mateo et al., 2016; Punekar et al., 2016). It is one of the most remarkable and important geological events in the history of species evolution relative to the environment. In 1991, the International Commission on Stratigraphy (ICS) and the International Union of Geological Sciences (IUGS) adopted the Tunisian El Kef section as "Global Stratotype Section and Point" (GSSP) of the K/T boundary on the base of five main criteria summarized by Keller (2011): (1) the major lithological change from carbonate-rich sediments in Late-Maastrichtian to more organic-rich clay layer in Early-Danian, called the "boundary clay", (2) the mass extinction of tropical and subtropical planktic foraminifera and calcareous nannofossils at the end of Cretaceous, (3) the first appearances of Danian species immediately above the extinction horizon, (4) chemical markers such as negative shift (2–3 ‰) in $\delta^{13}C$ values of marine carbonate at the K/T boundary clay, and (5) an iridium anomaly at the KTB with sometimes Ni-rich spinels. Numerous studies carried out around Mediterranean Sea and in the southern part of European North Atlantic margin have highlighted several K/T sections mapped in Premovic (2011). Gubbio in Italy (Alvarez et al., 1980) is one of these sections as well as Bidart in France (Perch Nielsen et al., 1985), El Kef (Perch-Nielsen, 1981a; b; Perch-Nielsen et al., 1982; Keller, 1988a; b), Elles (Karoui-Yaakoub et al., 1995; 1996; Zaghbib-Turki et al., 2000; 2001) and Ain Settara (Dupuis et al., 1998) in Tunisia, and Zumaya (Percival and Fischer, 1977; Smit and Romein, 1985), Sopelana (Orue-etxebarria, 1982, Lamolda et al., 1983) and Monte Urko (Orue-Etxebarria et al., 1991) in Spain.

The Zumaya section is one of the most complete K/T sections of southern part of European North Atlantic margin. Since Percival and Fischer (1977) till Pujalte et al. (2016), including Lamolda (1990), almost all the studies have been focused on biostratigraphy using mainly planktic foraminifera and calcareous nannofossils to reconstruct paleoenvironment changes. Few authors such as Margolis et al. (1987) added other method (stable isotope of carbon and oxygen) to the Zumaya K/T transition study. In this chapter, a multi-approach which integrates, besides biostratigraphy and stable isotopes, a combination of whole rock geochemistry, mercury, bulk and clay mineralogy and magnetic susceptibility analyses have

been applied to Zumaya K/T transition for a high resolution reconstruction of depositional environment, sea level changes and paleoclimate.

2. GEOLOGICAL AND STRATIGRAPHICAL SETTING

The Zumaya section, also called the MPI (Upper Maastrichtian, Paleocene and Ilerdian; Baceta et al., 2016), belongs to the north-eastern margin of the Basque-Cantabrian Basin (western Pyrenees) (Fig. 24). This Mesozoic-Early Tertiary basin is a pericratonic rift related to the Bay of Biscay opening and Iberian plate drift. The sediments were deposited during an interval of relative tectonic calm that preceded the main Alpine orogenic phase (Puigdefàbregas and Souquet, 1986; Vergés, 1993; Baceta, 1996; Pujalte et al., 2002). Moreover, this interval was characterised by a general transgressive trend and a predominantly warm and semiarid climatic conditions (Medus and Colombo, 1991; Schmitz and Pujalte, 2003).

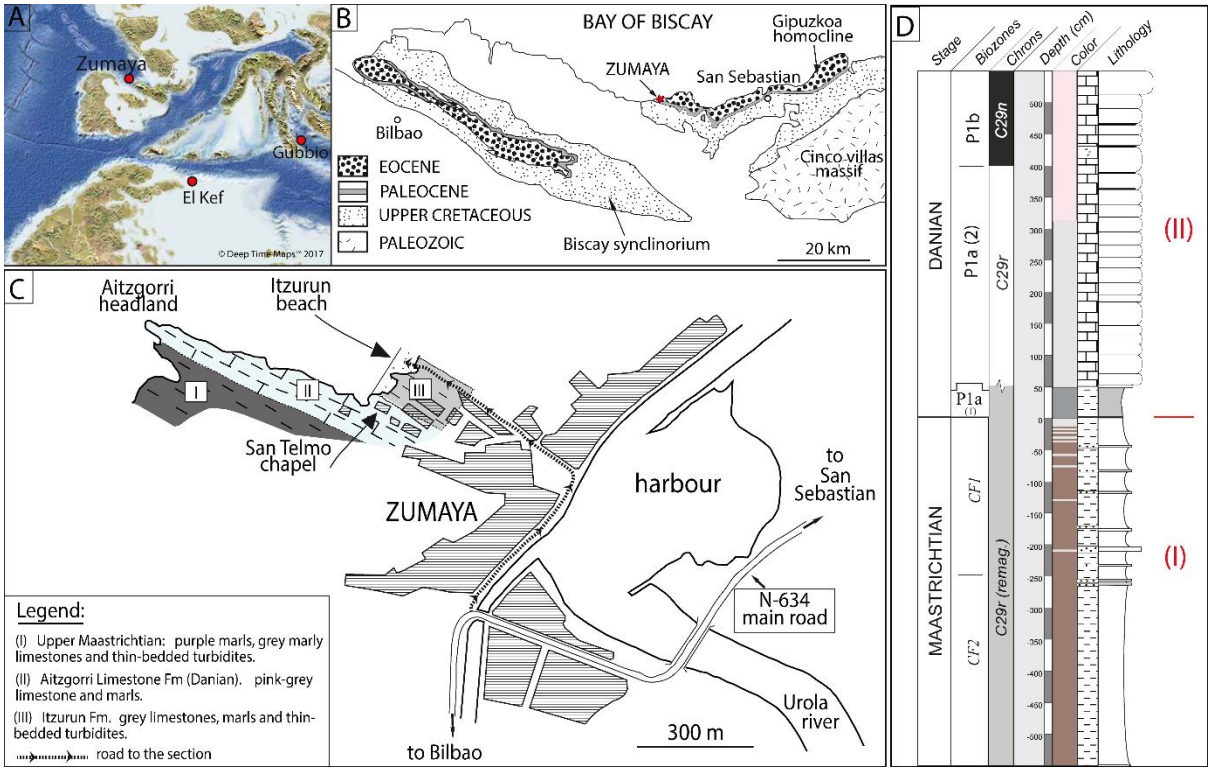

Figure 24*. (A) Generalized early Paleogene paleogeographic map of Western Mediterranean area (from Deep Time Maps 2017); (B) Simplified geological map of the Basque Basin, showing outcrops and location of Zumaya beach section, and (C) Geological map of the Cretaceous-Lower Paleogene outcrops in the Zumaya area (from Schmitz et al., 2011 modified); (D) Revised lithostratigraphical log of Zumaya beach matched to foraminifera biozones and chronostratigraphic units across the K/Pg boundary.*

Zumaya's is lithologically and stratigraphically made up of four units (see Fig. 24C): (1) the Zumaya- Algorri (Mathey, 1982); (2) the Aitzgorri Limestone Fm (Bernaola et al., 2009); (3) the Itzurun Fm (Baceta et al., 2004); and (4) the Eocene Flysch (Baceta et al., 2016). Lithological descriptions of these units are provided by Pujalte et al. (2016).

According to Baceta and Pujalte (2016), the detailed stratigraphy of the K/Pg boundary in the Basque Basin (including Zumaya section) represents five well-defined lithologic intervals (Fig. 24D). Some of them may be locally missing due to tectonic deformation during the Alpine Orogeny:

- *Interval 1* (upper Maastrichtian) includes 20-30 cm thick of alternated grey and reddish marls, marked by two biozones (Abathomphalus mayaroensis and Micula). At Zumaya, this interval consists of intercalations of thin mixed carbonate-siliciclastic turbidites with silt/fine sand sized detritic quartz (50-65 %) and tests of planktic foraminifera (10-20%) embedded in a matrix of micritic mud.

- *Interval 2* (uppermost Masstrichtian) is mainly characterized by a gradual but rapid decrease in the carbonate content with an abundance of calcareous plankton, clearly marked by the uppermost part of Abathomphalus mayaroensis and Micula prinsii biozones.

- *Interval 3* (K/Pg boundary clay) consists of three clay layers of variable thickness, where the lowest (a) is a grey or yellowish silty bed that usually contains planktic foraminifera tests with indications of dissolution. The intermediate layer (b) is a reddish to brownish siltstone where microspherules with Ni-rich spinel crystals are significantly present. The uppermost layer (c) includes thinly laminated, dark grey siltstones. The highest iridium anomaly occurs at the contact between the upper two layers. In the Zumaya section, boundary clay is not laterally continuous but it appears as small patches.

- *Interval 4* (lowermost Danian) which corresponds to a succession of grey marls that become marlstones in the upper part is characterized by several biozones (Gb. cretacea and Civisina euskalherriensis biozones; Biantholithus sparsus biozone). The first 4 cm of this interval have darker color in the Zumaya section.

- *Interval 5* (lower Danian) is mainly composed of hemipelagic limestones with minor intercalations of hemipelagic marls. In the Zumaya section there are also a few turbidites of mixed composition.

3. LOCATION AND METHODS

3.1. Location and sample preparations

The Zumaya section, latitude / longitude: 42°18.00'N / 2°15.30'W, is located in the coast of the Gipuzkoa province, between the cities of Bilbao and San Sebastian (Fig. 24). One hundred and thirteen (113) samples have been collected and a detailed description of each one is subsequently made. These samples were dried at 45 °C and a part of each one crushed in an agate mortar and subjected to bulk mineralogy, geochemistry, mercury and total organic carbon (TOC) analyses. The remaining part of each sample have been used for the clay mineralogy and biostratigraphy analyses.

3.2. XRD mineralogy

Mineralogy analyses were performed at the University of Lausanne using a X-TRA Thermo-ARL Diffractometer based on semi-quantitative method, following the procedure described in Klug and Alexander (1974), Kübler (1987) and Adatte et al. (1996). The whole rock mineralogical composition was obtained by XRD patterns on 800 mg of random powder samples pressed (20 bars) into a powder holder. External standards are used with error margins between 5 and 10% for the phyllosilicate and 5% for grain minerals.

For the clay mineral fraction, triturated samples are introduced into glass containers with deionized water and then decarbonized by HCl 10% (1.25 N) during 20 minutes, including an ultrasonic disaggregation of 3 minutes for each sample. The insoluble residues are washed by centrifugation and repeated until a neutral solution (pH 7) is obtained. Following the Stockes law, two granulometric fractions (<2 μm and 2–16 μm) are pipetted and deposited on a glass plate. After air-drying, samples are analyzed by XRD. Subsequently, the <2 μm fraction samples are saturated with ethylen-glycol and remeasured in order to check for swelling minerals. This method allows the semi-quantification of the proportion of clay minerals with a precision higher than 5%.

3.3. Whole rock geochemistry

Major (MEs) and trace (TEs) element concentrations were determinated by X-ray Fluorescence Spectrometry (XRFS) using a PANalytical PW2400 spectrometer at the

University of Lausanne based on different standard reference materials (NIM-G, NIM-N, SY-2, JCH-1, BHVO). Major elements were determined on fused lithium tetraborate glass discs. Samples were first heated to 1050 °C in an oven in order to determinate the loss of ignition (LOI). Then, 1.2000 ± 0.0002 g of ignited sample was mixed with 6.0000 ± 0.0002 g of lithium tetraborate ($Li_2B_4O_7$) and placed in a Bead machine PerlX'3 at 1250 °C to obtain the fused tablet. The obtained concentrations are given in weight percentages (wt.%). Trace element analyses were performed on pressed discs after mixing 15% of the powered samples with Mowiol 2%. The pressed discs were then placed in an oven at 110 °C for at least 6 hours before analysis by XRFS. The trace element concentrations are given in parts per million (ppm).

3.4. Stable isotopes

Stable carbon and oxygen isotope ratios ($\delta^{13}C_{carb}$ and $\delta^{18}O_{carb}$ values) were measured in whole rock samples following the procedure described by Spangenberg and Herlec (2006). The analyses were performed in aliquots of powdered whole rock samples (variable size depending on the $CaCO_3$ content) using a Thermo Fisher Scientific (Bremen, Germany) Gas Bench II carbonate preparation device connected to a Delta Plus XL isotope ratio mass spectrometer. The CO_2 extraction was done by reaction with anhydrous phosphoric acid at 70 °C. The stable carbon and oxygen isotope ratios are reported in the delta (δ) notation as the per mil (‰) deviation relative to the Vienna Pee Dee belemnite standard (VPDB). The standardization of the $\delta^{13}C_{carb}$ and $\delta^{18}O_{carb}$ values relative to the international VPDB scale was done by calibration of the reference gases and working standards with IAEA standards. Analytical uncertainty (2σ) monitored by replicate analyses of the international calcite standard NBS-19 and the laboratory standard Carrara Marble was not greater than ± 0.05 ‰ for $\delta^{13}C$ and ± 0.1 ‰ for $\delta^{18}O$.

The organic carbon isotope ratio ($\delta^{13}C_{org}$ values in ‰ VPDB) was determined from decarbonated (10% HCl treatment) samples based on continuous flow elemental analyser/isotope ratio mass spectrometry (EA/IRMS), as described previously (Spangenberg et al., 2010). Aliquots of samples were flash-combusted on a Carlo Erba 1108 (Milan, Italy) elemental analyser connected to a Thermo Fisher Scientific Delta V (Bremen, Germany) isotope ratio mass spectrometer that was operated in the continuous helium flow mode via a Conflo III split interface for the determination of the isotopic composition of the produced CO_2. Reproducibility and accuracy are better than ±0.1‰ for $\delta^{13}C_{org}$.

3.5. Total organic carbon (TOC*)*

Organic matter content was determined using Rock Eval 6 with an IFP16000 as standard following the method described by Behar et al. (2001). Samples were placed in an oven and first heated at 300 °C under an inert atmosphere and then gradually pyrolysed up to 650 °C. After the pyrolysis is completed, the samples are transferred into another oven and gradually heated up to 850 °C in the presence of air. The determined parameters are total organic carbon (TOC), Hydrogen Index (HI as mg HC/g TOC) and Oxygen Index (OI as mg CO_2/g TOC), which permit an overall characterization of the sedimentary organic.

3.6. Mercury (Hg) analysis

Hg content was determined using the Zeeman R-915F (Lumex, St. Petersburg, Russia), a high-frequency atomic absorption spectrometer specifically designed for Hg determination with a detection limit of 0.3–3 ppb. Measurements are based on the direct thermal evaporation of Hg from solid samples, without chemical pretreatment. Analyses were conducted on two aliquots. The accuracy was confirmed by the analysis of GSD-11 certified reference materials, from Chinese alluvium (Zintwana et al., 2012) with a Hg content of 72.0 ppb.

3.7. Biostratigraphy

Biostratigraphic and faunal analyses based on planktic foraminifera were performed at Princeton University, from washed sediment residues (method described in Keller et al., 1995) and thin sectioning at the University of Lausanne. Quantitative species analysis was based on washed residues of the fine fraction (38-63μm) to evaluate dwarfing, >63μm to assess dominant species components, and the >150μm size fraction was searched for rare large species. A total of 34 samples with an average spacing of 15 cm were analyzed for the top 5 m of the Maastrichtian. For the 5.5 m of the early Danian a total of 15 samples yielded good faunal assemblages for biostratigraphic analysis but only the 50 cm above the KPB yielded well preserved fauna for quantitative analysis. Biostratigraphic zonation is based on Keller et al., 1995; Keller, 2014) with biozones correlated with the El Kef KPB stratotype and auxiliary stratotype at Elles, Tunsia.

3.8. Magnetic susceptibility analysis

Rock magnetic experiments were performed in the Paleomagnetism Laboratory of the Instituto Dom Luís (IDL) of Lisbon, Portugal, and consist of magnetic susceptibility (MS) measurements. Rock fragments were crushed by using an agate mortar and filled within typical cubic plastic boxes of 8 cm^3 in volume. Mass specific magnetic susceptibility was measured with a MFK1 (AGICO) apparatus and reported relative to mass (m^3/kg). Frequency-dependent magnetic susceptibility (Kfd) was calculated by using the following formula: Kfd (%) = [(Klf-Khf)/Klf]×100; where lf is the low frequency (976 Hz) and hf is the high frequency (15916 Hz).

4. RESULTS

4.1. Lithology

About 11 m of sediment thickness (5.5 m of both K/T boundary side) have been studied in Zumaya (Figs. 24D and 25A). The late Maastrichtian sediments below the KTB clay consists of about 5 m of dark reddish marlstones extensively crossed by thin turbidites correlates to CF2 and CF1 zones and remagnetized C29r (Figs. 24D, 25A and B). These marls are increasingly clear to the top passing gradually over about 25 cm to light red color, then to light grey (pre-KTB layer; Z-77) just below the K/T boundary. Some biotubations (Figs. 25C and D) are also identified in this part.

K/T boundary (KTB) in this section is a 3 cm thick well differentiated layer, composed of three levels (Fig. 25E): (1) 2 cm thick basal yellowish and bioclastic-rich layer named KTB-1 (sample Z-78). This layer show undulation at its top, suggesting erosion after formation; (2) KTB-2 is a 0.8 cm thick discontinuous thin grey clay layer (sample Z-79) which overcomes KTB-1; (3) the uppermost layer (KTB-3), not sampled in this study, is a very thin yellowish bioclastic level of about 0,2 cm. The top of the KTB bed is clearly marked on a large scale by distinct undulations, characteristic of an erosional surface. This bed is the onset place of the δ13C shift (Fig. 25F). Using biostratigraphic data, it is correlated to uppermost part of the CF1 biozone (Fig. 26) and corresponds to C29r remagnetized chron (Font et al., 2018).

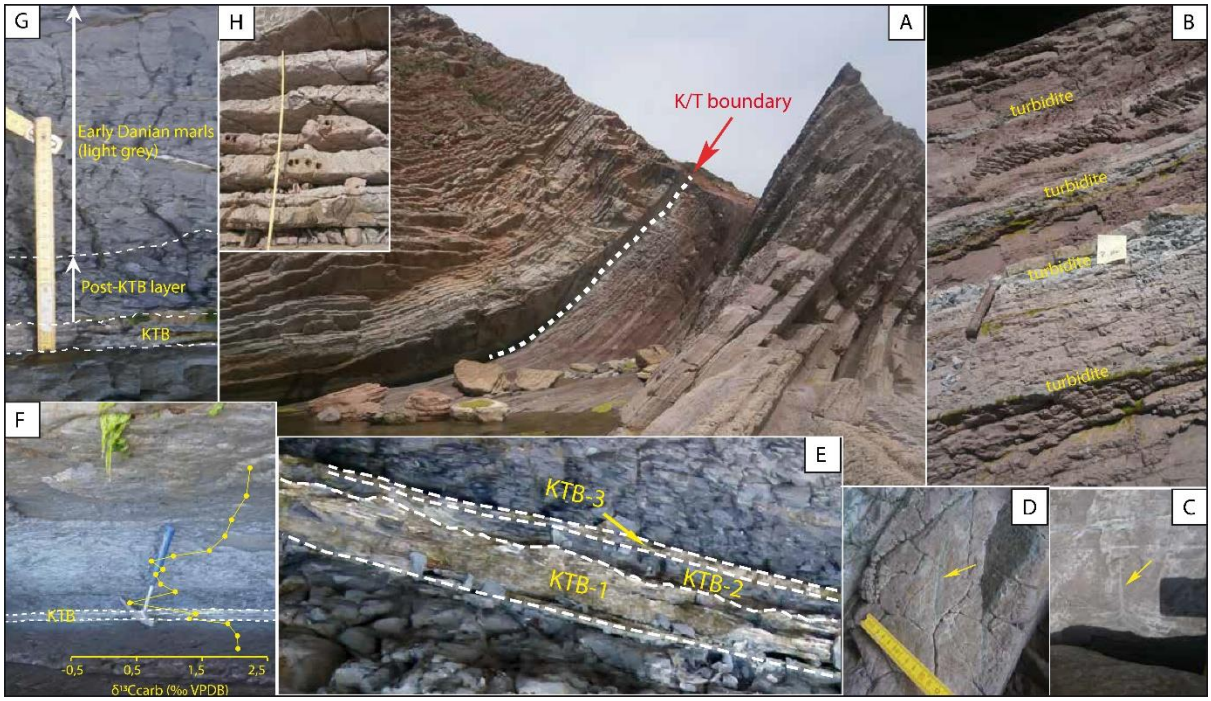

Figure 25. *Detailed lithology of the Zumaya beach K/T transition; (A) General overview of Zumaya K/T section; (B) Late Maastrichtian red marlstone cut crossed by thin turbidite layers; (C) & D) Bioturbations in Maastrichtian red marlstones; (E) Detailed Zumaya KTB level; (F) Zumaya K/T boundary (KPB) and early Danian marls matched to* $\delta^{13}C_{carb}$ *excursion; (G) Detailed succession of layers across the K/T transition; (H) Light grey to pink Danian limestones of Zumaya area.*

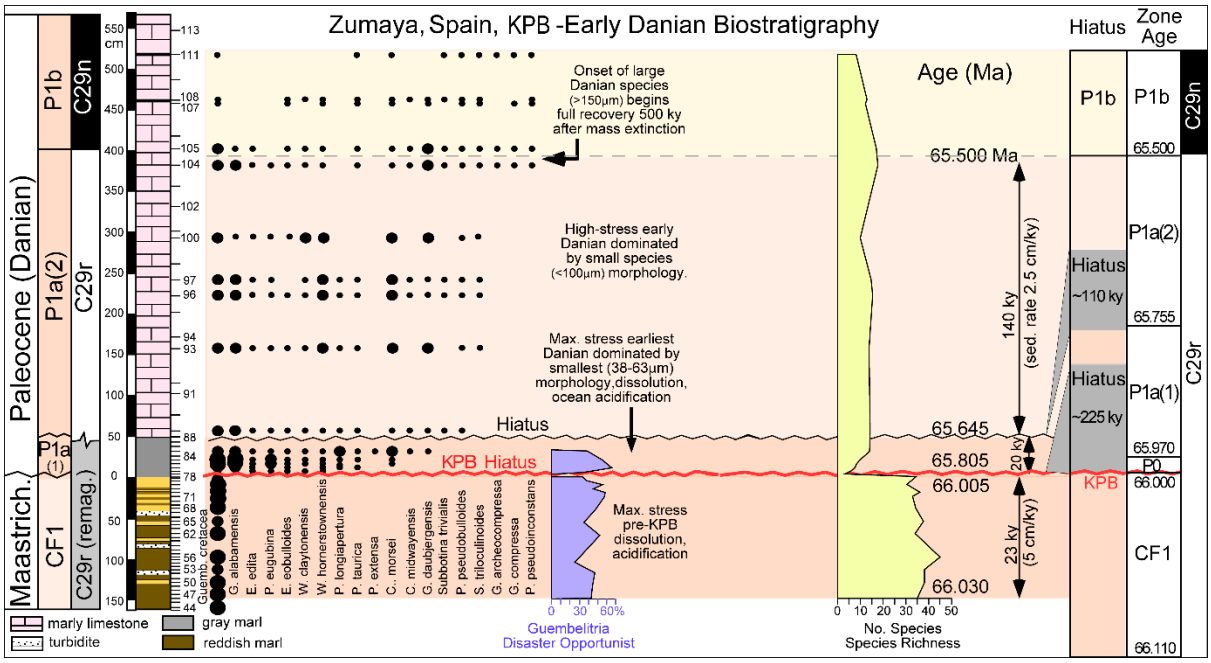

Figure 26*. New biostratigraphy zonation of Zumaya K/T section.*

A 40 cm thick grey marlstone level overlies the KTB. This level is clay-rich and dark in the first centimeters close to the KTB level (post-KTB layer: Z-80; Fig. 25G). It becomes clay-depleted, carbonate-rich and light grey few centimeters above the dark clay-rich portion with contact with KTB clay (samples Z-81 to 89) (Fig. 25G). This marly level was setup during 20 kyrs and corresponds to the upper part of P1a(1) biozone (Fig. 26). The followed massive limestone beds (Early Danian) present various thickness and color. They are light grey (P1a(2) zone), pink (P1a(2) – P1b zones), and overcome the post-KTB marly level (Figs. 25H) while presenting thin interbedded marls layers at the top (Z-108; Z-111).

4.2. Biostratigraphy

The most important planktic foraminiferal index species for the latest Maastrichtian is *Plummerita hantkeninoides,* which marks CF1 zone and corresponds to the upper part of C29r below the KTB. This species has not been previously reported in Zumaya, but was observed at Sopelana at 4.57m below KTB and inferred in Zumaya at ~4.00 m below KTB based on cyclostratigraphic correlation with Sopelana (Batenburg et al., 2012). Foraminifera at Zumaya consist mainly of internal molds of foraminifera, which do not preserve the characteristic spines of *Plummerita hantkeninoides.* However, *Plummerita hantkeninoides* can be identified based on characteristic chamber elongation preceding spinal development, similar to those illustrated by Robascynski et al. (1984). The first *P. hantkeninoides* at Zumaya were found 4.00 m below the KTB, similar to that of Sopelana in Batenburg et al. (2012) studies. Planktic foraminiferal assemblages in CF1 zone reveal high-stress marine environment characteristics marked by relatively low diversity (average 40 species), low abundance and sporadic occurrences of large specialized species (globotrunanids) dominated by low oxygen tolerant biserial species and dwarfed disaster opportunist *Guembelitria* (Fig. 26).

Abrupt termination of all Cretaceous species, except *Guembelitria cretacea*, marks the mass extinction at Zumaya and rare reworked Cretaceous species are present in the early Danian. This abrupt termination marks a hiatus across the KTB (Fig. 26) as also observed at Bidart (France) (Punekar et al., 2016). In KTB complete evolution sections of the earliest Danian species occurs in the boundary clay (zone P0) where five species evolved within a few thousand years after the mass extinction (Keller et al., 1995, 2002). The first appearances of *Parvularugoglobigerina eugubina* and *P. longiapertura* mark the P0/P1a(1) boundary. At Zumaya zone P0 and most of zone P1a(1) are missing due to a KTB hiatus. The index taxon, *P. eugubina,* is already present in the 1cm above the extinction level followed by 7 new Danian

species which are within the first 10 cm above the KTB (Fig. 26). By 30 cm above the KTB hiatus, a total of 14 Danian species are present and at 50 cm the first *Parasubbotina pseudobulloides* appear marking the subdivision of the *P. eugubina* zone into P1a(1)/P1a(2). The short P1a(1) interval and absence of P0 indicates a KTB hiatus that likely eroded part of the top Maastrichtian. This hiatus may account for the small Ir anomaly and boundary clay, as well as absence of small survivor species in zone P1a(1).

Another hiatus is indicated at the P1a(1)/P1a(2) boundary by a dramatic lithologic change from Maastrichtian type marls to pink limestone. Species morphologies in P1a(2) are slightly larger and assemblages change from *P. eugubina* and *Guembelitria* dominated to biserial low oxygen tolerant which is characteristic of this zone. Another abrupt faunal change occurs at 4 m above the KTB hiatus with the extinction of *P. eugubina* and *P. longiapertura* and reduced abundance of *Guembelitria* species that thrived during high-stress environments. Abruptly above this interval the first larger Danian morphologies appear (>150μm), and mark the onset of full recovery after the mass extinction.

Hiatuses are commonly present worldwide at the KPB, P1a(1)/P1a(2), and P1a(2)/P1b boundary in shallow and deep marine sections and correlate with sea level fluctuations. (e.g., MacLeod and Keller, 1991; Keller et al., 2016; Mateo et al., 2016).

4.3. Mineralogy

4.3.1. Whole rock mineralogy

The bulk mineralogical assemblage at the K/T transition of Zumaya is mainly consist of calcite, phyllosilicates and quartz. There are also minor amounts of Na-plagioclases and sometimes K-feldspar, dolomite and unquantified fraction (Fig. 27, Annex IV.1). Red marlstone of CF2 and CF1 zones (turbidites not included) present increased proportions of phyllosilicates (mean value: 35.93 %) and calcite (44.01 % as mean value), fairly high content in quartz (mean value: 14.88 %) and low content in sodic-plagioclase (average value: 2.91 %). Average detrital index (DI) of these materials is 0.84. Turbiditic layers that crossed red marlstone present an increased average detritus amounts (28.94 % of phyllosilicates and 27.34 % of quartz) and diminished average calcite content (37.11 %), with consequently a low detrital index (DI = 0.59). Sodic-plagioclases are also present (mean value: 5.50 %). Near the K/T boundary where marlstones become light grey (pre-KTB layer, Z-77), there is a slight decrease in calcite abundance (42.70 %), quartz (14.15 %) and Na-plagioclases (2.30 %) relative to

average red marlstone values, in contrast to phyllosilicate content (37,31 %) which slightly increase suggesting a higher chemical weathering.

At KTB-1, a sharp increase in calcite (72.92 %) coincides with a drop of phyllosilicates (16.41 %) and quartz (9.95 %) contents, and a complete disappearance of sodic-plagioclases. Detrital index (2.77) reaches his maximum value suggesting a very low chemical weathering and probably a higher sea level. In KTB-2, the sudden enrichment in Na-plagioclases (maximum value: 8.25%), yet absent in KTB-1 correlates to a net decrease of calcite content (54.02%) and a slight increase in phyllosilicates (24.02%) and quartz (11.82%) relative to KTB-1, suggesting a relatively low chemical weathering and decreased sea level as reflected by detrital index (DI = 1.23). Above of K/T boundary clay, dark grey marls (pre-KTB layer) associated to P1a (1) sub-zone present an atypical bulk mineralogical composition. Phyllosilicates (44.94 %) and quartz (27.85 %) contents have notably increased while calcite (19.41 %) abundance drops. Na-plagioclases (3.05 %) and K-feldspaths (1.15 %) are also in traces and, the very low DI (0.25) implies a very high detritism. They are overcomed by more carbonated ligh grey marls (average content in calcite: 46.42 %) always associated to P1a (1) sub-zone, with moderated contents in quartz (18.51 %) and phyllosilicates (28.41 %). Average content of Na-plagioclase (3.05%) remains unchanged, whereas DI = 0.95 (mean value) exhibits relatively high detritism. Furthermore, the early Danian limestones of the upper part of studied Zumaya section are characterized by average contents of 7,80 % of phyllosilicates, 3.58 % of quartz and 86.58 % of calcite and a deficit in feldspars.

4.3.2. Clay mineralogy

In the studied transect, clay mineral aggregations consist of interstratified (IS), mica, kaolinite and chlorite (Fig. 28). Red marlstones and turbidites cut crossing them present roughly similar clay mineral contents. For example, 18.11 % and 17.86 % for the kaolinite mean values, 52.16 % and 54.20 % for mica, 14.78 % and 14.03 % for IS, and 14.95 % and 13.91 % for chlorite, respectively for red marlstones and turbidites. Interstratified (IS: 19.05 %) and mica (55.11 %) contents increase in the fine grey marl layer near the K/T boundary (Z-77) whereas kaolinite (13.78 %) and chlorite (12.07 %) contents decrease slightly. At the basal layer of the K/T boundary (sample Z-78), the drop in mica content (36.63 %) and gradual decrease in chlorite (11.60 %) coincide with a sharp and moderate increase in kaolinite (up to 30.47 %) and IS (21.29 %) respectively.

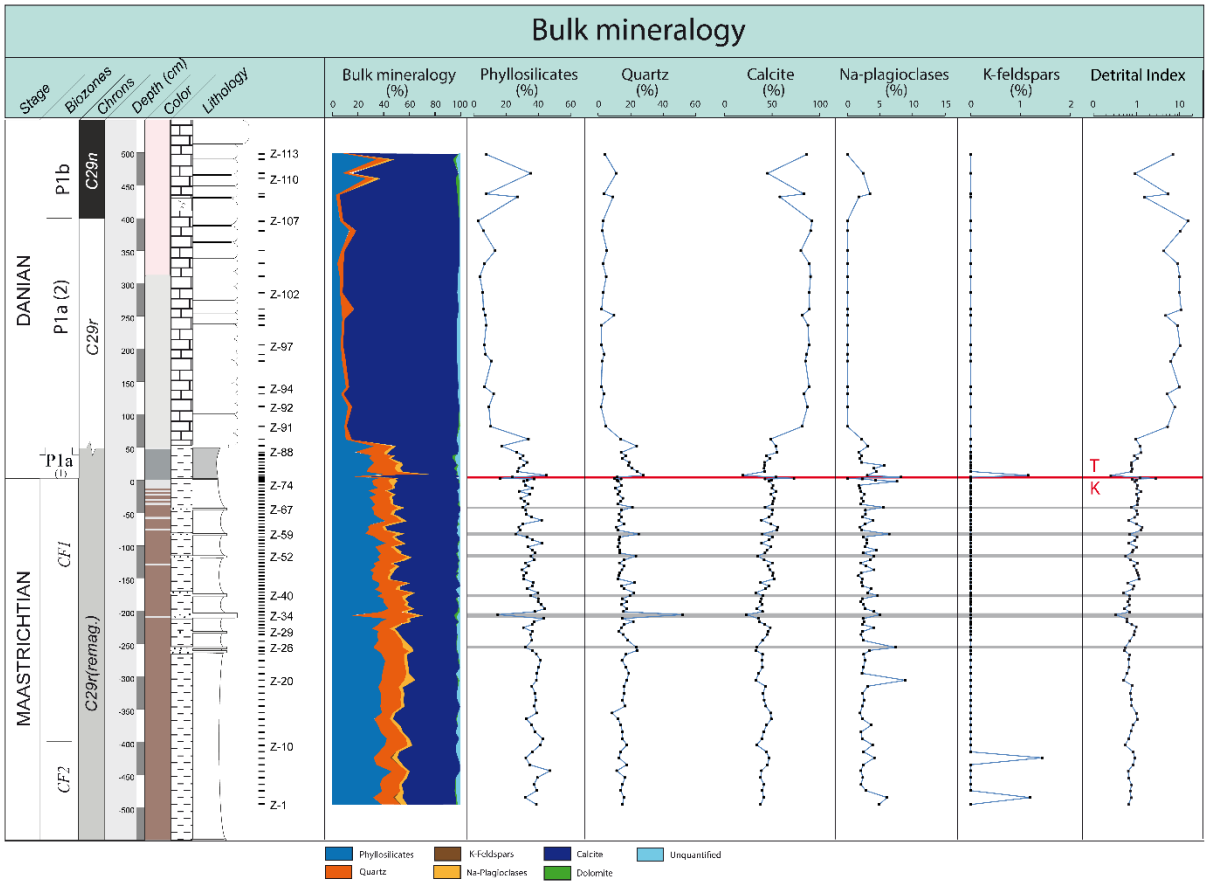

Figure 27. *Bulk mineralogical composition at the Zumaya transect. Note the decreased phyllosilicates and quartz, and increase of calcite abundance in K/T boundary clay (KTB-1 and -2) associated to a drop in Na-plagioclases in KTB-1 which sharply increase in KTB-2. The first 50 cm above KTB clay show relatively high contents in detrital minerals (phyllosilicates and quartz) with a maximum in the post- KTB layer.*

The intermediate clayey layer of the K/T boundary is characterized by rapid increase in IS (28.44 %) and mica (50.41 %) which is concomitant with abrupt decrease in kaolinite (15.23 %) and chlorite (5.92 %). Above the K/T boundary, dark grey marls (Z-80) present a slight decrease of IS content (24.32 %), moderate increase in kaolinite (18.69 %) and chlorite (7.47 %), and similar mica content (49.52 %) relatively to intermediate clay layer of K/T boundary. In the light grey marls which overcome previous marl level, mica (mean value 55.05 %) and chlorite (mean value 10.14 %) contents increase gradually while IS (mean value 17.16 %) and kaolinite (mean value 17.66 %) contents decrease. This average clay composition is similar to the grey marls composition observed below K/T boundary. Mica (mean value 49.52 %) is the major component of limestones, followed by IS (mean value 18.02 %), chlorite (mean value 17.19 %) and kaolinite (mean value 15.27%).

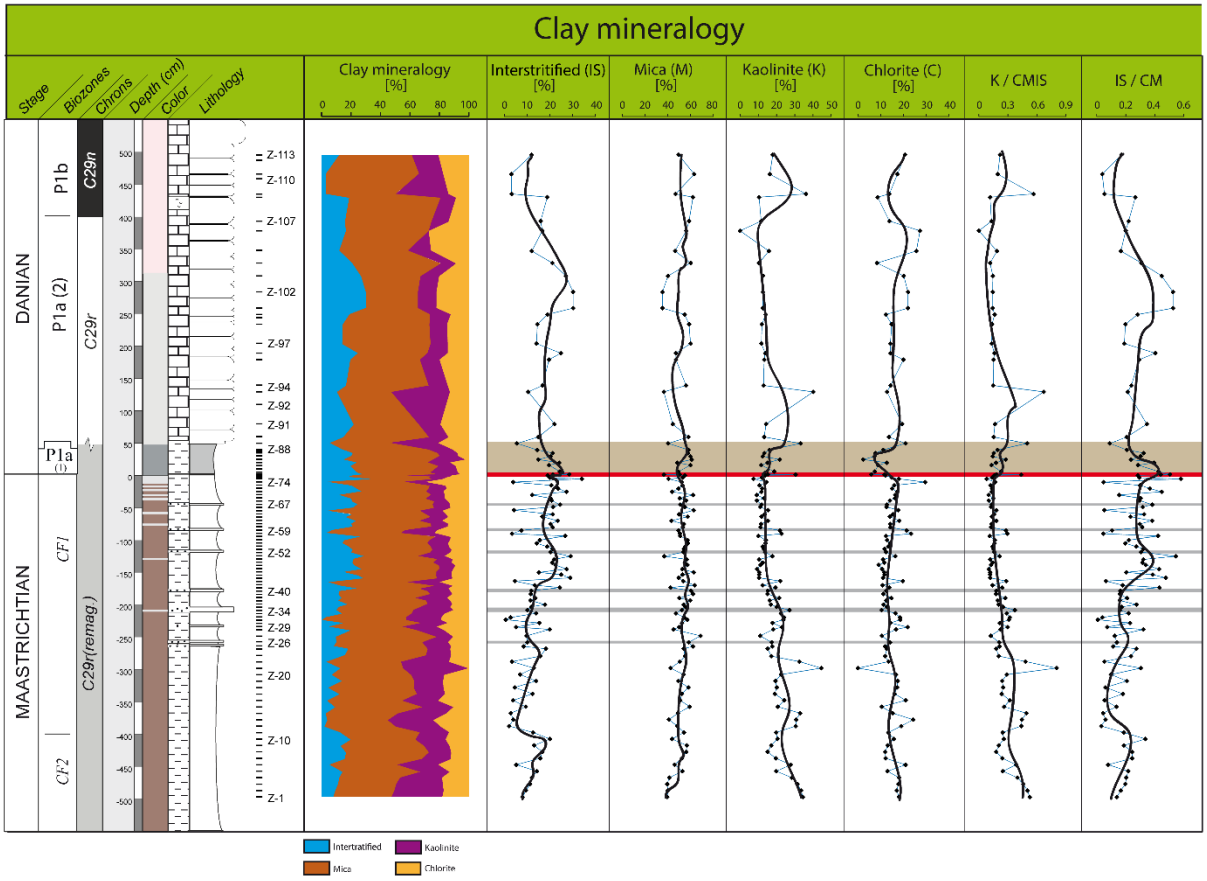

Figure 28. *Relative percent and ratios (K/CMIS and IS/CM) of clay minerals in the Zumaya section. Kaolinite and is strongly increase in KTB clay contrary to mica and chlorite. Note that kaolinite abundance as well as mica globally increase at the 50 cm above the KPB clay to the detriment of chlorite and IS.*

4.4. Majors and traces elements

4.4.1. Majors elements

The composition of the Zumaya major elements (MEs) along the studied section (Fig. 29, Annex IV.2) is variable. This variability is linked to lithology and especially in clay contents. For this, ME proportions are compared with the PAAS (Post-Archean Australian average Shales) values from Wedepohl (1971, 1991).

SiO_2 and CaO contents present, in the red marlstones, values range from 21 %wt. to 41 %wt. for SiO_2 with an average value of 29.79 %wt. which is very low relative to the PAAS value (58.90 %wt.), and from 19 %wt. to 34 %wt. for CaO (mean value, 24.14 %wt.) which are high relative to the PAAS value (2.20 %wt.). These proportions coincide with moderate contents in TiO_2 (0.38 % wt, mean value), Al_2O_3 (mean value of 10.58 %wt.), Fe_2O_3 (with average value of 3.60 %wt.), K_2O (with 2.00 %wt. as mean value) and Na_2O (mean value 0,53

%wt.). They are very low relative to their respective PAAS value (0.78 %wt. for TiO_2; 16.70 %wt. for Al_2O_3; 6.90 %wt. for Fe_2O_3; 3.60 %wt. for K_2O; 1.60 %wt. for Na_2O). MnO (0.07 %wt) and P_2O_5 (0.06 %wt) contents are low while loss on ignition contents (LOI: 19 %wt. to 30 %wt. with 24.64 % as mean value) are high. Turbidites cut crossing the red marlstones have an average SiO_2 (37.85 %wt.) and TiO_2 (0.43 %wt.) contents higher than in red marlstones. Al_2O_3 (mean value 8.71 %wt.), MnO (mean value 0.06 %wt.), MgO (mean value 1.33 %wt.), CaO (mean value 23.72 %wt.), N_2O (mean value 0.60 %wt.), K_2O (mean value 1.67 %wt.), P_2O_5 (mean value 0.06 %wt.) and LOI (mean value: 22.20 %wt.) contents are very similar to those of red marlstone while the average content of Fe_2O_3 (2.72 %wt.) is lower.

In the pre-KTB grey marls, the KTB-1 layer undergoes a drop in SiO_2 (11,76 %wt.), TiO_2 (0.20 %wt.), Al_2O_3 (4.00 %wt.), Fe_2O_3 (2.07 %wt.), MgO (0.83 %wt.), N_2O (0.18 %wt.) and K_2O (0.60 %wt.) contents while CaO (43.75 %wt.) and MnO (0.1 %wt.) contents, and LOI (35.76 %wt.) have sharply increased (Fig. 28; Annex IV.2). At the opposite, SiO_2 (19,72 %wt.), TiO_2 (0.28 %wt.), Al_2O_3 (6.53 %wt.), Fe_2O_3 (2.39 %wt.), MgO (1.08 %wt.), N_2O (0.26 %wt.) and K_2O (1.22 %wt.) contents observed in KTB-2 increase gradually whereas CaO (36.05 %wt.) and LOI (31.35 %wt.) contents decrease. This general trend continues up to post-KTB marls where a sudden inflection is clearly seen in almost all ME curves (Fig. 28). The abrupt increase in SiO_2 (47.49 %wt.), TiO_2 (0.61 %wt.), Al_2O_3 (14.74 %wt.), N_2O (0.66 %wt.), K_2O (3.18 %wt.), Fe_2O_3 (3.75 %wt.) and MgO (1.94 %wt.) coincide with a gradual drop in CaO (12.27 %wt.) content. LOI have also decreased, from 31.35 %wt. in KTB-2 to 15.16 %wt. in post-KTB marls. MnO (0.03 %wt.) and P_2O_5 (0.08 %wt.) have low contents.

Grey marls that overlying the post-KTB layer are characterized by a decreasing in SiO_2 contents (average value: 31.93 %wt.), TiO_2 (mean value of 0.40 %wt.), Al_2O_3 (mean value of 9.05 %wt.), Fe_2O_3 (mean value: 2.75 %wt.), MgO (mean value: 1.50 %wt.), N_2O (mean value of 0.46 %wt.) and K_2O (mean value of 1.87 %wt.). Contents of CaO (mean value: 26.40 %wt.) increase gradually, and the MnO (mean value: 0.07 %wt.) and P_2O_5 (from 0.08 %wt. to 0.12 %wt) concentrations are very low. In the upper limestones, some MEs such as TiO_2, MnO, N_2O, K_2O and P_2O_5 have low contents (Annex IV.2). Meanwhile, the highest contents in CaO (mean value: 50.16 %wt.) and LOI (mean value: 40.45 %wt.) whereas the lowest contents in SiO_2 (mean value: 5.19 %wt.), Al_2O_3 (1.15 %wt. as mean value), Fe_2O_3 (mean value: 0.83 % wt.) and MgO (mean value: 0.86 %wt.) are in this layer.

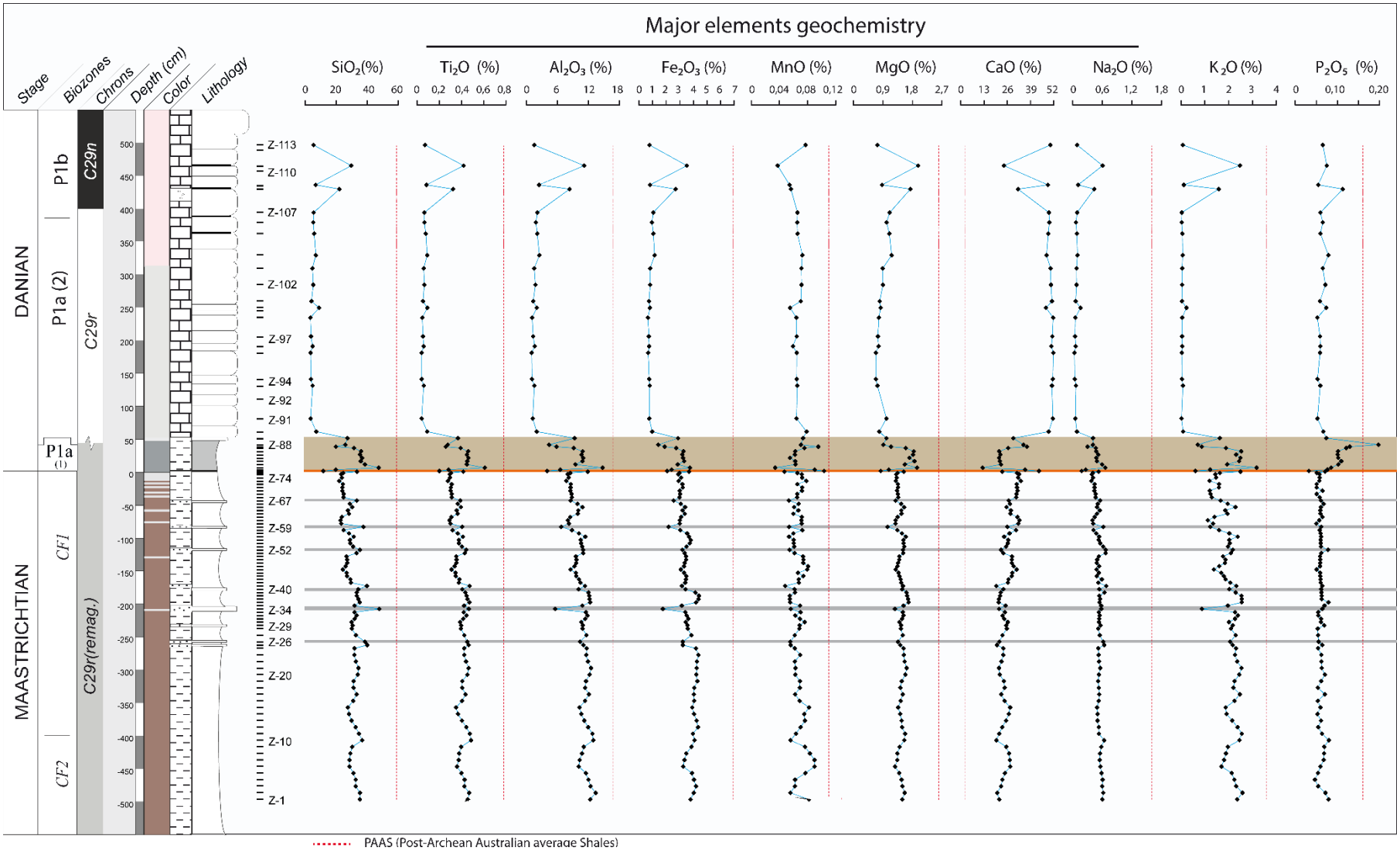

Figure 29. *Major element composition across the Zumaya K/T transition. Increased Si, Ti, Al, Fe, Mg, Na and K at the pre-KTB layer and in the early Danian marls suggest a high detrital input whereas high Mn and Ca at the KTB clay reflect increased productivity.*

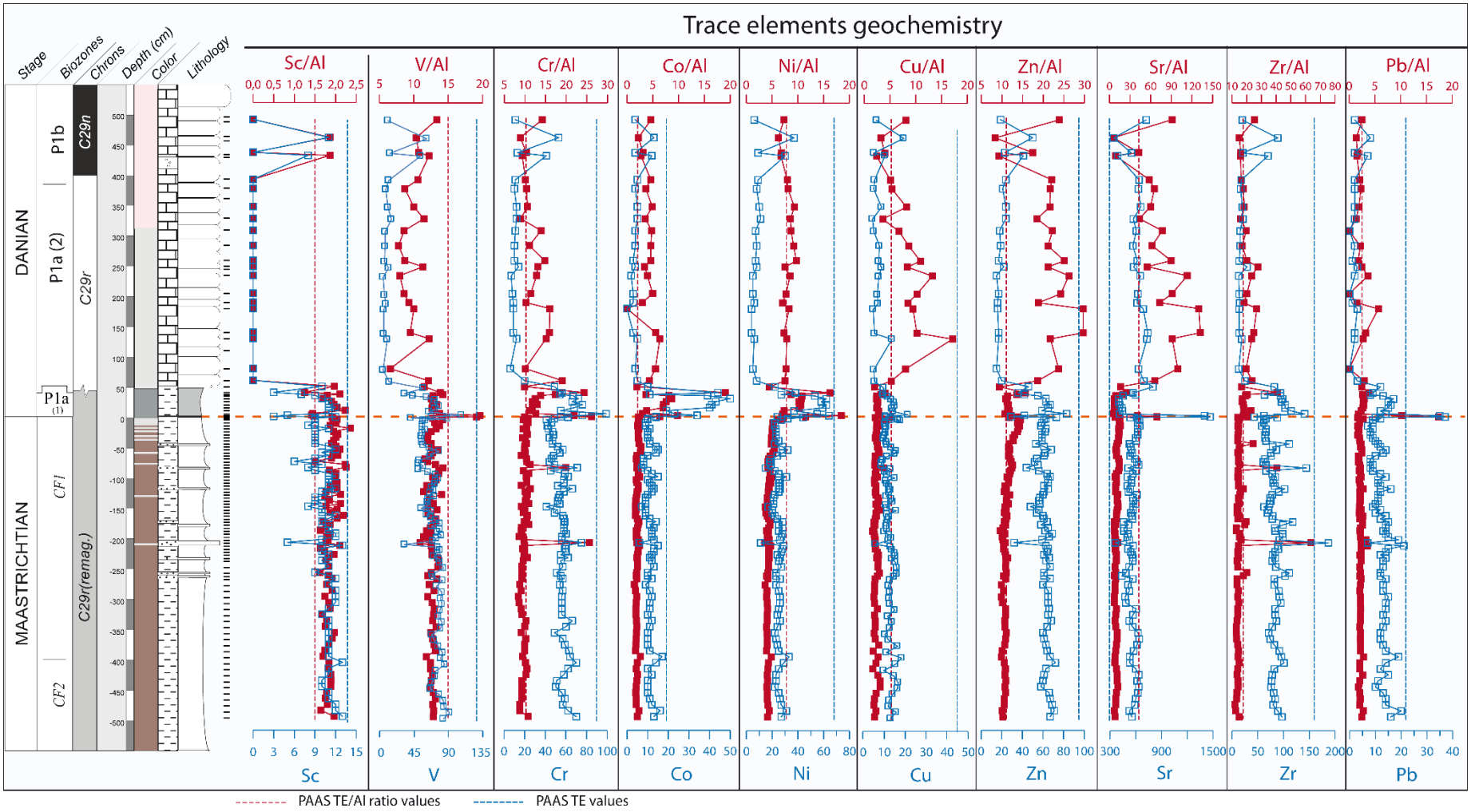

Figure 30. *Trace elements geochemistry of the Zumaya K/T beach. The red curves (Al-normalized) show the mobility of different elements around the K/T boundary and the blue curves present variation of concentration of these elements across the K/T boundary.*

4.4.2. Traces elements

Trace elements (TEs) concentrations (Table 1 in ppm) are normalized to the Al-content following Van der Weijden (2002) and Tribovillard et al. (2006) because of the low mobility of Al during diagenesis processes. This enables the estimation of element relative to reference materials.

Significant fluctuations of TEs/Al curves are mainly observed around the KTB zone (Fig. 30). At the pre-KTB layer, Sc/Al, Zn/Al and Rb/Al ratios are enriched while Cu/Al and Zr/Al ratios are low. In contrast, Al-normalized V, Cr, Co, Ni, Sr, Ba, Pb, Th and U show values very close to their respective PAAS values. KTB-1 and 2 are strongly enriched in V, Cr, Ni, Co, U, Pb, Sr and Ba whereas Sc shows very close values to that of Al from PAAS. All these Al-normalized elements (except Sc) roughly decreased in post-KTB layer showing the values similar to that of pre-KTB layer. Meanwhile, Cu/Al reach to the PAAS value in KTB-1 before returning in KTB-2 and post-KTB to pre-KTB values. Zn/Al slightly increase in KTB-1 before gradually decrease in KTB-2 then in post-KTB, very close to the PAAS value. Al-normalized Zr is slightly enriched in KTB-1 before to go down to the PAAS values in KTB-2 and post-KTB layer. Rb/Al gradually decreases since pre-KTB and reaches to a normal value in KTB-2.

4.5. Mercury (Hg) content

The Hg content curve of basal part (red marlstones) of the Zumaia section presents several fluctuations, mainly correlated to turbidites layers with shifts values reaching until 30.90 ppb (Fig. 31). Around the KT boundary, this content drops from the pre-KTB layer (7.10 ppb) and reaches its minimum value (3.30 ppb) in KTB-2. This drop is followed by an abrupt increase in the pre-KTB layer with a maximum value of 47.50 ppb in overlying grey marls (Fig. 31). In the limestone part, these values are very low (0.50 ppb to 4.80 ppb) with a mean value of 1.44 ppb.

4.6. Organic carbon content (TOC)

The total organic carbon content remains very low (< 0,2 %) in Zumaya deposits (Fig. 31). It is fairly constant in red marlstones (range from 0.03 % to 0.08 % with 0.05 % as mean value) except in samples Z-54 and Z-56, where a sudden increase is observed reaching 0.19 % and 0.17 % values respectively. However, fluctuations are observed around the KT boundary.

At the pre-KTB marls layer, total carbon organic content increase abruptly, from 0.06 % to 0.12 %, before returning in KTB-1 to 0.07 %, similar to red marlstones values. Then, there is a gradual increase in the TOC content (0.10 % in KTB-2) up to the post-KTB layer (0.14 %). Above the post-KTB layer, TOC content varies from 0.05 % to 0.11 % with an average value of about 0.08 %.

4.7. Stable isotopes

4.7.1. Organic carbon isotope ($\delta^{13}C_{org}$)

The $\delta^{13}C_{org}$ curve obtained around the KT boundary of studied section fluctuates over a range of -26.6 to -23.2 ‰ PDB (Fig. 31). $\delta^{13}C_{org}$ values are relatively constant in red marlstones (-26 to -24 ‰ PDB) except some small shifts corresponding to turbidites. Late Maastrichtian (light red marlstones to pre-KTB clay) is characterized by a fluctuation in $\delta^{13}C_{org}$ values whose extremities are -26.6 and -23,3 ‰ PDB. It's of -24.7 ‰ PDB in the pre-KTB layer and abruptly increases at the KT boundary reaching the maximum value (-23.2 ‰ PDB) in KTB-2. These values gradually decrease from the post-KTB layer and reach in the overlying grey marls to isotopic values of the late Maastrichtian.

4.7.2. Inorganic carbon ($\delta^{13}C_{carb}$) and oxygen ($\delta^{18}O$) isotopes

The Zumaya studied section shows positive $\delta^{13}C_{carb}$ values (0.40 to 2.40 ‰) with one negative value (-0.30 ‰) corresponding to a turbidite, and negative $\delta^{18}O$ values range from -1.60 to -6.40 ‰. In addition, these two curves have a similar trend (Fig. 31). Several fluctuations corresponding to turbidites are observed in red marlstones. $\delta^{13}C_{carb}$ remains almost stable in the upper Maastrichtian whereas $\delta^{18}O$ continues to fluctuate before returning to the red marlstone values in the uppermost Maastrichtian. A shift of $\delta^{13}C_{carb}$ from KTB-1 to early Paleocene with a minimum value (0,4 ‰ PDB) in pre-KTB layer coincide with negative excursion of $\delta^{18}O$ at the KT boundary (minimum value: -6,4 ‰ PDB) before a gradual increasing to early Paleocene.

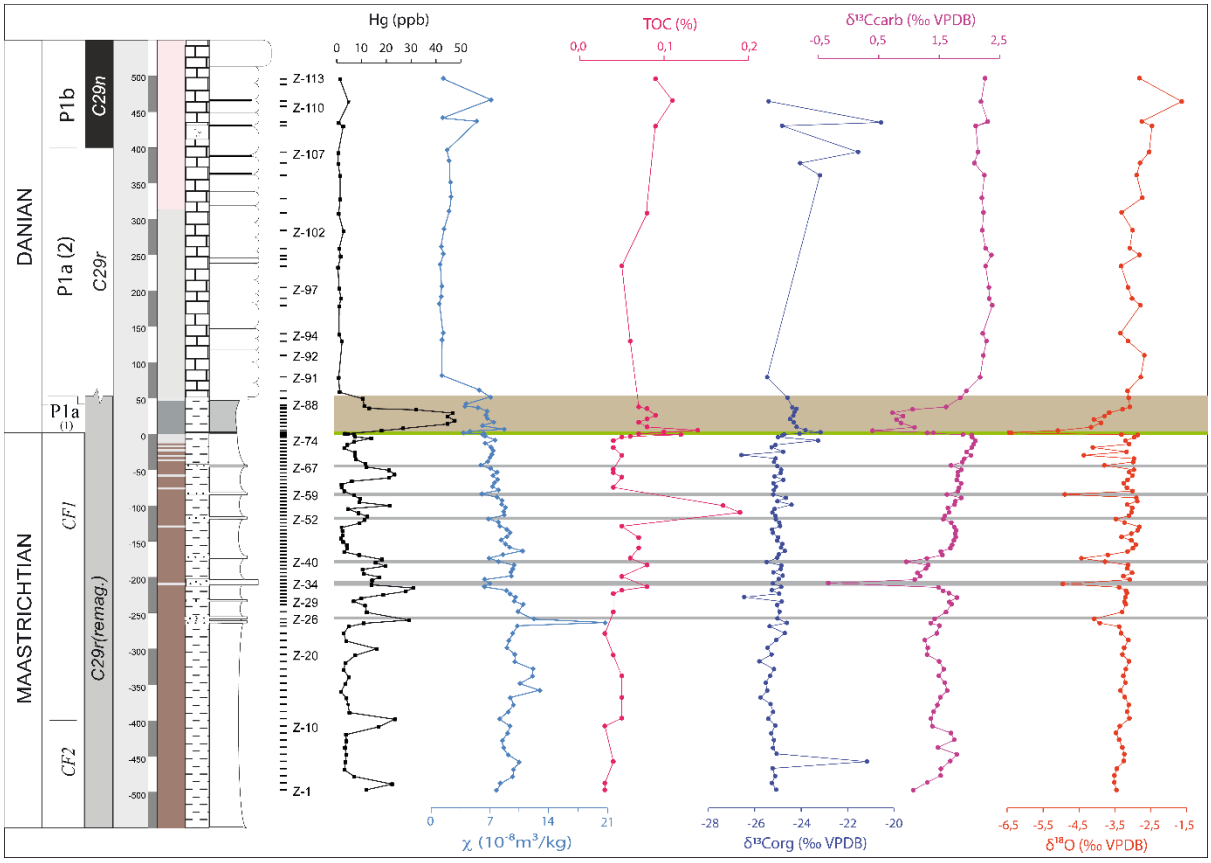

Figure 31. *Relative variation of mass specific magnetic susceptibility (χ in m3/kg), Hg, TOC and stable isotopes ($\delta^{13}C_{org}$, $\delta^{13}C_{carb}$ and $\delta^{18}O$) at the Zumaya studied section. Magneto-stratigraphy is based on Dinares-Turell et al. (2003).*

4.8. Magnetic susceptibility

In marine sediments, magnetic susceptibility (MS) is strongly linked to the mineralogical composition and depends on grain size and concentration of magnetic minerals (Stüben et al., 2003; Punekar et al., 2016), which are distinguished in diamagnetic (e.g., calcite, phyllosilicates, quartz and plagioclases), paramagnetic (e.g., clay) and ferromagnetic (e.g., magnetite and hematite) minerals. Magnetic susceptibility is generally correlated to detrital input, mainly to the phyllosilicate trend. Consequently, increased MS suggests high phyllosilicate contents whereas low MS implies carbonate productivity.

At the Zumaya studied section, mass magnetic susceptibility values (χ in m^3/kg) range from 6×10^{-8} to 13×10^{-8} m^3/kg in Maastrichtian marls and from 1×10^{-8} to 4×10^{-8} in Danian limestones, and are relatively comparable to Bidart (France), Gamsbach (Austria) and Elles (Tunisia) MS values (Font et al., 2011; 2014; Punekar et al., 2016). Mass magnetic susceptibility increases from the transect base to sample Z-15 (12.90×10^{-8} m^3/kg) which is likely the transitional zone between CF2 and CF1, before gradually decreasing through CF1

zone in contact with KTB (Fig. 31). At the KTB interval (green line, Fig. 31), there is a drastic drop in MS which is correlated to a decrease in phyllosilicates content and conversely with an increase in calcite (Fig. 31). Quartz remains very low in this interval as well as sodic plagioclases in KTB-1, which however increase suddenly in KTB-2 (Fig. 31). Above the KTB interval, the early Danian marls is materialized at the post-KTB layer by abrupt change in sedimentation (high MS values) thus suggesting KTB hiatus, then a slightly decrease of MS values until P1a(1)/P1a(2) transition before dropping in Danian limestones which are correlated to a high abundance in carbonate and probably a high sea level.

5. DISCUSSION

5.1. Redox conditions, Deccan volcanism and extraterrestrial indices

Many proxies are suggested for the characterization of redox conditions in sedimentary environments (see Hatch and Leventhal, 1992; Jones and Manning, 1994; Tribovillard et al., 2006). In Zumaya, three depositional environments are clearly identified: pre-KTB, KTB and post-KTB environments. Correlations between different elements and mineralogical phases were established on the full section (Table 3) in order to assess detritism influence (Al_2O_3 and phyllosilicates) and selecting substantially redox elements. It emerges that Co, U and Ni are weakly to moderately correlated with Al_2O_3 and phyllosilicates (Table 3), evidence of a slight detritism influence. At the KTB layers, because of its high enrichment factor (EF) and low positive correlation with Th (r = 0,39) and other substantially redox elements (Fig. 33C; Table 3), uranium through the U/Th ratio is coupled to V/(V+Ni) proxy and applied only to KTB (Fig 33B). The cross plot reveals a dyoxic to anoxic environment generally known at the KT boundary (Gertsch et al., 2011b). Ni/Co and V/Cr ratios applied to pre- and post-KTB materials suggest an oxic environment (Fig. 33A). This is confirmed by the low TOC content (0.03-0.19%) of these materials and the almost total absence of specific elements such as Mo (below the limit of detection) which has a conservative behaviour in the oxygenated waters (Tribovillard et al., 2006).

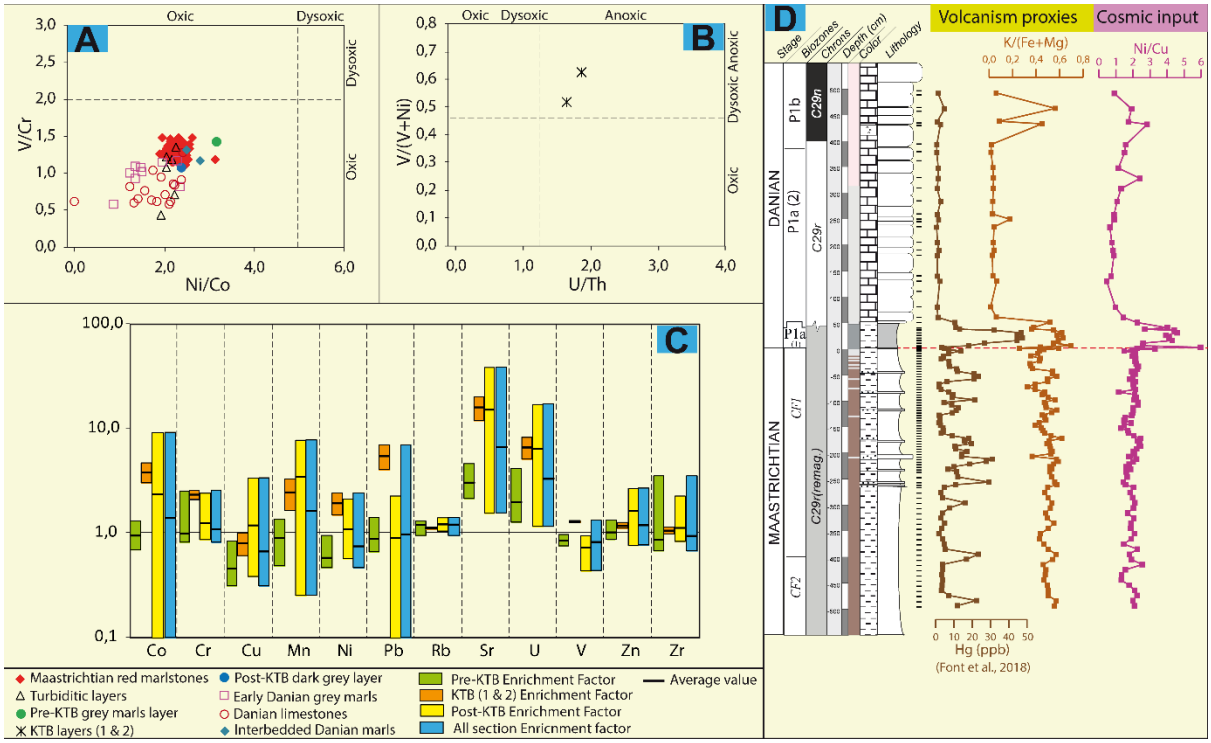

Figure 32. *(A and B) cross plot of various redox proxies. V/Cr vs. Ni/Co, V/(V+Ni) vs. U/Th. Ranges for V/Cr, U/Th and Ni/Co are from jones and manning (1994), and range for V/(V+Ni) are from Hatch and Leventhal (1992). (C) comparison of enrichment factor of some trace elements for pre-KPB marlstones (including turbidites), KTB layers and post-KTB materials (marls and limestones). The extend of the boxes corresponds to the range of values (minimum-maximum) and the inner black line to their average value. (D) volcanism proxies showing a clear similarity between mercury data variation and K/(Fe+Mg) ratio, and cosmic input across Zumaya KT boundary.*

Moreover, the high Hg contents (20-45 ppb) observed from late Maastrichtian to early Danian can easily be correlated to K/(Fe+Mg) proxy (Fig. 32D), evidence of a volcanism corresponding to the main phase of the Deccan as reported by Font et al. (2018). However, in KTB interval, a decrease of Hg content (4.60 ppb for KTB-1 and 3.30 ppb for KTB-2) and low K/(Fe+Mg) ratios (0.26 and 0.44 respectively for KTB-1 and -2) probably indicate a decrease of volcanic gases in atmosphere. This decrease coincides with an enrichment in Co, Cr, Mn, Ni, Pb, Sr, U (Fig. 32C), and a cosmic input mainly in KTB-2 through Ni/Co proxy (Fig. 32D), that suggests the Chicxulub impact. Similar results have been documented by Gertsch et al. (2011a) and Keller (2014).

Table 3. *Correlation coefficients of elemental geochemistry and bulk mineralogy of complete Zumaya beach transect.*

	SiO_2	TiO_2	Al_2O_3	Fe_2O_3	MnO	MgO	CaO	N_2O	K_2O	P_2O_5	Sc	V	Cr	Mn	Co	Ni	Cu	Zn	Rb	Sr	Zr	Ba	Pb	Th	U	Phyl	Qtz	S-pla	Calte
SiO_2	1																												
TiO_2	0,99	1																											
Al_2O_3	0,91	0,96	1																										
Fe_2O_3	0,84	0,90	0,97	1																									
MnO	-0,31	-0,28	-0,22	-0,12	1																								
MgO	0,84	0,88	0,89	0,84	-0,37	1																							
CaO	-0,99	-1,00	-0,97	-0,91	0,28	-0,89	1																						
Na_2O	0,96	0,96	0,94	0,88	-0,25	0,83	-0,97	1																					
K_2O	0,91	0,96	0,99	0,94	-0,29	0,91	-0,96	0,91	1																				
P_2O_5	0,15	0,12	0,00	-0,10	-0,06	0,15	-0,10	0,06	0,05	1																			
Sc	0,89	0,94	0,97	0,95	-0,17	0,87	-0,95	0,94	0,95	-0,01	1																		
V	0,90	0,95	0,98	0,96	-0,17	0,86	-0,95	0,91	0,97	0,01	0,96	1																	
Cr	0,93	0,94	0,87	0,81	-0,14	0,79	-0,93	0,88	0,88	0,21	0,86	0,90	1																
Mn	-0,03	0,01	0,09	0,21	0,90	-0,09	-0,02	0,06	0,01	-0,14	0,17	0,14	0,12	1															
Co	0,46	0,46	0,37	0,28	-0,08	0,50	-0,44	0,34	0,44	0,67	0,35	0,41	0,58	-0,02	1														
Ni	0,65	0,68	0,63	0,53	-0,16	0,72	-0,66	0,55	0,68	0,48	0,60	0,67	0,77	-0,03	0,90	1													
Cu	0,70	0,74	0,76	0,69	-0,19	0,69	-0,74	0,72	0,78	0,05	0,74	0,77	0,70	0,03	0,38	0,60	1												
Zn	0,88	0,92	0,97	0,95	-0,19	0,87	-0,94	0,91	0,95	-0,01	0,97	0,97	0,86	0,14	0,39	0,64	0,76	1											
Rb	0,90	0,95	0,99	0,96	-0,23	0,91	-0,96	0,93	0,99	0,02	0,97	0,98	0,86	0,09	0,40	0,65	0,77	0,97	1										
Sr	-0,47	-0,43	-0,39	-0,30	0,63	-0,55	0,45	-0,44	-0,42	-0,26	-0,37	-0,29	-0,22	0,48	-0,14	-0,15	-0,26	-0,35	-0,40	1									
Zr	0,96	0,92	0,78	0,69	-0,34	0,73	-0,91	0,89	0,79	0,22	0,78	0,77	0,90	-0,09	0,45	0,60	0,61	0,75	0,76	-0,45	1								
Ba	0,06	0,11	0,08	0,12	0,37	-0,02	-0,07	0,04	0,09	-0,12	0,07	0,18	0,30	0,34	0,22	0,31	0,12	0,07	0,06	0,76	0,07	1							
Pb	0,62	0,68	0,66	0,64	0,13	0,53	-0,65	0,59	0,67	0,03	0,64	0,72	0,77	0,30	0,52	0,68	0,56	0,63	0,65	0,27	0,56	0,73	1						
Th	0,96	0,98	0,95	0,90	-0,25	0,89	-0,98	0,94	0,95	0,10	0,95	0,94	0,91	0,05	0,46	0,67	0,75	0,93	0,95	-0,42	0,88	0,08	0,66	1					
U	0,38	0,40	0,38	0,39	0,30	0,14	-0,38	0,38	0,35	0,08	0,40	0,47	0,53	0,42	0,27	0,38	0,37	0,42	0,36	0,40	0,38	0,53	0,63	0,39	1				
Phyl	0,85	0,90	0,95	0,94	-0,13	0,81	-0,91	0,90	0,92	-0,06	0,94	0,94	0,81	0,17	0,28	0,54	0,73	0,94	0,94	-0,31	0,72	0,09	0,62	0,90	0,41	1			
Qtz	0,85	0,77	0,59	0,51	-0,26	0,55	-0,76	0,74	0,60	0,23	0,59	0,59	0,77	-0,09	0,38	0,45	0,45	0,57	0,56	-0,39	0,92	0,07	0,44	0,71	0,32	0,53	1		
S-pla	0,65	0,62	0,54	0,48	-0,18	0,45	-0,62	0,60	0,54	0,13	0,55	0,57	0,63	0,00	0,34	0,49	0,50	0,55	0,52	-0,14	0,66	0,20	0,51	0,58	0,45	0,49	0,59	1	
Calte	-0,97	-0,97	-0,93	-0,87	0,23	-0,82	0,97	-0,96	-0,91	-0,08	-0,92	-0,92	-0,92	-0,06	-0,39	-0,61	-0,72	-0,90	-0,91	0,39	-0,92	-0,10	-0,64	-0,95	-0,44	-0,91	-0,81	-0,66	1

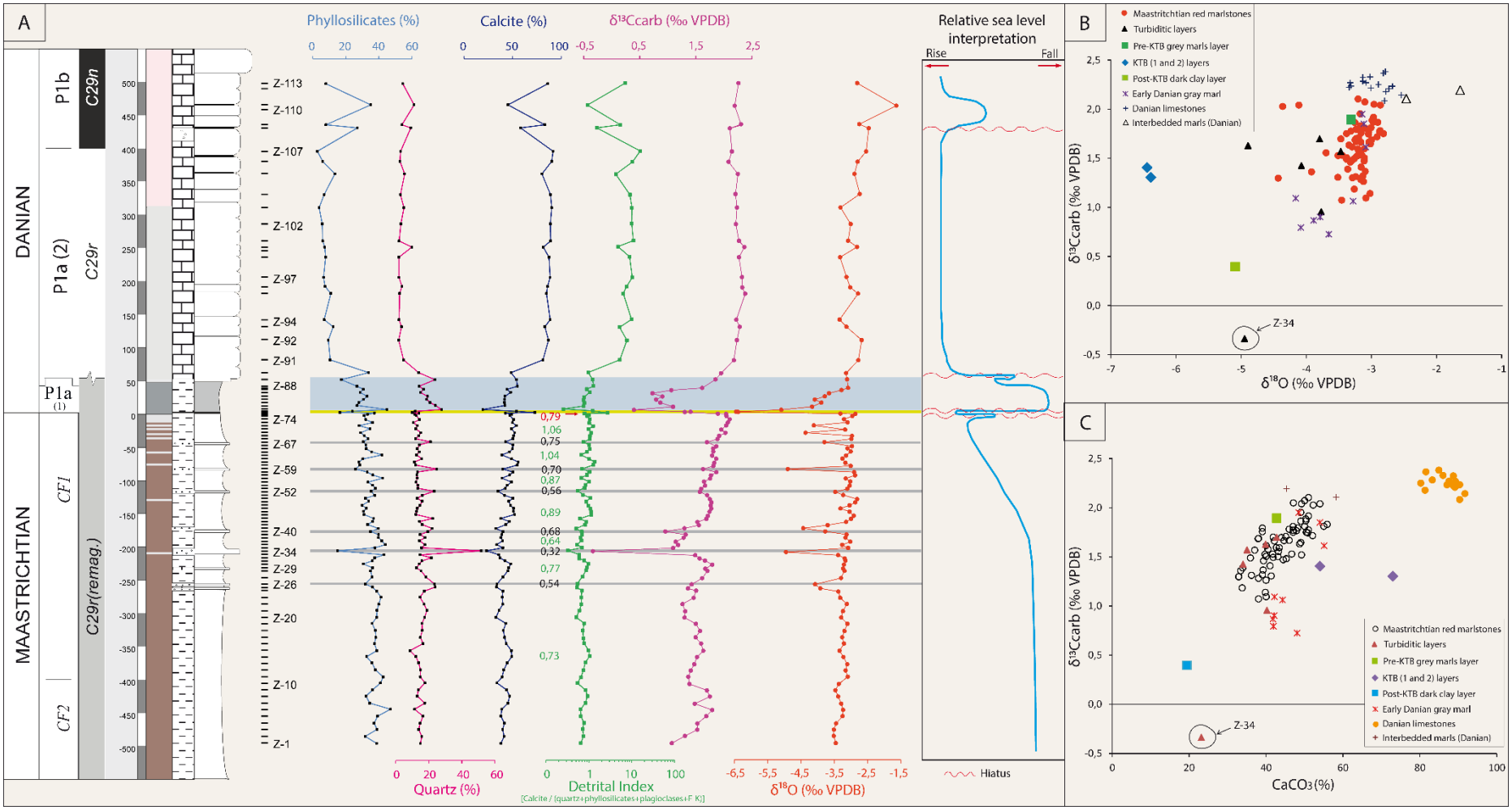

Figure 33. *(A) Relative sea level changes during late-Maastrichtian to early-Danian period at the Zumaya area. Increased DI reflects a high sea level and, an abrupt change of DI curve suggests a hiatus. (B) and (C) Diagenetic overprint across K/T transition of Zumaya studied section. Note a more meteoritic diagenesis in post-KTB layer and a burial diagenesis in the KTB layer*

5.2. Relative sea-level changes: lithology, bulk mineralogy and stable isotopes

Combination of lithology, bulk mineralogy and stable isotopes is an excellent environmental proxy to infer fluctuations in sea-level, diagenetic influence, continental runoff with associated erosion and relative position to the platform (Adatte et al., 2002; Jarvis et al., 2002; Swart and Eberli, 2005; Gertsch et al., 2011; Swart, 2015; Açikalin et al., 2016). High calcite content generally indicates deeper environment, diminish erosion and low continental runoff, whereas high detritus input suggests shallower environment and high continental runoff (Adatte et al., 2002).

At Zumaya section, CF2 and CF1 marlstones (Fig. 33A) present globally a relatively low detrital index (high content in detritus and relatively low carbonate content) ranging from 0.30 to 1.40 with 0.82 as average reflects a proximal source and consequently a lower sea level (Adatte et al., 2002). In addition, negative $\delta^{13}C_{carb}$ (-0.3 ‰) and $\delta^{18}O$ (-4.9 ‰) values at Z-34 (turbidite layer; Figs. 33B and C) could be strongly influenced by early meteoric diagenesis (Nelson and Smith, 1996; Immenhauser et al., 2003) implicitly confirming the continental runoff effect, and/or different source materials (Swart, 2015). Furthermore, DI values coupled to positive trend of δ^{13}Ccarb curve (Figs. 33A) confirm a gradual rising sea level observed in upper Maastrichtian up to the pre-KTB layer (about 1 cm below KTB), where the low detrital index value (0.79 in red color, Fig. 33A) suggests a drop in sea level. Calcite dissolution observed in this layer is probably result from acidification linked to the Deccan phase-2 volcanism (Font et al., 2018). In addition, its correlation to similar sea level changes (last falling sea level before KTB) observed in Tunisia (50 to 100 cm below KTB; Adatte et al., 2002), Texas (60 cm below KTB; Keller et al., 2007) and India (66 cm below KTB; Gertsch et al., 2011) suggest a short hiatus due either to sea level lowstand leading to erosion of the uppermost CF1 zone and the juxtaposition of KTB over it (Keller et al., 2003) and/or to a non-deposition phase.

Above the pre-KTB layer, there is an abrupt increase of DI reaching highest values at the KTB-1 (DI = 2,77) and KTB-2 (DI = 1,23), which correlate to a drop in $\delta^{13}C_{carb}$ (1,3 ‰ PDB for KTB-1 and 1,4 ‰ PDB for KTB-2) and negative shift of $\delta^{18}O$ (-6,4 ‰ PDB for KTB-1 and -2). These results, associated at the lowermost P1a(1) biozone, coincide with a planktic foraminiferal packstone observed on the field in KTB-1 and -3 (not sampled) layers, that suggest a maximum flooding surface (MFS) during significant sea level rise (Adatte et al., 2002) coupled to a massive extinction and dissolution-recrystallization processes due to

acidification linked to main phase of Deccan volcanism as indicated by Font et al. (2018) and many other authors (Keller et al., 2008; Gertsch et al., 2011; Punekar et al., 2016; Mateo et al., 2017). However, some fluctuations are also observed within the KT boundary interval. A first rise in sea level allowed in outer neritic to deeper environments a deposition of KTB-1 layer (foraminiferal packstone; Fig. 25D). This is probably interrupted by a small marine regression marked at the top of KTB-1 by a lower erosive surface (Fig. 25H), before gradually rising to reach MFS while allowing deposition of KTB-2 (Fig. 11A: DI = 1,23; middle to outer neritic environments) and -3 (condensed bioclastes thin layer probably in outer neritic to deeper environment; Fig. 25H) layers. Post-KTB layer (sample Z-80) marks the minimum sea level (Fig. 33A). It is characterized by an increase in quartz (27.85 %) and phyllosilicates (44.94 %) contents while calcite content (19.41 %) decreases, with consequently a very low detrital index (DI = 0.25) which reflects an inner neritic environment confirmed by a low amount of K-feldspars (1.15 %) and plagioclases (3.05 %) in this layer. This suggests an abrupt drop in sea level, which by erosion, as evidenced by field observations, induces a significant hiatus revealed by biostratigraphic data (P0 zone and lower part of P1a(1) zone are missing). Subsequently, sea level gradually increases until Z-89 (DI = 0.97; abrupt increase in kaolinite content: 33.26 %), top of P1a(1) zone, where the early interruption of drop suggests a P1a(1) zone missing part, probably the uppermost part. This hiatus marks a sea level lowstand and erosion in shallow water and correlated with biostratigraphy data. Similar hiatuses have been documented in the same interval by several authors (e.g., MacLeod and Keller 1991a, b; Schmitz et al., 1992; Keller, 1993; Keller et al., 2003; Adatte et al., 2002; Gertsch et al., 2011). Furthermore, very negative $\delta^{18}O$ values (-6.4 to -3.1 ‰VPDB) observed across KTB (Table 4; Z-77 to Z-89) implies a strong diagenetic overprint linked to dissolution-precipitation processes (Jenkyns et al., 1995; Mitchell et al., 1997 and Gertsch et al., 2011). This assumption is confirmed by the coincidence with very low $\delta^{13}C$ values (0.4 to 2.0 %VPDB) (Anderson and Arthur, 1983). However, the diagenetic effect on $\delta^{13}C_{carb}$ trend is limited at Zumaya as indicated by low coefficients of correlation between bulk carbonate $\delta^{13}C$ values and $\delta^{18}O$ ($R^2 \approx 0.077$; Fig. 34B), and $\delta^{13}C_{carb}$ and calcite percentages ($R^2 = 0.285$; Fig. 34C). Similar observations were made in India by Gertsch et al. (2011).

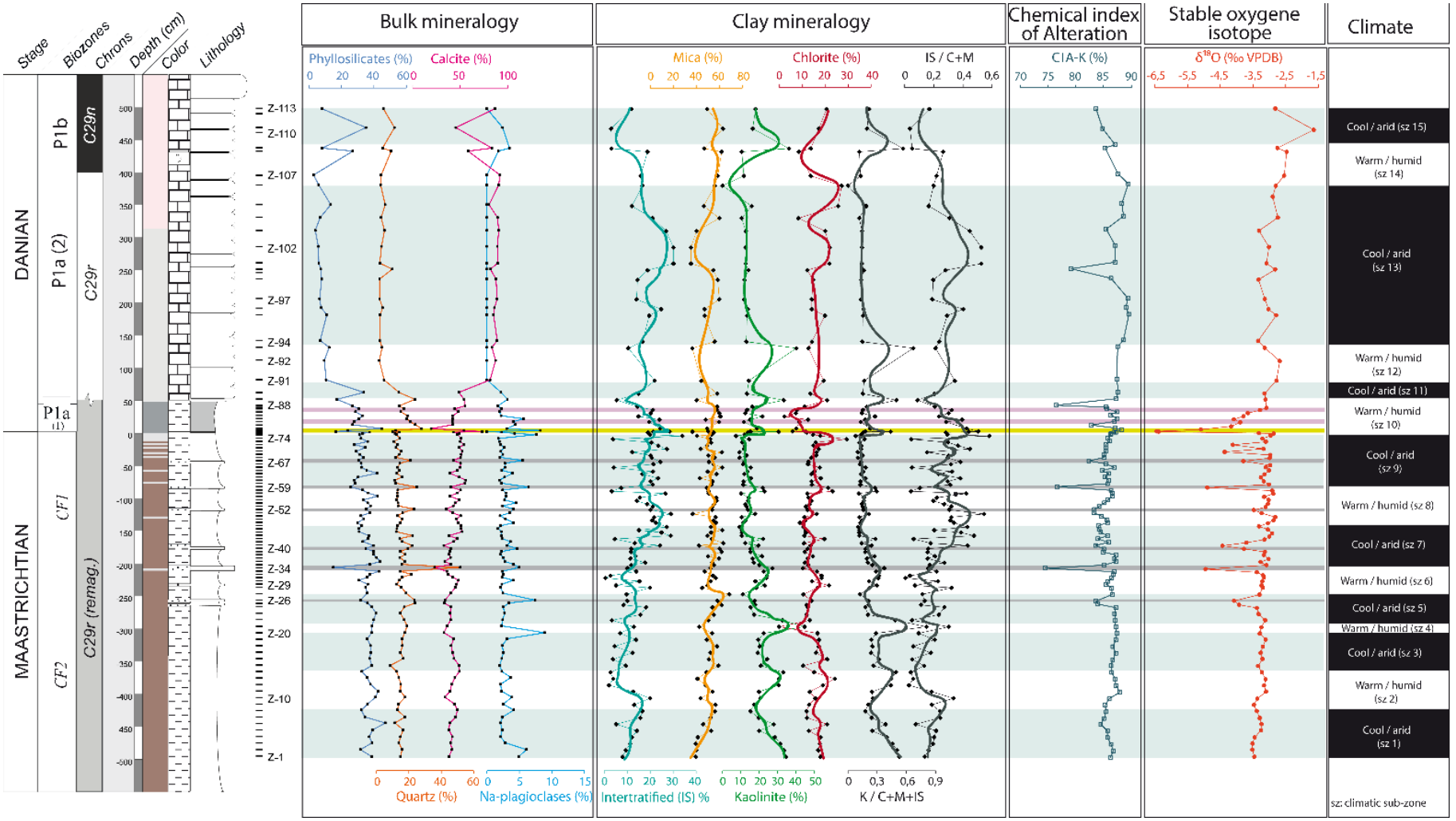

Figure 34. *Late Maastrichtian to early Danian climate fluctuations of Zumaya area, inferred from mineralogical proxies (phyllosilicates, quartz, calcite, intertratified, mica, kaolinite, chlorite, and ratios K/CMIS and IS/CM) and others, including chemical index of alteration (CIA) and $\delta^{18}O$ stable isotope. Note increased kaolinite and K/CMIS ratio coinciding to a negative shift in $\delta^{18}O$ and high CIA reflect warm/humid climate. Increasing chlorite, IS and mica associated to increased IS/CM ratio globally suggest cool/arid climate.*

Table 4. *Correlation coefficients of elemental geochemistry and bulk mineralogy of some samples (Z-77 to Z-89) at the Zumaya K/T transition*

	SiO_2	TiO_2	Al_2O_3	Fe_2O_3	MnO	MgO	CaO	N_2O	K_2O	P_2O_5	Sc	V	Cr	Mn	Co	Ni	Cu	Zn	Rb	Sr	Zr	Ba	Pb	Th	U	Phyl	Qtz	S-pla	Calte
SiO_2	1																												
TiO_2	0,98	1																											
Al_2O_3	0,90	0,96	1																										
Fe_2O_3	0,78	0,87	0,96	1																									
MnO	-0,94	-0,91	-0,89	-0,78	1																								
MgO	0,88	0,90	0,87	0,83	-0,76	1																							
CaO	-0,99	-0,99	-0,96	-0,86	0,93	-0,91	1																						
Na_2O	0,97	0,92	0,85	0,72	-0,93	0,80	-0,94	1																					
K_2O	0,91	0,96	0,99	0,95	-0,89	0,92	-0,97	0,84	1																				
P_2O_5	0,14	-0,04	-0,21	-0,43	-0,10	0,00	-0,02	0,18	-0,17	1																			
Sc	0,83	0,85	0,91	0,90	-0,77	0,83	-0,88	0,81	0,90	-0,18	1																		
V	0,78	0,87	0,93	0,92	-0,81	0,79	-0,85	0,71	0,92	-0,35	0,77	1																	
Cr	0,59	0,68	0,63	0,56	-0,58	0,63	-0,62	0,45	0,67	-0,11	0,32	0,78	1																
Mn	-0,89	-0,86	-0,84	-0,72	0,98	-0,69	0,88	-0,89	-0,83	-0,10	-0,67	-0,80	-0,61	1															
Co	0,32	0,26	0,13	0,08	-0,23	0,44	-0,29	0,20	0,27	0,49	0,04	0,08	0,38	-0,18	1														
Ni	0,53	0,56	0,52	0,52	-0,47	0,71	-0,57	0,38	0,63	0,07	0,38	0,61	0,75	-0,43	0,77	1													
Cu	0,82	0,88	0,83	0,76	-0,79	0,80	-0,84	0,76	0,84	-0,20	0,64	0,86	0,81	-0,78	0,13	0,50	1												
Zn	0,92	0,95	0,97	0,92	-0,92	0,91	-0,96	0,88	0,98	-0,10	0,89	0,93	0,66	-0,88	0,18	0,57	0,86	1											
Rb	0,90	0,95	0,99	0,95	-0,85	0,93	-0,96	0,84	0,99	-0,17	0,94	0,89	0,59	-0,78	0,20	0,56	0,80	0,97	1										
Sr	-0,81	-0,71	-0,64	-0,47	0,73	-0,74	0,77	-0,82	-0,65	-0,51	-0,70	-0,40	-0,21	0,65	-0,35	-0,30	-0,47	-0,70	-0,70	1									
Zr	0,97	0,91	0,79	0,62	-0,90	0,77	-0,92	0,95	0,79	0,28	0,68	0,66	0,58	-0,87	0,32	0,44	0,79	0,82	0,78	-0,78	1								
Ba	-0,69	-0,58	-0,53	-0,34	0,63	-0,54	0,65	-0,73	-0,51	-0,58	-0,62	-0,26	-0,03	0,57	-0,22	-0,12	-0,26	-0,55	-0,57	0,94	-0,68	1							
Pb	-0,53	-0,40	-0,37	-0,17	0,52	-0,33	0,47	-0,62	-0,32	-0,61	-0,47	-0,11	0,15	0,48	0,00	0,13	-0,13	-0,40	-0,38	0,85	-0,55	0,95	1						
Th	0,95	0,98	0,94	0,86	-0,86	0,93	-0,98	0,90	0,95	-0,03	0,89	0,80	0,58	-0,78	0,30	0,53	0,83	0,92	0,96	-0,77	0,87	-0,63	-0,44	1					
U	-0,78	-0,74	-0,66	-0,57	0,59	-0,85	0,77	-0,74	-0,70	-0,21	-0,72	-0,46	-0,29	0,53	-0,40	-0,42	-0,58	-0,68	-0,73	0,84	-0,69	0,69	0,53	-0,82	1				
Phyl	0,75	0,82	0,91	0,83	-0,77	0,67	-0,81	0,73	0,83	-0,23	0,79	0,86	0,55	-0,75	-0,14	0,30	0,72	0,86	0,85	-0,53	0,64	-0,51	-0,42	0,78	-0,47	1			
Qtz	0,76	0,66	0,46	0,25	-0,69	0,51	-0,65	0,78	0,46	0,50	0,37	0,35	0,43	-0,69	0,28	0,25	0,64	0,53	0,45	-0,66	0,89	-0,57	-0,53	0,61	-0,52	0,35	1		
S-pla	0,15	0,14	0,10	0,08	-0,13	0,10	-0,14	0,07	0,13	0,10	0,08	0,26	0,37	-0,13	0,31	0,56	0,09	0,13	0,09	0,11	0,17	0,09	0,22	0,04	0,12	0,00	0,16	1	
Calte	-0,93	-0,93	-0,90	-0,74	0,89	-0,79	0,93	-0,91	-0,86	-0,11	-0,76	-0,83	-0,68	0,87	-0,17	-0,49	-0,83	-0,90	-0,86	0,71	-0,92	0,64	0,51	-0,88	0,61	-0,86	-0,74	-0,23	1

An increasing of calcite content (86.80 % as mean value) and detrital index (DI = 8.55 as mean value) in P1a (2) zone reflects deeper marine conditions. However, the upper part of Danian limestones characterized by a drop of DI (1.54 for Z-108 and 0.93 for Z-111: thin interbedded marlstones) and high kaolinite content (36.13 % for Z-109; see Fig. 28) suggest a sea level lowstand and short hiatus (Fig. 34A). This hiatus is probably associated to P1a-P1b boundary (Macleod and Keller, 1991a, b; Keller and Benjamini, 1991; Canudo et al., 1991; Keller and Stinnesbeck, 1996).

5.3. Mineralogy, CIA and $\delta^{18}O$ isotope as climate proxies

Clay minerals assemblage as well as bulk rock mineralogy and geochemistry of stable isotopes ($\delta^{18}O$) are commonly used to infer paleoclimatic conditions in sedimentary deposits (Singer, 1984; Chamley, 1989; Robert and Maillot, 1989; Li et al., 2000; Adatte et al., 2002; Ruffell et al., 2002; Bristow et al., 2009; Gerstch et al., 2011). Combination of these proxies associated to Chemical Index of Alteration (CIA) are applied to Zumaya K/Pg transition for a high-resolution reconstruction of paleoclimatic conditions (Fig. 34). Cretaceous cycle is mainly characterized by smectite, kaolinite, mica (illite) and other mixed-layers clays (Chamley, 1989). Generally, high kaolinite content indicates warm or humid climates, high precipitations and intense chemical weathering in the hinterland while abundance of chlorite and mica suggests cool or arid conditions, high physical weathering and poorly developed soils (Millot, 1970; Singer, 1984; Chamley, 1989; Li et al., 2000; Adatte et al. 2002; Keller et al., 2002; Gerst et al. 2011). Also, interstratified abundance is linked to a strong burial diagenesis (Chamley, 1989; Meunier, 2005; Duchamp-Alphonse et al., 2011) and/or transitional climatic conditions. Consequently, increased K/(C+M+IS) ratio suggests warm/climatic conditions whereas high IS/(C+M) reflects major diagenesis impact. Furthermore, more positive $\delta^{18}O$ values correspond to a cold climate in contrast to negative values reflecting to a warm climate. However, from the mid-latitude areas lower $\delta^{18}O$ values of bulk carbonate could be due to the burial diagenetic effect (Schrag et al. 1995).

CF3 zone is characterized by an alternation of cool/arid and warm/humid climatic sub-zones (sz). Gradual decrease in kaolinite abundance and K/C+M+IS ratio indicate a cool climatic conditions at the base of studied transect (sz 1), rapidly followed by a similar warming/humid period (sz 2) indicated by a global increase of kaolinite and chlorite contents and K/C+M+IS ratio which coincide with a high CIA and lower burial diagenesis impact (Fig.

34). The following sub-zones (sz 3 and 5) are a very long gradual cooling and/or drying period until CF2/CF1 boundary where the maximum cooling is reached. These sub-zones are punctuated by a short humid climate period marked by an abrupt enrichment in kaolinite content associates to slight increase in quartz content and relatively high CIA (sz 4; Fig. 34), probably reflecting a low sea level. At the base of CF1 zone (sz 6), increasing of K/CMIS ratio and chlorite content reflects warm/humid climatic sub-zone with a fluctuated chemical weathering. At the sz 7, there is a decreasing in kaolinite abundance with consequently decreased K/CMIS ratio, associated to relatively stable chlorite and mica contents and increasing diagenetic impact confirmed by many negative $\delta^{18}O$ shifting in this sub-zone. All these informations reflect a most arid than cold climate. The next climatic sub-zone (sz 8) is a warm/humid interval (gradual increase of kaolinite and chlorite associated with a high CIA) subsequently followed by a long cold/arid climate period (sz 9) at the upper part of CF1 zone with a maximum cooling at Z-75 (kaolinite: 7,34 %, chlorite: 17,97 % and mica: 40,67 %; Fig. 34) near the pre-KTB layer just below the first short hiatus. This hiatus (at the pre-KTB layer) marks the outset of warm and humid period (sz 10) which continuous until major hiatus (~ 110 ky) at the top of P1a (1) zone at about 50 cm above KT boundary clay (Figs. 26, 33 and 34) including the major KTB hiatus (~ 225 ky). Similar climatic conditions have been observed just below the KTB in Tunisia (Adatte et al., 2002). This climatic zone is globally enriched in bulk and clay detrital minerals (quartz, phyllosilicate and kaolinite) and Na-plagioclases. The chlorite and calcite contents are low except at the KTB where calcite content is enough raised. This suggests a recrystallization processes probably due to the ocean acidification. In addition, the $\delta^{18}O$ strong negative shift confirms this climate. It is also characterized by low seasonality contrasts marked by slight positive inflexion of mica, chlorite and $\delta^{18}O$ curves, and negative kaolinite inflexion (pink bands, Fig. 34), which reflect predominately mechanical erosion. Sz 8, 9 and 10 correspond to maximum stressed intervals (Fig. 26) linked to Deccan-2 phase.

Within the P1a (2) and P1b zones, trend of bulk and clay mineralogy curves as well as K/CMIS ratio and $\delta^{18}O$ delimits five climatic sub-zones (sz 11, sz 12, sz 13, sz 14 and sz 15; Fig. 34). The first sub-zone (sz 11) is a short time interval characterized by a decrease in kaolinite and chlorite contents, and an increasing mica, Na-plagioclase and phyllosilicate abundance suggesting a most arid than cool climate (Chamley, 1989). It is followed by an atypical humid period (sz 12) with a raised sea level, a strong kaolinite abundance associates to slight $\delta^{18}O$ inflexion and very low chemical weathering. Meanwhile, chlorite, mica and interstratified contents remain low. A very long cool/arid period follows the last one and is

characterized by a gradual decreasing in kaolinite and K/CMIS ratio reaching the maximum cooling near to the P1a (2) – P1b boundary (Fig. 34). Chlorite and mica curves show slight fluctuations at the upper part of sz 13 suggesting alternately short dried and cooled episodes. P1a to P1b transition (sz 14) is generally marked by a warm/humid conditions (Adatte et al., 2002; Keller et al., 2002) and associated to a hiatus as it is the case in Egypt and Tunisia (Adatte et al., 2002; Keller et al., 2002; Punekar et al. 2014) and an increase in kaolinite abundance reflecting high chemical weathering (CIA curve, Fig. 34), contrary to Egypt where mica and chlorite contents increase to the detriment to kaolinite (Keller et al., 2002), suggesting rather a high mechanical erosion. The top of studied transect (sz 15) is characterized by a cool/arid climate reflected by a decreasing of K/CMIS ratio and kaolinite abundance and an increasing in chlorite, mica and interstratified. Nevertheless, enrichment in detrital materials (phyllosilicates and quartz) over calcite in this time period coincide with a high chemical weathering (Fig. 34) and a low sea level that suggest a short warm humid period and consequently a contrasted climatic sub-zone.

6. CONCLUSIONS

(a) The Zumaya Cretaceous-Tertiary boundary (KTB) section consists on the one side, by Late Maastrichtian red marlstones showing bioturbations and crossed by thin turbiditic beds and on the other side by 40 cm thick of early Danian grey marls, corresponding to the top of the P1a(1) biozone, which is followed by light grey to pink Danian limestones. A 3 cm thick foraminiferal packstone (KTB) layer of the uppermost CF1 zone membership separates Maastrichtian and Danian deposits. This one, differentiated in three levels and showing, on a large scale, net undulations at the top, was set up following of brief sea-level fluctuations in a middle neritic to deeper environment.

(b) This KTB layer indicates a deposition in depleted-oxygen water conditions, and an enrichment in cosmic inputs. It is preceded by a well oxygenated Late Maastrichtian environment constrained to a strong Hg injection from a distal volcanism, probably the main phase of Deccan volcanism, which pursue until the lowermost Danian period whereas the calcareous Danian environment is oxic and quiet (no volcanism).

(c) Besides minor hiatuses at the pre-KTB layer and P1a(2)/P1b transition, two significant hiatuses have been recorded across the Zumaya K/T section: KTB hiatus (P0 and lowermost P1a(1) missing) and P1a(1)/P1a(2) hiatus (top of P1a(1) zone missing). Both are resulting from a marine regression.

(d) Interval including pre-KTB, KTB and P1a(1) sediments is marked by a high stressed environment linked to Deccan-2 phase during a contrasted warm/humid climate.

CHAPTER IV. FIRST EVIDENCE OF PALEOCENE-EOCENE THERMAL MAXIMUM (PETM) IN DOUALA SEDIMENTARY SUB-BASIN, CAMEROON, CENTRAL AFRICA

1. INTRODUCTION

The Paleocene-Eocene Thermal Maximum (PETM) is one of the most intense and abrupt intervals of global warming in the geological records, occurred during a short interval (170 to ~217 kyr; Röhl et al., 2007; Murphy et al., 2010) in the Cenozoic time about 55.7–56 Myr ago (Hilgen et al., 2010; Charles et al., 2011). Depending on geodynamic setting and the possible related effects, marine or continental domain membership and the position of sections relatively to the equator, the manifestations associated with the PETM may be diverse with varied magnitude. The most interesting and common manifestation of this event is a prominent negative excursion of $\delta^{13}C$ known as the Carbon Isotope Excursion (CIE) with as much as 2.5-6‰ drop in $\delta^{13}C$ recorded from marine as well as terrestrial sedimentary archives (e.g., Kennett and Stott, 1991; Koch et al., 1992, 2003; Bralower et al., 1995; Thomas and Shackleton, 1996; Thompson and Schmitz, 1997; Zachos et al., 2001; Magioncalda et al., 2004; McInerney and Wing, 2011; Bowen et al., 2015). Others manifestations may also be associate with the PETM event. These include: (1) a strong dissolution of seafloor carbonate followed by gradual recovery (Zachos et al., 2005; Bralower et al., 2014), (2) a rapid 3-8 °C global warming from high latitudes to equator, and from terrestrial to marine sedimentary archives (e.g., Kennett and Stott, 1991; Bralower et al., 1995; Zachos et al., 2003; Tripati and Elderfield, 2005; Wing et al., 2005; Sluijs et al., 2006; Zachos et al., 2008), (3) a mass extinctions and/or turnovers among land and marine organisms, which indicates dramatic change in terrestrial, shallow marine and deep marine conditions (e.g., Tjalsma and Lohmann, 1983; Miller et al., 1987; Katz and Miller, 1991; Canudo et al., 1995; Kelly et al., 1996, 1998; Aubry et al., 1998; Thomas, 1998, 2003, 2007; Crouch et al., 2001, 2003; Kaminski and Gradstein, 2005; Sluijs et al., 2006; Alegret et al., 2009a, 2009b; Stassen et al., 2012; Arreguín-Rodríguez et al., 2016; Ouda, 2018), (4) profound changes in the global hydrologic cycle (Robert and Kennett, 1994; Gibson et al., 2000; Schmitz and Pujalte, 2007; Handley et al., 2012; Carmichael et al., 2017), and (5) geochemical and mineralogical changes such as fluctuation in phyllosilicate abundances and change in sensitive trace elements (Zwingmann et al., 1999; Crouch et al., 2003; Zachos et al., 2005; Tribovillard et al., 2006; Sluijs et al., 2007; Storey et al., 2007; Dypvik et al., 2011; Schulte et al., 2011, 2013; Solimann et al., 2011; Handley et al., 2012; Khozyem, 2013; Khozyem et al., 2013). Numerous studies conducted on the subject reveal the potential causes of the PETM. These include the release of methane hydrate from methane clathrate reservoirs present on shallow ocean floors (Dickens et al., 1997; Dickens, 2000; Higgins and Schrag, 2006), the comet impact (Kent et al., 2003; Cramer and Kent, 2005), the explosive distal

volcanism (Bralower et al., 1997; Schmitz et al., 2004; Dickson et al., 2015; Khozyem et al., 2016, 2017a, 2017b), the intrusion-forced injection of thermogenic methane (Svensen et al., 2004; Frieling et al., 2016), the sub-lithospheric gas explosion (Morgan et al., 2004), and the tectonically forced desiccation of epicontinental seas (Higgins and Schrag, 2006).

Several PETM sections, from the high to middle latitudes, were studied throughout the world. Some of them are from deep sea sites (e.g., Stott et al., 1990; Thomas and Shackleton, 1996), bathyal to outer shelf outcrops (e.g. Corfield et al.,1991; Lu et al., 1996; Schmitz et al., 1997; Arenillas et al., 1999; Berggren and Ouda, 2003; Dupuis et al., 2003; Knox et al., 2003; Ouda et al. 2013; Khozyem et al., 2015) and from shallow marine environment (e.g., Schmitz et al., 1996; Cramer et al., 1999; Gibbs et al., 2006) whereas, others, in contrast, are from terrestrial environments (e.g., Thiry et al., 1998, 2006; Cojan et al., 2000; Bowen et al., 2001; Magioncalda et al., 2001; Magioncalda et al., 2004). But only a few studies were made on the PETM in the low latitude to near-equator regions (e.g., Bralower et al., 1995; Bown and Pearson, 2009; Handley et al., 2012; Aze et al., 2014; Frieling et al., 2017).

In the Gulf of Guinea (Central African region), many investigations have already been made on Paleocene and Eocene sediments exposed and/or cored at several places mainly in Nigeria (Bio-Lakoto et al., 1998; Gebhardt et al., 2010; Chukwura et al., 2017; Frieling et al., 2017; Oboh-Ikuenobe et al., 2017) and in Cameroon (Njike Ngaha, 1984; Mbesse et al., 2012; Ngon Ngon et al., 2012, 2014, 2016; Mfayankouo Chavom et al., 2014). However, only Gebhardt et al. (2010) and Frieling et al. (2017) in Dahomey basin (Nigeria) have so far focused on the Paleocene-Eocene transition in order to elucidate any effects that may be related to PETM. The present work, focused on two main sections of Douala sub-basin (Bongue and Dibamba), is an attempt to identify the PETM signatures and to discuss its possible causes through a multiproxy approach based on benthic and planktic foraminifera as well as ostracods, carbon stable isotopes, mineralogy, whole rock geochemistry and mercury (Hg) anomalies.

2. LOCATION AND GEOLOGICAL SETTING

Bongue and Dibamba sections are located respectively in North-West (N 04°21’38,95”; E 09°37’12,43”) and South-East (N 04°00’21,8”; E 09°51’32,9”) of the northern part of Douala sub-basin (Cameroon, Central Africa), within a humid equatorial climatic zone. According to Njike Ngaha (1984) and the geological report of SNH (2005), the relative age of the deposits of both localities is Paleocene and Eocene (Fig. 35) corresponding to the N’kapa Formation (Fig. 36). Douala sub-basin is located in the Gulf of Guinea and covers a total surface area of

12250 km^2, of which 6955 km^2 represents the onshore part (SNH, 2005). This onshore part is limited by the Cameroon Volcanic Line in the north, the Wouri estuary river at the west, the Kribi-Campo sub-basin in the south and the Precambrian basement at the east (Fig. 35).

The geological history of this basin begins in Late Jurassic and falls within of the breaking continental process responsible for genesis of the Cameroonian Atlantic margin (Giresse et al., 1996). Lithostratigraphy of Douala sub-basin is made of seven major formations related to three stage of geodynamic and sedimentary evolution (Regnoult, 1986; Nguene et al., 1992; Lawrence et al., 2002; SNH, 2005) (Fig. 36). *(i)* The syn-rift period (Late Jurassic - Early Cretaceous) marked by the establishment of major normal faults and represented by (1) the Mundeck Formation (Aptian- Cenomanian), which lies unconformably on the Precambrian basement and consists of continental and fluvio-deltaic deposits, i.e., clays, coarse-grained sandstones, conglomerates. *(ii)* The drift I sequence (Upper Cretaceous - Lower Tertiary) includes: (2) the Logbadjeck Formation (Cenomanian – Campanian), lies unconformably on the Mundeck Formation and composed of micro-conglomerates, sand, sandstone, limestone, and clay; (3) the Logbaba Formation (Maastrichtian), mainly composed of sandstone, sand and fossiliferous clay; (4) the N'kapa Formation (Paleocene-Eocene), rich in marl and clay with lenses of sand and fine to coarse-grained unconsolidated sandstone. The drift II phase in the Tertiary, during which expands passive margin. It is marked by (5) the Souellaba Formation (Oligocene) lying unconformably on N'kapa deposits and characterised by marl deposits with some interstratified lenses of channel sands; (6) the Matanda Formation (Miocene), dominated by deltaic facies interstratified with volcano- clasties layers, and (7) the Wouri Formation (Plio-Pleistocene) which consists of gravelly and sandy deposits with a clayey or kaolinitic matrix.

3. METHODS

3.1. Sample preparations

63 samples (30 samples from Bongue section and 33 from Dibamba) were collected and a detailed description of each one was subsequently made. These samples were dried at 45 °C and a part of each one crushed with an agate mortar was subjected to bulk mineralogy, geochemistry, mercury and total organic carbon (TOC) analyses at the Institute of Earth Sciences (ISTE) and the Institute of Earth Surface Dynamics (IDYST) of University of Lausanne (Switzerland). The remaining part of each sample allowed the clay mineralogy and biostratigraphy analyses.

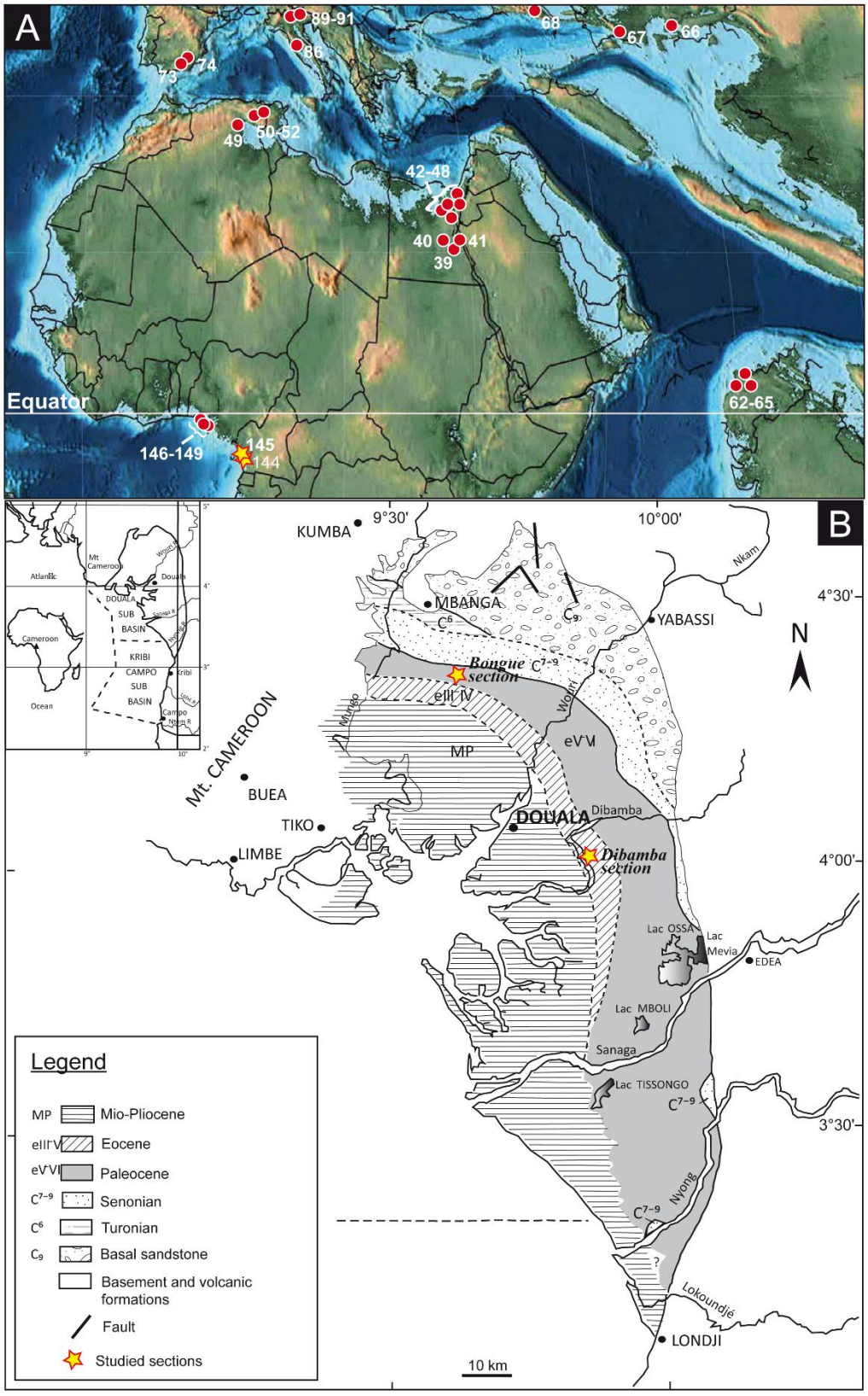

Figure 35. *A. Global Paleocene-Eocene (~56 Mya) paleogeographic map with PETM interval sites from Central Africa to Tethys (from McInery and Wing, 2011; modified). Sites 144 and 145 (this study), 146 to 148 (Frieling et al., 2017) and 149 (Gebhardt et al., 2011) have been added. B. Location and geological map of Douala sub-basin (from Njike-Ngaha, 1984; SNH, 2005; modified)*

3.2. XRD mineralogy

Mineralogy analyses were performed using a X-TRA Thermo-ARL Diffractometer based on semi-quantitative method, following the procedure described in Klug and Alexander (1974), Kübler (1987) and Adatte et al. (1996). The whole rock mineralogical composition was obtained by XRD patterns on 800 mg of random powder samples pressed (20 bars) into a powder holder, and external standards are used with error margins varying between 5 and 10% for the phyllosilicate and 5% for grain minerals. For the clay mineral fraction, triturated samples are introduced into glass containers with deionized water and then decarbonized by HCl 10% (1.25 N) during 20 minutes, including an ultrasonic disaggregation of 3 minutes for each sample. The insoluble residues are washed by centrifugation and repeated until a neutral solution (pH 7) is obtained. Following the Stockes law, two granulometric fractions (<2 µm and 2–16 µm) are pipetted and deposited on a glass plate. After air-drying, samples are analyzed by XRD. Subsequently, the <2 µm fraction samples are saturated with ethylen-glycol and remeasured in order to check for swelling minerals. This method allows the semi-quantification of the proportion of clay minerals with a precision better than 5%.

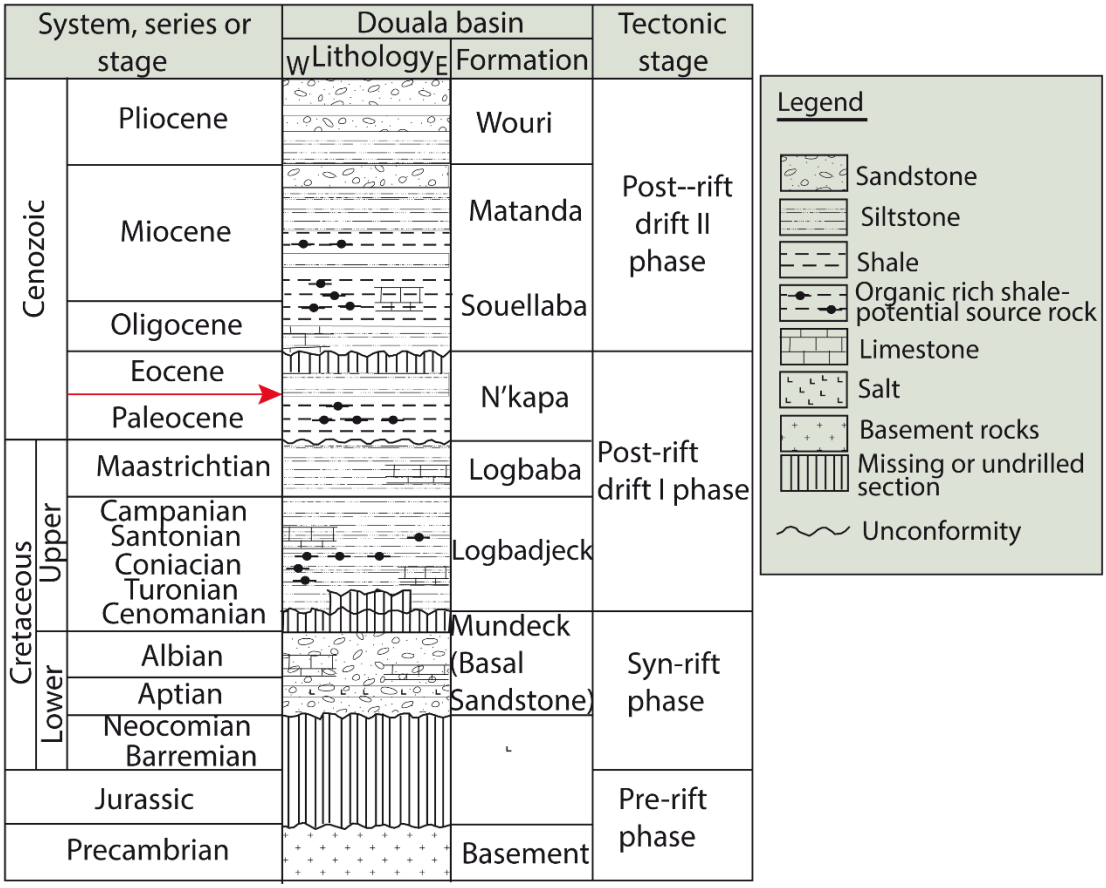

Figure 36. *Tectono-lithostratigraphy of Douala sub-basin (modified from Regnoult, 1985; Nguene et al., 1992; Manga, 2008)*

3.3. Whole rock geochemistry

Major (MEs) and trace (TEs) elements concentration were determinated by X-ray Fluorescence Spectrometry (XRFS) using a PANalytical PW2400 spectrometer at the University of Lausanne based on different standard reference materials (SY-2, NIM-N, NIM-G, BHVO). Major elements were determined on fused lithium tetraborate glass discs. For this purpose, samples were first heated to 1050 °C in an oven in order to calculate the loss of ignition (LOI). Then, 1.2000 ± 0.0002 g of ignited sample was mixed with 6.0000 ± 0.0002 g of lithium tetraborate ($Li_2B_4O_7$) and placed in a Bead machine PerlX'3 at 1250 °C to obtain the fused tablet. The obtained concentrations are given in weight percentages (wt.%). Trace element analyses were performed on pressed discs after mixing 15% of the powered samples with Mowiol 2%. The pressed discs were then placed in an oven at 110 °C for at least 6 h before analysis by XRFS. The trace element concentrations are given in parts per million (ppm).

3.4. Organic carbon isotope ($\delta^{13}C_{org}$)

The organic carbon isotope ratio ($\delta^{13}C_{org}$ values in ‰ VPDB) was determined from decarbonated (10% HCl treatment) samples based on continuous flow elemental analyser/isotope ratio mass spectrometry (EA/IRMS), as described previously (Spangenberg et al., 2010). Aliquots of samples were flash-combusted on a Carlo Erba 1108 (Milan, Italy) elemental analyser connected to a Thermo Fisher Scientific Delta V (Bremen, Germany) isotope ratio mass spectrometer that was operated in the continuous helium flow mode via a Conflo III split interface for the determination of the isotopic composition of the produced CO2. Reproducibility and accuracy are better than ±0.1‰ for $\delta^{13}C_{org}$.

3.5. Total organic carbon (TOC)

Organic matter content was determined using Rock Eval 6 with an IFP16000 as standard following the method described by Behar et al. (2001). Samples were placed in an oven and first heated at 300 °C under an inert atmosphere and then gradually pyrolysed up to 650 °C. After the pyrolysis is completed, the samples are transferred into another oven and gradually heated up to 850 °C in the presence of air. The determined parameters are total

organic carbon (TOC), Hydrogen Index (HI as mg HC/g TOC) and Oxygen Index (OI as mg CO2/g TOC), which permit an overall characterization of the sedimentary organic.

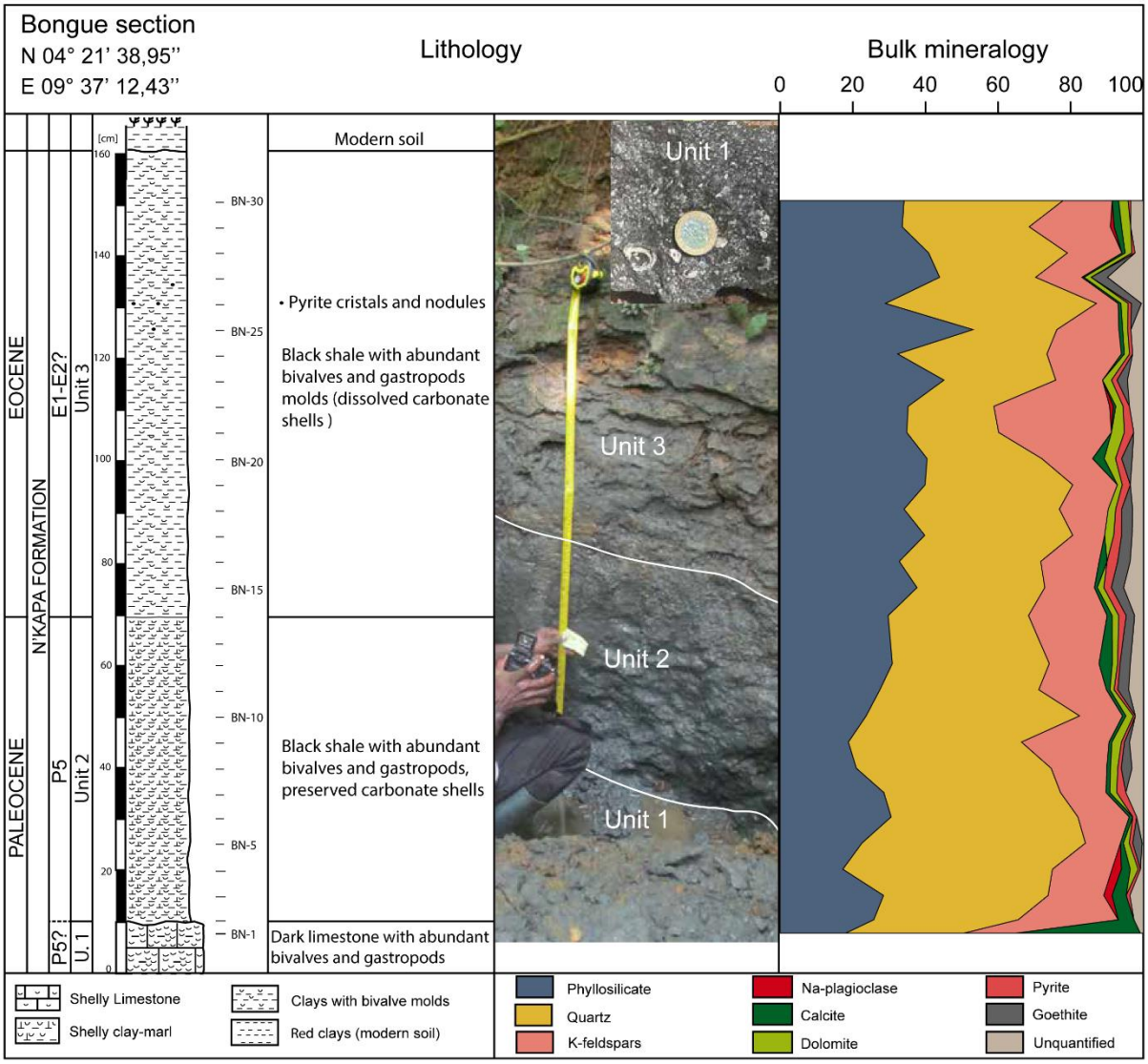

Figure 37. *Lithology and mineralogy of the Bongue section. Lithology reflects anoxic to dysoxic marine environment. Note that the PETM and post-PETM intervals are characterized by more humid conditions and increase in detrital input.*

3.6. Mercury (Hg) analysis

Hg content was determined using the Zeeman R-915F (Lumex, St. Petersburg, Russia), a high-frequency atomic absorption spectrometer specifically designed for Hg determination with a detection limit of 0.3–3 ppb. Measurements are based on the direct thermal evaporation of Hg from solid samples, without chemical pretreatment. Analyses were conducted on two aliquots. The accuracy was confirmed by the analysis of a GSD-11 certified reference materials, from Chinese alluvium (Zintwana et al., 2012) with a Hg content of 72.0 ppb.

3.7. Biostratigraphy

Biostratigraphic and faunal analyses based on planktic foraminifera and ostracod were performed at Princeton University, based on washed sediment residues (method described in Keller et al., 1995) prepared at the University of Lausanne. Quantitative species analysis was based on washed residues of the fine fraction (38-63μm) to evaluate dwarfing, >63μm to assess dominant species components, and the >150μm size fraction was searched for rare large species.

4. RESULTS

4.1. Lithology and mineralogy

Generally, N'kapa Formation (Paleocene-Eocene) is characterized as rich in marl and clay with unconsolidated sandstones. In this study, focused investigations in Bongue and Dibamba areas show lithological units slightly different of the known standard lithologies (Figs. 37 and 38). At the base of Bongue section, unit 1 (~10 cm thick) is a dark limestone with abundant bivalves and gastropods which consist to 34 % of calcite, 33 % of quartz, 18 % of phyllosilicates and 14 % of potassic feldspars. Smectites (50 %), mica (23 %), interstratified (I/S; 19 %) and zeolites (8 %) are essentials clay minerals in these materials. The overlying lithological unit is black shales of about 60 cm thick (unit 2; Fig. 37) presenting abundant preserved carbonate shells (bivalves and gastropods). This unit is globally characterized, from bottom (BN-2) to top (BN-13), by a gradual decrease in quartz (with a mean value of 50 %) and inversely for phyllosilicates of which average content is of 25 % (Fig. 37). K-feldspars (16 %) are abundant, and calcite (1,89 %), dolomite (1.37 %) and goethite (1.16%) are very low. Pyrite (0.93 %) and Na-plagioclases (0.44 %) are in traces. Limestone – black shales transition is marked by chlorite enrichment with a maximum at BN-4 (Fig.37) where kaolinite is absent, mica, zeolite and I/S are in low proportion (about 3 % for each one), and smectites 17 %. Beyond BN-4, chlorite reappears intermittently with relatively small proportions (6 - 11%) before its complete disappearance at the top of this unit (Fig. 37). Proportions of kaolinite vary between 31 – 72 % (with an average of 57 %) and that of smectite between 23 – 59 % with 36 % as mean value. Unit 3 (BN-14 to BN-30) is also consisting of black shales of 80 cm thick (Fig. 37) with abundant relics of carbonate shells (bivalves and gastropods) dissolution, usually

indicative of acidification in marine environment (e.g. Khozyem et al., 2015, Font et al., 2018 and Keller et al., 2018). Relatively to the top of previous unit, the base of unit 3 (BN-14) is marked by a net decrease in kaolinite (from 65,67 to 49.52 %), quartz (from 43.22 to 38.65 %) and calcite (from 3.65 to 1.37 %) which is associate to an abrupt increase in smectite (from 28.63 to 46.62 %), K-feldspars (from 13.7 to 21.65 %) and pyrite (from 0.67 to 2.05 %). Phyllosilicates remain relatively stable. Above BN-14 (BN-15 to BN-20), there is a sudden increase in phyllosilicates reaching 40 % at BN-20, as well as that of kaolinite which reaches maximum value (76 %) at BN-20 with a mean of ~64 %. Quartz content decrease gradually (39 % to 32 % with 38 % as average value) whereas that of K-feldspars returns to that of top of unit 2 (~13 %) and stays relatively uniform until the BN-20. Smectite is relatively high (18 – 45 % with 28.78 % as a mean value) and calcite is almost absent. Pyrite and goethite are globally low and yet reach their maximum values. Beyond BN-20, quartz, phyllosilicates and kaolinite globally increase while K-feldspars, pyrite and goethite decrease (Fig. 37). Smectite, although present in high content (mean value: 32.2 %), show a sawtooth trend. Chlorite is absent in this part except at BN-22 (~12 %) where it reappears.

Dibamba section (about 6.2 m thick) is meanwhile differentiated into five essentially clayey lithological units (Fig. 38). From the bottom to top, unit 1 (~45 cm thick) consists of black clay with small quartz pebbles and pyrite nodules, and rarely small bivalve molds. Unit 2 (~170 cm) is silty grey clays characterized by small quartz pebbles, bivalve and gastropod molds and small bioturbations. Modern iron crusts are also abundantly present. Unit 3 is consisting by dark grey clays of about 100 cm thick with rare bivalves and small bioturbations near the top. It is overcome by an atypic dark clay level (unit 4; Fig. 38) of about 55 cm thick consisting by large bioturbations infilled by silts, glauconite and abundant bivalves, and which is greatly characteristic of a maximum flooding surface. The last unit (unit 5) is consisting by silty clays with some clay pebbles and presenting abundant glauconite at the bottom, but disappearing towards the top. Bivalve shells are also abundant near the base and increasingly rare towards the top. Mineralogical trends in this section show, from the base of unit 1 to the top of unit 4, a gradual increase in phyllosilicates and smectite contrary to quartz, K-feldspars and kaolinite which decrease (Fig. 38). Mica is in low content (~5.75 %) and I/S appear intermittently in very low content at unit 3 and 4. The base of unit 5 (DI-19 to 20) presents a similar mineralogical composition to that of the top of the previous unit. Beyond BN-20, there is a drop in phyllosilicates from 56.43 % at DI-20 to 16.67 % at DI-23 before stabilizing around 22.45 % until the top of the section and inversely for the quartz content which presents a sudden increase from 32.89 % to 62.52 % before stabilizing at 63.64%. In the same time, smectite, I/S

and mica gradually increase and reach their maximum between DI-23 and DI-26 (except smectite) and where chlorite appears, before to decrease towards the top. Contrary to all these clay minerals, kaolinite decrease gradually and reaches the minimum (21 %) at DI-26. Also, pyrite and calcite are almost absent in DI section.

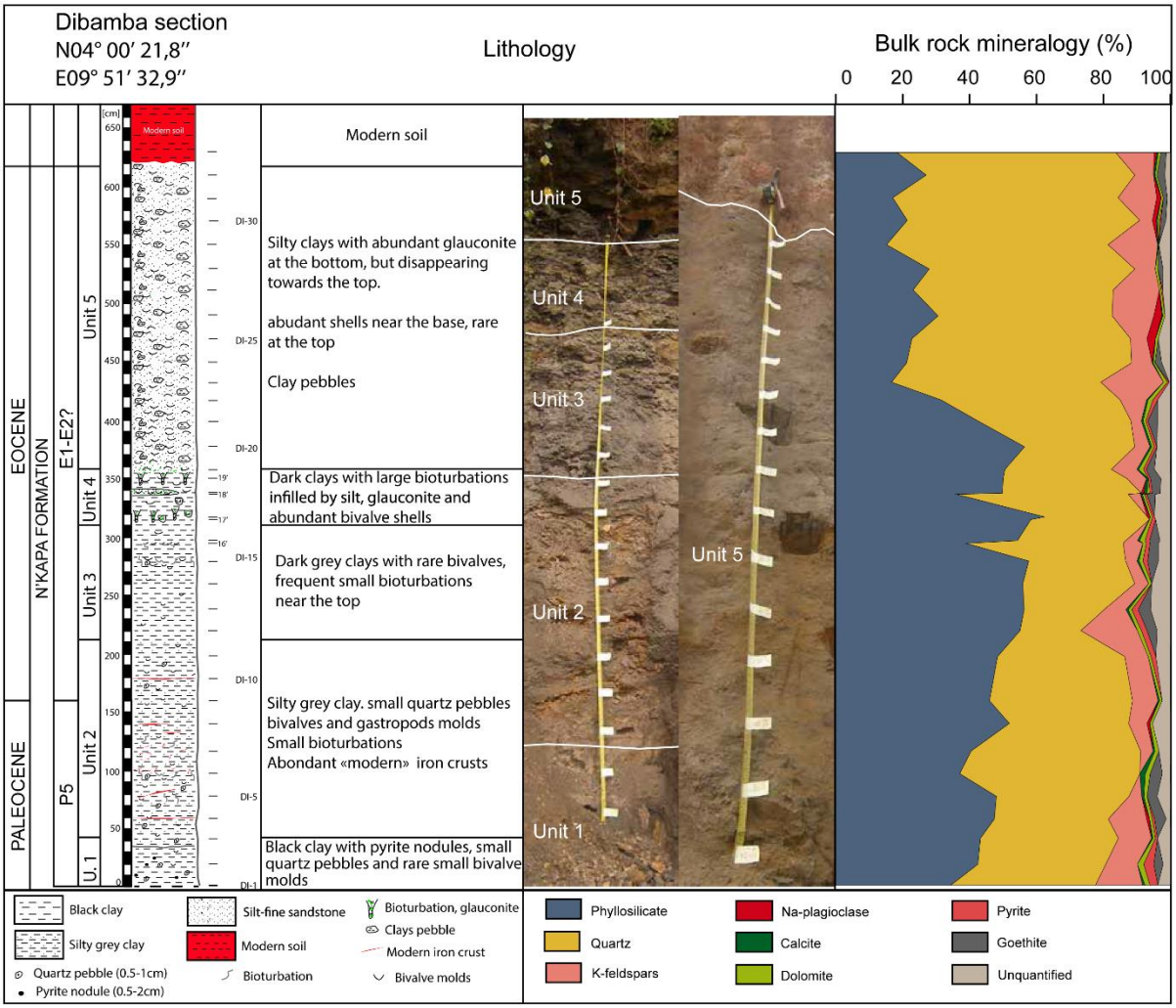

Figure 38. *Lithology and mineralogy of the Dibamba section. Lithology reflects marine environment. Note that the PETM and post-PETM intervals are characterized by more humid conditions and increase in detrital input.*

4.2. Biostratigraphy and age constraints

The biostratigraphy analysis based on foraminifera (benthics and planktics) and ostracods was applied to both sections (Bongue and Dibamba). It follows that some foraminiferal index species like rare *Acarinina esnaensis*, *Chiloguembelina trinitatensis* and mainly *Morozovella occlusa* as well as ostracods like *Cyntherella sylvesterbradleyi* and *Paracosta kefensis* identified in the lower part of Bongue section (BN-2 to BN-14) are correlated to the lower Dibamba section and correspond to latest Paleocene age (P5 zone)

preceding the PETM (Figs. 39 and 40). In the upper part of Dibamba section, *Chiloguembelina crinita* is identified and constitutes a common specie above the PETM in E1-E2 zones (Farouk, 2016).

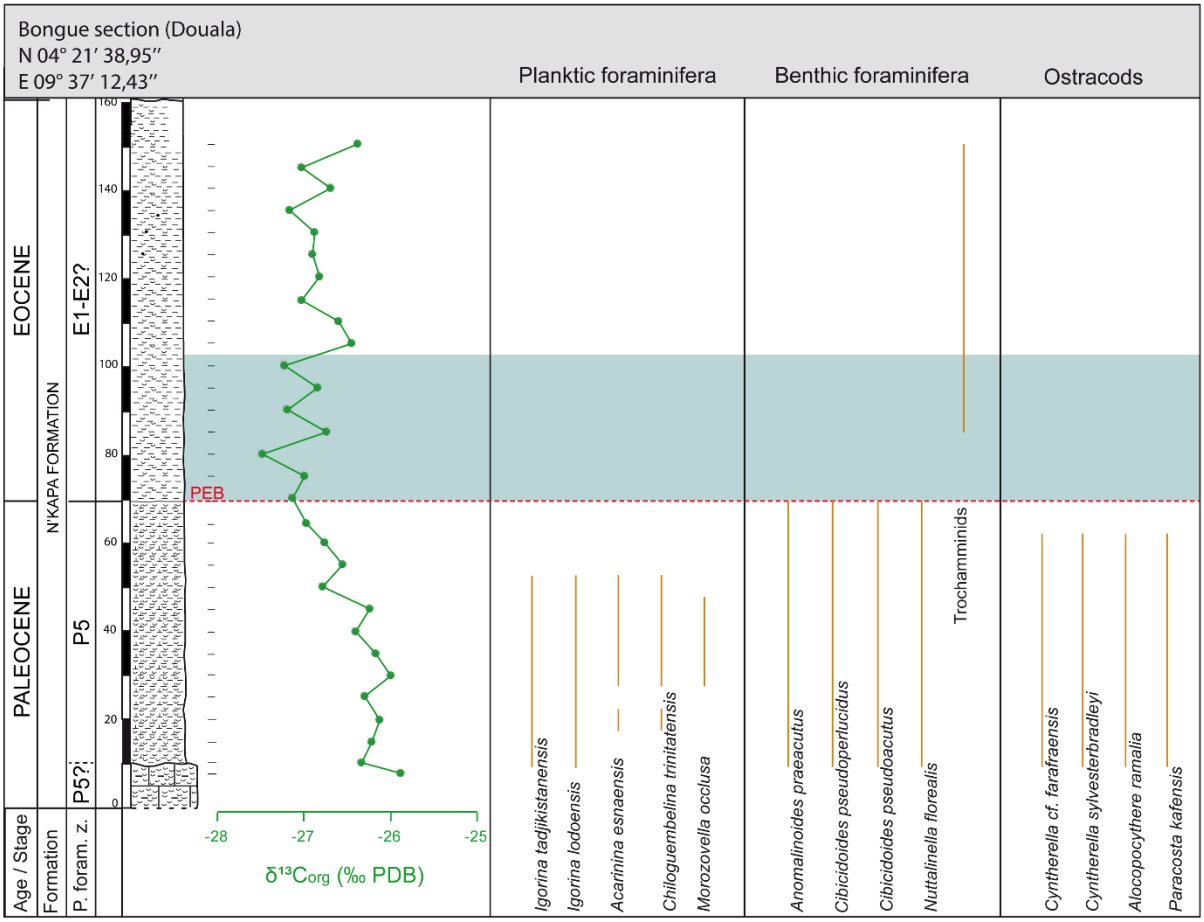

Figure 39. *Carbon isotope ($\delta^{13}C_{org}$), carbonate content ($CaCO_3$) variation and stratigraphic distribution of identified microfossils (ostracods, planktic and benthic foraminifera) along the Bongue section. Note that, decreased carbonate content interval coincides with minimum $\delta^{13}C_{org}$ values and disappearance of calcareous microfossil species across the PETM interval (blue shaded).*

The bottom samples of Bongue section (BN-2 to BN-14) have common bivalve shells, ostracods and benthic foraminifera with the latter assemblages dominated (~90%) by *Cibicidoides cf. C. pseudoperlucidus* (Bykova) 1956 and common *Anomalinoides praeacutus* (Vasilenko) 1950. For the most part these species are dwarfed, broken, thin shelled with holes due to dissolution. These benthic species suggest an inner to middle shelf environment and deposition during the late Paleocene because these species are rare after the PETM (e.g., Dababiya, Speijer et al., 1996; Alegret et al., 2005; Alegret and Ortiz, 2006). A late Paleocene age is in agreement with planktic foraminifera based on the great abundance of mostly dwarfed *Igorina tadjikistanensis*, rare *Igorina lodoensis*, *Acarinina esnaensis* and *Chiloguembelina*

trinitatensis, and one specimen of *Morozovella occlusa*. All of these species are only as calcite infillings where shells are dissolved plus carbonate blobs of recognizable species, and indicate a deposition during the latest Paleocene zone P5 just below the PETM. Ostracods *Cyntherella cf. farafraensis*, *Cyntherella sylvesterbradleyi*, *Alocopocythere ramalia* and *Paracosta kefensis* identified in this interval also indicate a late Paleocene age (Reyment 1963; Benson 1977; Bassiouni & Luger 1990; Bassoiuni & Morsi 2000). Based on above descriptions and correlative with a gradual decrease in carbonate and $\delta^{13}C$ values (Fig. 39), carbonate dissolution is present in the lower part of this section as evident by benthic foraminifera shell dissolution effects, including thin shells with holes and generally broken chambers.

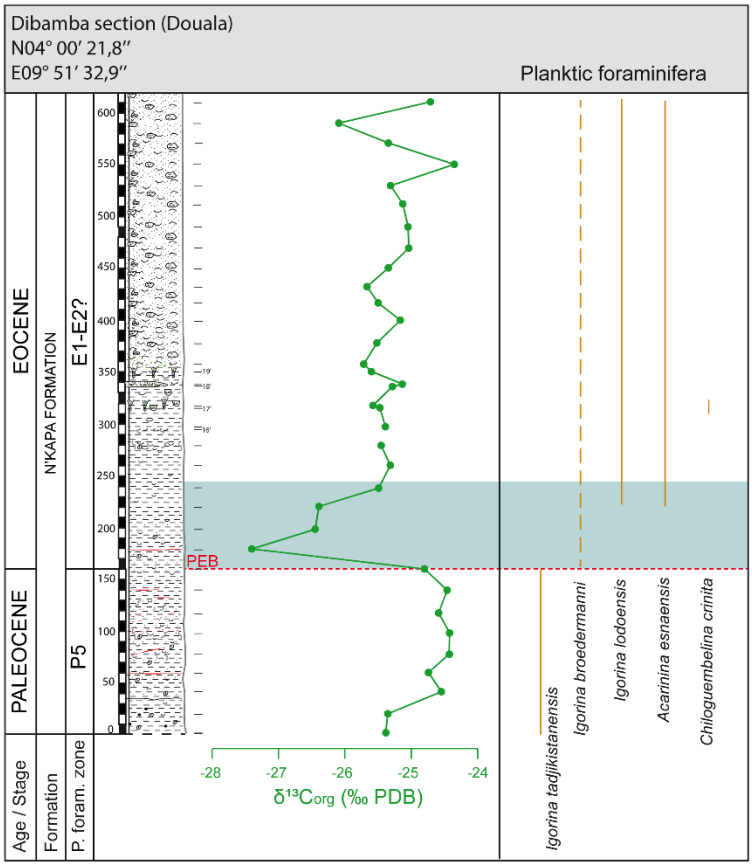

Figure 40. *Carbon isotope ($\delta^{13}C_{org}$), carbonate content ($CaCO_3$) variation and stratigraphic distribution of identified planktic foraminifera species along the Dibamba section. Note that, decreased carbonate content interval coincides with minimum $\delta^{13}C_{org}$ values and disappearance of calcareous microfossil species across the PETM interval (blue shaded). Only tiny carbonate blobs are present and recognised as a one renewed planktic species.*

In the sample BN-15 benthics are rare and ostracods absent. This means that carbonate dissolution increased significantly through the upper part of the Bongue section beginning with sample 15, thus excluding calcareous benthic foraminifera, ostracods and bivalve shells, possibly due to severe ocean acidification generally associated with the PETM. In the

uppermost part (BN-21 to BN-30) of this section, bivalve shells, ostracods and calcareous benthics are absent and only some arenaceous benthic foraminifera (Trochamminids, Fig. 39) are present. This part seems to be post PETM (See Alegret et al., 2005; Alegret and Ortiz, 2006).

As in the Bongue section, the lower half of Dibamba section (DI-1 to DI-10) consists by carbonate blobs of dissolved foraminifera that are rarely identifiable; some rare bivalve shells are observed, no calcareous benthic foraminifera but arenaceous benthics are present. Some *Igorina tadjikistanensis* are identified. This species is very abundant in the latest Paleocene and disappears at the PETM, that correlates this part to the lower half of Bongue. In the upper part of the section (DI-11 to DI-32), some tiny white carbonate blobs which can be identified as *Igorina broedermanni* of which the Paleocene ancestor is *Igorina tadjikistanensis* are present, as well as *Chiloguembelina crinita*, *Igorina lodoensis* and *Acarinina esnaensis* (Fig. 40). The two last species begin in zone P5 but are only common above PETM (Keller et al., 2018) while *Chiloguembelina crinita* indicates the E1-E2 zones (Farouk, 2016). Few unidentified small benthic infillings are also observed. The planktic assemblage of this part as well as the dissolution effects observed above the PEB correspond to Eocene E1-E2 zones, which correlate the upper half of Dibamba to that of Bongue.

4.3. Organic carbon isotope ($\delta^{13}C_{org}$), total organic carbon (TOC) and mercury content (Hg)

The Bongue and Dibamba $\delta^{13}C$ values show a negative excursion that culminates from BN-14 to BN-20 for Bongue and from DI-9 to DI-13 for Dibamba (CIE: carbone isotope excursion) and which are associated at the onset to a gradual decrease (pre-CIE) and recovery above (Figs. 41A and 42A). At the base of both sections (sample BN-2 to 6 for Bongue and DI-3 to 6 for Dibamba) during the late Paleocene, $\delta^{13}C$ values are relatively. Above, the pre-CIE is marked by a gradual decrease from -26,00 ‰ at BN-6 to -27,13 ‰ at BN-14 and from -24,42 ‰ at DI-6 to -24,80 ‰ at DI-9, i.e. 1,13 ‰ of variation for Bongue and 0,38 ‰ for Dibamba, and corresponds to latest Paleocene P5 zone. Correlatively to pre-CIE $\delta^{13}C$ values, high Hg/TOC values prior to BN-14 (Fig. 41A) and DI-9 (Fig. 42A) suggest volcanic activity and decreasing productivity leading up to the PETM. This is similar to Dababiya. Although the TOC content is low throughout the Bongue section (<1 %) and in the lower half of Dibamba, it however shows a slightly increase in the latest Paleocene P5 zone correlated with the pre-

CIE interval (Figs. 41A and 42A). This probably results of the gradually extinction of planktic and benthic species due to the increasing ocean acidification.

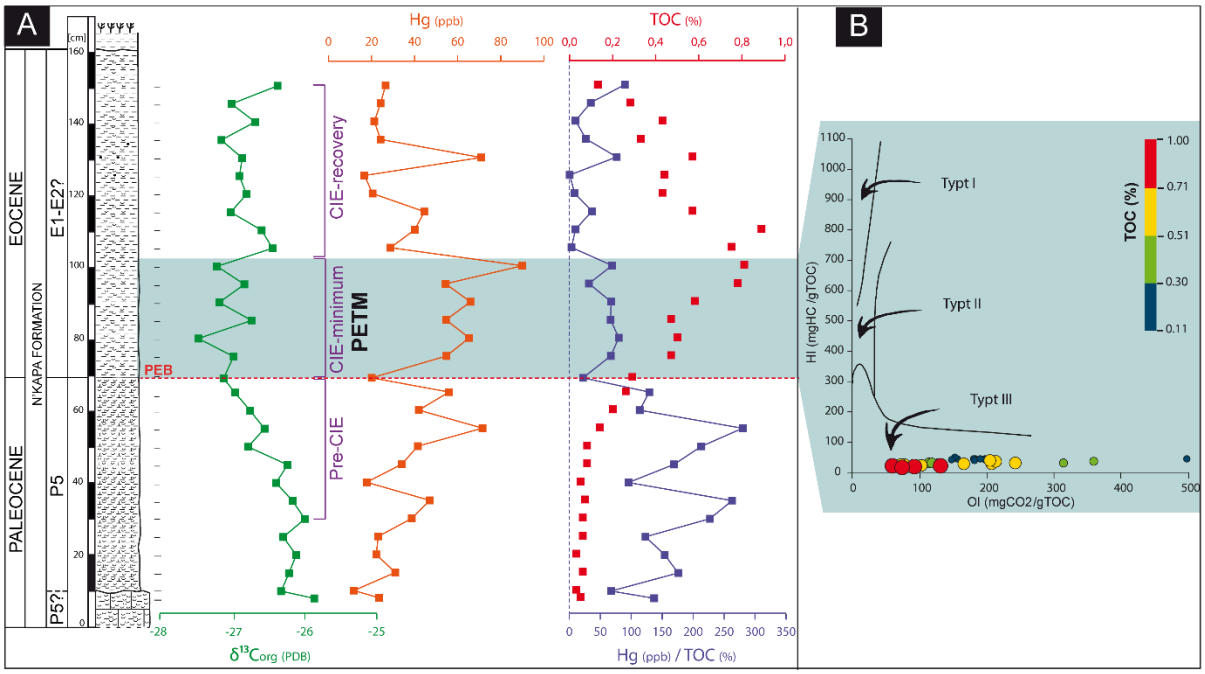

Figure 41. *A. $\delta^{13}C_{org}$, Hg concentration, TOC and Hg/TOC ratio from Bongue section. Note the gradual decrease in δ^{13}Corg values starting 40 cm below the PEB (pre-CIE interval) coupled with high Hg/TOC ratio reflecting volcanism prior the PEB. CIE-minimum values correlate with high Hg and TOC contents suggesting a strong link between organic matter and Hg concentration during the PETM. B. HI vs. OI cross plot of the PETM interval at Bongue. Note that the low HI values coupled with increased OI reflect a typt-III organic matter suggesting a terrestrial origin or a highly reworked marine organic matter.*

Between BN-14 and BN-20 at Bongue and DI-9 and DI-13 at Dibamba, the δ^{13}C values reach their minimum and thus constitute the CIE-minimum (Figs. 41A and 42A) generally associated with the PETM (see Khozyem et al., 2015). Also, the sharply increase in Hg is coupled by that of TOC (Figs. 42A and 42A), showing a strong link between TOC and Hg contents in these intervals. This suggests a strong accumulation of organic matter as a result of mass extinction due to a severe ocean acidification. These results agree with the biostratigraphic data. In addition, TOC of PETM intervals is mainly Type-III organic matter (Figs. 41B and 42B) that reflected a continental source or highly weathered marine organic matter.

Above the PETM interval in both sections (from BN-21 to BN-30 for Bongue and from D-14 to DI-18), the δ^{13}C values gradually increase and constitute the CIE-recovery phase during early Eocene (Figs. 41A and 42A). Hg content decreases progressively (from 28,80 ppb to 26,50 ppb at Bongue and 38,30 ppb to 23,80 ppb at Dibamba) correlatively to TOC.

However, Hg/TOC ratio values remain relatively low in this interval, evidence of a quiet period (no volcanism) during earliest Eocene. This quiet period continues in the Dibamba area up to sample DI-22, beyond which a new volcanic episode is materialized by an abrupt increase in Hg/TOC ratio (Fig. 42A).

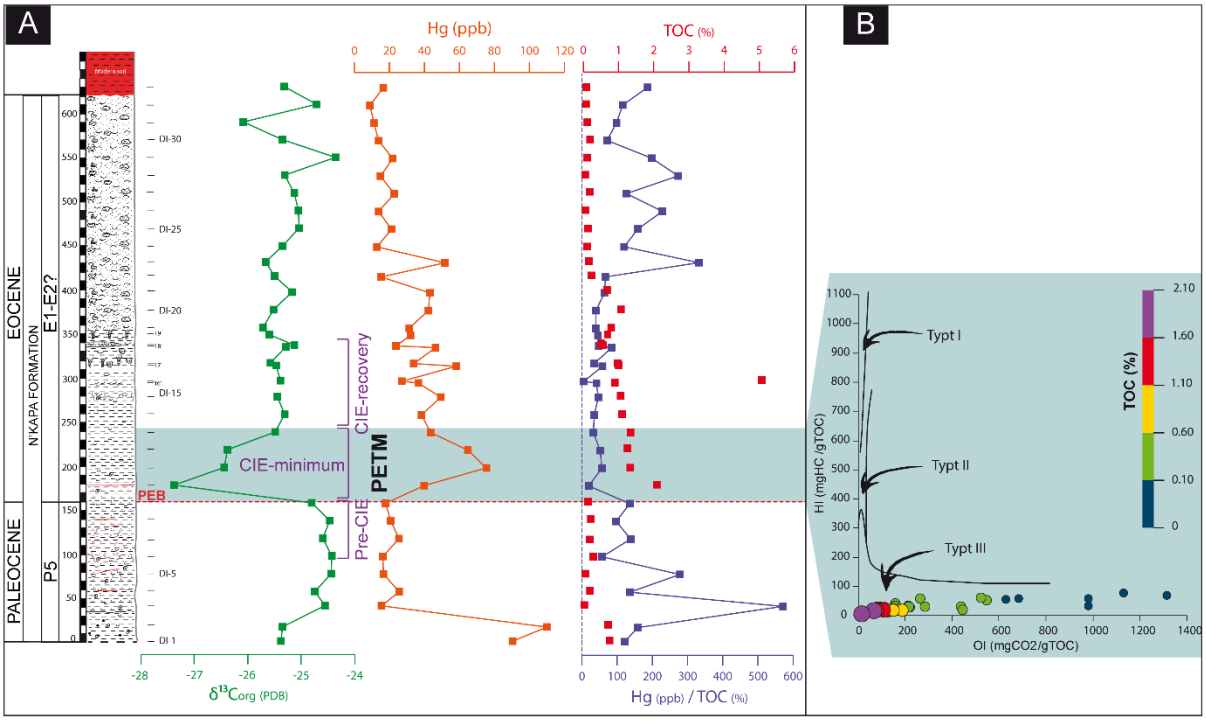

Figure 42. *A. $\delta^{13}C_{org}$, Hg concentration, TOC and Hg/TOC ratio from Dibamba section. Note the gradual decrease in δ^{13}corg values starting 60 cm below the PEB (pre-CIE interval) coupled with high Hg/TOC ratio reflecting volcanism prior the PEB. CIE-minimum values correlate with high hg and toc contents suggesting a strong link between organic matter and hg concentration during the PETM. B. HI vs. OI cross plot of the PETM interval at Dibamba. Note that the low HI values coupled with increased OI reflect a typt-III organic matter suggesting a terrestrial origin or a highly reworked marine organic matter.*

4.4. Major and trace elements geochemistry

4.4.1. Major elements

Major element (ME) concentrations (Figs. 43A and B) show along both sections significant variations which allow to materialize, for example, different trend values across the PEB. Enrichment Factor (EF= $(X/Al)_{sample}/(X/Al)_{PAAS}$) for each trend or interval were determined to evaluate enrichment in major and trace elements of modern and ancient sediments (Table 5). Several authors have used this approach (e.g., Algeo and Maynard, 2004; Rimmer, 2004; Tribovillard et al., 2006; Soliman et al., 2011).

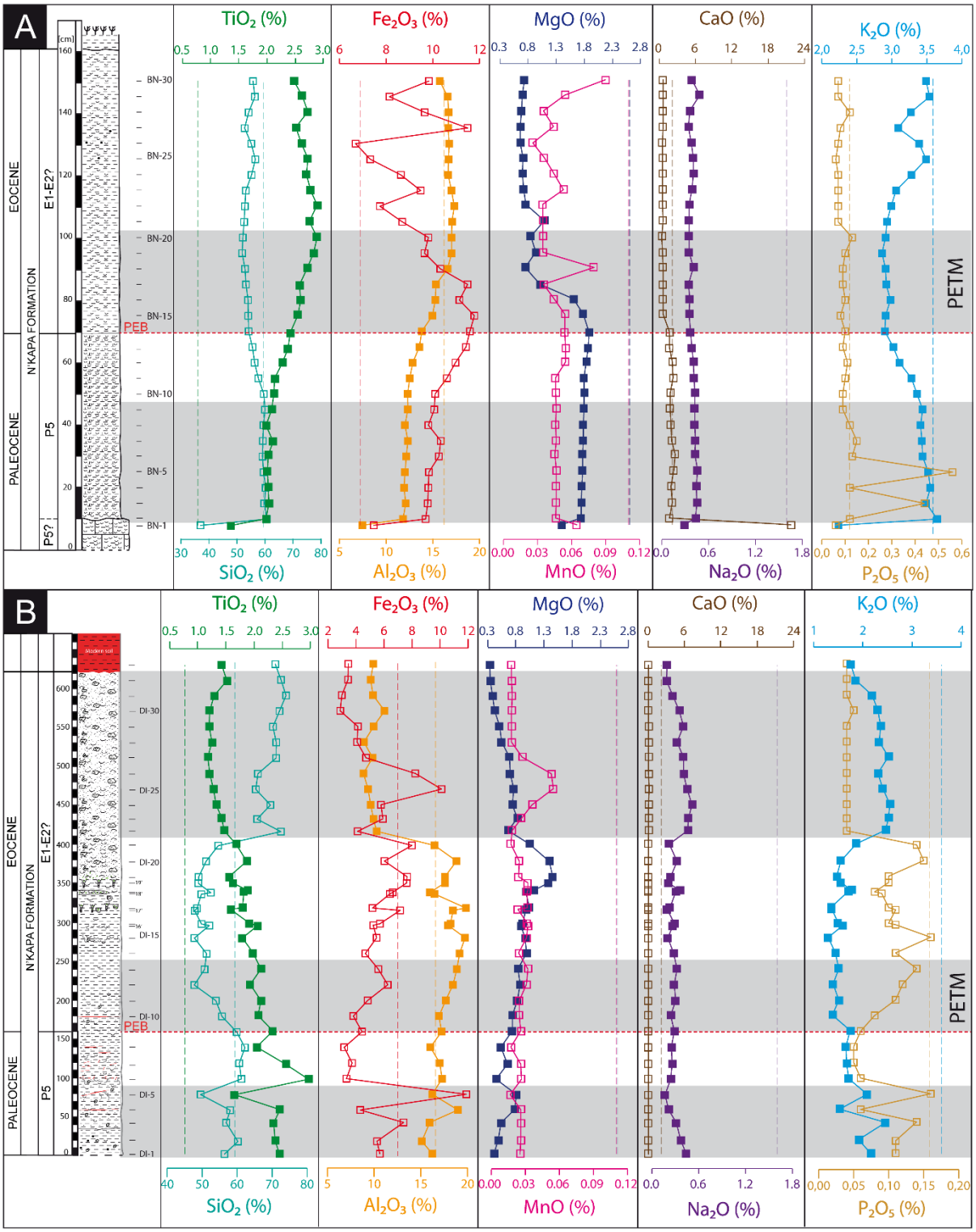

Figure 43. *Major elements (MEs) stratigraphy of (A) Bongue and (B) Dibamba sections. Note that increase in Fe, Al and Mg oxides below and above the PEB reflect gradual increase of chemical weathering and continental runoff.*

For the case of Bongue section, five intervals marked by the alternation of grey and light strips show trends of MEs (Fig. 43A). Globally, the bottom limestone sample (BN-1; interval 1) presents a large difference in ME concentrations probably linked to strong variation

of clay content. It is highly enriched in CaO (EF=21.87) with a moderated EF in TiO_2 (3.89) and Fe_2O_3 (2.40). SiO_2, MgO, K_2O, and P_2O_5 exhibit concentrations very close to average shale values while Na_2O depleted. In the interval 2 (from BN-2 to BN-9; Fig. 43A), except P_2O_5 fluctuating values with an EF(P)= 1.84, all ME concentrations exhibit relatively stable values. SiO_2 is in high proportions range from 59.10 to 60.61% with a mean of 59.74% very close to the shale value (58.90%). Al_2O_3 and Fe_2O_3 are in moderated proportions and range respectively from 11,80 to 12,33% (with 12.08% as mean value) and from 9.69 to 10.34% (with a mean value of 9,95%). Fe_2O_3 is slightly enriched with an EF=1,98. TiO_2, MgO and K_2O contents are relatively low and present a respectively variation and mean value of 0.12% and 2.03% for TiO_2, 0.05% and 1.77% for MgO and, 0.24% and 3.49% for K_2O. In contrast, TiO_2 (EF=3.59) is moderately enriched whereas MgO (EF=0.93) and K_2O (EF=1.33) remain close to their respective average shale values

Table 5. *Enrichment factor (EF) relative to PAAS of major and trace elements across the Paleocene-Eocene boundary samples from Bongue and Dibamba sections. PAAS data are from Wedepohl (1971; 1991).*

Elements	Enrichment Factor (EF)										Average Shale
	Bongue section					Dibamba section					
	Inter. 1	Inter. 2	Inter. 3	Inter. 4	Inter. 5	Inter. 1	Inter. 2	Inter.3	Inter. 4	Inter. 5	
SiO_2	1,40	1,40	1,27	0,97	0,93	0,97	1,04	0,86	0,78	2,04	58,90 %
TiO_2	3,89	3,59	3,72	3,61	3,43	2,94	3,21	2,55	2,14	2,89	0,78 %
Al_2O_3	1,00	1,00	1,00	1,00	1,00	1,00	1,00	1,00	1,00	1,00	16,70 %
Fe_2O_3	2,40	1,98	2,02	1,67	1,26	1,03	0,49	0,67	0,82	1,25	4,90 %
MgO	1,19	0,93	0,90	0,52	0,28	0,23	0,21	0,29	0,39	0,38	2,60 %
CaO	21,87	1,27	1,17	0,36	0,25	0,00	0,00	0,00	0,00	0,03	2,20 %
Na_2O	0,42	0,39	0,34	0,25	0,25	0,20	0,16	0,17	0,16	0,41	1,60 %
K_2O	1,38	1,33	1,15	0,86	0,90	0,58	0,46	0,39	0,39	1,09	3,60 %
P_2O_5	0,89	1,84	0,79	0,65	0,46	0,74	0,34	0,59	0,62	0,40	0,16 %
Sc	1,89	1,18	1,20	1,08	0,99	1,19	0,69	0,61	0,65	0,93	13 ppm
V	1,91	1,83	1,80	1,38	1,18	1,22	0,63	0,68	1,23	1,26	130 ppm
Cr	2,65	2,52	2,51	2,00	1,65	2,03	0,96	1,09	1,26	1,76	90 ppm
Mn	1,16	0,44	0,44	0,36	0,32	0,13	0,14	0,16	0,18	0,28	850 ppm
Co	2,41	2,06	2,16	1,77	1,28	0,57	0,36	0,52	0,72	0,83	19 ppm
Ni	0,76	0,70	0,76	0,79	0,72	0,41	0,29	0,40	0,50	0,48	68 ppm
Cu	0,30	0,21	0,25	0,31	0,30	0,29	0,28	0,26	0,21	0,22	45 ppm
Zn	3,40	3,10	3,04	2,38	2,73	1,31	0,96	1,20	2,35	2,39	95 ppm
Rb	0,73	0,71	0,63	0,48	0,47	0,31	0,33	0,26	0,30	0,55	140 ppm
Sr	3,18	0,99	0,90	0,47	0,43	0,23	0,26	0,17	0,16	0,31	300 ppm
Zr	12,33	12,04	11,28	6,19	4,20	6,81	5,20	3,59	3,09	8,51	160 ppm
Ba	1,81	1,66	1,45	1,13	1,34	0,89	0,62	0,37	0,33	0,98	580 ppm
Pb	0,95	1,13	1,10	1,14	1,09	1,69	1,13	0,99	0,86	0,93	22 ppm
Th	3,35	2,70	2,64	1,84	1,49	1,98	1,53	1,18	1,16	1,75	12 ppm
U	3,31	2,23	2,08	1,42	1,24	1,31	1,23	0,97	0,82	1,45	3,7 ppm

The latest Paleocene P5 zone (interval 3) just below the PEB is marked by a net variation of the trend of ME curves (Fig. 43A). There is a gradual depletion in SiO_2 (EF=1.27), CaO (EF=1.17), Na_2O (EF=0.35) and K_2O (EF=1.15) contents whereas TiO_2 (EF=3.72),

Al_2O_3, Fe_2O_3 (EF=2.02) and MgO (EF=0.90) slightly increase. Also, P_2O_5 (EF=0.79) gradually depleted relatively to underlying values (EF=1.84). At the Bongue PETM interval (interval 4), a suddenly change of Fe_2O_3 (EF=1.67) and MgO (EF=0.52) curves trends is observed while TiO_2 and Al_2O_3 contents gradually increase reaching their maximum values between BN-18 and BN-20 (Fig. 43A). In this interval, SiO_2, CaO, Na_2O and K_2O also continuous the decreasing and reach their minimum values between BN-18 and BN-20. P_2O_5 remains relatively stable. Beyond sample BN-20, except Fe_2O_3 that fluctuates and CaO and P_2O_5 which remain stable until the top of the section, all other ME curves globally change tendency showing a recovery phase during early Eocene.

Furthermore, Dibamba section is also differentiated into five trend zones of ME curves (Fig. 44B), but the second, third and fourth zones will all be treated as the middle group because of a great similarity of ME curves evolution. The first, from DI-1 to DI-5, globally exhibits a depleted interval in MgO (EF=0.23), CaO (absent), Na_2O (EF=0.20), K_2O (EF=0.58) and P_2O_5 (EF=0.74) whereas SiO_2 and Fe_2O_3 contents are similar to shale values, and TiO_2 slightly enriched. At the onset of the middle group (DI-6 – DI-21), there is a spurt of the SiO_2, TiO_2 and Na_2O contents (reaching the maximum TiO_2 value), then SiO_2 and TiO_2 gradually decrease across the middle zone while Na_2O increases. Fe_2O_3, Al_2O_3 and MgO drop at the beginning of interval 2, before gradually increase across this zone. P_2O_5 content also gradually increases contrary to that of K_2O which decreases (light grey, Fig. 43B). CaO is always in trace. The fifth interval is marked by an abrupt increase of SiO_2, MnO, CaO, Na_2O and K_2O contents followed by their gradual decrease toward the top of section. Fe_2O_3, Al_2O_3 and MgO drop abruptly and the two last pursue their decreasing toward the top while Fe_2O_3 shows a spurt reaching the maximum value before decreasing.

4.4.2. Trace elements

For the marine sedimentary deposits, trace elements (TEs) are commonly normalized to Al because of his immobility during diagenetic processes. This allows to avoid dilution effects by carbonates (Van der Weijden, 2002; Tribovillard, 2006). EF was also calculated according to equation above.

In the case of Bongue section, Al-normalized TE curves are distinct and show globally, except the bottom limestone sample (BN-1), four main trends through the section (Fig. 44A). From BN-2, Sc, V, Cr, Mn, Co, Zn, Rb, Sr, Zr Th and U deplete toward the top of the section (Fig. 44A; Table 5). This depletion is more pronounced in the interval 4 and in most cases reaches the minimum values between BN-18 and 20. Ni and Cu proportions, although being

below average shale values, however show an increase up to the interval 4 ($EF_{(Ni)}$=0.70 to 0.79; $EF_{(Cu)}$=0,21 to 0.31) before slightly decreasing through the interval 5. For almost all the Al-normalized TE, interval 5 seems be a recovery phase.

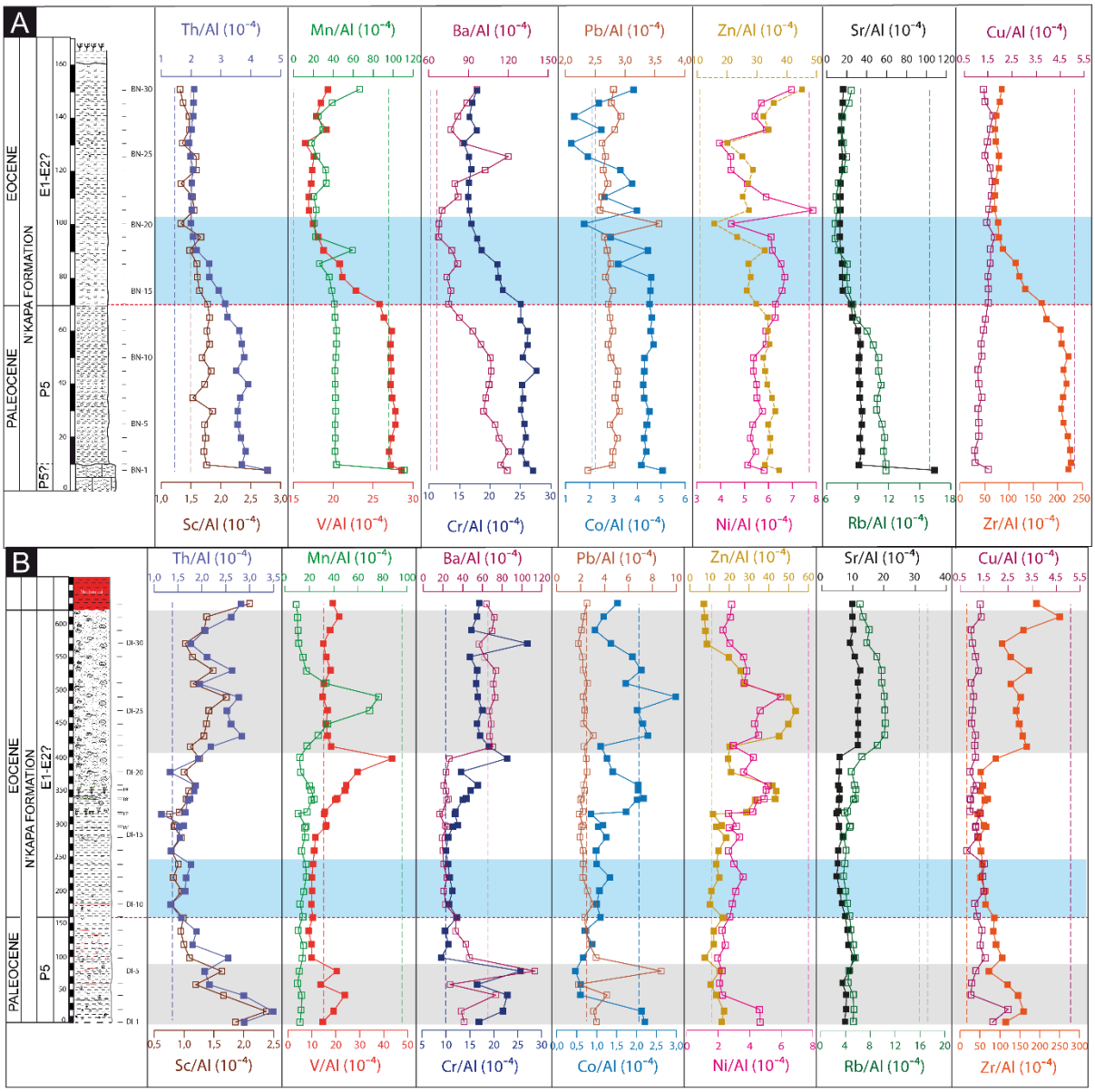

Figure 44. *Al-normalized trace elements (TEs) distribution from lithologs of (A) Bongue and (B) Dibamba. Decrease in Mn, V, Ba, Cr, Zn, Rb, Sr and Zr in the PETM suggest a low mobility of these element relatively to Al whereas a slight positive spurt in Ni/Al and Cu/Al ratios reflect a high mobility of Ni and Cu.*

As for Dibamba section, Al-normalized TE curves are characterized by three distinct trends (Fig. 44B). The bottom shaded samples (DI-1 to 5) show significant fluctuations in almost all TE/Al ratios (Fig. 44B). This interval is depleted in Mn (0,13), Co (0,57), Ni (0,47), Cu (0,29), Rb (0,31) and Sr (0,23) contrary to Zr (6,81) highly enriched. Sc, V, Ba, Zn and U contents are very close to that of average shales while Cr, Pb and Th are moderately enriched.

From BN-6 to 21, there is a globally depletion in Th, Sc, Ba, Cr, Rb, Sr, Zr, V and U followed by a sharply increase through the upper shaded zone. In contrast, Mn, Co, Ni and Zn increase gradually in this interval then sharply increase from BN-17 until the top of the section.

5. DISCUSSION

5.1. Dissolution and genuine paleoecological signal across the PETM: an overview in Gulf of Guinea

The dissolution at the onset of PETM is one of the features that worldwide characterizes this event. According to Zachos et al. (2005), it is caused by a progressive shoaling of the lysocline/CCD. Hence, the bottom samples globally show a slight progressive decrease of $CaCO_3$ prior to the PEB (Figs. 39 and 40) indicating the beginning of a gradual and continuous dissolution. This hypothesis is in agreement with the microfossil assemblage, where the shells of calcareous benthics are clearly affected by dissolution, but always present even in the last 15 cm below the PEB (Fig. 39). In the P5 zone, the dwarfism of identified planktic species, also reported in Dahomey basin (SW of Nigeria) by Bio-Lokoto et al. (1998), is undoubtedly the result of physico-chemical conditions that are inimical to pelagic forms linked to the PETM effects.

The dissolution intervals (from BN-14 to 20 in Bongue and from DI-9 to DI-13 in Dibamba) show a sharp drop in $CaCO_3$ contents due to a severe ocean acidification generally linked to the PETM. Calcareous benthic foraminifera are rare, and planktic foraminifera and ostracods absent except in Dibamba, where some tiny white carbonate blobs are identified as *I. broedermanni*. Similar phenomena (rarity and/or absence of the same planktic species: *Chiloguembelina*, *Morozovella*, *Acarinina* and *Igorina*) have also been reported in the early Eocene of Dahomey basin, suggesting a reduced water depth, or a risen oxygen minimum zone related to the carbon release connected with the PETM (Gebhardt et al., 2010). The disappearance continues throughout the top part of sections and only a few arenaceous benthics are present in Bongue and some *I. lodoensis*, *A. esnaensis* and *C. crinita* in Dibamba. The entire upper half of the Bongue section beginning with BN-15 and PETM interval in Dibamba are therefore the place of a mass extinction in relation to the sudden variation of paleoecology.

These results, including those of Bio-Lokoto et al. (1998), Gebhardt et al. (2011) and Frieling et al. (2017), testify to the presence of the PETM event in the Gulf of Guinea so far

little studied and mapped in figure 35. For this, a correlation of different results shows an overview of the PETM interval in the Gulf of Guinea (Fig. 45).

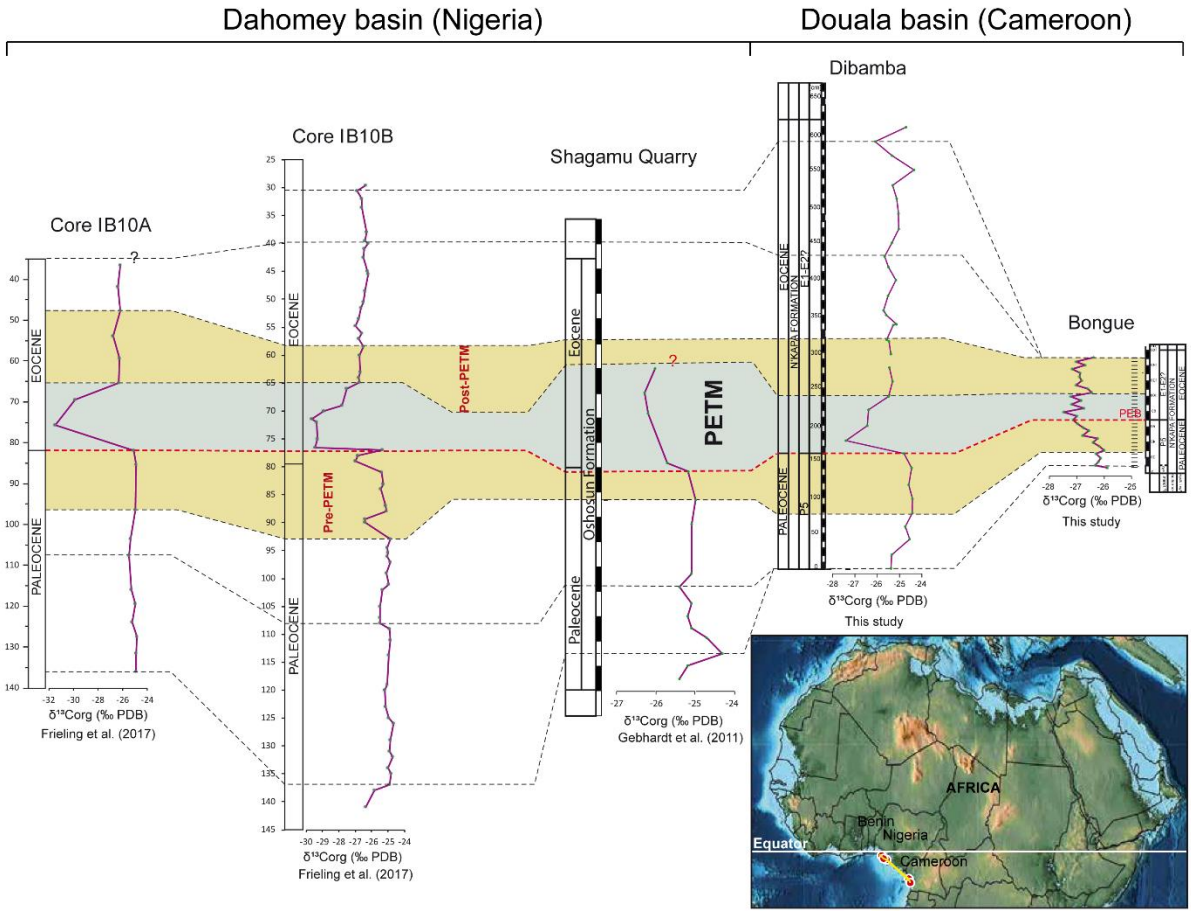

Figure 45. *Local correlation of the PETM interval in Gulf of Guinea (Nigeria and Cameroon) based on organic carbon isotope excursion ($\delta^{13}C_{org}$-CIE). IB10A and IB10B cores data as well as Shamagu Quarry data are from Gebhardt et al. (2010) and Frieling et al. (2017) in Dahomey basin, and Bongue and Dibamba section data are from Douala sub-basin in this study.*

5.2. Geochemical and mineralogical signatures across the PETM

The major mineralogical and geochemical changes associated with the PETM observed throughout the world include negative shift in $\delta^{13}C$, carbonate dissolution, enhanced fluvial input, fluctuation in phyllosilicate abundances and some clay minerals, change in detritus sensitive trace elements, ocean acidification and other attendant effects (Zwingmann et al., 1999; Crouch et al., 2003; Zachos et al., 2005; Tribovillard et al., 2006; Sluijs et al., 2007; McInerney and Wing, 2011; Schulte et al., 2011, 2013; Handley et al., 2012).

In sedimentary deposits, chemical elements abundance is generally or partly controlled by bulk mineralogy. This is the case for example of carbonate rich sample BN-1 in Bongue

section, which presents a large difference in elemental concentration with respect to overlying rich-clayey samples (Figs. 43A, 44A and 46). However, both sections are constituted by rich-clay materials with very low or no carbonate content (Figs. 39 and 40), this allows to appreciate clearly the relative abundance and variation of elements regardless of the lithology along the sections.

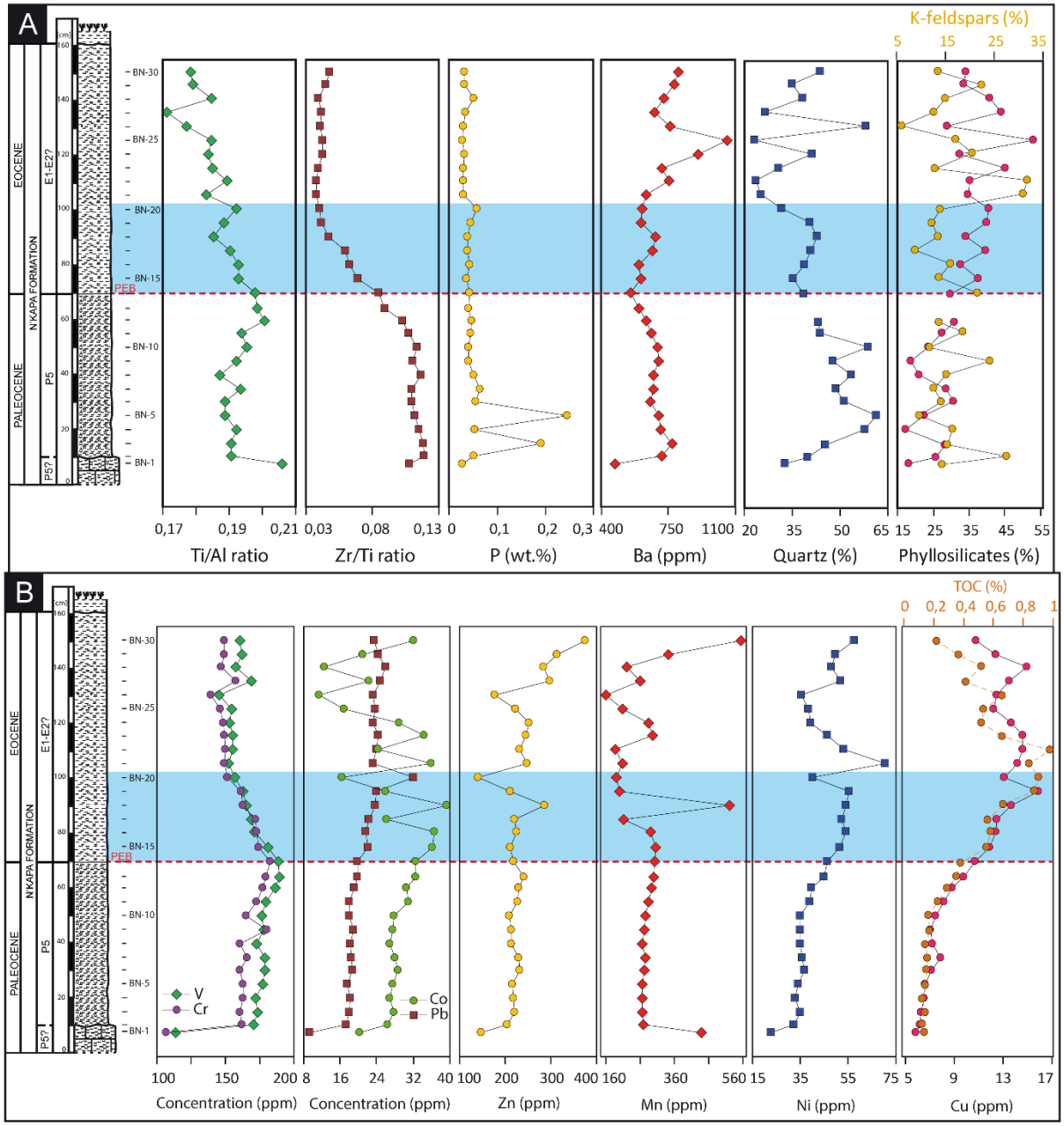

Figure 46. *Stratigraphic evolution of selected significant ratios and elements across the Paleocene-Eocene boundary (PEB) in Bongue area. A. Noted increase in Ba, quartz and phyllosilicates during the PETM suggests an increased productivity, intense chemical weathering and continental runoff. B. Note that increase in Co, Pb, Ni, Cu and TOC contents in the PETM interval indicates dysoxic to anoxic conditions.*

At the latest Paleocene P5 zone just below the PEB, the globally increasing in Ti/Al and decreasing in Zr/Ti ratios in the both sections reflect a Ti enrichment of sediments towards the PEB (Figs. 46 and 47). In addition, the strong mobility of Si, Ti and Zr relative to their respective PAAS values (Fig. 47) is an evidence of a high detritism at this period. These results coincide with a gradual increase in some significant elements (V, Cr, Pb, Co, Mn, Ni, Cu) as well as COT content (Figs. 12 and 13). Phyllosilicates abundance and the Chemical Index of Alteration (CIA) also increase gradually towards the PEB and agree to the pre-CIE and the gradual decrease of carbonates. Similar results, also observed in several sections around the world, constitute precursors of the PETM climate change (Solimann et al., 2011; Khozyem et al., 2015; Gupta and Kumar, 2018).

In the assumed PETM interval, the enriched Ti and Zr contents (Figs. 48A and B; Table 5) combined to increased phyllosilicate abundance and a slight positive inflection in quartz (Figs. 46A and 47A), reflect a strong period of fluvial discharge (Khozyem et al., 2015). Among the chalcophile elements, we note the high concentrations of V, Cr, Ni, Co, Mn, Cu, Zn and Pb (Figs. 46B and 47B). High amounts of these elements can be incorporated in sediments deposited under reducing conditions (Brumsack, 1980; Jacobs et al., 1985, 1987; Brumsack, 1989; El-Kammar et al., 1990; Hatch and Leventhal, 1992; Calvert and Pedersen, 1993; Brumsack, 2006; Tribovillard et al., 2006). In addition, the slightly increased P values coupled with increased TOC contents as observed in both sections are generally recorded under dysoxic to intermittently anoxic conditions (Fantasia et al., 2018a). These hypotheses agree with less oxidizing conditions along the sea floor; which at this span period is reflected by the amount of crystals and nodules of pyrite observed in the field (Fig. 37) and the associated negative $\delta^{13}C_{org}$ shift as seen at the early Eocene in both sections. On the other hand, the increased detritus mineral fraction (quartz, phyllosilicates, kaolinite and feldspars) across the assumed PETM indicates a severe intensification in chemical weathering, as evidenced by the very high observed CIA values (67%-92%; Figs. 47A and B).

The post-PETM in Douala sub-basin is characterized by a slight CIE recovery (Figs. 41B and 42A), a gradual decrease of TOC and related mercury contents and a detritism intensity very close to that at PETM due to similar trends of detrital fractions (Figs. 48A and B). In contrast, there is a slight enrichment in some sensitive trace elements (Zn, Mn and Ni) which would probably be linked to increasing productivity expressed by increasingly Ba and P contents, respectively in Bongue and Dibamba. Similar observations were made at Dababiya NW (see Khozyem et al., 2015).

5.3. Problem of productivity across the PETM and related volcanism effects

Phosphorus (P) and barium (Ba) are useful proxies allowing to trace primary productivity (see Bains et al., 2000; Bralower, 2002; Solimann et al., 2011; Schulte et al., 2013; Fantasia et al., 2018a, 2018b). This productivity represents the amount of nutrients produced by different sources and archived in sedimentary deposits. As the continent is the main supplier of nutrients to the marine realm, an increasing temperatures and precipitations coupled with that of CO_2, would be expected to affect the marine realm, via increased marine primary productivity due to continental chemical weathering rates and nutrient runoff (Bralower, 2002). In contrast, high detrital inputs can dilute the nutrient-rich water involving for example a considerable decrease of phosphorous (Fantasia et al., 2018b) and barium contents. On the other hand, mercury (Hg) is more recently used by several authors to trace signals of probable volcanism activities archived in sediments during extreme environmental turnovers (e.g. Sial et al., 2013; Grasby et al., 2013, 2016; Font et al., 2016; Thibodeau et al., 2016; Bond and Grasby, 2017; Charbonier et al., 2017; Fantasia et al. 2018b). Because of his sequestration in sediments is controlled by the increasing of biologic productivity and burial organic matter (Outridge et al., 2007; Sanei et al., 2012; Grasby et al., 2013), Hg is normalized to TOC in order to elucidate its origin (Font et al. 2016; Thibodeau et al., 2016).

The lower halves of Bongue and Dibamba sections globally exhibit a gradual decrease of P and Ba contents toward the PEB (Figs. 12 and 13) that are coupled to Hg/TOC values with a similar trend (Figs. 41A and 42A) and low proportions of zeolite (Figs. 37 and 38). The correlation between these results and the gradual decrease of $\delta^{13}C$ values prior to PEB suggests, as in the case of Dababiya, volcanic activity and decreasing productivity leading up to the PETM. The related volcanic activity would be linked to the Cameroon Volcanic Line (CVL) of which magma generation and intrusion have been sustained for more than 70 Myr (Milelli et al., 2012) with probably volcanic eruptions coupled to gas injections into the atmosphere especially during the late Paleocene which modified basin geometry and atmosphere composition (Eldholm and Thomas, 1993). This volcanism could have disrupted the supply in nutrient-rich water from the hinterland, inducing therefore a gradual diminishing of P and Ba contents as well as that of some detrital proxies (SiO_2, quartz) towards the PEB (Figs. 43A-B, 46A and 47A).

During the PETM, the increase in Ba to Bongue (Fig. 46A) and P in Dibamba (Fig. 47A) suggests a gradual feedback to normal supplying conditions. This is in agreement with slight inflection of quartz curves observed at the onset of PETM (Figs. 46A and 47A) in both

sections as well as enrichment in Fe_2O_3 and Al_2O_3 (Figs. 43A and B). The increasingly enrichment in Ba and P respectively in Bongue and Dibamba alongside to quartz and phyllosilicate contents in both sections reflects a restoring of nutrient supply conditions across the post-PETM (BN-21 to BN-30 at Bongue and DI-14 to DI-21 at Dibamba). Moreover, PETM and post-PETM intervals appear as quiet periods (no volcanism; see Figs. 41A and 42A).

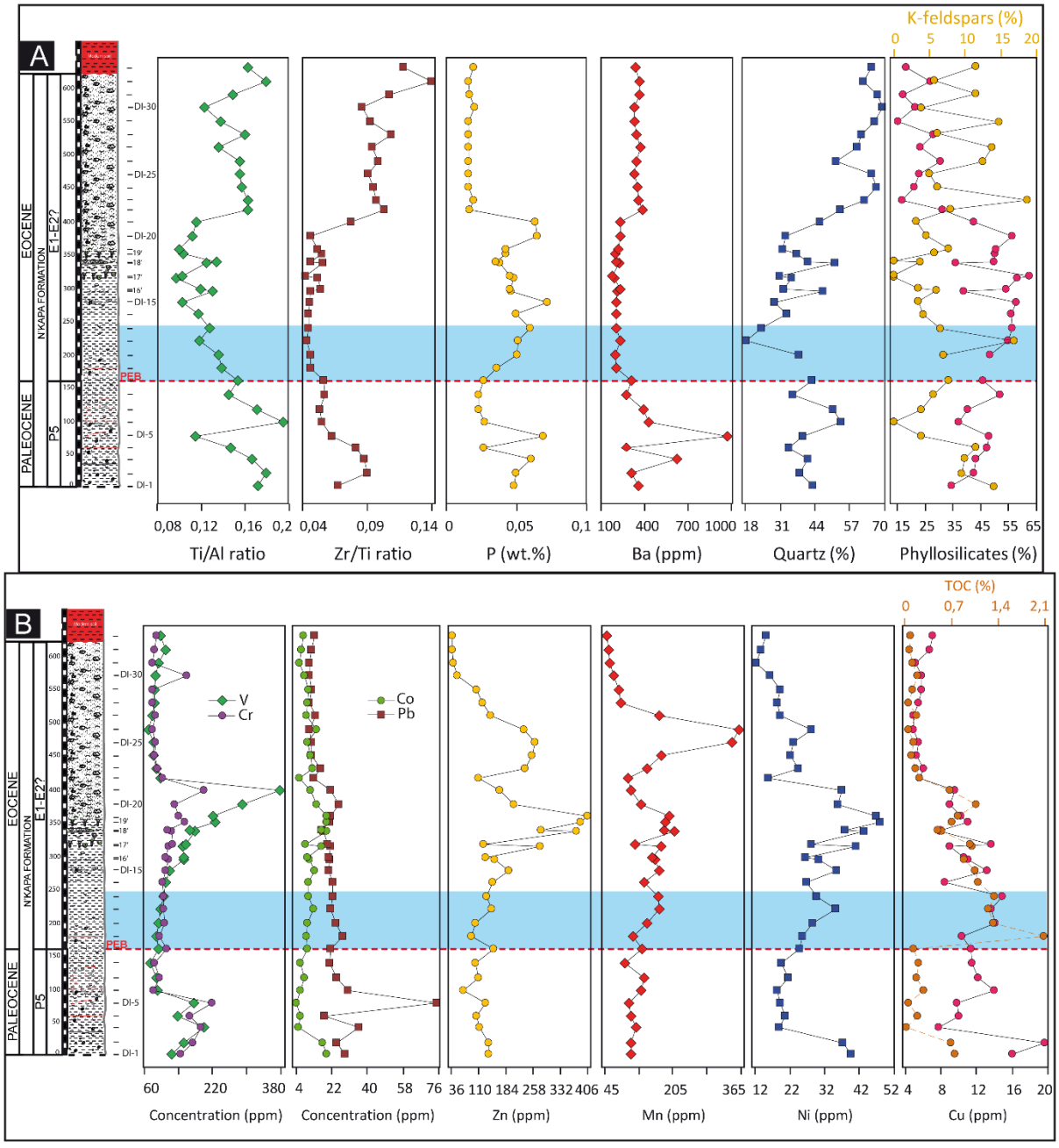

Figure 47. *Stratigraphic evolution of selected significant ratios and elements across the Paleocene-Eocene boundary (PEB) at Dibamba. A) Noted increase in P, K-feldspars and phyllosilicates during the PETM suggests an increased productivity, intense chemical weathering and continental runoff. B) Note that increase in V, Cr, Co, Zn, Ni, Cu and TOC contents in the PETM interval indicates dysoxic to anoxic conditions.*

In the uppermost Dibamba part (DI-22 to DI-29), high Hg/TOC ratio values (Fig. 42A) and appearance of zeolite (in traces; Fig. 38) suggest a short volcanic episode during which the sudden increase in Ba, Zn, Mn and Ni observed (Fig. 47A) indicates high primary productivity due to the nutrient supply via continental runoff. However, the rising silicoclastic influx (Fig. 48B) would probably have diluted nutrient-rich water and considerably reduced organic matter and phosphorous contents (Murphy et al., 2000; Fantasia et al., 2018b).

5.4. Sea level fluctuations and paleoclimate reconstruction

Distribution of bulk rock and clay minerals as well as some of their ratios such as kaolinite/smectite (K/S) is strongly linked to sea level fluctuations and past climate conditions (Singer,1984; Chamley, 1989; Robert and Maillot, 1990; Bolle et al., 2000; Adatte et al., 2002). Coupled to Chemical Index of Alteration (CIA=[Al2O3/(Al2O3+CaO*+K2O+Na2O)]×100, Nesbitt and Young, 1984, 1989; Price and Velbel, 2003) as observed in Khozyem et al. (2015), we could make a high-resolution simulation of the prevailing climate of this epoch in relation to intensity of the chemical weathering and relative abundance in mineral phases. It is however conceded that smectite formation might as well have been the result from submarine volcanogenic phenomena (Robert, 1980; Singer, 1984). But, no volcanoclastic components (debris, glass or ash) were observed throughout the studied sedimentary sections, just a distal volcanism signal traced by high mercury contents. In addition, distribution of smectite bundance in both sections is independent of localized volcanic intervals (high Hg/TOC values). According to Robert (1980), there is no evidence of burial diagenetic evolution of clays in South Atlantic area. Consequently, the Paleocene-Eocene clay minerals of the Douala sub-basin have a detrital origin in agreement with Robert et al. (1979) and Robert (1980). Thus, high kaolinite content and increased abundance of detrital fraction (phyllosilicate and feldspar) associated to increased CIA suggest warm/humid climate, coastal areas and probably lower sea level, whereas increased smectite abundance and decreased detrital fraction and CIA reflect dry and seasonal climate, open marine environments and higher sea level (Millot, 1970; Singer, 1984; Chamley, 1989; Weaver, 1989; Adatte et al., 2000, 2002; Bolle et al., 2000; Li et al., 2000; Khozyem et al., 2013).

Latest Paleocene P5 zone is marked, over the world, by a general rising sea level leading up to the PEB (Haq et al., 1988; Gavrilov, 1997; Bolle et al., 2000; Sluijs et al., 2008). This is also the case in Douala sub-basin thought the studied sections, where simultaneous decrease in terrigenous inputs (but always higher than average shale values), K/S ratio values and calcite

content towards the PEB suggest decreased erosion, moved coastline landward, increasing sea level which initiated prior to the CIE and a dominated sedimentation by fine detrital particles as phyllosilicates (Figs. 46A and 13A; Bolle et al., 2000). This agrees with benthic species encountered, suggesting an inner to middle shelf environment and deposition during the late Paleocene because these species are rare after the PETM (e.g., Dababiya, Alegret et al., 2005; Alegret and Ortiz, 2006; Speijer et al., 1996). However, an abrupt change of K/S curve trend is noted at Dibamba during the late Paleocene suggesting a hiatus. But no discontinuity (eroded and/or omission surface) have been evidenced by sedimentological observations. Consequently, it appears that the sudden change of K/S ration trend is the result of a regressive episode as recognised on the continental scale (Ly et Anglada, 1991) or a warm dry climate characterized by alternating humid and dry seasons (Robert, 1980; Singer, 1984, Chamley, 1998). The last hypothesis seems be consolidated because of, in addition to slight positive detrital inflections observed at Dibamba during the late Paleocene, it clearly appears that in Bongue the climate is arid to humid whereas in Dibamba it is humid to tropical (Figs. 48A and B). The much difference in CIA values observed in Bongue and Dibamba sections, which inferred paleoclimates during the late Paleocene, may probably due to the position of sections relatively to hinterland and volcanic edifice.

A falling sea-level with lesser magnitude, which is reflected by higher CIA, increase in topographic relief and more kaolinite abundance (increasing K/S ratio), encompasses the PETM (CIE interval) in both Douala sections (Figs. 46A and B; Schmitz and Pujalte, 2003). This small regression is followed at the onset of post-PETM (CIE-recovery phase) by a large transgression, which reaches, at the end of post-PETM interval, the maximum flooding surface (MFS) in Dibamba area during early Eocene (e.g. Speijer and Wagner, 2002; Gavrilov et al., 2003; Ernst et al., 2006; Sluijs et al., 2008) in agreement with Okosun (1989). Some field data like large bioturbations infilled by silt, glauconite and abundant bivalve shells, also reveal a MFS, as observed in other sequences over the world (Sluijs et al., 2008). These periods (PETM and post-PETM) are characterized by sub-tropical to tropical climate with abundant rainfall and continental runoff, reflected by high CIA values, alternative dominance of kaolinite and smectite (Figs. 48A and B), and increasing abundance in phyllosilicates (Figs. 47A and 48A) during transgressive system tract (TST).

Above, the sudden increase in K/S ratio whose peak coincides with increased detrital inputs (quartz and K-feldspars included) as well as decreased chemical weathering and phyllosilicate contents, suggests intense erosion and continental runoff, more humid climate and falling sea level. This is rapidly followed by a relatively long-time rising sea level, which

is characterized by gradual decrease in K/S ratio during which erosion is intense, and climate humid with lesser rainfall. The uppermost Eocene sediments beginning with DI-27 are characterized by gradual dominance in kaolinite abundance and increased sedimentation rates, which are interpreted to reflect enhanced hinterland erosion due to an increase in topographic relief resulting from marine regression (Schmitz and Pujalte, 2003; Sluijs et al., 2008) during humid to tropical climate towards the top of the section.

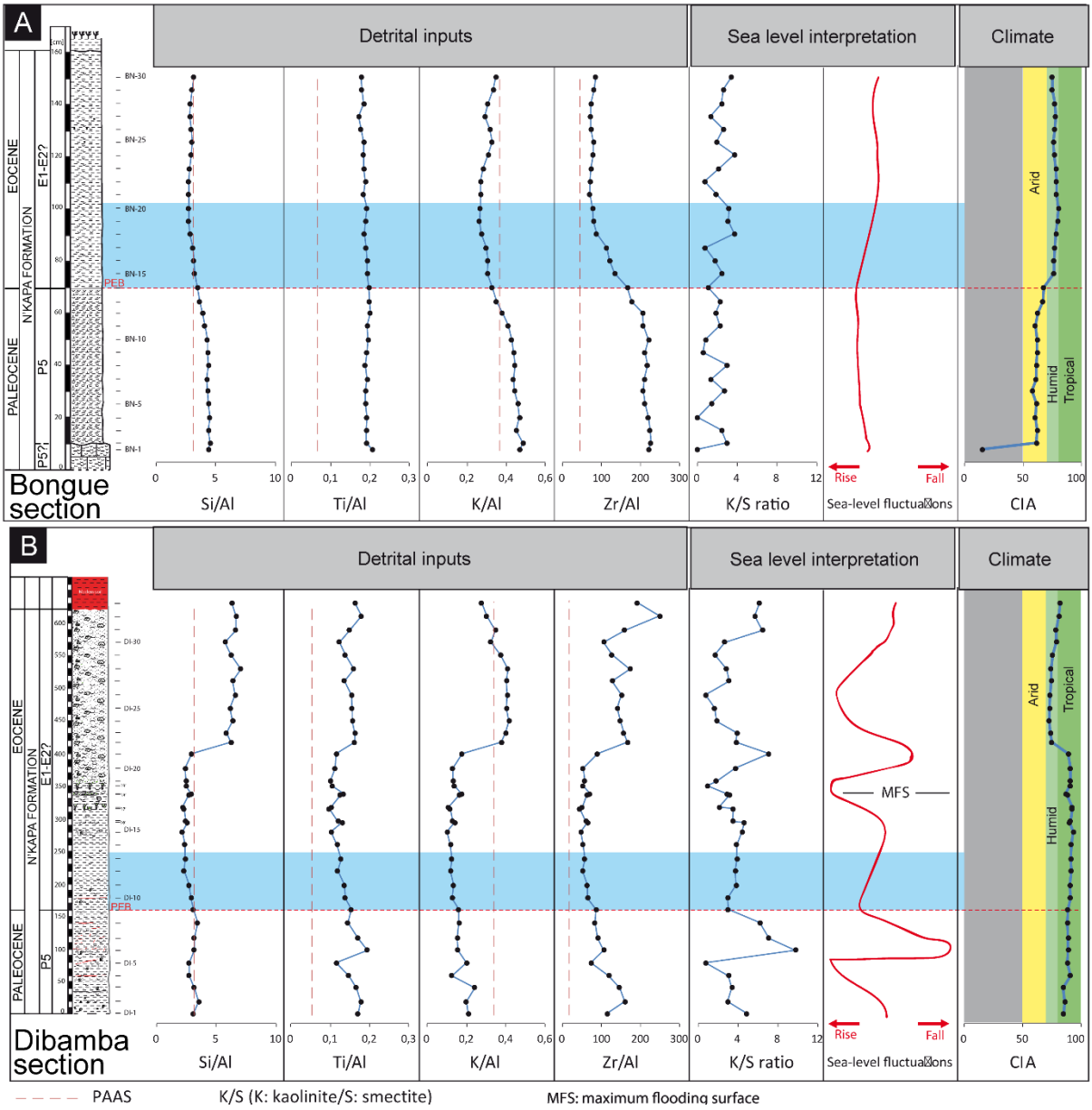

Figure 48. *A) Detrital inputs, sea level fluctuations and climate changes along the Bongue Paleocene-Eocene transect. Note that high Ti/Al and Zr/Al ratios relative to their PAAS as well as increase of kaolinite/smectite (K/S) ratio and high CIA values during the PETM indicate increased detrital inputs, rising sea level and more humid to tropical climate. B) detrital inputs, sea level fluctuations and climate changes along the Dibamba Paleocene-Eocene transect. Note that high Ti/Al and Zr/Al ratios relative to their PAAS as well as increase of*

kaolinite/smectite (K/S) ratio and high CIA values during the PETM indicate increased detrital inputs, rising sea level and more humid to tropical climate.

6. CONCLUSIONS

This study represents the preliminary investigations on the PETM in Central African region, where the event was identified in fine grained sediments (shales for Bongue and clays for Dibamba) of inner to middle shelf constituting a part of N'kapa Formation in the Cameroonian Douala sub-basin. Based on $\delta^{13}C_{org}$ and biostratigraphic data, three mainly intervals namely pre-PETM, PETM and post-PETM have been recognised, in addition to lowermost interval in both sections, and an uppermost interval only in Dibamba section. The most crucial results are summarized as follow: (1) The pre-PETM interval corresponds to a gradual $\delta^{13}C_{org}$ decrease period (pre-CIE zone) prior the Paleocene-Eocene boundary (PEB), during which the encountered microfauna assemblage (benthic and planktic foraminifera and ostracods) represents the latest Paleocene P5 zone, just below the PETM. These microfossils are widely affected by the ocean acidification, as certified by gradual decrease in $CaCO_3$ content. This period is characterized by a distal volcanism activity coupled to decreasing productivity during a rising sea level leading up to PETM, under contrasted warm climate. (2) During the PETM (zone E1), the severe ocean acidification induces a mass extinction where only few *I. broedermanni*, evolved species of *I. Tadjikistanensis*, are present and where CIE-minimum interval coincides to calcite minimum values. Also, *Trochamminids* and some *I. lodensis* and *A. esnaensis* species reappear at the end of this high stress environmental change period during which the high sediment deposition rate took place under dysoxic to anoxic conditions and subtropical to tropical climate during a slight falling sea level. (3) The post-PETM, correlated interval with the CIE-recovery phase, is the place, at the early Eocene (biozones E1-E2), of intense erosion and chemical weathering associated with a considerable rise in productivity. The depositional environment, dysoxic to anoxic, is almost similar to that of PETM. However, there is a rise in sea level reaching the maximum flooding surface (MFS) at the top of related interval, as evidenced by sedimentological data. N'kapa Formation (Douala sub-basin, Cameroon) appears to be the lateral equivalent of Oshosun Formation (Dahomey basin, Nigeria) in the regional geology of Gulf of Guinea.

CHAPTER V. PALYNOLOGY, MINERALOGY AND GEOCHEMISTRY OF SEDIMENTS IN TONDE LOCALITY, NORTHERN PART OF DOUALA SUB-BASIN, CAMEROON, CENTRAL AFRICA: IMPLICATION ON PALEOENVIRONMENT

1. INTRODUCTION

Clastic rocks may preserve minerals and elements from the long-eroded source rocks which may provide crucial informations on the composition and exposure time of such parent rocks (Armstrong-Altrin et al., 2004). Depending on originated area of materials and prevailing climate, these rocks are more or less enriched in clay minerals (Chamley, 1989; Thiry, 2000; Flagel, 2007; Abdoullayev and Leroy, 2016). Indeed, major and trace element concentrations of clastic sediments coupled to their bulk and/or clay mineralogy provide more informations about their provenance, the nature of parent rock as well as the weathering conditions and sedimentary processes (Taylor and McLennan, 1985; Wronkiewicz and Condie, 1987; Cullers, 1988; Chamley, 1989; Nesbitt and Young, 1989; Thiry, 2000; Adatte et al. 2002; Bertolino et al., 2007; Flagel, 2007; Singh, 2009; Armstrong-Altrin et al., 2018; Ramos-Vázquez et al., 2018; Armstrong-Altrin et al., 2019; Ramos-Vázquez and Armstrong-Altrin, 2019). Therefore, several trace elements (TE) such as REE, Ni, Co, U, Cr, V, Pb, Zn, Sr, Ba, Th, Sc and Zr from deposits resulting of sedimentary processes can be used to characterize the global paleoenvironment, not only because of their relatively low mobility and solubility, but also in relation to their redox and productivity sensitivity. (Taylor and McLennan, 1985; Condie et al., 1995; Schaller et al., 1997; McLennan, 2001; Tribovillard et al. 2006; Singh, 2009; Piper and Bau, 2013; Lim et al., 2014; Acharya et al., 2015; Armstromg-Altrin et al., 2015). Moreover, sedimentary pyrite may result from the interaction of H_2S (from bacterial sulphate reduction) with reactive detrital iron minerals (Berner, 1984). It is one of the few minerals for which a combination of elemental (trace and rare earth elements) and isotopic ($\delta^{34}S$ and $\delta^{56}Fe$) studies as well as the characterization of crystal textures can be an useful tool to trace the history of the formation of deposits (Hofmann et al. 2009; Zhou and Jiang, 2009; Ding et al., 2014; Large et al. 2014; Botsou et al., 2015). In Central Africa region particularly in the Douala sub-basin in Cameroon, only few studies combining geochemistry and mineralogy to reconstruct paleoenvironment has been undertaken (e.g., Ndome Effoudou-Priso et al., 2014; Ngon Ngon et al., 2014, 2016, 2019).

Moreover, palynological study can also be used to understand the paleoenvironment and to suggest a relative age. In Douala sub-basin, a number of studies were performed from Cretaceous (Salard-Schebodaeff, 1977, 1990; Njike Ngaha, 2004) to Late Quaternary (Salard-Schebodaeff, 1977, 1990) and from Paleocene to Eocene (Kenfack et al., 2012; Mbesse et al., 2012; Ngon Ngon et al., 2016) times.

The goals of this study are to reconstruct the paleoenvironmental and paleoclimatic evolution of the Tondè deposits, based on mineralogical, geochemical, texture of pyritic crystals and to infer a relative age using palynological data.

2. GEOLOGICAL SETTING

The Tondè area (4°10'–4°12' N and 9°50'–9°52' E) is located in South-East of the northern part of Douala sub-basin (Cameroon, Central Africa), within the humid equatorial climatic zone. The geomorphology of this area consists of a coastal plain (height: 20–60) overlain by smooth and sharp hills summits in alternation with V valleys. According to Njike Ngaha (1984) and the geological report of SNH (2005), the relative geological age of the Tondè deposits is Paleocene-Eocene corresponding to N'kapa Formation (Fig. 49).

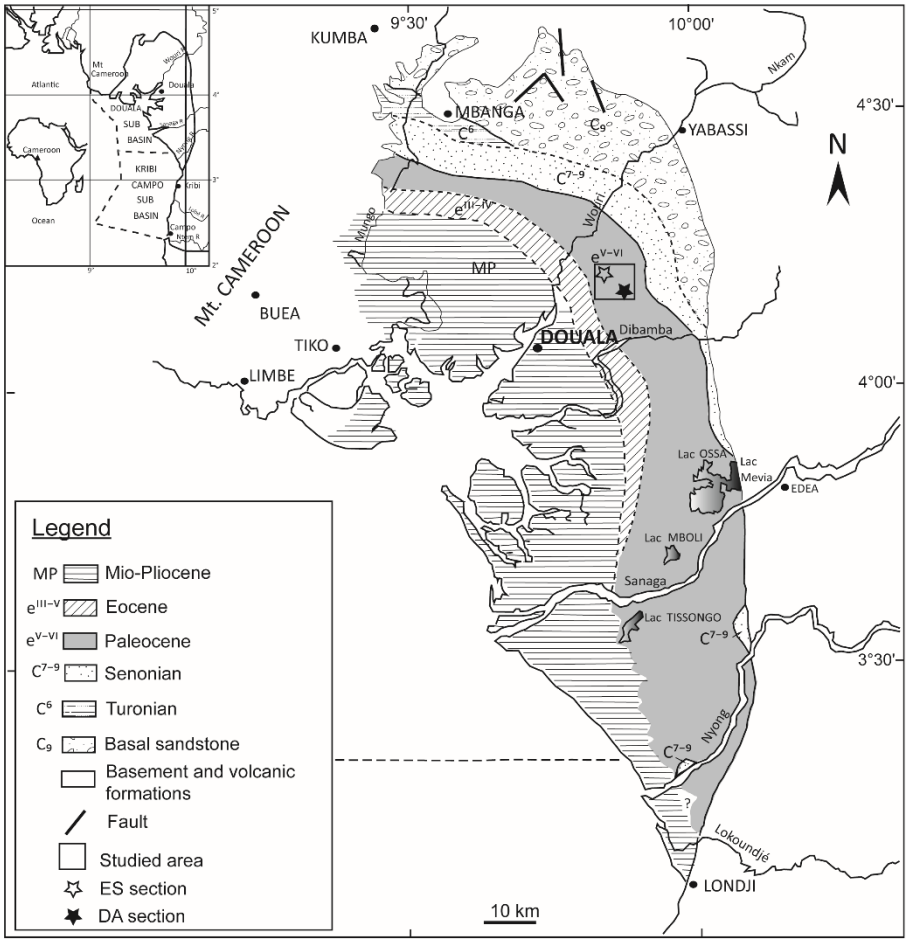

Figure 49. *Location and geological map of Douala sub-basin (from Njike-Ngaha, 1984; SNH/UD, 2005; modified). Square refers to Tondè area while stars (empty: ES; black: DA) are sites.*

The Douala sub-basin is located in the Gulf of Guinea and covers a total surface area of 12,250 km^2, of which 6,955 km^2 represents the onshore part (SNH/UD, 2005). This onshore

part is limited by the Cameroon Volcanic Line in the north, the Wouri estuary river at the west, the Kribi-Campo sub-basin in the south and the Precambrian basement at the east (Fig. 49).

The geological history of this basin begins in Late Jurassic and includes the breaking continental process leading to the formation of Cameroon Atlantic margin (Giresse et al., 1996). The lithostratigraphy of Douala sub-basin consits of seven major formations related to three stage of geodynamic and sedimentary evolution (Regnoult, 1986; Nguene et al., 1992; Lawrence et al., 2002; SNH/UD, 2005).

3. MATERIALS AND METHODS

3.1. Sampling and sample preparations

A well (ES) and core drilling (DA) of 7 m and 23 m depth respectively were performed at coordinates 04°11’21,1” N - 09°50’17,2” E for the ES site and 04°09’52,8” N - 09°51’36,8” E for DA. The study was carried out on 64 bulk samples: 15 samples from ES site, are collected over the entire extent of well wall mainly at regular intervals of 50 cm while sampling of the 49 others is made at high resolution on ~ 12 m of core sediments (DA), between heights -23 and -11 m. In order to precise the depositional environment, 10 pyrite samples, free of any clay coating, were also collected along ES profile based on textures encountered. A detailed description of all samples was made subsequently. A part of each sample is dried at 45 °C (except samples of pyrite) and crushed with an agate mortar. Powders obtained from bulk sediment samples were subjected to mineralogical and geochemical analyses at the Institute of Earth Sciences of University of Lausanne (Switzerland) while those from pyrite samples were analysed for major, trace and rare earth elements by Australian Laboratory Services (ALS) of Vancouver (Canada). Moreover, 10 DA core samples were selected after drying, for palynomorph preparations in the palynological laboratory at GeoTechniques Research Ltd., Sunbury on Thames, UK.

3.2. Bulk mineralogy

Bulk rock mineralogy was performed at the ISTE, University of Lausanne using a X-TRA Thermo-ARL Diffractometer based on semi-quantitative method, following the procedure described in Klug and Alexander (1974), Kübler (1987), Adatte et al. (1996). The whole rock mineralogical composition was obtained by XRD patterns of random powder

samples pressed into a powder holder, used external standards with error margins varying between 5 and 10% for the phyllosilicate and 5% for grain minerals.

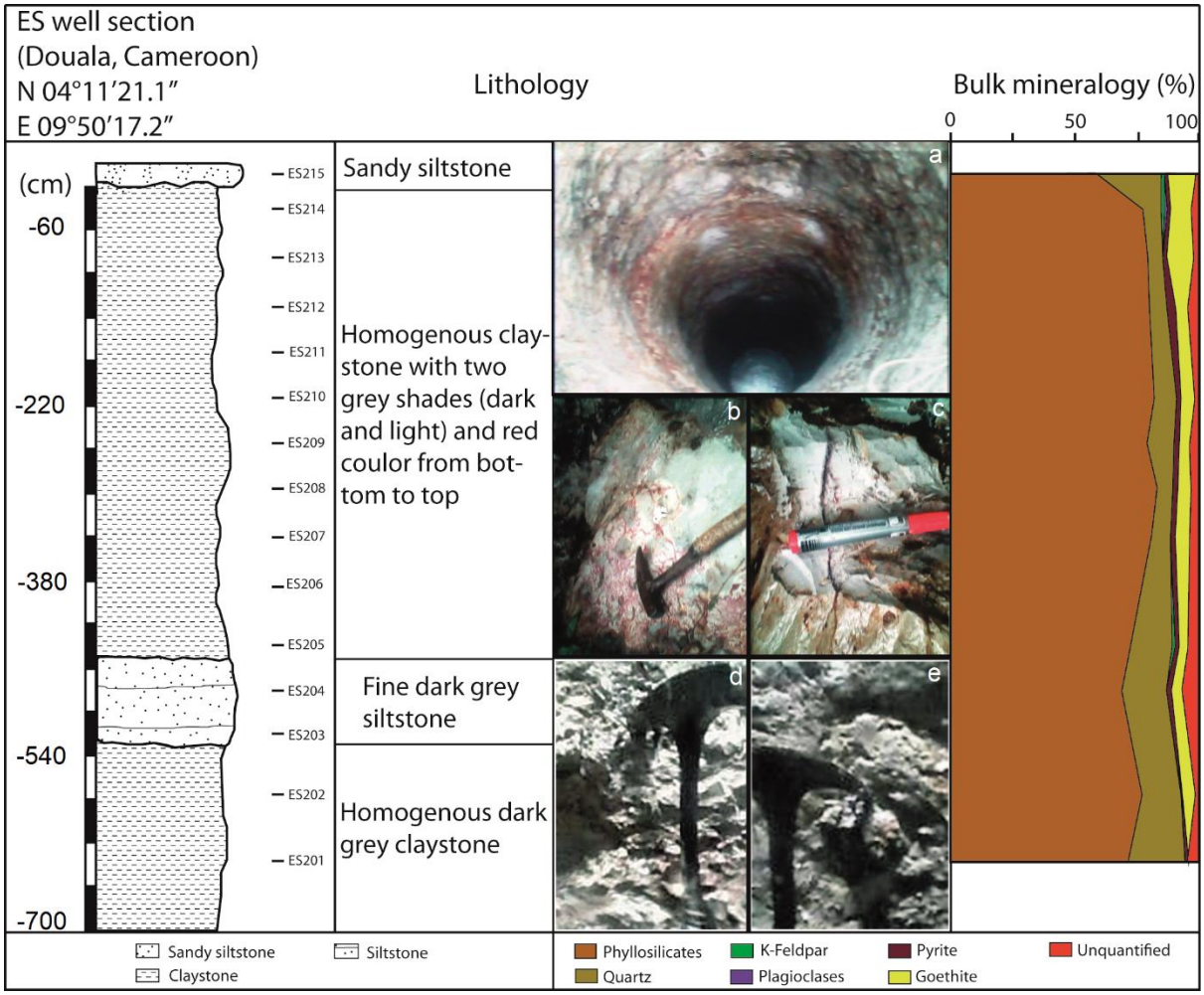

Figure 50. *Lithology and mineralogy of the ES well section. Photograph (a) represents the entire section while (b), (c) and (d) represent different encountered clayey lithologies. Photograph (e) shows a pyrite cluster in place in the section. Main minerals are phyllosilicates and quartz with low contents in goethite and pyrite.*

3.3. Scanning electron microscopy (SEM)

In order to characterize clay minerals and pyrite textures, some selected samples are studied by scanning electron microscopy (SEM, Tescan Mira/LMU) at the ISTE, University of Lausanne after gold coating.

3.4. Major, trace and rare earth elements

3.4.1. Whole rock geochemistry

Major (MEs) and trace (TEs) elements concentration of 64 whole rock samples were determinated by X-ray Fluorescence Spectrometry (XRFS) using a PANalytical PW2400 spectrometer at the ISTE of the University of Lausanne based on different standard reference materials (NIM-G, NIM-N, SY-2, JCH-1, BHVO). Major elements were determined on fused lithium tetraborate glass discs. For this purpose, samples were first heated to 1050 °C in an oven in order to calculate the loss of ignition (LOI). Then, 1.2000 ± 0.0002 g of ignited sample was mixed with 6.0000 ± 0.0002 g of lithium tetraborate ($Li_2B_4O_7$) and placed in a Bead machine PerlX'3 at 1250 °C to obtain the fused tablet. The obtained concentrations are given in weight percentages (wt.%). Trace element analyses were performed on pressed discs after mixing 15% of the powered samples with Mowiol 2%. The pressed discs were then placed in an oven at 110 °C for at least 6 h before analysis by XRFS. The trace element concentrations are given in parts per million (ppm).

3.4.2. Geochemistry of pyrite

MEs, TEs and rare earth elements (REEs) analysis of the pyrite samples were carried out by both inductively coupled plasma mass spectrometry (ICP-MS) and inductively coupled plasma atomic emission spectrometry (ICP-AES) at the Australian Laboratories Services of Vancouver. The accuracies of these analyses were assessed by analyses of standard reference materials, AMIS0085, AMIS0167, OREAS-14P and SY-4 for MEs and, OREAS-104, TRHB et DUP for TEs and REEs.

3.5. Palynology

Palynomorphs were extracted from 10 selected samples from DA section using HCl, HF and HNO_3 followed by 5% solution of KOH. The sample residue was washed with water through a 15µm screen. The slides were prepared in polyvinyl alcohol and mounted in Canada balsam. A determination of some pollens and spores have been done in Institute of Earth Sciences of Paris (ISTeP), Université Pierre et Marie Curie by Jean-Pierre Suc.

4. RESULTS

4.1. Lithology

4.1.1. ES profile

The ES well section (Fig. 50a) is characterized by a succession of fine grained lithofacies such as claystone (dark and light grey, and reddish; Figs 50b, c, d and e), siltstone and sandy siltstone. Basal dark grey claystone (height: -700 to -528 cm) is highly consolidated and globally uniform, presenting locally black patches. Pyrite is abundant and consists of globular clusters and massive concretions, with varying sizes up to 5 cm and more or less altered. This facies is overlain by a siltstone (~ 80 cm thick) which presents similar physical characteristics (dark grey colour and black patches) to those of previous facies. Pyrite included are also massive, and materials are relatively high consolidated.

Above, the next facies is a claystone of about 4.4 m thick, which presents from bottom to top a gradual change of coloration ranging from dark to light grey, and reddish. Many black patches are also present. Pyrite occurs as clusters, which seem to be more altered in the light grey interval. In the reddish part, pyrite consists of small nearly unaltered granules ($\Phi < 1.5$ cm). The superficial facies is a weakly consolidated light brown sandy siltstone of ~ 17 cm thick. Its contact with facies below is very clear and marked by slight undulations. No pyrite occurrence is there, but rather extensive plant debris and bioturbations.

4.1.2. DA profile

The DA section is characterized by an alternation of sandstone, siltstone and claystone extended between heights -2300 and -1100 cm (Fig. 51). The lowermost facies is made of about 2 m thick of coarse sandstone Fig. 51j), more or less consolidated, and soaked by an argillaceous matrix. Its colour gradually changes bottom up from purple to dark red, and then light grey. This unit contains groundwater and can be considered as a reservoir. It is overlayed by is a 2.8 m thick fine to medium grey siltstone (Fig. 51h and i) which can be locally purple, reddish and may include black patches. Encountered pyrite are in form of isolated crystals which sometimes organize in cluster. This unit is following by a homogeneous well consolidated dark grey claystone (5.6 m thick; Fig. 51b, c, d, e, f and g) with several black patches and a reddish-purple interval near the top. There is a wide distribution of pyrite crystals associated with the quartz in a kaolinitic matrix (Fig. 52d and e).

In contrast to underlying lithologies, the next argillaceous siltstone (~ 1.2 m of thick) is unconsolidated and shows mixture of grey and reddish colour. No pyrite crystal has been encountered. This unit appears as the transition between underlying claystone and the topmost facies. The superficial part of this section is an unconsolidated red recent sandstone, which is associated in its lower part with few remnants of light grey materials. This unit is similar to a modern soil, commonly found in equatorial zone.

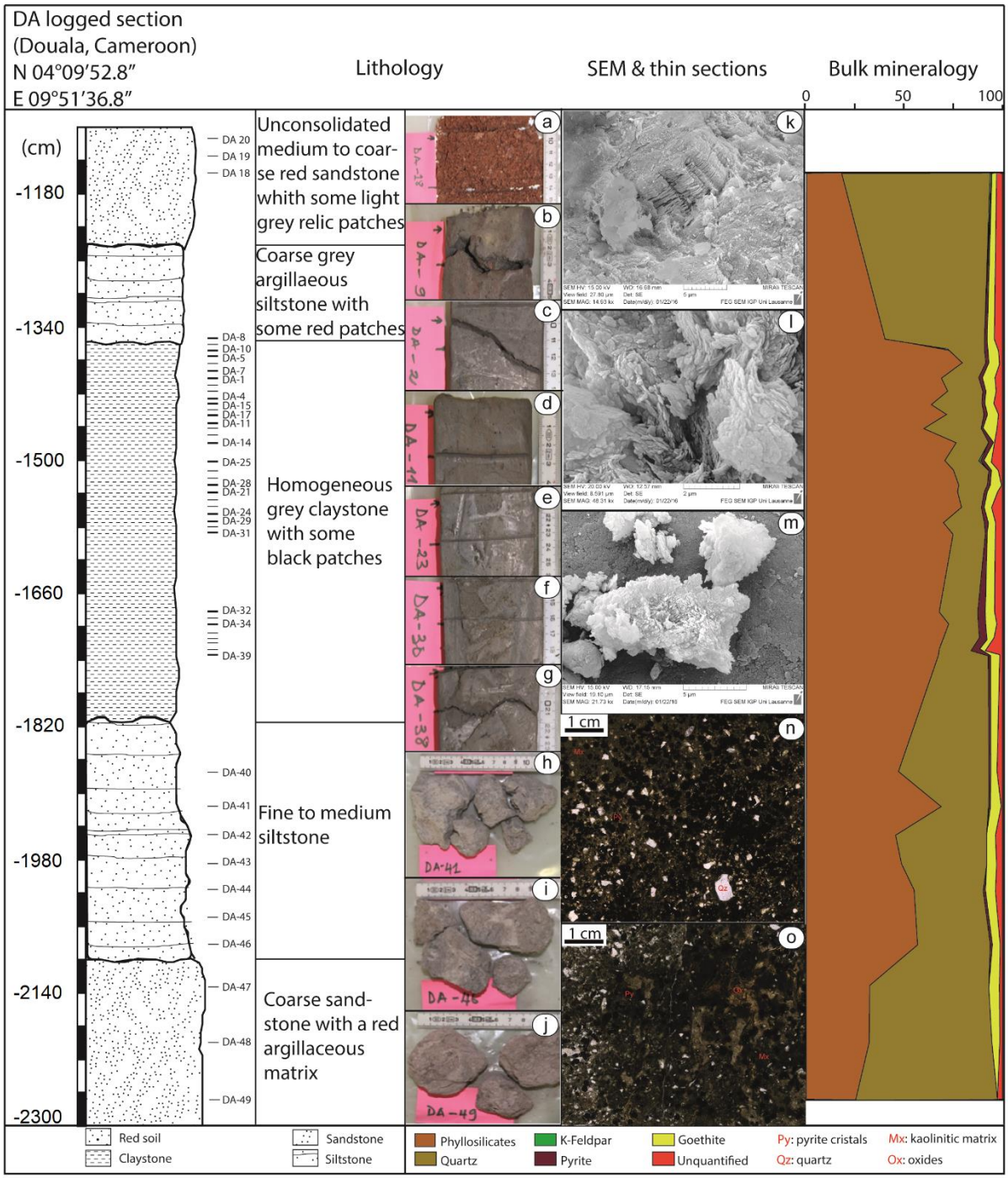

Figure 51. *Lithology and mineralogy of the da drill core section. Photographs a – j represent different crossed lithologies (unconsolidated red sandstone, grey clayey facies, sandstone). Main minerals are phyllosilicates and quartz with low contents in goethite and pyrite. SEM micrographs k, l and m showing*

kaolinite as dominant phyllosilicate are respectively from DA-2, -9 and -13. Thin micrographs n and o (from DA-4 and -31 respectively) show abundant pyrite crystals (Py), quartz (Qz), kaolinitic matrix (Mx) and oxides (Ox).

4.2. Mineralogy

Whole rock mineralogical compositions of the Tondè materials reflect the dominant lithologies at both sites (ES and DA), i.e. clay and siltstone, in addition to sandstone for the DA profile. For the ES well section, claystone lithologies (basal and upper; Fig. 50) are mainly consist of phyllosilicates (71.0 – 84.0 %; mean value: 78.3 %), quartz (6.1 – 23.1 %; mean value: 11.1 %) and goethite (0.0 – 11.4 %; with 5.9 % as average value) (Fig. 2 and supplementary file). Pyrite is well identified in these XRF results with a maximum concentration in grey to reddish claystone lithology (height: -448 to -80 cm), in line with lithological data. Siltstones in this section also exhibit a high content in phyllosilicate (69.0 % for lower siltstone and 58.0 % for the upper sandy), but slightly decreased relative to that of average content of claystones (78.3 %). Quartz is relatively more abundant, 18.0 % for dark grey siltstone and 26.9 % for sandy siltstone. Goethite is scarcely represented in dark grey siltstone (4.9 %) while it is more abundant in sandy siltstone.

For the DA profile, mineralogical composition of basal coarse sandstone matrix consists of quartz (60.2 – 72.1 %, with 64.8 % as mean value), phyllosilicates (25.6 – 32.8 %; mean value: 30.3 %) and goethite (0.0 – 5.41 %; mean values: 3.2 %). Pyrite is absent. Above, grey siltstone averages 54.0% phyllosilicates, 38.5% quartz and about 4.6% goethite, with trace pyrite (~ 0.6 %). The following dark claystone exhibits a mineralogical composition ranging from 60.1 to 79.3 % (with ~ 72 % as average value) phyllosilicates, 10.0 to 29.0 % (mean value: ~ 18.1 %) quartz and 0.6 to 7.2 % (mean value: ~ 4.7 %) goethite, which is very close to that of same lithology at the ES profile. SEM observations show that kaolinite is almost the only clay mineral species present, with a characteristic layered hexagonal structure observable on the SEM micrographs (Fig. 51a and b). Thin sections from this claystone (samples DA-4 and 31) show abundant pyrite crystals associated with a few quartz grains, all soaked by a kaolinitic matrix (Fig. 51n and o). The next lithology, coarse grey argillaceous siltstone, consists of 40.0 % phyllosilicates and 48.9 % quartz, with about 3.7 % of goethite. Pyrite is nevertheless present in trace amounts (1.1 %), although no occurrence has been identified. The red sandstone is enriched in quartz (~ 75.3 %) with a relatively low proportion of phyllosilicates (18.4 %) and goethite (2.42%).

Table 6. *Major (ME) and trace (TE) elements composition of DA section. Note that CaO content is null*

Sample	Major elements (wt.%)										Trace elements (ppm)																	
	SiO_2	TiO_2	Al_2O_3	Fe_2O_3	MgO	Na_2O	K_2O	P_2O_5	LOI	Total	Sc	V	Cr	Mn	Co	Ni	Cu	Zn	Rb	Sr	Y	Zr	Nb	Ba	Nd	Hf	Pb	Th	U
DA-1	46.74	1.43	26.32	9.22	0.03	0.03	0.16	0.07	15.28	99.33	22	134	120	98	19	39	25	23	10	50	19	274	28	166	54	8	81	24	3
DA-2	45.78	1.37	24.52	11.33	0.03	0.04	0.15	0.06	16.12	99.44	25	157	138	98	23	40	29	23	10	42	22	322	29	166	48	10	62	25	3
DA-3	46.34	1.37	23.31	10.97	0.02	0.03	0.14	0.05	17.08	99.35	22	146	141	44	17	38	25	21	9	36	17	374	29	148	38	12	55	23	3
DA-4	46.91	1.38	23.03	11.94	0.02	0.03	0.14	0.04	15.62	99.16	21	136	129	36	16	32	18	19	9	34	19	435	31	141	34	13	48	21	3
DA-5	42.71	1.32	24.79	12.42	0.03	0.03	0.16	0.04	17.76	99.31	24	163	151	74	24	47	23	24	10	34	17	219	25	149	36	7	49	26	3
DA-6	43.59	1.32	25.16	11.08	0.03	0.04	0.16	0.05	17.86	99.35	22	152	137	83	20	42	31	23	10	37	18	227	26	157	43	7	50	28	3
DA-7	44.99	1.38	25.70	10.08	0.03	0.03	0.16	0.06	16.80	99.28	22	143	125	99	23	40	25	24	10	41	19	249	27	141	47	3	58	23	3
DA-8	79.92	0.53	8.97	4.92	0.03	0.09	0.07	0.02	4.61	99.17	11	251	78	31	3	13	13	8	3	15	7	215	11	62	17	7	15	11	1
DA-9	44.83	1.09	21.53	13.35	0.03	0.04	0.14	0.04	18.36	99.46	22	164	146	64	26	49	25	20	9	28	17	172	22	129	30	4	36	21	2
DA-10	41.50	1.26	24.51	12.76	0.03	0.04	0.15	0.05	19.19	99.54	24	154	144	69	31	53	25	23	9	36	22	210	25	142	37	6	53	24	3
DA-11	44.45	1.34	21.78	13.14	0.02	0.03	0.14	0.04	18.45	99.43	24	156	134	39	16	36	38	20	9	33	19	420	30	158	39	13	69	12	<d.l.
DA-12	46.24	1.49	25.75	9.44	0.03	0.03	0.17	0.05	16.09	99.33	24	140	121	29	14	29	39	20	10	43	20	295	32	147	41	10	55	22	3
DA-13	42.78	1.45	28.01	5.32	0.01	0.03	0.15	0.10	21.43	99.31	37	130	108	26	28	53	44	22	10	82	29	171	29	182	107	5	110	36	3
DA-14	42.26	1.40	27.41	11.01	0.01	0.05	0.14	0.09	17.04	99.43	27	168	140	35	20	47	41	27	9	73	23	181	27	212	104	5	94	33	3
DA-15	64.20	0.94	16.35	6.76	0.03	0.04	0.12	0.04	10.77	99.27	17	147	109	65	13	28	21	16	6	27	16	245	19	113	33	8	33	17	2
DA-16	45.61	1.36	22.81	11.75	0.02	0.05	0.14	0.04	17.30	99.14	22	132	119	35	16	31	25	19	9	33	21	421	31	136	33	14	40	18	3
DA-17	55.54	1.23	21.37	8.07	0.03	0.03	0.13	0.05	12.72	99.22	21	152	125	62	15	32	21	19	8	38	17	313	25	162	46	9	51	22	3
DA-18	93.82	0.46	2.96	1.03	0.03	0.02	0.02	0.02	1.08	99.44	3	72	24	8	<d.l.	<d.l.	6	<d.l.	<d.l.	10	2	155	6	26	31	6	3	6	<d.l.
DA-19	93.50	0.34	2.56	1.65	0.03	0.02	0.02	0.02	1.14	99.29	3	44	31	9	<d.l.	1	5	1	<d.l.	5	2	205	6	20	9	7	3	4	<d.l.
DA-20	89.61	0.52	3.60	2.82	0.03	0.03	0.03	0.02	2.60	99.26	5	53	44	14	<d.l.	2	4	3	<d.l.	6	3	209	8	21	15	6	8	5	3
DA-21	39.14	1.56	25.58	9.62	0.01	0.04	0.14	0.03	23.27	99.42	24	177	154	25	15	46	15	27	9	15	26	216	33	95	44	7	15	27	2
DA-22	36.02	1.43	23.70	13.04	0.01	0.03	0.14	0.04	25.09	99.52	40	195	168	28	25	59	25	29	9	18	33	191	29	100	86	5	21	29	2
DA-23	36.68	1.45	24.10	13.58	0.02	0.04	0.15	0.04	23.34	99.44	33	189	173	30	24	54	21	29	9	20	35	197	29	115	86	7	20	33	3
DA-24	38.61	1.52	24.99	10.68	0.02	0.04	0.18	0.03	23.45	99.57	23	142	121	26	22	41	13	23	9	15	26	171	26	89	47	5	13	24	2
DA-25	36.76	1.35	23.88	11.27	0.01	0.04	0.13	0.03	25.91	99.41	22	153	131	22	16	40	37	22	7	10	21	167	25	63	27	4	16	20	2
DA-26	39.84	1.55	26.20	8.79	0.00	0.03	0.14	0.03	22.56	99.17	28	180	159	23	19	45	25	27	9	12	25	205	31	89	39	6	17	25	3
DA-27	39.12	1.47	24.52	12.44	0.01	0.03	0.13	0.02	21.34	99.12	26	155	132	21	15	41	19	24	8	12	25	201	29	77	37	5	14	23	3
DA-28	38.47	1.48	24.55	14.99	0.01	0.03	0.13	0.03	19.71	99.45	29	215	178	30	18	54	23	32	10	16	25	198	31	111	42	8	12	27	5
DA-29	38.69	1.54	24.43	14.90	0.03	0.04	0.19	0.03	19.43	99.32	21	183	168	35	18	46	18	29	10	16	23	207	30	120	38	8	15	26	2
DA-30	40.23	1.60	24.88	10.18	0.03	0.04	0.21	0.03	21.90	99.13	24	172	160	32	31	50	17	27	10	11	29	190	29	103	32	5	13	18	3
DA-31	41.95	1.61	25.54	11.33	0.03	0.04	0.22	0.03	18.58	99.39	22	176	162	36	15	45	16	29	11	12	24	210	30	125	24	12	13	18	2
DA-32	36.87	1.22	20.63	16.47	0.02	0.04	0.12	0.47	23.31	99.19	35	195	153	28	20	42	40	24	7	93	41	198	25	390	101	3	17	28	3
DA-33	44.66	1.54	25.99	9.54	0.03	0.04	0.16	0.39	16.83	99.21	28	207	154	31	15	40	24	28	9	188	47	226	29	894	131	3	23	41	4
DA-34	47.97	1.63	27.07	5.83	0.03	0.03	0.18	0.05	16.55	99.37	24	177	140	27	14	36	34	25	9	24	34	231	30	123	59	6	21	34	2
DA-35	46.74	1.56	26.09	2.82	0.02	0.03	0.18	0.04	21.60	99.11	16	124	101	22	9	25	53	19	8	16	27	206	28	80	24	5	12	19	2
DA-36	36.90	1.22	20.80	20.16	0.04	0.04	0.15	0.02	19.85	99.22	25	193	171	26	11	36	36	23	8	10	24	213	25	116	28	8	12	20	2
DA-37	44.80	1.47	24.31	11.43	0.03	0.03	0.17	0.02	17.02	99.33	26	195	156	31	11	31	26	24	9	11	27	235	29	116	27	9	11	22	3
DA-38	39.39	1.28	21.51	17.36	0.04	0.03	0.15	0.03	19.44	99.27	27	212	174	35	23	40	65	25	9	10	31	198	25	115	52	5	14	28	2
DA-39	41.48	1.36	22.92	13.12	0.04	0.04	0.18	0.03	20.04	99.25	29	222	171	43	15	37	76	28	10	14	32	223	29	127	45	8	14	27	2
DA-40	52.12	1.32	21.53	9.53	0.02	0.04	0.11	0.04	14.60	99.34	22	165	127	30	19	36	25	24	7	21	23	237	26	108	43	8	21	22	2
DA-41	54.69	1.34	25.77	3.63	0.03	0.25	0.18	0.04	13.39	99.34	15	130	95	44	19	29	30	21	9	29	18	255	27	95	41	6	30	23	4
DA-42	62.61	1.17	21.60	3.09	0.02	0.04	0.15	0.05	10.40	99.15	14	129	95	33	18	24	40	16	8	35	15	305	24	107	45	9	40	18	4
DA-43	69.52	0.89	17.59	2.45	0.02	0.01	0.12	0.04	8.66	99.32	12	126	85	26	16	20	19	13	5	26	13	279	18	93	42	8	31	14	2
DA-44	70.16	0.84	15.32	3.30	0.02	0.02	0.11	0.04	9.45	99.28	13	133	120	30	18	21	23	13	5	28	13	274	19	102	49	10	27	16	3
DA-45	59.37	1.10	19.96	3.12	0.01	0.02	0.14	0.04	15.41	99.18	22	118	104	45	33	37	35	17	7	31	21	272	23	91	59	8	32	19	4
DA-46	65.64	1.08	19.47	3.37	0.02	0.01	0.13	0.04	9.56	99.33	14	115	104	30	24	27	25	14	6	25	14	253	21	101	45	8	26	17	3

DA-47	85.30	0.38	8.72	1.14	0.02	0.07	0.05	0.05	3.51	99.25	6	96	128	21	5	7	5	6	2	50	14	336	9	92	75	11	28	8	1
DA-48	89.12	0.27	6.29	0.86	0.02	0.02	0.03	0.03	2.53	99.18	6	74	106	16	3	5	3	4	1	20	14	173	6	75	49	6	15	4	<d.l.
DA-49	87.71	0.33	7.02	1.13	0.02	0.02	0.04	0.03	2.85	99.15	6	87	89	16	4	6	4	4	1	18	19	233	7	63	46	8	17	6	2

***Table 7**. Major (ME) and trace (TE) elements composition of ES section. Note that CaO content is null*

Sample	Major elements (wt.%)										Trace elements (ppm)																		
	SiO_2	TiO_2	Al_2O_3	Fe_2O_3	MgO	Na_2O	K_2O	P_2O_5	LOI	Total	Sc	V	Cr	Mn	Co	Ni	Cu	Zn	Rb	Sr	Y	Zr	Nb	Ba	Nd	Hf	Pb	Th	U
ES-201	47.73	1.60	27.09	4.37	0.02	0.04	0.25	0.03	17.96	99.12	19	207	137	24	26	39	66	25	11	27	11	237	30	116	24	7	8	21	<d.l.
ES-202	51.74	1.58	29.63	2.13	0.02	0.04	0.25	0.05	13.73	99.21	17	156	112	19	9	24	11	20	10	49	13	230	28	136	50	7	30	26	2
ES-203	45.95	1.61	33.01	2.04	0.02	0.04	0.28	0.06	16.29	99.34	19	196	124	18	12	39	48	24	13	62	12	108	24	133	41	3	38	15	3
ES-204	45.05	1.70	28.47	4.20	0.02	0.04	0.29	0.05	19.41	99.27	19	211	136	20	17	40	14	26	13	40	15	218	26	131	36	6	25	24	3
ES-205	41.40	1.52	27.11	7.74	0.01	0.04	0.21	0.05	21.13	99.23	20	186	118	21	17	36	10	26	11	45	11	168	27	113	39	4	29	24	4
ES-206	45.06	1.73	31.28	3.00	0.00	0.03	0.22	0.06	17.95	99.35	20	191	102	21	17	38	12	33	11	41	14	157	30	100	33	4	30	25	4
ES-207	44.26	1.64	32.01	3.22	0.00	0.03	0.15	0.07	18.07	99.48	22	204	124	19	18	42	38	37	10	59	11	120	28	105	58	2	49	26	4
ES-208	38.85	1.45	28.46	6.58	0.00	0.03	0.14	0.08	23.99	99.60	20	178	104	21	20	46	32	30	9	69	10	96	25	109	72	3	55	28	2
ES-209	41.57	1.61	28.71	6.48	0.03	0.05	0.33	0.09	20.51	99.41	22	230	146	25	16	45	19	27	14	55	11	158	26	407	48	3	13	28	2
ES-210	45.35	1.77	32.37	2.47	0.00	0.04	0.24	0.08	16.98	99.34	19	191	123	27	14	35	18	30	11	50	9	180	30	192	56	5	20	26	3
ES-211	36.75	1.34	27.71	6.98	0.00	0.03	0.16	0.05	26.45	99.49	16	185	119	19	19	37	13	27	8	33	7	120	22	123	35	3	18	24	3
ES-212	31.25	1.23	24.36	14.57	0.00	0.03	0.08	0.03	27.65	99.23	20	220	169	10	17	45	27	30	6	16	6	91	22	60	24	2	15	25	4
ES-213	42.95	1.69	34.55	3.09	0.00	0.03	0.09	0.03	16.81	99.29	18	187	127	11	18	49	39	35	7	21	7	115	29	55	20	3	14	28	5
ES-214	38.76	1.35	32.05	12.22	0.00	0.03	0.08	0.17	14.52	99.22	19	149	98	7	16	55	10	31	7	231	9	79	23	246	241	<d.l.	255	40	1
ES-215	65.32	1.24	17.84	6.20	0.00	0.04	0.05	0.11	8.34	99.16	15	139	127	7	10	39	10	19	4	236	7	256	20	245	154	10	50	20	2

Feldspars (K-feldspars and Na-plagioclases), hematite as well as calcite are in trace or null in both sections (see raw data in supplementary file). Also, undosed part of these components, 1.0 – 7.0 % for ES and 0.5 – 8.6 % for DA, consists of poorly crystallized minerals (e.g., opal, Fe-oxides).

4.3. Major and trace element geochemistry

Major element composition of deposits from Tondè locality is shown in Tables 6 and 7, respectively for DA and ES sections. In order to assess mobility of elements during diagenesis processes, trace element concentrations of Tondè materials (Table 6 for DA section, and 2 for ES section) are normalized to aluminum following Van der Weijden (2002) and Tribovillard et al. (2006). Then, Al-normalized trace elements as well as major elements are compared to the PAAS (Post-Archean Australian average Shales) values (Fig. 52).

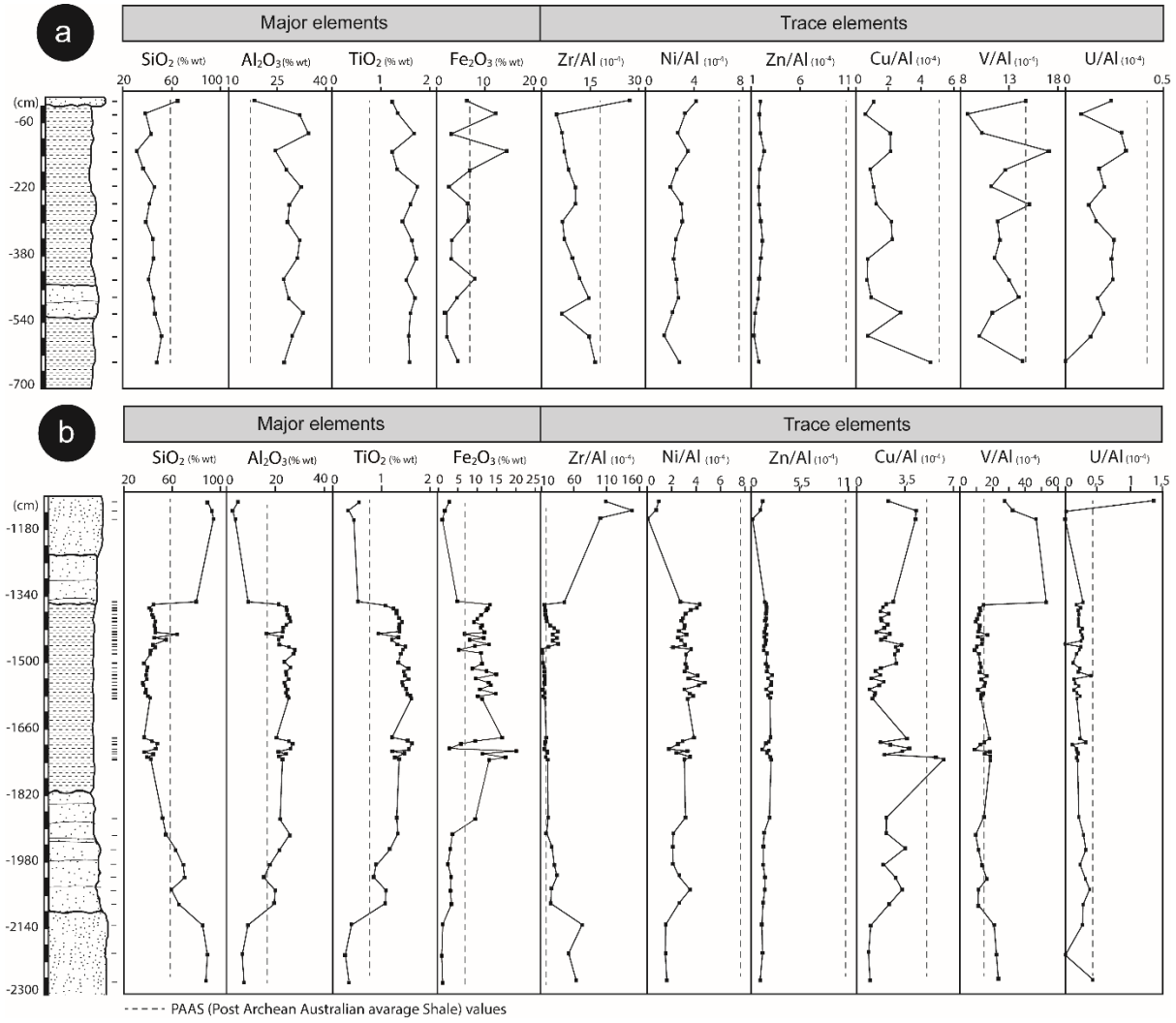

Figure 52. *Significant major and Al-normalized trace elements from (a) ES section and (b) DA section. Grey dashed line represents PAAS value (Wedepohl, 1971; 1991). Note that clayey*

facies are globally depleted in SiO_2 and enriched in Al_2O_3 and TiO_2 while Ni, Zn and Cu remain little mobile.

In the DA section, the sandstone facies is highly enriched in SiO_2 (85.00 – 90.00 wt.%) in contrast to Al_2O_3 (6.00 – 9.00 wt.%), Fe_2O_3 (0.86 – 1.14 wt.%) and TiO_2 (0.27 – 0.38 wt.%), which present very low contents related to their respective PAAS values (16.70 wt.% for Al_2O_3, 6.91 wt.% for Fe_2O_3 and 0.77 wt.% for TiO_2). The siltstone in the same section, presents average contents of Al_2O_3 (20.18 wt.%), Fe_2O_3 (4.01 wt.%), SiO_2 (62.01 wt.%) and TiO_2 (1.10 wt.%) relatively close to those of respective PAAS values. Zr and V are relatively mobile in both facies in contrast to Ni, Zn and Cu which exhibit a very low mobility (Fig. 52a and b).

The clayey intervals show the same trends in both sections. The entire ES section (except sandy siltstone) and the homogeneous grey claystone in DA section show SiO_2 contents fluctuating between 31.00 – 65.00 wt.%, with a mean value of 42.62 wt.% (ES) and 43.11 wt.% (DA), which are quite low compared to the PAAS value (58.91 wt.%); This trend is quite common in tropical areas, where silica removal is significant. In the same time, TiO_2 contents show values between 1.20 to 1.80 wt.%, with an average of 1.56 wt.% (ES) and 1.40 wt.% (DA) significantly higher than the PAAS value (0.77 wt.%). Increase in Al_2O_3 content in these facies is very similar to that of TiO_2. The mean values, 29.77 wt.% for ES section and 24.23 wt.% for DA section, are very high related to the PAAS value (16.70 wt.%). Apart from Zr/Al (19.14 average value of grey claystone and 18.10 PAAS value) and V/Al (12.35 and 13.22 respective average values of ES section and grey claystone and 14.71), all other TEs/Al ratios offer overall low values compared to their respective PAAS, typical of low mobility of these elements during diagenetic processes.

The superficial lithology, characterized by sandy siltstone in the ES section, and unconsolidated sandstone and argillaceous siltstone in the DA section (Fig. 52a and b), present high SiO_2 contents relative to PAAS value (58.00 wt.%) value, ranging from 65.00 to 94.00 wt.%. They globally contain relatively lower proportions in Al_2O_3 (2.00 – 9.00 wt.%), TiO_2 (0.30 – 0.60 wt.%) and Fe_2O_3 (1.00 – 5.00 wt.%), except in the sandy siltstone of the ES section which exhibit Al_2O_3 and Fe_2O_3 contents close PAAS value. Compared to Zn, Ni and Cu, zircon and vanadium appear highly mobile with averages values of 14.70 and 13.21 for V/Al ratio, and 18.10 and 19.14 for Zr/Al respectively for ES and DA sections.

4.4. Occurrences and whole rock geochemistry of pyrite

Two main pyrite morphologies can be found (euhedral and massive) along the ES profile. Euhedral pyrite represents well shaped pyrite crystals (Kortenski and Kostova, 1996; Taylor and Macquaker, 2000; Widodo et al, 2010; Wang et al., 2012). In this study, they appear as isolated (Figs.53a and b) and clusters (Figs.53c, d and e) euhedral crystals, with various sizes and morphologies. Massive pyrite is usually found as filling in cleats, joints and cell structures in exinites, cementing, coating framboids, euhedra or detrital minerals, and as replacement of organic matter in different macerals (Querol et al., 1989). These forms are illustrated in figures 53f, g and h.

***Table 8**. Geochemical composition (ME, TE and REE) of pyritic occurrences of Tondè locality. Me are in wt.% while TE and REE are in ppm. Mean values were calculated; average shale data are from Wedepohl (1971, 1991)*

Element	AP1	AP2	AP3	AP4	AP5	AP6	AP7	AP8	AP9	AP10	Mean value	Average shale
SiO_2	7.34	5.66	4.39	4.83	9.24	7.11	8.59	0.82	4.41	1.72	5.41	58.90
Al_2O_3	3.76	3.21	3.09	3.35	6.14	4.35	6.33	0.61	3.51	1.10	3.55	16.70
Fe_2O_3	56.30	57.90	59.00	59.00	51.10	55.00	51.40	60.10	57.90	61.70	56.94	6.90
MgO	0.01	0.01	0.01	0.01	0.02	0.01	0.01	<d.l.	<d.l.	<d.l.	0.01	2.60
K_2O	0.05	0.04	0.03	0.04	0.07	0.06	0.03	<d.l.	0.01	0.01	0.04	3.60
Na_2O	<d.l.	<d.l.	<d.l.	<d.l.	<d.l.	<d.l.	<d.l.	<d.l.	<d.l.	<d.l.	0.00	1.60
CaO	0.01	0.01	0.01	0.01	0.01	0.01	0.01	<d.l.	<d.l.	<d.l.	0.01	2.20
TiO_2	0.33	0.27	0.21	0.21	0.39	0.31	0.39	0.04	0.18	0.08	0.24	0.78
P_2O_5	0.07	0.07	0.07	0.02	0.30	0.09	0.02	0.03	0.03	0.01	0.07	0.16
MnO	0.01	0.01	<d.l.	0.01	0.01	0.01	0.01	0.01	0.01	<d.l.	0.01	0.11
LOI	33.00	34.10	33.90	33.30	31.90	33.10	33.40	35.20	34.00	33.90	33.58	-
Cr	430.00	500.00	350.00	580.00	670.00	750.00	980.00	570.00	320.00	530.00	568.00	90.00
V	52.00	37.00	30.00	24.00	51.00	43.00	72.00	<d.l.	13.00	<d.l.	40.25	130.00
Ba	90.10	106.00	117.50	27.20	87.90	345.00	218.00	7.20	18.30	6.10	102.33	580.00
Zr	74.00	48.00	14.00	12.00	37.00	42.00	39.00	2.00	11.00	7.00	28.60	160.00
Sr	46.50	61.60	59.90	8.70	19.60	44.10	25.40	8.40	20.30	2.40	29.69	300.00
Y	4.90	5.30	4.50	1.20	2.50	5.40	3.30	<d.l.	0.80	0.60	3.17	41.00
Ga	6.30	5.40	5.10	5.30	9.90	7.20	11.10	1.10	5.40	1.70	5.85	19.00
Nb	5.40	4.70	3.50	3.50	6.50	4.90	6.80	0.70	3.30	1.40	4.07	18.00
Hf	2.10	1.50	0.50	0.50	1.20	1.20	1.20	0.20	0.50	0.30	0.92	2.80
Th	6.90	6.64	5.35	3.53	6.83	5.93	8.10	0.62	3.05	1.05	4.80	12.00
U	0.72	0.72	0.51	0.38	0.76	0.60	0.94	0.11	0.45	0.17	0.54	3.70
Cs	0.38	0.27	0.23	0.18	0.40	0.27	0.30	<d.l.	0.13	0.05	0.25	5.50
Rb	3.00	2.20	1.60	1.80	3.80	3.00	2.60	0.20	1.10	0.70	2.00	140.00
Sn	10.00	13.00	15.00	7.00	8.00	6.00	6.00	5.00	2.00	5.00	7.70	6.00
La	25.50	24.60	31.50	6.70	13.40	10.30	7.80	6.00	14.40	2.10	14.23	40.00
Ce	62.80	65.60	80.90	14.40	30.90	30.00	18.20	12.40	27.60	4.20	34.70	95.00
Pr	7.97	8.83	10.55	1.63	3.90	4.67	2.48	1.29	2.70	0.45	4.45	0.70
Nd	31.00	37.00	43.00	5.90	14.80	22.00	9.80	3.90	8.00	1.50	17.69	39.00
Sm	6.53	8.67	9.14	0.97	2.58	5.13	1.72	0.61	1.14	0.25	3.67	7.30
Eu	1.40	1.94	1.92	0.18	0.49	1.01	0.36	0.12	0.20	0.05	0.77	1.60
Gd	4.37	6.23	5.89	0.56	1.41	3.11	1.09	0.31	0.51	0.15	2.36	7.00
Tb	0.51	0.66	0.64	0.07	0.17	0.37	0.16	0.03	0.07	0.02	0.27	1.20
Dy	1.93	2.46	2.33	0.29	0.75	1.54	0.78	0.12	0.28	0.11	1.06	5.50
Ho	0.27	0.32	0.29	0.05	0.11	0.23	0.14	0.02	0.04	0.02	0.15	1.60
Er	0.53	0.55	0.46	0.11	0.25	0.46	0.31	0.04	0.09	0.06	0.29	3.90
Tm	0.06	0.05	0.04	0.02	0.03	0.04	0.04	<d.l.	0.02	0.01	0.03	0.60
Yb	0.35	0.30	0.19	0.13	0.22	0.25	0.24	<d.l.	0.10	0.06	0.20	3.70
Lu	0.06	0.04	0.02	0.02	0.03	0.04	0.03	<d.l.	0.01	0.01	0.03	0.70
ΣREE	143.28	157.25	186.87	31.03	69.04	79.15	43.15	24.84	55.16	8.99	79.88	-
LREE	135.20	146.64	177.01	29.78	66.07	73.11	40.36	24.32	54.04	8.55	75.51	-
HREE	8.08	10.61	9.86	1.25	2.97	6.04	2.79	0.52	1.12	0.44	4.37	-
LREE/HREE	16.73	13.82	17.95	23.82	22.25	12.10	14.47	46.77	48.25	19.43	23.56	-
$(La/Yb)_{PAAS}$	5.37	6.04	12.22	3.80	4.49	3.04	2.39	0.00	10.61	2.58	5.05	-
$(Ce/Ce^*)_{PAAS}$	0.91	1.02	1.21	0.18	0.43	0.52	0.27	0.15	0.31	0.05	0.50	-
$(Eu/Eu^*)_{PAAS}$	1.14	1.63	1.53	0.14	0.36	0.78	0.28	0.08	0.13	0.04	0.61	-

Geochemical data obtained from analyse of these pyrite occurrences (Table 8) present a high proportion in Fe_2O_3 (51.00 – 62.00 wt%) and relatively low proportions in Al_2O_3 (0.61 – 6.14% wt) and SiO_2 (0.82 – 9.24 wt%). The PAAS-normalized TE diagrams (Fig. 6a) generally show a Cr an Sn enrichment. There is also observed a relatively significant depletion in Rb and Cs. The PAAS-normalized REE patterns show a deficit in REE compared to the PAAS values with a slight positive Eu anomaly, and a particular enrichment in LREE compared to HREE (Fig. 54b).

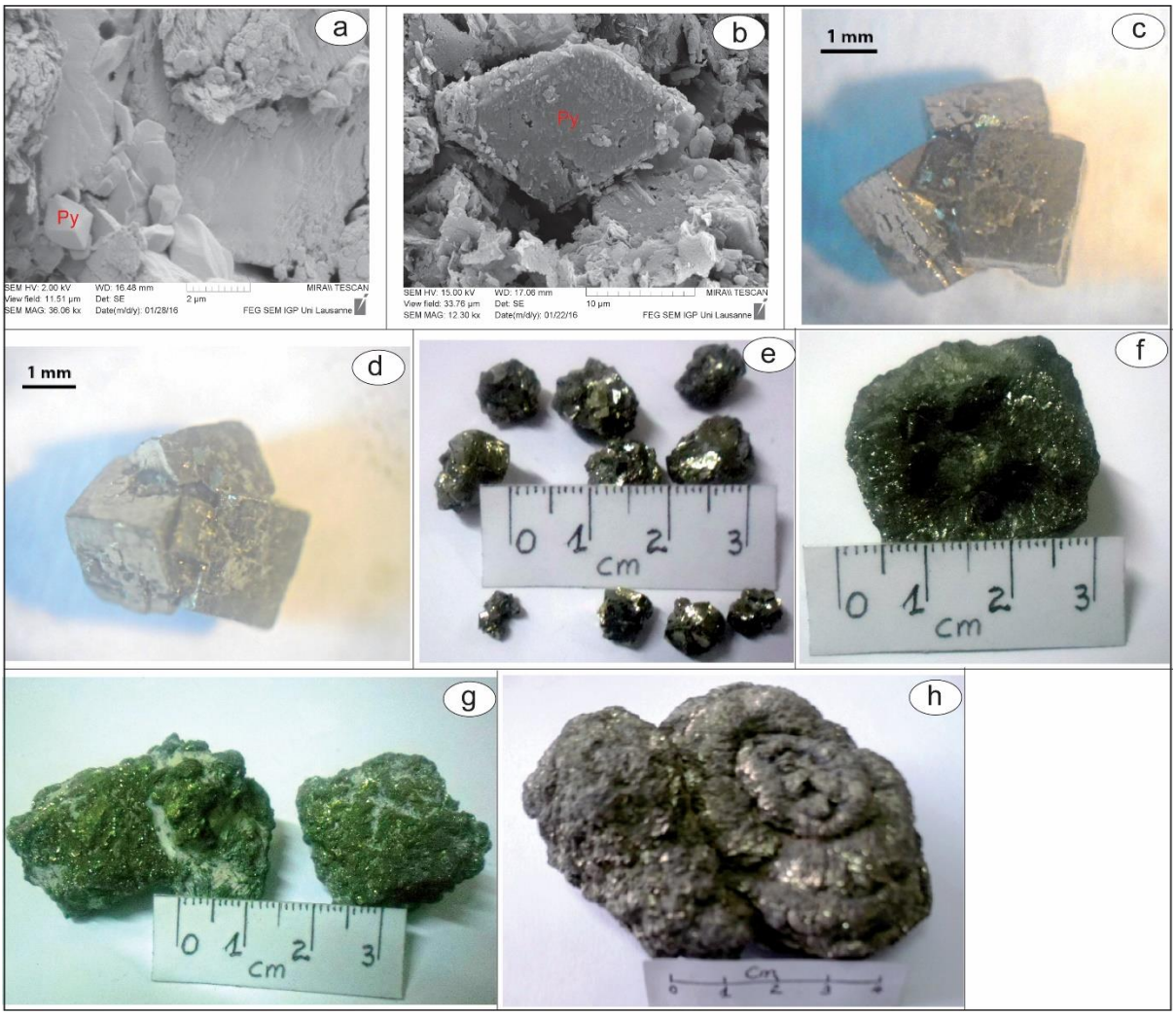

Figure 53. *Pyrite occurrences of Tondè locality (from ES section). SEM micrographs (a) and (b) show well crystallized isolated tiny pyrite crystals (Py) while (c), (d) and (e) are macroscopic euhedral clusters. Photographs f, g and h refer to massive pyrite. Note that the well-shaped forms imply diagenetic origin.*

5. DISCUSSION

5.1. Provenance

Scandium (Sc) and thorium (Th) are trace elements recognized as very immobile during the chemical weathering (Middelburg et al. 1988; Braun et al., 1993; Condie et al., 1995; Nesbitt and Markovics., 1997; Ma et al, 2007). Associated with Lanthanum (La), as in this study, and other trace elements (La/Sc, Th/Sc, La/Co, Th/Co and Cr/Th), they provide crucial informations on the origin of sedimentary rocks (Cullers, 1988, 1994, 2000; Wronkiewicz and Condie, 1989; Condie and Wronkiewicz, 1990; Tapia-Fernandez et al 2017; Hernández-Hinojosa et al 2018; Tawfik et al 2018).

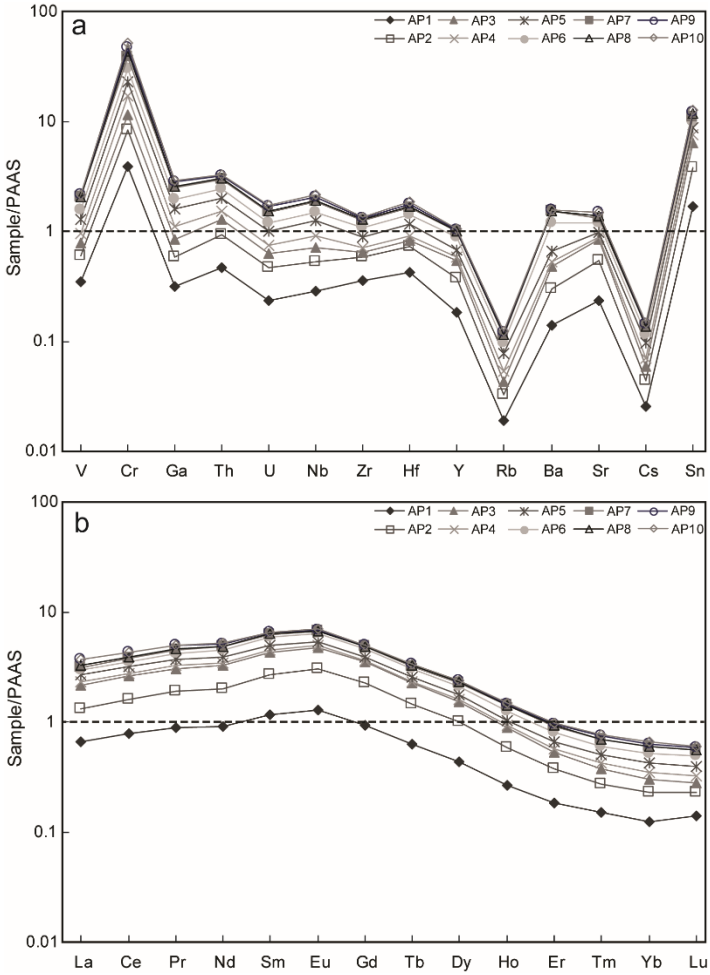

Figure 54. *Geochemical diagrams for pyrite samples of Tondè area (es section). Normalizing values from Wedepohl (1971; 1991). (a) PAAS-normalized TE diagrams. Note enrichment in Cr and Sn, and significant depletion in Rb and Cs. (b) PAAS-normalized REE patterns, showing deficit in REE and weak positive Eu anomaly.*

Two diagrams, Th/Sc vs. Zr/Sc (McLennan et al., 1993) and La-Sc-Th (Taylor and McLennan, 1985) (Fig. 55), have been used for this determination and show that materials of Tonde locality have an intermediate source between felsic and mafic rocks with a mean value of Th/Sc ratio of 1.35 and 1.06 respectively for ES and DA sections (fig.55a). They would probably be the result of the alteration of surrounding Panafrican basement (gneiss and micashist) (Ngon Ngon et al., 2014, Bukalo et al., 2019). According to Potter et al. (1980), most clay minerals come from the erosion of preexisting mudstones while Curtis (1990) suggests that most clay minerals come from soil erosion, which should be the case in this study. In addition, some clays from rock alteration often transform by means of a soil so that their source has both rock and soil characteristics (Hillier, 1995).

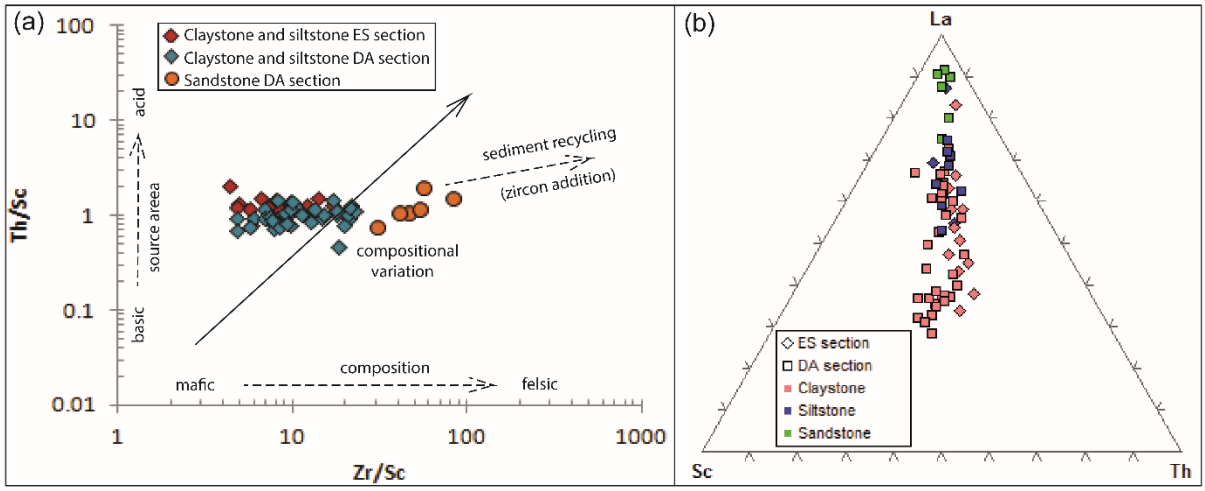

Figure 55. *Discrimination diagrams of Tondè detrital materials illustrating (a) variation of composition (Th/Sc) and recycling of sediments (Zr/Sc) (McLennan et al., 1993), and (b) Post-Archean Shales (Taylor and McLennan, 1985).*

Furthermore, Al_2O_3/TiO_2 ratio is generally used in sedimentary environments in order to detect source rock composition and consequently, to predict the provenance of clastic sediments (see Girty et al., 1996; Nagarajan et al., 2015; Ngon Ngon et al., 2019). The Al_2O_3/TiO_2 values ranging from 3 to 8, from 8 to 21, and from 21 to 70 respectively indicate mafic source rocks, intermediate source rocks and felsic source rocks. (Hayashi et al., 1997). At Tondè, the Al_2O_3/TiO_2 values of ES profile vary between 14.38 – 20.64 and only one sample (ES214; Al_2O_3/TiO_2 = 23.68) exhibits a ratio value more than 21. Likewise, excepted the upper part (unconsolidated red sandstone) which presents low values (6.48 – 7.52) probably due to processes of modern soil formation, most of the Al_2O_3/TiO_2 values from DA profile range from

15.56 to 19.84, with however, values of the three basal samples higher than 21. All these observations suggest, in agreement with trace elemental ratios above, an intermediate source rocks with a relative influence of felsic materials, also reported in this area by Ngon Ngon et al. (2019).

5.2. Paleoweathering and sediment recycling

Si/Al, Ti/Al and Zr/Al ratios characterize detritism and source rocks materials in continental environments. For example, Ti is usually associated with heavy minerals and therefore not mobile. In addition, high Ti/Al ratios imply high transportation energy (the river for example). Ti/Al enrichment may also be linked to volcanic input if this enrichment is correlated with high Zr/Al ratios (Khozyem et al., 2013). Similarly, the Chemical Index of Alteration (CIA) is a method, which compares abundances of soluble cations of calcium and sodium against relatively stable aluminium to determine the relative amount of chemical weathering (e.g. weathering of plagioclase into clay minerals) to estimate the intensity of weathering in relation to climate (Nesbit and Young, 1984, 1989, Price and Velbel, 2003). Its formula, based on molar ratios, is: CIA = (100 [Al_2O_3 / (Al_2O_3 + CaO* + Na_2O + K_2O)] where Ca* represents the proportion of CaO of the silicate minerals (Nesbit and Young, 1984, 1989 and Price and Velbel, 2003).

In the ES section, Ti/Al ratio values are moderately high (5.00 – 6.80) over most of profile relative to PAAS value (5.20), except in the upper part (sandy siltstone) where the ratio is very high reaching a value very close to 8.00 (Fig. 52a). In the same time, DA section presents moderately high Ti/Al ratios (4.78 – 7.27) in the entire section except in the unconsolidated red sandstone, where Ti/Al ratio values are very high (15.00 – 17.50). Moreover, no correlation is observed between Ti and Zr in both sections (Figs. 56a and b) thus excluding any volcanic influence. These results suggest therefore intense chemical weathering in Tondè locality which also attested by higher CIA values, from 98.45 % to 99.43 % and from 97.35 % to 99.10 %, respectively observed in both ES and DA sections.

The Si_2O_3/Al_2O_3 elemental ratio is widely used as proxy to infer sediment maturity and recycling (Anaya-Gregorio et al., 2018; Armstrong-altrin et al., 2018; Tawfik et al., 2018). In clastic sediments, Si_2O_3/Al_2O_3 values > 5 indicate mature and/or high recycled sediments whereas values < 5 suggest immature and/or first-cycle sediments. For the ES samples, Si_2O_3/Al_2O_3 values range from 1.21 to 1.76, except at the superficial lithology (ES-215) this ratio is 3.66, that indicate immature and moderated mature sediments. The Si_2O_3/Al_2O_3 ratio

from DA samples exhibit values ranging, for sand-rich lithologies (included basal and superficial sandstone), from 9.79 to 36.49, and for intermediate clay-rich lithologies, between 1.52 and 4.58. These values indicate mature sediments from sand-rich lithologies and immature to moderate mature deposits from clay-rich lithologies.

In addition, combination of some significant trace elements through McLennan et al., (1993) and Taylor and McLennan (1985) diagrams (Figs. 55a and b respectively), also testify that sand-rich lithologies of the DA profile is more recycled (Fig.55a) and enriched in lanthanum (Fig. 55b) during the deposition process. Likewise, siltstone in both profiles are also relatively recycled (Fig. 55a) and enriched in lanthanum (Fig. 55b).

5.3. Paleoclimate evaluation

In humid climatic conditions, and based on the combination of empirical data of Marbut (1935) and modern calculation methods, Sheldon et al. (2002) and Sheldon and Tabor (2009) quantify the mean annual precipitation (MAP) through the relation MAP ($mm.y^{-1}$) = $221.1e^{0.0197(CIA-K)}$. This parameter assesses intensity of chemical weathering depending to precipitations. The standard error (SE) of this parameter as well as correlation coefficient relative to empirical relation are ± 181 $mm.y^{-1}$ and $R^2 = 0.72$ respectively. Also, MAT (°C) = 46,9*C* + 4 applicable to Cenozoic paleosols allows an estimation of mean annual temperature (Sheldon et al. 2002; Sheldon et Retallack, 2004; Hamer et al, 2007). The SE of the present relation is ± 0.6 °C, *C* (Al/Si ratio) the clayeyness and $R^2 = 0.96$ (Sheldon, 2006c), the correlation coefficient.

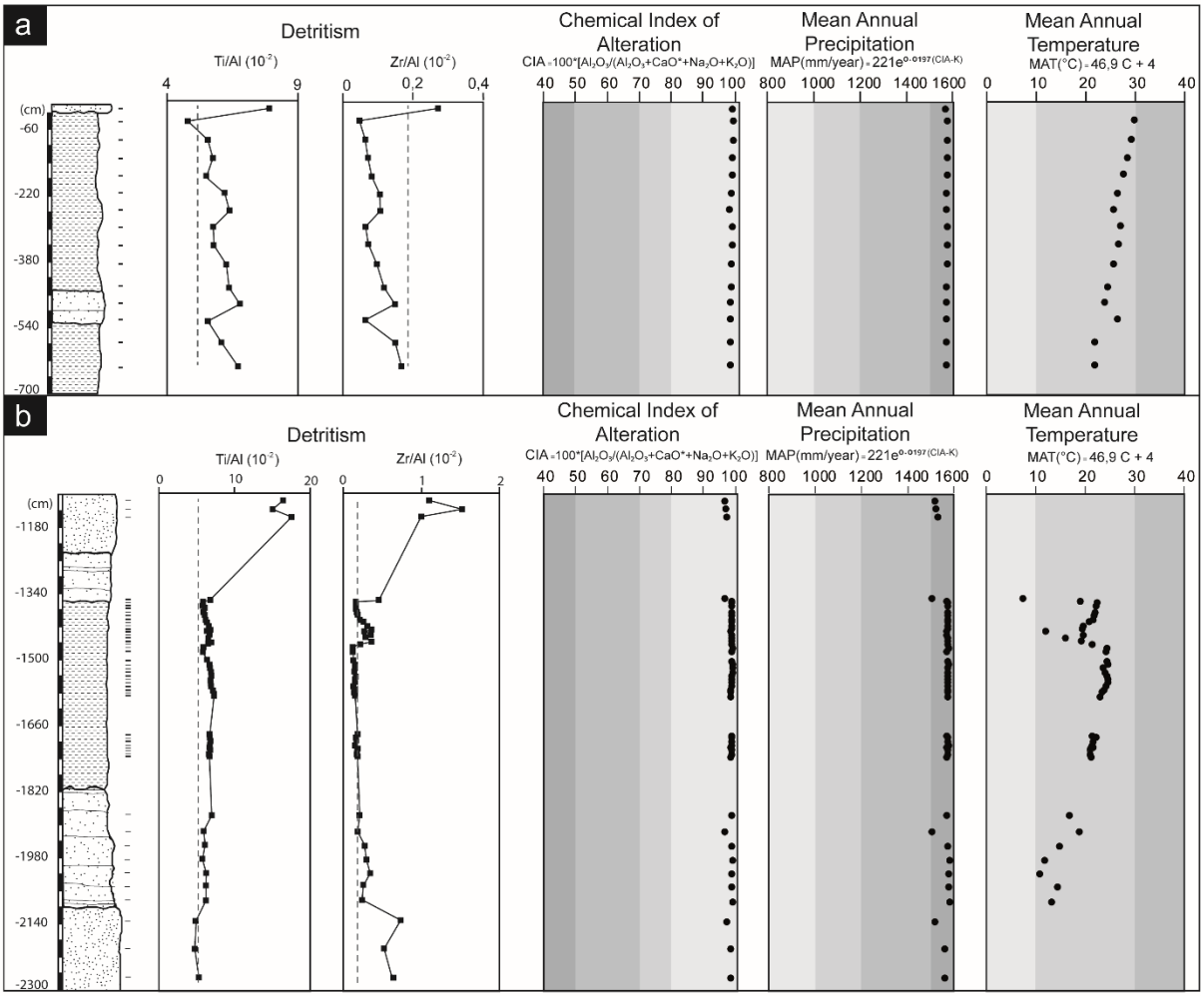

Figure 56. *Summary of environmental and climatic proxies (detritism, chemical index of alteration, mean annual precipitation and mean annual temperature) from (a) ES section and (b) DA section, based on major element geochemistry. The high Ti/Al ratio correlates to high CIA values indicates intense alteration processes. MAP and MAT values indicate a warm/humid seasonal climatic regime.*

The present study shows MAP values globally high, range from 1567 to 1578 $mm.y^{-1}$ in ES section (Fig. 56a) with an average value of ~1575 $mm.y^{-1}$ and from 1506 to 1582 $mm.y^{-1}$ for DA section (Fig. 56b) with a mean of 1566 $mm.y^{-1}$, testifying of a more humid climate period. Moreover, MAT values from clayey facies (claystones, siltstone and clayey sandstone) in both sections fluctuate between 12 and 30 °C (with average values of 25.2 °C for ES and 20.3 °C for DA) thus corresponding to a warm climate. The MAP and MAT values from the Tondè locality are correlated to those suggested by Quantin (1965), 1500 – 1600 $mm.y^{-1}$; 25.5 °C, for a warm/humid climate of subequatorial zones. In addition, the relative simplicity of clayey phase (mainly kaolinite) reflects an abundant and permanent rainfall (Righi et Meunier, 1995).

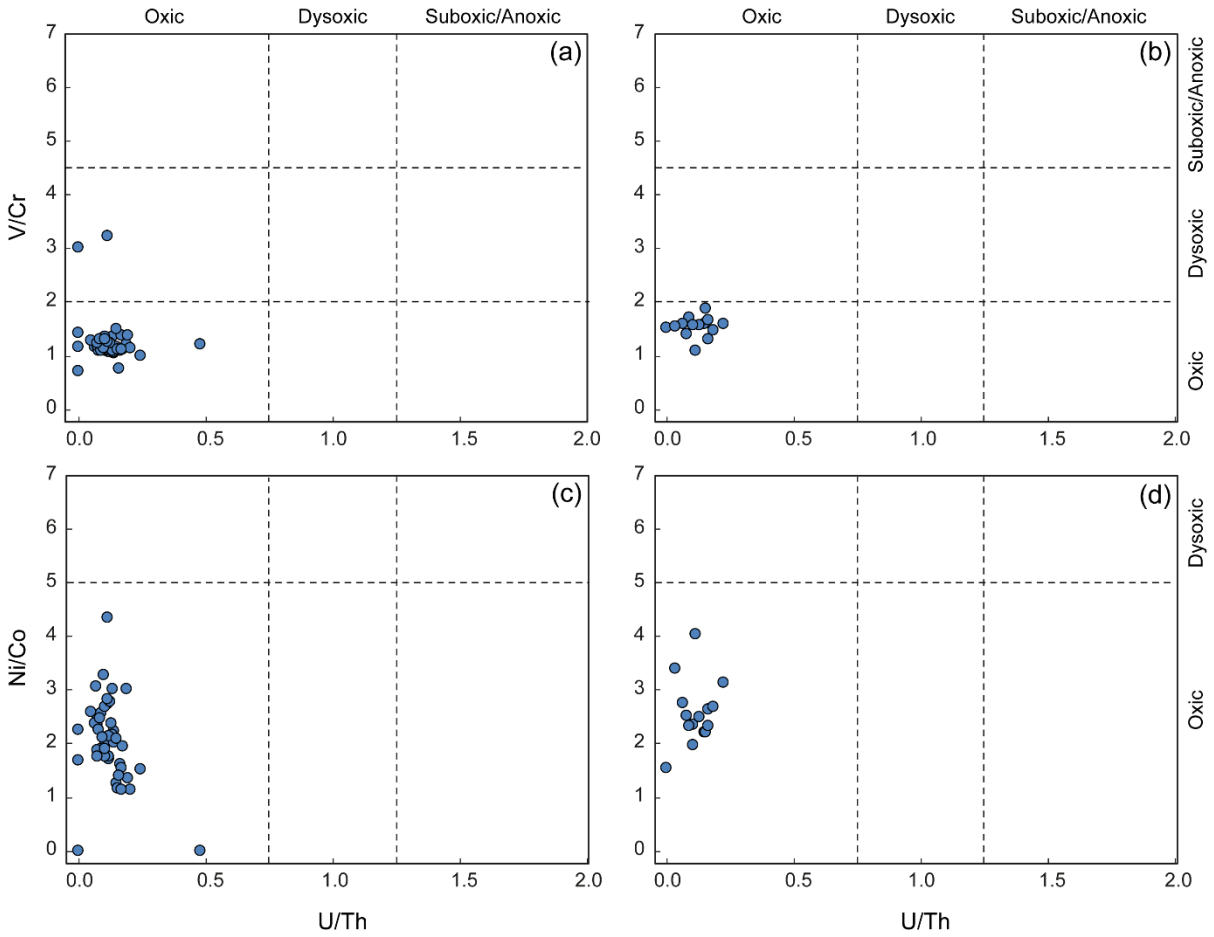

Figure 57. *Trace element cross plots from da (a and c) and es (b and d) sections as redox sensibility proxies. (a) and (b) are V/Cr vs. U/Th while (c) et (d) represent Ni/Co vs. U/Th diagrams.*

5.4. Age constrain and depositional environment

The study of pollen residue (Fig. 58) of some selected samples enables to distinguish, among others, fungi (Figs. 58a, b, c, j, n, r and s) and algae (fig. 58d, g, h, k, m) spores, graminaceae (Figs. 58e et i), stomata (Fig. 58o), silicoflagellates (Fig. 58p), triletes (Fig. 58q) and well-differentiated pollen from the Malvaceae species (Figs. 58t and u). The latter characterize the pantropical plants of swampy bays of the seaside (Salard-Cheboldaeff, 1980) and hinterlands (Barreda et al., 2008), with a very wide interval of age ranges from the upper Eocene up to the Holocene. Some other species such as graminaceae are typical of Quaternary. Considering therefore the abundance of spores and mycelia in the pollen residue as well as the very good preservation of the encountered species, the deposits of Tondè locality represent Pleistocene to Holocene soils and sandstones sequences.

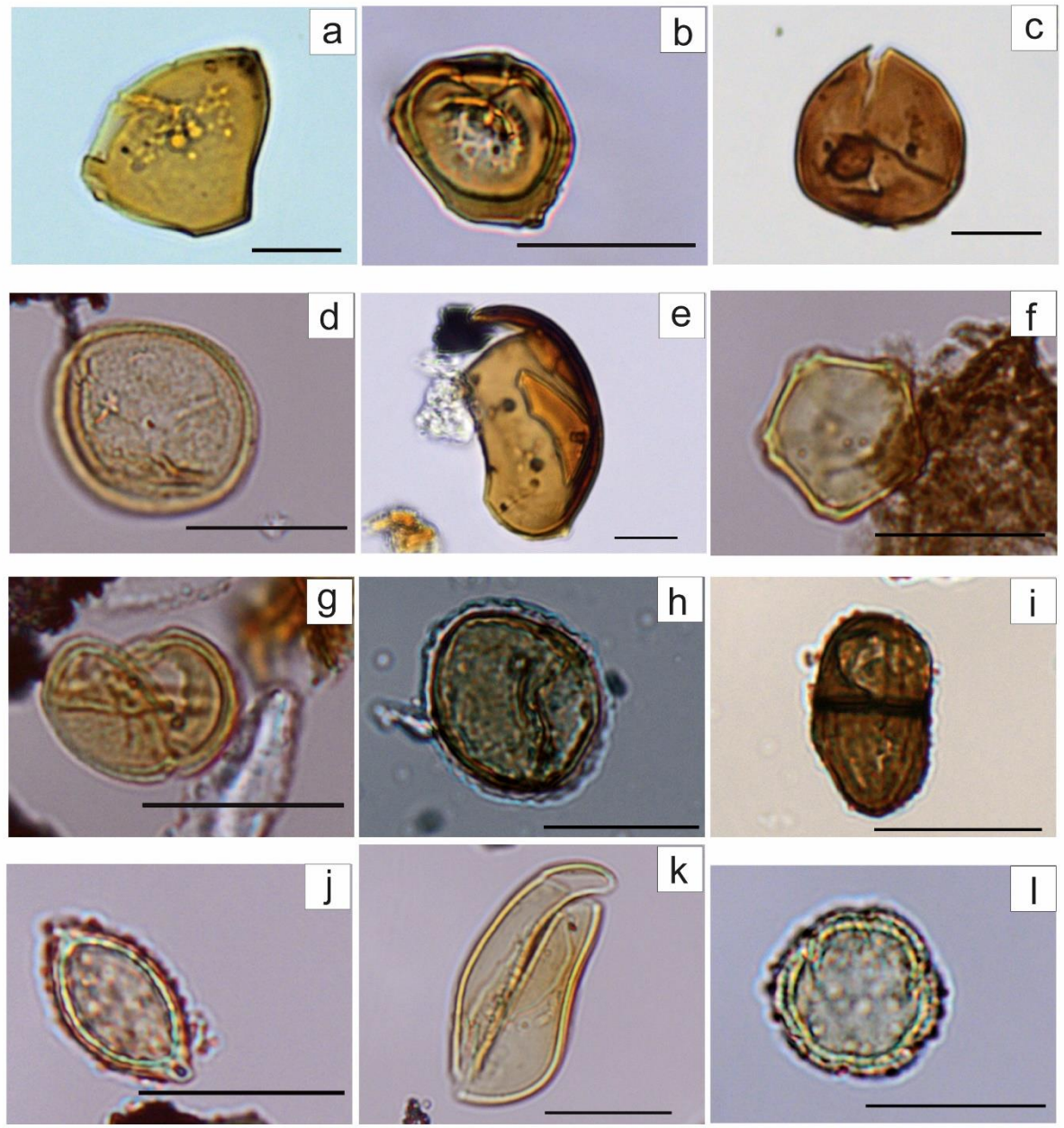

Figure 58. *Spores and pollens of Tondè continental deposits (Douala sub-basin). Spores are from fungi (a, b, c, j, n, r and s) and algae (d, g, h, k, m) while pollen derive of graminaceae (e and i), silicoflagellates (p), triletes (q) and Malvaceae (t and u) species. Malvaceae species suggest sub-recent to recent age. Scale is 20µm.*

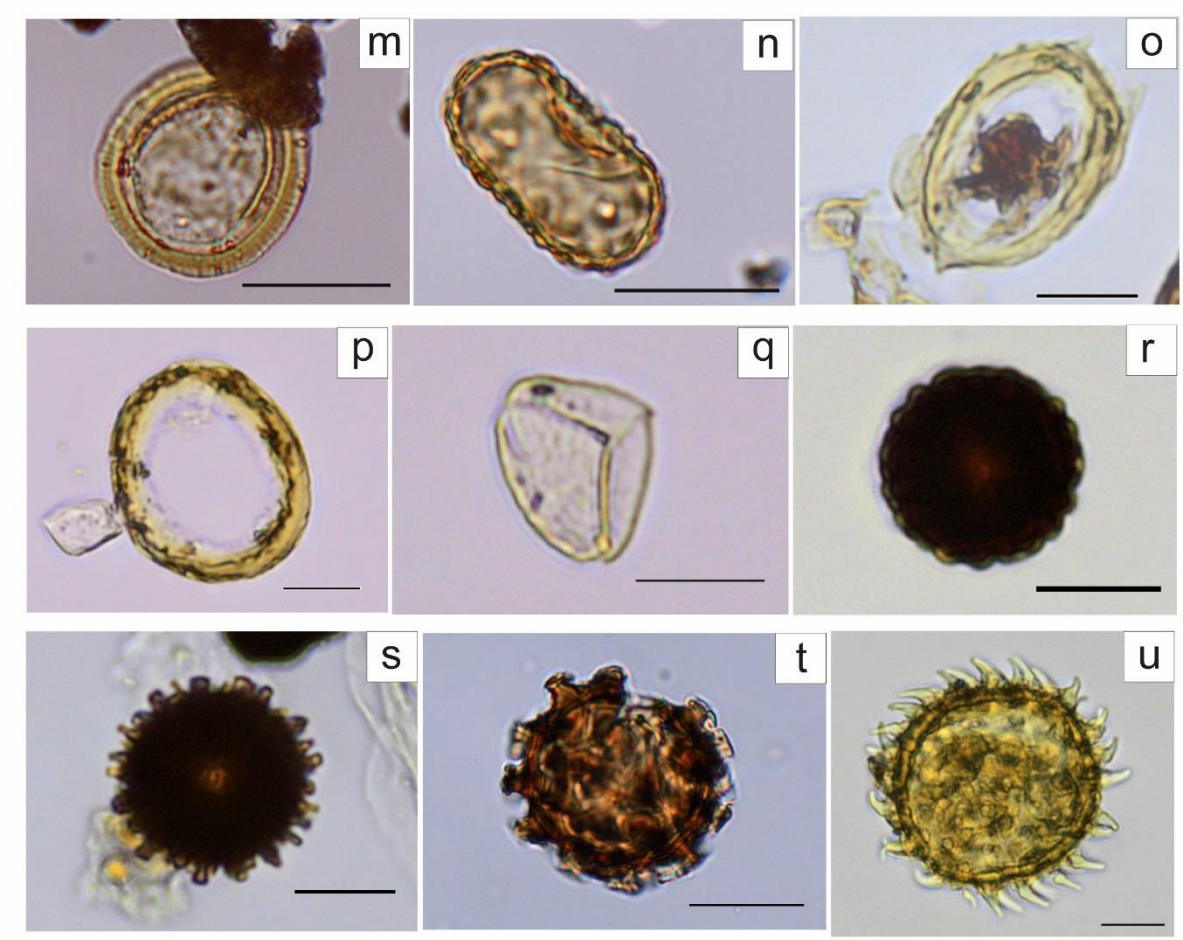

Figure 58. (Continued)

The U/Th, V/Cr and Ni/Co ratios, as well as the proportion in authigenic uranium (AU = U_{total} - Th/3) of clastic sediments (Wignall and Myers, 1988) are generally used as proxies to infer the redox sensibility of depositional environments (Hatch and Leventhal 1992, Jones and Manning 1994, Pattan et al 2005, Nagarajan et al 2007, Madhavaruja and Lee 2009, Armstrong-Altrin et al 2015; Anaya-Gregorio et al., 2018). High ratios in U/Th (> 1.25), V/Cr (> 4.5) and AU (> 5) suggest anoxic environment while values of U/Th < 0.75, V/Cr < 2 and AU < 5 are associated to oxic environment (Jones and Manning, 1994). Similarly, a Ni/Co ratio > 5 characterizes suboxic to anoxic conditions while Ni/Co < 5 suggests an oxic environment (Jones and Manning, 1994).

Figure 9 presents the combination of these different proxies in order to constrain redox sensibility. The U/Th values range from 0.06 to 0.20 and from 0.06 to 0.50 respectively for the ES and DA sections while those of V/Cr are between 1.08 – 1.90 and 0.69 – 1.50 respectively for ES and DA sections. Both proxies reflect an oxic depositional environment. In addition, the AU whose values range between -12.00 – 0.80 in the two sections as well as Ni/Co ratio (1.50 – 4.05 for ES and 1.12 – 4.40 for DA) also suggest an oxic depositional environment. Similar

observations have also been suggested by Ngon Ngon et al., 2019. However, two samples (DA-8 and DA-18) show high values of V/Cr ratios (≥ 3) thus suggesting a dysoxic environment. This could be due to a depletion of Cr probably remobilized in the pyrite genesis process.

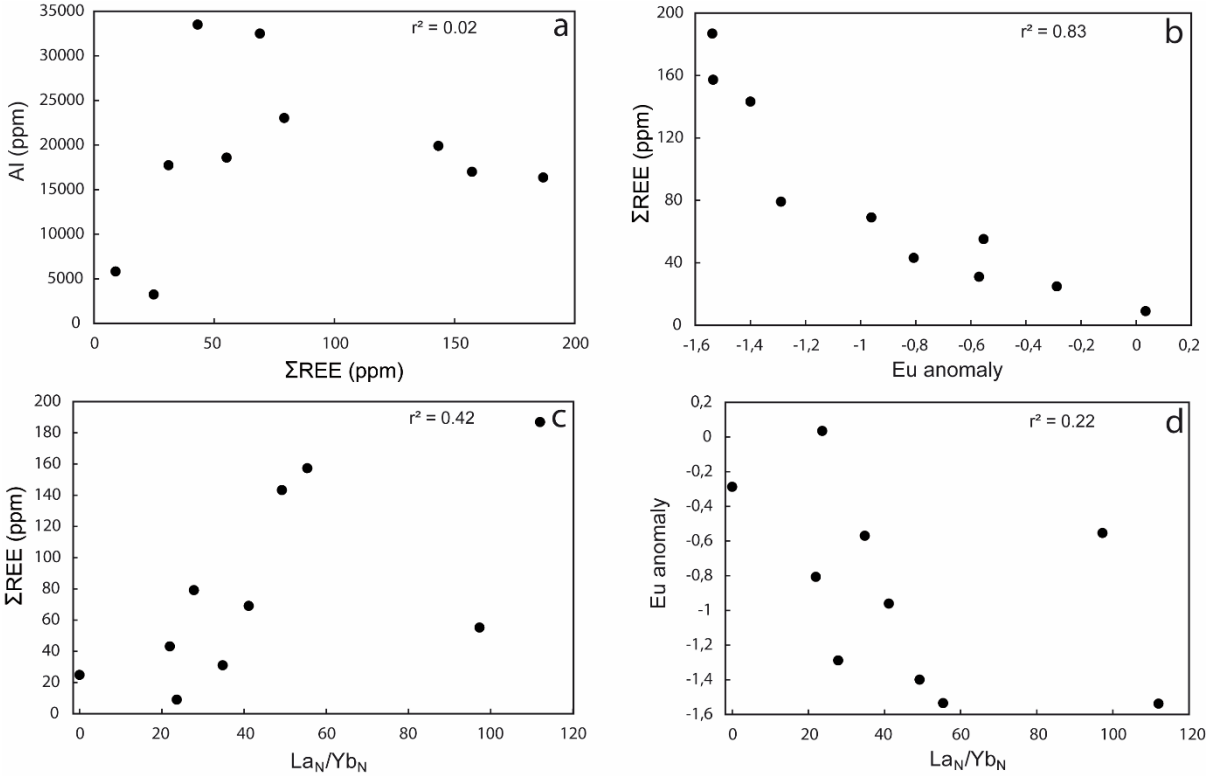

Figure 59. *Correlation between (a) Al and ΣREE, (b) ΣREE and Eu anomaly, (c) ΣREE and La_N/Yb_N, and (d) Eu anomaly and La_N/Yb_N. Europium anomaly is defined as log [$Eu_N/(Sm_N*Gd_N)$] (after Budakoglu et al., 2015).*

5.5. Genesis of pyrite

In sedimentary environments, the formation of pyrite results from the reaction between H_2S, from bacterial sulphate-reduction, and the reactive iron from detrital minerals (Berner, 1984). This process, however, is limited in river sediments because of the low concentration of dissolved sulphates and therefore cannot be correlated to organic matter (Berner, 1984). For this, some TEs such as thorium and the REE ratios (example: (La_N/Yb_N; Eu/Eu*) and the correlations between them and with other elements (example: Eu/Eu* vs. La_N/Yb_N; ΣREE vs. La_N/Yb_N, ΣREE vs. Eu/Eu*, Al vs. ΣREE) are commonly used to globally determine genesis processes in sediments (Singh and Ramajani 2001, Kütterrolf et al., 2008, Madhavajaru and Lee 2009; Garzanti et al., 2010, Dabard and Loi 2012, Budakoglu et al., 2015).

The low Th content (4.80 ppm as mean) of the pyrite relatively to PAAS (14.60 ppm), which is still high in the clayey coating (average value: 25.00 ppm) and the weak positive correlation between Al and ΣREE ($r^2 = 0.02$) (Fig. 59a), testify a very weak detrital influence, and consequently, a post-depositional. The positive Eu anomaly relative to PAAS reflects an intense diagenesis (Murray et al., 1991, MacRae et al., 1992). This hypothesis is confirmed by the strong negative correlation ($r^2 = -0.83$) between ΣREE and the Eu anomaly (fig. 59b). Also, Cr enrichment (568.00 ppm; average value) relatively to PAAS (110.00 ppm) and coating (124.00 ppm as mean) values is probably due to the remobilization of a part of Cr in oxic sediments during the diagenesis (Chiffoleau, 1994). The pyrite textures encountered (euhedral with cubic and rhomboidal crystals, and massive) are typically characteristic of early and late epigenetic stages (Querol et al., 1989).

6. CONCLUSIONS

The present study conducted on 64 samples of clayey and sandy materials from two sections (ES and DA) and 15 samples of pyrite (section ES) of the locality of Tondè (Douala sedimentary sub-basin), in order to constrain the paleoenvironmental and paleoclimatic conditions. Four (04) main conclusions are resulted:

1. The wide distribution of elements such as Th and Sc in the majority of clayey samples suggest an intermediate original source rock, probably the surrounding basement (gneiss and micaschist), from which the paleosols sequence would be derived. These paleosols overlies the Paleocene-Eocene sedimentary deposits (Nkapa Formation). Palynological data attribute a Pleistocene to Holocene age to these paleosoils sequences.
2. The high concentration in some trace elements (Ti and Zr) often associated with heavy minerals, as well as high CIA values in sandstones and siltstones suggests the recycling of a part of original material and intense weathering.
3. The mineralogical phase mainly consisting of kaolinite and quartz, with low proportions of goethite, reflecting intense alteration under a warm/humid equatorial climate, all deposited in a sub-recent to recent well-oxygenated environment as testify the palynological data.
4. Pyrite, however, formed by late secondary enrichment and precipitation predominately in clayey materials, implying alternating oxic and reducing conditions linked to water table fluctuations.

SUMMARY AND GENERAL CONCLUSIONS

The Earth's evolution over geological time has been punctuated by numerous crises that have affected both marine and continental environments. One no less important of these crises occurred during the Cretaceous-Paleogene transition (66.043 ± 0.011 Ma) and is therefore called KPB mass extinction (or KTB mass extinction). The evoked causes are the Chicxulub meteorite impact on the Yucatan Peninsula in Mexico, and more recently, the super Deccan Traps volcanism in India. On the other hand, Paleocene-Eocene thermal maximum (PETM) is also another crisis that occurred at the Paleocene-Eocene transition about 55.7–56.0 Ma ago, and whose potential causes are a massive carbon dioxide injection from multiple potential sources. The main manifestation of both crises is the rapid global warming that induces irreversible disasters on the marine and continental ecosystem. The importance of the KPB and PETM studies is due to the fact that they have similarities with the human-induced climate change taking place today. Therefore, accurate knowledge of what happened during these crises could help us to predict future climate change. The present work, based on a multiproxy approach, has been conducted on K/Pg sections at Gorgonilla (Colombia) and Zumaya (Spain) for KPB mass extinction studies as well as P/E sections and others for PETM signatures in Douala sub-basin (Cameroon).

The studied KPB mass extinction event, although taking place in the same time (~ 66 Ma) at Gorgonilla and Zumaya, is marked in both sites by proven dissimilarities, from the major cause responsible for triggering the event to its manifestations. At Gorgonilla, our results reveal that materials mainly consist of alternating calcareous mudstones and turbiditic litharenites. The first facies, deposited in bathyal environment between lysocline and CCD, contains a various microfossil species including abundant radiolarians, benthic and planktic foraminifera, a few nannofossil species and sponge spicules, while the second is composed by eroded basaltic lithics (and/or breccia) and a large amount of plagioclases probably resulted from the CLIP, reaching deep sea water via turbidity currents. The KPB is materialized by a 3 cm spherules-rich layer which triplicates in one edge of outcrop due to minor syn- and post-depositional faults, and shows an erosional surface at the base. Tektites are black to light yellow with various sizes ranging from 0.80 to 1.50 mm, normally size-graded and soaked in calcareous matrix containing lithic fragments. The large size tektites show a depletion in common cosmic elements and rather an enrichment in detrital ones (with a chemical composition very close to that of matrices), contrary to smaller tektites. This, combined to normal size-gradation of tektites as well as mixing Danian and Maastrichtian fossils in spherule-rich layers, suggests that a long and intense reworking of tektites preceded their deposition. Whole rock geochemistry of all lithological units reveals dysoxic to anoxic

environment, probably due to the large paleodepth which induces strong O_2-depletion. At the Zumaya Cretaceous-Paleogene transition, Late Maastrichtian are consisting by bioturbated red marlstones crossed by thin turbiditic beds whereas Danian materials is done by 40 cm thick of grey marls corresponding to the top of the P1a(1) zone, followed by light grey to pink Danian limestones. KTB is marked by a foraminiferal packstone layer of 3 cm thick which is differentiated in three levels (KTB-1, 2 and 3) and showing, on a large scale, net undulations at the top which set up following of brief sea-level fluctuations in a middle neritic to deeper environment. The KTB layer indicates a deposition in O_2-depleted water conditions, and an enrichment in cosmic inputs. It is preceded by a well oxygenated Late Maastrichtian environment constrained to a strong Hg injection from a distal volcanism which pursue until the lowermost Danian period whereas the calcareous Danian environment is oxic and quiet (no distal volcanism).

Five planktic biozones including CF3, CF2, CF1, P1a(2) and P1b, are highlighted along of Gorgonilla transect. Two hiatuses, the major KPB hiatus materialized by the erosional surface at the base of spherule-rich layer and the missing of top part of zone CF1, zone P0, zone P1a(1) and lower part of zone P1a(2), and another short hiatus above the KPB globally correlated by a sudden change in carbonate production rate, have been evidenced the combination of the biostratigraphy and stable isotope data. No Deccan volcanism (and/or another intense distal volcanism) and hydrothermalism influences have been detected at Gorgonilla. However, hydrothermal plume particles, probably from CLIP volcanic processes, would have impregnated Gorgonilla materials through fallout from the nearby hydrothermal fields. A weak thermal and a globally contrasted climate mark the Cretaceous-Paleogene transition at Gorgonilla, during which the cooler conditions are generally associated to a rising sea level while the more warm/humid conditions are indexed to falling sea level, especially at the KPB. Four planktic zones (CF1 for the Maastrichtian, and P1a(1), P1a(2) and P1b for Danian) are distinguished on Zumaya section. Besides minor hiatuses observed at the pre-KTB layer and P1a(2)/P1b transition, two significant hiatuses, resulting from a marine regression, have been recorded across the Zumaya K/T section: KTB hiatus implying missing of zone P0 and lower part of zone P1a(1), and P1a(1)/P1a(2) hiatus involving the missing of top P1a(1) zone. Interval including pre-KTB, KTB and P1a(1) sediments is marked by a high stressed environment linked to Deccan-2 phase during a contrasted warm/humid climate.

The PETM, which is an event taking place at the Paleocene-Eocene transition (~55,8 Ma), has been detected in fine grained sediments (shales for Bongue and clays for Dibamba)

of inner to middle shelf constituting a part of N'kapa Formation in the Cameroonian Douala sub-basin. Three main intervals including pre-PETM, PETM and post-PETM are identified.

- The pre-PETM interval corresponds to a gradual $\delta^{13}C_{org}$ decrease period (pre-CIE zone) prior the Paleocene-Eocene boundary (PEB), during which the encountered microfauna assemblage (benthic and planktic foraminifera and ostracods) represents the latest Paleocene P5 zone, just below the PETM. These microfossils are widely affected by the ocean acidification, as certified by gradual decrease in $CaCO_3$ content. This period is characterized by a distal volcanism activity coupled to decreasing productivity during a rising sea level leading up to PETM, under contrasted warm climate.
- During the PETM (zone E1), the severe ocean acidification induces a mass extinction where only few *I. broedermanni*, evolved species of *I. Tadjikistanensis*, are present and where CIE-minimum interval coincides to calcite minimum values. Also, *Trochamminids* and some *I. lodensis* and *A. esnaensis* species reappear at the end of this high stress environmental change period during which the high sediment deposition rate took place under dysoxic to anoxic conditions and subtropical to tropical climate during a slight falling sea level.
- The post-PETM, correlated interval with the CIE-recovery phase, is the place, at the early Eocene (biozones E1-E2), of intense erosion and chemical weathering associated with a considerable rise in productivity. The depositional environment, dysoxic to anoxic, is almost similar to that of PETM. However, there is a rise in sea level reaching the maximum flooding surface (MFS) at the top of related interval, as evidenced by sedimentological data.

The N’kapa Formation in Douala sedimentary sub-basin (Cameroon) appears to be the lateral equivalent of Oshosun Formation in Dahomey basin (Nigeria), that indicates a regional correlation of geology in the Gulf of Guinea.

For the Tonde area, these are mainly Pleistocene to Holocene paleosols, probably from surrounding basement (gneiss and micaschist) deposited in well-oxygenated environment under a warm/humid equatorial climate. However, included pyrite is formed by late secondary enrichment and precipitation predominately in clayey materials, under alternating oxic and reducing conditions linked to water table fluctuations.

Future challenges

The KTB mass extinction and PETM had a significant impact on the existing ecosystem. This impact is generally assessed following two axes: climate change and fossil fuels.

(a) From a climatic point of view, the understanding of such rapid global warming processes would be an asset for the prediction of future climate change with local and even global trends. It would therefore be a good idea to intensify and deepen research on this type of event throughout Cameroon and even the Central Africa sub-region by adding to a fine biostratigraphy, based on palynology.

(b) The massive extinction of fauna and flora species caused by the rapid increase in temperature and observed in the marine and continental environment implies, when conditions permit, a strong accumulation and preservation of organic matter. Detailed study of these events also may reveal potential hydrocarbon rocks and/or coal, with the economic repercussions that may result.

REFERENCES

Abdullayev, E. and Leroy, S., 2016, Provenance of clay minerals in the sediments from the Pliocene Productive Series, western South Caspian Basin. Marine and Petroleum Geology, 73, 517–527.

Acharya, S., Panigrahi, M., Gupta, A. and Tripathy, S., 2015, Response of trace metal redox proxies in continental shelf environment: the eastern Arabian Sea scenario. *Continental Shelf Research*, 106, 70–84.

Açıkalın, S., Ocakoğlu, F., Yılmaz, İ., Vonhof, H., Hakyemez, A. and Smit, J. (2016). Stable isotopes and geochemistry of a Campanian–Maastrichtian pelagic succession, Mudurnu–Göynük Basin, NW Turkey: Implications for palaeoceanography, palaeoclimate and sea-level fluctuations. *Palaeogeography, Palaeoclimatology, Palaeoecology*, 441, pp.453-466.

Adatte T., Bolle M.P., de Kaenel E., Gawenda P., Winkler W. & Von Salis K. (2000) Climatic evolution from Paleocene to earliest Eocene inferred from clay mineral: a transect from northern Spain (Zumaia) to southern (Spain, Tunisia) and southeastern Tethys margins (Israel, Negev). *Geologiska Förenings i Stockholm Förhandlingar*, 112, pp. 7-8.

Adatte, T., Keller, G. and Stinnesbeck, W. (2002). Late Cretaceous to early Paleocene climate and sea-level fluctuations: the Tunisian record. *Palaeogeography, Palaeoclimatology, Palaeoecology*, 178(3-4), pp.165-196.

Adatte, T., Keller, G., and Baum, R. (2011). Age and origins of the Chicxulub impact and sandstone complex, Brazos River, Texas: Evidence from lithostratigraphy and sedimentology, in Keller, G., and Adatte, T., eds., The End-Cretaceous Mass Extinction and the Chicxulub Impact in Texas: Society for Sedimentary Geology (SEPM) Special Publication 100, p. 43–80.

Adatte, T., Keller, G., Stüben, D., Harting, M., Kramar, U., Stinnesbeck, W., Abramovich, S. and Benjamini, C. (2005). Late Maastrichtian and K/T paleoenvironment of the eastern Tethys (Israel): mineralogy, trace and platinum group elements, biostratigraphy and faunal turnovers. *Bulletin de la Société Géologique de France*, 176(1), pp.37-55.

Adatte, T., Stinnesbeck, W. and Keller, G. (1996). Lithostratigraphic and mineralogic correlations of near K/T boundary clastic sediments in northeastern Mexico: implications for origin and nature of deposition. In Ryder, G., Fastovsky, D.E. and Gartner, S. (eds), The Cretaceous-Tertiary Event and Other Catastrophes in Earth History. Geological Society of America, Boulder, p. 211–226.

Agnini, C., Fornaciari, E., Rio, D., Tateo, F., Backman, J. and Giusberti, L. (2007). Responses of calcareous nannofossil assemblages, mineralogy and geochemistry to the environmental perturbations across the Paleocene/Eocene boundary in the Venetian Pre-Alps. *Marine Micropaleontology*, 63(1-2), pp.19-38.

Alegret, L. and Ortiz, S. (2006). Global extinction event in benthic foraminifera across the Paleocene/Eocene boundary at the Dababiya Stratotype section. *Micropaleontology*, 52(5), pp.433-447.

Alegret, L., Molina, E. and Thomas, E. (2001). Benthic foraminifera at the Cretaceous-Tertiary boundary around the Gulf of Mexico. *Geology*, 29(10), p.891.

Alegret, L., Ortiz, S. and Molina, E. (2009b). Extinction and recovery of benthic foraminifera across the Paleocene–Eocene Thermal Maximum at the Alamedilla section (Southern Spain). *Palaeogeography. Palaeoclimatology. Palaeoecology*. 279, 186–200.

Alegret, L., Ortiz, S., Arenillas, I. and Molina, E. (2005). Palaeoenvironmental turnover across the Palaeocene/Eocene boundary at the Stratotype section in Dababiya (Egypt) based on benthic foraminifera. *Terra Nova*, 17(6), pp.526-536.

Alegret, L., Ortiz, S., Orue-Etxebarria, X., Bernaola, G., Baceta, J.I., Monechi, S., Apellániz, E. and Pujalte, V. (2009a). The Paleocene–Eocene Thermal Maximum: new data on microfossil turnover at the Zumaia section, Spain. Palaios 24, 318–328.

Alegret, L., Reolid, M. and Vega Pérez, M. (2018). Environmental instability during the latest Paleocene at Zumaia (Basque-Cantabric Basin): The bellwether of the Paleocene-Eocene Thermal Maximum. *Palaeogeography, Palaeoclimatology, Palaeoecology*, 497, pp.186-200.

Algeo, T. and Maynard, J. (2004). Trace-element behavior and redox facies in core shales of Upper Pennsylvanian Kansas-type cyclothems. *Chemical Geology*, 206(3-4), pp.289-318.

Alvarez, L., Alvarez, W., Asaro, F. and Michel, H. (1980). Extraterrestrial Cause for the Cretaceous-Tertiary Extinction. *Science*, 208(4448), pp.1095-1108.

Alvarez, L.W., Alvarez, W., Asaro, F., and Michel, H.V., 1980. Extraterrestrial cause for the Cretaceous-Tertiary extinction. *Science*, 208, pp. 1095–1108.

Alvarez, W., Smit, J., Lowrie, W., Asaro, F., Margolis, S.V., Claeys, P., Kaster, M. and Hildebrand A.R. (1992). Proximal impact deposits at the Cretaceous-Tertiary boundary in the Gulf of Mexico: A restudy of DSDP Leg 77 Sites 536 and 540. *Geology*, 20, pp.697-700.

Anaya-Gregorio, A., Armstrong-Altrin, J., Machain-Castillo, M., Montiel-García, P. and Ramos-Vázquez, M., 2018, Textural and geochemical characteristics of late Pleistocene to Holocene fine-grained deep-sea sediment cores (GM6 and GM7), recovered from southwestern Gulf of Mexico. *Journal of Palaeogeography*, 7, pp.1–19.

Anders, E. and Grevesse, N. (1989). Abundances of the elements: meteoritic and solar. *Geochimica et Cosmochimica Acta*, 53, pp.197–214.

Anderson, T.F. and Arthur, M.A. (1983). Stable isotopes of oxygen and carbon and their application to sedimentologic and paleoenvironmental problems. In: Arthur, M.A., Anderson, T.F., Kaplan, I.R., Veizer, J., Land, L.S. (Eds.), Stable Isotopes in Sedimentary Geology. SEPM Short Course, 10. SEPM, Tulsa, pp. 111-151

Archibald, J., Clemens, W., Padian, K., Rowe, T., Macleod, N., Barrett, P., Gale, A., Holroyd, P., Sues, H., Arens, N., Horner, J., Wilson, G., Goodwin, M., Brochu, C., Lofgren, D., Hurlbert, S., Hartman, J., Eberth, D., Wignall, P., Currie, P., Weil, A., Prasad, G., Dingus, L., Courtillot, V.,

Milner, A., Milner, A., Bajpai, S., Ward, D. and Sahni, A. (2010). Cretaceous Extinctions: Multiple Causes. *Science*, 328(5981), pp.973-973.

Arenillas, I., Molina, E. and Schmitz, B. (1999). Planktic foraminiferal and $\delta^{13}C$ isotopic changes across the Paleocene/Eocene boundary at Possagno (Italy). *International Journal of Earth Sciences*, 88(2), pp.352-364.

Arens, N.C., Thompson, A. and Jahren, A.H. (2014). A Preliminary Test of the Press-Pulse Extinction Hypothesis: Palynological Indicators of Vegetation Change Preceding the Cretaceous-Paleogene Boundary. *Geological Society of America Special Pape*r, pp. 209–227.

Arens, N.C., West, I.D., 2008. Press-pulse: a general theory of mass extinction? *Paleobiology* 34(4), pp.456–471.

Armstrong-Altrin, J., Botello, A., Villanueva, S. and Soto, L. (2019). Geochemistry of surface sediments from the northwestern Gulf of Mexico: implications for provenance and heavy metal contamination. *Geological Quarterly*, 63, 522–538.

Armstrong-Altrin, J., Lee, Y., Verma, S. and Ramasamy, S. (2004). Geochemistry of sandstones from the upper Miocene Kudankulam Formation, southern India: implications for provenance, weathering, and tectonic setting. *Journal of Sedimentary Research*, 74, 285–297.

Armstrong-Altrin, J., Machain-Castillo, M., Rosales-Hoz, L., Carranza-Edwards, A., Sanchez-Cabeza, J. and Ruíz-Fernández, A. (2015). Provenance and depositional history of continental slope sediments in the Southwestern Gulf of Mexico unraveled by geochemical analysis. *Continental Shelf Research*, 95, 15–26.

Armstrong-Altrin, J., Ramos-Vázquez, M., Zavala-León, A. and Montiel-García, P. (2018). Provenance discrimination between Atasta and Alvarado beach sands, western Gulf of Mexico, Mexico: Constraints from detrital zircon chemistry and U-Pb geochronology. *Geological Journal*, 53, 2824–2848.

Arreguín-Rodríguez, G.J., Alegret, L., Thomas, E. (2016). Late Paleocene-middle Eocene benthic foraminifera on a Pacific seamount (Allison Guyot, ODP Site 865): greenhouse climate and superimposed hyperthermal events. *Paleoceanography* 31, 346–364.

Aubry, M., Lucas, S. and Berggren, W. (1998). *Late Paleocene-early Eocene climatic and biotic events in the marine and terrestrial records*. New York: Columbia University Press.

Aze, T., Pearson, P., Dickson, A., Badger, M., Bown, P., Pancost, R., Gibbs, S., Huber, B., Leng, M., Coe, A., Cohen, A. and Foster, G. (2014). Extreme warming of tropical waters during the Paleocene–Eocene Thermal Maximum. *Geology*, 42(9), pp.739-742.

Baceta, J. and Pujalte, V. (2016). Lithostratigraphy of the K/Pg boundary interval. In: V. Pujalte, X. Orue-Etxebarria, F. Caballero, E. Apellaniz and A. Hilario, ed., *The upper Maastrichtian, Paleocene and lowermost Ypresian of the Zumaia section (Basque Basin, Western Pyrenees)*, 2nd ed. Donostia-San Sebastian: Diputación Foral de Gipuzkoa - Gipuzkoako Foru Aldundia, pp.38-40.

Baceta, J. I., Pujalte, V., Serra-Kiel, J., Robador, A. and Orue-Etxebarria, X. (2004). El Maastrichtiense final, Paleoceno e Ilerdiense inferior de la Cordillera Pirenaica. In: J.A. Vera (Ed.), Geología de España. Sociedad Geológica de España-Instituto Geológico y Minero de España, Madrid, 308-313.

Baceta, J.I. (1996). El Maastrichtiense superior, Paleoceno e Ilerdiense inferior de la Región Vasco-Cantábrica: Secuencias Deposicionales, Facies y Evolución Paleogeográfica. Tesis Doctoral Univ. País Vasco, 372 p.

Baceta, J.I., Pujalte, V., Bernaola, G., Orue-Etxebarria, X. and Apellaniz, A. (2016). The Zumaia section. In: Pujalte, V, Orue-Etxebarria, X., Apellaniz, E., Caballero, F. and Hilario, A. (eds.), 20–24.

Bains, S., Norris, R., Corfield, R. and Faul, K. (2000). Termination of global warmth at the Palaeocene/Eocene boundary through productivity feedback. *Nature*, 407(6801), pp.171-174.

Barreda, V., Guler, V. and Palazzesi, L. (2008). Late Miocene continental and carine palynological assemblages from Patagonia. *Developments in Quaternary Sciences*, 11, 343–350.

Barrera, E. and Keller, G. (1990). Stable isotope evidence for gradual environmental changes and species survivorship across the Cretaceous/Tertiary Boundary. *Paleoceanography*, 5(6), pp.867-890.

Bassiouni, M. A. A.; Luger, P. (1990). Maastrichtian to Early Eocene Ostracoda from southern Egypt. Palaeontology, palaeoecology, palaeobiogeography and biostratigraphy. *Berliner Geowissenschaftliche Abhandlungen Reihe A Geologie und Palaeontologie*. 120 (2): 755-928.

Bassiouni, M.A.A., Morsi, A.M. (2000). Paleocene–Lower Eocene ostracodes from El Quss Abu Said Plateau (Farafra Oasis), Western Desert, Egypt. *Palaeontographica A* 257, 27–84.

Behar, F., Beaumont, V. and De B. Penteado, H. (2001). Rock-Eval 6 Technology: Performances and Developments. *Oil & Gas Science and Technology*, 56(2), pp.111-134.

Benson, R.H. (1977). Evolution of Oblitacythereis from Paleocosta (Ostracoda: Trachyleberididae) during the Cenozoic in the Mediterranean and Atlantic. *Smithsonian Contributions to Paleobiology* 33, 1–47.

Berggren, W. A., Ouda, Kh. (2003). Upper Paleocene-Lower Eocene planktonic foraminifera biostratigraphy of the Qreiya (Gebel Abu Had) section, Upper Nile Valley (Egypt). In: Ouda Kh., Aubry M-P. (Eds.), The Upper Paleocene-Lower Eocene of the Upper Nile Valley: Part 1: Stratigraphy. *Micropaleontology*, 49, supplement 1: 105-122.

Bermúdez, H., García, J., Stinnesbeck, W., Keller, G., Rodríguez, J., Hanel, M., Hopp, J., Schwarz, W., Trieloff, M., Bolívar, L. and Vega, F. (2016). The Cretaceous-Palaeogene boundary at Gorgonilla Island, Colombia, South America. *Terra Nova*, 28(1), pp.83-90.

Bermúdez, H.D., Arenillas, I., Arz, J.A., Vajda, V., Renne, P.R., Gilabert, V. and Rodríguez, J.V. (2019). The Cretaceous/Paleogene boundary deposits on Gorgonilla Island. In: Gómez, J. &

Mateus–Zabala, D. (Eds), The Geology of Colombia, Volume 3 Paleogene – Neogene. Servicio Geológico Colombiano, Publicaciones Geológicas Especiales, 37, 19p.

Bernaola, G., Martín-Rubio, M. and Baceta, J.I. (2009). New high resolution calcareous nannofossil analysis across the Danian/Selandian transition at the Zumaia section: comparison with South Tethys and Danish sections. *Geologica Acta* 7, 79–92.

Berner, R., 1984, Sedimentary pyrite formation: an update. *Geochimica et Cosmochimica* Acta, 48, 605–615.

Berner, R., 2006. GEOCARBSULF: A combined model for Phanerozoic atmospheric O2 and CO2. *Geochimica et Cosmochimica Acta*, 70(23), pp.5653-5664.

Bertolino, S., Zimmermann, U. and Sattler, F. (2007) Mineralogy and geochemistry of bottom sediments from water reservoirs in the vicinity of Córdoba, Argentina: environmental and health constraints. *Applied Clay Science*, 36, 206–220.

Bio-Lokoto, A., Carbonnel, G., De Klasz, I., De Klasz, S., Lang, J., Salard-Cheboldaeff, M. (1998). Données nouvelles biochronologiques et paléoécologiques sur le bassin sédimentaire côtier du bénin entre le Crétacé supérieur et l'Eocène basal (Afrique de l'ouest), 41(1), pp. 29-57

Bolle, M., Pardo, A., Hinrichs, K., Adatte, T., Von Salis, K., Burns, S., Keller, G. and Muzylev, N. (2000). The Paleocene-Eocene transition in the marginal northeastern Tethys (Kazakhstan and Uzbekistan). *International Journal of Earth Sciences*, 89(2), pp.390-414.

Bond, D. and Grasby, S. (2017). On the causes of mass extinctions. *Palaeogeography, Palaeoclimatology, Palaeoecology*, 478, pp.3-29.

Bond, D. and Wignall, P. (2014). Large igneous provinces and mass extinctions: An update. In: Keller, G., Kerr, A.C. (Eds.), *Volcanism, Impacts, and Mass Extinctions: Causes and Effects*. The Geological Society of America

Bond, D.P.G., Grasby, S.E. (2017). On the causes of mass extinctions. *Palaeogeography, Palaeoclimatology, Palaeoecology*, 478, pp. 3–29.

Boström, K., Kraemer, T. and Gartner, S. (1973). Provenance and accumulation rates of opaline silica, Al, Ti, Fe, Mn, Cu, Ni and Co in Pacific pelagic sediments. *Chemical Geology*, 11(2), pp.123-148.

Botsou, F., Godelitsas, A., Kaberi, H., Mertzimekis, T., Goettlicher, J., Steininger, R. and Scoullos, M. (2015). Distribution and partitioning of major and trace elements in pyrite-bearing sediments of a Mediterranean coastal lagoon. *Geochemistry*, 75, 219–236.

Bowen, G. J., Koch, P., Gingerich, P.D., Norris, R. C., Bains, S. and Corfield, R. M. (2001). Refined isotope stratigraphy across the continental Paleocene-Eocene boundary on Polecat Bench in the northern Bighorn Basin. In: Gingerich, P. R. (Ed.), Paleocene-Eocene Stratigraphy and Biotic Change in the Bighorn and Clarks Fork Basins, Wyoming. University of Michigan Papers on Paleontology, 33: 73–88.

Bowen, G., Maibauer, B., Kraus, M., Röhl, U., Westerhold, T., Steimke, A., Gingerich, P., Wing, S. and Clyde, W. (2015). Two massive, rapid releases of carbon during the onset of the Palaeocene–Eocene thermal maximum. *Nature Geoscience*, 8(1), pp.44-47

Bowen, G.J., 2013. Up in smoke: a role for organic carbon feedbacks in Paleogene hyperthermals. *Global and Planetary Change* 109, pp.18–29.

Bowen, G.J., Beerling, D.J., Koch, P.L., Zachos, J.C., Quattlebaum, T. (2004). A humid climate state during the Palaeocene/Eocene Thermal Maximum. *Nature* 432, pp.495–499.

Bown, P. and Pearson, P. (2009). Calcareous plankton evolution and the Paleocene/Eocene thermal maximum event: New evidence from Tanzania. *Marine Micropaleontology*, 71(1-2), pp.60-70.

Bralower, T., Kelly, D., Gibbs, S., Farley, K., Eccles, L., Lindemann, T. and Smith, G. (2014). Impact of dissolution on the sedimentary record of the Paleocene–Eocene thermal maximum. *Earth and Planetary Science Letters*, 401, pp.70-82.

Bralower, T., Thomas, D., Zachos, J., Hirschmann, M., Röhl, U., Sigurdsson, H., Thomas, E. and Whitney, D. (1997). High-resolution records of the late Paleocene thermal maximum and circum-Caribbean volcanism: Is there a causal link? *Geology*, 25(11), p.963.

Bralower, T., Zachos, J., Thomas, E., Parrow, M., Paull, C., Kelly, D., Silva, I., Sliter, W. and Lohmann, K. (1995). Late Paleocene to Eocene paleoceanography of the equatorial Pacific Ocean: Stable isotopes recorded at Ocean Drilling Program Site 865, Allison Guyot. *Paleoceanography*, 10(4), pp.841-865.

Bralower, T.J. (2002). Evidence of surface water oligotrophy during the Paleocene-Eocene thermal maximum: Nannofossil assemblage data from Ocean Drilling Program Site 690, Maud Rise, Weddell Sea. *Paleoceanography*, 17(2), pp.

Braun, J., Pagel, M., Herbilln, A. and Rosin, C., 1993, Mobilization and redistribution of REEs and thorium in a syenitic lateritic profile: a mass balance study. *Geochimica et Cosmochimica Acta*, 57, 4419–4434.

Bristow, T., Kennedy, M., Derkowski, A., Droser, M., Jiang, G. and Creaser, R. (2009). Mineralogical constraints on the paleoenvironments of the Ediacaran Doushantuo Formation. *Proceedings of the National Academy of Sciences*, 106(32), pp.13190-13195.

Brumsack, H.-J. (1980). Geochemistry of black shales from the Atlantic Ocean (DSDP Legs 11, 14, 36 and 41). *Chemical Geology* 31, 1–25.

Brumsack, H.-J. (1989). Geochemistry of recent TOC-rich sediments from the Gulf of California and the Black Sea. *Geologische Rundschau*. 78, 851–882.

Brumsack, H.J. (2006). The trace metal content of recent organic carbon-rich sediments: implications for Cretaceous black shale formation. *Palaeogeography, Palaeoclimatology, Palaeoecology*, 232, 344–361.

Budakoglu, M., Abdelnasser, A., Karaman, M. and Kumral, M. (2015). The rare earth element geochemistry on surface sediments, shallow cores and lithological units of Lake Acıgöl basin, Denizli, Turkey. *Journal of Asian Earth Sciences*, 111, 632–662.

Buffetaut E. (2004). Polar dinosaurs and the question of dinosaur extinction: A brief review. *Palaeogeography, Palaeoclimatology, Palaeoecology*, 214, pp.225–231

Bukalo, N., Ekosse, G., Odiyo, J. and Ogola, J. (2019). Paleoclimatic implications of hydrogen and oxygen isotopic compositions of Cretaceous–Tertiary kaolins in the Douala Sub-Basin, Cameroon. *Comptes Rendus Geoscience*, 351, 17–26.

Calvert, S.E. and Pedersen, T.F. (1993). Geochemistry of recent oxic and anoxic marine sediments: implications for the geological record. *Marine Geology* 113, 67–88.

Canudo, J., Keller, G. and Molina, E. (1991). Cretaceous/Tertiary boundary extinction pattern and faunal turnover at Agost and Caravaca, S.E. Spain. *Marine Micropaleontology*, 17(3-4), pp.319-341.

Canudo, J.I., Keller, G., Molina, E., Ortiz, N. (1995). Planktic foraminiferal turnover and $\delta^{13}C$ isotopes across the Paleocene–Eocene transition at Caravaca and Zumaya, Spain. *Palaeogeography, Palaeoclimatology, Palaeoecology* 114, 75–100.

Carmichael, M.J., Inglis, G.N., Badger, M.P.S., Naafs, B.D.A., Behrooz, L., Remmelzwaal, S., Monteiro, F.M., Rohrssen, M., Farnsworth, A., Buss, H.L., Dickson, A.J., Valdes, P.J., Lunt, D.J. and Pancost, R.D. (2017). Hydrological and associated biogeochemical consequences of rapid global warming during the Paleocene-Eocene Thermal Maximum. *Global and Planetary Change*, 157, 114–138.

Cave, R., German, C., Thomson, J. and Nesbitt, R. (2002). Fluxes to sediments underlying the Rainbow hydrothermal plume at 36°14′N on the Mid-Atlantic Ridge. *Geochimica et Cosmochimica Acta*, 66(11), pp.1905-1923.

Chamley H. (1998). Clay mineral sedimentation in the Ocean. pp. 269-302 in: Soils and Sediments (Mineralogy and Geochemistry) (H. Paquet & N. Clauer, editors). Springer-Verlag, Berlin.

Chamley, H., 1989. Clay Sedimentology. Springer-Verlag, Berlin. 623p.

Charbonnier, G., Duchamp-Alphonse, S., Deconinck, J., Adatte, T., Spangenberg, J., Colin, C. and Föllmi, K. (2020). A global palaeoclimatic reconstruction for the Valanginian based on clay mineralogical and geochemical data. *Earth-Science Reviews*, 202, p.103092.

Charbonnier, G., Morales, C., Duchamp-Alphonse, S., Westermann, S., Adatte, T., Föllmi, K.B. (2017). Mercury enrichment indicates volcanic triggering of Valanginian environmental change. *Scientific Report* 7, 40808.

Charles, A., Condon, D., Harding, I., Pälike, H., Marshall, J., Cui, Y., Kump, L. and Croudace, I. (2011). Constraints on the numerical age of the Paleocene-Eocene boundary. *Geochemistry, Geophysics, Geosystems*, 12(6).

Chiffoleau J-F., 1994, Le chrome en milieu marin. Repères Océan n°8, Rapports Scientifiques et Techniques de l'IFREMER, Plouzané, 43 p.

Chukwura, E., Onuigbo, E.N., Okoro, A.U., Okafor, P.N., and Okolo, C.M. (2017). Palynological evaluation of the Imo Formation at Isiagu, Niger Delta basin, Nigeria: age and paleoenvironmental significance. *Journal of Basic Physical Research*, 7(2), pp.6-16.

Cohen, A. S., A. L. Coe, and D. B. Kemp (2007), The Late Palaeocene–Early Eocene and Toarcian (Early Jurassic) carbon isotope excursions: A comparison of their time scales, associated environmental changes, causes and consequences, *Journal of Geological Society*, 164, pp.1093–1108

Cojan, I., Moreau, M.-G. and Stott, L. E. (2000). Stable carbon isotope stratigraphy of the Paleogene pedogenic series of southern France as a basis for continental-marine correlation. *Geology*, 28 (3): 259–262.

Condie, K. and Wronkiewicz, D. (1990). The Cr/Th ratio in Precambrian pelites from the Kaapvaal Craton as an index of craton evolution. *Earth and Planetary Science Letters*, 97, 256–267.

Condie, K., Dengate, J. and Cullers, R. (1995). Behavior of rare earth elements in a paleoweathering profile on granodiorite in the Front Range, Colorado, USA. *Geochimica et Cosmochimica Acta*, 59, 279–294.

Corfield, R. M., Cartlidge, J. E., Premoli-Silva I. and Housley, R. A. (1991). Oxygen and carbon isotope stratigraphy of the Palaeogene and Cretaceous limestones in the Bottaccione Gorge and the Contessa Highway sections, Umbria, Italy. *Terra Nova*, 3: 414–422.

Courtillot, V. (1999). Evolutionary catastrophes: The Science of Mass Extinctions. Cambridge University Press, Cambridge, 171p

Courtillot, V. and Fluteau, F. (2014). A review of the embedded time scales of flood basalt volcanism with special emphasis on dramatically short magnetic pulses. In Keller G. and Kerr A. (Eds), Volcanism, Impacts, and Mass Extinctions: Causes and effects. Geological Society of America Special paper 505.

Courtillot, V., and Fluteau, F. (2010). Cretaceous extinctions: The volcanic hypothesis. *Science*, 328, pp.973–974

Courtillot, V., Fluteau, F. and Besse, J. (2015). Evidence for volcanism triggering extinctions: a short history of IPGP contributions with emphasis on paleomagnetism. In: Schmidt, Anja, Fristad, Kirsten E., Elkins Tanton, Linda T. (Eds.), Volcanism and Global Environmental Change. Vol 2015 Cambridge University Press.

Cowie, J., Ziegler, W. and Remane, J. (1989). Stratigraphic Commission Accelerates Progress, 1984 to 1989. *Episodes*, 12(2), pp.79-82.

Cox, R., Lowe, D. and Cullers, R., 1995, The influence of sediment recycling and basement composition on evolution of mudrock chemistry in the southwestern United States. *Geochimica et Cosmochimica Acta*, 59, 2919–2940.

Cramer, B., Aubry, M.-P., Miller, K. G., Olsson, R. K., Wright, J. D. and Kent, D. V. (1999). An exceptional chronologic, isotopic, and clay mineralogic record of the latest Paleocene thermal maximum, Bass River, NJ, ODP 174AX. *Bulletin de la Société géologique de France*, 170: 883–897.

Cramer, B.S. and Kent, D.V. (2005). Bolide summer: The Paleocene/Eocene thermal maximum as a response to an extraterrestrial trigger, *Palaeogeography, Palaeoclimatology, Palaeoecology* 224 (1–3), 144–166.

Crouch, E.M., Brinkhuis, H., Visscher, H., Adatte, T. and Bolle, M.-P. (2003). Late Paleocene– early Eocene dinoflagellate cyst records from the Tethys: Further observations on the global distribution of Apectodinium. *Special Paper of the Geological Society of America* 369, 113–132.

Crouch, E.M., Heilmann-Clausen, C., Brinkhuis, H., Morgans, H.E.G., Rogers, K.M., Egger, H. and Schmitz, B. (2001). Global dinoflagellate event associated with the late Paleocene thermal maximum. *Geology* 29, 315–318.

Cui, Y., Kump, L.R., Ridgewell, A.J., Charles, A.J., Junium, C.K., Diefendorf, A.F., Freeman, K.H., Urban, N.M. and Harding, I.C. (2011). Slow release of fossil carbon during the Palaeocene–Eocene Thermal Maximum. *Nature Geoscience*, 4, pp.481–485

Cullers, R. (1988). Mineralogical and chemical changes of soil and stream sediment formed by intense weathering of the Danburg granite, Georgia, U.S.A. *Lithos*, 21, 301–314.

Cullers, R. (1994). The controls on the major and trace element variation of shales, siltstones, and sandstones of Pennsylvanian-Permian age from uplifted continental blocks in Colorado to platform sediment in Kansas, USA. *Geochimica et Cosmochimica Acta*, 58, 4955–4972.

Cullers, R. (2000). The geochemistry of shales, siltstones and sandstones of Pennsylvanian–Permian age, Colorado, USA: implications for provenance and metamorphic studies. *Lithos*, 51, 181–203.

Curtis, C. (1990). Aspects of climatic influence on the clay mineralogy and geochemistry of soils, palaeosols and clastic sedimentary rocks. *Journal of the Geological Society*, 147, 351–357.

Dabard, M. and Loi, A. (2012). Environmental control on concretion-forming processes: Examples from Paleozoic terrigenous sediments of the North Gondwana margin, Armorican Massif (Middle Ordovician and Middle Devonian) and SW Sardinia (Late Ordovician). *Sedimentary Geology*, 267-268, 93–103.

Dameron, S., Leckie, R., Clark, K., MacLeod, K., Thomas, D. and Lees, J., 2017. Extinction, dissolution, and possible ocean acidification prior to the Cretaceous/Paleogene (K/Pg) boundary in the tropical Pacific. *Palaeogeography, Palaeoclimatology, Palaeoecology*, 485, pp.433-454.

Deconinck, 1984. Sédimentation et diagenèse des minéraux argileux du Jurassique supérieur-Crétacé dans le Jura méridional et le domaine subalpin (France, Sud-Est). Comparaison avec le domaine Atlantique Nord. Doctorat 3^{e} cycle, Université des Sciences et Technologie de Lille, 150p.

Deconinck, J.F. and Debrabant, P., 1985. Diagenèse des argiles dans le domaine subalpin : rôles respectifs de la lithologie, de l'enfouissement et de la surcharge tectonique, *Revue de géologie dynamique et de géographie physique*, 26(5), pp.321-330.

DeConto, R.M., Galeotti, S., Pagani, M., Tracy, D., Schaefer, K., Zhang, T., Pollard, D., Beerling, D.J., 2012. Past extreme warming events linked to massive carbon re-lease from thawing permafrost. *Nature*, 484, pp.87–91

Dessert, C., Dupré, B., Gaillardet, J., François, L. and Allègre, C., 2003. Basalt weathering laws and the impact of basalt weathering on the global carbon cycle. *Chemical Geology*, 202(3-4), pp.257-273.

Dias, Á. and Barriga, F., 2006. Mineralogy and geochemistry of hydrothermal sediments from the serpentinite-hosted Saldanha hydrothermal field (36°34′N; 33°26′W) at MAR. *Marine Geology*, 225(1-4), pp.157-175.

Dickens, G., 2011, Down the Rabbit Hole: toward appropriate discussion of methane release from gas hydrate systems during the Paleocene-Eocene thermal maximum and other past hyperthermal events. *Climate of the Past*, 7, pp.831–846.

Dickens, G., O'Neil, J., Rea, D. and Owen, R., 1995. Dissociation of oceanic methane hydrate as a cause of the carbon isotope excursion at the end of the Paleocene. *Paleoceanography*, 10(6), pp.965-971.

Dickens, G.R., 2000. Methane oxidation during the late Palaeocene thermal maximum. *Bulletin de la Société géologique de France* 171 (1), 37–49.

Dickens, G.R., Castillo, M.M., Walker, J.C.G., 1997. A blast of gas in the latest Paleocene: Simulating first-order effects of massive dissociation of oceanic methane hydrate. *Geology* 25 (3), 259–262.

Dickson, A., Cohen, A., Coe, A., Davies, M., Shcherbinina, E. and Gavrilov, Y. (2015). Evidence for weathering and volcanism during the PETM from Arctic Ocean and Peri-Tethys osmium isotope records. *Palaeogeography, Palaeoclimatology, Palaeoecology*, 438, pp.300-307.

Dinares-Turell, J., Baceta, J.I., Pujalte, V., Orue-Etxebarria, X., Bernaola, G. and Lorito, S., 2003. Untangling the Palaeocene climatic rhythm: an astronomically calibrated Early Palaeocene magnetostratigraphy and biostratigraphy at Zumaia (Basque basin, northern Spain). *Earth Planetary Science Letters* 216, 483-500.

Ding, H., Yao, S. and Chen, J., 2014, Authigenic pyrite formation and re-oxidation as an indicator of an unsteady-state redox sedimentary environment: Evidence from the intertidal mangrove sediments of Hainan Island, China. *Continental Shelf Research*, 78, 85–99.

Duchamp-Alphonse, S., Fiet, N., Adatte, T. and Pagel, M. (2011). Climate and sea-level variations along the northwestern Tethyan margin during the Valanginian C-isotope excursion: Mineralogical evidence from the Vocontian Basin (SE France). *Palaeogeography, Palaeoclimatology, Palaeoecology*, 302(3-4), pp.243-254.

Dupuis, C., Steurbaut, E. and Matmati, M.F., 1998. The Ain Settara K/T boundary section. Main results and comparison with the El Kef stratotype. In Abstracts, International Workshop on Cretaceous-Tertiary Transition, Tunis, May 1998, Geol. Surv. Tunisia, Tunis, pp. 67-68.

Dupuis, D., Aubry, M-P., Steurbaut, E., Berggren, W. A., Ouda, Kh., Magioncalda, C., Cramer, B. S., Kent, D. V., Speijer, R. P., Heilmann-Clausen, C., 2003. The Dababiya Quarry Section: Lithostratigraphy, clay mineralogy, geochemistry and paleontology. In: Ouda Kh., Aubry M-P. (Eds.), The Upper Paleocene-Lower Eocene of the Upper Nile Valley: Part 1: Stratigraphy. *Micropaleontology*,49, supplement 1: 41-59.

Dypvik, H., Riber, L., Burca, F., Rüther, D., Jargvoll, D., Nagy, J. and Jochmann, M. (2011). The Paleocene–Eocene thermal maximum (PETM) in Svalbard — clay mineral and geochemical signals. *Palaeogeography, Palaeoclimatology, Palaeoecology*, 302(3-4), pp.156-169.

Eldholm, O. and Thomas, E. (1993). Environmental impact of volcanic margin formation. *Earth and Planetary Science Letters*, 117(3-4), pp.319-329.

El-Kammar, A.M., Darwish, M., Philip, G., El-Kammar, M.M., 1990. Composition and origin of black shales from Quseir Area, Red Sea, Egypt. *Journal of the University of Kuwait-Science* 17, 177–1989.

Erba, E., 2004. Calcareous nannofossils and Mesozoic oceanic anoxic events. *Marine Micropaleontology*, 52(1-4), pp.85-106.

Ernst, 2014. Large Igneous Provinces. Cambridge University Press, 635p.

Ernst, R. and Youbi, N., 2017. How Large Igneous Provinces affect global climate, sometimes cause mass extinctions, and represent natural markers in the geological record. *Palaeogeography, Palaeoclimatology, Palaeoecology*, 478, pp.30-52.

Ernst, S.R., Guasti, E., Dupuis, C., Speijer, R.P., 2006. Environmental perturbation in the southern Tethys across the Paleocene/Eocene boundary (Dababiya, Egypt): Foraminiferal and clay mineral records. *Marine Micropaleontology*, 60, pp. 89–111.

Estrada, J.J., and MacDonald, W.D., 1994. Andean accretionary Cretaceous terranes: Paleomagnetic evidence supporting large latitudinal displacement component at Gorgona Island, Colombia: Eos (Washington, D.C.), v. 75, p. 127.

Fagel, N., 2007, Clay minerals, deep circulation and climate. In: Hillaire–Marcel, C. and De Vernal, A. (eds.), Proxies in Late Cenozoic Paleoceanography, 1st ed. Developments in Marine Geology, p. 139–184.

Fantasia, A., Föllmi, K.B., Adatte, T., Bernárdez, E., Spangenberg, J.E., Mattioli, E. (2018). The Toarcian Oceanic Anoxic Event in southwestern Gondwana: An example from the Andean Basin, northern Chile. *Journal of the Geological Society*, 175, pp.883-902.

Fantasia, A., Föllmi, K.B., Adatte, T., Spangenberg, J.E., Montero-Serrano, J.-C. (2018). The Early Toarcian oceanic anoxic event: Paleoenvironmental and paleoclimatic change across the Alpine Tethys (Switzerland). *Global and Planetery Change*, 162, pp.53-58.

Farouk, S. (2016). Paleocene stratigraphy in Egypt. *Journal of African Earth Sciences*, 113, pp.126-152.

Fedo, C., Wayne Nesbitt, H. and Young, G. (1995). Unraveling the effects of potassium metasomatism in sedimentary rocks and paleosols, with implications for paleoweathering conditions and provenance. *Geology*, 23(10), p.921.

Font, E., Adatte, T., Andrade, M., Keller, G., Mbabi Bitchong, A., Carvallo, C., Ferreira, J., Diogo, Z. and Mirão, J. (2018). Deccan volcanism induced high-stress environment during the Cretaceous–Paleogene transition at Zumaia, Spain: Evidence from magnetic, mineralogical and biostratigraphic records. *Earth and Planetary Science Letters*, 484, pp.53-66.

Font, E., Adatte, T., Sial, A., Drude de Lacerda, L., Keller, G. and Punekar, J., 2016. Mercury anomaly, Deccan volcanism, and the end-Cretaceous mass extinction. *Geology*, 44(2), pp.171-174.

Font, E., Fabre, S., Nedelec, A., Adatte, T., Keller, G., Veiga-Pires, C., Ponte, J., Mirao, J., Khozyem, H., Spangenberg, J.E. (2014). Atmospheric halogen and acid rains during the main phase of Deccan eruptions: Magnetic and mineral evidence. Volcanism, Impacts, and Mass Extinctions: Causes and Effects. *The Geological Society of America Special Papers* 505, 353-368.

Font, E., Nedelec, A., Ellwood, B.B., Mirao, J., Silva, P.F. (2011). A new sedimentary benchmark for the Deccan Traps volcanism? *Geophysical Research Letters* 38.

Frakes, l.,A,, J.K. Francis, and 11 Syktus. 1992. Climate modes of the Phanerozoic. Cambridge University Press, Cambridge, United Kingdom, 274 p.

Frank, T.D., Arthur, M.A. and Dean, W.E., 1999. Diagenesis of Lower Cretaceous pelagic carbonates, North Atlantic; paleoceanographic signals obscured. *Journal of Foraminiferal Research*, 29(4), pp.340–351.

Friedman, I. and O'Neil, J.R., 1977. Compilation of stable isotope fractionation factors of geochemical interest. U.S.G.S. Professional Paper 440-KK.

Frieling, J., Gebhardt, H., Huber, M., Adekeye, O.A., Akande, S.O., Gert-Jan Reichart, G.-J., Middelburg, J.J., Schouten, S., Sluijs, A. (2017). Extreme warmth and heat-stressed plankton in the tropics during the Paleocene-Eocene Thermal Maximum. *Science Advances*, 3(3) e1600891, pp. 1-9.

Frieling, J., Svensen, H., Planke, S., Cramwinckel, M., Selnes, H. and Sluijs, A. (2016). Thermogenic methane release as a cause for the long duration of the PETM. *Proceedings of the National Academy of Sciences*, 113(43), pp.12059-12064.

Gardin, S. (2002). Late Maastrichtian to early Danian calcareous nannofossils at Elles (Northwest Tunisia). A tale of one million years across the K–T boundary. *Palaeogeography, Palaeoclimatology, Palaeoecology*, 178(3-4), pp.211-231.

Garzanti, E., Andò, S., France-Lanord, C., Vezzoli, G., Censi, P., Galy, V. and Najman, Y., 2010, Mineralogical and chemical variability of fluvial sediments1. Bedload sand (Ganga–Brahmaputra, Bangladesh). *Earth and Planetary Science Letters*, 299, 368–381.

Gavrilov, Y., Shcherbinina, E.A., Oberhänsli, H., 2003. Paleocene-Eocene boundary events in the northeastern Peri-Tethys, in Causes and Consequences of Globally Warm Climates in the Early Paleogene, edited by S. L. Wing et al., *Special Paper the Geological Society of America*, 369, 147–168.

Gavrilov, Y.O., Kodina, L.A., Lubchenko, I.Yu., Muzylev, N.G., 1997. The Late Paleocene anoxic event in epicontinental seas of Peri-Tethys and formation of the Sapropelite Unite: sedimentology and geochemistry. *Lithology and Mineral Resources* 32, 427–450.

Gebhardt, H., Adekeye, O.A., Akande, S. O., 2011. Late Paleocene to Initial Eocene Thermal Maximum (IETM) foraminiferal biostratigraphy and paleoecology of the Dahomey Basin, Southwestern Nigeria. *Jahrbuch der Geologische Bundesanstalt* 3, 407–419 (2011).

Gersch, B., Keller, G., Adatte, T., Bartels, D. (2011b). Trace-element geochemistry of Brazos sections, Texas, USA, *in* Keller, G. and Adatte, T. eds., End-Cretaceous Mass Extinction and the Chicxulub Impact in Texas: *Society for Sedimentary Geology (SEPM)* Special Publication 100, p. 228-249.

Gertsch, B., Keller, G., Adatte, T., Garg, R., Prasad, V., Berner, Z. and Fleitmann, D. (2011a). Environmental effects of Deccan volcanism across the Cretaceous–Tertiary transition in Meghalaya, India. *Earth and Planetary Science Letters*, 310(3-4), pp.272-285.

Gibbs, S., Bown, P., Sessa, J., Bralower, T. and Wilson, P., 2006. Nannoplankton Extinction and Origination Across the Paleocene-Eocene Thermal Maximum. *Science*, 314(5806), pp.1770-1773.

Gibson, T.G., Bybell, L.M., Mason, D.B., 2000. Stratigraphic and climatic implications of the clay mineral changes around the Paleocene/Eocene boundary of the northeastern US margin. *Sedimentary Geology* 134, 65–92.

Giresse P., Megope-Foonde J.P., Ngueutchoua G., Aloisi J.C., Kuete M., Monteillet J., 1996, Carte sédimentologique du plateau continental du Cameroun à 1 : 200000 (Notice Explicative 111). Institut Français de Recherche Scientifique pour le Développement en Coopération, ORSTOM, Paris, 41 p.

Giresse, P., 1990. Esquisse géologique de l'Afrique centrale occidentale. In : Paysages quaternaires de l'Afrique centrale occidentale. ORSTOM, n.s.: 15-19.

Girty G.H., Ridge, D.L., Knaack, C., Johnson, D. and Al-Riyami, R.K., 1996, Provenance and Depositional Setting of Paleozoic Chert and Argillite, Sierra Nevada, California. *SEPM Journal of Sedimentary Research*, 66, 107–118.

Grasby, S.E., Beauchamp, B., Bond, D.P.G., paul b. Wignall, P.B., Sanei, H., 2016. Mercury anomalies associated with three extinction events (Capitanian Crisis, Latest Permian Extinction and the Smithian/Spathian Extinction) in NW Pangea. *Geological Magasine*, 153 (2), pp. 285–297.

Grasby, S.E., Sanei, H., Beauchamp, B., and Chen, Z.H., 2013. Mercury deposition through the Permo-Triassic biotic crisis: *Chemical Geology*, 351, pp. 209–216,

Gupta, S. and Kumar, K. (2018). Precursors of the Paleocene–Eocene Thermal Maximum (PETM) in the Subathu Group, NW sub-Himalaya, India. *Journal of Asian Earth Sciences*, In press.

Hamer, J., Sheldon, N., Nichols, G. and Collinson, M., 2007, Late Oligocene–Early Miocene paleosols of distal fluvial systems, Ebro Basin, Spain. *Palaeogeography, Palaeoclimatology, Palaeoecology*, 247, 220–235.

Handley, L., O'Halloran, A., Pearson, P., Hawkins, E., Nicholas, C., Schouten, S., McMillan, I. and Pancost, R. (2012). Changes in the hydrological cycle in tropical East Africa during the Paleocene–Eocene Thermal Maximum. *Palaeogeography, Palaeoclimatology, Palaeoecology*, 329-330, pp.10-21.

Haq, B.U., Hardenbol, J., Vail P., 1988. Mesozoic and Cenozoic chronostratigraphy and cycles, of relative sea-level changes. pp. 71-108 in: Sea-level Changes: An Integrated Approach (C. Wilgus, B. Hastings, C.A. Ross, H.W. Posamentier, J. Van Wagoner & C.G. Kendall, editors). *SEPM, Special Publication*, 42.

Harnois, L., 1988. The CIW index: A new chemical index of weathering. *Sedimentary Geology*, 55(3-4), pp.319-322.

Hatch, J. and Leventhal, J., 1992, Relationship between inferred redox potential of the depositional environment and geochemistry of the Upper Pennsylvanian (Missourian) Stark Shale Member of the Dennis Limestone, Wabaunsee County, Kansas, U.S.A. *Chemical Geology*, 99, 65–82.

Hayashi, K., Fujisawa, H., Holland, H. and Ohmoto, H., 1997, Geochemistry of ~1.9 Ga sedimentary rocks from northeastern Labrador, Canada. *Geochimica et Cosmochimica Acta*, 61, 4115–4137.

Hernández-Hinojosa, V., Montiel-García, P., Armstrong-Altrin, J., Nagarajan, R. and Kasper-Zubillaga, J., 2017, Textural and geochemical characteristics of beach sands along the western gulf of mexico, mexico. Carpathian Journal of Earth and Environmental Sciences, 13, 161–174.

Higgins, J. and Schrag, D. (2006). Beyond methane: Towards a theory for the Paleocene–Eocene Thermal Maximum. *Earth and Planetary Science Letters*, 245(3-4), pp.523-537.

Hildebrand, A., Penfield, G., Kring, D., Pilkington, M., Camargo Z., A., Jacobsen, S. and Boynton, W., 1991. Chicxulub Crater: A possible Cretaceous/Tertiary boundary impact crater on the Yucatán Peninsula, Mexico. *Geology*, 19(9), p.867.

Hilgen, F., Kuiper, K. and Lourens, L. (2010). Evaluation of the astronomical time scale for the Paleocene and earliest Eocene. *Earth and Planetary Science Letters*, 300(1-2), pp.139-151.

Hillier, S., 1995, Erosion, sedimentation and sedimentary origin of clays. In: Velde, B. (ed.), Origin and Mineralogy of Clays: Clays and the Environment. Springer, Berlin Heidelberg New York, p. 162–219.

Hofmann, A., Bekker, A., Rouxel, O., Rumble, D. and Master, S., 2009, Multiple sulphur and iron isotope composition of detrital pyrite in Archaean sedimentary rocks: A new tool for provenance analysis. *Earth and Planetary Science Letters*, 286, 436–445.

Immenhauser, A., Della Porta, G., Kenter, J. and Bahamonde, J. (2003). An alternative model for positive shifts in shallow-marine carbonate $\delta^{13}C$ and δ18O. *Sedimentology*, 50(5), pp.953-959.

Jablonski, D., 1994. Extinctions in the fossil record. *Philosophical Transactions of the Royal Society of London. Series B: Biological Sciences*, 344(1307), pp.11-17.

Jacobs, L., Emerson, S., Huested, S.S., 1987. Trace metal geochemistry in the Cariaco Trench. *Deep Sea Research* 34, 965–981.

Jacobs, L., Emwrson, S., Skei, J., 1985. Partitioning and transport of metals across the O_2/ H_2S interface in permanently anoxic basin: Framvarn Fjord, Norway. *Geochimica et Cosmochimica Acta* 49, 1433–1444.

Jarvis, I., Mabrouk, A., Moody, R. and de Cabrera, S. (2002). Late Cretaceous (Campanian) carbon isotope events, sea-level change and correlation of the Tethyan and Boreal realms. *Palaeogeography, Palaeoclimatology, Palaeoecology*, 188(3-4), pp.215-248.

Jenkyns, H., 2003. Evidence for rapid climate change in the Mesozoic–Palaeogene greenhouse world. *Philosophical Transactions of the Royal Society of London. Series A: Mathematical, Physical and Engineering Sciences*, 361(1810), pp.1885-1916.

Jenkyns, H., 2010. Geochemistry of oceanic anoxic events. *Geochemistry, Geophysics, Geosystems*, 11(3), p.n/a-n/a.

Jenkyns, H., Gale, A. and Corfield, R. (1994). Carbon- and oxygen-isotope stratigraphy of the English Chalk and Italian Scaglia and its palaeoclimatic significance. *Geological Magazine*, 131(01), p.1.

John, C. M., S. M. Bohaty, J. C. Zachos, A. Sluijs, S. Gibbs, H. Brinkhuis, and T. J. Bralower (2008), North American continental margin records of the Paleocene-Eocene thermal maximum: Implications for global carbon and hydrological cycling, *Paleoceanography*, 23, PA2217

Jones, B. and Manning, D. (1994). Comparison of geochemical indices used for the interpretation of palaeoredox conditions in ancient mudstones. *Chemical Geology*, 111(1-4), pp.111-129.

Kaminski, M.A., Gradstein, F., 2005. Atlas of Paleogene Cosmopolitan Deep-water Agglutinated Foraminifera. 10. *Grzybowski Foundation Special Publication*, pp. 1–548.

Karoui, N., Saïd-Benzarti, R., Zaghbib-Turki, D., 1995. Le passage Crétacé-Tertiaire dans la coupe d'Elles (Tuisie centro-septentrionale). In: Actes du troisième Colloque Africain de Micropaléontologie, p. 99.

Katz M.E., Pak D.K., Dickens G.R. and Miller K.G. (1999). The source and fate of massive carbon input during the Latest Paleocene Thermal Maximum. *Science*, 286, pp.1531–33

Katz, M.E., Miller, K.G., 1991. Early Paleogene benthic foraminiferal assemblages and stable isotopes in the Southern Ocean. *Proceedings of the Ocean Drilling Project, Scientific Reports* 114, 481–512.

Keller, 2014. Cretaceous mass extinction: Coincidence? Cause and effect? In Keller, G., and Kerr, A.C., eds., Volcanism, Impacts, and Mass Extinctions: Causes and Effects: *Geological Society of America Special Paper* 505, pp.57–89.

Keller, G. (1988a). Biotic turnover in benthic foraminifera across the cretaceous/tertiary boundary at El Kef, Tunisia. *Palaeogeography, Palaeoclimatology, Palaeoecology*, 66(3-4), pp.153-171.

Keller, G. (1988b). Extinction, survivorship and evolution of planktic foraminifera across the Cretaceous/Tertiary boundary at El Kef, Tunisia. *Marine Micropaleontology*, 13(3), pp.239-263.

Keller, G. (1993). The Cretaceous-Tertiary boundary transition in the Antarctic Ocean and its global implications. *Marine Micropaleontology*, 21(1-3), pp.1-45.

Keller, G. (2008). Cretaceous climate, volcanism, impacts, and biotic effects. *Cretaceous Research*, 29(5-6), pp.754-771.

Keller, G. and Abramovich, S., 2009. Lilliput effect in late Maastrichtian planktic foraminifera: Response to environmental stress. *Palaeogeography, Palaeoclimatology, Palaeoecology*, 284(1-2), pp.47-62.

Keller, G. and Benjamini, C. (1991). Paleoenvironment of the Eastern Tethys in the Early Paleocene. *PALAIOS*, 6(5), p.439.

Keller, G. and Lindinger, M., 1989. Stable isotope, TOC and $CaCO_3$ record across the cretaceous/tertiary boundary at El Kef, Tunisia. *Palaeogeography, Palaeoclimatology, Palaeoecology*, 73(3-4), pp.243-265.

Keller, G., 1989. Extended Cretaceous/Tertiary boundary extinctions and delayed population change in planktonic foraminifera from Brazos River, Texas. *Paleoceanography*, 4(3), pp.287-332.

Keller, G., 2001. The end-cretaceous mass extinction in the marine realm: year 2000 assessment. Planetary and Space Science, 49, pp. 817-830.

Keller, G., 2005. Impacts, volcanism and mass extinctions: random coincidence or cause and effect? *Australian Journal of Earth Sciences*, 52, pp.725–757.

Keller, G., 2008. Cretaceous climate, volcanism, impacts, and biotic effects. *Cretaceous Research*, 29(5-6), pp.754-771.

Keller, G., 2011. The Cretaceous-Tertiary mass extinction: Theories and controversies. In Keller, G., and Adatte, T., eds., The End-Cretaceous Mass Extinction and the Chicxulub Impact in Texas: Society for Sedimentary Geology (SEPM) Special Publication 100, p. 7–22.

Keller, G., 2014. Deccan volcanism, the Chicxulub impact, and the end-Cretaceous mass extinction: Coincidence? Cause and effect? In Keller, G. and Kerr, A.C. (Eds), *Volcanism, Impacts, and Mass Extinctions: Causes and Effects*, Geological Society of America, pp.57-89.

Keller, G., Adatte, M., Berner, T., Harting, Z., Baum, G., Prauss, M., Tantawy, A.A., Stueben, D., 2007. Chicxulub impact predates K-T boundary: new evidence from Texas. *Earth and Planetary Science Letters*, 255, pp.339–356.

Keller, G., Adatte, T., Burns, S. and Tantawy, A. (2002). High-stress paleoenvironment during the late Maastrichtian to early Paleocene in Central Egypt. *Palaeogeography, Palaeoclimatology, Palaeoecology*, 187(1-2), pp.35-60.

Keller, G., Adatte, T., Gardin, S., Bartolini, A. and Bajpai, S. (2008). Main Deccan volcanism phase ends near the K–T boundary: Evidence from the Krishna–Godavari Basin, SE India. *Earth and Planetary Science Letters*, 268(3-4), pp.293-311.

Keller, G., Adatte, T., Juez, A. and Lopez-Oliva, J., 2009. New evidence concerning the age and biotic effects of the Chicxulub impact in NE Mexico. *Journal of the Geological Society*, 166(3), pp.393-411.

Keller, G., Adatte, T., Pardo, A., Bajpai, S., Khosla, A., and Samant, B., 2010, Cretaceous extinctions: Evidence overlooked. *Science*, 328, pp.974– 975.

Keller, G., Adatte, T., Stinnesbeck, W., Luciani, V., Karoui-Yaakoub, N. and Zaghbib-Turki, D., 2002. Paleoecology of the Cretaceous–Tertiary mass extinction in planktonic foraminifera. *Palaeogeography, Palaeoclimatology, Palaeoecology*, 178(3-4), pp.257-297.

Keller, G., Adatte, T., Stinnesbeck, W., Rebolledo-Vieyra, M., Urrutia Fucugauchi, J., Kramar, U. and Stuben, D. (2004). From The Cover: Chicxulub impact predates the K-T boundary mass extinction. *Proceedings of the National Academy of Sciences*, 101(11), pp.3753-3758.

Keller, G., Adatte, T., Stinnesbeck, W., Rebolledo-Vieyra, M., Urrutia Fucugauchi, J., Kramar, G., and Stüben, D., 2004. Chicxulub predates the K/T boundary mass extinction: Proceedings of the National Academy of Sciences of the United States of America, 101, p. 3753–3758.

Keller, G., Adatte, T., Stinnesbeck, W., Stüben, D. and Berner, Z., 2001. Age, chemo- and biostratigraphy of Haiti spherule-rich deposits: a multi-event K–T scenario. *Canadian Journal of Earth Sciences*, 38(2), pp.197-227.

Keller, G., Adatte, T., Stinnesbeck, W., Stüben, D., Berner, Z., Kramar, U., Harting, M., 2004. More evidence that the Chicxulub impact predates the K/T mass extinction. *Meteoritics & Planetary Science*, 39, pp.1127–1144.

Keller, G., Adatte, T., Stinnesbeck, W., Stüben, D., Kramar, U., Berner, Z., Li, L. and Perch-Nielsen, K. (1997). The cretaceous-tertiary transition on the shallow Saharan Platform of southern tunisia. *Geobios*, 30(7), pp.951-975.

Keller, G., Adatte, T., Tantawy, A., Berner, Z., Stinnesbeck, W., Stueben, D. and Leanza, H. (2007). High stress late Maastrichtian – early Danian palaeoenvironment in the Neuquén Basin, Argentina. *Cretaceous Research*, 28(6), pp.939-960.

Keller, G., and Stinnesbeck, W., 1996, Sea-level changes, clastic deposits and megatsunami across the Cretaceous-Tertiary boundary, in MacLeod, N., and Keller, G., eds., The Cretaceous/Tertiary mass extinction: Biotic and environmental events: New York,W.W. Norton

Keller, G., Khozyem, H., Adatte, T., Malarkodi, N., Spangenberg, J. and Stinnesbeck, W. (2013). Chicxulub impact spherules in the North Atlantic and Caribbean: age constraints and Cretaceous–Tertiary boundary hiatus. *Geological Magazine*, 150(05), pp.885-907.

Keller, G., Li, L. and MacLeod, N. (1996). The Cretaceous/Tertiary boundary stratotype section at El Kef, Tunisia: how catastrophic was the mass extinction? *Palaeogeography, Palaeoclimatology, Palaeoecology*, 119(3-4), pp.221-254.

Keller, G., Mateo, P., Punekar, J., Khozyem, H., Gertsch, B., Spangenberg, J., Mbabi Bitchong, A. and Adatte, T. (2018). Environmental changes during the Cretaceous-Paleogene mass extinction and

Paleocene-Eocene Thermal Maximum: Implications for the Anthropocene. *Gondwana Research*, 56, pp.69-89.

Keller, G., Punekar, J. and Mateo, P. (2016). Upheavals during the Late Maastrichtian: Volcanism, climate and faunal events preceding the end-Cretaceous mass extinction. *Palaeogeography, Palaeoclimatology, Palaeoecology*, 441, pp.137-151.

Keller, G., Punekar, J. and Mateo, P. (2016). Upheavals during the Late Maastrichtian: Volcanism, climate and faunal events preceding the end-Cretaceous mass extinction. *Palaeogeography, Palaeoclimatology, Palaeoecology*, 441, pp.137-151.

Keller, G., Stinnesbeck, W., Adatte, T. and Stüben, D. (2003). Multiple impacts across the Cretaceous–Tertiary boundary. *Earth-Science Reviews*, 62(3-4), pp.327-363.

Kelly, D.C., Bralower, T.J., Zachos, J.C., 1998. Evolutionary consequences of the latest Paleocene thermal maximum for tropical planktonic foraminifera. *Palaeogeography, Palaeoclimatology, Palaeoecology*, 141:139–161.

Kelly, D.C., Bralower, T.J., Zachos, J.C., Premoli-Silva, I., Thomas, E., 1996. Rapid diversification of planktonic foraminifera in the tropical Pacific (ODP Site 865) during the late Paleocene Thermal Maximum. *Geology*, 24, pp.423–426.

Kenfack P. L., Njike Ngaha P. R., Ekodeck, G.E., Ngueutchoua, G., 2012, Fossils dinoflagellates from the northern border of the Douala sedimentary sub-Basin (South-West Cameroon): age assessment and paleoecological interpretations. *Geosciences*, 2, 117–124.

Kennan, L., and Pindell, J.L., 2009, Dextral shear, terrane accretion and basin formation in the Northern Andes: Best explained by interaction with a Pacific-derived Caribbean plate?, in James, K., Lorente, M.A., and Pindell, J., eds., The Geology and Evolution of the Region between North and South America: *Geological Society* [London] Special Publication 328, p. 487–531.

Kennett, J. and Stott, L. (1991). Abrupt deep-sea warming, palaeoceanographic changes and benthic extinctions at the end of the Palaeocene. *Nature*, 353(6341), pp.225-229

Kent, D.V., Cramer, B.S., Lanci, L., Wang, D., Wright, J. D., Van der Voo, R., 2003. A case for a comet impact trigger for the Paleocene/Eocene thermal maximum and carbon isotope excursion. *Earth and Planetary Science Letters* 211 (1), 13–26.

Kerr, A. and Tarney, J., 2005. Tectonic evolution of the Caribbean and northwestern South America: The case for accretion of two Late Cretaceous oceanic plateaus. *Geology*, 33(4), p.269.

Khozyem 2013. Sedimentology, geochemistry and mineralogy of the paleocene eocene thermal maximum (PETM): sediment records from Egypt, India, and Spain. Thèse de Doctorat, Université de Lausanne, 174p.

Khozyem H., Adatte T., Mbabi Bitchong A., Chevalier Y. and Keller G. (2016). Paleocene-Eocene Thermal maximum triggered by volcanism? Evidence from mercury anomalies. *GSA Annual Meeting in Denver*, Colorado, USA (25-28 September 2016).

Khozyem H., Adatte T., Mbabi Bitchong A., Chevalier Y. and Keller G. (2017a). Paleocene-Eocene Thermal Maximum triggered by Volcanism revealed by Mercury anomalies. *Geophysical Research Abstracts*, vol. 19, EGU2017-9160, EGU General Assembly 2017.

Khozyem H., Adatte T., Mbabi Bitchong A., Mohamed A. and Keller G. (2017b). The role of volcanism (North Atlantic Igneous Province) in the PETM events revealed by mercury anomalies. *GSA Annual Meeting in Seattle*, Washington, USA (22-25 October 2017).

Khozyem, H., Adatte, T., Spangenberg, J., Keller, G., Tantawy, A. and Ulianov, A. (2015). New geochemical constraints on the Paleocene–Eocene thermal maximum: Dababiya GSSP, Egypt. *Palaeogeography, Palaeoclimatology, Palaeoecology*, 429, pp.117-135.

Khozyem, H., Adatte, T., Spangenberg, J.E., Tantawy, A.A., Keller, G., 2013. Palaeoenvironmental and climatic changes during the Paleocene–Eocene Thermal Maximum (PETM) at Wadi Nukhul Section, Sinai, Egypt. *Journal of the Geological Society, London* 170, 341–352.

Klemme and Ulminshek, 1991. Effective petroleum source rocks of the world: Stratigraphic distribution and controlling depositional factors. *American Association of Petroleum Geologists Bulletin*, 75, pp.1809-1851.

Klug, H.P. and Alexander, L. (1974). X-ray Diffraction Procedures for Polycrystalline and Amorphous Materials. John Willey and Sons, Inc. First and second editions, New York.

Knauth, L. and Kennedy, M., 2009. The late Precambrian greening of the Earth. *Nature*, 460(7256), pp.728-732.

Knox, R.W.O.B., Aubry, M.-P., Berggren, W.A., Dupuis, C., Ouda, Kh., Magioncalda, R., Soliman, M.F., 2003. The Qreiya section at Gebel Abu Had: lithostratigraphy, clay mineralogy, geochemistry and biostratigraphy. *Micropaleontology* 49, 93–104.

Koch, P., Zachos, J. and Gingerich, P. (1992). Correlation between isotope records in marine and continental carbon reservoirs near the Palaeocene/Eocene boundary. *Nature*, 358(6384), pp.319-322.

Kortenski, J. and Kostova, I., 1996, Occurrence and morphology of pyrite in Bulgarian coals. International Journal of Coal Geology, 29, 273–290.

Kübler, B., 1987. Cristallinité de l'illite: méthode normalisée de préparation de mesure, méthode automatique normalisées de mesure. Cahiers de l'Institut de Géologie de Neuchâtel, Series AX n°3.1 and 3.2..

Kuhnt, W., Hess, S., Holbourn, A., Paulsen, H. and Salomon, B. (2005). The impact of the 1991 Mt. Pinatubo eruption on deep-sea foraminiferal communities: A model for the Cretaceous–Tertiary (K/T) boundary?. *Palaeogeography, Palaeoclimatology, Palaeoecology*, 224(1-3), pp.83-107.

Kurtz, A., Kump, L., Arthur, M., Zachos, J. and Paytan, A., 2003. Early Cenozoic decoupling of the global carbon and sulfur cycles. *Paleoceanography*, 18(4), p.n/a-n/a.

Kutterolf, S., Diener, R., Schacht, U. and Krawinkel, H., 2008, Provenance of the Carboniferous Hochwipfel Formation (Karawanken Mountains, Austria/Slovenia) — Geochemistry versus petrography. Sedimentary Geology, 203, 246–266.

Kvenvolden, K., 1993. Gas hydrates-geological perspective and global change. *Reviews of Geophysics*, 31(2), pp.173-187.

Labandeira C. C., Johnson K. R., and Wilf P. 2002. Impact of the terminal Cretaceous event on plant-insect associations. *Proceedings of the Academy of Science*, 99, pp.2061–2066.

Lamolda, M. (1990). The Cretaceous-Tertiary boundary crisis at Zumaya (Northern Spain). Micropaleon-tological data. In: E. Kauffman and O. Walliser, ed., *Extinction Events in Earth History. Proceedings of the Project 216: Global Biological Events in Earth History*. Berlin: Springer.

Lamolda, M., Orue-Etxebarria, X. and Proto-Decima, F. (1983). The Cretaceous-Tertiary boundary in Sopelana (Biscay, Basque Country). *Zitteliana*, 10, pp.663-670.

Lanson, B., Sakharov, B., Claret, F. and Drits, V., 2009. Diagenetic smectite-to-illite transition in clay-rich sediments: A reappraisal of X-ray diffraction results using the multi-specimen method. *American Journal of Science*, 309(6), pp.476-516.

Large, R., Halpin, J., Danyushevsky, L., Maslennikov, V., Bull, S., Long, J., Gregory, D., Lounejeva, E., Lyons, T., Sack, P., McGoldrick, P. and Calver, C., 2014, Trace element content of sedimentary pyrite as a new proxy for deep-time ocean–atmosphere evolution. Earth and Planetary Science Letters, 389, 209–220.

Lawrence, S., Munday, S. and Bray, R. (2002). Regional geology and geophysics of the eastern Gulf of Guinea (Niger Delta to Rio Muni). *The Leading Edge*, 21(11), pp.1112-1117.

Li, L. and Keller, G., 1998. Maastrichtian climate, productivity and faunal turnovers in planktic foraminifera in South Atlantic DSDP sites 525A and 21. *Marine Micropaleontology*, 33(1-2), pp.55-86.

Li, L., Keller, G., Adatte, T. and Stinnesbeck, W. (2000). Late Cretaceous sea-level changes in Tunisia: a multi-disciplinary approach. *Journal of the Geological Society*, 157(2), pp.447-458.

Lim, D., Jung, H. and Choi, J., 2014. REE partitioning in riverine sediments around the Yellow Sea and its importance in shelf sediment provenance. *Marine Geology*, 357, 12–24.

Lu, G., Keller, G., Adatte, T., Ortiz, N., Molina, E., 1996. Long-term (105) or short-term (103) $\delta^{13}C$ excursion near the Palaeocene-Eocene transition: Evidence from the Tethys. *Terra Nova*, 8: 347–355.

Ly A., Anglada R., 1991. Le bassin sénégalo-mauritanien dans l'évolution des marges périatlantiques au Tertiaire. *Cahier de Micropaléontologie, Paris*, 6(2), pp. 23-47

Lyons, S., Baczynski, A., Babila, T., Bralower, T., Hajek, E., Kump, L., Polites, E., Self-Trail, J., Trampush, S., Vornlocher, J., Zachos, J. and Freeman, K., 2018. Palaeocene–Eocene Thermal Maximum prolonged by fossil carbon oxidation. *Nature Geoscience*, 12(1), pp.54-60.

Lyson, T., Miller, I., Bercovici, A., Weissenburger, K., Fuentes, A., Clyde, W., Hagadorn, J., Butrim, M., Johnson, K., Fleming, R., Barclay, R., Maccracken, S., Lloyd, B., Wilson, G., Krause, D. and Chester, S., 2019. Exceptional continental record of biotic recovery after the Cretaceous–Paleogene mass extinction. *Science*, 366(6468), pp.977-983.

MacLeod, N. and Keller, G. (1991). Hiatus distributions and mass extinctions at the Cretaceous/Tertiary boundary. *Geology*, 19(5), p.497.

Macleod, N. and Keller, G. (1991). How complete are Cretaceous /Tertiary boundary sections? A chronostratigraphic estimate based on graphic correlation. *Geological Society of America Bulletin*, 103(11), p.1439.

MacLeod, N.D., 2003. The causes of phanerozoic extinctions. In: Rothschild, L.J., Lister, A.M. (Eds.), Evolution on Planet Earth: Impact of the Physical Environment. Academic Press, Amsterdam, pp. 235–252.

MacRae, N., Nesbitt, H. and Kronberg, B, 1992, Development of a positive Eu anomaly during diagenesis. Earth and Planetary Science Letters, 109, 585–591.

Madhavaraju, J. and Lee, Y.I., 2009, Geochemistry of the Dalmiapuram Formation of the Uttatur Group (early Cretaceous), Cauvery basin, southeastern India: implications on provenance and paleo-redox conditions. Revista Mexicana de Ciencias Geológicas, 26, 380–394.

Madhavaraju, J., Tom, M., Lee, Y., Balaram, V., Ramasamy, S., Carranza-Edwards, A. and Ramachandran, A., 2016, Provenance and tectonic settings of sands from Puerto Peñasco, Desemboque and Bahia Kino beaches, Gulf of California, Sonora, México. Journal of South American Earth Sciences, 71, 262–275.

Magioncalda, R., Dupuis, C., Blamart, D., Fairon-Demaret. M., Perreau, M., Renard, M., Riveline, J., Roche, M., Keppens, E., 2001. L'excursion isotopique du carbone organique ($\delta^{13}C_{org}$) dans les paléoenvironnements continentaux de l'intervalle Paléocène/Eocène de Varengeville (Haute-Normandie). *Bulletin de la Société géologique de France*, 172 (3): 349–358

Magioncalda, R., Dupuis, C., Smith, T., Steurbaut, E., Gingerich, P. D., 2004. Paleocene- Eocene carbon isotope excursion in organic carbon and pedogenic carbonate: Direct compaison in a continental stratigraphic section. *Geology*, 32 (7): 553–556.

Manga, C. S. (2008). Stratigraphy structure and prospectivity of the Southern onshore Douala Basin Cameroon – Central Africa, In Guest Editors: Ntamak-Nida MJ, Ekodeck GE, Guiraud M. Cameroon and neighboring basins in the Gulf of Guinea (Petroleum Geology Tectonics Geophysics Paleontology and Hydrogeology). *African Geosciences Review Special Publication*, 1 & 2, 13-37.

Marbut, C.F., 1935, Soils of the United States. In: Baker, O.E. (ed.), Atlas of American agriculture. USDA Bureau of Chemistry and Soils, U.S. Gov. Print. Office, Washington DC. p. 1–98.

Margolis, S., Mount, J., Doehne, E., Showers, W. and Ward, P. (1987). The Cretaceous/Tertiary boundary carbon and oxygen isotope stratigraphy, diagenesis, and paleoceanography at Zumaya, Spain. *Paleoceanography*, 2(4), pp.361-377.

Mateo, P., Keller, G., Adatte, T. and Spangenberg, J. (2016). Mass wasting and hiatuses during the Cretaceous-Tertiary transition in the North Atlantic: Relationship to the Chicxulub impact?. *Palaeogeography, Palaeoclimatology, Palaeoecology*, 441, pp.96-115.

Mateo, P., Keller, G., Adatte, T., Mbabi Bitchong, A., Spangenberg, J., Vennemann, T. and Hollis, C., 2019. Deposition and age of Chicxulub impact spherules on Gorgonilla Island, Colombia. *GSA Bulletin*, 132(1-2), pp.215-232.

Mathey, B. (1982). El Cretácico superior del Arco Vasco. In: El Cretácico de España. Universidad Complutense de Madrid, 111-135

Mbesse, C.O., Roche, E. and Ngos III, S., 2013, The Paleocene-Eocene boundary in the Douala Basin (Cameroon). Dinocysts biostratigraphy and tentative of paleoenvironmental reconstruction. *International journal of tropical geology, geography and ecology*, 36, 83–119.

McInerney, F. and Wing, S. (2011). The Paleocene-Eocene Thermal Maximum: A Perturbation of Carbon Cycle, Climate, and Biosphere with Implications for the Future. *Annual Review of Earth and Planetary Sciences*, 39(1), pp.489-516.

McLennan, S., 2001, Relationships between the trace element composition of sedimentary rocks and upper continental crust. *Geochemistry, Geophysics, Geosystems*, 2, n/a–n/a.

McLennan, S.M., Hemming, S., McDaniel, D.K., Hanson, G.N., 1993, Geochemical approaches to sedimentation, provenance, and tectonics. In: Johnsson, M.J. and Basu, A. (eds.), Processes Controlling the Composition of Clastic Sediments, *Geological Society of America*, p. 21–40.

Medus, J. and Colombo, F. (1991). Sucession climatique et limite stratigrafique Crétacé-Tertiaire dans le N.E. de l'Espagne. *Acta Geologica Hispanica* 26, 27-35

Meunier, A. (2005). *Clays*. Berlin: Springer.

Mfayakouo Chavom, B., Njike Ngaha, P.R., and Bitom, D.L. (2014). Sedimentary facies and depositional environments of Cenozoic sedimentary formations cropping out at the central part of the Douala basin. *American Journal of Geosciences* 4 (1), 8-22.

Middelburg, J., van der Weijden, C. and Woittiez, J., 1988, Chemical processes affecting the mobility of major, minor and trace elements during weathering of granitic rocks. *Chemical Geology*, 68, 253–273.

Milelli, L., Fourel, L., Jaupart, C., 2012. A lithospheric instability origin for the Cameroon Volcanic Line. *Earth and Planetary Science Letters*, 335-336, pp. 80-87.

Miller, K.G., Janecek, T.R., Katz, M.E., Keil, D.J., 1987. Abyssal circulation and benthic foraminiferal changes near the Paleocene/Eocene boundary. *Paleoceanography* 2, 741–761.

Millot, G., 1970. Geology of clays. Springer, Berlin Heidelberg New York (429 p.).

Mitchell, J., Roopnarine, P. and Angielczyk, K., 2012. Late Cretaceous restructuring of terrestrial communities facilitated the end-Cretaceous mass extinction in North America. *Proceedings of the National Academy of Sciences*, 109(46), pp.18857-18861.

Mitchell, S., Ball, J., Crowley, S., Marshall, J., Paul, C., Veltkamp, C. and Samir, A. (1997). Isotope data from Cretaceous chalks and foraminifera: Environmental or diagenetic signals?. *Geology*, 25(8), p.691.

Moore EA, Kurtz AC. 2008. Black carbon in Paleocene-Eocene boundary sediments: a test of biomass combustion as the PETM trigger. *Palaeogeography, Palaeoclimatology, Palaeoecology*, 267, pp.147–52.

Munsel, D., Berner, Z., Stueben, D., 2011. The sandstone complex in the Brazos Riverbed section: geochemical constraints on genesis and depositional conditions. In: Keller, G., Adatte, T. (Eds.), End-Cretaceous mass extinction and the Chicxulub impact in Texas: *SEPM Special Publication*, No. 100.

Murphy, A.E., Sageman, B.B., Hollander, D.J., Lyons, T.W., Brett, C.E., 2000. Black shale deposition and faunal overturn in the Devonian Appalachian basin: Clastic starvation, seasonal water-column mixing, and efficient biolimiting nutrient recycling. *Paleoceanography*, 15(3), pp. 280-291.

Murphy, B., Farley, K. and Zachos, J. (2010). An extraterrestrial 3He-based timescale for the Paleocene–Eocene thermal maximum (PETM) from Walvis Ridge, IODP Site 1266. *Geochimica et Cosmochimica Acta*, 74(17), pp.5098-5108.

Murray, R., Buchholtz Ten Brink, M., Gerlach, D., Russ, G. and Jones, D., 1991, Rare earth, major, and trace elements in chert from the Franciscan Complex and Monterey Group, California: Assessing REE sources to fine-grained marine sediments. *Geochimica et Cosmochimica Acta*, 55, 1875–1895.

Mussard, M., Le Hir, G., Fluteau, F., Lefebvre, V., Goddéris, Y., 2014. Modeling the carbonsulfate interplays in climate changes related to the emplacement of continental flood basalts. *Geological Society of America Special Pape*r, 505, pp.339–352.

Nagarajan, R., Armstrong-Altrin, J., Kessler, F., Hidalgo-Moral, E., Dodge-Wan, D. and Taib, N., 2015, Provenance and tectonic setting of Miocene siliciclastic sediments, Sibuti formation, northwestern Borneo. *Arabian Journal of Geosciences*, 8, 8549–8565.

Nagarajan, R., Madhavaraju, J., Nagendra, R., Armstrong-Altrin, J.S., Moutte, J., 2007, Geochemistry of Neoproterozoic shales of the Rabanpalli Formation, Bhima Basin, Northern Karnataka, Southern India: implications for provenance and paleoredox conditions. *Revista Mexicana de Ciencias Geológicas*, 24, 150–160.

Nascimento-Silva, M., Sial, A., Ferreira, V., Neumann, V., Barbosa, J., Pimentel, M. and de Lacerda, L., 2011. Cretaceous-Paleogene transition at the Paraíba Basin, Northeastern, Brazil: Carbon-isotope and mercury subsurface stratigraphies. *Journal of South American Earth Sciences*, 32(4), pp.379-392.

Ndome Effoudou-Priso, E., Onana, V., Boubakar, L., Beyala, V. and Ekodeck, G., 2014, Relationships between major and trace elements during weathering processes in a sedimentary context: Implications for the nature of source rocks in Douala, Littoral Cameroon. *Chemie der Erde*, 74, 765–781.

Nederbragt, A., 1991. Late Cretaceous Biostratigraphy and Development of Heterohelicidae (Planktic Foraminifera). *Micropaleontology*, 37(4), p.329.

Nelson, C. and Smith, A. (1996). Stable oxygen and carbon isotope compositional fields for skeletal and diagenetic components in New Zealand Cenozoic nontropical carbonate sediments and limestones: A synthesis and review. *New Zealand Journal of Geology and Geophysics*, 39(1), pp.93-107.

Nesbitt, H.W. and Markovics, G., 1997, Weathering of granodioritic crust, long-term storage of elements in weathering profiles, and petrogenesis of siliciclastic sediments. *Geochimica et Cosmochimica Acta*, 61, 1653–1670.

Nesbitt, H.W. and Young, G.M., 1989, Formation and Diagenesis of Weathering Profiles. Journal of Geology, 97, 129–147.

Nesbitt, H.W., Young, G.M., 1984. Prediction of some weathering trends of plutonic and volcanic rocks based on thermodynamic and kinetic considerations. *Geochemica Cosmochemica Acta* 48, 1523–1534.

Nesbitt, H.W., Young, G.M., 1989. Formation and diagenesis of weathering profiles. *Journal of Geology*, 97, 129–147.

Nesbitt, H.W., Young, G.M., 1989. Formation and diagenesis of weathering profiles. *Journal of Geology*, 97, 129–147.

Ngon Ngon, G., Etame, J., Ntamak-Nida, M., Mbesse, C., Mbai, J., Bayiga, É. and Gerard, M. (2016). Geochemical and palaeoenvironmental characteristics of Missole I iron duricrusts of the Douala sub-basin (Western Cameroon). *Comptes Rendus Geoscience*, 348(2), pp.127-137.

Ngon Ngon, G., Mbog, M., Etame, J., Ntamak-Nida, M., Logmo, E., Gerard, M., Yongue-Fouateu, R. and Bilong, P. (2014). Geochemistry of the Paleocene-Eocene and Miocene-Pliocene clayey materials of the eastern part of the Wouri River (Douala sub-basin, Cameroon): Influence of parent rocks. *Journal of African Earth Sciences*, 91, pp.110-124.

Ngon Ngon, G.-F., Bayiga, E., Ntamak-Nida, M. J., Etame, J., Noa Tang, S., Yongue-Fouateu, R. (2012). Trace elements geochemistry of clay deposits of Missole II from the Douala sub-basin in Cameroon (Central Africa): a provenance study. *Sciences, Technologie & Développement*, 13(1), pp.20-35.

Ngon Ngon, G.-F., Mbabi Bitchong, A., Mbaï, J.S., Ngos III, S., Yongue Fouateu, R. and Bilong, P., 2019, Geochemistry of pyriteous mudrocks of the cenozoic N'Kapa formation in Douala Sub-basin, western Cameroon (Central Africa): Source rock weathering, provenance, paleo-redox conditions and tectonic settings. *Journal of African Earth Sciences*, 156, 44–57.

Nguene, F.R., Tamfu, S.F., Loule, J.-P. and Ngassa, C. (1992). Paleoenvironments of the Douala and Kribi/Campo sub basins, in Cameroon, West Africa. In: Curnelle, R. (Ed.), Géologie Africaine. 1er Colloque de Stratigraphie et de Paléogéographie des Bassins Sédimentaires Ouest-Africains, 2e Colloque Africain de Micropaléontologie, 6-8 mai 1991, Libreville, Gabon. Bull. Centres de Recherches, Exploration–Production, Elf Aquitaine 13, pp. 129–139.

Nichols D. and Johnson K. 2002. Palynology and microstratigraphy of Cretaceous-Tertiary boundary sections in southwestern North Dakota. In The Hell Creek Formation and the Cretaceous- Tertiary boundary in the northern Great Plains: An integrated continental record of the end of the Cretaceous, edited by Hartman J. H., Johnson K. R., and Nichols D. J. GSA Special Paper #361. Boulder, Colorado: *Geological Society of America*. pp. 95–143.

Nichols, G., 2009, Sedimentology and Stratigraphy (2nd ed.): London, Wiley-Blackwell, 432 p.

Njike Ngaha, P.R., 1984, Contribution à l'étude géologique, stratigraphique et structurale de la bordure Atlantique du Cameroun. Thèse 3ème cycle, Université de Yaoundé, Yaoundé, 131 p.

Njike Ngaha, P.R., 2005, Palynostratigraphie et reconstitution des paléoenvironnements du Crétacé de l'Est du bassin sédimentaire de Douala (Cameroun). Thèse d'Etat, Université de Yaoundé I, Yaoundé, 259 p.

Oboh-Ikuenobe, F., Antolinez-Delgado, H. and Awad, W. (2017). Dinoflagellate cyst assemblages, biostratigraphy and paleoenvironment of a Paleocene-Early Eocene sedimentary succession in the northern Niger Delta Basin: Comparison with low, mid and high latitude regions. *Palaeogeography, Palaeoclimatology, Palaeoecology*, 481, pp.29-43.

Oehlert, A. and Swart, P., 2014. Interpreting carbonate and organic carbon isotope covariance in the sedimentary record. *Nature Communications*, 5(1).

Ogorelec, B., Dolenec, T. and Drobne, K. (2007). Cretaceous–Tertiary boundary problem on shallow carbonate platform: Carbon and oxygen excursions, biota and microfacies at the K/T boundary sections Dolenja Vas and Sopada in SW Slovenia, Adria CP. *Palaeogeography, Palaeoclimatology, Palaeoecology*, 255(1-2), pp.64-76.

Okosun, E.A., 1989. Eocene ostracoda from Oshosun Formation southwesthern Nigeria. *Journal of African Earth Sciences*, 9(3/4), pp. 669-676.

Olsson, R.K., Hemleben, C., Berggren, W.A., and Huber, B.T., 1999. Atlas of Paleocene Planktonic Foraminifera: *Smithsonian Contributions to Paleobiology*, 85, 252 p.

Orue-Etxebarria, X. (1982). - Los foraminíferos planctónicos del Paleó-geno del Sinclinorio de Bizkaia (Corte de Sopelana Punta de la Galea). - Universidad del País Vasco, 271 p. (Unpublished Ph. D. Thesis)

Orue-Etxebarria, X., Rocía, R., Pujalte, V., Apellaniz, E. and Baceta, J. I. (1991): Estudio preliminar del tránsito Cretácico/Terciario en la sección del monte Urko (Eibar, País Vasco). - / Congreso del Grupo Español del Terciario, Vic, 240-243.

Ouda, K. (2018). Morphologic change and evolution of Acarinina sibaiyaensis and its descendants during the earliest Eocene CIE/PETM interval in southern Egypt. *Journal of African Earth Sciences*, 147, pp.78-125.

Ouda, Kh, Berggren, W. A., Abdel Sabour, A., 2013. Planktonic foraminiferal biostratigraphy of the Paleocene/Eocene boundary interval in the Dababiya Quarry Corehole, Upper Nile Valley, Egypt. In: Berggren W. A., Ouda Kh. (Eds.), Early Paleocene Geohistory of Egypt: the Dababiya Quarry Corehole. *Stratigraphy*, 9 (3-4), pp.213-227.

Outridge, P.M., Sanei, H., Stern, G.A., Hamilton, P.B., and Goodarzi, F., 2007, Evidence for control of mercury accumulation rates in Canadian High Arctic lake sediments by variations of aquatic primary productivity. *Environmental Science & Technology*, 41, pp. 5259–5265.

Pagani, M., Pedentchouk, N., Huber, M., Sluijs, A., Schouten, S., Brinkhuis, H., Damste, J.S.S., Dickens, G.R.Expedition 302 Scientists, 2006. Arctic hydrology during global warming at the Palaeocene/Eocene Thermal Maximum. *Nature*, 442, pp.671– 675.

Pan, A., Yang, Q., Zhou, H., Ji, F., Wang, H. and Pancost, R., 2018. Geochemical impacts of hydrothermal activity on surface deposits at the Southwest Indian Ridge. *Deep Sea Research Part I: Oceanographic Research Papers*, 139, pp.1-13.

Pattan, J.N., Masuzawa, T. and Yamamoto M., 2005, Variations in terrigenous sediment discharge in a sediment core from southeastern Arabian Sea during the last 140 ka. *Current Science*, 89, 1421–1425.

Pearson, P., Ditchfield, P., Singano, J., Harcourt-Brown, K., Nicholas, C., Olsson, R., Shackleton, N. and Hall, M., 2001. Warm tropical sea surface temperatures in the Late Cretaceous and Eocene epochs. *Nature*, 413(6855), pp.481-487.

Perch Nielsen, K. (1981a). Nouvelles observations sur les nannofossiles calcaires a la limite Crétacé-Tertiaire, près d'E1 Kef, Tunisie. *Cahier de Micropaléontologie*, 3, pp.25-36.

Perch-Nielsen, K. (1981b): Les nannofossiles calcaires á la limite Crétacé-Tertiaire près de El Kef, Tunisie. *Cahiers de Micropaleontologie* 3, 25-37.

Perch-Nielsen, K. (1985): Mesozoic calcareous nannofossils, In: H.M. Bolli, J.B. Saunders, K. Perch-Nielsen (Eds.), Plankton Stratigraphy, Cambridge University Press, 329-426.

Perch-Nielsen, K., McKenzie, J. and He, Q. (1982). Biostratigraphy and isotope stratigraphy and the 'catastrophic' extinction of calcareous nannoplankton at the Cretaceous/Tertiary boundary. *Geological Society of America Special Papers*, pp.353-372.

Percival, S. and Fischer, A. (1977). Changes in Calcareous nannoplankton in the Cretaceous–Tertiary biotic crisis at Zumaya, Spain. *Evolutionary Theory*, 1(1-35).

Pierret, M., Clauer, N. and Blanc, G., 2000. Influence hydrothermale dans les sédiments de fosses de la mer Rouge par l'étude de quelques éléments traces. *Oceanologica Acta*, 23(7), pp.783-792.

Piper, D. and Bau, M., 2013, Normalized Rare Earth Elements in Water, Sediments, and Wine: Identifying Sources and Environmental Redox Conditions. *American Journal of Analytical Chemistry*, 4, 69–83.

Potter, P E., Maynard, J.B. and Pryor, W.A., 1980, Sedimentology of Shale: Study Guide and Reference Source. Springer-Verlag, New York, 310 p.

Prasad G.V.R., Parmar V. (2020) Phanerozoic Mass Extinctions and Indian Stratigraphic Records. In: Gupta N., Tandon S. (eds) Geodynamics of the Indian Plate. Springer Geology. Springer, Cham, pp.291-362.

Price, J.R., Velbel, M.A., 2003. Chemical weathering indices applied to weathering profiles developed on heterogeneous felsic metamorphic parent rocks. *Chemical Geology*, 202, pp. 397–416.

Puigdefàbregas, C. and Souquet, P. (1986). Tecto-sedimentary cycles and depositional sequences of the Mesozoic and Tertiary from the Pyrenees. *Tectonophysics*, 129, pp. 173-203

Pujalte, V., Baceta, J.I. and Payros, A. (2002). Tertiary: Western Pyrenees and Basque-Cantabrian region. In: *The Geology of Spain* (W. Gibbons y T. Moreno, Eds.), Geol. Soc. (London), pp. 293-301

Pujalte, V., Baceta, J.I., Orue-Etxebarria, X. and Payros, A. (1998b). Paleocene strata of the Basque Country, western Pyrenees, northern Spain: Facies and sequence development in a deep-water starved basin. In: Mesozoic and Cenozoic Sequence Stratigraphy of European Basins (P.C. de Graciansky, J. Hardenbol, T. Jacquin y P.R. Vail, Eds.), Soc. Econ. Paleont. Miner., Sp. Publ., 60, pp. 311-325.

Pujalte, V., Orue-Etxebarria Urkiza, X., Caballero, F., Apellaniz Ingunza, E. and Hilario, A. (2016). *The upper Maastrichtian, Paleocene and lowermost Ypresian of the Zumaia section*. [Donostia-San Sebastián]: Gipuzkoa Foru Aldundia = Diputación Foral de Gipuzkoa.

Pujol, F., Berner, Z. and Stüben, D., 2006. Palaeoenvironmental changes at the Frasnian/Famennian boundary in key European sections: Chemostratigraphic constraints. *Palaeogeography, Palaeoclimatology, Palaeoecology*, 240(1-2), pp.120-145.

Punekar, J., Keller, G., Khozyem, H., Adatte, T., Font, E. and Spangenberg, J. (2016). A multi-proxy approach to decode the end-Cretaceous mass extinction. *Palaeogeography, Palaeoclimatology, Palaeoecology*, 441, pp.116-136.

Punekar, J., Keller, G., Khozyem, H., Hamming, C., Adatte, T., Tantawy, A. and Spangenberg, J., 2014b. Late Maastrichtian–early Danian high-stress environments and delayed recovery linked to Deccan volcanism. *Cretaceous Research*, 49, pp.63-82.

Punekar, J., Mateo, P., and Keller, G., 2014a, Environmental and biological effects of Deccan volcanism: A global survey. In Keller, G., and Kerr, A.C., eds., Volcanism, Impacts, and Mass Extinctions: Causes and Effects: Geological Society of America Special Paper 505, p. 91–116.

Quantin, P., 1965, Les sols de la République Centrafricaine, Paris: ORSTOM, 16, 113 p.

Querol, X., Chinchon, S. and Lopez-Soler, A., 1989, Iron sulfide precipitation sequence in Albian coals from the Maestrazgo Basin, southeastern Iberian Range, northeastern Spain. *International Journal of Coal Geology*, 11, 171–189.

Ramos-Vázquez, M. and Armstrong-Altrin, J., 2019, Sediment chemistry and detrital zircon record in the Bosque and Paseo del Mar coastal areas from the southwestern Gulf of Mexico. *Marine and Petroleum Geology*, 110, 650–675.

Ramos-Vázquez, M., Armstrong-Altrin, J., Machain-Castillo, M. and Gío-Argáez, F., 2018, Foraminiferal assemblages, ^{14}C ages, and compositional variations in two sediment cores in the western Gulf of Mexico. *Journal of South American Earth Sciences*, 88, 480–496.

Raup, D. M., and J. Sepkoski (1982), Mass extinctions in the marine fossil record, *Science*, 215(4539), pp.1501–1503.

Regnoult, J.M., 1986, Synthèse géologique du Cameroun. Ministère des Mines et de l'Energie, Yaoundé, Cameroun, 119 p.

Reineck, H.E., and Singh, I.B., 1980. Depositional sedimentary environments, with reference to terrigenous Clastics (2nd ed.), Berlin, Springer-Verlag, 551 p.

Renne, P., Arenillas, I., Arz, J., Vajda, V., Gilabert, V. and Bermúdez, H., 2018. Multi-proxy record of the Chicxulub impact at the Cretaceous-Paleogene boundary from Gorgonilla Island, Colombia. *Geology*, 46(6), pp.547-550.

Renne, P., Deino, A., Hilgen, F., Kuiper, K., Mark, D., Mitchell, W., Morgan, L., Mundil, R. and Smit, J., 2013. Time Scales of Critical Events Around the Cretaceous-Paleogene Boundary. *Science*, 339(6120), pp.684-687.

Reyment, R.A. (1963) Studies on Nigerian Upper Cretaceous and Lower Tertiary Ostracoda. Part 2: Danian, Paleocene and Eocene Ostracoda. *Acta Universitatis Stockholmiensis, Stockholm Contributions in Geology* 10, 1–286.

Ridgwell, A. and Schmidt, D., 2010. Past constraints on the vulnerability of marine calcifiers to massive carbon dioxide release. *Nature Geoscience*, 3(3), pp.196-200.

Ridgwell, A., 2005. A Mid Mesozoic Revolution in the regulation of ocean chemistry. *Marine Geology*, 217(3-4), pp.339-357.

Righi, D. and Meunier, A. 1995, Origin of clays by rock weathering and soil formation. In: Velde, B, (ed.), Origin and Mineralogy of clays. Clays and the environment. Springer, Berlin Heidelberg New York, p 43–161.

Rimmer, S. (2004). Geochemical paleoredox indicators in Devonian–Mississippian black shales, Central Appalachian Basin (USA). *Chemical Geology*, 206(3-4), pp.373-391.

Robaszynski, F., Caron, M., Gonzalez Donoso, J.M., and Wonders, A.A.H., 1983–1984, Atlas of Late Cretaceous globotruncanids. *Micropaleontology*, 26(3-4), pp.145–305.

Robert C., Herbin J. P., Deroo G., Giroud d'Argoud G., Chamley H., 1979. L'Atlantique Sud au Crétacé d'après l'étude des minéraux argileux et de la matière organique (legs 39 et 40 DSDP), *Oceanologica Acta*, 2(2), pp. 209-218.

Robert, C., 1980. Climats et courants cénozoïques dans l'Atlantique Sud d'après l'étude des minéraux argileux (legs 3, 39 et 40 DSDP). *Oceanologica Acta*, 3(3), pp. 369-376.

Robert, C., and Maillot, H. (1990). Paleoenvironments in the weddell sea area a n d antarctic climates, as deduced from clay mineral associations a n d geochemical data, odp leg 11. In Barker, P. R, Kennett, J. P., et al. (Eds), Proceedings of the Ocean Drilling Program, Scientific Results, Vol. 113

Robert, C., Kennett, J.P., 1994. Antarctic subtrobical humid episode at the Paleocene– Eocene boundary: clay mineral evidence. *Geology* 22, 211–214.

Rodríguez-Cuicas, M., Montero-Serrano, J. and Garbán, G., 2019. Paleoenvironmental changes during the late Albian oceanic anoxic event 1d: An example from the Capacho Formation, southwestern Venezuela. *Palaeogeography, Palaeoclimatology, Palaeoecology*, 521, pp.10-29.

Rohde, R. A., and R. A. Muller (2005), Cycles in fossil diversity, *Nature*, 434(7030), pp.208–210.

Röhl, U., Westerhold, T., Bralower, T. and Zachos, J. (2007). On the duration of the Paleocene-Eocene thermal maximum (PETM). *Geochemistry, Geophysics, Geosystems*, 8(12), pp.1-13.

Rudnick, R. and Gao, S., 2003. Composition of the Continental Crust. *Treatise on Geochemistry*, pp.1-64.

Ruffell, A., McKinley, J. and Worden, R. (2002). Comparison of clay mineral stratigraphy to other proxy palaeoclimate indicators in the Mesozoic of NW Europe. *Philosophical Transactions of the Royal Society A: Mathematical, Physical and Engineering Sciences*, 360(1793), pp.675-693.

Sageman, B. and Lyons, T., 2003. Geochemistry of Fine-grained Sediments and Sedimentary Rocks. *Treatise on Geochemistry*, pp.115-158.

Salard-Chebodaeff, M., 1980, Palynologie camerounaise. I. Pollens de la Mangrove et des fourrés arbustifs côtiers. Compte rendus Congres National des Sociétés savantes, 106, p. 125–136.

Salard-Cheboldaeff, M., 1977, Palynologie du bassin sédimentaire littoral du Cameroun dans ses rapports avec la stratigraphie et la paleoécologie. Thèse de Doctorat d'Etat ès sciences naturelles, Université Pierre et Marie Curie, Paris, 262p.

Salard-Cheboldaeff, M., 1990, Intertropical African palynostratigraphy from Cretaceous to late quaternary times. *Journal of African Earth Sciences* (and the Middle East), 11, 1–24.

Sanders, D., Keller, G., Schlagintweit, F. and Studeny, M., 2019. Cretaceous-Paleocene transition along a rocky carbonate shore: Implications for the Cretaceous-Paleocene boundary event in shallow platform environments and correlation to the deep sea. In: T. Adatte, D. Bond and G. Keller, ed., *Mass Extinctions, Volcanism, and Impacts: New Developments*. Geological Society of America.

Sanei, H., Grasby, S.E., and Beauchamp, B., 2012. Latest Permian mercury anomalies. *Geology*, 40, pp. 63–66.

Schaller, T., Moor, H. and Wehrli, B., 1997, Sedimentary profiles of Fe, Mn, V, Cr, As and Mo as indicators of benthic redox conditions in Baldeggersee. *Aquatic Sciences*, 59, 345–361.

Schlanger, S., 1988. Strontium Storage and Release During Deposition and Diagenesis of Marine Carbonates Related to Sea-Level Variations. *Physical and Chemical Weathering in Geochemical Cycles*, pp.323-339.

Schmidt, A., Skeffington, R., Thordarson, T., Self, S., Forster, P., Rap, A., Ridgwell, A., Fowler, D., Wilson, M., Mann, G., Wignall, P. and Carslaw, K., 2015. Selective environmental stress from sulphur emitted by continental flood basalt eruptions. *Nature Geoscience*, 9(1), pp.77-82.

Schmitz, B. and Pujalte, V. (2003). Sea-level, humidity, and land-erosion records across the Initial Eocene Thermal Maximum from a continental-marine transect in northern Spain. *Geology*, 31, pp. 689-692

Schmitz, B. and Pujalte, V. (2007). Abrupt increase in seasonal extreme precipitation at the Paleocene-Eocene boundary. *Geology*, 35(3), p.215.

Schmitz, B., Asaro, F., Molina, E., Monechi, S., von Salis, K. and Speijer, R. (1997). High-resolution iridium, $\delta^{13}C$, $\delta^{18}O$, foraminifera and nannofossil profiles across the latest Paleocene benthic extinction event at Zumaya, Spain. *Palaeogeography, Palaeoclimatology, Palaeoecology*, 133(1-2), pp.49-68.

Schmitz, B., Keller, G. and Stenvall, O. (1992). Stable isotope and foraminiferal changes across the Cretaceous—Tertiary boundary at Stevns Klint, Denmark: Arguments for long-term oceanic instability before and after bolide-impact event. *Palaeogeography, Palaeoclimatology, Palaeoecology*, 96(3-4), pp.233-260.

Schmitz, B., Peucker-Ehrenbrink, B., Heilmann-Clausen, C., Åberg, G., Asaro, F. and Lee, C. (2004). Basaltic explosive volcanism, but no comet impact, at the Paleocene–Eocene boundary: high-resolution chemical and isotopic records from Egypt, Spain and Denmark. *Earth and Planetary Science Letters*, 225(1-2), pp.1-17.

Schmitz, B., Pujalte, V., 2003. Sea-level, humidity, and land-erosion records across the initial Eocene thermal maximum from a continental-marine transect in northern Spain. *Geology* 31, 689–692.

Schmitz, B., Pujalte,V., Molina,E., Monechi,S., Orue-Etxebarria,X., Speijer,R.P., Alegret, L., Apellaniz,E., Arenillas,I., Aubry,M.P., Baceta,J.I., Berggren,W.A., Bernaola, G., Caballero,F., Clemmensen, A., Dinarès-Turell, J., Dupuis, C., Heilmann-Clausen, C., Hilario Orús, A., Knox, R., Martín-Rubio, M., Ortiz,S., Payros, A., Petrizzo, M.R., von Salis, K., Sprong,J., Steurbaut,E. and Thomsen, E. (2011). The Global Stratotype Sections and Points for the bases of the Selandian (Middle Paleocene) and Thanetian (Upper Paleocene) stages at Zumaia, Spain. *Episodes* 34, pp. 220–243.

Schmitz, B., Speijer, R. and Aubry, M. (1996). Latest Paleocene benthic extinction event on the southern Tethyan shelf (Egypt): Foraminiferal stable isotopic ($\delta^{13}C$, $\delta^{18}O$) records. *Geology*, 24(4), p.347.

Schobben, M., Ullmann, C., Leda, L., Korn, D., Struck, U., Reimold, W., Ghaderi, A., Algeo, T. and Korte, C., 2016. Discerning primary versus diagenetic signals in carbonate carbon and oxygen isotope records: An example from the Permian–Triassic boundary of Iran. *Chemical Geology*, 422, pp.94-107.

Schöllhorn, I., Adatte, T., Van de Schootbrugge, B., Houben, A., Charbonnier, G., Janssen, N. and Föllmi, K., 2020. Climate and environmental response to the break-up of Pangea during the Early Jurassic (Hettangian-Pliensbachian); the Dorset coast (UK) revisited. *Global and Planetary Change*, 185, p.103096.

Schrag, D., DePaolo, D. and Richter, F. (1995). Reconstructing past sea surface temperatures: Correcting for diagenesis of bulk marine carbonate. *Geochimica et Cosmochimica Acta*, 59(11), pp.2265-2278.

Schulte, P., Alegret, L., Arenillas, I., Arz, J., Barton, P., Bown, P., Bralower, T., Christeson, G., Claeys, P., Cockell, C., Collins, G., Deutsch, A., Goldin, T., Goto, K., Grajales-Nishimura, J., Grieve, R., Gulick, S., Johnson, K., Kiessling, W., Koeberl, C., Kring, D., MacLeod, K., Matsui, T., Melosh, J., Montanari, A., Morgan, J., Neal, C., Nichols, D., Norris, R., Pierazzo, E., Ravizza, G., Rebolledo-Vieyra, M., Reimold, W., Robin, E., Salge, T., Speijer, R., Sweet, A., Urrutia-Fucugauchi, J., Vajda, V., Whalen, M. and Willumsen, P., 2010. The Chicxulub Asteroid Impact and Mass Extinction at the Cretaceous-Paleogene Boundary. *Science*, 327(5970), pp.1214-1218.

Schulte, P., Scheibner, C. and Speijer, R. (2011). Fluvial discharge and sea-level changes controlling black shale deposition during the Paleocene–Eocene Thermal Maximum in the Dababiya Quarry section, Egypt. *Chemical Geology*, 285(1-4), pp.167-183.

Schulte, P., Schwark, L., Stassen, P., Kouwenhoven, T., Bornemann, A. and Speijer, R. (2013). Black shale formation during the Latest Danian Event and the Paleocene-Eocene Thermal Maximum in central Egypt: Two of a kind?. *Palaeogeography, Palaeoclimatology, Palaeoecology*, 371, pp.9-25.

Scotese, C.R., 2013. Map folio 14, PETM (55.8 Ma, Thanetian/Ypresian boundary), PALEOMAP PaleoAtlas for ArcGIS. Cenozoic. vol. 1. PALEOMAP Project, Evanston, IL.

Scotese, C.R., 2014. Atlas of Late Cretaceous Paleogeographic Maps, PALEOMAP Atlas for ArcGIS, volume 2, The Cretaceous, Maps 16 – 22, Mollweide Projection, PALEOMAP Project, Evanston, IL.

Self, S., Jay, A., Widdowson, M. and Keszthelyi, L., 2008. Correlation of the Deccan and Rajahmundry Trap lavas: Are these the longest and largest lava flows on Earth? *Journal of Volcanology and Geothermal Research*, 172(1-2), pp.3-19.

Sepúlveda, J., Alegret, L., Thomas, E., Haddad, E., Cao, C. and Summons, R., 2019. Stable Isotope Constraints on Marine Productivity Across the Cretaceous-Paleogene Mass Extinction. *Paleoceanography and Paleoclimatology*, 34(7), pp.1195-1217.

Serrano, L., Ferrari, L., Martínez, M., Petrone, C. and Jaramillo, C., 2011. An integrative geologic, geochronologic and geochemical study of Gorgona Island, Colombia: Implications for the formation of the Caribbean Large Igneous Province. *Earth and Planetary Science Letters*, 309(3-4), pp.324-336.

Sheehan P. and Fastovsky D. 1992. Major extinctions of land-dwelling vertebrates at the Cretaceous-Tertiary boundary, eastern Montana. *Geology*, 20, pp.556–560.

Sheldon, N. and Retallack, G., 2004, Regional Paleoprecipitation Records from the Late Eocene and Oligocene of North America. *The Journal of Geology*, 112, 487–494.

Sheldon, N. and Tabor, N., 2009, Quantitative paleoenvironmental and paleoclimatic reconstruction using paleosols. *Earth-Science Reviews*, 95, 1–52.

Sheldon, N., 2006, Quaternary Glacial-Interglacial Climate Cycles in Hawaii. The Journal of Geology, 114, 367–376.

Sheldon, N., Retallack, G. and Tanaka, S., 2002, Geochemical Climofunctions from North American Soils and Application to Paleosols across the Eocene-Oligocene Boundary in Oregon. *The Journal of Geology*, 110, 687–696.

Shrivastava, J., Mukhopadhyay, S. and Pal, S. (2013). Chemico-mineralogical attributes of clays from the late Cretaceous–early Palaeogene succession of the Um Sohryngkew river section of Meghalaya, India: Palaeoenvironmental inferences and the K/Pg boundary. *Cretaceous Research*, 45, pp.247-257.

Sial, A., Chen, J., Lacerda, L., Frei, R., Tewari, V., Pandit, M., Gaucher, C., Ferreira, V., Cirilli, S., Peralta, S., Korte, C., Barbosa, J. and Pereira, N., 2016. Mercury enrichment and Hg isotopes in Cretaceous–Paleogene boundary successions: Links to volcanism and palaeoenvironmental impacts. *Cretaceous Research*, 66, pp.60-81.

Sial, A., Chen, J., Lacerda, L., Peralta, S., Gaucher, C., Frei, R., Cirilli, S., Ferreira, V., Marquillas, R., Barbosa, J., Pereira, N. and Belmino, I., 2014. High-resolution Hg chemostratigraphy: A contribution to the distinction of chemical fingerprints of the Deccan volcanism and Cretaceous–Paleogene Boundary impact event. *Palaeogeography, Palaeoclimatology, Palaeoecology*, 414, pp.98-115.

Sial, A.N., Lacerda, L.D., Ferreira, V.P., Frei, R., Marquillas, R.A., Barbosa, J.A., Gaucher, C., Windmoller, C.C., and Pereira, N.S., 2013, Mercury as a proxy for volcanic activity during extreme environmental turnover: The Cretaceous- Paleogene transition: *Palaeogeography, Palaeoclimatology, Palaeoecology*, 387, pp. 153–164.

Singer, A. (1984). The paleoclimatic interpretation of clay minerals in sediments — a review. *Earth-Science Reviews*, 21(4), pp.251-293.

Singh, P. and Rajamani, V., 2001, REE geochemistry of recent clastic sediments from the Kaveri floodplains, southern India: Implication to source area weathering and sedimentary processes. *Geochimica et Cosmochimica Acta*, 65, 3093–3108.

Singh, P., 2009, Major, trace and REE geochemistry of the Ganga River sediments: Influence of provenance and sedimentary processes. *Chemical Geology*, 266, 242–255.

Slack, J., Grenne, T. and Bekker, A., 2009. Seafloor-hydrothermal Si-Fe-Mn exhalites in the Pecos greenstone belt, New Mexico, and the redox state of ca. 1720 Ma deep seawater. *Geosphere*, 5(3), pp.302-314.

Sluijs, A. and Dickens, G., 2012. Assessing offsets between the $\delta^{13}C$ of sedimentary components and the global exogenic carbon pool across early Paleogene carbon cycle perturbations. *Global Biogeochemical Cycles*, 26(4), p.n/a-n/a.

Sluijs, A., Bowen, G.J., Brinkhuis, H., Lourens, L.J., Thomas, E., 2007. The Palaeocene– Eocene Thermal Maximum super greenhouse: biotic and geochemical signatures, age models and mechanisms of global change. In: Williams, M., Haywood, A.M., Gregory, F.J., Schmidt, D.N. (Eds.), Deep time perspectives on climate change: marrying the signal from computer models and biological proxies. The Micropalaeontological Society, Special Publications, *The Geological Society, London* 2, 323–349.

Sluijs, A., Brinkhuis, H., Schouten, S., Bohaty, S.M., John, C.M., Zachos, J.C., Reichart, G.-J., Sinninghe Damsté, J.S., Crouch, E.M., Dickens, G.R., 2007. Environmental precursors to rapid light carbon injection at the Palaeocene/Eocene boundary. *Nature*, 450 (7173), pp.1218–1221.

Sluijs, A., Schouten, S., Pagani, M.,Woltering,M., Brinkhuis, H., Damsté, J.S.S., Dickens, G.R., Huber, M., Reichart, G.-J., Stein, R., Matthiessen, J., Lourens, L.J., Pedentchouk, N., Backman, J., Moran, K., the Expedition 302 Scientists, 2006. Subtropical Arctic Ocean temperatures during the Palaeocene/Eocene thermal maximum. *Nature*, 441 (7093):610–613.

Sluijs, A., U. Röhl, S. Schouten, H.-J. Brumsack, F. Sangiorgi, J. S. Sinninghe Damsté, and H. Brinkhuis (2008), Arctic late Paleocene–early Eocene paleoenvironments with special emphasis on the Paleocene-Eocene thermal maximum (Lomonosov Ridge, Integrated Ocean Drilling Program Expedition 302), *Paleoceanography*, 23, PA1S11.

Smit J. 1999. The global stratigraphy of the Cretaceous-Tertiary boundary impact ejecta. *Annual Review of Earth and Planetary Science*, 27, pp.75–113.

Smit, J. (1990). Meteorite impact, extinctions and the Cretaceous- Tertiary Boundary. *Geologie en Mijnbouw*, 69, pp.187-204.

Smit, J. and Hertogen, J. (1980). An extraterrestrial event at the Cretaceous–Tertiary boundary. *Nature*, 285(5762), pp.198-200.

Smit, J. and Romein, A. (1985). A sequence of events across the Cretaceous-Tertiary boundary. *Earth and Planetary Science Letters*, 74(2-3), pp.155-170.

SNH, 2005. Stratigraphie séquentielle et tectonique des dépôts mesozoic syn-rifts du Bassin de Kribi/Campo. (Auteurs : Ntamak-Nida, M.J., Mpesse, J.E., Ketchemen-Tandia, B., Ndong Ondo, S., Courville, P., Baudin, F., Rapport Interne, 11 planches, 2 rapports annexes d'analyses).

Soliman, M., Aubry, M., Schmitz, B. and Sherrell, R. (2011). Enhanced coastal paleoproductivity and nutrient supply in Upper Egypt during the Paleocene/Eocene Thermal Maximum (PETM): Mineralogical and geochemical evidence. *Palaeogeography, Palaeoclimatology, Palaeoecology*, 310(3-4), pp.365-377.

Spangenberg, J. and Herlec, U. (2006). Hydrocarbon Biomarkers in the Topla-Mezica Zinc-Lead Deposits, Northern Karavanke/Drau Range, Slovenia: Paleoenvironment at the Site of Ore Formation. *Economic Geology*, 101(5), pp.997-1021.

Spangenberg, J., Ferrer, M., Tschudin, P., Volken, M. and Hafner, A. (2010). Microstructural, chemical and isotopic evidence for the origin of late neolithic leather recovered from an ice field in the Swiss Alps. *Journal of Archaeological Science*, 37(8), pp.1851-1865.

Speijer, R. and Van Der Zwaan, G. (1996). Extinction and survivorship of southern Tethyan Benthic foraminifera across the Cretaceous/Palaeogene boundary. *Geological Society, London, Special Publications*, 102(1), pp.343-371.

Speijer, R. P., and T. Wagner (2002), Sea-level changes and black shales associated with the Late Paleocene Thermal Maximum (LPTM): Organic-geochemical and micropaleontologic evidence from the southern Tethyan margin (Egypt– Israel), in Catastrophic Events and Mass Extinctions: Impacts and Beyond, edited by C. Koeberl and K. G. MacLeod, *Geological Society of America Special Pape*r, 356, pp.533–549.

Speijer, R.P., Scheibner, C., Stassen, P., Morsi, A.M.M., 2012. Response of marine ecosystems to deep-time global warming: a synthesis of biotic patterns across the Paleocene–Eocene Thermal Maximum (PETM). *Austrian Journal of Earth Sciences*, 105, pp.6–16.

Speijer, R.P., Van der Zwaan, G.J., and Schmitz, B. (1996). The impact of Paleocene/Eocene boundary events on middle neritic benthic foraminiferal assemblages from Egypt. *Marine Micropaleontology*, 28, pp. 99– 132.

Speijer, R.P., Wagner, T. (2002). Sea-level changes and black shales associated with the late Paleocene Thermal Maximum: Organic-geochemical and Micropaleontologic Evidence from the Southern Tethyan Margin (Egypt-Israel). 356. *GSA Spec. Publ.*, pp. 533–549.

Sprain, C., Renne, P., Vanderkluysen, L., Pande, K., Self, S. and Mittal, T., 2019. The eruptive tempo of Deccan volcanism in relation to the Cretaceous-Paleogene boundary. *Science*, 363(6429), pp.866-870.

Stanley, S.M. 1999. Earth System History. W.H. Freeman and Company, New York, 615 p.

Stassen, P., Dupuis, C., Steurbaut, E., Yans, J., Speijer, R.P. (2012). Perturbation of a Tethyan coastal environment during the Paleocene-Eocene thermal maxium in Tunisia (Sidi Nasseur and Wadi Mezaz). *Palaeogeography. Palaeoclimatology. Palaeoecology*. 317-318, 66–92.

Storey, M., Duncan, R. and Swisher, C. (2007). Paleocene-Eocene Thermal Maximum and the Opening of the Northeast Atlantic. *Science*, 316(5824), pp.587-589.

Storey, M., Mahoney, J., Kroenke, L. and Saunders, A., 1991. Are oceanic plateaus sites of komatiite formation? *Geology*, 19(4), p.376.

Stott, L. D., Kennett, J. P., Shackleton, N. J., Corfield, R. C., 1990. The evolution of Antarctic surface waters during the Paleogene: Inferences from the stable isotopic composition of planktonic foraminifers, ODP Leg 113. In: Barker, P. F, Kennett, J. P. et al. (Eds.), Proc. Ocean Drill, Progr, Scient. Res., 113 - College Station, TX, Ocean Drill. Progr,: 849–863.

Stüben, D., Kramar, U., Berner, Z., Meudt, M., Keller, G., Abramovich, S., Adatte, T., Hambach, U. and Stinnesbeck, W., 2003. Late Maastrichtian paleoclimatic and paleoceanographic changes inferred from Sr/Ca ratio and stable isotopes. *Palaeogeography, Palaeoclimatology, Palaeoecology*, 199(1-2), pp.107-127.

Stüben, D., Kramar, U., Berner, Z., Stinnesbeck, W., Keller, G. and Adatte, T., 2002. Trace elements, stable isotopes, and clay mineralogy of the Elles II K–T boundary section in Tunisia: indications for sea level fluctuations and primary productivity. *Palaeogeography, Palaeoclimatology, Palaeoecology*, 178(3-4), pp.321-345.

Stüben, D., Kramar, U., Harting, M., Stinnesbeck, W. and Keller, G. (2005). High-resolution geochemical record of Cretaceous-Tertiary boundary sections in Mexico: New constraints on the K/T and Chicxulub events. *Geochimica et Cosmochimica Acta*, 69(10), pp.2559-2579.

Šucha, V., Kraust, I., Gerthofferová, H., Peteš, J. and Sereková, M., 1993. Smectite to Illite Conversion in Bentonites and Shales of the East Slovak Basin. *Clay Minerals*, 28(2), pp.243-253.

Svensen, H., Planke, S. and Corfu, F., 2010. Zircon dating ties NE Atlantic sill emplacement to initial Eocene global warming. *Journal of the Geological Society*, 167(3), pp.433-436.

Svensen, H., Planke, S., Malthe-Sørenssen, A., Jamtveit, B., Myklebust, R., Rasmussen Eidem, T. and Rey, S. (2004). Release of methane from a volcanic basin as a mechanism for initial Eocene global warming. *Nature*, 429(6991), pp.542-545.

Swart, P. and Eberli, G. (2005). The nature of the $\delta^{13}C$ of periplatform sediments: Implications for stratigraphy and the global carbon cycle. *Sedimentary Geology*, 175(1-4), pp.115-129.

Swart, P., 2015. The geochemistry of carbonate diagenesis: The past, present and future. *Sedimentology*, 62(5), pp.1233-1304.

Sweet R., Braman D., and Lerbekmo J. 1990. Palynifloral response to K/T boundary events: A transitory interruption within a dynamic system. Global catastrophes in Earth history: The proceedings of an interdisciplinary conference on impacts, volcanism and mass mortality, edited by Sharpton V. L. and Ward P. W. GSA Special Paper #247. Boulder, Colorado: *Geological Society of America.* pp.457–469.

Takashima, R., Nishi, H., Huber, B. and Leckie, R., 2006. Greenhouse World and the Mesozoic Ocean. *Oceanography*, 19(4), pp.82-92.

Takayama, H., Tada, R., Matsui, T., Iturralde-Vinent, M., Oji, T., Tajika, E., Kiyokawa, S., Garcia, D., Okada, H., Hasegawa, T. and Toyoda, K., 2000. Origin of the Peñalver Formation in northwestern Cuba and its relation to K/T boundary impact event. *Sedimentary Geology*, 135(1-4), pp.295-320.

Tapia-Fernandez, H., Armstrong-Altrin, J. and Selvaraj, K., 2017, Geochemistry and U–Pb geochronology of detrital zircons in the Brujas beach sands, Campeche, Southwestern Gulf of Mexico, Mexico. *Journal of South American Earth Sciences*, 76, 346–361.

Tawfik, H., Salah, M., Maejima, W., Armstrong-Altrin, J., Abdel-Hameed, A. and El Ghandour, M., 2017, Petrography and geochemistry of the Lower Miocene Moghra sandstones, Qattara Depression, north Western Desert, Egypt. *Geological Journal*, 53(5), 1938–1953.

Taylor, K., Willumsen, P., Hollis, C. and Pancost, R., 2018. South Pacific evidence for the long-term climate impact of the Cretaceous/Paleogene boundary event. *Earth-Science Reviews*, 179, pp.287-302.

Taylor, K.G., and Macquaker, J.H.S., 2000, Spatial and temporal distribution of authigenic minerals in continental shelf sediments: implications for sequence stratigraphic analysis. In Glenn, C., Prévôt-Lucas, L. and Lucas, J. (eds.), Marine Authigenesis: Microbial to Global. SEPM Society for Sedimentary Geology, Special Publication, 66, p. 309–323.

Taylor, S.R. and MacLennan, S.M., 1985, The continental crust: its composition and evolution. Blackwell Scientific Publications, Oxford, 312 p.

Thibodeau, A.M., Ritterbush, K., Yager, J.A., West, A.J., Ibarra, Y., Bottjer, D., Berelson, W.M., Bergquist, B.A., Corsetti, F.A., 2016. Mercury anomalies and the timing of biotic recovery following the end-Triassic mass extinction. *Nature Communications*, 7, 11147.

Thiry, M., 2000. Palaeoclimatic interpretation of clay minerals in marine deposits: an outlook from the continental origin. *Earth-Science Reviews*, 49(1-4), pp.201-221.

Thiry, M., Aubry, M.-P., Dupuis, C., Sinha, A., Stott, L.D., Berggren, W. A., 2006. The Sparnacian deposits of the Paris Basin: $\delta^{18}O$ Isotope stratigraphy. *Stratigraphy*, 2: 65– 100.

Thiry, M., Dupuis, C., Aubry, M.-P., Berggren, W. A., Ellison, R. A., Knox, O'B, R., Sinha, A., Stott, L., 1998. Tentative correlations between continental deposits of the Argiles Plastiques (Paris Basin) and Reading Beds (London Basin), based on chemostratigraphy. In: Rey, J., (Ed.). Strata, 1: 125–129

Thomas, E. (2007). Cenozoic mass extinctions in the deep sea: What perturbs the largest habitat on Earth? *Special Paper 424: Large Ecosystem Perturbations: Causes and Consequences*, pp.1-23.

Thomas, E., 1998. The biogeography of the late Paleocene benthic foraminiferal extinction. In: Aubry, M.-P., Lucas, S., Berggren, W.A. (Eds.), Late Paleocene–Early Eocene Biotic and Climatic Events in the Marine and Terrestrial Records. *University Press, Columbia*, pp. 214–243.

Thomas, E., 2003. Extinction and food at the seafloor: a high-resolution benthic foraminiferal record across the Initial Eocene Thermal Maximum, Southern Ocean Site 690. In: Wing, S.L., Gingerich,

P.D., Schmitz, B., Thomas, E. (Eds.), Causes and Consequences of Globally Warm Climates in the Early Paleogene. 369. *Geological Society of America Special Publication*, pp. 319–332.

Thomas, E., 2007. Cenozoic mass extinctions in the deep sea: what perturbs the largest habitat on Earth? In: Monechi, S., Coccioni, R., Rampino, M.R. (Eds.), Large Ecosystem Perturbations: Causes and Consequences. 424. *Geological Society of America Speial. Papers*, pp. 1–23.

Thomas, E., Shackleton, N. J., 1996. The Paleocene-Eocene benthic foraminiferal extinction and stable isotope anomalies. In:. Knox, R. W. O'B., Corfield, R. M., Dunay, R. E. (Eds.), Correlation of the early Paleogene in Northwest Europe. *Geological Society, Special Publication*, 101: 401–441.

Thompson, E. and Schmitz, B. (1997). Barium and the Late Paleocene δ13C maximum: Evidence of increased marine surface productivity. *Paleoceanography*, 12(2), pp.239-254.

Tjalsma, R. and Lohmann, G. (1983). *Paleocene-Eocene bathyal and abyssal benthic Foraminifera from the Atlantic Ocean*. New York: Micropaleontology Press, American Museum of Natural History.

Toon, O., Zahnle, K., Morrison, D., Turco, R. and Covey, C., 1997. Environmental perturbations caused by the impacts of asteroids and comets. *Reviews of Geophysics*, 35(1), pp.41-78.

Tribovillard, N., Algeo, T., Lyons, T. and Riboulleau, A. (2006). Trace metals as paleoredox and paleoproductivity proxies: An update. *Chemical Geology*, 232(1-2), pp.12-32.

Tripati, A., Elderfield, H., 2005. Deep-sea temperature and circulation changes at the Paleocene–Eocene thermal maximum. *Science* 308, 1894–1898.

Vajda V. and McLoughlin S. 2007. Extinction and recovery patterns of the vegetation across Cretaceous–Palaeogene boundary—A tool for unravelling the causes of the end-Permian mass-extinction. *Review of Palaeobotany and Palynology*, 144, pp.99–112.

Vajda V., Raine J. I., and Hollis C. 2001. Indication of global deforestation at the Cretaceous-Tertiary boundary by New Zealand fernspike. *Science*, 294, pp.1700–1702.

Vajda, V. and McLoughlin, S., 2005. A new Maastrichtian-PaleoceneAzollaspecies from of Bolivia, with a comparison of the global record of coeval Azolla microfossils. *Alcheringa: An Australasian Journal of Palaeontology*, 29(2), pp.305-329.

Vajda, V., 2004. Fungal Proliferation at the Cretaceous-Tertiary Boundary. *Science*, 303(5663), pp.1489-1489.

Van der Weijden, C. (2002). Pitfalls of normalization of marine geochemical data using a common

Vergés, J. (1993). Estudi geologic del vessant sud del Pirineu oriental i central, Evolució cinematica en 3D. PhD thesis, University of Barcelona

Wang, L., Shi, X. and Jiang, G., 2012, Pyrite morphology and redox fluctuations recorded in the Ediacaran Doushantuo Formation. Palaeogeography, Palaeoclimatology, Palaeoecology, 333-334, 218–227.

Weaver, C.E., 1989. Clays, muds and shales. In: Development in Sedimentology vol. 44. Elsevier, Amsterdam, 819 pp

Wedepohl, K.H., 1971, Environmental Influences on the Chemical Composition of Shales and Clays. *Physics and Chemistry of the Earth*, 8, 307–333.

Wedepohl, K.H., 1991, Chemical-Composition and Fractionation of the Continental-Crust. Geologische Rundschau, 80, 207–223.

Wedepohl, K.H., 1991. The composition of the upper earth's crust and the natural cycles of selected metals. Metals in natural raw materials. Natural Resources. In: Merian, E. (Ed.), Metals and Their Compounds in the Environment. VCH, Weinheim, pp. 3 – 17.

Westerhold, T., Rohl, U., McCarren, H.K., Zachos, J.C., 2009. Latest on the absolute age of the Paleocene–Eocene Thermal Maximum (PETM): new insights from exact stratigraphic position of key ash layers +19 and −17. *Earth and Planetary Science Letters*, 287, pp.412–419.

White, R.V., Saunders, A.D., 2005. Volcanism, impact and mass extinctions: incredible or credible coincidences? In: Kerr, A. (Ed.), Volcanism, Impact and Mass Extinctions. *Lithos*, 79, pp.299–316.

Widodo, S., Oschmann, W., Bechtel, A., Sachsenhofer, R., Anggayana, K. and Puettmann, W., 2010, Distribution of sulfur and pyrite in coal seams from Kutai Basin (East Kalimantan, Indonesia): Implications for paleoenvironmental conditions. *International Journal of Coal Geology*, 81, 151–162.

Wiedmann, J. (1988). The Basque coastal sections of the K/T boundary - A key to understanding "mass extinction" in the fossil record. *Revista Española de Micropaleontologia*, (Extra), pp.127-140.

Wignall, P. and Myers, K., 1988, Interpreting benthic oxygen levels in mudrocks: A new approach. *Geology*, 16, p.452–455.

Wignall, P.B., 2001. Large igneous provinces and mass extinctions. *Earth Science Reviews*, 53, pp.1–33.

Wing, S.L., Harrington, G.J., Smith, F.A., Bloch, J.I., Boyer, D.M., Freeman, K.H., 2005. Transient floral change and rapid global warming at the Paleocene–Eocene boundary. *Science* 310, 993–996.

Wronkiewicz, D. and Condie, K., 1987, Geochemistry of Archean shales from the Witwatersrand Supergroup, South Africa: Source-area weathering and provenance. *Geochimica et Cosmochimica Acta*, 51, 2401–2416.

Wronkiewicz, D. and Kent C., 1989, Geochemistry and provenance of sediments from the Pongola Supergroup, South Africa: Evidence for a 3.0-Ga-old continental craton. *Geochimica et Cosmochimica Acta*, 53, 1537–1549.

Zachos, J., Lohmann, K., Walker, J. and Wise, S., 1993. Abrupt Climate Change and Transient Climates during the Paleogene: A Marine Perspective. *The Journal of Geology*, 101(2), pp.191-213.

Zachos, J., Pagani, M., Sloan, L., Thomas, E. and Billups, K. (2001). Trends, Rhythms, and Aberrations in Global Climate 65 Ma to Present. *Science*, 292(5517), pp.686-693.

Zachos, J.C., Dickens, G.R., Zeebe, R.E., 2008. An early Cenozoic perspective on greenhouse warming and carbon-cycle dynamics. *Nature* 451, 279–283.

Zachos, J.C., Röhl, U., Schellenberg, S.A., Sluijs, A., Hodell, D.A., Kelly, D.C., Thomas, E., Nicolo, M., Raffi, I., Lourens, L.J., McCarren, H., Kroon, D., 2005. Rapid acidification of the ocean during the Paleocene–Eocene Thermal Maximum. *Science* 308 (5728), 1611– 1615.

Zachos, J.C., Wara, M.W., Bohaty, S., Delaney, M.L., Petrizzo, M.R., Brill, A., Bralower, T.J., Premoli-Silva, I., 2003. A transient rise in tropical sea surface temperature during the Paleocene–Eocene Thermal Maximum. *Science* 302 (5650), 1551–1554.

Zaghbib-Turki, D., Karoui-Yaakoub, N., Rocchia, R., Robin, E. and Belayouni, H. (2000). Enregistrement des événements remarquables de la limite Crétacé–Tertiaire dans la coupe d'Ellès (Tunisie). *Comptes Rendus de l'Académie des Sciences - Series IIA - Earth and Planetary Science*, 331(2), pp.141-149.

Zaghbib-Turki, D., Karoui-Yaakoub, N., Said-Benzarti, R., Rocchia, R. and Robin, E. (2001). Révision de la limite Crétacé-Tertiaire de la coupe d'Ellès (Tunisie): proposition d'un nouveau parastratotype. *Geobios*, 34(1), pp.25-37.

Zeebe, R.E., 2013. What caused the long duration of the Paleocene–Eocene Thermal Maximum? *Paleoceanography*, 28, pp.440–452.

Zhou, C. and Jiang, S., 2009, Palaeoceanographic redox environments for the lower Cambrian Hetang Formation in South China: Evidence from pyrite framboids, redox sensitive trace elements, and sponge biota occurrence. *Palaeogeography, Palaeoclimatology, Palaeoecology*, 271, 279–286.

Zintwana, M., Cawthorn, R., Ashwal, L., Roelofse, F. and Cronwright, H. (2012). Mercury in the Bushveld Complex, South Africa, and the Skaergaard Intrusion, Greenland. *Chemical Geology*, 320-321, pp.147-155.

Zwingmann, H., Clauer, N. and Gaupp, R. (1999). Structure-related geochemical (REE) and isotopic (K-Ar, Rb-Sr, $\delta^{18}O$) characteristics of clay minerals from Rotliegend sandstone reservoirs (Permian, northern Germany). *Geochimica et Cosmochimica Acta*, 63(18), pp.2805-2823.

ANNEXES

ANNEX I: AFFILIATED PAPERS

1. **André Mbabi Bitchong**, Thierry Adatte, Gilbert-François Ngon Ngon, Simon Ngos III and Paul Bilong (2020). Palynology, mineralogy and geochemistry of sediments in Tondè locality, northern part of Douala sub-basin, Cameroon, Central Africa: implication on paleoenvironment. *Geosciences Journal*, pp.

2. Gilbert François Ngon Ngon, **André Mbabi Bitchong**, Joël Simon Mbaïa, Simon Ngos III, Rose Yongue Fouateu and Paul Bilong (2019). Geochemistry of pyriteous mudrocks of the cenozoic N'Kapa formation in Douala Sub-basin, western Cameroon (Central Africa): Source rock weathering, provenance, paleo-redox conditions and tectonic settings. *Journal of African Earth Sciences*, 156, pp. 44-57.

3. Paula Mateo, Gerta Keller, Thierry Adatte, **André M. Bitchong**, Jorge E. Spangenberg, Torsten Vennemann, and Christopher J. Hollis (2019). Deposition and age of Chicxulub impact spherules on Gorgonilla Island, Colombia. *GSA Bulletin*, 132 (1-2), pp. 215–232.

4. Gerta Keller, Paula Mateo, Jahnavi Punekar, Hassan Khozyem, Brian Gertsch, Jorge Spangenberg, **Andre Mbabi Bitchong** and Thierry Adatte (2018). Environmental changes during the Cretaceous-Paleogene mass extinction and Paleocene-Eocene Thermal Maximum: Implications for the Anthropocene. *Gondwana Research*, 56, pp. 69–89.

5. Eric Font, Thierry Adatte, Mariana Andrade, Gerta Keller, **André Mbabi Bitchong**, Claire Carvallo, Joana Ferreira, Zenaida Diogo, José Mirão. Deccan volcanism induced high-stress environment during the Cretaceous–Paleogene transition at Zumaia, Spain: Evidence from magnetic, mineralogical and biostratigraphic records. *Earth and Planetary Science Letters*, 484, pp. 53–66.

Article

https://doi.org/10.1007/s12303-020-0021-z
pISSN 1226-4806 eISSN 1598-7477

Geosciences Journal GJ

Palynology, mineralogy and geochemistry of sediments in Tondè locality, northern part of Douala sub-basin, Cameroon, Central Africa: implication on paleoenvironment

André Mbabi Bitchong[1,2]*, Thierry Adatte[3], Gilbert-François Ngon Ngon[4], Simon Ngos III[1,2], and Paul Bilong[2]

[1]Department of Mining, Petroleum, Gas and Water Resources Exploration, Faculty of Mines and Petroleum Industries (FMIP), University of Maroua, P.O. Box 08 Kaélé, Cameroon
[2]Department of Earth Sciences, Faculty of Science, University of Yaoundé 1, P.O. Box 812 Yaoundé, Cameroon
[3]Institute of Earth Sciences (ISTE), University of Lausanne, 1015 Lausanne, Switzerland
[4]Department of Earth Sciences, Faculty of Science, University of Douala, P.O. Box 24157 Douala, Cameroon

ABSTRACT: A multi-proxy study, including mineralogy, whole rock geochemistry and palynology analyses, was conducted on 79 samples (64 bulk sediment and 10 pyrite samples) from two sites (ES and DA) located in the Tondè area, Douala sub-basin (Cameroon) to unravel the paleoenvironmental and paleoclimatic conditions prevailing in recent continental deposits. Lithologies of this locality mainly consist of pyriteous claystones (grey and red) and unconsolided sandstones. Encountered pyrite is euhedral (isolated and clusters crystals) and massive with diverse morphologies and sizes. In both sections, major and trace elements show that the clayey materials result from weathering of an intermediate source rock, probably from the surrounding basement (gneiss and micaschist), whereas the sandy materials appear to be recycled. Palynological data consists of a few index species such as Malvaceae and graminaceae which indicate Pleistocene–Holocene age deposits of continental origin (swampy bays of seaside and hinterland). This area was subjected to intense chemical alteration (high CIA values: 97.35–99.43%) as testified by the mineralogical phases, mainly consist of kaolinite, quartz and goethite. Mean annual precipitation (MAP = $221.1e^{0.0197(CIA\text{-}K)}$; ±181 mm.y^{-1}) and mean annual temperature (MAT = 46.9*C* + 4; ±0.6 °C) are 1575 ± 181 mm.y^{-1} and 25.2 ± 0.6 °C for ES site and then 1566 ± 181 mm.y^{-1} and 20.3 ± 0.6 °C for DA, thus reflecting a subequatorial to equatorial climate. The pyrite geochemistry is characterized by a weak Al vs. ΣREE positive correlation (r^2 = 0.02), a positive Eu anomaly relative to PAAS and a significant negative correlation between ΣREE and the Eu anomaly (r^2 = –0.83). These results indicate that pyrite is a late diagenesis product formed by a secondary enrichment and coupled with precipitation under more reducing conditions, linked to the water table fluctuation.

Key words: Douala sub-basin, Pleistocene–Holocene age deposits, equatorial climate, pyrite occurrences, clay minerals, Cameroon

Manuscript received January 6, 2020; Manuscript accepted April 3, 2020

1. INTRODUCTION

Clastic rocks may preserve minerals and elements from the long-eroded source rocks which may provide crucial information on the composition and exposure time of such parent rocks (Armstrong-Altrin et al., 2004). Depending on originated area of materials and prevailing climate, these rocks are more or less enriched in clay minerals (Singer, 1980; Chamley, 1989; Thiry, 2000; Flagel, 2007; Abdoullayev and Leroy, 2016). Indeed, major and trace element concentrations of clastic sediments coupled to their bulk and/or clay mineralogy provide more information about their provenance, the nature of parent rock as well as the weathering conditions and sedimentary processes (Singer, 1980;

***Corresponding author:**
André Mbabi Bitchong
Department of Mining, Petroleum, Gas and Water Resources Exploration, Faculty of Mines and Petroleum Industries, University of Maroua, P.O. Box 08 Kaélé, Cameroon
Tel: +237-696623866, E-mail: andrembabi@gmail.com; mbabiandre@yahoo.fr

Electronic supplementary material
The online version of this article (https://doi.org/10.1007/s12303-020-0021-z) contains supplementary material, which is available to authorized users.

Journal of African Earth Sciences 156 (2019) 44–57

Contents lists available at ScienceDirect

Journal of African Earth Sciences

journal homepage: www.elsevier.com/locate/jafrearsci

Geochemistry of pyriteous mudrocks of the cenozoic N'Kapa formation in Douala Sub-basin, western Cameroon (Central Africa): Source rock weathering, provenance, paleo-redox conditions and tectonic settings

Gilbert François Ngon Ngon[a,*], André Mbabi Bitchong[c], Joël Simon Mbaï[a], Simon Ngos III[c], Rose Yongue Fouateu[b], Paul Bilong[b]

[a] Laboratory of Geosciences and Environment, Department of Earth Sciences, Faculty of Science, University of Douala, P.O. Box 24157, Douala, Cameroon
[b] Laboratory of Applied Geology–Metallogeny, Department of Earth Sciences, Faculty of Science, University of Yaounde I, P.O. Box 812, Yaounde, Cameroon
[c] Laboratory of Sedimentology, Department of Earth Sciences, Faculty of Science, University of Yaounde I, P.O. Box 812, Yaounde, Cameroon

ARTICLE INFO

Keywords:
Douala sub-basin
Geochemistry
Mudrock
Provenance
Pyriteous mudrock

ABSTRACT

Pyriteous mudrocks of the pyritic deposit situated at 28 km of Douala (pK28) were studied in a tropical forest setting of Douala Sub-basin (Cameroon, Central Africa), using physicochemical analyses, X-ray diffraction and ICP-AES and ICP-MS in order to decipher source rock weathering, provenance, paleo-redox conditions and tectonic setting. Three main types of sediments were differentiated in the area that include mudstones (claystones and siltstones), sandstones (fine sandstones and coarse sandstones) and lenses of conglomerates. All the pyriteous mudstones facies of the study area contain between 88.15 and 98.45 wt% (clay and silt fractions). Siltstones and claystones containing pyrite are more acid and more acid and relatively homogenous, and have organic carbon content higher than the sandstone facies and red laminated mudstone. All these mudrocks are essentially Fe-shales. Mineralogically, they are essentially composed of quartz, kaolinite, smectite, goethite, hematite, K-feldspar and pyrite. The CIA is more than 98% and Th/U ratios are higher than 4. This shows that these mudrocks have been derived from significantly weathered source rock. The Al_2O_3/TiO_2 ratios between 12.19 and 21.69, Cr/Th and Th/Cr ratios respectively 4.59–48.46 and 0.02–0.22, La/Th versus Th/Yb, a negative Eu anomaly and higher LREE/HREE ratios showed that they were mostly composed of felsic rocks with lesser contribution of mafic rocks like source rocks of Bomkoul, Missole, Kumba and Delta of Niger mudstones. The U/Th ratios below 1.25, V/Cr ratios less than 2 and Ce anomaly ranged from 1 to 1.12 are indicators that investigated mudrocks were deposited in an oxic fully marine environment in the area of active continental margin field like those of Bomkoul, Missole, Kumba mudrocks and Delta of Niger mudstones.

1. Introduction

The Douala Sub-basin is located at the bottom of the gulf of Guinea in Central Africa (Fig. 1). It is the northern part of the Douala/Kribi-Campo basin, which is one of the series of continental shelf basins in West Africa. Several studies have been carried out to understand the geological evolution and to constrain the productive petroleum systems of the Douala Sub-basin (Belmonte, 1966; Dumort, 1968; Njike Ngaha, 1984; Pauken et al., 1991; Nguene et al., 1992; Tamfu et al., 1995; Meyers et al., 1996; Brownfield and Carpenter, 2006). However, Mesozoic and Cenozoic mudstones of this basin were characterized mineralogically, geochemically and industrially in order to set up industrial units in the Douala region for manufacturing construction materials and ceramics (Thibaut and Le Berre, 1985; Njopwouo and Wandji, 1985; Njopwouo and Kong, 1986; Elimbi and Njopwouo, 2002; Njopwouo, 1984; Ngon et al., 2012; Diko and Ekosse, 2013; Logmo et al., 2013; Ngon et al., 2014; Diko et al., 2016; Mbog, 2016; Bukalo et al., 2018a). Some of the studies were focused to determine depositional palaeo-environment of sedimentary rocks (Salard-Chebodaeff, 1981, 1990; Njike Ngaha, 2004; Kenfack et al., 2012; Mbesse et al., 2012; Ngon et al., 2016). Furthermore, few geochemical studies have recently been carried out on the sedimentary rocks of the Cameroon's coastal basins and particularly the Douala Sub-basin (Ngon et al., 2014; Nguetchoua et al., 2017), and the delta of Niger (Oni et al., 2014), to record their geological evolution in the gulf of Guinea. The age of the source rocks of these sediments were determined by Bukalo et al. (2018b).

* Corresponding author.
E-mail address: gngonngon@yahoo.fr (G.F. Ngon Ngon).

https://doi.org/10.1016/j.jafrearsci.2019.04.011
Received 1 October 2018; Received in revised form 13 April 2019; Accepted 18 April 2019
Available online 30 April 2019
1464-343X/

THE GEOLOGICAL SOCIETY OF AMERICA®

Deposition and age of Chicxulub impact spherules on Gorgonilla Island, Colombia

Paula Mateo[1,†], Gerta Keller[2], Thierry Adatte[3], André M. Bitchong[4,5], Jorge E. Spangenberg[6], Torsten Vennemann[6], and Christopher J. Hollis[7]

[1]*Division of Geological and Planetary Sciences, California Institute of Technology, Pasadena, California 91125, USA*
[2]*Department of Geosciences, Princeton University, Princeton, New Jersey 08544, USA*
[3]*Institute of Geology and Paleontology, University of Lausanne, Lausanne 1015, Switzerland*
[4]*Department of Earth Sciences, Faculty of Science, University of Yaounde 1, Yaounde, Cameroon*
[5]*Department of Petroleum and Gas Exploration, Institute of Mines and Petroleum Industries, University of Maroua, Kaele, Cameroon*
[6]*Institute of Earth Surface Dynamics (IDYST), University of Lausanne, Lausanne 1015, Switzerland*
[7]*GNS Science, Lower Hutt, 5040, New Zealand*

ABSTRACT

The end-Cretaceous mass extinction (66 Ma) has long been associated with the Chicxulub impact on the Yucatan Peninsula. However, consensus on the age of this impact has remained controversial because of differing interpretations on the stratigraphic position of Chicxulub impact spherules relative to the mass extinction horizon. One side argues that the impact occurred precisely at the Cretaceous-Paleogene boundary, thus coinciding with the mass extinction; the other side argues that the impact predated the Cretaceous-Paleogene boundary, based on the discovery of primary impact spherules deposits in NE Mexico and Texas near the base of planktic foraminiferal zone CF1, dated at 170 k.y. before the Cretaceous-Paleogene boundary. A recent study of the most pristine Chicxulub impact spherules discovered on Gorgonilla Island, Colombia, suggested that they represent a primary impact deposit with an absolute age indistinguishable from the Cretaceous-Paleogene boundary. Here, we report on the Gorgonilla section with the main objective of evaluating the nature of deposition and age of the spherule-rich layer relative to the Cretaceous-Paleogene boundary.

The Gorgonilla section consists of light gray-yellow calcareous siliceous mudstones (pelagic deposits) alternating with dark olive-brown litharenites (turbidites). A 3-cm-thick dark olive-green spherule-rich layer overlies an erosional surface separating Maastrichtian and Danian sediments. This layer consists of a clast-supported, normally graded litharenite, with abundant Chicxulub impact glass spherules, lithics (mostly volcanic), and Maastrichtian as well as Danian microfossils, which transitions to a calcareous mudstone as particle size decreases. Mineralogical analysis shows that this layer is dominated by phyllosilicates, similar to the litharenites (turbidites) that characterize the section. Based on these results, the spherule-rich layer is interpreted as a reworked early Danian deposit associated with turbiditic currents. A major hiatus (>250 k.y.) spanning the Cretaceous-Paleogene boundary and the earliest Danian is recorded at the base of the spherule-rich layer, based on planktic foraminiferal and radiolarian biostratigraphy and carbon stable isotopes. Erosion across the Cretaceous-Paleogene boundary has been recorded worldwide and is generally attributed to rapid climate changes, enhanced bottom-water circulation during global cooling, sea-level fluctuations, and/or intensified tectonic activity. Chicxulub impact spherules are commonly reworked and redeposited into younger sediments overlying a Cretaceous-Paleogene boundary hiatus of variable extent in the Caribbean, Central America, and North Atlantic, while primary deposits are rare and only known from NE Mexico and Texas. Because of their reworked nature, Gorgonilla spherules provide no stratigraphic evidence from which the timing of the impact can be inferred.

INTRODUCTION

The end-Cretaceous mass extinction (66 Ma) is one of the five major biotic crises in Earth's history, and since 1980, it has been attributed to a meteorite impact (Alvarez et al., 1980) related to the impact crater (Chicxulub) discovered on the Yucatan Peninsula (Hildebrand et al., 1991; review in Schulte et al., 2010). Ever since the discovery of the Chicxulub crater, impact spherules at or near the Cretaceous-Paleogene boundary in Mexico, the Caribbean, Central America, the United States, and the North Atlantic have become major players in solving the age of the impact relative to the mass extinction based on their stratigraphic positions. However, consensus on the age of the Chicxulub impact has remained controversial, primarily because of differing interpretations regarding these impact deposits, with one side arguing that the impact occurred precisely at the Cretaceous-Paleogene boundary, thus coinciding with the mass extinction (review in Schulte et al., 2010), and the other side arguing that the impact predated the Cretaceous-Paleogene boundary (Keller et al., 2004a, 2009a; review in Keller, 2011).

The discovery of the Cretaceous-Paleogene boundary mass extinction in planktic foraminifera between major Deccan eruptions in India (Keller et al., 2011a, 2012) and recent studies pointing to Deccan volcanism as an important contributor to environmental stress across the Cretaceous-Paleogene boundary (e.g., Font et al., 2016; Keller et al., 2016; Punekar et al., 2014a; Schoene et al., 2015, 2019) have revived the mass extinction debate challenging a Cretaceous-Paleogene boundary role for the Chicxulub impact.

When did the Chicxulub impact occur relative to the Cretaceous-Paleogene boundary? What was its contribution to the Cretaceous-Paleogene boundary mass extinction? To answer these questions, the study of impact deposits that can be evaluated both stratigraphically (i.e., relative

†pmateo@caltech.edu

GSA Bulletin; https://doi.org/10.1130/B35287.1; 15 figures; 1 table; Data Repository item 2019245.

Gondwana Research 56 (2018) 69–89

Contents lists available at ScienceDirect

Gondwana Research

journal homepage: www.elsevier.com/locate/gr

Environmental changes during the Cretaceous-Paleogene mass extinction and Paleocene-Eocene Thermal Maximum: Implications for the Anthropocene

Gerta Keller [a,*], Paula Mateo [h], Jahnavi Punekar [b], Hassan Khozyem [c], Brian Gertsch [i], Jorge Spangenberg [e], Andre Mbabi Bitchong [f,g], Thierry Adatte [d]

[a] Department of Geosciences, Princeton University, Princeton, NJ 08544, USA
[b] Indian Institute of Technology Bombay, Mumbai 400076, India
[c] Department of Geology, Faculty of Sciences, Aswan University, Aswan, Egypt
[d] Institute of Earth Sciences (ISTE), University of Lausanne, 1015 Lausanne, Switzerland
[e] Institute of Earth Surface Dynamics (IDYST), University of Lausanne, Switzerland, 1015 Lausanne, Switzerland
[f] Department of Earth Sciences, Faculty of Science, University of Yaounde 1, P.O. Box 812, Yaounde, Cameroon
[g] Department of Petroleum and Gas Exploration, Institute of Mines and Petroleum Industries, University of Maroua, P.O. Box 08, Kaele, Cameroon
[h] Division of Geological and Planetary Sciences, California Institute of Technology, Padadena, 91125, CA
[i] Swiss National Science Foundation (SNSF), Wildhainweg 3, P.O. Box, CH 3001 Berne, Switzerland

ARTICLE INFO

Article history:
Received 6 August 2017
Received in revised form 30 November 2017
Accepted 1 December 2017
Available online 24 December 2017

Handling Editor: I. Somerville

ABSTRACT

The Cretaceous-Paleogene boundary (KPB) mass extinction (~66.02 Ma) and the Paleocene-Eocene Thermal Maximum (PETM) (~55.8 Ma) are two remarkable climatic and faunal events in Earth's history that have implications for the current Anthropocene global warming and rapid diversity loss. Here we evaluate these two events at the stratotype localities in Tunisia and Egypt based on climate warming and environmental responses recorded in faunal and geochemical proxies. The KPB mass extinction is commonly attributed to the Chicxulub impact, but Deccan volcanism appears as a major culprit. New mercury analysis reveals that major Deccan eruptions accelerated during the last 10 ky and reached the tipping point leading up to the mass extinction. During the PETM, climate warmed rapidly by ~5 °C, which is mainly attributed to methane degassing from seafloor sediments during global warming linked to the North Atlantic Igneous Province (NAIP). Biological effects were transient, marked by temporary absence of most planktic foraminifera due to ocean acidification followed by the return of the pre-PETM fauna and diversification. In contrast, the current rapid rise in atmospheric CO_2 and climate warming are magnitudes faster than at the KPB or PETM events leading to predictions of a PETM-like response as best case scenario and rapidly approaching sixth mass extinction as worst-case scenario.

1. Introduction

One of the greatest challenges to our planet is the looming Anthropocene mass extinction commonly attributed to human activity as the dominant influence on rapid climate warming and changing environments as a result of fossil fuel burning (IPCC 5th Assessment Report, 2013). This climate warming is commonly compared with the rapid short-term ~5 °C warming known as the Paleocene-Eocene Thermal Maximum (PETM) ~55.8 Ma. However, the PETM led to opposite results: major diversification in marine and terrestrial life and significant species extinctions only in deep-water benthic foraminifera. A better understanding of the impending Anthropocene catastrophe can be gained from the rapid warming and mass extinction culminating at the Cretaceous-Paleogene boundary (KPB also known as KPgB or KTB). In this study we examine both the PETM and KPB events to gain insights into potential Anthropocene scenarios.

The PETM event (55.8 ± 0.2 Ma) lasted ~170 ky and is commonly attributed to North Atlantic Igneous Province (NAIP) volcanism and methane degassing of seafloor sediments (e.g., Dickens et al., 1995; Dickens, 2000; Westerhold et al., 2009; Charles et al., 2011; Wieczorek et al., 2013; Gutjahr et al., 2017). The resulting global negative $\delta^{13}C$ excursion of 2–6‰ and rapid warming of 4.5–5 °C from tropical to high latitudes was accompanied by ocean acidification and shoaling of the carbonate compensation depth (CCD) by ~2000 m (e.g., Kennett and Stott, 1991; Sluijs et al., 2006; Zachos et al., 2003, 2005, 2006; Weijers et al., 2007; McInerney and Wing, 2011; Coccioni et al., 2012; Gutjahr et al., 2017). In the marine realm

* Corresponding author.
E-mail addresses: gkeller@exchange.Princeton.EDU (G. Keller), pmateo@caltech.edu (P. Mateo), jpunekar@iitb.ac.in (J. Punekar), jorge.spangenberg@unil.ch (J. Spangenberg), thierry.adatte@unil.ch (T. Adatte).

https://doi.org/10.1016/j.gr.2017.12.002
1342-937X/

Earth and Planetary Science Letters 484 (2018) 53–66

Contents lists available at ScienceDirect

Earth and Planetary Science Letters

www.elsevier.com/locate/epsl

Deccan volcanism induced high-stress environment during the Cretaceous–Paleogene transition at Zumaia, Spain: Evidence from magnetic, mineralogical and biostratigraphic records

Eric Font [a,*], Thierry Adatte [b], Mariana Andrade [a], Gerta Keller [c], André Mbabi Bitchong [b,d,e], Claire Carvallo [f], Joana Ferreira [a], Zenaida Diogo [a], José Mirão [g]

[a] IDL-FCUL, Instituto Dom Luís, Faculdade de Ciências da Universidade de Lisboa, Campo Grande, Lisbon, Portugal
[b] ISTE, Lausanne University, Geopolis, CH-1015 Lausanne, Switzerland
[c] Department of Geosciences, Princeton University, Princeton, NJ 08544, USA
[d] Department of Earth Sciences, Faculty of Science, University of Yaounde 1, P.O. Box 812 Yaounde, Cameroon
[e] Department of Petroleum and Gas Exploration, Faculty of Mines and Petroleum Industries, University of Maroua, P.O. Box 08 Kaele, Cameroon
[f] Institut de Minéralogie, de Physique des Minéraux et de Cosmochimie, Sorbonne Universités-Pierre and Marie Curie, University of Paris 06, UMR CNRS 7590, Muséum National d'Histoire Naturelle, IRD UMR 206, Paris, France
[g] HERCULES Centre, ECT-Geosciences Department, University of Évora, Évora, Portugal

ARTICLE INFO

Article history:
Received 2 September 2017
Received in revised form 27 November 2017
Accepted 30 November 2017
Available online xxxx
Editor: D. Vance

Keywords:
Cretaceous–Paleogene mass extinction
Deccan
volcanism
akaganéite
mercury
acidification

ABSTRACT

We conducted detailed rock magnetic, mineralogical and geochemical (mercury) analyses spanning the Cretaceous–Paleogene boundary (KPB) at Zumaia, Spain, to unravel the signature of Deccan-induced climate and environmental changes in the marine sedimentary record. Our biostratigraphic results show that Zumaia is not complete, and lacks the typical boundary clay, zone P0 and the base of zone P1a(1) in the basal Danian. Presence of an unusual ~1m-thick interval spanning the KPB is characterized by very low detrital magnetite and magnetosome (biogenic magnetite) contents and by the occurrence of akaganéite, a very rare mineral on Earth in oxidizing, acidic and hyper-chlorinated environments compatible with volcanic settings. These benchmarks correlate with higher abundance of the opportunist *Guembelitria cretacea* species. Detrital magnetite depletion is not linked to significant lithological changes, suggesting that iron oxide dissolution by acidification is the most probable explanation. The concomitant decrease in magnetosomes, produced by magnetotactic bacteria at the anoxic–oxic boundary, is interpreted as the result of changes in seawater chemistry induced by surficial ocean acidification. Mercury peaks up to 20–50 ppb are common during the last 100 kyr of the Maastrichtian (zone CF1) but only one significant anomaly is present in the early Danian, which is likely due to the missing interval. Absence of correlation between mercury content ($R^2 = 0.009$) and total organic carbon ($R^2 = 0.006$) suggest that the former originated from the Deccan Traps eruptions. No clear relation between the stratigraphic position of the mercury peaks and the magnetite-depleted interval is observed, although the frequency of the mercury peaks tends to increase close to the KPg boundary. In contrast to Bidart (France) and Gubbio (Italy), where magnetite depletion and akaganéite feature within a ~50cm-thick interval located 5 cm below the KPg boundary, the same benchmarks are observed in a 1m-thick interval encompassing the KPg boundary at Zumaia. Results reinforce the synchronism of the major eruptions of the Deccan Traps Magmatic Province with the Cretaceous–Paleogene (KPg) mass extinction and provide new clues to better correlate the Deccan imprint of the global sedimentary record.

1. Introduction

Recent advances in U–Pb and Ar–Ar radiometric dating have improved constraints for the onset and duration of the entire Deccan Magmatic Province (Renne et al., 2015; Schoene et al., 2015). More than 3000 m of continental flood basalts, representing more than 1.1 million of km^3 in volume, erupted within ca. 750,000 years, spanning Chron 29r and encompassing the Cretaceous–Paleogene boundary (KPB), the mass extinction and the Chicxulub impact (Schoene et al., 2015). The KPB mass extinction has been documented by planktic foraminifera assemblages within

* Corresponding author at: IDL-FCUL, Instituto Dom Luís, Universidade de Lisboa, Edifício C8-8.3.22, Campo Grande, 1749-016, Lisboa, Portugal.
E-mail address: font_eric@hotmail.com (E. Font).

https://doi.org/10.1016/j.epsl.2017.11.055
0012-821X/

ANNEX II: AFFILIATED MEETING ABSTRACTS

1. Adatte T., Keller, G., Font, E., Mateo, P., Punekar, J., Schoene, B., Eddy, M., Samperton, K.M., Spangenberg, J., **Mbabi Bitchong, A.**, Sharma, N., Lorenzo, V. and Cujean, S. (2019). Timing and Paleoenvironmental implications of Deccan volcanism relative to the KPg. 3rd International Congress on Stratigraphy. ST3.8 Cretaceous integrated stratigraphy, greenhouse climate change and events.
2. Adatte, T., Keller, G., Font, E., Mateo, P., Punekar, J., Schoene, B., Eddy, M., Spangenberg, J., **Mbabi Bitchong, A.**, Sharma, N., Lorenzo, V. and Cujean S. (2019). Timing and paleoenvironmental implications of Deccan volcanism relative to the KPg extinction revealed by mercury anomalies. Geophysical Research Abstracts, vol. 21, EGU2019-5666, EGU General Assembly 2019.
3. Adatte, T., Keller, G., Font, E., **Mbabi Bitchong, A**., Schoene, B. (2017). Timing and tempo of Deccan volcanism relative to the KPg boundary, evidence from mercury anomalies. Berichte der Geologischen Bundesanstalt (ISSN 107-8880), Band 120, Wien 2017. 10th Int. Symp. Cretaceous.
4. Adatte, T., Keller, G., Font, E., **Mbabi Bitchong, A.**, Schoene, B., Samperton, K. and M. P. Eddy (2017). Near coincidence of maximum Deccan volcanism with the Cretaceous-Paleogene boundary revealed by mercury anomalies. GSA Annual Meeting in Seattle, Washington, USA (22-25 October 2017). Abstracts with Programs Vol. 49, No. 6, doi: 10.1130/abs/2017AM-302876
5. Adatte, T., Font, E., **Mbabi Bitchong, A**., Keller, G., Schoene, B., Samperton, K. and S. Khadri (2017). Timing and tempo of Deccan volcanism: evidence from mercury anomalies. Geophysical Research Abstracts, vol. 19, EGU2017-7709, EGU General Assembly 2017.
6. Font, E., Adatte, T., Andrade, M., Keller, G., **Mbabi Bitchong, A**., Carvallo, C., Ferreira, J., Diogo, Z. and J. Mirão (2017). Deciphering the magnetic and mineralogical record of the Deccan Traps at the Cretaceous-Paleogene boundary of the Zumaia section, Basque-Cantabric basin (Spain). Geophysical Research Abstracts, vol. 19, EGU2017-9160, EGU General Assembly 2017
7. Khozyem Hassan, Adatte Thierry, **Mbabi Bitchong André**, Chevalier Yoann and Keller Gerta (2017). Paleocene-Eocene Thermal Maximum triggered by Volcanism revealed by Mercury anomalies. Geophysical Research Abstracts, vol. 19, EGU2017-9160, EGU General Assembly 2017

8. Khozyem Hassan, Adatte Thierry, **Mbabi Bitchong André**, Mohamed Abdallah and Keller Gerta (2017). The role of volcanism (North Atlantic Igneous Province) in the PETM events revealed by mercury anomalies. GSA Annual Meeting in Seattle, Washington, USA (22-25 October 2017). Abstracts with Programs Vol. 49, No. 6, doi:10.1130/abs/2017AM-302839.
9. Adatte Thierry, Font Eric, **Mbabi Bitchong André**, Keller Gerta, Schoene Blair, Samperton Kyle M. and Khadri Syed F.R. (2016). Timing and tempo of Deccan volcanism revealed by mercury anomalies. GSA Annual Meeting in Denver, Colorado, USA (25-28 September 2016). doi: 10.1130/abs/2016am-285123.
10. Khozyem Hassan, Adatte Thierry, **Mbabi Bitchong André**, Chevalier Yoann and Keller Gerta (2016). Paleocene-Eocene Thermal maximum triggered by volcanism? Evidence from mercury anomalies. GSA Annual Meeting in Denver, Colorado, USA (25-28 September 2016)
11. Mateo Paula, Keller Gerta, Adatte Thierry, **Mbabi Bitchong André**, Spangenberg Jorge, Vennemann Torsten, Heizler Matthew, Hodges Kip, McDonald Christopher, Hollis Chris and Stinnesbeck Wolfgang (2016). Age, Biostratigraphy, geochemistry and mineralogy of Chicxulub Impact spherules on Gorgonilla Island, Colombia. GSA Annual Meeting in Denver, Colorado, USA (25-28 September 2016)
12. **André Mbabi Bitchong**, Gilbert-François Ngon Ngon, Simon Ngos III, Izuchukwu Mike Akaegbobi, Chakravadhanula Manikyamba, Paul Bilong (2014). Characterization of materials in a clayey sequence of the pk 27 area, Douala sedimentary sub-basin, Cameroon. First International Workshop on West African Sedimentology and Sedimentary Basins (27 July – 2 August 2014)
13. **A. Mbabi Bitchong**, G.-F. Ngon Ngon, J. Etame, M.J. Ntamak-Nida, S. Ngos III, P. Bilong (2013). Caractérisation morphologique et distribution de la pyrite dans une séquence argileuse de pk 27, sous-bassin sédimentaire de Douala, Cameroun. Colloque Géosciences et Appui au Développement, Douala, Cameroun (16-17 mai 2013).

Thanks Thierry Adatte, check the entered data and press send to submit the abstract or press back button to change

ST3.8 Cretaceous integrated stratigraphy, greenhouse climate change and events

Alternative Session: ST11.4 General session on Stratigraphy

Timing and Paleoenvironmental implications of Deccan volcanism relative to the KPg

Adatte T. *1, Keller, G. 2, Font, E. 3, Mateo, P. 4, Punekar, J. 5, Schoene, B. 2, Eddy, M. 2, Samperton, K.M. 6, Spangenberg, J. 7, Bitchong, A.M. 8, Sharma, N. 1, Lorenzo, V. 1, Cujean, S. 1

1. ISTE, University of Lausanne, Switzerland 2. Department of Geosciences, Princeton University, USA 3. Departamento de Ciências da Terra, Universidade de Coimbra Portugal 4. Division of Geological and Planetary Sciences, California Institute of Technology, USA 5. Indian Institute of Technology, Mumbai, India 6. Nuclear and Chemical Science Division, Lawrence Livermore National Laboratory, USA 7. IDYST, University of Lausanne, Switzerland, 8. Department of Earth Sciences, University of Yaounde 1, Cameroon and Institute of Mines and Petroleum Industries, University of Maroua, Cameroon

Corresponding author email: Thierry.adatte@unil.ch

Mercury (Hg) as indicator of large-scale volcanism in marine sediments provides new insights into relative timing between biological and environmental changes, mass extinctions and delayed recovery. Several studies evaluated the relationship between Hg anomalies in sediments and LIP activity across mass extinction horizons. The bulk (80%) of Deccan Trap eruptions occurred over a relatively short time interval in magnetic polarity C29r. U-Pb zircon geochronology reveals the onset of this main eruption phase 250 ky before the Cretaceous-Tertiary (KT) mass extinction and continued into the early Danian suggesting a cause-and-effect relationship. Maximum eruption rates occurred before and after the K-Pg extinction, with one such pulse initiating tens of thousands of years prior to both the bolide impact and extinction. These findings support extinction models that incorporate both catastrophic events as drivers of environmental deterioration associated with the K-Pg extinction and its aftermath.

We present the first comprehensive high-resolution analysis of Deccan Traps Hg loading, climate change and end-Cretaceous mass extinction from a transect, which includes 25 sections deposited in both shallow and deep environments. We investigate the Hg contents of around sections located in France (Bidart), Spain (Zumaya, Caravaca, Agost), Denmark (Nye Klov, Stevn Klint), Austria (Gams), Italy (Gubbio), Tunisia (Elles, El Kef), Turkey (Goniuk, Okcular), Egypt (Wadi Nukhul, Sinai, Duwi), Israel (Negev), Oman (Abat), India (Megalaya, Anjar, Podgavan, Cauvery Basin), Demarara Rise, Texas USA (Brazos River) and NE Mexico (El Penon, La Parida). In all sections, results show that Hg concentrations are more than 2 orders of magnitude greater during the last 100ky of the Maastrichtian up to the early Danian P1a zone (first 380 Ky of the Paleocene). These Hg anomalies are correlative with the main Deccan eruption phases. Hg anomalies generally show no correlation with clay or total organic carbon contents, suggesting that the mercury enrichments resulted from higher input of atmospheric Hg species into the marine realm, rather than organic matter scavenging and/or increased run-off. Significant and coeval Hg enrichments are observed in multiples basins characterized by proximal and distal, as well as shallow and deep-water settings, supporting a direct direct fallout from volcanic aerosols. At Gams, Bidart, Elles and Demerara, the highest Hg anomalies correlate with high shell fragmentation and dissolution effects in planktic foraminifera indicating that paleoenvironmental and paleoclimate changes drastically affected marine biodiversity especially during the last 25 ky preceding the KPg. These observations provide further support that Deccan volcanism played a key role in increasing atmospheric CO_2 and SO_2 levels that resulted in global warming and acidified oceans, increasing biotic stress that predisposed faunas to eventual extinction at the KPg

---

Keywords: Mass Extinction, Cretaceous-Paleogene, Deccan Volcanism

Notes:

Send

Geophysical Research Abstracts
Vol. 21, EGU2019-5666-4, 2019
EGU General Assembly 2019

Timing and paleoenvironmental implications of Deccan volcanism relative to the KPg extinction revealed by mercury anomalies.

Thierry Adatte (1), Gerta Keller (2), Eric Font (3), Paula Mateo (4), Jahnavi Punekar (6), Blair Schoene (2), Michael Eddy (2), Jorge Spangenberg (7), André Mbabi Bitchong (5), Nikhil Sharma (1), Valentin Lorenzo (1), and Cujean Sébastien (1)

(1) ISTE, Institute of Earth Sciences, Lausanne, Switzerland (thierry.adatte@unil.ch), (2) Department of Geosciences, Princeton University, Guyot Hall, Princeton, NJ 08544, USA (gkeller@Princeton.EDU), (3) Departamento de Ciências da Terra, Faculdade de Ciências e Tecnologia, Universidade de Coimbra, 3000-272 Coimbra, Portugal (font_eric@hotmail.com), (4) Division of Geological and Planetary Sciences, California Institute of Technology, Pasadena, CA 91125, USA (chiripiorca@gmail.com), (6) Indian Institute of Technology Bombay, Mumbai, 400 076, India (jahnavi.punekar@gmail.com), (7) IDYST, Institute of Earth Surface Dynamics , University of Lausanne, Lausanne, 1015, Switzerland (Jorge.spangenberg@unil.ch), (5) Department of Earth Sciences, Faculty of Science, University of Yaounde 1, Yaounde Cameroon, P.O.Box 812, Cameroon; Department of Petroleum and Gas Exploration, Institute of Mines and Petroleum Industries,University of Maroua, Kaele, P.O.Box 08, Cameroon

Mercury (Hg) as indicator of large-scale volcanism in marine sediments provides new insights into relative timing between biological and environmental changes, mass extinctions and delayed recovery. Several studies evaluated the relationship between Hg anomalies in sediments and LIP activity across mass extinction horizons. The bulk (80%) of Deccan Trap eruptions occurred over a relatively short time interval in magnetic polarity C29r. U-Pb zircon geochronology reveals the onset of this main eruption phase 250 ky before the Cretaceous-Tertiary (KT) mass extinction and continued into the early Danian suggesting a cause-and-effect relationship.
We present the first comprehensive high-resolution analysis of Deccan Traps Hg loading, climate change and end-Cretaceous (KTB or KPB) mass extinction from a transect, which includes 27 sections deposited in both shallow and deep environments. We investigate the Hg contents of around sections located in France (Bidart), Spain (Zumaya, Caravaca, Agost), Denmark (Nye Klov, Stevn Klint), Austria (Gams), Croatia (Hvar, Brac) Italy (Gubbio), Tunisia (Elles, El Kef), Turkey (Goynuk, Okçular), Egypt (Wadi Nukhul, Sinai, Duwi), Israel (Negev), Oman (Abat), India (Megalaya, Anjar, Podgavan, Cauvery Basin), Demarara Rise, Texas USA (Brazos River) and NE Mexico (El Penon, La Parida). In all sections, results show that Hg concentrations are more than 2 orders of magnitude greater during the last 100ky of the Maastrichtian up to the early Danian P1a zone (first 380 Ky of the Paleocene). These Hg anomalies are correlative with the main Deccan eruption phases. Hg anomalies generally show no correlation with clay or total organic carbon contents, suggesting that the mercury enrichments resulted from higher input of atmospheric Hg species into the marine realm, rather than organic matter scavenging and/or increased run-off. Significant and coeval Hg enrichments are observed in multiples basins characterized by proximal and distal, as well as shallow and deep-water settings, supporting a direct direct fallout from volcanic aerosols. At Gams, Bidart, Elles and Demerara, the highest Hg anomalies correlate with high shell fragmentation and dissolution effects in planktic foraminifera indicating that paleoenvironmental and paleoclimate changes drastically affected marine biodiversity especially during the last 25 ky preceding the KPg. These observations provide further support that Deccan volcanism played a key role in increasing atmospheric CO_2 and SO_2 levels that resulted in global warming and acidified oceans, increasing biotic stress that predisposed faunas to eventual extinction at the KPB

Timing and tempo of Deccan volcanism relative to the KPg boundary, evidence from mercury anomalies

***Adatte, T.*[1], *Keller, G.*[2], *Font, E.*[3], *Mbabi Bitchong, A.*[4], *Schoene, B.*[2]**

1) Institute of Earth Sciences, Lausanne University, Lausanne, Switzerland, E-mail: thierry.adatte@unil.ch
2) Department of Geosciences, Princeton University, Princeton, USA
3) IDL-FCUL, Universidade de Lisboa, Lisbon, Portugal
4) Institute of Mines and Petroleum, Maroua University, Maroua, Cameroon

Mercury is a very toxic element, with a long residence time (1–2 years) and wide distribution by aerosols. Volcanic emissions and coal combustion are the two main natural sources of mercury. Several studies evaluated the relationship between Hg anomalies in sediments and LIP activity across mass extinction horizons. The bulk (80 %) of Deccan Trap eruptions occurred over a relatively short time interval in magnetic polarity C29r. U-Pb zircon geochronology reveals the onset of this main eruption phase 250 ky before the Cretaceous-Tertiary (KT) mass extinction and continued into the early Danian suggesting a cause-and-effect relationship (SCHOENE et al., 2015). In a related study, we investigate the mercury (Hg) contents of sections in France (Bidart), Spain (Zumaya, Caravaca, Agost), Denmark (Nye Klov), Austria (Gams), Italy (Gubbio), Tunisia (Elles, El Kef), Egypt (Sinai), Israel (Negev), India (Megalaya), Texas USA (Brazos River) and Mexico (La Parida). In all sections, results show Hg concentrations are more than 2 orders of magnitude greater during the last 100 ky of the Maastrichtian up to the early Danian P1a zone (first 380 ky of the Paleocene). These Hg anomalies are correlative with the main Deccan eruption phase. Hg anomalies generally show no correlation with clay or total organic carbon contents, suggesting that the mercury enrichments resulted from higher input of atmospheric Hg species into the marine realm, rather than organic matter scavenging and/or increased run-off. At Gams, Bidart, Elles and Caravaca, Hg anomalies correlate with high shell fragmentation and dissolution effects in planktic foraminifera indicating that paleoenvironmental and paleoclimate changes drastically affected marine biodiversity. These observations provide further support that Deccan volcanism played a key role in increasing atmospheric CO_2 and SO_2 levels that resulted in global warming and acidified oceans, increasing biotic stress that predisposed faunas to eventual extinction at the KTB.

SCHOENE, B. et al., 2015. Science, **347**/6218, 182–184.

GSA Annual Meeting in Seattle, Washington, USA - 2017

Paper No. 197-12
Presentation Time: 11:00 AM

NEAR COINCIDENCE OF MAXIMUM DECCAN VOLCANISM WITH THE CRETACEOUS-PALEOGENE BOUNDARY REVEALED BY MERCURY ANOMALIES

ADATTE, Thierry[1], KELLER, Gerta[2], FONT, Eric[3], MBABI BITCHONG, André[4], SCHOENE, Blair[2], SAMPERTON, Kyle[2] and EDDY, Michael P.[5], (1)Institute of Earth Sciences, University of Lausanne, Géopolis, Lausanne, 1015, Switzerland, (2)Department of Geosciences, Princeton University, Guyot Hall, Princeton, NJ 08544, (3)Faculdade de Ciencias, University of Lisbon, Campo Grande, Edificio C8, Piso 3, Lisbon, 1749-016, Portugal, (4)Department of Earth Sciences, Faculty of Science, University of Yaounde 1, Yaounde Cameroon, P.O.Box 812, Cameroon; Department of Petroleum and Gas Exploration, Institute of Mines and Petroleum Industries,, University of Maroua, Kaele, P.O.Box 08, Cameroon, (5)Department of Geosciences, Princeton University, Princeton, NJ 08544, Thierry.Adatte@unil.ch

Mercury is a very toxic element, with a long residence time (1-2 years) and wide distribution by aerosols. Several studies evaluated the relationship between Hg anomalies in sediments and LIP activity across mass extinction horizons. The bulk (80%) of Deccan Trap eruptions occurred over a relatively short time interval in magnetic polarity C29r. U-Pb zircon geochronology reveals the onset of this main eruption phase 250 ky before the Cretaceous-Tertiary (KT) mass extinction and continued into the early Danian suggesting a cause-and-effect relationship. We investigate the mercury (Hg) contents of sections in France (Bidart), Spain (Zumaya), Denmark (Nye Klov), Austria (Gams), Italy (Gubbio), Tunisia (Elles, El Kef), Egypt (Wadi Nukhul, Sinai, Duwi, Eastern Desert), Israel (Negev), India (Megalaya), Texas USA (Brazos River) and NE Mexico (El Penon, La Parida). In all sections, results show Hg concentrations are more than 2 orders of magnitude greater during the last 100ky of the Maastrichtian up to the early Danian P1a zone (first 380 Ky of the Paleocene). These Hg anomalies are correlative with the main Deccan eruption phase. Hg anomalies generally show no correlation with clay or total organic carbon contents, suggesting that the mercury enrichments resulted from higher input of atmospheric Hg species into the marine realm, rather than organic matter scavenging and/or increased run-off. At Gams, Bidart and Elles, Hg anomalies correlate with high shell fragmentation and dissolution effects in planktic foraminifera indicating that paleoenvironmental and paleoclimate changes drastically affected marine biodiversity. Hg isotope data from Bidart support a direct fallout from volcanic aerosols. PGEs data from Mishor Rotem (Israel) from the KPg layer and two uppermost Maastritchian red clay layers provide some important clues about the Hg deposited in the KPg layer, which appears to be more linked to volcanism than impact, suggesting a major pulse of Deccan activity just before and at the KPg.

These observations provide further support that Deccan volcanism played a key role in increasing atmospheric CO_2 and SO_2 levels that resulted in global warming and acidified oceans, increasing biotic stress that predisposed faunas to eventual extinction at the KPg

Session No. 197

T56. Mass Extinctions I: Past, Present, and Future?
Tuesday, 24 October 2017: 8:00 AM-12:00 PM

Room 608 (Washington State Convention Center)

Geological Society of America *Abstracts with Programs.* Vol. 49, No. 6
doi: 10.1130/abs/2017AM-302876

Back to: T56. Mass Extinctions I: Past, Present, and Future?

<< Previous Abstract | Next Abstract >>

Geophysical Research Abstracts
Vol. 19, EGU2017-7709, 2017
EGU General Assembly 2017

Timing and tempo of Deccan volcanism: evidence from mercury anomalies

Thierry Adatte (1), Eric Font (2), André Mbabi Bitchong (1,3,4), Gerta Keller (5), Blair Schoene (5), Kyle Samperton (5), and Syed Khadri (6)

(1) Lausanne, Institute of Earth Sciences, ISTE, Lausanne, Switzerland (thierry.adatte@unil.ch), (2) IDL-FCUL (Instituto Dom Luís, Faculdade de Ciências da Universidade de Lisboa), Campo Grande, Edifício C1, Piso 1, 1749-016 Lisbon, Portugal , (3) Department of Earth Sciences, Faculty of Science, University of Yaounde 1, P.O.Box 812 Yaounde Cameroon, (4) Department of Petroleum and Gas Exploration, Institute of Mines and Petroleum Industries, University of Maroua, P.O.Box 08 Kaele, Cameroon , (5) Department of Geosciences, Princeton University, Princeton, NJ 08544, USA, (6) Department of Geology, Amravati University, Amravati, India

Mercury is a very toxic element, with a long residence time (1-2 years) and wide distribution by aerosols. Volcanic emissions and coal combustion are the two main natural sources of mercury. Several studies [1-4] evaluated the relationship between Hg anomalies in sediments and LIP activity across mass extinction horizons. The bulk (80%) of Deccan Trap eruptions occurred over a relatively short time interval in magnetic polarity C29r. U-Pb zircon geochronology reveals the onset of this main eruption phase 250 ky before the Cretaceous-Tertiary (KT) mass extinction and continued into the early Danian suggesting a cause-and-effect relationship [5]. In a related study we investigate the mercury (Hg) contents of sections in France (Bidart), Spain (Zumaya), Denmark (Nye Klov), Austria (Gams), Italy (Gubbio), Tunisia (Elles, El Kef), Egypt (Sinai), India (Megalaya), Texas USA (Brazos River) and Mexico (La Parida). In all sections, results show Hg concentrations are more than 2 orders of magnitude greater during the last 100ky of the Maastrichtian up to the early Danian P1a zone (first 380 Ky of the Paleocene). These Hg anomalies are correlative with the main Deccan eruption phase. Hg anomalies generally show no correlation with clay or total organic carbon contents, suggesting that the mercury enrichments resulted from higher input of atmospheric Hg species into the marine realm, rather than organic matter scavenging and/or increased run-off. At Gams, Bidart and Elles, Hg anomalies correlate with high shell fragmentation and dissolution effects in planktic foraminifera indicating that paleoenvironmental and paleoclimate changes drastically affected marine biodiversity. These observations provide further support that Deccan volcanism played a key role in increasing atmospheric CO_2 and SO_2 levels that resulted in global warming and acidified oceans, increasing biotic stress that predisposed faunas to eventual extinction at the KTB.

Geophysical Research Abstracts
Vol. 19, EGU2017-9160, 2017
EGU General Assembly 2017

Deciphering the magnetic and mineralogical record of the Deccan Traps at the Cretaceous-Paleogene boundary of the Zumaia section, Basque-Cantabric basin (Spain)

Eric Font (1), Thierry Adatte (2), Mariana Andrade (1), Gerta Keller (3), André Mbabi Bitchong (2,4,5), Claire Carvallo (6), Joana Ferreira (1), Zenaida Diogo (1), and José Mirão (7)

(1) Universidade de Lisboa, Faculdade de Ciencias, IDL, Lisbon, Portugal (font_eric@hotmail.com), (2) ISTE, Geopolis, CH-1015 Lausanne, Switzerland, (3) Department of Geosciences, Princeton University, Princeton, NJ 08544, USA, (4) Department of Earth Sciences, Faculty of Science, University of Yaounde 1, P.O.Box 812 Yaounde Cameroon, (5) Department of Petroleum and Gas Exploration, Institute of Mines and Petroleum Industries, University of Maroua, P.O.Box 08 Kaele, Cameroon, (6) Institut de Minéralogie, de Physique des Minéraux et de Cosmochimie, Sorbonne Universités-Pierre and Marie Curie, University of Paris 06, UMR CNRS 7590, Muséum National d'Histoire Naturelle, IRD UMR 206, Paris, France, (7) HERCULES Centre, ECT-Geosciences Department, University of Évora, Évora, Portugal

The Deccan Traps Magmatic Province coincides with the Cretaceous-Paleogene (KPg) boundary and probably contributed to the associated mass extinctions by inducing rapid and abrupt climate changes, including continental and superficial seawater acidification. However, how such environmental acidification is expressed in the marine sedimentary record is still poorly constrained. Recent environmental magnetic studies of the Bidart (France) and Gubbio (Italy) sections proposed new benchmarks to identify the Deccan Traps fingerprint in the marine sedimentary record, namely anomalous concentration in mercury, presence of akagenéite (a Cl-rich oxy-hydroxide forming in hyper-chlorinated and acid conditions) and the loss of detrital and biogenic magnetite by acid reductive dissolution. Here we test this scenario on the Zumaia section, Spain, a reference KPg section cropping out in the Basque-Cantabric basin. Our results confirm the presence of an iron-depleted interval located just below the KPg boundary, similarly to Bidart and Gubbio, and which contains significant amounts of akaganéite grains as well as high content in mercury. These results consolidate the use of the previously cited benchmarks to identify environmental and climate changes induced by the Deccan volcanism. It also suggests that the main eruptive Deccan phase began just before the KPg extinction, reinforcing its contribution in the KPg mass extinction.

Publication supported by FCT- project UID/GEO/50019/2013 - Instituto Dom Luiz

Geophysical Research Abstracts
Vol. 19, EGU2017-18553, 2017
EGU General Assembly 2017

Paleocene-Eocene Thermal Maximum triggered by Volcanism revealed by Mercury anomalies

Hassan Khozyem (1), Thierry Adatte (2), André Mbabi Bitchong (2,3,4), Yoann Chevalier (2), and Gerta Keller (5)

(1) Department of Geology, Faculty of Sciences, Aswan University, Aswan, Egypt, (2) Institute of Earth Sciences (ISTE), University of Lausanne, 1015 Lausanne, Switzerland , (3) Department of Earth Sciences, Faculty of Science, University of Yaounde 1, P.O.Box 812 Yaounde Cameroon, (4) Department of Petroleum and Gas Exploration, Institute of Mines and Petroleum Industries, University of Maroua, P.O.Box 08 Kaele, Cameroon , (5) Department of Geosciences, Princeton University, Princeton, NJ 08544, USA

The Paleocene-Eocene Thermal Maximum (PETM, ∼55.8±0.2 Ma) is marked by a global drop of 2-6‰ in [U+F064]13C values and rapid warming of 4-5°C in tropical surface waters and 4-8°C in high latitudes. Climate warming persisted for several tens of thousands of years and resulted in rapid diversification in terrestrial mammals and marine planktic foraminifera. Deep-water bathyal benthic foraminifera suffered a mass extinction (∼40% species) but no significant extinctions occurred shallow shelf environments. Benthic extinctions are commonly explained as the effects of the initial stage of climate warming due to North Atlantic Volcanic Province volcanism (NAVP), which triggered methane release from ocean sediments causing global warming and ocean acidification. But the relationship between NAPV and the PETM events are not clearly demonstrated. Several studies [1-4] demonstrated the relationship between Hg anomalies in sediments and LIP activity associated with mass extinctions. We investigated the mercury (Hg) content of several sections located in deep bathyal (Zumaya, Trabakua, N-Spain) and outer shelf environments (Dababiya GSSP, Duwi, Egypt). At Zumaya the PETM is marked by a red clayey and marly interval poor in organic matter and coincident with a pronounced ∂13C negative shift. A comparable clay interval with low TOC content is also present in the Dababyia section in the lower part of the negative ∂13C shift, whereas the upper part of is enriched in TOC, reflecting increased productivity. A significant but unique Hg enrichment is observed at the onset of the PETM just below the carbone isotope shift in Spain as well as in Egypt. This increase, which is not correlated with clay or total organic carbon contents, suggests the Hg anomaly resulted from higher atmospheric Hg input into the marine realm, rather than organic matter scavenging and/or increased run-off. This Hg anomaly at the onset of the PETM provides the first direct evidence that volcanism played a crucial role in triggering the PETM events by initiating the warming that likely released methane gases that accelerated greenhouse warming and ocean acidification.

GSA Annual Meeting in Seattle, Washington, USA - 2017

Paper No. 228-5
Presentation Time: 2:30 PM

THE ROLE OF VOLCANISM (NORTH ATLANTIC IGNEOUS PROVINCE) IN THE PETM EVENTS REVEALED BY MERCURY ANOMALIES

KHOZYEM, Hassan[1], ADATTE, Thierry[2], MBABI BITCHONG, André[3], MOHAMED, Abdallah[1] and KELLER, Gerta[4], (1)Department of Geology, University of Aswan, Aswan, 81528, Egypt, (2)Institute of Earth Sciences, University of Lausanne, Géopolis, Lausanne, 1015, Switzerland, (3)Department of Earth Sciences, Faculty of Science, University of Yaounde 1, Yaounde Cameroon, P.O.Box 812, Cameroon; Department of Petroleum and Gas Exploration, Institute of Mines and Petroleum Industries,, University of Maroua, Kaele, P.O.Box 08, Cameroon, (4)Department of Geosciences, Princeton University, Guyot Hall, Princeton, NJ 08544, hkhozyem@gmail.com

The Paleocene-Eocene Thermal Maximum (PETM, ≈55.8±0.2 Ma) is marked by a global change in carbon cycle and rapid warming. Climate warming persisted for several tens of thousands of years and resulted in rapid diversification in terrestrial mammals and marine planktic foraminifera.

Deep-water benthic foraminifera suffered a mass extinction (≈40% species) but no significant extinctions occurred shallow shelf environments. Benthic extinctions are commonly explained as the effects of the initial stage of climate warming due to North Atlantic Volcanic Province volcanism (NAVP), which triggered methane release from ocean sediments causing global warming and ocean acidification. But the relationship between NAPV and the PETM events are till now not clearly demonstrated.

Several studies demonstrated the relationship between Hg anomalies in sediments and LIP activity associated with mass extinctions. Mercury (Hg) content of several sections located in different sedimentary environments (deep bathyal: Zumaya, Trabakua, N-Spain and outer shelf: Dababiya GSSP, Duwi, Wadi Nukhul, Egypt, terrestrial: Esplugafreda) were determined. At Zumaya the PETM is marked by a red clayey and marly interval poor in organic matter and coincident with a pronounced $\delta^{13}C$ negative shift. A comparable clay interval with low TOC content is also present in the Dababyia section in the lower part of the negative $\delta^{13}C$ shift, whereas the upper part of is enriched in TOC, reflecting increased productivity. The Esplugafreda section located in South Central Pyrenees shows an excellent terrestrial record of the early Eocene warm events. High-resolution $\delta^{13}C$ and $\delta^{18}O$ analyses of two types of calcareous paleosoil nodules reveal two distinct negative excursions a Pre-Onset Excursion (POE) and the Paleocene Eocene Thermal Maximum (PETM), both characterized by significant Hg enrichments.

This Hg enrichment is not linked to clays or total organic carbon contents, and suggests that Hg anomaly resulted from higher atmospheric Hg input into the marine realm, rather than organic matter scavenging and/or increased run-off.

The presence of several peaks of mercury coincident with both POE and PETM intervals supports the role of volcanism (North Atlantic Igneous Province) to initiate the concomitant warming and sea-level rise characterizing the POE and PETM.

Session No. 228

T56. Mass Extinctions II: Past, Present, and Future?
Tuesday, 24 October 2017: 1:30 PM-5:30 PM

Room 608 (Washington State Convention Center)

Geological Society of America *Abstracts with Programs.* Vol. 49, No. 6
doi: 10.1130/abs/2017AM-302839

Back to: T56. Mass Extinctions II: Past, Present, and Future?

<< Previous Abstract | Next Abstract >>

GSA Annual Meeting in Denver, Colorado, USA - 2016

Paper No. 106-6
Presentation Time: 9:00 AM

TIMING AND TEMPO OF DECCAN VOLCANISM REVEALED BY MERCURY ANOMALIES

ADATTE, Thierry[1], FONT, Eric[2], MBABI BITCHONG, André[1], KELLER, Gerta[3], SCHOENE, Blair[3], SAMPERTON, Kyle M.[3] and KHADRI, Syed F.R.[4], (1)Institute of Earth Sciences (ISTE), University of Lausanne, Lausanne, 1015, Switzerland, (2)Faculdade de Ciencias, University of Lisbon, Campo Grande, Edificio C8, Piso 3, Lisbon, 1749-016, Portugal, (3)Department of Geosciences, Princeton University, Guyot Hall, Princeton, NJ 08544, (4)Department of Geology, Amravati University, Amravati, 444602, India, Thierry.Adatte@unil.ch

Mercury is a very toxic element, with a long residence time (1-2 years) and wide distribution by aerosols. Volcanic emissions and coal combustion are the two main natural sources of mercury. Several studies [1-4] evaluated the relationship between Hg anomalies in sediments and LIP activity across mass extinction horizons. The bulk (80%) of Deccan Trap eruptions occurred over a relatively short time interval in magnetic polarity C29r. U-Pb zircon geochronology reveals the onset of this main eruption phase 250 ky before the Cretaceous-Tertiary (KT) mass extinction and continued into the early Danian suggesting a cause-and-effect relationship [5]. In a related study we investigate the mercury (Hg) contents of sections in France (Bidart), Spain (Zumaya), Denmark (Nye Klov), Austria (Gams), Italy (Gubbio), Tunisia (Elles, El Kef), Egypt (Sinai), India (Megalaya), Texas USA (Brazos River) and Mexico (La Parida). In all sections, results show Hg concentrations are more than 2 orders of magnitude greater during the last 100ky of the Maastrichtian up to the early Danian P1a zone (first 380 Ky of the Paleocene). These Hg anomalies are correlative with the main Deccan eruption phase. Hg anomalies generally show no correlation with clay or total organic carbon contents, suggesting that the mercury enrichments resulted from higher input of atmospheric Hg species into the marine realm, rather than organic matter scavenging and/or increased run-off. At Gams, Bidart and Elles, Hg anomalies correlate with high shell fragmentation and dissolution effects in planktic foraminifera indicating that paleoenvironmental and paleoclimate changes drastically affected marine biodiversity. These observations provide further support that Deccan volcanism played a key role in increasing atmospheric CO_2 and SO_2 levels that resulted in global warming and acidified oceans, increasing biotic stress that predisposed faunas to eventual extinction at the KTB.

[1] Grasby et al., 2013, Geology 351, 209–216. [2] Font et al., 2016. Geology 44, 171–174. [3] Sanei et al., H., 2012, Geology 40, 63–66. [4] Percival et al., 2015, EPSL 428, 267–280. [5] Schoene et al., 2015, Science 347, 182-184.

Session No. 106

T145. Volcanism, Mass Extinctions, and Environmental Change
Monday, 26 September 2016: 8:00 AM-12:00 PM

Mile High Ballroom 3C (Colorado Convention Center)

Geological Society of America *Abstracts with Programs.* Vol. 48, No. 7
doi: 10.1130/abs/2016AM-285123

Back to: T145. Volcanism, Mass Extinctions, and Environmental Change

<< Previous Abstract | Next Abstract >>

GSA Annual Meeting in Denver, Colorado, USA - 2016

Paper No. 106-2
Presentation Time: 8:15 AM

PALEOCENE-EOCENE THERMAL MAXIMUM TRIGGERED BY VOLCANISM? EVIDENCE FROM MERCURY ANOMALIES

KHOZYEM, Hassan[1], ADATTE, Thierry[2], MBABI BITCHONG, André[2], CHEVALIER, Yoann[2] and KELLER, Gerta[3], (1)Department of Geology, University of Aswan, Aswan, 81528, Egypt, (2)Institute of Earth Sciences (ISTE), University of Lausanne, Lausanne, 1015, Switzerland, (3)Department of Geosciences, Princeton University, Guyot Hall, Princeton, NJ 08544, hkhozyem@gmail.com

The Paleocene-Eocene Thermal Maximum (PETM, ~55.8±0.2 Ma) is marked by a global drop of 2-6‰ in $\delta^{13}C$ values and rapid warming of 4-5°C in tropical surface waters and 4-8°C in high latitudes. Climate warming persisted for several tens of thousands of years and resulted in rapid diversification in terrestrial mammals and marine planktic foraminifera. Deep-water bathyal benthic foraminifera suffered a mass extinction (~40% species) but no significant extinctions occurred shallow shelf environments. Benthic extinctions are commonly explained as the effects of the initial stage of climate warming due to North Atlantic Volcanic Province volcanism (NAVP), which triggered methane release from ocean sediments causing global warming and ocean acidification. But the relationship between NAPV and the PETM events are not clearly demonstrated. Several studies [1-4] demonstrated the relationship between Hg anomalies in sediments and LIP activity associated with mass extinctions. We investigated the mercury (Hg) content of several sections located in deep bathyal (Zumaya, Trabakua, N-Spain) and outer shelf environments (Dababiya GSSP, Duwi, Egypt). At Zumaya the PETM is marked by a red clayey and marly interval poor in organic matter and coincident with a pronounced $\delta^{13}C$ negative shift. A comparable clay interval with low TOC content is also present in the Dababyia section in the lower part of the negative $\delta^{13}C$ shift, whereas the upper part of is enriched in TOC, reflecting increased productivity. A significant but unique Hg enrichment is observed at the onset of the PETM just below the carbone isotope shift in Spain as well as in Egypt. This increase, which is not correlated with clay or total organic carbon contents, suggests the Hg anomaly resulted from higher atmospheric Hg input into the marine realm, rather than organic matter scavenging and/or increased run-off. This Hg anomaly at the onset of the PETM provides the first direct evidence that volcanism played a crucial role in triggering the PETM events by initiating the warming that likely released methane gases that accelerated greenhouse warming and ocean acidification.

[1] Grasby et al., 2013, Geology 351, 209–216. [2] Font et al., 2016. Geology 44, 171–174. [3] Sanei et al., H., 2012, Geology 40, 63–66. [4] Percival et al., 2015, EPSL 428, 267–280. [5

Session No. 106

T145. Volcanism, Mass Extinctions, and Environmental Change
Monday, 26 September 2016: 8:00 AM-12:00 PM

Mile High Ballroom 3C (Colorado Convention Center)

Geological Society of America *Abstracts with Programs.* Vol. 48, No. 7
doi: 10.1130/abs/2016AM-283712

Back to: T145. Volcanism, Mass Extinctions, and Environmental Change

<< Previous Abstract | Next Abstract >>

GSA Annual Meeting in Denver, Colorado, USA - 2016

Paper No. 106-9
Presentation Time: 9:45 AM

AGE, BIOSTRATIGRAPHY, GEOCHEMISTRY AND MINERALOGY OF CHICXULUB IMPACT SPHERULES ON GORGONILLA ISLAND, COLOMBIA

MATEO, Paula[1], KELLER, Gerta[1], ADATTE, Thierry[2], BITCHONG, André[2], SPANGENBERG, Jorge[3], VENNEMANN, Torsten[4], HEIZLER, Matthew[5], HODGES, Kip[6], MCDONALD, Christopher[7], HOLLIS, Chris[8] and STINNESBECK, Wolfgang[9], (1)Department of Geosciences, Princeton University, Guyot Hall, Princeton, NJ 08544, (2)Institute of Geology and Paleontology, University of Lausanne, Anthropole, Lausanne, CH-2000, Switzerland, (3)Idyst, University of Lausanne, UNIL-Mouline, Bâtiment Géopolis, Lausanne, 1015, Switzerland, (4)Institute of Earth Surface Dynamics, University of Lausanne, Geopolis - CH-1015 Lausanne - Suisse, Lausanne, 1015, Switzerland, (5)New Mexico Geochronology Research Laboratory, New Mexico Bureau of Mines & Mineral Resources, 801 Leroy Place, New Mexico Tech, Socorro, NM 87801-4796, (6)School of Earth and Space Exploration, Arizona State University, Tempe, AZ 85282, (7)School of Earth and Space Exploration, Arizona State University, Tempe, AZ 85287, (8)GNS Science, Avalon, 5010, New Zealand, (9)Institute of Earth Sciences, Heidelberg University, Im Neuenheimer Feld 234-236, Heidelberg, 69120, Germany, mmateo@princeton.edu

The age of the Chicxulub impact is still controversial. Impact spherules found at or near the Cretaceous-Paleogene boundary (KPB) in the North Atlantic, Caribbean, Belize and Guatemala are reworked in early Danian sediments above a KP hiatus [1-3]. But, in NE Mexico and Texas where impact spherules are beyond erosion by the Gulf Stream, they are found in late Maastrichtian sediments with the primary spherule layer predating the KPB by ~100 ky [4,5]. Recent discovery of pristine Chicxulub impact glass spherules on Gorgonilla Island, Colombia [6], and re-sampling of the section sheds new light on this controversy. Sediments consist of radiolarian-rich marls alternating with volcanic-rich turbidites depleted in calcite. Three closely spaced ~2 cm-thick spherule beds, two discontinuously present, overlie a late Maastrichtian erosion surface and have a similar mineralogical composition as the turbidites, suggesting spherule re-deposition marked by decreasing grain size and repetition of beds due to slumping. Spherule beds contain reworked Maastrichtian species and clay clasts with early Danian planktic foraminifera typical of zone P1a(2) about 150-200 ky after the KPB indicating re-deposition during the early Danian. Study of radiolaria is in progress. $\delta^{13}C_{org.carb}$ values show no negative shift near the spherule bed, confirming a KPB hiatus, as also indicated by absence of significant Ni and Co enrichments. $\delta^{18}O$ by laser ablation of spherules have a wide range of values (8.5 to 10.4‰) typical of andesitic-dacitic (~8‰) and rhyolitic glass (9 to 10‰), suggesting melt contaminated with sedimentary material. While these analyses confirm an impact origin, spherules with higher SiO_2 content also have higher $d^{18}O$ values, indicating crystal fractionation processes or assimilation of sedimentary material. Preliminary $^{40}Ar/^{39}Ar$ dating of Gorgonilla impact spherules is currently underway at two laboratories.

[1] Keller et al., 2003. J Geol Soc London 160, 1-13. [2] Keller et al., 2013. Geol Mag 150, 885-907. [3] Mateo et al., 2016. Palaeogeogr Palaeoclimatol Palaeoecol 441, 96-115. [4] Keller et al., 2007. Earth Planet Sci Lett 255, 339-356. [5] Keller et al., 2009. J Geol Soc London 166, 393-411. [6] Bermudez et al., 2016. Terra Nova 28(1), 83-90.

Session No. 106

T145. Volcanism, Mass Extinctions, and Environmental Change
Monday, 26 September 2016: 8:00 AM-12:00 PM

Mile High Ballroom 3C (Colorado Convention Center)

Geological Society of America *Abstracts with Programs.* Vol. 48, No. 7
doi: 10.1130/abs/2016AM-282848

Back to: T145. Volcanism, Mass Extinctions, and Environmental Change

<< Previous Abstract | Next Abstract >>

INTERNATIONAL ASSOCIATION OF SEDIMENTOLOGISTS

Workshop on West African Sedimentology and Sedimentary Basins.
Date: July 27 – August 2, 2014

Ibadan, June 3, 2014

Mr. Mbabi Bitchong André
Department of Earth Sciences
Faculty of Science
University of Yaounde 1 (Cameroon)

Dear Andre,

ACCEPTANCE LETTER

We are pleased to inform you that your co-authored abstract titled '**Characterization of materials in a clayey sequence of the pk 27 area, Douala Sedimentary sub-basin, Cameroon'** has been accepted for oral presentation at the IAS-supported Inaugural Workshop on *West African Sedimentology and Sedimentary Basins* to be held at the Faculty of Science, University of Ibadan, Ibadan, Nigeria from Sunday July 27 to Saturday August 2, 2014. The presentation will be on MS-PowerPoint within a timeframe of 12 minutes. Please confirm that you will make the oral presentation by sending an email to the convener (izumike1970@gmail.com or izumike@daad-alumni.de).

The technical papers presented at the workshop will be published in a special volume of SEDIMENTOLOGY – the journal of the International Association of Sedimentologists (IAS). The guidelines for preparing the manuscript will be distributed at the workshop venue.

Kindly accept our hearty congratulations as we look forward to seeing you at the workshop.

Yours sincerely,

Dr. Izuchukwu Mike Akaegbobi (Workshop Convenor)

Department of Geology
University of Ibadan
Ibadan – Nigeria

Email: izumike1970@gmail.com, izumike@daad-alumni.de
Tel.: +234 803 339 3641

Caractérisation des sols ferralitiques – podzols d'Amazonie brésilienne

André Guy Tranquille Temgoua[1], Jean-Loup Robert[1], Christophe Wonkam[2], Yves Lucas[3]

[1]Department of Civil Engineering, Laval University, Québec, QC, Canada, G1K 7P4
[2]Département de Géosciences, Université de Douala, BP 24157 Douala, Cameroun
[3]Université du Sud Toulon-Var, Directeur du Laboratoire PROTEE - Bâtiment R BP 20132 - 83957 LA GARDE Cedex France
Corresponding author: Andre_Guy_Tranquille.Temgoua@ete.inrs.ca

Résumé

La modélisation numérique est une approche répandue de représentation des milieux géologiques. L'objectif principal de la présente étude est de reproduire l'hétérogénéité des milieux poreux de l'Amazonie brésilienne dans un modèle géométrique bidimensionnel qui peut être utilisé pour effectuer des simulations numériques en hydrogéologie. L'hétérogénéité des milieux poreux de l'Amazonie brésilienne est représentée dans cette étude sur une toposéquence à l'aide d'un algorithme développé sur la plateforme du logiciel MATLAB (2010). Des analyses granulométriques des échantillons prélevés en Amazonie brésilienne ont été effectuées à l'aide d'une tamiseuse digitale (SPARTAN) et d'un appareil électronique à diffraction laser. L'appareil laser (Analysette 22 MicroTec Plus) utilisé est doté d'une technologie double laser avec alignement automatique. Les analyses granulométriques, réalisées conformément à la norme de qualité ISO 9001, ont révélé cinq classes de granulométrie. Ces classes de granulométrie sont représentatives des sols d'Amazonie brésilienne. Les techniques de caractérisation géologiques utilisées permettent de représenter l'hétérogénéité des sols à partir des analyses granulométriques sur une toposéquence. Cette représentation géomorphologique correspond à l'objectif spécifique de la présente étude. De plus, l'utilisation de la méthode de WIND (méthode par évaporation au laboratoire (MEL)) a permis de définir les paramètres hydrodynamiques requis pour le développement d'un modèle hydrogéologique. Il a été ainsi possible de définir les courbes de conductivités hydrauliques et de teneur en eau. Ce travail présente une contribution à la caractérisation granulométrique et hydrodynamique des milieux poreux d'Amazonie.

Mots clés: *Sols ferrallitiques, Podzols, Analyses granulométriques, Paramètres hydrodynamiques*

Caractérisation morphologique et distribution de la pyrite dans une séquence argileuse de pk 27, sous-bassin sédimentaire de Douala, Cameroun

André Mbabi Bitchong[1]*, Gilbert-François Ngon Ngon[2], Etame Jacques[2], Ntamak-Nida Marie Joseph[2], Simon Ngos III[1], Paul Bilong[1]

[1]Département des Sciences de la Terre, Faculté des Sciences, Université de Yaoundé I
[2]Département des Sciences de la Terre, Faculté des Sciences, Université de Douala
Auteur de correspondance : mbabiaandre@yahoo.fr

Résumé :

A pk 27, au Sud-est de la partie nord du sous-bassin de Douala au Cameroun, la pyrite est contenue dans l'argile de la formation de N'kapa d'âge Paléocène-Eocène. Ces matériaux affleurent généralement dans les zones basses, d'altitude comprise entre 20 et 40 m. Un puits de 700 cm de profondeur, foré aux coordonnées N 04°11'21.1'' et E 009°50'17.2'', a révélé la superposition de haut en bas, de deux faciès. (1) Un faciès d'argile rouge brique de 34 cm d'épaisseur présentant de fines laminations blanches et contenant environ 10 % de la masse totale de la pyrite récoltée. Il présente des caractéristiques (% C.O, ph et Eh) favorables à la genèse et à la stabilité de la pyrite. La pyrite de ce facies apparait en cristaux millimétriques isolés de forme cubique ou octaédrique, et surtout en amas globuleux ou allongés de cristaux euédriques millimétriques ou centimétriques; (2) un faciès d'argile grise de 650 cm d'épaisseur contenant la quasi-totalité (90 %) de la pyrite récoltée. Le pH, le Eh et la teneur en carbone organique de ce facies lui confèrent les caractéristiques d'un milieu propice à la genèse et à la stabilité de la pyrite. La pyrite y est euédrique ou massive. La pyrite euédrique, sous forme de coquilles ou de moules assimilables aux formes de la classe des gastéropodes est observée de 200 à 500 cm. Sur l'ensemble du faciès gris, la pyrite se trouve sous forme de cristaux isolés en amas millimétriques. Ses proportions et sa distribution sont variables en fonction du degré de gris. Le niveau supérieur, de couleur gris clair, présente des masses denses de formes irrégulières et de taille pluri centimétrique. Le niveau inférieur a une couleur gris sombre et présente des masses de formes irrégulières, de taille et de densité décroissant avec la profondeur. Toutes ces masses laissent parfois apparaître les caractéristiques des concrétions pyriteuses. En dehors du faciès gréseux superficiel, tout le profil restant présente des caractéristiques des dépôts d'un environnement de mer profonde riches en fer ferreux (Fe^{2+}). Tout ceci porte à croire que la minéralisation pyriteuse des argiles de pk 27 est authigène et s'est développée lors d'épisodes diagénétique précoce et épigénétique.

Mots clés : *pyrite ; pk 27 ; formation de N'kapa ; sous-bassin de Douala ; Cameroun.*

ANNEX III: GEOCHEMICAL AND MINERALOGICAL DATA FROM GORGONILLA SECTION

1. Trace element enrichment factor values $EF_{(TE)}$ of tektites (T) and matrixes (M) relative to PAAS (S) and chondrite (C) from Gorgonilla spherule-rich layers

Sample	Ba		Co		Cr		Cs		Cu		Mo		Ni		Pb		Sc		Sr		U		V		Zn		Zr	
	S	C	S	C	S	C	S	C	S	C	S	C	S	C	S	C	S	C	S	C	S	C	S	C	S	C	S	C
GI-40																												
T1	0.24	52.56	0.75	0.02	0.59	0.02	0.03	0.85	0.34	1.10	1.00	1.28	2.28	0.01	0.08	0.66	0.43	0.84	1.37	47.18	0.30	121.98	0.41	0.86	0.52	0.14	0.20	7.18
T2	1.17	220.09	0.90	0.02	0.32	0.01	0.15	3.23	0.53	0.12	1.25	1.35	0.31	0.00	0.10	0.70	2.31	3.82	6.38	184.62	0.44	153.09	0.85	1.49	0.47	0.11	1.21	36.80
T3	0.79	177.35	0.70	0.02	0.30	0.01	0.19	5.05	0.65	0.08	0.43	0.55	0.17	0.00	0.24	1.98	1.72	3.41	2.19	76.28	0.33	137.04	0.96	2.04	0.69	0.20	0.80	29.19
T4	0.83	178.63	0.60	0.02	0.15	0.00	0.15	3.93	0.27	0.07	0.43	0.53	0.14	0.00	0.04	0.28	1.77	3.36	2.29	76.41	0.17	67.53	0.53	1.08	0.07	0.02	0.91	31.73
T5	0.49	105.13	0.74	0.02	0.54	0.02	0.11	2.90	0.50	0.84	1.66	2.04	1.81	0.01	0.10	0.75	0.95	1.79	2.02	66.92	0.38	150.62	0.57	1.16	0.33	0.09	0.49	17.13
T6	0.81	181.20	0.67	0.02	0.21	0.01	0.17	4.61	0.30	0.07	0.10	0.13	0.14	0.00	0.05	0.40	1.71	3.38	2.12	73.85	0.16	66.54	0.74	1.56	0.08	0.02	0.82	29.95
T7	0.89	145.73	4.51	0.11	4.90	0.11	0.15	2.95	2.50	4.83	3.09	2.90	13.61	0.06	0.39	2.30	2.20	3.18	4.17	105.38	2.45	738.27	2.87	4.42	2.54	0.52	0.98	25.89
T8	0.80	118.38	4.43	0.10	4.37	0.09	0.14	2.48	1.00	4.12	0.96	0.81	12.85	0.05	0.06	0.30	2.18	2.84	3.21	73.33	1.03	280.25	2.28	3.17	0.14	0.03	0.99	23.63
T9	0.73	124.79	2.06	0.05	1.84	0.04	0.17	3.49	1.47	1.74	0.32	0.32	4.69	0.02	0.03	0.16	1.87	2.82	2.53	66.92	0.89	280.25	1.89	3.04	0.09	0.02	0.87	24.21
T10	0.65	146.15	1.49	0.05	1.73	0.05	0.16	4.26	0.93	1.92	0.35	0.46	3.93	0.02	0.05	0.38	1.51	3.01	1.41	49.23	0.73	301.23	1.32	2.81	0.10	0.03	0.64	23.43
T11	0.78	120.09	4.53	0.10	5.52	0.12	0.15	2.69	0.96	3.94	0.69	0.60	11.86	0.05	0.04	0.20	2.15	2.91	2.56	60.64	1.35	381.48	2.59	3.73	0.11	0.02	0.85	21.02
T12	1.20	216.24	2.63	0.07	2.48	0.06	0.27	5.67	0.56	2.62	0.50	0.52	6.73	0.03	0.08	0.54	2.90	4.58	2.84	78.85	0.92	303.70	2.14	3.61	0.15	0.03	1.37	39.85
T13	0.60	116.24	1.33	0.04	1.20	0.03	0.14	3.22	0.38	1.44	0.26	0.29	3.45	0.02	0.05	0.35	1.58	2.69	1.44	42.95	0.48	169.14	1.04	1.89	0.04	0.01	0.83	25.89
T14	0.62	83.33	3.14	0.06	2.75	0.05	0.11	1.70	2.22	2.35	3.35	2.59	8.04	0.03	0.16	0.78	1.68	1.99	5.13	106.92	1.70	420.99	2.54	3.22	0.61	0.10	0.77	16.78
T15	0.61	89.32	5.77	0.13	5.40	0.11	0.18	3.16	3.44	7.94	1.04	0.87	24.91	0.09	0.33	1.75	1.75	2.26	3.44	78.21	1.70	459.26	2.47	3.42	2.06	0.38	0.82	19.52
M	4.55	539.82	2.41	0.04	0.75	0.01	0.11	1.57	2.71	0.47	12.62	8.58	1.84	0.01	0.51	2.19	2.15	2.25	2.22	40.70	0.33	72.16	0.97	1.08	3.49	0.52	0.93	17.78
GI-41																												
T1	0.25	58.12	0.37	0.01	0.12	0.00	0.03	0.76	0.28	0.05	0.52	0.69	0.10	0.00	0.05	0.38	0.66	1.35	1.50	53.59	0.16	68.77	0.33	0.72	0.19	0.05	0.30	11.22
T2	0.83	186.75	0.75	0.03	0.27	0.01	0.21	5.51	0.45	0.09	0.12	0.16	0.18	0.00	0.08	0.68	1.76	3.51	1.43	50.00	0.26	106.67	0.96	2.05	0.15	0.04	0.86	31.47
T3	0.80	184.62	0.74	0.03	0.27	0.01	0.17	4.55	0.30	0.08	0.37	0.48	0.16	0.00	0.13	1.05	1.87	3.78	2.69	95.51	0.22	93.70	0.78	1.69	0.24	0.07	0.85	31.47
T4(a)	0.83	189.74	0.73	0.02	0.20	0.01	0.19	5.06	0.36	0.08	0.10	0.13	0.16	0.00	0.05	0.37	1.78	3.60	1.47	52.05	0.16	66.30	0.76	1.65	0.07	0.02	0.89	32.99
T4(b)	0.87	200.00	0.76	0.03	0.21	0.01	0.19	5.26	0.40	0.09	0.13	0.17	0.18	0.00	0.04	0.30	1.81	3.67	1.46	51.92	0.18	77.16	0.85	1.84	0.05	0.01	0.93	34.52
T5	0.84	194.02	0.80	0.03	0.26	0.01	0.20	5.40	0.72	0.10	0.17	0.22	0.21	0.00	0.07	0.55	1.88	3.85	1.59	57.18	0.26	111.11	0.94	2.05	0.10	0.03	0.88	32.99
T6	0.71	155.13	0.69	0.02	0.21	0.01	0.15	3.80	0.24	0.08	0.34	0.43	0.17	0.00	0.07	0.58	1.49	2.89	2.19	74.62	0.19	75.80	0.63	1.31	0.15	0.04	0.66	23.53
T7(a)	0.85	193.59	0.69	0.02	0.23	0.01	0.21	5.61	0.43	0.08	0.32	0.41	0.15	0.00	0.05	0.43	1.78	3.56	1.41	49.62	0.19	81.48	0.78	1.68	0.08	0.02	0.92	33.76
T7(b)	0.83	188.89	0.74	0.03	0.21	0.01	0.20	5.45	0.38	0.09	0.13	0.17	0.18	0.00	0.07	0.59	1.79	3.58	1.45	50.90	0.19	80.12	0.88	1.88	0.14	0.04	0.89	32.99
T8	0.68	138.03	1.91	0.06	1.89	0.05	0.08	1.97	0.52	1.70	0.43	0.49	3.89	0.02	0.03	0.25	1.80	3.19	2.41	75.13	0.36	134.57	1.12	2.12	0.07	0.02	0.82	26.65
T9	0.71	113.68	2.17	0.05	1.63	0.04	0.14	2.63	0.98	1.56	0.32	0.30	4.49	0.02	0.03	0.18	1.81	2.55	2.77	68.46	0.66	195.06	1.64	2.46	0.05	0.01	0.89	23.07
T10	0.63	102.99	4.02	0.10	3.47	0.08	0.09	1.66	0.86	3.96	0.57	0.53	11.24	0.05	0.02	0.14	1.89	2.70	3.05	76.67	0.63	188.89	1.82	2.78	0.05	0.01	0.85	22.34
T11	0.68	136.32	1.66	0.05	2.02	0.06	0.09	2.20	0.77	1.64	0.51	0.59	3.76	0.02	0.05	0.39	1.86	3.29	2.33	72.56	0.73	269.14	1.59	3.01	0.11	0.03	0.85	27.66
GI-43																												
M	4.51	546.90	2.73	0.05	0.75	0.01	0.08	1.18	3.52	0.44	11.45	7.96	1.66	0.00	0.65	2.84	2.37	2.53	1.42	26.71	0.38	84.38	1.12	1.27	6.57	1.00	1.03	20.26
GI-45																												
T3	0.85	192.31	0.69	0.02	0.18	0.01	0.19	5.04	0.26	0.07	0.10	0.13	0.14	0.00	0.05	0.41	1.98	3.95	2.25	78.85	0.13	56.17	0.63	1.35	0.09	0.03	0.95	35.03
T4	0.84	170.09	1.03	0.03	0.70	0.02	0.15	3.47	0.49	0.23	2.83	3.27	0.53	0.00	0.07	0.53	1.91	3.40	3.98	123.85	0.46	170.37	0.79	1.49	0.16	0.04	0.90	29.44
T6	0.77	173.08	0.74	0.02	0.23	0.01	0.17	4.55	0.70	0.11	0.07	0.10	0.23	0.00	0.05	0.40	1.68	3.31	1.11	38.33	0.18	74.44	0.67	1.42	0.10	0.03	0.86	31.22
T7	1.07	229.49	0.73	0.02	0.17	0.01	0.19	4.68	0.25	0.07	0.25	0.31	0.15	0.00	0.05	0.37	2.21	4.16	2.86	94.74	0.19	74.32	0.65	1.31	0.12	0.03	1.18	40.86
T8	0.79	129.06	0.60	0.01	0.22	0.00	0.02	0.34	0.46	0.11	0.78	0.73	0.30	0.00	0.09	0.53	1.55	2.23	8.10	205.13	0.37	111.48	0.67	1.04	0.46	0.09	0.84	22.36
T9	0.70	143.59	0.91	0.03	0.56	0.02	0.13	3.24	0.53	0.61	0.16	0.19	1.37	0.01	0.01	0.10	1.44	2.60	1.49	47.44	0.21	80.49	0.78	1.52	0.02	0.00	0.77	25.63
T10	0.85	181.62	0.77	0.02	0.23	0.01	0.17	4.30	0.47	0.12	0.05	0.07	0.25	0.00	0.02	0.14	1.70	3.21	1.09	35.90	0.18	69.38	0.69	1.39	0.03	0.01	0.92	31.73

T11	0.85	146.58	2.23	0.06	3.30	0.08	0.13	2.58	1.40	2.61	8.97	8.87	6.98	0.03	0.20	1.25	1.76	2.67	3.87	103.33	1.02	322.22	1.20	1.95	1.18	0.26	0.88	24.64
T12	0.68	112.82	2.55	0.06	1.93	0.04	0.07	1.38	0.96	2.25	2.46	2.33	6.28	0.03	0.45	2.65	1.50	2.18	4.41	112.56	1.37	417.28	1.85	2.87	1.86	0.38	0.74	19.90
T13	0.79	153.85	0.77	0.02	0.23	0.01	0.07	1.57	0.48	0.10	0.29	0.32	0.24	0.00	0.09	0.65	1.78	3.04	5.48	164.10	0.29	103.09	0.88	1.61	0.43	0.10	0.82	25.63
T14	0.69	128.21	2.15	0.06	2.00	0.05	0.15	3.22	0.77	2.67	3.70	3.97	6.60	0.03	0.02	0.11	1.72	2.84	2.02	58.46	0.71	244.44	1.83	3.22	0.04	0.01	0.83	25.15
T15	0.96	162.39	2.25	0.06	1.81	0.04	0.18	3.60	0.69	1.71	0.35	0.34	4.65	0.02	0.02	0.13	2.49	3.73	2.42	63.72	0.46	143.21	1.43	2.28	0.03	0.01	1.13	31.22
T16	0.70	124.79	2.37	0.06	1.88	0.05	0.13	2.65	1.02	2.19	0.36	0.37	5.69	0.03	0.02	0.14	1.97	3.07	2.22	60.90	0.51	165.43	1.46	2.44	0.04	0.01	0.92	26.40

2. Rare earth element enrichment factor values $EF_{(REE)}$ of tektites (T) and matrixes (M) relative to PAAS (S) and chondrite (C) from Gorgonilla spherule-rich layers

Sample	Ce		Dv		Er		Eu		Gd		Ho		La		Lu		Nd		Pr		Sm		Tb		Tm		Yb	
	S	C	S	C	S	C	S	C	S	C	S	C	S	C	S	C	S	C	S	C	S	C	S	C	S	C	S	C
GI-40																												
T1	0.12	19.40	0.19	4.29	0.16	3.90	0.18	5.18	0.14	5.09	0.14	3.96	0.13	22.16	0.14	4.12	0.14	12.11	0.15	15.04	0.15	7.68	0.13	4.41	0.16	4.13	0.19	4.31
T2	0.56	88.69	0.97	21.96	0.84	20.70	0.88	25.00	0.74	26.35	0.69	19.96	0.66	111.63	0.75	21.40	0.68	58.58	0.72	71.60	0.77	38.34	0.66	21.76	0.81	20.25	0.99	22.58
T3	0.42	65.48	0.75	16.98	0.63	15.36	0.70	20.00	0.58	20.65	0.53	15.11	0.48	80.95	0.57	16.46	0.51	43.77	0.53	52.97	0.62	30.52	0.52	17.08	0.64	16.12	0.72	16.31
T4	0.47	73.77	0.84	18.99	0.74	18.06	0.74	21.07	0.64	22.79	0.60	17.27	0.55	93.74	0.65	18.52	0.57	48.85	0.59	59.03	0.64	31.61	0.58	19.01	0.72	17.77	0.81	18.34
T5	0.22	34.81	0.40	9.02	0.34	8.37	0.32	9.29	0.30	10.53	0.28	7.91	0.26	43.46	0.31	9.05	0.26	22.33	0.28	27.50	0.30	14.89	0.26	8.54	0.33	8.26	0.39	8.98
T6	0.44	69.96	0.79	17.84	0.68	16.74	0.71	20.18	0.60	21.41	0.55	15.65	0.51	87.35	0.58	16.46	0.54	46.86	0.56	56.34	0.62	30.86	0.54	17.91	0.65	16.12	0.75	17.11
T7	0.38	59.52	0.74	16.81	0.63	15.42	0.70	20.00	0.57	20.40	0.54	15.47	0.45	76.27	0.56	16.05	0.49	42.22	0.52	51.52	0.60	29.64	0.50	16.53	0.63	15.70	0.69	15.75
T8	0.33	52.72	0.64	14.46	0.54	13.34	0.59	16.79	0.48	16.99	0.45	12.95	0.35	60.08	0.49	13.99	0.41	35.59	0.41	41.41	0.50	24.88	0.43	14.05	0.52	12.81	0.62	14.09
T9	0.32	49.73	0.68	15.37	0.55	13.47	0.58	16.61	0.48	17.14	0.46	13.31	0.37	62.63	0.48	13.99	0.42	35.81	0.41	41.19	0.50	24.81	0.45	14.88	0.52	12.81	0.62	14.03
T10	0.37	57.86	0.63	14.17	0.54	13.28	0.59	16.79	0.48	17.19	0.45	12.95	0.39	65.62	0.48	13.58	0.42	36.03	0.45	44.89	0.48	23.73	0.42	14.05	0.52	12.81	0.61	13.85
T11	0.35	55.04	0.64	14.46	0.55	13.40	0.65	18.57	0.48	17.14	0.45	12.77	0.37	62.21	0.47	13.58	0.42	36.25	0.44	43.77	0.51	25.22	0.45	14.88	0.53	13.22	0.61	13.91
T12	0.55	86.21	1.07	24.19	0.92	22.53	0.94	26.79	0.80	28.48	0.78	22.48	0.62	106.09	0.82	23.46	0.67	57.91	0.69	68.57	0.78	38.68	0.68	22.59	0.89	21.90	0.98	22.34
T13	0.33	51.72	0.57	13.02	0.54	13.34	0.51	14.64	0.47	16.89	0.45	12.95	0.38	64.76	0.48	13.99	0.36	31.39	0.40	39.84	0.45	22.43	0.38	12.67	0.47	11.57	0.57	12.98
T14	0.28	43.93	0.45	10.30	0.38	9.38	0.42	11.96	0.33	11.85	0.30	8.63	0.25	41.76	0.32	9.05	0.29	25.42	0.30	30.42	0.34	16.86	0.31	10.19	0.38	9.50	0.43	9.85
T15	0.25	39.46	0.51	11.50	0.43	10.51	0.45	12.68	0.37	13.28	0.35	10.25	0.27	46.02	0.38	10.70	0.31	26.75	0.32	31.54	0.37	18.49	0.34	11.29	0.43	10.74	0.49	11.08
M	0.16	25.36	0.33	7.42	0.30	7.43	0.43	12.14	0.24	8.60	0.24	7.01	0.20	34.04	0.32	9.05	0.22	18.83	0.23	22.90	0.24	12.10	0.22	7.44	0.32	7.85	0.38	8.68
GI-41																												
T1	0.18	28.02	0.32	7.25	0.27	6.67	0.30	8.57	0.26	9.10	0.23	6.47	0.20	34.09	0.24	7.00	0.21	18.52	0.22	22.45	0.25	12.24	0.22	7.16	0.27	6.61	0.30	6.89
T2	0.46	72.94	0.85	19.16	0.73	17.87	0.76	21.79	0.66	23.55	0.59	17.09	0.53	90.33	0.63	18.11	0.57	49.29	0.59	58.92	0.67	33.45	0.58	19.28	0.69	16.94	0.82	18.71
T3	0.44	69.79	0.81	18.34	0.69	16.87	0.73	20.89	0.63	22.43	0.58	16.73	0.52	88.20	0.60	17.28	0.55	47.75	0.56	56.23	0.64	31.82	0.57	18.73	0.65	16.12	0.78	17.66
T4(a)	0.47	73.61	0.86	19.41	0.75	18.38	0.73	20.89	0.67	23.96	0.61	17.63	0.54	92.46	0.66	18.93	0.57	48.85	0.59	59.15	0.67	33.17	0.58	19.01	0.73	18.18	0.86	19.57
T4(b)	0.51	80.74	0.93	21.05	0.81	19.89	0.81	23.04	0.71	25.38	0.66	19.06	0.59	100.55	0.73	20.99	0.60	51.50	0.63	62.85	0.70	34.87	0.62	20.39	0.77	19.01	0.88	20.12
T5	0.48	75.76	0.91	20.60	0.75	18.44	0.84	24.11	0.69	24.47	0.64	18.53	0.54	91.18	0.65	18.93	0.58	49.96	0.61	60.61	0.69	34.06	0.60	19.83	0.76	18.60	0.85	19.45
T6	0.39	61.01	0.65	14.83	0.54	13.28	0.66	18.75	0.51	18.06	0.44	12.59	0.44	75.42	0.47	13.58	0.47	40.23	0.49	48.93	0.54	26.65	0.43	14.33	0.52	12.81	0.60	13.72
T7(a)	0.49	76.43	0.84	19.08	0.75	18.50	0.76	21.61	0.68	24.21	0.61	17.45	0.55	93.74	0.65	18.52	0.57	49.51	0.61	60.83	0.67	33.04	0.58	19.28	0.75	18.60	0.83	18.83
T7(b)	0.47	74.60	0.84	18.99	0.74	18.12	0.76	21.79	0.64	22.94	0.60	17.27	0.54	92.46	0.67	19.34	0.57	49.29	0.60	59.82	0.65	32.09	0.56	18.73	0.73	18.18	0.84	19.20
T8	0.35	54.38	0.71	16.19	0.60	14.66	0.59	16.79	0.52	18.57	0.50	14.39	0.39	66.04	0.54	15.64	0.43	37.36	0.45	44.78	0.51	25.42	0.47	15.70	0.59	14.46	0.65	14.77
T9	0.33	51.72	0.60	13.68	0.55	13.40	0.54	15.36	0.47	16.73	0.44	12.77	0.35	59.65	0.47	13.58	0.38	32.71	0.40	39.62	0.46	23.05	0.41	13.50	0.51	12.40	0.59	13.54
T10	0.30	47.41	0.60	13.51	0.51	12.52	0.51	14.64	0.47	16.63	0.43	12.23	0.32	54.96	0.44	12.76	0.37	31.61	0.38	37.49	0.44	21.96	0.40	13.22	0.50	12.40	0.55	12.55
T11	0.35	55.87	0.71	16.11	0.63	15.36	0.64	18.21	0.55	19.53	0.51	14.75	0.40	68.17	0.54	15.64	0.44	38.24	0.46	46.02	0.54	26.72	0.48	15.70	0.60	14.88	0.71	16.25
GI-43																												
M	0.17	25.99	0.44	9.93	0.38	9.44	0.52	15.00	0.33	11.75	0.31	8.99	0.22	37.67	0.40	11.52	0.29	24.62	0.29	28.96	0.33	16.52	0.29	9.64	0.40	9.92	0.48	10.95
GI-45																												
T3	0.47	74.44	0.85	19.16	0.70	17.24	0.71	20.36	0.65	23.14	0.62	17.81	0.56	94.59	0.67	19.34	0.58	49.73	0.60	60.38	0.68	33.58	0.59	19.28	0.73	18.18	0.80	18.22
T4	0.44	69.13	0.75	17.10	0.69	16.93	0.67	19.11	0.59	21.06	0.56	16.19	0.52	88.62	0.65	18.52	0.51	43.99	0.54	54.21	0.60	29.57	0.51	16.80	0.69	17.36	0.79	17.91
T6	0.45	70.13	0.82	18.54	0.67	16.49	0.66	18.75	0.60	21.36	0.57	16.19	0.50	84.79	0.63	18.11	0.53	45.98	0.55	54.66	0.61	30.05	0.53	17.63	0.66	16.53	0.77	17.48

T7	0.60	94.50	1.04	23.65	0.95	23.41	0.92	26.25	0.84	29.81	0.77	22.12	0.72	121.86	0.84	24.28	0.72	62.33	0.76	76.32	0.84	41.47	0.72	23.69	0.91	22.73	1.04	23.69
T8	0.31	48.91	0.54	12.24	0.45	11.14	0.48	13.75	0.42	14.90	0.37	10.79	0.37	62.21	0.39	11.11	0.37	31.61	0.40	39.62	0.43	21.21	0.38	12.40	0.45	11.16	0.52	11.75
T9	0.33	52.39	0.58	13.19	0.52	12.65	0.46	13.04	0.45	16.07	0.42	12.05	0.39	65.62	0.45	12.76	0.40	34.26	0.42	42.09	0.45	22.37	0.39	12.67	0.50	12.40	0.57	13.05
T10	0.47	73.44	0.85	19.20	0.73	17.87	0.69	19.64	0.66	23.60	0.62	17.81	0.55	93.74	0.65	18.52	0.56	48.19	0.59	58.92	0.65	32.29	0.58	19.28	0.75	18.60	0.83	18.83
T11	0.36	57.19	0.64	14.54	0.57	13.91	0.55	15.71	0.48	17.14	0.46	13.31	0.42	71.15	0.50	14.40	0.43	36.91	0.45	44.78	0.49	24.41	0.43	14.33	0.55	13.64	0.62	14.15
T12	0.30	47.41	0.52	11.87	0.44	10.76	0.53	15.00	0.40	14.39	0.37	10.43	0.32	53.69	0.38	11.11	0.35	30.28	0.37	36.59	0.39	19.51	0.35	11.57	0.43	10.74	0.52	11.82
T13	0.35	55.37	0.67	15.16	0.55	13.53	0.64	18.39	0.49	17.50	0.47	13.49	0.40	68.60	0.48	13.58	0.43	37.36	0.45	44.89	0.50	24.68	0.44	14.60	0.55	13.64	0.62	14.09
T14	0.33	52.39	0.65	14.75	0.54	13.34	0.57	16.43	0.50	17.85	0.46	13.31	0.38	65.19	0.50	14.40	0.40	34.70	0.42	41.75	0.49	24.47	0.43	14.33	0.54	13.64	0.62	14.22
T15	0.41	64.32	0.82	18.67	0.70	17.12	0.68	19.29	0.62	22.18	0.57	16.55	0.47	79.68	0.62	18.11	0.51	43.77	0.52	51.52	0.58	29.03	0.55	18.18	0.67	16.53	0.79	18.03
T16	0.34	53.55	0.68	15.45	0.60	14.79	0.60	17.32	0.52	18.41	0.50	14.39	0.39	65.62	0.51	14.81	0.43	37.14	0.44	43.88	0.52	25.83	0.47	15.43	0.56	13.64	0.67	15.32

3. Raw data of mineralogy and stable isotopes

Sample	Bulk rock mineralogy (%)									Clay mineralogy (%)			Stable isotopes (PDVB)		
	Phyllosilicate	Quartz	K-feldspar	Na-plagioclase	Calcite	Dolomite	Pyrite	Goethite	Undosed	Smectit	Illite	Zeolite	$\delta^{13}C_{org}$	$\delta^{13}C_{carb}$	$\delta^{18}O$
GI-101	30.68	2.67	5.84	10.27	19.36	0.00	0.00	0.00	31.18	-	-	-	-26.47	-	-
GI-100	25.37	0.98	1.84	0.00	30.89	0.00	1.00	0.00	39.92	-	-	-	-24.43	-9.35	-2.50
GI-99	22.57	1.09	0.00	44.20	5.66	0.62	1.08	3.08	21.70	15.40	8.67	75.93	-29.23	-	-
GI-98	18.06	1.62	0.00	9.50	55.89	0.00	0.00	0.00	14.92	-	-	-	-23.34	-12.94	-3.64
GI-97	60.34	1.13	0.00	23.89	5.21	0.00	0.99	3.07	5.37	-	-	-	-22.80	-	-
GI-96	12.09	1.48	0.00	37.03	23.09	0.00	0.88	0.00	25.42	9.06	3.99	86.95	-27.94	-21.53	-2.38
GI-95	21.82	2.34	3.86	27.94	2.89	0.73	0.00	4.89	35.53	-	-	-	-26.32	-	-
GI-94	12.02	1.08	0.00	8.66	65.02	0.00	0.00	0.00	13.22	21.61	8.31	70.08	-25.80	-12.66	-2.07
GI-93	43.29	1.08	3.64	12.88	17.03	0.00	0.00	0.00	22.08	-	-	-	-29.64	-13.78	-2.54
GI-92	23.02	1.92	0.00	34.02	22.69	0.00	1.17	0.00	17.18	-	-	-	-20.46	-3.61	-2.98
GI-91	19.14	1.60	0.00	8.01	51.83	0.00	1.05	0.00	18.37	5.06	2.35	92.59	-25.06	-11.18	-2.54
GI-90	52.93	1.35	4.89	24.30	3.89	0.69	0.80	2.71	8.45	53.10	20.15	26.74	-28.62	-	-
GI-89	43.03	2.53	0.00	19.38	15.99	0.73	0.90	2.28	15.16	24.43	7.35	68.23	-28.86	-7.54	-2.56
GI-88	31.45	2.30	4.80	9.94	39.99	0.00	0.00	0.00	11.52	14.94	6.30	78.76	-31.98	-7.94	-1.66
GI-87	54.12	2.25	1.74	21.83	4.78	1.78	2.17	0.00	11.33	33.76	5.24	61.00	-25.36	-	-
GI-86b	59.32	1.69	2.08	2.89	1.15	1.78	1.40	3.78	25.91	-	-	-	-28.06	-	-
GI-86	60.02	0.80	17.02	7.98	2.87	0.95	0.00	3.05	7.30	37.23	16.79	45.99	-27.97	-	-
GI-85	23.99	1.30	1.79	9.30	30.88	0.94	1.26	0.00	30.55	-	-	-	-27.51	-4.86	-2.56
GI-84	15.30	1.03	0.00	10.14	29.77	0.99	1.54	8.71	32.53	-	-	-	-26.92	-10.05	-2.34
GI-83	39.09	0.44	14.88	8.38	0.00	0.68	0.00	2.83	33.70	-	-	-	-24.42	-	-
GI-82	40.03	2.81	0.00	7.90	34.99	1.14	1.92	2.99	8.22	-	-	-	-29.07	-9.22	-2.09
GI-81	19.99	1.60	0.00	25.82	31.44	0.00	1.91	6.28	12.97	7.05	7.72	85.23	-29.04	-7.25	-2.95
GI-80	43.55	0.99	0.00	10.88	27.54	0.00	1.17	2.17	13.70	64.34	35.66	0.00	-26.65	-4.69	-2.23

GI-79	9.78	2.26	2.56	6.89	54.10	0.00	1.65	0.00	22.77	-	-	-	-28.99	-4.34	-2.12
GI-78	19.55	2.67	2.91	17.00	41.77	0.00	1.69	4.34	10.06	-	-	-	-28.90	-7.06	-1.86
GI-1	17.55	2.75	10.67	4.67	37.90	1.58	1.73	5.67	17.48	3.99	1.21	94.80	-23.39	-5.62	-2.92
GI-2	43.67	0.61	1.28	12.67	20.84	0.00	2.22	3.06	15.64	-	-	-	-24.48	-5.95	-2.29
GI-3	54.34	0.67	0.00	33.67	6.56	0.00	0.00	0.00	4.76	52.38	47.62	0.00	-23.19	-	-
GI-4	14.23	1.03	0.00	7.74	62.55	0.00	0.00	0.00	14.45	7.88	6.39	85.73	-25.31	-6.68	-2.45
GI-5	18.70	3.06	4.01	10.45	43.76	3.52	0.00	2.45	14.04	12.31	2.11	85.58	-25.50	-7.91	-2.24
GI-6	16.85	1.42	0.00	39.46	25.86	0.00	1.04	0.00	15.37	18.23	7.11	74.66	-23.75	-4.21	-2.13
GI-7	51.56	0.76	14.66	10.90	5.78	0.00	0.00	2.62	13.71	55.87	22.07	22.07	-24.23	-	-
GI-8	23.67	1.48	3.32	16.95	40.56	0.00	0.00	0.00	14.02	28.61	6.07	65.32	-22.53	-5.57	-1.79
GI-9	23.26	0.65	2.48	54.23	11.08	0.00	0.67	1.54	6.11	14.39	5.16	80.44	-21.53	-6.07	-2.26
GI-10	23.12	3.00	5.10	21.54	34.89	0.00	0.00	0.00	12.35	-	-	-	-22.63	-6.77	-1.58
GI-11	21.79	2.67	0.00	26.89	31.82	0.00	1.46	2.78	12.59	11.52	7.06	81.41	-24.34	-5.97	-3.30
GI-12	20.84	1.34	0.00	43.24	16.13	0.00	1.03	0.00	17.41	13.32	10.14	76.54	-21.47	-9.06	-3.88
GI-13	14.85	1.33	2.36	45.25	15.69	0.00	0.63	0.00	19.89	4.47	3.63	91.90	-22.10	-8.23	-3.52
GI-14	15.47	1.65	3.25	30.12	36.18	0.00	0.00	0.00	13.33	4.97	3.79	91.25	-23.93	-11.29	-4.16
GI-15	34.23	1.69	0.00	28.67	5.89	0.75	0.79	0.00	27.98	3.38	3.22	93.40	-22.41	-	-
GI-16	53.22	0.94	0.00	19.82	4.89	0.00	0.86	3.89	16.39	44.69	27.93	27.37	-22.29	-	-
GI-17	32.56	0.98	4.18	22.67	3.78	0.87	1.18	3.89	29.88	-	-	-	-22.43	-	-
GI-18	22.54	2.51	0.00	38.09	1.76	0.83	0.00	3.02	31.25	-	-	-	-22.18	-	-
GI-19	15.00	3.63	4.89	21.78	18.89	0.00	1.49	2.94	31.38	-	-	-	-22.79	-15.98	-5.47
GI-20	35.90	1.56	0.00	26.94	3.37	0.00	0.96	5.10	26.17	-	-	-	-23.63	-	-
GI-21	25.03	2.74	6.87	32.67	0.00	0.00	0.89	0.00	31.80	2.57	2.16	95.28	-22.58	-	-
GI-22	37.04	2.18	0.00	25.00	6.90	0.00	0.00	0.00	28.88	-	-	-	-22.74	-	-
GI-23	19.75	5.36	0.00	34.22	3.93	0.00	1.77	3.83	31.15	4.61	2.26	93.13	-24.38	-	-
GI-24	16.43	1.76	0.00	20.74	32.09	0.00	1.03	0.00	27.94	-	-	-	-21.57	-5.43	-2.46
GI-25	20.94	2.12	0.00	29.03	39.02	0.00	0.84	2.44	5.61	4.15	2.83	93.02	-22.43	-3.79	-2.39
GI-26	30.56	2.31	0.00	9.38	25.33	0.80	1.26	0.00	30.36	10.34	6.79	82.87	-24.57	-4.17	-3.10
GI-27	35.96	1.14	3.90	23.93	1.73	1.41	0.70	2.01	29.23	45.06	31.48	23.46	-24.89	-	-
GI-28	21.67	3.25	2.72	25.92	19.99	0.00	1.01	2.93	22.51	-	-	-	-25.39	-8.42	-3.94
GI-29	28.05	3.03	0.00	19.55	32.56	0.63	0.98	0.00	15.19	-	-	-	-22.37	-11.22	-3.20
GI-30	20.44	4.35	0.00	12.45	31.43	1.09	1.63	0.00	28.62	-	-	-	-24.03	-6.46	-4.01
GI-31	39.45	1.05	0.00	23.44	12.55	0.00	2.44	2.38	18.68	26.71	15.84	57.45	-24.95	-13.67	-3.15
GI-32	24.94	2.49	0.00	4.33	55.90	0.00	0.00	4.91	7.43	-	-	-	-20.51	-6.59	-2.24
GI-33	15.03	2.78	2.62	5.03	62.44	0.00	1.86	0.00	10.24	-	-	-	-24.45	-5.11	-2.54
GI-34	13.00	10.94	2.67	3.90	59.05	0.00	1.73	3.02	5.69	-	-	-	-23.91	-5.00	-1.87

GI-35	19.04	2.31	0.00	8.94	60.02	1.12	1.40	2.77	4.40	-	-	-	-24.03	-8.45	-2.37
GI-36	2.71	0.53	0.00	0.00	86.02	0.00	0	2.17	5.43	-	-	-	-21.61	-7.49	-3.42
GI-37	34.93	2.56	0.00	32.55	17.05	0.00	0.00	2.09	10.82	-	-	-	-24.02	-8.52	-2.52
GI-37b	42.04	1.54	0.00	23.05	26.03	0.00	0.00	1.56	5.78	-	-	-	-22.74	-5.79	-2.74
GI-38	23.56	2.71	3.07	17.43	23.55	0.69	1.45	0.00	27.54	-	-	-	-22.51	-4.64	-2.74
GI-39	8.54	0.67	3.14	0.00	74.30	0.00	0.00	0.00	13.35	-	-	-	-22.98	-12.31	-2.89
GI-40	35.99	0.88	0.00	1.88	57.30	0.00	1.44	1.43	1.07	50.00	25.77	24.23	-22.94	-5.13	-2.65
GI-41	50.33	0.77	2.61	2.49	34.04	0.98	0.98	2.12	5.68	-	-	-	-24.50	-3.56	-3.02
GI-42	20.89	2.87	0.00	9.93	35.05	0.74	1.08	0.00	29.44	-	-	-	-23.05	-10.01	-2.81
GI-43	49.04	0.65	2.67	5.90	32.37	0.00	1.02	2.78	5.57	-	-	-	-24.60	-8.13	-2.59
GI-44	19.04	1.55	0.00	11.56	51.03	0.00	1.52	1.89	13.41	-	-	-	-20.06	-10.02	-3.13
GI-45	39.83	0.97	2.93	3.89	43.04	0.92	1.10	2.86	4.45	-	-	-	-25.33	-6.36	-3.27
GI-46	22.12	1.93	0.00	29.73	38.02	0.00	1.30	0.00	6.89	25.16	9.48	65.36	-23.72	-5.39	-2.23
GI-47	23.93	2.59	0.00	34.95	34.95	0.00	1.46	0.56	1.56	-	-	-	-24.44	-4.44	-1.59
GI-48	27.03	2.20	2.80	38.20	27.04	0.00	0.00	0.00	2.73	-	-	-	-24.05	-3.30	-2.21
GI-49	39.02	1.17	0.00	15.94	20.85	0.00	1.21	2.47	19.35	-	-	-	-23.01	-2.98	-2.15
GI-50	37.84	1.92	0.00	22.20	25.54	0.89	0.94	3.13	7.54	-	-	-	-22.70	-4.94	-2.34
GI-51	22.04	2.21	0.00	33.82	39.03	0.00	1.16	0.00	1.74	-	-	-	-23.17	-7.05	-1.75
GI-52	31.45	1.15	0.00	32.67	30.05	0.00	0.95	2.26	1.46	18.53	12.47	69.00	-22.23	-5.56	-2.23
GI-53	31.56	2.22	0.00	26.04	33.85	0.00	1.32	1.56	3.46	-	-	-	-21.99	-5.82	-1.61
GI-54	32.10	1.17	4.88	26.90	29.03	1.00	0.00	1.65	3.27	-	-	-	-24.31	-5.29	-1.57
GI-55	28.45	0.88	0.00	39.04	18.44	0.00	0.87	2.94	9.39	29.29	10.76	59.95	-21.74	-5.96	-1.79
GI-56	9.18	0.91	0.80	7.23	78.98	0.00	0.00	0.00	2.91	-	-	-	-21.19	-5.08	-1.37
GI-57	65.02	3.20	0.00	22.56	5.40	0.00	0.00	0.00	3.81	24.73	13.55	61.72	-22.83	-	-
GI-58	27.03	3.27	3.56	28.04	32.94	0.00	0.00	0.00	5.16	-	-	-	-20.49	-6.53	-2.51
GI-59	25.89	1.68	3.69	23.66	34.03	0.00	2.45	2.55	6.05	-	-	-	-21.57	-8.82	-1.57
GI-60	9.03	3.47	3.58	6.44	42.67	0.00	2.33	5.33	27.16	-	-	-	-24.10	-5.49	-1.65
GI-61	27.56	1.82	0.00	29.56	14.94	0.00	0.00	0.00	26.12	-	-	-	-27.01	-4.76	-2.42
GI-62	35.99	0.49	3.00	34.94	7.90	0.00	0.00	2.28	15.40	-	-	-	-19.93	-	-
GI-63	24.95	1.18	5.93	21.54	25.04	0.68	1.33	0.00	19.35	-	-	-	-23.75	-12.02	-4.78
GI-64	47.03	1.38	0.00	27.33	7.04	0.00	0.00	0.00	17.22	-	-	-	-23.73	-	-
GI-65	42.56	1.33	0.00	32.55	2.19	0.00	0.88	2.03	18.46	-	-	-	-23.86	-	-
GI-66	57.02	0.61	0.00	14.94	5.03	1.02	1.17	4.95	15.26	-	-	-	-25.18	-	-
GI-67	30.02	3.66	0.00	46.03	1.03	0.80	0.89	3.97	13.61	-	-	-	-27.97	-	-
GI-68	50.20	2.31	4.25	19.43	0.00	0.00	0.09	0.00	23.73	14.61	5.92	79.46	-25.24	-	-
GI-69	50.23	0.64	4.67	15.30	0.96	0.00	1.04	0.00	27.15	-	-	-	-29.47	-	-

GI-70	52.94	1.36	0.00	25.48	1.45	0.00	0.00	0.00	18.77	-	-	-	-28.96	-	-
GI-71	55.93	0.78	0.00	10.89	3.45	0.00	1.15	0.00	27.80	-	-	-	-28.46	-	-
GI-72	48.04	0.86	0.00	41.56	0.00	0.00	0.68	0.00	8.86	-	-	-	-28.62	-	-
GI-73	54.02	1.17	3.00	10.93	16.44	1.13	0.00	0.00	13.31	80.53	19.47	0.00	-26.61	-	-
GI-74	58.02	0.99	0.00	15.95	4.93	0.00	0.76	2.12	17.24	-	-	-	-26.90	-	-
GI-75	34.23	1.48	6.07	36.04	1.53	0.00	0.00	0.00	20.65	-	-	-	-24.54	-	-
GI-76	53.94	1.53	9.25	19.03	2.39	0.00	0.00	0.00	13.85	50.66	13.10	36.24	-27.98	-	-
GI-77	40.46	1.21	0.00	32.03	2.09	0.72	0.77	2.18	20.53	-	-	-	-26.79	-	-

4. Major, trace and rare earth element raw data of tektites (T) and matrixes (M) from Gorgonilla spherule-rich layers

Samples		Major Elements (MEs)									Rare Earth Elements (REE)													
		MgO	CaO	Na_2O	MnO	K_2O	Al_2O_3	TiO_2	SiO_2	FeO	La	Ce	Pr	Nd	Sm	Eu	Gd	Tb	Dy	Ho	Er	Tm	Yb	Lu
		[%]	[%]	[%]	[%]	[%]	[%]	[%]	[%]	[%]	[ppm]	[ppm]	[ppm]	[ppm]	[ppm]	[ppm]	[ppm]	[ppm]	[ppm]	[ppm]	[ppm]	[ppm]	[ppm]	[ppm]
GI-40	T1	2.53	6.43	3.89	0.10	1.46	14.97	0.63	63.11	4.61	5.20	11.70	1.34	5.48	1.13	0.29	1.00	0.16	1.04	0.22	0.62	0.10	0.70	0.10
	T2	4.48	21.33	1.67	0.15	0.49	12.55	0.58	52.73	4.77	26.20	53.50	6.38	26.50	5.64	1.40	5.18	0.79	5.33	1.11	3.29	0.49	3.67	0.52
	T3	3.01	8.53	3.49	0.13	1.29	15.13	0.75	60.83	5.61	19.00	39.50	4.72	19.80	4.49	1.12	4.06	0.62	4.12	0.84	2.44	0.39	2.65	0.40
	T4	2.57	9.38	3.17	0.14	1.34	14.48	0.64	63.02	4.53	22.00	44.50	5.26	22.10	4.65	1.18	4.48	0.69	4.61	0.96	2.87	0.43	2.98	0.45
	T5	3.00	8.31	4.20	0.15	1.28	14.38	0.68	62.55	4.80	10.20	21.00	2.45	10.10	2.19	0.52	2.07	0.31	2.19	0.44	1.33	0.20	1.46	0.22
	T6	2.66	8.38	3.15	0.12	1.36	15.07	0.71	62.49	5.00	20.50	42.20	5.02	21.20	4.54	1.13	4.21	0.65	4.33	0.87	2.66	0.39	2.78	0.40
	T7	3.26	18.36	3.56	0.13	1.01	10.96	0.52	55.74	5.47	17.90	35.90	4.59	19.10	4.36	1.12	4.01	0.60	4.08	0.86	2.45	0.38	2.56	0.39
	T8	3.76	12.99	3.11	0.07	0.82	9.91	0.53	60.84	6.87	14.10	31.80	3.69	16.10	3.66	0.94	3.34	0.51	3.51	0.72	2.12	0.31	2.29	0.34
	T9	2.61	11.03	4.89	0.09	1.57	11.46	0.59	61.84	5.09	14.70	30.00	3.67	16.20	3.65	0.93	3.37	0.54	3.73	0.74	2.14	0.31	2.28	0.34
	T10	2.66	8.50	3.07	0.11	1.35	15.12	0.71	62.59	4.96	15.40	34.90	4.00	16.30	3.49	0.94	3.38	0.51	3.44	0.72	2.11	0.31	2.25	0.33
	T11	4.47	11.53	3.05	0.19	0.94	10.26	0.64	59.86	8.01	14.60	33.20	3.90	16.40	3.71	1.04	3.37	0.54	3.51	0.71	2.13	0.32	2.26	0.33
	T12	3.03	13.22	5.23	0.11	1.22	12.03	0.52	57.29	5.74	24.90	52.00	6.11	26.20	5.69	1.50	5.60	0.82	5.87	1.25	3.58	0.53	3.63	0.57
	T13	3.02	9.48	3.69	0.17	1.17	12.96	0.66	62.45	5.36	15.20	31.20	3.55	14.20	3.30	0.82	3.32	0.46	3.16	0.72	2.12	0.28	2.11	0.34
	T14	3.07	15.58	4.28	0.08	0.80	9.03	0.50	59.83	5.40	9.80	26.50	2.71	11.50	2.48	0.67	2.33	0.37	2.50	0.48	1.49	0.23	1.60	0.22
	T15	3.61	12.91	5.58	0.11	1.69	9.85	0.51	57.83	6.57	10.80	23.80	2.81	12.10	2.72	0.71	2.61	0.41	2.79	0.57	1.67	0.26	1.80	0.26
	M	4.47	14.83	1.77	0.26	0.81	7.95	0.35	38.16	5.87	7.99	15.30	2.04	8.52	1.78	0.68	1.69	0.27	1.80	0.39	1.18	0.19	1.41	0.22
GI-41	T1	2.58	6.90	3.88	0.19	1.61	15.50	0.70	62.68	5.22	8.00	16.90	2.00	8.38	1.80	0.48	1.79	0.26	1.76	0.36	1.06	0.16	1.12	0.17
	T2	2.44	6.11	3.75	0.14	1.64	15.15	0.70	64.24	5.14	21.20	44.00	5.25	22.30	4.92	1.22	4.63	0.70	4.65	0.95	2.84	0.41	3.04	0.44
	T3	3.10	11.04	2.96	0.19	1.23	15.38	0.71	58.99	5.36	20.70	42.10	5.01	21.60	4.68	1.17	4.41	0.68	4.45	0.93	2.68	0.39	2.87	0.42
	T4(a)	2.51	6.29	3.60	0.14	1.52	15.38	0.75	63.80	5.22	21.70	44.40	5.27	22.10	4.88	1.17	4.71	0.69	4.71	0.98	2.92	0.44	3.18	0.46
	T4(b)	-	-	-	-	-	-	-	-	-	23.60	48.70	5.60	23.30	5.13	1.29	4.99	0.74	5.11	1.06	3.16	0.46	3.27	0.51
	T5	2.69	6.86	3.88	0.16	1.48	15.56	0.76	62.29	5.54	21.40	45.70	5.40	22.60	5.01	1.35	4.81	0.72	5.00	1.03	2.93	0.45	3.16	0.46
	T6	2.71	8.90	3.32	0.09	1.45	14.74	0.70	61.96	5.05	17.70	36.80	4.36	18.20	3.92	1.05	3.55	0.52	3.60	0.70	2.11	0.31	2.23	0.33

	T7(a)	2.30	6.11	3.56	0.13	1.58	15.25	0.73	64.52	4.93	22.00	46.10	5.42	22.40	4.86	1.21	4.76	0.70	4.63	0.97	2.94	0.45	3.06	0.45
	T7(b)	-	-	-	-	-	-	-	-	-	21.70	45.00	5.33	22.30	4.72	1.22	4.51	0.68	4.61	0.96	2.88	0.44	3.12	0.47
	T8	3.71	11.68	2.37	0.14	0.68	13.51	0.64	60.00	5.40	15.50	32.80	3.99	16.90	3.74	0.94	3.65	0.57	3.93	0.80	2.33	0.35	2.40	0.38
	T9	2.65	11.13	4.21	0.10	1.06	10.70	0.53	62.91	5.31	14.00	31.20	3.53	14.80	3.39	0.86	3.29	0.49	3.32	0.71	2.13	0.30	2.20	0.33
	T10	3.84	12.99	3.34	0.11	0.59	10.89	0.52	59.20	6.67	12.90	28.60	3.34	14.30	3.23	0.82	3.27	0.48	3.28	0.68	1.99	0.30	2.04	0.31
	T11	3.56	10.94	3.97	0.11	0.82	13.51	0.64	59.41	5.50	16.00	33.70	4.10	17.30	3.93	1.02	3.84	0.57	3.91	0.82	2.44	0.36	2.64	0.38
GI-43	M	5.92	9.44	1.75	0.27	0.74	8.13	0.40	39.97	7.80	8.84	15.68	2.58	11.14	2.43	0.84	2.31	0.35	2.41	0.50	1.50	0.24	1.78	0.28
GI-45	T3	2.74	8.99	3.27	0.15	1.33	15.17	0.72	61.54	5.21	22.20	44.90	5.38	22.50	4.94	1.14	4.55	0.70	4.65	0.99	2.74	0.44	2.96	0.47
	T4	3.23	12.38	2.91	0.12	0.81	13.50	0.61	59.91	5.23	20.80	41.70	4.83	19.90	4.35	1.07	4.14	0.61	4.15	0.90	2.69	0.42	2.91	0.45
	T6	2.47	5.69	4.06	0.14	1.58	15.02	0.73	64.21	5.49	19.90	42.30	4.87	20.80	4.42	1.05	4.20	0.64	4.50	0.90	2.62	0.40	2.84	0.44
	T7	3.38	11.02	2.57	0.18	1.03	14.34	0.71	59.65	6.09	28.60	57.00	6.80	28.20	6.10	1.47	5.86	0.86	5.74	1.23	3.72	0.55	3.85	0.59
	T8	3.42	28.92	2.22	0.11	0.47	10.98	0.53	48.10	3.61	14.60	29.50	3.53	14.30	3.12	0.77	2.93	0.45	2.97	0.60	1.77	0.27	1.91	0.27
	T9	2.01	7.36	4.50	0.10	1.39	13.78	0.59	65.71	3.90	15.40	31.60	3.75	15.50	3.29	0.73	3.16	0.46	3.20	0.67	2.01	0.30	2.12	0.31
	T10	2.11	5.33	3.63	0.11	1.50	14.34	0.65	66.79	4.76	22.00	44.30	5.25	21.80	4.75	1.10	4.64	0.70	4.66	0.99	2.84	0.45	3.06	0.45
	T11	3.65	15.41	4.12	0.11	0.98	11.56	0.51	57.73	5.30	16.70	34.50	3.99	16.70	3.59	0.88	3.37	0.52	3.53	0.74	2.21	0.33	2.30	0.35
	T12	3.16	18.45	2.31	0.07	0.60	11.06	0.48	57.18	5.31	12.60	28.60	3.26	13.70	2.87	0.84	2.83	0.42	2.88	0.58	1.71	0.26	1.92	0.27
	T13	3.32	21.52	2.79	0.14	0.89	12.99	0.63	52.01	4.78	16.10	33.40	4.00	16.90	3.63	1.03	3.44	0.53	3.68	0.75	2.15	0.33	2.29	0.33
	T14	3.03	10.67	3.81	0.11	1.29	12.53	0.58	62.02	5.46	15.30	31.60	3.72	15.70	3.60	0.92	3.51	0.52	3.58	0.74	2.12	0.33	2.31	0.35
	T15	3.13	11.09	4.16	0.13	1.54	11.39	0.59	61.88	5.60	18.70	38.80	4.59	19.80	4.27	1.08	4.36	0.66	4.53	0.92	2.72	0.40	2.93	0.44
	T16	3.14	10.43	4.41	0.12	1.42	11.90	0.57	61.70	5.57	15.40	32.30	3.91	16.80	3.80	0.97	3.62	0.56	3.75	0.80	2.35	0.33	2.49	0.36

Samples		Trace Elements (TEs)																				
		Sc [ppm]	V [ppm]	Cr [ppm]	Co [ppm]	Ni [ppm]	Cu [ppm]	Zn [ppm]	Rb [ppm]	Sr [ppm]	Y [ppm]	Zr [ppm]	Nb [ppm]	Mo [ppm]	Cs [ppm]	Ba [ppm]	Hf [ppm]	Ta [ppm]	W [ppm]	Pb [ppm]	Th [ppm]	U [ppm]
GI-40	T1	4.95	48.70	47.80	12.40	139.00	13.90	45.10	11.50	368.00	5.78	28.30	1.81	1.19	0.16	123.00	0.76	0.11	0.85	1.64	1.46	0.99
	T2	22.60	84.30	21.80	12.50	15.60	17.80	34.30	34.20	1440.00	30.20	145.00	8.00	1.25	0.60	515.00	3.85	0.50	0.73	1.73	7.05	1.24
	T3	20.20	115.00	24.80	11.80	10.20	26.60	61.10	48.10	595.00	23.20	115.00	5.48	0.52	0.94	415.00	3.08	0.36	0.56	4.89	5.27	1.11
	T4	19.90	60.80	12.10	9.69	8.44	10.40	6.18	42.00	596.00	26.30	125.00	6.73	0.49	0.74	418.00	3.46	0.41	0.40	0.69	6.00	0.55
	T5	10.60	65.30	41.60	11.80	106.00	19.60	27.80	29.60	522.00	12.10	67.50	3.86	1.89	0.54	246.00	1.80	0.26	1.27	1.86	3.52	1.22
	T6	20.00	88.40	17.10	11.30	8.67	12.40	6.88	43.10	576.00	24.10	118.00	6.18	0.12	0.86	424.00	3.17	0.39	0.30	0.98	5.55	0.54
	T7	18.80	250.00	290.00	54.90	608.00	74.00	162.00	36.50	822.00	23.50	102.00	4.95	2.69	0.55	341.00	2.67	0.32	5.28	5.69	4.51	5.98
	T8	16.80	179.00	234.00	48.80	519.00	26.80	7.96	27.80	572.00	19.70	93.10	4.90	0.75	0.46	277.00	2.46	0.30	1.19	0.74	3.84	2.27
	T9	16.70	172.00	114.00	26.30	219.00	45.40	5.90	44.10	522.00	20.50	95.40	5.02	0.29	0.65	292.00	2.52	0.31	0.45	0.39	3.99	2.27
	T10	17.80	159.00	141.00	25.00	242.00	38.10	9.20	55.30	384.00	19.30	92.30	5.44	0.42	0.80	342.00	2.53	0.35	0.67	0.94	4.51	2.44
	T11	17.20	211.00	306.00	51.60	496.00	26.70	6.45	27.90	473.00	20.00	82.80	4.58	0.56	0.50	281.00	2.15	0.26	0.77	0.49	3.38	3.09
	T12	27.10	204.00	161.00	35.10	330.00	18.10	10.60	63.40	615.00	33.30	157.00	8.41	0.48	1.06	506.00	4.24	0.53	0.67	1.34	7.40	2.46
	T13	15.90	107.00	83.70	19.10	182.00	13.30	3.38	35.00	335.00	18.80	102.00	4.60	0.27	0.60	272.00	2.59	0.30	0.38	0.86	4.53	1.37
	T14	11.80	182.00	134.00	31.50	296.00	54.10	32.10	21.40	834.00	13.40	66.10	4.24	2.40	0.32	195.00	1.88	0.21	2.93	1.93	2.60	3.41

	T15	13.40	193.00	287.00	63.20	1000.00	91.50	118.00	43.90	610.00	15.30	76.90	3.84	0.81	0.59	209.00	2.10	0.25	1.29	4.32	3.27	3.72
	M	13.30	60.99	31.99	21.28	59.66	58.09	161.36	14.03	317.45	11.51	70.05	3.17	7.97	0.29	1263.19	1.93	0.22	0.62	5.41	3.08	0.58
GI-41	T1	7.97	40.80	10.10	6.29	6.51	11.80	17.00	7.42	418.00	9.92	44.20	2.12	0.64	0.14	136.00	1.19	0.14	0.38	0.94	2.05	0.56
	T2	20.80	116.00	22.10	12.70	11.20	18.50	13.20	50.80	390.00	25.80	124.00	6.12	0.15	1.03	437.00	3.41	0.40	0.35	1.69	5.86	0.86
	T3	22.40	95.70	22.10	12.60	9.79	12.50	21.70	40.60	745.00	25.40	124.00	5.74	0.45	0.85	432.00	3.30	0.37	0.36	2.59	5.56	0.76
	T4(a)	21.30	93.30	16.30	12.40	9.73	14.80	6.26	49.80	406.00	27.40	130.00	6.27	0.12	0.95	444.00	3.50	0.42	0.24	0.93	6.10	0.54
	T4(b)	21.70	104.00	17.40	13.00	11.10	16.70	4.41	49.20	405.00	28.70	136.00	6.68	0.16	0.98	468.00	3.70	0.43	0.30	0.73	6.51	0.63
	T5	22.80	116.00	21.50	13.80	13.20	30.10	9.32	48.50	446.00	27.00	130.00	6.20	0.21	1.01	454.00	3.55	0.40	0.41	1.37	5.96	0.90
	T6	17.10	73.90	17.00	11.30	10.20	9.67	13.00	31.60	582.00	19.70	92.70	4.96	0.40	0.71	363.00	2.49	0.30	0.28	1.44	4.43	0.61
	T7(a)	21.10	94.80	19.30	11.70	9.47	17.60	7.04	53.40	387.00	26.80	133.00	6.80	0.39	1.05	453.00	3.64	0.42	0.49	1.07	6.09	0.66
	T7(b)	21.20	106.00	16.90	12.60	11.20	15.50	12.50	48.30	397.00	27.30	130.00	6.24	0.16	1.02	442.00	3.47	0.41	0.35	1.45	6.00	0.65
	T8	18.90	120.00	138.00	28.70	214.00	18.80	5.40	20.40	586.00	21.40	105.00	5.24	0.46	0.37	323.00	2.92	0.35	0.67	0.61	4.62	1.09
	T9	15.10	139.00	94.10	25.80	196.00	28.30	3.42	30.50	534.00	18.70	90.90	4.89	0.28	0.49	266.00	2.54	0.28	0.43	0.44	3.87	1.58
	T10	16.00	157.00	204.00	48.70	499.00	25.30	3.12	17.90	598.00	18.40	88.00	4.42	0.49	0.31	241.00	2.34	0.28	0.71	0.33	3.50	1.53
	T11	19.50	170.00	147.00	25.00	207.00	28.00	8.37	23.10	566.00	22.20	109.00	5.45	0.54	0.41	319.00	2.95	0.36	0.92	0.97	4.64	2.18
GI-43	M	15.00	72.00	32.94	24.68	54.82	77.17	310.86	10.45	208.32	14.41	79.83	3.66	7.39	0.22	1279.74	2.22	0.27	0.52	7.01	4.05	0.68
GI-45	T3	23.40	76.20	15.00	11.70	8.53	10.70	7.90	50.20	615.00	27.60	138.00	7.03	0.12	0.94	450.00	3.57	0.41	0.20	1.02	5.95	0.46
	T4	20.10	84.40	51.00	15.50	28.90	18.00	12.20	30.10	966.00	25.10	116.00	6.44	3.03	0.65	398.00	3.22	0.41	0.87	1.32	6.26	1.38
	T6	19.60	80.40	18.40	12.30	14.30	28.30	8.56	54.30	299.00	25.20	123.00	6.60	0.09	0.85	405.00	3.32	0.39	0.16	0.98	5.60	0.60
	T7	24.60	74.10	13.30	11.60	8.59	9.72	10.10	53.00	739.00	33.40	161.00	8.45	0.29	0.88	537.00	4.48	0.52	0.32	0.91	7.86	0.60
	T8	13.20	58.60	12.90	7.35	13.40	13.60	29.30	6.43	1600.00	16.50	88.10	4.37	0.68	0.06	302.00	2.35	0.28	0.34	1.30	4.09	0.90
	T9	15.40	85.60	41.30	14.00	77.00	19.80	1.43	41.50	370.00	18.30	101.00	5.67	0.18	0.61	336.00	2.78	0.38	0.97	0.26	5.15	0.65
	T10	19.00	78.50	17.70	12.20	14.90	18.10	2.09	46.90	280.00	26.40	125.00	7.22	0.06	0.81	425.00	3.48	0.44	0.19	0.36	6.24	0.56
	T11	15.80	110.00	206.00	28.70	329.00	43.60	79.60	31.60	806.00	19.80	97.10	5.39	8.23	0.48	343.00	2.70	0.35	5.26	3.08	5.05	2.61
	T12	12.90	162.00	115.00	31.30	283.00	28.60	120.00	15.40	878.00	15.70	78.40	4.32	2.16	0.26	264.00	2.14	0.25	2.23	6.55	3.37	3.38
	T13	18.00	90.70	15.80	11.10	12.60	16.90	32.30	17.90	1280.00	20.30	101.00	4.68	0.30	0.29	360.00	2.64	0.30	0.37	1.60	4.28	0.84
	T14	16.80	182.00	135.00	30.00	337.00	26.10	2.70	35.80	456.00	20.40	99.10	4.95	3.68	0.60	300.00	2.66	0.30	2.29	0.28	4.43	1.98
	T15	22.10	129.00	111.00	28.50	216.00	21.20	2.09	40.60	497.00	25.30	123.00	6.37	0.31	0.67	380.00	3.39	0.42	0.49	0.32	5.68	1.16
	T16	18.20	138.00	121.00	31.40	276.00	32.90	2.69	29.20	475.00	22.00	104.00	5.18	0.34	0.50	292.00	2.82	0.33	0.56	0.35	4.43	1.34

5. Major and trace elements raw data of Gorgonilla bulk samples

Samples	SiO2	TiO2	Al2O3	Fe2O3	MnO	MgO	CaO	Na2O	K2O	P2O5	LOI
	wt-%	wt-%	wt-%	wt-%	wt-%	wt-%	wt-%	wt-%	wt-%	wt-%	wt-%
GI-1	63.51	0.22	5.80	2.76	0.08	1.59	7.75	1.19	0.89	0.12	15.60
GI-2	45.95	0.56	11.93	9.41	0.20	4.47	9.86	2.20	1.24	0.18	13.50
GI-3	47.18	0.59	12.71	8.95	0.13	4.55	5.10	2.18	1.20	0.25	16.97
GI-4	59.85	0.24	6.21	2.44	0.09	1.60	11.72	1.39	1.31	0.14	14.11
GI-5	62.77	0.24	6.53	2.64	0.08	1.66	10.03	1.31	1.23	0.18	13.28
GI-6	55.98	0.35	8.69	4.07	0.08	2.45	8.20	1.89	1.70	0.21	15.55
GI-7	47.98	0.54	11.63	9.44	0.12	4.84	3.80	2.22	1.19	0.19	18.00
GI-8	40.74	0.33	8.28	3.89	0.17	2.56	18.45	1.66	1.57	0.24	21.36
GI-9	45.39	0.47	10.92	8.28	0.17	4.26	8.56	1.99	1.15	0.16	18.06
GI-10	35.77	0.30	8.36	4.32	0.22	2.55	23.26	1.40	1.16	0.18	21.68
GI-11	64.24	0.30	8.87	4.49	0.05	2.63	4.63	1.56	1.26	0.13	11.87
GI-12	64.95	0.34	10.11	5.07	0.06	2.91	5.37	1.61	1.19	0.11	7.44
GI-13	64.11	0.25	7.37	3.68	0.07	2.33	6.12	1.12	0.99	0.11	13.22
GI-14	63.13	0.23	6.64	2.77	0.08	1.91	9.18	1.17	1.13	0.11	13.27
GI-15	68.28	0.33	10.30	3.44	0.03	2.27	3.24	1.84	1.73	0.23	7.78
GI-16	51.42	0.47	13.08	10.00	0.15	5.36	5.50	1.96	1.06	0.18	10.39
GI-17	75.35	0.25	7.20	2.60	0.03	1.70	2.48	1.49	1.40	0.14	7.22
GI-18	67.23	0.28	9.21	4.01	0.03	2.46	3.43	1.66	1.26	0.12	9.92
GI-19	72.98	0.23	7.75	2.88	0.04	1.72	4.24	1.35	1.01	0.12	7.11
GI-20	56.41	0.41	12.24	6.44	0.06	3.40	4.64	1.95	1.89	0.18	11.55
GI-21	66.69	0.35	10.51	4.37	0.05	2.38	4.30	1.76	1.61	0.18	7.36
GI-22	55.80	0.43	14.11	6.77	0.08	3.67	5.77	2.55	1.80	0.21	8.25
GI-23	64.38	0.33	11.19	3.99	0.05	2.31	4.37	1.91	1.55	0.19	9.27
GI-24	55.16	0.31	9.49	3.09	0.13	2.05	11.64	1.85	1.74	0.19	13.51
GI-25	49.12	0.39	11.71	7.79	0.13	4.23	8.32	2.37	1.80	0.15	13.24
GI-26	74.91	0.13	4.42	1.38	0.06	1.14	5.19	1.06	0.69	0.09	10.06
GI-27	48.21	0.43	13.43	8.34	0.10	4.57	4.55	2.06	1.06	0.19	17.09
GI-28	58.07	0.32	10.02	3.97	0.05	2.13	6.36	2.03	2.13	0.17	14.02
GI-29	61.49	0.29	9.07	4.11	0.07	2.26	5.21	1.71	1.87	0.19	13.49
GI-30	76.58	0.15	4.48	1.46	0.05	0.94	5.15	0.98	0.84	0.07	8.60
GI-31	50.01	0.52	13.62	9.68	0.12	4.64	7.08	2.58	1.56	0.13	9.87
GI-32	48.03	0.24	6.82	3.13	0.14	1.71	16.21	1.37	1.47	0.10	19.94
GI-33	57.09	0.15	4.53	1.80	0.12	0.96	15.59	0.90	0.87	0.08	17.50
GI-34	72.70	0.11	3.15	1.40	0.07	0.80	7.83	0.64	0.65	0.05	11.66
GI-35	61.87	0.24	6.71	2.90	0.10	1.66	10.08	1.45	1.31	0.11	12.65
GI-36	51.30	0.13	3.80	1.40	0.13	0.86	19.28	0.84	0.69	0.08	20.58
GI-37	50.26	0.43	12.75	9.69	0.11	4.55	5.75	2.44	1.49	0.12	11.51
GI-37B	44.93	0.47	12.84	8.57	0.18	4.57	10.81	2.28	1.03	0.13	14.14
GI-38	72.09	0.24	6.82	2.47	0.04	1.57	4.82	1.36	1.19	0.12	9.10
GI-39	50.09	0.18	4.88	1.97	0.16	1.22	18.28	1.00	0.93	0.10	20.45
GI-40	46.99	0.44	10.23	7.33	0.23	5.39	11.70	2.21	1.08	0.10	14.22
GI-41	42.05	0.39	8.91	7.13	0.23	5.44	11.35	2.02	0.93	0.07	21.42
GI-42	72.16	0.17	5.38	1.82	0.05	1.04	6.62	1.14	1.02	0.12	9.94
GI-43	46.79	0.44	9.98	8.33	0.23	5.80	9.28	2.13	1.01	0.07	15.80
GI-44	58.34	0.30	8.13	3.40	0.11	1.71	10.34	1.78	1.80	0.12	13.78
GI-45	45.85	0.39	9.47	7.57	0.23	4.94	11.55	1.97	1.11	0.09	16.38
GI-46	40.77	0.35	10.76	5.42	0.16	3.11	17.30	1.86	1.20	0.26	18.06
GI-47	35.99	0.30	9.35	4.62	0.18	2.74	20.19	1.55	1.01	0.22	23.01
GI-48	41.05	0.35	10.90	5.54	0.12	3.42	13.61	1.92	1.19	0.30	21.00
GI-49	44.49	0.42	11.21	7.16	0.10	4.15	8.31	2.22	1.26	0.30	20.05

GI-50	44.94	0.43	11.39	7.27	0.11	4.06	8.58	2.24	1.29	0.28	19.20
GI-51	41.94	0.34	9.58	4.74	0.16	2.75	15.20	1.73	1.30	0.33	21.72
GI-52	45.19	0.38	10.97	5.56	0.16	3.24	14.21	2.04	1.43	0.27	15.85
GI-53	45.58	0.36	10.32	5.48	0.13	3.13	12.35	1.88	1.44	0.23	18.77
GI-54	45.63	0.37	10.19	5.31	0.12	2.88	12.29	1.96	1.37	0.20	19.12
GI-55	48.44	0.41	10.38	8.87	0.13	4.67	7.56	1.98	1.25	0.15	16.05
GI-56	47.22	0.37	9.88	5.65	0.13	3.15	12.85	1.96	1.43	0.21	16.51
GI-57	45.70	0.40	12.61	8.86	0.08	4.80	5.50	1.97	1.28	0.11	18.73
GI-58	45.34	0.25	7.92	2.97	0.17	1.93	19.02	1.32	1.12	0.14	19.74
GI-59	59.23	0.14	3.87	1.56	0.16	1.01	15.55	0.89	0.63	0.13	16.26
GI-60	71.23	0.15	4.27	2.29	0.07	1.30	6.36	0.93	0.72	0.09	11.78
GI-61	64.39	0.31	7.98	3.69	0.06	2.06	5.04	1.43	1.25	0.17	12.75
GI-62	51.02	0.50	12.22	11.44	0.15	5.19	5.60	2.38	1.28	0.17	9.89
GI-63	66.89	0.34	7.84	4.54	0.06	2.84	3.75	1.61	1.76	0.18	9.97
GI-64	54.14	0.52	12.23	8.56	0.07	4.72	3.08	2.32	2.30	0.18	11.28
GI-65	53.81	0.52	14.50	6.97	0.08	3.66	5.46	2.53	1.92	0.27	10.37
GI-66	51.52	0.58	13.39	10.44	0.12	4.92	4.42	2.29	1.28	0.20	10.74
GI-67	60.22	0.47	12.56	6.50	0.06	3.49	4.37	1.98	2.02	0.26	7.18
GI-68	55.45	0.56	12.26	8.13	0.07	4.61	2.76	2.22	2.40	0.29	11.10
GI-69	53.41	0.60	12.86	10.58	0.16	4.67	4.22	2.30	1.42	0.24	8.95
GI-70	53.53	0.61	13.23	8.93	0.07	4.51	3.26	2.29	2.09	0.21	10.54
GI-71	48.73	0.56	12.45	9.27	0.10	4.70	3.66	2.07	1.28	0.20	16.93
GI-72	52.80	0.62	13.72	9.59	0.12	4.61	4.15	2.43	1.28	0.22	10.26
GI-73	51.55	0.62	13.33	9.50	0.12	4.69	4.06	2.45	1.25	0.20	11.56
GI-74	49.19	0.58	12.57	8.96	0.12	4.31	4.07	2.28	1.22	0.21	16.57
GI-75	59.73	0.49	13.85	5.26	0.06	3.41	5.79	2.29	1.69	0.24	6.68
GI-76	53.76	0.56	14.15	8.51	0.08	4.93	5.06	2.33	1.43	0.14	9.03
GI-77	51.31	0.53	14.28	9.41	0.11	5.98	6.81	2.28	1.02	0.13	7.56
GI-78	62.42	0.16	4.48	1.97	0.12	1.22	12.32	0.99	0.63	0.09	15.35
GI-79	64.59	0.22	5.45	2.44	0.09	1.53	9.99	1.15	0.82	0.13	12.73
GI-80	48.61	0.45	10.35	9.51	0.13	4.95	6.83	1.99	1.14	0.16	15.91
GI-81	63.57	0.27	6.92	3.69	0.08	1.87	7.71	1.46	1.31	0.17	12.33
GI-82	60.35	0.30	7.43	3.85	0.09	2.06	8.98	1.57	1.60	0.19	12.76
GI-83	49.25	0.60	12.98	9.24	0.14	4.37	5.29	2.37	1.14	0.22	14.27
GI-84	69.19	0.23	6.10	2.07	0.06	1.27	6.49	1.51	1.43	0.21	10.96
GI-85	70.42	0.25	6.29	1.81	0.05	1.31	5.17	1.51	1.48	0.24	11.07
GI-86	53.14	0.63	13.90	8.76	0.14	4.45	3.57	2.37	1.21	0.28	11.35
GI-86B	52.40	0.92	12.54	7.69	0.06	5.72	3.07	3.58	2.18	0.27	11.51
GI-87	55.00	0.56	12.59	5.17	0.07	3.90	2.69	2.58	2.90	0.62	13.80
GI-88	44.83	0.37	8.95	5.07	0.21	2.84	15.64	1.74	1.59	0.20	18.07
GI-89	55.06	0.46	11.27	6.27	0.11	3.86	6.19	2.13	1.88	0.23	11.88
GI-90	51.50	0.61	13.02	10.19	0.13	4.51	4.53	2.52	1.34	0.19	11.48
GI-91	59.74	0.30	8.04	2.98	0.12	2.11	8.45	1.84	1.82	0.23	13.41
GI-92	56.95	0.34	9.42	4.20	0.09	3.00	8.56	2.03	1.75	0.24	12.57
GI-93	58.64	0.32	9.39	3.99	0.07	2.40	5.68	1.96	1.64	0.25	14.68
GI-94	53.08	0.24	7.09	3.06	0.21	2.54	13.52	1.50	1.23	0.21	16.57
GI-95	69.13	0.28	7.73	3.09	0.04	1.89	1.82	1.73	1.62	0.18	11.73
GI-96	62.69	0.29	7.77	3.03	0.10	1.97	7.33	1.72	1.64	0.28	12.37
GI-97	46.79	0.59	12.51	8.89	0.10	4.73	4.14	2.14	1.28	0.22	18.48
GI-98	56.79	0.23	6.37	2.11	0.26	1.63	13.24	1.53	1.44	0.13	16.02
GI-99	64.37	0.31	9.94	3.28	0.06	2.05	3.87	2.29	2.03	0.21	10.64
GI-100	63.32	0.24	6.65	1.18	0.14	1.30	7.85	1.67	1.73	0.15	15.38
GI-101	75.14	0.22	6.01	1.96	0.07	1.03	4.10	1.32	1.06	0.12	8.11

Sample	Sc (ppm)	V (ppm)	Cr (ppm)	Mn (ppm)	Co (ppm)	Ni (ppm)	Cu (ppm)	Zn (ppm)	Ga (ppm)	Br (ppm)	Rb (ppm)	Sr (ppm)	Y (ppm)	Zr (ppm)	Ba (ppm)	La (ppm)	Ce (ppm)	Nd (ppm)
GI-1	11	80	14	582	9	10	70	39	8	5	15	181	13	36	211	12	15	11
GI-2	18	214	11	1450	23	13	145	75	14	7	19	237	14	78	312	14	17	10
GI-3	18	209	8	929	20	9	132	77	15	6	18	209	15	81	224	8	22	12
GI-4	12	91	11	655	10	8	62	48	8	5	16	254	13	39	836	<LLD	13	10
GI-5	12	74	8	572	7	7	54	40	9	6	20	198	17	41	433	16	11	12
GI-6	14	116	8	577	15	11	79	61	12	8	22	347	19	62	817	14	20	16
GI-7	16	173	3	952	20	8	110	75	14	7	19	223	14	92	453	11	18	11
GI-8	17	112	9	1152	13	9	65	50	11	5	20	398	22	55	872	18	25	15
GI-9	15	144	8	1251	18	9	84	75	13	5	19	273	14	82	658	16	13	9
GI-10	20	113	26	1543	13	13	67	52	11	4	16	414	18	42	732	18	20	14
GI-11	14	117	27	404	14	17	82	55	12	6	23	203	14	43	235	<LLD	8	9
GI-12	17	153	46	503	14	17	73	49	12	3	20	227	11	38	417	9	15	9
GI-13	13	106	22	522	10	12	66	45	9	2	17	213	13	36	392	13	10	9
GI-14	10	64	16	596	7	7	55	44	6	2	13	150	9	24	580	9	<LLD	3
GI-15	17	130	28	185	11	11	93	61	12	4	23	321	20	48	877	22	23	17
GI-16	19	164	8	1122	19	7	96	93	12	4	17	293	14	58	505	7	15	10
GI-17	11	81	14	225	8	7	63	52	8	4	17	214	12	31	952	11	11	9
GI-18	15	114	30	225	14	14	78	58	12	5	18	232	13	39	509	7	5	8
GI-19	13	92	18	286	9	9	61	50	9	4	15	175	12	31	388	9	7	8
GI-20	26	163	44	493	19	19	111	84	16	5	27	400	18	56	803	19	18	17
GI-21	19	131	29	345	13	14	81	61	13	6	25	292	19	51	678	19	15	16
GI-22	26	191	27	597	21	21	107	77	17	9	25	426	21	62	818	15	17	18
GI-23	19	139	26	391	13	15	89	67	15	7	25	290	20	50	460	20	16	17
GI-24	19	123	22	826	11	11	84	57	12	7	23	349	18	45	1034	22	13	14
GI-25	19	140	13	925	23	18	89	77	13	8	20	397	14	55	1383	15	11	10
GI-26	9	46	11	515	5	5	38	32	7	6	13	145	9	25	194	11	6	6
GI-27	20	184	10	761	18	8	93	73	14	5	15	320	15	58	728	15	17	12
GI-28	15	135	11	424	15	12	83	66	12	8	25	356	15	50	1383	15	12	10
GI-29	14	117	13	511	13	12	72	62	12	8	28	261	19	50	527	19	14	16
GI-30	7	46	8	343	5	6	29	21	6	3	14	113	8	27	178	9	5	6
GI-31	23	240	36	848	27	23	116	89	15	5	24	335	11	71	673	8	10	7
GI-32	14	96	8	958	12	11	58	44	10	8	19	266	15	41	569	12	11	10
GI-33	9	47	8	901	6	6	36	23	6	3	13	210	12	28	229	14	9	9
GI-34	7	30	61	554	5	6	34	22	6	2	15	120	9	23	110	9	5	8
GI-35	11	74	11	681	9	10	55	35	9	4	19	214	14	44	328	15	11	10
GI-36	8	36	5	1071	4	4	25	40	5	3	10	133	10	23	217	15	10	8
GI-37	19	192	6	832	23	14	107	64	11	9	15	408	10	57	1423	7	5	5
GI-37B	22	213	32	1368	23	18	106	75	13	4	15	280	12	64	721	12	16	8

GI-38	12	87	10	349	8	8	59	30	10	4	19	202	12	40	553	11	10	12
GI-39	10	57	6	1114	5	6	39	32	7	4	15	135	12	28	420	15	11	9
GI-40	12	70	27	1964	30	66	61	134	11	7	17	361	15	88	619	13	16	10
GI-41	12	61	28	1931	27	57	62	123	9	9	14	295	12	76	707	12	5	7
GI-42	9	54	7	450	5	5	46	40	7	4	14	179	11	29	633	14	9	9
GI-43	13	78	27	1816	27	60	67	145	9	7	13	257	10	83	880	<LLD	6	7
GI-44	14	110	12	842	10	13	71	51	9	6	20	336	13	45	1378	13	12	9
GI-45	14	85	31	1788	26	58	63	109	10	7	16	357	13	82	1126	11	6	8
GI-46	19	118	20	1183	18	21	74	65	11	7	18	405	29	53	311	27	21	24
GI-47	18	101	21	1305	16	21	65	55	12	5	16	393	26	47	369	31	20	22
GI-48	18	124	21	910	17	20	76	67	13	8	17	409	31	53	329	23	27	25
GI-49	19	139	17	793	20	21	86	74	13	8	18	335	28	76	377	26	21	20
GI-50	18	141	15	810	20	20	92	73	13	7	17	329	26	74	353	24	24	20
GI-51	19	125	17	1068	15	17	73	61	12	7	19	328	29	53	228	24	23	24
GI-52	20	151	17	1067	17	19	88	66	14	9	21	352	24	56	322	26	24	21
GI-53	20	142	13	926	17	17	88	68	13	10	22	330	22	50	414	12	15	16
GI-54	20	157	13	838	16	15	85	60	13	8	20	339	20	53	202	20	13	15
GI-55	15	135	5	965	21	13	61	65	11	10	19	278	12	53	346	14	12	10
GI-56	20	154	12	921	18	14	85	63	13	11	20	339	19	50	351	12	16	14
GI-57	19	188	9	618	22	15	113	71	14	6	20	312	9	45	236	13	10	10
GI-58	15	105	12	1151	9	9	62	46	10	4	17	228	13	34	395	15	18	12
GI-59	11	49	11	1187	6	5	41	28	7	4	12	147	13	24	86	9	7	11
GI-60	8	38	19	553	24	13	34	26	9	4	13	109	9	28	59	9	6	7
GI-61	19	110	22	451	17	14	87	51	15	5	24	190	20	52	94	19	9	16
GI-62	21	216	7	1102	27	13	126	87	14	11	20	325	13	58	580	12	16	10
GI-63	17	114	20	542	13	13	96	66	12	7	24	178	20	48	530	13	12	14
GI-64	24	208	22	537	22	20	152	86	17	7	32	324	20	71	765	16	15	15
GI-65	29	219	43	614	22	22	146	109	19	9	29	372	28	78	649	18	28	25
GI-66	22	261	7	869	25	12	125	96	16	9	21	279	14	67	210	16	12	11
GI-67	25	164	49	458	18	26	190	104	19	5	40	229	26	73	83	19	23	22
GI-68	20	186	33	508	24	26	137	106	18	7	32	359	23	82	1060	16	21	17
GI-69	19	220	5	1106	26	10	119	93	16	6	24	353	16	79	417	14	20	14
GI-70	21	223	20	511	25	21	142	90	16	6	30	360	16	88	1122	13	18	11
GI-71	18	227	6	796	24	12	138	85	15	9	21	282	13	71	274	9	20	13
GI-72	20	256	2	893	25	9	145	90	16	10	20	308	15	79	313	7	22	14
GI-73	18	251	2	899	25	8	147	87	16	11	20	305	14	80	269	12	14	13
GI-74	18	241	1	896	22	7	136	81	15	12	21	317	15	74	429	12	23	13
GI-75	24	184	57	415	18	18	95	62	16	9	26	339	20	72	436	11	25	17
GI-76	27	266	42	623	26	18	113	80	15	8	19	275	13	63	300	9	13	10
GI-77	24	257	77	824	29	20	110	77	16	8	16	309	11	64	262	8	10	10

GI-78	10	57	15	849	8	7	45	28	6	6	13	185	11	25	61	11	9	9
GI-79	11	74	10	641	8	7	68	36	7	5	14	191	13	32	164	10	9	7
GI-80	17	159	10	1030	18	13	117	67	13	9	19	246	14	66	345	12	11	10
GI-81	12	95	9	578	10	10	77	41	9	6	19	219	16	38	543	16	14	11
GI-82	15	114	12	624	13	11	106	63	11	6	23	276	18	48	625	18	17	11
GI-83	18	217	7	1022	22	7	122	95	16	10	18	243	16	80	286	9	15	11
GI-84	10	101	9	472	9	5	48	45	9	6	16	245	16	33	985	11	16	12
GI-85	11	79	10	386	8	5	56	44	9	6	17	220	18	39	463	17	17	13
GI-86	18	178	1	1006	19	4	93	105	18	9	18	244	21	96	477	18	21	16
GI-86B	33	113	371	423	46	87	31	199	12	4	35	318	25	45	708	14	14	10
GI-87	19	189	14	506	22	12	116	107	17	17	27	410	40	79	1299	29	44	30
GI-88	19	156	19	1484	17	14	95	61	13	8	22	322	19	48	554	15	19	14
GI-89	22	188	21	777	18	16	123	89	15	11	27	317	20	61	572	16	23	16
GI-90	21	283	3	979	23	9	154	85	16	12	23	264	14	72	553	15	14	8
GI-91	15	118	9	856	16	8	73	73	9	9	18	285	19	40	1260	17	20	12
GI-92	16	104	20	640	14	12	151	68	12	12	23	271	21	56	714	22	26	15
GI-93	15	104	14	524	11	9	88	53	12	10	22	284	24	56	1064	20	19	14
GI-94	14	82	13	1537	12	7	325	58	8	7	15	243	19	38	814	22	19	14
GI-95	11	83	11	329	9	7	177	49	11	11	20	208	16	54	355	12	14	12
GI-96	14	126	14	689	12	7	200	43	10	7	20	234	20	41	773	16	27	18
GI-97	20	252	9	733	22	9	217	78	15	11	21	242	15	77	816	12	10	8
GI-98	12	80	6	1802	9	5	135	71	7	6	15	235	14	35	1341	17	9	8
GI-99	17	100	18	433	11	8	141	81	12	12	19	318	21	52	1043	12	14	10
GI-100	9	32	4	1036	5	3	84	46	8	5	15	294	21	62	994	21	20	13
GI-101	9	70	15	553	7	8	44	39	8	3	14	156	14	34	645	12	<LLD	8

ANNEX IV: MINERALOGICAL AND GEOCHEMICAL RAW DATA FROM ZYMAYA OUTCROP

1. Bulk rock and clay mineralogical raw data

Samples	Bulk rock mineralogy							Clay mineralogy			
	Phyllo	Quartz	K-felds	Na-plagio	Calcite	Dolomite	Undosed	I/S	Mica	Kaolonite	Chlorite
Z-1	38.68	14.96	0.00	4.88	38.03	1.03	2.42	7.99	39.54	34.46	18.01
Z-2	31.74	15.82	1.19	6.09	41.33	1.12	2.71	9.46	40.02	33.46	17.06
Z-3	38.94	13.90	0.00	2.81	39.73	0.86	3.75	11.28	39.53	31.46	17.73
Z-4	37.11	14.85	0.00	2.10	41.70	0.91	3.33	12.12	41.34	28.49	18.06
Z-5	39.24	16.56	0.00	2.37	37.93	0.00	3.90	14.30	52.86	19.84	12.99
Z-6	47.03	11.43	0.00	2.07	39.02	0.00	0.45	5.22	45.98	27.85	20.94
Z-7	34.46	17.63	0.00	2.42	45.23	0.00	0.27	15.77	52.46	19.62	12.16
Z-8	32.21	12.95	1.43	4.13	47.03	0.00	2.24	16.69	56.22	15.13	11.96
Z-9	36.12	13.76	0.00	2.50	44.02	0.00	3.60	13.06	56.70	17.14	13.09
Z-10	40.97	17.74	0.00	3.86	33.93	0.00	3.49	20.00	43.74	20.51	15.75
Z-11	42.65	14.93	0.00	2.25	39.23	0.00	0.95	12.63	54.21	19.79	13.38
Z-12	37.84	15.02	0.00	2.11	41.03	0.00	4.00	2.12	48.31	30.53	19.03
Z-13	35.89	13.86	0.00	3.68	44.45	0.00	2.12	3.97	41.01	30.78	24.23
Z-14	32.59	12.32	0.00	2.30	49.23	0.73	2.84	2.82	48.92	32.98	15.28
Z-15	38.76	8.64	0.00	1.95	48.74	0.00	1.91	9.44	59.29	20.75	10.51
Z-16	37.34	16.60	0.00	2.30	43.44	0.00	0.32	3.85	50.91	24.25	20.99
Z-17	38.18	14.94	0.00	2.54	41.83	0.00	2.51	12.38	52.43	19.08	16.11
Z-18	37.91	16.07	0.00	2.36	40.48	0.00	3.19	4.55	58.12	20.11	17.21
Z-19	35.93	15.89	0.00	3.11	43.10	0.00	1.97	13.90	49.22	19.42	17.45
Z-20	38.65	17.51	0.00	8.88	32.93	1.10	0.92	6.90	53.93	22.43	16.74
Z-21	38.90	18.93	0.00	2.25	36.20	0.00	3.72	12.92	42.50	44.58	0.00
Z-22	39.95	17.16	0.00	2.44	40.00	0.00	0.46	3.39	50.60	32.57	13.44
Z-23	41.29	14.67	0.00	2.73	39.35	0.85	1.11	15.83	55.10	17.10	11.97
Z-24	38.67	17.27	0.00	2.51	40.04	0.00	1.51	18.24	53.94	15.17	12.65
Z-25	36.11	23.92	0.00	3.39	33.39	0.82	2.36	8.41	62.00	17.66	11.94
Z-26	31.82	23.52	0.00	7.42	34.00	0.00	3.24	10.09	58.40	17.38	14.12
Z-27	35.94	18.32	0.00	2.46	40.02	0.71	2.55	9.76	68.69	10.99	10.56
Z-28	34.97	15.40	0.00	2.10	45.12	0.00	2.41	19.93	45.08	18.23	16.76
Z-29	36.24	12.59	0.00	2.32	46.02	0.00	2.83	5.19	50.04	22.98	21.78
Z-30	30.65	14.25	0.00	4.05	48.22	0.00	2.83	15.37	52.52	17.81	14.31
Z-31	36.02	15.88	0.00	2.34	42.15	0.85	2.76	0.58	57.08	23.75	18.59
Z-32	37.51	21.63	0.00	2.53	37.02	0.00	1.31	2.77	54.54	24.19	18.50
Z-33	43.12	14.73	0.00	2.39	35.92	0.96	2.88	14.00	47.15	22.38	16.47
Z-34	15.02	51.77	0.00	4.98	23.18	2.50	2.55	10.11	52.36	27.12	10.40
Z-35	37.66	15.65	0.00	4.10	40.03	1.57	0.99	11.81	55.42	20.06	12.71
Z-36	43.94	17.67	0.00	2.76	33.80	0.84	1.00	17.84	53.94	16.97	11.25
Z-37	41.70	14.44	0.00	2.50	39.78	0.00	1.58	11.48	59.76	16.29	12.47
Z-38	39.78	17.82	0.00	2.06	38.02	0.76	1.56	13.62	50.17	21.46	14.74
Z-39	39.82	14.85	0.00	2.29	39.02	1.24	2.78	11.62	62.10	15.12	11.16
Z-40	35.03	19.52	0.00	4.65	40.23	0.00	0.57	11.86	60.47	15.26	12.41
Z-41	39.71	22.14	0.00	3.11	32.84	0.00	2.20	24.31	42.42	19.46	13.81
Z-42	33.19	16.02	0.00	3.62	43.20	0.00	3.97	13.34	63.49	12.35	10.83
Z-43	36.32	14.45	0.00	2.34	46.65	0.00	0.25	4.66	53.52	22.07	19.75
Z-44	36.82	22.35	0.00	2.20	38.03	0.00	0.60	28.88	49.59	10.46	11.07
Z-45	30.99	12.26	0.00	2.27	52.10	0.00	2.38	24.94	52.89	10.45	11.71
Z-46	30.78	12.73	0.00	1.70	50.83	1.13	2.83	15.16	62.75	10.56	11.53
Z-47	32.45	13.11	0.00	2.12	51.02	0.00	1.30	27.27	52.77	9.32	10.64
Z-48	29.90	14.66	0.00	4.11	47.89	1.21	2.23	22.43	57.24	11.22	9.11
Z-49	33.83	16.02	0.00	2.85	46.02	0.00	1.28	20.97	54.97	12.48	11.58
Z-50	31.99	13.08	0.00	2.03	50.45	1.06	1.40	21.80	56.68	10.44	11.07
Z-51	37.54	16.17	0.00	3.53	41.81	0.00	0.96	29.03	36.84	17.71	16.42
Z-52	35.40	23.26	0.00	4.05	35.03	0.76	1.50	20.23	53.67	13.74	12.35

Z-53	37.95	13.42	0.00	2.40	42.67	0.94	2.61	21.15	54.16	12.98	11.71
Z-54	36.18	13.36	0.00	4.49	44.66	0.00	1.31	18.76	55.53	12.38	13.34
Z-55	33.40	12.38	0.00	2.73	49.02	0.00	2.47	14.22	57.67	13.96	14.15
Z-56	42.36	13.07	0.00	2.99	39.03	1.46	1.09	15.56	57.47	14.21	12.77
Z-57	36.35	12.86	0.00	2.95	47.02	0.00	0.82	26.72	50.87	10.08	12.32
Z-58	33.03	13.28	0.00	2.43	50.33	0.00	0.93	3.33	50.61	22.76	23.30
Z-59	25.85	24.88	0.00	6.42	39.87	0.00	2.98	7.46	49.27	21.87	21.39
Z-60	28.55	12.03	0.00	2.23	55.02	0.00	2.17	21.18	53.30	11.25	14.26
Z-61	27.93	11.32	0.00	1.96	55.90	0.00	2.89	20.23	54.11	11.50	14.16
Z-62	30.33	15.79	0.00	2.73	49.02	1.29	0.83	23.43	43.12	15.33	18.12
Z-63	41.91	12.70	0.00	3.97	39.02	0.00	2.39	16.66	57.53	11.77	14.04
Z-64	35.59	14.30	0.00	2.29	46.98	0.00	0.84	21.27	49.89	13.54	15.31
Z-65	32.36	13.04	0.00	2.78	50.02	0.00	1.80	4.23	62.69	15.35	17.74
Z-66	32.19	14.48	0.00	2.77	50.33	0.00	0.22	21.42	54.94	11.08	12.56
Z-67	30.52	21.08	0.00	5.49	42.74	0.00	0.17	24.42	51.03	11.80	12.76
Z-68	33.46	12.03	0.00	2.01	50.33	1.21	0.96	20.73	56.00	9.22	14.05
Z-69	31.25	14.06	0.00	2.46	51.02	0.00	1.22	20.21	50.45	13.08	16.25
Z-70	29.06	15.23	0.00	2.15	52.23	0.00	1.33	12.19	62.30	9.14	16.36
Z-71	34.69	12.15	0.00	2.64	49.02	0.00	1.50	27.31	43.75	11.74	17.20
Z-72	28.02	13.17	0.00	2.08	54.02	0.00	2.71	23.56	49.36	12.11	14.97
Z-73	36.22	10.73	0.00	1.93	50.02	0.00	1.09	20.57	52.84	10.64	15.95
Z-74	32.10	14.43	0.00	1.76	51.02	0.00	0.69	3.86	52.14	14.51	29.49
Z-75	31.08	12.47	0.00	7.62	47.12	0.87	0.83	34.03	40.67	7.34	17.97
Z-76	33.15	11.54	0.00	4.29	49.23	0.00	1.80	19.99	53.15	12.03	14.82
Z-77	37.31	14.15	0.00	2.30	42.70	0.00	3.55	19.05	55.11	13.78	12.07
Z-78	16.41	9.95	0.00	0.00	72.92	0.00	0.72	21.29	36.63	30.47	11.60
Z-79	24.02	11.82	0.00	8.25	54.02	0.00	1.89	28.44	50.41	15.23	5.92
Z-80	44.94	27.85	1.15	3.05	19.41	1.08	2.51	24.32	49.52	18.69	7.47
Z-81	26.92	24.02	0.00	4.41	42.12	0.00	2.53	-	-	-	-
Z-82	27.93	20.83	0.00	4.07	41.77	2.66	2.74	19.60	59.93	11.59	8.88
Z-83	30.78	18.78	0.00	5.62	41.92	1.21	1.69	24.04	48.26	15.06	12.65
Z-84	32.92	19.25	0.00	2.19	42.11	0.00	3.53	14.93	60.99	21.74	2.34
Z-85	28.72	15.02	0.00	1.93	48.02	1.97	4.34	20.32	59.90	12.47	7.30
Z-86	30.62	16.88	0.00	2.21	44.29	2.25	3.75	21.25	57.72	13.33	7.71
Z-87	26.78	14.17	0.00	1.71	55.08	0.00	2.26	-	-	-	-
Z-88	17.26	23.75	0.00	3.17	54.01	0.00	1.81	14.42	58.23	16.20	11.15
Z-89	33.81	13.90	0.00	2.17	48.49	0.00	1.63	5.52	40.30	33.26	20.92
Z-90	10.59	4.77	0.00	0.00	81.31	0.00	3.32	14.90	58.23	13.24	13.63
Z-91	9.45	1.81	0.00	0.00	87.05	1.29	0.40	22.00	44.34	14.26	19.40
Z-93	12.40	3.53	0.00	0.00	83.21	0.00	0.86	10.51	36.55	40.11	12.82
Z-94	6.92	2.05	0.00	0.00	88.73	0.00	2.30	16.78	55.98	12.92	14.32
Z-95	11.00	2.40	0.00	0.00	84.94	0.00	1.66	19.59	47.18	13.26	19.97
Z-96	7.45	3.82	0.00	0.00	86.02	0.00	2.71	24.81	47.12	13.80	14.27
Z-97	6.58	2.00	0.00	0.00	88.67	0.00	2.75	14.11	59.95	11.69	14.24
Z-98	7.82	2.00	0.00	0.00	87.52	0.00	2.66	14.53	58.68	11.98	14.81
Z-100	7.29	9.82	0.00	0.00	81.56	0.00	1.32	18.90	54.81	14.01	12.27
Z-101	6.07	2.08	0.00	0.00	89.22	0.00	2.63	30.14	35.34	12.54	21.98
Z-102	5.75	3.15	0.00	0.00	88.92	0.00	2.18	27.01	40.21	12.65	20.14
Z-103	3.89	5.01	0.00	0.00	90.32	0.00	0.78	-	-	-	-
Z-104	6.89	2.92	0.00	0.00	89.10	0.00	1.09	21.10	60.10	10.40	8.40
Z-105	13.40	5.43	0.00	0.00	80.23	0.00	0.94	12.04	46.49	15.82	25.65
Z-106	6.02	2.59	0.00	0.00	90.34	0.00	1.05	16.63	56.11	0.00	27.25
Z-107	2.81	2.99	0.00	0.00	91.72	1.74	0.74	15.94	58.65	11.58	13.83
Z-108	27.03	9.14	0.00	1.75	58.22	2.67	1.19	18.83	62.07	10.44	8.66
Z-109	8.02	3.78	0.00	3.46	83.20	0.00	1.53	3.21	46.84	36.13	13.82
Z-111	35.10	11.15	0.00	2.43	45.33	2.28	3.71	3.06	63.23	16.36	17.35
Z-113	8.03	4.30	0.00	0.00	86.34	0.00	1.33	11.96	49.44	17.95	20.65

2. Stable isotopes ($\delta^{13}C_{org}$, $\delta^{13}C_{carb}$ and $\delta^{18}O$), TOC and mercury (Hg) raw data of representative samples at the Zumaya K/T section.

Samples	Hg	TOC	Stable isotopes		
			$\delta^{13}C_{org}$	$\delta^{13}C_{carb}$	$\delta^{18}O$
Z-1	11,9	0,03	-25,1	1,1	-3,5
Z-2	22,3	0,03	-25,3	1,3	-3,5
Z-3	7,1	-	-25,1	1,5	-3,5
Z-4	3,1	-	-25,2	1,5	-3,4
Z-5	3,5	0,04	-21,2	1,7	-3,3
Z-6	3,9	-	-25,1	1,8	-3,2
Z-7	3,3	-	-25,2	1,5	-3,3
Z-8	3,9	-	-25,2	1,8	-3,4
Z-9	3,7	-	-25,3	1,7	-3,5
Z-10	16,9	0,03	-25,1	1,4	-3,4
Z-11	23,4	0,05	-25,4	1,4	-3,1
Z-12	5,1	-	-25,2	1,4	-3,2
Z-13	4,6	-	-25,3	1,5	-3,1
Z-14	3,9	0,05	-25,7	1,5	-3,2
Z-15	1,7	-	-25,5	1,6	-3,3
Z-16	3,4	-	-25,5	1,6	-3,2
Z-17	4,9	0,05	-25,3	1,5	-3,3
Z-18	2,7	-	-25,2	1,6	-3,2
Z-19	3,6	-	-25,8	1,5	-3,1
Z-20	7,5	0,04	-25,3	1,3	-3,3
Z-21	16,1	-	-25,4	1,3	-3,2
Z-22	3,8	-	-25,1	1,3	-3,1
Z-23	2,8	0,03	-24,7	1,5	-3,3
Z-24	4,8	-	-25,4	1,5	-3,4
Z-25	10,8	-	-24,6	1,4	-3,9
Z-26	29,1	-	-25,0	1,4	-4,1
Z-27	12,1	0,04	-24,9	1,6	-3,3
Z-28	11,4	-	-25,0	1,7	-3,2
Z-29	6,8	-	-24,8	1,7	-3,2
Z-30	9,9	-	-26,5	1,8	-3,2
Z-31	18,7	0,04	-24,9	1,7	-3,2
Z-32	27,7	0,05	-25,3	1,6	-3,2
Z-33	30,9	0,08	-24,9	1,5	-3,4
Z-34	14,1	-	-25,2	-0,3	-4,9
Z-35	14,2	-	-25,0	1,1	-3,1
Z-36	17,3	0,05	-24,8	1,2	-3,3
Z-37	11	-	-25,2	1,1	-3,0
Z-38	10,4	-	-24,9	1,3	-3,2
Z-39	19,6	0,08	-24,8	1,3	-3,1
Z-40	15,6	-	-25,5	1,0	-3,8
Z-41	18,2	0,06	-25,0	1,3	-4,4
Z-42	9	-	-25,0	1,6	-3,7
Z-43	3	-	-24,7	1,5	-3,1
Z-44	4,1	0,07	-24,9	1,7	-3,0
Z-45	4	-	-24,8	1,7	-2,9
Z-46	2,6	-	-25,0	1,7	-3,0
Z-47	1,7	0,07	-25,0	1,8	-3,3
Z-48	2,4	-	-25,2	1,8	-3,0
Z-49	2,3	-	-25,3	1,8	-2,9
Z-50	2	0,05	-24,9	1,8	-2,8
Z-51	9,2	-	-24,9	1,7	-3,2
Z-52	11,2	-	-25,1	1,6	-3,5
Z-53	12,4	-	-25,1	1,6	-3,1
Z-54	8,8	0,19	-25,2	1,7	-3,0

Z-55	4,5	-	-25,1	1,6	-3,0
Z-56	21,3	0,17	-24,4	1,8	-3,2
Z-57	9,1	-	-25,0	1,8	-2,9
Z-58	9,4	-	-24,7	1,9	-2,9
Z-59	7	-	-25,2	1,6	-4,9
Z-60	3	-	-25,2	1,8	-3,0
Z-61	2	0,04	-25,1	1,8	-3,2
Z-62	1,9	-	-25,2	1,9	-3,3
Z-63	6,1	-	-24,8	1,8	-3,1
Z-64	21,1	0,05	-25,1	1,8	-3,0
Z-65	23,3	0,04	-24,9	1,8	-3,1
Z-66	21,1	0,04	-24,9	1,9	-3,0
Z-67	12	-	-25,0	1,7	-3,8
Z-68	11,5	-	-25,2	1,9	-3,0
Z-69	7,7	-	-25,1	1,9	-3,0
Z-70	7,3	0,05	-26,6	2,0	-4,4
Z-71	7,3	-	-24,8	2,0	-3,2
Z-72	3	0,04	-25,3	2,0	-4,1
Z-73	4,3	-	-25,1	2,1	-3,1
Z-74	7,1	0,04	-23,3	2,1	-3,2
Z-75	13,9	0,05	-25,0	2,0	-3,0
Z-76	7,3	0,06	-24,8	2,0	-2,9
Z-77	7,1	0,12	-24,7	1,9	-3,3
Z-78	4,6	0,07	-24,1	1,3	-6,4
Z-79	3,3	0,1	-23,2	1,4	-6,4
Z-80	18,1	0,14	-23,8	0,4	-5,1
Z-81	26,8	0,08	-24,2	1,1	-4,2
Z-82	44,6	0,07	-24,3	0,9	-3,9
Z-83	47,5	0,08	-24,5	0,8	-4,1
Z-84	44,6	0,09	-24,3	0,9	-3,8
Z-85	46,7	-	-24,3	0,7	-3,7
Z-86	32	0,08	-24,2	1,1	-3,3
Z-87	13,1	0,07	-24,4	1,6	-3,1
Z-88	11,1	-	-18,2	1,9	-3,1
Z-89	10,5	-	-24,6	2,0	-3,1
Z-90	1,2	-	-19,1	2,2	-2,8
Z-91	0,8	-	-25,5	2,2	-2,7
Z-93	2,2	0,06	-17,9	2,3	-3,1
Z-94	0,9	-	-22,9	2,2	-3,3
Z-95	1	-	-16,9	2,4	-2,8
Z-96	1,7	-	-22,7	2,3	-3,0
Z-97	1	-	-19,9	2,3	-3,1
Z-98	0,5	0,05	-14,8	2,3	-3,3
Z-100	1,6	-	-19,5	2,4	-2,8
Z-101	0,9	-	-22,2	2,3	-3,1
Z-102	2,7	-	-20,4	2,2	-3,0
Z-103	0,8	0,08	-20,6	2,2	-3,3
Z-104	1,4	-	-22,1	2,2	-2,7
Z-105	1,4	-	-23,2	2,3	-2,9
Z-106	0,6	-	-24,0	2,1	-2,8
Z-107	0,6	-	-21,5	2,1	-2,5
Z-108	2,6	0,09	-24,8	2,1	-2,5
Z-109	0,8	-	-20,6	2,3	-2,7
Z-111	4,8	0,11	-25,4	2,2	-1,6
Z-113	1,3	0,09	-16,9	2,3	-2,8

3. Major and trace element raw data from Zumaya K/Pg section

Sample	SiO_2 (%wt)	TiO_2	Al_2O_3	Fe_2O_3	MnO	MgO	CaO	Na_2O	K_2O	P_2O_5	LOI	Sc (ppm)	V	Cr	Mn	Co	Ni	Cu	Zn	Rb	Sr	Zr	Ba	Pb	Th	U
Z-1	35,32	0,46	12,34	3,79	0,06	1,49	21,55	0,60	2,36	0,08	21,31	13	84	70	455	13	27	13	67	127	555	97	256	16	9	5
Z-2	35,38	0,47	13,40	4,02	0,06	1,57	20,39	0,62	2,58	0,07	20,79	12	91	62	404	16	31	16	71	137	525	89	271	20	9	4
Z-3	32,66	0,43	12,40	4,19	0,06	1,49	22,56	0,60	2,32	0,05	22,34	12	84	57	436	12	27	12	69	129	589	80	257	14	8	4
Z-4	32,66	0,43	12,00	4,04	0,06	1,47	23,27	0,61	2,24	0,05	22,62	11	83	59	459	11	26	12	67	127	599	84	263	14	8	5
Z-5	31,20	0,40	11,50	3,90	0,08	1,40	24,71	0,58	2,13	0,05	23,53	11	78	56	527	10	25	14	66	122	625	81	265	13	8	5
Z-6	28,68	0,36	10,12	3,25	0,09	1,27	27,71	0,56	1,70	0,06	25,53	10	67	50	608	10	22	16	58	102	636	76	222	10	7	4
Z-7	28,65	0,37	10,30	3,34	0,09	1,34	27,46	0,55	1,81	0,07	25,44	10	68	51	632	10	23	17	60	107	617	77	230	11	7	5
Z-8	29,18	0,38	10,75	3,48	0,08	1,34	27,02	0,55	1,89	0,07	24,88	11	72	58	599	12	23	15	61	111	636	78	237	15	7	5
Z-9	30,39	0,40	11,09	3,86	0,08	1,41	25,50	0,58	1,97	0,07	24,05	11	73	62	529	10	25	10	63	113	602	82	236	12	9	5
Z-10	36,85	0,49	12,93	4,08	0,06	1,55	19,94	0,64	2,46	0,08	20,12	13	85	70	401	14	29	15	72	133	531	101	281	14	10	5
Z-11	34,71	0,48	12,78	3,96	0,06	1,58	21,54	0,53	2,55	0,06	21,30	11	80	64	456	17	33	18	67	129	531	96	256	19	9	5
Z-12	32,61	0,44	11,94	4,34	0,07	1,49	23,19	0,53	2,37	0,05	22,58	11	83	63	496	11	25	11	64	123	577	92	241	14	8	4
Z-13	30,00	0,40	11,19	4,23	0,08	1,47	25,31	0,50	2,15	0,06	24,11	11	77	59	548	10	24	16	63	115	615	82	227	13	8	5
Z-14	28,31	0,37	10,62	4,05	0,08	1,43	26,90	0,50	1,91	0,05	25,19	11	71	57	554	10	23	12	61	109	641	74	232	12	7	4
Z-15	27,59	0,35	10,26	3,91	0,08	1,37	27,67	0,49	1,87	0,06	25,66	11	68	49	565	10	22	11	60	105	627	71	219	12	7	5
Z-16	31,00	0,40	11,33	4,06	0,07	1,44	24,52	0,53	2,25	0,05	23,51	11	80	60	493	11	24	13	64	117	563	78	250	13	7	4
Z-17	33,20	0,44	12,09	4,03	0,06	1,51	22,64	0,54	2,47	0,07	22,17	11	81	66	462	12	26	14	68	127	524	86	267	14	8	5
Z-18	31,21	0,41	11,34	4,06	0,07	1,43	24,61	0,53	2,20	0,05	23,44	10	77	56	486	10	24	12	65	120	568	84	247	13	8	5
Z-19	31,27	0,41	11,52	4,29	0,07	1,47	24,17	0,51	2,25	0,06	23,22	11	79	56	491	11	25	15	66	120	604	84	242	14	8	5
Z-20	33,96	0,45	12,21	4,21	0,06	1,59	21,86	0,53	2,45	0,07	21,74	12	82	56	434	11	26	13	65	124	484	95	249	14	9	5
Z-21	34,39	0,46	12,49	4,25	0,06	1,63	21,40	0,56	2,54	0,06	21,42	12	80	56	424	12	26	13	65	124	476	92	250	15	9	5
Z-22	32,76	0,44	11,90	4,26	0,06	1,56	22,80	0,53	2,36	0,06	22,42	12	82	57	464	11	25	13	65	123	527	91	255	13	9	4
Z-23	31,77	0,42	11,57	4,37	0,07	1,54	23,80	0,53	2,26	0,06	22,99	11	75	54	452	9	23	12	60	112	509	82	231	13	8	5
Z-24	31,83	0,42	11,65	4,19	0,06	1,53	23,81	0,52	2,31	0,05	23,02	12	82	57	457	12	26	13	67	123	567	82	244	14	8	5
Z-25	40,07	0,46	11,03	3,22	0,06	1,43	20,30	0,64	2,17	0,06	19,91	11	70	55	346	10	23	15	61	111	439	103	238	12	8	4
Z-26	38,68	0,45	10,38	3,22	0,06	1,36	21,63	0,62	2,07	0,06	20,71	9	69	51	376	10	23	16	61	106	485	111	233	12	8	4
Z-27	32,77	0,43	11,61	3,85	0,06	1,51	23,38	0,55	2,30	0,05	22,58	11	83	57	437	13	27	16	67	119	523	85	248	13	9	4
Z-28	30,12	0,39	10,86	3,58	0,07	1,45	25,80	0,52	2,10	0,05	24,36	10	79	55	495	12	25	15	63	111	563	78	228	13	8	5
Z-29	30,68	0,40	10,92	3,56	0,07	1,46	25,40	0,56	2,17	0,07	24,11	11	78	62	513	11	26	14	66	116	570	84	233	14	8	5
Z-30	29,99	0,39	10,60	3,43	0,08	1,40	26,34	0,53	2,01	0,06	24,62	11	71	55	524	12	24	15	61	106	556	79	214	12	8	4
Z-31	31,92	0,42	11,37	3,62	0,07	1,48	24,34	0,54	2,27	0,06	23,25	10	76	60	495	13	27	15	64	116	539	84	226	14	7	5
Z-32	33,26	0,44	11,81	3,50	0,06	1,53	23,38	0,55	2,39	0,05	22,55	10	79	59	425	13	28	14	65	117	509	90	234	15	9	5
Z-33	31,85	0,42	11,50	3,41	0,07	1,51	24,73	0,53	2,27	0,05	22,94	13	76	60	489	15	29	13	63	117	570	89	237	21	8	5
Z-34	47,80	0,47	5,55	1,75	0,06	1,27	21,42	0,58	0,88	0,06	19,58	5	32	75	383	6	11	6	32	44	359	187	123	7	8	4
Z-35	31,86	0,42	10,82	3,15	0,07	1,53	25,06	0,58	1,97	0,07	23,68	10	70	56	476	13	26	12	59	108	529	92	219	19	8	4
Z-36	35,27	0,47	12,34	4,20	0,06	1,68	21,22	0,54	2,55	0,08	21,21	12	75	56	382	12	27	13	66	124	503	99	251	15	9	4
Z-37	34,35	0,45	12,21	4,38	0,05	1,67	21,38	0,56	2,55	0,06	21,53	12	80	60	402	12	28	13	69	129	508	98	254	14	10	4

Z-38	33,39	0,45	12,15	4,41	0,05	1,64	22,07	0,54	2,54	0,06	21,99	11	76	58	377	12	25	10	62	115	461	84	220	13	8	3
Z-39	33,31	0,43	12,00	4,15	0,06	1,62	22,36	0,64	2,30	0,06	22,21	11	79	58	415	13	28	12	65	120	464	83	230	14	9	4
Z-40	34,31	0,41	10,09	3,42	0,06	1,49	23,83	0,54	2,03	0,06	22,99	10	68	58	448	11	25	11	58	104	515	99	210	14	9	5
Z-41	39,87	0,47	11,34	3,15	0,05	1,51	19,86	0,68	2,32	0,06	19,96	10	79	59	323	14	28	11	64	117	459	118	249	15	9	5
Z-42	29,53	0,38	10,45	3,40	0,07	1,46	26,39	0,52	2,07	0,06	25,07	11	73	58	482	11	24	12	61	109	562	78	215	12	7	4
Z-43	29,22	0,38	10,17	3,45	0,07	1,44	26,70	0,59	1,87	0,06	25,30	12	67	57	479	9	22	13	60	108	557	79	216	14	8	5
Z-44	27,03	0,35	9,63	3,48	0,07	1,41	28,54	0,49	1,80	0,06	26,53	10	62	49	484	9	20	12	54	95	543	69	193	10	6	3
Z-45	26,82	0,35	9,55	3,32	0,07	1,38	28,87	0,53	1,69	0,06	26,74	10	68	51	481	9	20	16	56	98	570	71	195	12	7	5
Z-46	24,32	0,31	8,50	3,07	0,08	1,29	31,30	0,48	1,38	0,05	28,52	8	54	41	520	7	17	11	48	81	569	62	165	9	6	4
Z-47	26,14	0,34	9,29	3,31	0,08	1,34	29,60	0,54	1,60	0,06	27,15	10	63	54	573	9	21	11	57	99	600	73	202	10	7	4
Z-48	27,16	0,35	9,62	3,36	0,07	1,37	28,54	0,49	1,85	0,06	26,46	9	62	52	500	9	21	14	56	99	572	75	200	11	7	4
Z-49	27,13	0,36	9,68	3,46	0,07	1,40	28,54	0,50	1,87	0,06	26,50	9	63	53	522	9	21	13	57	99	564	74	200	11	6	4
Z-50	26,75	0,35	9,56	3,46	0,07	1,40	28,70	0,53	1,76	0,06	26,77	11	71	54	571	10	22	11	60	104	613	78	210	11	8	6
Z-51	33,17	0,43	10,98	3,36	0,06	1,52	23,76	0,67	2,10	0,06	23,17	10	67	58	394	12	25	13	61	111	515	91	225	12	8	5
Z-52	35,36	0,44	10,97	3,19	0,05	1,51	22,53	0,67	2,17	0,08	22,15	12	71	66	390	13	26	13	65	117	536	102	239	16	9	5
Z-53	30,97	0,40	10,79	3,49	0,06	1,55	25,31	0,62	1,97	0,06	24,12	11	68	52	426	12	25	13	61	109	504	83	216	12	8	5
Z-54	29,13	0,38	10,57	3,73	0,06	1,53	26,32	0,56	2,05	0,06	24,95	11	72	58	467	11	26	11	65	113	551	80	226	11	8	5
Z-55	28,91	0,38	10,49	3,81	0,06	1,53	26,54	0,53	2,02	0,06	25,10	11	74	58	448	10	25	11	65	110	549	80	218	11	8	5
Z-56	31,41	0,41	11,39	3,68	0,05	1,60	24,27	0,54	2,38	0,06	23,40	12	77	62	389	15	31	15	67	118	505	84	241	14	7	4
Z-57	28,35	0,37	10,14	3,54	0,06	1,48	27,30	0,48	2,03	0,06	25,51	11	73	59	459	12	25	11	64	107	563	78	219	12	7	4
Z-58	24,79	0,32	8,80	3,03	0,07	1,34	30,94	0,42	1,60	0,06	28,00	9	64	45	528	10	22	10	56	91	609	66	183	9	6	4
Z-59	37,61	0,41	6,72	2,17	0,05	1,04	26,05	0,62	1,23	0,06	23,33	8	51	71	364	7	15	13	44	65	512	144	174	8	8	4
Z-60	23,31	0,30	8,22	2,99	0,07	1,29	32,25	0,41	1,34	0,05	28,98	10	57	49	518	8	19	9	55	86	635	66	171	9	6	5
Z-61	22,80	0,29	8,00	3,00	0,07	1,29	32,85	0,40	1,12	0,06	29,29	6	51	44	502	8	18	9	52	79	613	61	164	8	5	4
Z-62	23,65	0,31	8,46	3,10	0,07	1,35	31,70	0,45	1,40	0,06	28,68	9	52	46	494	8	19	10	54	85	591	64	165	8	6	4
Z-63	28,29	0,37	9,93	3,36	0,06	1,47	27,74	0,49	1,95	0,06	25,81	11	66	48	433	10	24	11	61	100	535	76	202	10	7	4
Z-64	27,60	0,36	10,01	3,20	0,07	1,46	28,06	0,55	1,86	0,06	26,14	10	68	54	467	14	28	15	62	104	561	75	202	13	7	5
Z-65	30,39	0,40	10,86	3,39	0,06	1,55	25,62	0,49	2,29	0,06	24,33	12	78	57	428	15	32	16	68	119	546	86	244	14	9	5
Z-66	28,89	0,37	9,87	3,07	0,07	1,46	27,53	0,51	1,96	0,07	25,57	11	66	52	458	14	28	13	61	102	542	79	207	12	7	4
Z-67	33,34	0,39	8,56	2,54	0,05	1,29	26,85	0,56	1,66	0,06	24,44	9	57	47	391	11	22	11	53	85	527	111	190	11	7	5
Z-68	24,76	0,31	8,80	2,98	0,07	1,37	31,02	0,46	1,29	0,06	28,00	9	56	47	496	11	25	11	59	90	604	66	179	10	7	4
Z-69	24,89	0,31	8,74	3,02	0,07	1,36	31,20	0,46	1,24	0,05	27,91	9	56	44	472	10	23	10	59	88	600	64	177	9	6	4
Z-70	24,00	0,30	8,49	2,99	0,07	1,33	31,79	0,44	1,20	0,06	28,53	9	54	48	494	10	23	10	59	87	622	64	176	8	6	4
Z-71	24,09	0,30	8,53	3,22	0,07	1,36	31,50	0,44	1,59	0,05	28,03	9	56	47	489	10	23	11	62	89	627	66	174	8	7	5
Z-72	24,36	0,31	8,59	3,19	0,07	1,36	31,32	0,44	1,60	0,05	27,88	11	60	43	477	11	23	11	63	90	621	66	178	9	7	4
Z-73	21,99	0,28	7,71	2,91	0,08	1,30	33,64	0,38	1,20	0,06	29,52	8	56	42	504	9	22	11	58	78	645	58	157	7	6	4
Z-74	23,71	0,30	8,18	3,10	0,07	1,32	32,09	0,41	1,47	0,06	28,24	9	56	46	477	9	22	10	59	84	625	62	160	9	6	4
Z-75	23,20	0,29	7,97	2,88	0,07	1,31	32,69	0,39	1,44	0,06	28,82	9	60	41	498	10	27	18	61	80	644	62	162	9	6	7
Z-76	24,55	0,31	8,48	2,98	0,07	1,35	31,41	0,41	1,63	0,05	27,72	9	57	49	457	10	32	17	63	86	624	66	172	12	6	5
Z-77	33,44	0,42	11,86	3,68	0,05	1,54	23,24	0,53	2,50	0,07	22,18	12	89	62	294	14	44	13	73	121	535	88	228	10	8	6
Z-78	11,70	0,20	4,00	2,07	0,10	0,83	43,75	0,18	0,60	0,03	35,76	3	40	55	669	14	24	11	29	39	1465	43	3027	37	4	7
Z-79	19,72	0,28	6,53	2,39	0,09	1,08	36,05	0,26	1,22	0,08	31,35	5	68	76	553	34	64	11	42	61	1400	62	2351	35	5	7
Z-80	47,49	0,61	14,74	3,75	0,03	1,94	12,27	0,66	3,18	0,08	15,16	11	107	99	190	23	55	21	83	147	413	141	240	14	11	4

Z-81	38,55	0,45	9,47	2,84	0,06	1,57	22,50	0,60	1,94	0,10	21,36	11	64	55	409	19	37	14	59	101	445	115	166	12	9	4
Z-82	35,92	0,45	10,84	3,32	0,06	1,86	21,91	0,49	2,44	0,11	21,87	12	73	68	442	40	59	14	65	123	438	103	184	15	9	4
Z-83	36,76	0,46	10,98	3,24	0,05	1,71	21,42	0,48	2,50	0,10	21,36	11	78	76	401	41	62	15	67	123	411	103	191	16	9	5
Z-84	35,42	0,45	10,66	3,18	0,06	1,82	22,20	0,52	2,32	0,10	22,40	11	72	66	418	43	58	15	63	115	404	96	166	15	9	3
Z-85	36,09	0,46	10,88	3,27	0,06	1,84	21,50	0,48	2,53	0,10	21,79	10	72	72	390	50	62	14	63	119	404	98	176	17	9	3
Z-86	31,51	0,39	9,14	2,73	0,08	1,60	26,52	0,47	1,89	0,12	24,83	9	62	67	529	39	53	12	55	100	453	94	152	13	8	5
Z-87	19,87	0,26	5,82	1,88	0,10	1,15	37,01	0,30	0,87	0,13	31,71	7	44	54	603	11	27	10	42	63	596	63	106	8	5	5
Z-88	25,97	0,27	4,38	1,42	0,07	0,92	35,06	0,41	0,70	0,20	29,82	3	32	56	433	44	38	9	36	39	570	94	89	9	5	6
Z-89	27,30	0,37	9,31	2,86	0,07	1,01	29,44	0,41	1,63	0,07	26,87	10	57	49	492	10	22	10	46	91	799	82	146	12	7	6
Z-90	7,19	0,09	1,98	0,97	0,08	0,79	49,19	0,08	0,08	0,07	39,37	0	13	20	501	5	8	6	20	21	694	25	30	3	2	4
Z-91	3,50	0,04	1,20	0,75	0,06	1,01	51,56	0,05	0,02	0,05	41,55	0	4	6	379	4	5	5	15	12	633	13	8	0	3	2
Z-93	4,82	0,06	1,51	0,78	0,07	0,74	51,00	0,07	0,08	0,06	40,65	0	10	12	366	5	6	14	17	14	730	19	29	2	2	4
Z-94	3,71	0,04	1,06	0,75	0,06	0,69	51,52	0,04	0,04	0,05	41,17	0	5	9	380	3	4	6	17	12	740	14	13	2	0	4
Z-95	3,50	0,04	1,00	0,67	0,06	0,69	51,82	0,04	0,03	0,06	41,40	0	5	9	391	0	4	5	16	11	687	14	16	3	1	3
Z-96	4,82	0,06	1,59	0,74	0,06	0,77	50,71	0,06	0,05	0,06	40,59	0	8	9	357	3	6	7	16	16	616	15	56	1	2	4
Z-97	3,77	0,05	1,29	0,72	0,06	0,75	51,28	0,05	0,04	0,06	41,10	0	6	8	376	3	5	7	17	13	625	14	16	0	1	3
Z-98	3,39	0,05	1,09	0,65	0,06	0,78	51,72	0,05	0,05	0,05	41,57	0	5	7	395	2	5	8	15	12	652	13	11	2	2	3
Z-100	9,03	0,09	1,98	0,80	0,06	0,83	47,63	0,16	0,23	0,07	38,59	0	12	14	336	4	8	9	22	19	577	29	29	3	2	4
Z-101	4,08	0,05	1,30	0,73	0,07	0,80	51,06	0,06	0,04	0,06	41,13	0	6	10	432	3	7	8	17	14	618	14	12	1	0	3
Z-102	5,24	0,07	1,73	0,82	0,07	0,90	50,48	0,08	0,04	0,07	40,50	0	7	10	415	4	8	8	19	17	567	16	19	2	3	2
Z-103	4,69	0,06	1,49	0,82	0,07	0,90	50,26	0,08	0,05	0,07	40,75	0	7	11	453	4	7	5	18	16	607	16	29	0	0	2
Z-104	6,88	0,09	2,49	1,14	0,07	1,17	48,00	0,10	0,07	0,08	39,31	0	15	12	456	5	11	5	24	24	572	21	34	2	2	4
Z-105	5,84	0,08	2,08	1,05	0,07	1,10	48,96	0,08	0,05	0,06	40,02	0	11	12	428	5	10	9	24	22	658	20	26	2	3	2
Z-106	5,22	0,07	1,82	0,95	0,07	1,01	49,55	0,07	0,02	0,07	40,37	0	8	10	380	4	8	5	21	18	631	17	19	2	2	3
Z-107	5,49	0,07	2,09	1,04	0,07	1,11	49,36	0,09	0,03	0,06	40,26	0	12	11	405	5	9	6	24	21	639	18	20	2	1	3
Z-108	22,12	0,32	8,34	2,69	0,06	1,74	32,04	0,44	1,58	0,11	29,87	8	54	41	334	12	30	11	41	94	391	70	127	7	6	3
Z-109	6,81	0,08	2,43	0,80	0,05	0,88	48,73	0,11	0,11	0,05	39,39	0	14	13	319	4	9	5	23	22	550	21	32	2	1	4
Z-111	29,78	0,42	11,16	3,52	0,04	1,97	24,19	0,61	2,48	0,07	25,02	11	61	53	287	13	37	19	50	134	344	89	151	8	8	3
Z-113	5,41	0,07	1,50	0,77	0,08	0,74	50,12	0,09	0,07	0,07	40,38	0	11	11	485	4	6	6	19	17	722	20	22	2	2	5

ANNEX V: MINERALOGICAL AND GEOCHEMICAL RAW DATA FROM BONGUE AND DIBAMBA SECTIONS IN DOUALA SUB-BASIN

1. Raw data of bulk and clay mineralogy from Bongue and Dibamba sections

Samples	Bulk-rock mineralogy									Clay mineralogy					
	Calcite	Dolomite	Goethite	Indosed	K-feldspar	Phyllosilicate	Na-plagioclase	Pyrite	Quartz	Chlorite	I/S	Kaolinite	Mica	Smectite	Zeolite
	[%]	[%]	[%]	[%]	[%]	[%]	[%]	[%]	[%]	[cps]	[cps]	[cps]	[cps]	[cps]	[cps]
BN-1	34.32	0.00	0.00	0.82	14.29	18.03	0.00	0.00	32.54	0.00	60.00	0.00	74.17	224.17	27.50
BN-2	4.33	0.00	0.00	2.59	27.55	25.76	0.00	0.00	39.77	0.00	0.00	1045.83	69.17	391.67	0.00
BN-3	3.91	0.00	0.00	3.72	15.32	28.44	2.27	1.00	45.34	133.07	42.50	660.26	76.67	270.00	45.00
BN-4	2.43	2.20	0.00	0.79	16.42	17.24	2.58	0.61	57.72	0.00	31.67	771.67	70.00	180.83	33.33
BN-5	0.80	1.60	2.62	0.32	9.67	22.50	0.00	0.94	61.55	0.00	0.00	694.17	62.50	488.33	0.00
BN-6	0.98	0.00	0.00	1.84	14.13	30.55	0.00	1.07	51.43	0.00	0.00	838.33	62.50	309.17	0.00
BN-7	1.04	1.90	0.00	4.82	12.54	28.54	0.00	2.51	48.66	0.00	0.00	730.00	0.00	527.50	0.00
BN-8	1.03	2.00	2.94	3.13	15.30	20.96	0.00	0.99	53.65	0.00	0.00	1078.33	69.17	361.67	0.00
BN-9	0.79	2.64	1.37	3.81	24.12	18.77	0.00	0.83	47.66	140.44	0.00	659.56	65.00	1224.17	0.00
BN-10	0.92	2.06	0.00	2.20	11.84	23.66	0.00	0.54	58.78	240.12	0.00	833.21	0.00	1041.67	0.00
BN-11	0.95	1.14	2.97	4.06	18.63	27.44	0.00	1.05	43.77	0.00	0.00	826.67	0.00	362.50	0.00
BN-12	3.65	1.48	2.81	3.60	13.70	30.87	0.00	0.67	43.22	120.97	40.83	706.53	53.33	381.67	39.17
BN-13										0.00	0.00	698.33	60.00	304.17	0.00
BN-14	1.37	1.83	2.33	2.41	21.65	29.72	0.00	2.05	38.65	0.00	0.00	940.83	73.33	885.33	0.00
BN-15	0.81	1.80	3.39	5.43	13.66	37.67	0.00	2.05	35.19	121.95	0.00	638.88	0.00	258.33	0.00
BN-16	2.17	0.00	3.44	3.62	16.09	32.78	0.00	2.92	38.97	0.00	0.00	1321.67	0.00	747.50	0.00
BN-17	0.00	2.50	2.88	3.09	8.80	39.78	0.00	2.18	40.76	248.87	71.67	707.80	78.33	905.83	65.00
BN-18	0.00	2.05	3.00	2.97	13.47	34.09	0.00	1.66	42.77	0.00	65.00	999.17	83.33	268.33	0.00
BN-19	0.00	1.35	0.00	3.59	12.31	39.89	0.00	2.21	40.65	0.00	0.00	1779.17	0.00	561.67	0.00
BN-20	3.21	3.10	2.88	3.07	13.98	40.43	0.00	1.71	31.61	0.00	0.00	2221.67	0.00	705.00	0.00
BN-21	0.00	3.57	0.00	2.63	31.06	34.85	0.00	2.58	25.30	0.00	0.00	2032.50	0.00	1069.17	0.00
BN-22	0.70	2.01	0.00	3.82	31.87	35.22	1.01	1.73	23.62	151.14	0.00	464.69	0.00	632.50	0.00
BN-23	0.00	2.45	2.87	4.38	12.90	45.09	0.00	1.53	30.78	0.00	0.00	496.67	0.00	234.17	0.00
BN-24	0.83	1.40	0.00	2.95	20.52	32.35	0.00	0.86	41.09	0.00	0.00	1390.83	0.00	375.00	0.00
BN-25	1.05	1.38	0.00	3.43	17.09	53.09	0.00	0.87	23.09	0.00	0.00	1932.50	0.00	1010.00	0.00
BN-26	0.78	1.97	2.78	0.53	5.98	28.98	0.00	0.89	58.09	0.00	0.00	2946.67	0.00	1133.33	0.00
BN-27	0.59	1.97	4.49	9.89	12.73	43.90	0.00	0.00	26.44	0.00	0.00	1788.33	0.00	1354.17	0.00
BN-28	0.88	1.83	0.00	2.29	15.06	40.87	0.00	0.87	38.19	0.00	0.00	2082.50	0.00	875.00	0.00
BN-29	2.08	2.49	0.00	3.49	22.35	33.58	1.03	0.00	34.98	0.00	0.00	1848.33	0.00	705.83	0.00
BN-30	1.76	2.59	0.00	3.46	13.56	34.10	0.00	0.75	43.78	0.00	0.00	1305.00	0.00	382.50	0.00

DI-1	0.72	1.47	0.00	3.75	14.10	34.39	0.00	2.37	43.20	0.00	0.00	4441.67	0.00	912.50	0.00
DI-2	0.00	1.87	2.77	2.18	9.45	42.47	0.00	3.05	38.22	0.00	0.00	3240.83	0.00	1100.00	0.00
DI-3	0.43	0.74	0.00	3.86	9.91	43.23	0.00	0.61	41.22	0.00	0.00	4428.33	175.83	1310.00	0.00
DI-4	0.00	0.83	3.48	1.24	11.45	47.40	0.86	0.69	34.04	0.00	0.00	5245.00	0.00	1726.67	0.00
DI-5	0.65	0.97	2.96	4.00	3.78	48.00	0.00	0.00	39.64	0.00	0.00	1366.67	85.83	1930.00	0.00
DI-6	1.63	1.44	3.62	2.42	0.00	37.04	0.00	0.00	53.84	0.00	0.00	6612.50	0.00	677.50	0.00
DI-7	0.52	1.18	0.00	3.44	3.78	40.44	0.00	0.00	50.64	0.00	70.00	6025.83	245.83	701.67	62.50
DI-8	0.00	0.81	0.00	5.36	5.45	51.87	0.84	0.00	35.67	0.00	0.00	4750.83	0.00	768.33	0.00
DI-9	0.44	0.76	0.00	2.46	7.65	45.94	0.00	0.00	42.74	0.00	0.00	3621.67	115.83	1203.33	0.00
DI-10										0.00	0.00	3225.00	0.00	1090.00	0.00
DI-11	0.00	0.85	0.00	4.31	6.98	48.35	0.00	1.47	38.03	0.00	0.00	2620.83	117.50	689.17	0.00
DI-12	0.00	1.19	3.02	3.95	16.87	55.08	0.00	1.72	18.17	0.00	0.00	3185.00	106.67	853.33	0.00
DI-13	0.69	1.02	3.69	5.94	6.51	56.29	0.00	1.94	23.93	0.00	0.00	2772.50	104.17	715.00	0.00
DI-14	0.00	0.94	0.00	5.58	4.14	55.89	0.00	0.00	33.45	0.00	95.00	2597.50	115.00	679.17	0.00
DI-15	0.60	1.14	3.20	3.62	3.40	57.68	0.00	1.43	28.95	0.00	0.00	1837.50	110.00	418.33	0.00
DI-16'	0.00	0.96	2.55	3.58	5.88	38.94	0.00	1.11	46.98	0.00	0.00	2053.33	116.67	444.17	0.00
DI-16	0.63	1.65	3.12	3.13	3.46	54.30	0.00	1.33	32.38	0.00	0.00	2386.67	161.67	555.00	0.00
DI-17'	0.00	0.68	0.00	4.41	0.00	58.29	0.00	1.19	35.43	0.00	77.50	1981.67	113.33	562.50	0.00
DI-17	0.00	0.70	0.00	4.74	0.00	62.37	0.79	0.64	30.76	0.00	0.00	2830.00	117.50	1303.33	0.00
DI-18'	0.53	0.71	2.53	4.49	3.67	36.00	0.00	0.68	51.39	0.00	77.50	2047.50	119.17	670.00	0.00
DI-18	0.95	0.86	2.39	3.01	0.00	49.82	0.79	0.75	41.44	0.00	95.83	2118.33	121.67	736.67	0.00
DI-19'	0.58	0.00	3.13	2.81	5.71	50.02	0.00	0.63	37.12	0.00	0.00	1370.83	103.33	1540.83	0.00
DI-19	0.50	1.44	2.46	4.75	7.62	50.54	0.00	0.85	31.83	0.00	75.00	1957.50	129.17	1080.83	0.00
DI-20	0.52	0.74	0.00	4.03	4.57	56.43	0.00	0.82	32.89	0.00	0.00	1489.17	109.17	399.17	0.00
DI-21	0.51	0.82	2.90	3.84	3.11	42.43	0.00	0.61	45.78	0.00	58.33	921.67	130.83	130.00	0.00
DI-22	0.45	1.43	0.00	3.80	7.90	31.43	0.00	1.43	53.56	0.00	53.33	763.33	130.00	200.83	0.00
DI-23	0.00	1.23	0.00	0.32	18.72	16.67	0.00	0.54	62.52	106.60	44.17	304.23	134.17	78.33	0.00
DI-24	0.33	0.52	2.03	2.58	6.13	21.19	0.00	0.00	67.21	0.00	39.17	229.17	88.33	125.00	0.00
DI-25	0.00	0.81	0.00	3.63	4.92	22.78	2.57	0.00	65.29	64.18	0.00	153.32	84.17	95.00	0.00
DI-26	0.29	0.65	0.00	1.61	12.45	30.57	2.39	0.00	52.03	29.44	41.67	50.56	55.00	73.33	0.00
DI-27	0.00	0.57	0.00	2.27	13.82	23.12	0.00	0.42	59.79	0.00	53.33	806.67	146.67	263.33	0.00
DI-28	0.00	0.80	1.57	2.17	6.09	27.93	0.00	0.00	61.43	0.00	0.00	1454.17	124.17	518.33	0.00
DI-29	0.35	0.00	0.00	3.44	14.84	15.17	0.00	0.00	66.20	0.00	65.00	923.33	108.33	552.50	54.17
DI-30	0.34	0.62	1.49	1.34	3.81	21.37	1.11	0.47	69.45	0.00	60.83	1247.50	90.83	473.33	37.50
DI-31	0.00	0.63	1.18	0.91	11.56	17.03	1.36	0.00	67.33	0.00	0.00	695.00	85.83	107.50	0.00
DI-32	0.44	0.54	2.35	1.68	5.63	27.03	0.00	0.00	62.33	0.00	0.00	1572.50	114.17	277.50	0.00
DI-33	0.45	0.89	1.55	1.21	11.43	18.30	0.81	0.00	65.36	0.00	0.00	1510.83	99.17	245.83	0.00

2. Rock-Eval and stable isotope raw data of Bongue and Dibamba sections in Douala sub-basin

Samples	$\delta^{13}C$ (PDB)	Rock-Eval			
		TOC [%]	HI [mg HC/g TOC]	OI [mg CO_2/g TOC]	Tmax [°C]
BN-1	-25.87	0.14	38.06	242.37	418.00
BN-2	-26.33	0.12	43.29	184.15	419.00
BN-3	-26.22	0.15	43.31	181.78	422.00
BN-4	-26.12	0.12	42.82	199.48	418.00
BN-5	-26.30	0.15	28.55	166.59	425.00
BN-6	-26.00	0.15	40.87	199.08	419.00
BN-7	-26.17	0.16	38.93	183.66	423.00
BN-8	-26.40	0.14	43.68	192.24	429.00
BN-9	-26.24	0.17	43.34	157.74	421.00
BN-10	-26.79	0.17	50.27	154.23	424.00
BN-11	-26.56	0.23	41.46	149.53	424.00
BN-12	-26.76	0.29	32.53	128.25	426.00
BN-13	-26.97	0.35	32.44	113.59	424.00
BN-14	-27.13	0.38	32.75	118.82	431.00
BN-15	-26.99	0.56	26.26	78.09	430.00
BN-16	-27.48	0.59	24.94	74.30	431.00
BN-17	-26.74	0.56	20.44	131.28	428.00
BN-18	-27.19	0.67	28.19	209.24	433.00
BN-19	-26.84	0.87	20.33	93.19	430.00
BN-20	-27.22	0.90	21.94	131.75	432.00
BN-21	-26.45	0.84	21.18	60.70	428.00
BN-22	-26.60	0.98	17.18	74.56	425.00
BN-23	-27.03	0.66	27.12	167.60	429.00
BN-24	-26.81	0.52	36.02	215.00	434.00
BN-25	-26.91	0.53	39.35	206.36	430.00
BN-26	-26.87	0.66	22.13	103.61	424.00
BN-27	-27.16	0.42	37.31	359.57	435.00
BN-28	-26.69	0.52	30.15	243.43	439.00
BN-29	-27.02	0.37	34.13	314.27	442.00
BN-30	-26.38	0.22	42.84	499.26	443.00
DI-1	-25.38	0.74	25.14	107.59	394.00
DI-2	-25.35	0.70	25.38	82.02	396.00
DI-3	-24.55	0.03	76.47	1131.91	361.00
DI-4	-24.74	0.19	38.49	163.34	350.00
DI-5	-24.43	0.06	34.72	981.52	354.00
DI-6	-24.42	0.28	22.24	124.67	339.57
DI-7	-24.59	0.18	22.93	165.25	343.59
DI-8	-24.46	0.21	29.66	161.45	331.61
DI-9	-24.80	0.13	32.32	217.31	463.63
DI-10	-27.40	2.09	13.20	68.27	387.65
DI-11	-26.45	1.33	22.01	82.50	390.29
DI-12	-26.39	1.26	20.87	106.86	394.33
DI-13	-25.49	1.34	21.14	78.36	394.38
DI-14	-25.31	1.10	21.98	111.22	388.43
DI-15	-25.45	1.06	20.90	89.96	393.48
DI-16'	-	0.85	21.25	96.43	394.57
DI-16	-25.39	5.07	3.33	18.59	393.52
DI-17'	-25.47	1.00	13.75	126.99	380.67
DI-17	-25.58	0.98	21.69	113.57	389.62
DI-18'	-25.29	0.55	23.06	151.21	399.76
DI-18	-25.13	0.50	25.62	223.40	404.71
DI-19'	-25.60	0.70	16.67	190.37	396.86
DI-19	-25.72	0.79	16.10	142.85	392.81
DI-20	-25.52	1.07	19.00	124.65	393.90

DI-21	-25.17	0.67	15.90	150.92	400.95
DI-22	-25.50	0.23	27.79	221.01	412.75
DI-23	-25.67	0.16	27.26	443.04	417.50
DI-24	-25.35	0.11	49.23	551.42	409.25
DI-25	-25.04	0.13	15.85	447.10	408.00
DI-26	-25.05	0.06	69.97	1313.75	413.75
DI-27	-25.13	0.18	29.23	289.15	418.50
DI-28	-25.31	0.05	57.97	981.39	419.25
DI-29	-24.35	0.11	57.19	525.00	419.00
DI-30	-25.35	0.19	21.77	177.90	410.75
DI-31	-26.09	0.11	55.24	266.28	415.50
DI-32	-24.71	0.08	54.58	630.43	412.25
DI-33	-25.32	0.09	59.19	682.41	419.00

3. Major element raw data of Bongue and Dibamba in Douala sub-basin

Samples	Major elements									
	Al [ppm]	Ca [ppm]	Fe [ppm]	K [ppm]	Mg [ppm]	Mn [ppm]	Na [ppm]	P [ppm]	Si [ppm]	Ti [ppm]
BN-1	39529.77	155584.47	52246.55	18588.56	8435.99	500.84	2158.89	282.25	172722.21	8139.53
BN-2	62422.63	11873.02	67785.04	30263.70	10522.30	357.39	3217.99	523.66	283372.65	11892.89
BN-3	64017.89	15084.38	68418.43	28944.70	10544.35	360.04	3379.83	1907.29	279477.72	12204.10
BN-4	63017.04	13984.70	68629.68	29485.30	10572.86	359.10	3302.25	526.18	281655.80	12116.78
BN-5	63611.30	16725.80	68753.04	29219.37	10672.57	362.49	3402.83	2451.40	278184.45	12006.62
BN-6	64359.08	18689.00	71772.31	28543.54	10643.46	350.38	3154.89	552.88	276335.34	12147.76
BN-7	65260.80	14777.30	72313.72	28452.86	10730.89	360.65	3178.32	650.40	276906.35	12615.67
BN-8	63620.03	13358.81	68640.88	28295.46	10722.59	354.80	3126.75	519.87	278111.05	11916.74
BN-9	65221.91	12735.08	70346.55	28577.93	10805.12	361.26	3114.43	407.18	280510.36	12524.96
BN-10	65098.49	13190.11	70614.09	27884.05	10854.58	357.33	3149.01	402.75	278623.97	12720.56
BN-11	66240.69	16407.66	74125.59	27215.16	10801.93	355.59	3065.61	440.88	269458.35	12823.97
BN-12	68005.29	15544.74	76705.84	25837.34	11089.12	422.88	3038.06	476.63	263249.67	13635.96
BN-13	71688.77	11669.58	79884.46	25064.92	11280.19	423.87	2842.16	398.12	259559.13	14214.63
BN-14	73157.67	12245.26	81068.67	24053.23	11363.56	416.83	2728.45	430.67	253322.56	14462.63
BN-15	79142.69	4388.71	82368.54	24139.04	10731.35	419.62	2612.70	354.72	252609.19	15262.90
BN-16	80810.66	4406.09	77933.90	24699.30	9701.46	345.98	2651.32	428.96	252231.56	15583.22
BN-17	81234.89	4177.97	80355.82	24264.52	6144.40	274.38	2562.62	386.58	248843.29	15448.08
BN-18	87760.11	4106.34	72155.35	24142.04	4532.33	616.12	3016.46	385.80	247265.22	16264.49
BN-19	90027.62	3748.54	67443.76	23729.82	5695.01	270.80	2593.99	457.83	242322.68	16975.23
BN-20	90006.08	3001.20	68598.49	24184.30	5119.00	271.01	2596.04	572.74	243577.43	17303.23
BN-21	90238.05	4116.11	60793.60	24339.87	6579.80	270.32	2589.41	304.68	245648.14	16526.84
BN-22	91540.74	4009.66	54095.11	24791.71	4581.81	267.38	2625.28	301.37	247012.41	17330.02
BN-23	89946.81	3904.12	66313.07	25380.30	4358.18	409.41	2875.95	307.64	248523.00	16634.19
BN-24	88044.38	3816.99	60332.24	27192.80	4241.87	344.68	3037.56	310.80	258067.77	16164.88
BN-25	88284.12	3903.71	51233.78	28989.99	4321.13	277.39	2989.22	273.57	264376.47	16314.77
BN-26	88591.27	3221.73	46812.23	28138.38	4026.59	201.41	2829.68	302.69	257575.12	15691.09
BN-27	88105.94	4115.94	80380.69	25669.51	4008.46	343.09	2563.41	348.03	246517.68	15081.15
BN-28	88442.18	4261.05	67534.69	27110.88	4133.26	275.66	2706.59	504.90	253206.87	16320.10
BN-29	87764.00	4189.15	56958.14	29419.89	4242.94	419.03	3612.47	314.86	263634.85	15727.70
BN-30	83328.03	4110.69	68771.37	28946.93	4445.38	696.01	2866.82	313.79	260554.42	14866.33
DI-1	85901.10	0.00	39862.03	17951.91	2506.63	197.03	3271.41	481.17	263628.79	14689.00
DI-2	79967.39	0.00	38450.39	15931.98	2933.52	201.76	2770.18	492.72	281491.06	14261.06
DI-3	84478.45	0.00	51761.93	20453.15	3244.57	201.56	2316.89	605.82	265876.84	14038.78
DI-4	100433.05	0.00	30102.14	12681.45	4686.46	202.81	1618.95	266.69	271323.76	14753.80
DI-5	85888.93	0.00	83111.46	17316.95	4882.33	129.24	1238.01	691.94	231613.75	9901.94
DI-6	91438.91	0.00	23234.22	14189.56	2710.57	204.71	1830.15	269.18	286297.77	17795.94
DI-7	90139.89	0.00	25994.86	13872.07	3937.54	202.21	1936.97	227.91	283377.04	15388.13
DI-8	84814.71	0.00	22079.33	13715.55	3199.73	134.69	1870.76	227.71	290975.61	12299.73
DI-9	91122.06	0.00	30979.77	14503.76	4426.43	202.96	2138.58	266.89	279937.26	13979.31

DI-10	89701.07	0.00	26625.56	11459.88	4483.93	189.78	1817.93	356.51	260232.40	12435.15
DI-11	93456.60	0.00	33838.43	12549.91	4978.68	189.86	2243.02	499.32	252161.53	12734.04
DI-12	97617.28	0.00	43857.33	11530.93	5289.49	240.39	2129.98	508.02	223308.52	11580.69
DI-13	99788.03	0.00	39109.86	12524.92	5061.64	249.94	2394.17	598.64	237009.91	12717.83
DI-14	101424.91	0.00	32695.96	11975.66	5979.65	187.24	2092.55	492.44	239758.71	11882.44
DI-15	104465.42	0.00	38277.41	10708.01	5847.51	242.17	1507.86	716.51	223431.95	10729.62
DI-16'	94816.44	0.00	36582.05	13239.82	5371.96	250.79	1981.94	459.35	243346.65	12373.14
DI-16	96213.92	0.00	39957.01	12396.44	5576.28	244.76	2168.69	448.29	232945.85	11507.08
DI-17'	97687.24	0.00	49979.37	11316.85	5907.59	182.03	1453.04	478.72	223848.69	9485.31
DI-17	104923.75	56.68	36222.66	11257.54	6266.76	245.67	1706.11	449.96	226952.98	10789.40
DI-18'	87162.40	168.31	44916.96	14141.55	5919.32	243.19	2271.24	376.89	232771.40	10868.59
DI-18	84524.16	172.08	46314.30	14724.27	6729.46	248.62	2738.80	350.29	245255.95	11352.13
DI-19'	92992.46	114.58	53211.65	12843.35	8317.13	248.33	1546.17	419.84	228696.29	9705.01
DI-19	93052.92	114.60	53502.38	12180.25	8754.02	186.28	1784.38	419.92	229115.47	9322.46
DI-20	99666.63	0.00	42187.89	12874.86	8414.99	190.65	2374.14	644.66	239020.33	11213.46
DI-21	87174.79	0.00	55856.57	15514.92	6303.13	131.58	1638.56	630.31	255270.78	10081.29
DI-22	54378.79	330.49	28723.13	20499.37	4016.85	143.25	3430.53	161.46	339052.27	8813.54
DI-23	52506.76	565.25	41429.96	20937.12	4982.95	204.17	3455.19	191.77	307163.98	8532.45
DI-24	50949.11	323.33	40441.68	21181.55	4475.55	280.29	3826.00	157.96	325016.56	7971.68
DI-25	49502.65	583.57	70694.94	19958.57	4597.13	421.58	3365.23	158.39	305493.97	7667.02
DI-26	46862.83	568.44	57549.80	19147.63	4211.39	410.65	3015.74	154.28	308233.16	7256.36
DI-27	52073.54	260.94	32944.38	20989.01	4129.50	212.07	2979.38	159.35	332527.07	7057.09
DI-28	47138.50	448.30	28518.98	19340.89	3297.29	138.80	2393.13	156.44	332777.22	7518.91
DI-29	52628.83	255.89	28863.16	19616.76	3077.67	138.64	2988.12	156.27	328392.30	7242.38
DI-30	58862.13	64.94	20085.15	19084.85	2576.26	140.75	2629.02	198.30	337032.47	7243.42
DI-31	52286.33	0.00	20892.79	18158.10	2328.45	142.35	1977.21	160.45	345860.78	7766.70
DI-32	50887.37	64.59	23957.47	15379.28	2126.04	139.98	1407.87	157.77	339157.42	9099.45
DI-33	52465.56	127.09	24130.40	14540.50	2038.08	137.72	1451.10	194.03	331478.52	8526.23

4. Trace element raw data of Bongue and Dibamba in Douala sub-basin

Samples	Trace elements																					
	As [ppm]	Ba [ppm]	Ce [ppm]	Co [ppm]	Cr [ppm]	Cu [ppm]	Ga [ppm]	Hf [ppm]	La [ppm]	Nb [ppm]	Nd [ppm]	Ni [ppm]	Pb [ppm]	Rb [ppm]	Sc [ppm]	Sr [ppm]	Th [ppm]	U [ppm]	V [ppm]	Y [ppm]	Zn [ppm]	Zr [ppm]
BN-1	9.90	471.50	132.40	20.00	107.00	5.80	10.80	23.60	65.70	27.10	51.80	22.60	9.40	46.40	11.00	426.80	18.00	5.50	113.00	32.60	148.00	877.70
BN-2	10.00	712.40	180.60	26.00	162.00	6.20	17.80	41.30	81.70	43.40	70.50	32.30	17.40	73.20	11.00	201.00	23.10	6.20	170.00	33.10	204.00	1418.30
BN-3	14.20	768.60	182.80	28.00	161.00	6.30	18.00	40.70	78.10	44.20	74.80	34.80	17.90	73.80	11.00	223.30	24.50	5.40	173.00	43.60	221.00	1441.20
BN-4	11.40	711.50	181.90	27.00	163.00	6.50	17.60	38.40	77.50	43.90	71.20	33.00	18.10	73.30	11.00	208.10	23.10	5.90	172.00	35.50	217.00	1390.50
BN-5	11.40	700.70	189.60	28.00	163.00	6.60	17.70	36.60	86.50	43.40	77.60	34.30	17.50	72.40	11.00	222.50	22.60	6.30	177.00	48.10	215.00	1346.00
BN-6	19.80	652.60	177.60	29.00	161.00	7.10	17.90	37.70	76.10	43.30	71.00	36.80	18.70	70.00	12.00	228.10	22.90	5.80	179.00	33.70	233.00	1334.70
BN-7	15.40	670.90	187.00	28.00	166.00	7.90	18.40	3.00	83.60	45.20	73.60	35.70	18.50	71.20	10.00	215.80	23.80	5.70	179.00	36.30	229.00	1378.10
BN-8	13.70	671.50	184.00	27.00	161.00	7.20	18.10	40.80	84.70	44.30	73.70	34.80	18.20	71.80	11.00	210.30	24.90	6.30	173.00	35.10	213.00	1388.30
BN-9	13.70	698.60	180.20	28.00	180.00	7.00	18.20	4.00	82.10	44.90	71.70	34.80	18.80	71.90	12.00	207.20	22.90	6.20	178.00	34.10	214.00	1382.00
BN-10	12.40	693.10	189.70	28.00	165.00	7.50	18.30	41.00	89.70	45.70	73.80	35.10	18.00	71.70	11.00	210.30	24.60	6.20	177.00	37.10	209.00	1440.60
BN-11	17.60	658.50	196.50	31.00	173.00	8.10	19.10	39.60	88.90	46.60	76.00	38.70	18.00	69.40	12.00	223.70	24.50	5.60	180.00	36.30	227.00	1376.60
BN-12	17.90	633.50	194.30	31.00	178.00	8.80	20.20	42.20	93.20	48.70	77.90	39.80	19.00	67.50	12.00	211.60	24.60	5.80	186.00	37.10	229.00	1400.90
BN-13	22.30	595.60	184.00	33.00	179.00	9.80	21.10	36.10	81.20	50.50	72.70	45.10	19.70	64.10	13.00	181.80	23.10	6.10	189.00	36.30	241.00	1271.60
BN-14	23.80	549.20	182.00	33.00	183.00	10.70	21.70	34.90	86.00	50.70	73.10	46.20	19.90	62.40	13.00	179.20	23.00	5.70	189.00	38.50	218.00	1220.40
BN-15	27.00	607.80	179.90	36.00	175.00	11.90	23.40	27.80	82.00	54.10	70.30	51.60	22.10	63.80	13.00	126.60	23.10	5.40	181.00	36.70	211.00	1058.60
BN-16	27.60	596.30	170.90	37.00	173.00	12.40	24.10	29.10	84.20	54.10	69.00	54.20	21.60	64.20	13.00	125.80	21.10	5.40	171.00	36.50	226.00	979.70
BN-17	29.10	664.90	168.00	26.00	172.00	12.50	24.70	23.20	82.50	53.90	67.40	52.50	22.40	65.00	13.00	126.40	21.20	5.40	169.00	36.50	221.00	924.90
BN-18	32.40	680.10	154.60	39.00	163.00	13.70	26.20	20.90	79.20	56.30	68.60	54.30	23.70	62.80	13.00	121.60	19.20	3.90	165.00	41.40	286.00	768.30
BN-19	33.40	607.60	145.80	26.00	161.00	15.90	26.80	19.70	78.40	57.40	64.80	55.30	23.90	61.30	15.00	117.00	18.60	4.40	163.00	35.10	211.00	714.20
BN-20	56.90	610.70	134.30	16.00	152.00	13.10	27.90	18.70	73.00	58.20	57.50	40.40	32.10	61.40	12.00	116.80	17.90	3.90	157.00	34.30	141.00	697.70
BN-21	26.30	631.50	132.40	36.00	150.00	14.20	26.80	15.60	68.30	56.00	58.40	70.80	23.30	63.50	14.00	121.80	18.20	4.60	153.00	34.30	247.00	628.00
BN-22	26.40	752.90	119.80	24.00	150.00	14.60	26.70	17.60	68.30	57.20	50.50	53.50	23.90	63.30	14.00	122.20	18.40	5.00	155.00	28.90	231.00	653.00
BN-23	30.40	716.90	116.80	34.00	149.00	14.60	26.70	16.60	65.00	55.70	52.50	46.30	24.40	64.60	12.00	124.30	18.20	4.40	155.00	31.00	244.00	654.60
BN-24	26.20	902.80	133.40	29.00	149.00	13.70	26.20	18.20	91.60	54.50	69.90	39.30	23.20	67.60	14.00	132.90	18.20	4.30	153.00	40.40	253.00	692.30
BN-25	28.40	1058.80	123.20	17.00	146.00	12.20	25.30	17.10	86.90	54.50	70.40	38.50	23.60	69.70	14.00	137.60	17.50	4.40	155.00	38.50	222.00	700.20
BN-26	26.80	758.70	116.10	11.00	139.00	12.50	25.20	16.90	78.90	52.30	59.80	35.40	23.20	67.80	12.00	131.10	17.10	4.30	146.00	31.00	178.00	646.80
BN-27	46.50	675.90	115.60	22.00	157.00	13.50	27.10	16.80	111.70	52.20	82.50	52.00	24.90	65.30	13.00	127.10	17.70	4.30	169.00	59.70	299.00	634.20
BN-28	47.40	724.40	100.80	12.00	147.00	15.00	26.40	16.90	202.70	54.80	127.70	48.20	25.90	66.40	13.00	131.20	18.30	5.10	158.00	99.70	285.00	651.10
BN-29	27.90	778.30	115.10	21.00	150.00	12.40	25.60	18.40	138.60	52.90	129.00	50.00	24.30	71.40	12.00	139.30	18.30	4.60	162.00	84.10	313.00	712.10
BN-30	28.50	803.70	118.80	32.00	149.00	10.80	23.40	16.90	149.00	49.10	157.00	57.50	23.40	70.00	11.00	137.00	17.50	5.00	161.00	86.80	376.00	710.80
DI-1	25.60	354.90	157.50	19.00	145.00	16.00	28.10	27.30	72.10	78.40	66.40	40.00	28.50	45.10	16.00	63.00	24.80	6.20	125.00	38.50	138.00	986.30
DI-2	37.30	309.00	148.80	17.00	175.00	20.00	28.10	36.60	76.00	77.60	57.90	37.00	24.60	42.50	19.00	61.70	27.90	6.40	152.00	36.80	138.00	1280.00

DI-3	21.60	620.50	131.60	5.00	193.00	8.00	31.10	36.50	79.60	80.50	43.60	19.00	35.60	44.40	14.00	66.10	24.30	3.90	201.00	34.20	113.00	1233.70
DI-4	6.20	271.60	105.10	6.00	166.00	10.00	29.10	33.80	53.60	79.70	44.60	21.00	18.10	44.30	12.00	65.80	21.70	4.70	137.00	37.00	105.00	1196.90
DI-5	21.60	971.20	121.40	4.00	220.00	10.00	27.80	17.80	91.50	49.10	42.80	19.00	75.00	39.20	14.00	76.70	17.70	2.50	175.00	31.30	130.00	624.60
DI-6	3.00	428.40	119.50	6.00	82.00	14.00	31.00	27.10	70.70	92.30	48.70	18.00	30.10	50.90	10.00	93.70	23.30	5.30	90.00	40.10	69.00	972.50
DI-7	0.00	389.60	128.70	8.00	95.00	12.00	30.30	3.00	67.10	76.20	57.50	22.00	24.50	47.20	9.00	77.60	16.30	4.40	89.00	45.40	109.00	817.60
DI-8	0.00	276.30	118.80	6.00	83.00	12.00	28.90	19.50	63.80	64.40	52.80	19.00	21.00	41.30	8.00	69.00	16.00	4.10	73.00	37.40	102.00	708.20
DI-9	4.60	305.80	156.00	10.00	112.00	11.00	30.70	4.00	78.30	65.80	74.00	25.00	21.10	42.50	9.00	67.70	14.30	3.90	94.00	52.40	152.00	787.30
DI-10	10.00	204.00	140.70	9.00	95.00	10.00	32.10	16.60	69.50	62.70	64.50	26.00	27.30	38.40	7.00	57.40	12.10	3.00	88.00	44.10	91.00	578.70
DI-11	13.40	196.80	130.80	10.00	106.00	14.00	30.40	16.40	70.40	59.80	59.90	29.00	24.00	37.30	9.00	54.10	15.40	4.30	94.00	40.60	102.00	594.50
DI-12	14.00	233.90	178.50	13.00	105.00	14.00	26.00	14.20	80.10	53.80	82.80	35.00	21.20	35.70	8.00	46.10	16.30	3.80	97.00	48.90	145.00	503.40
DI-13	13.40	205.00	198.40	10.00	104.00	15.00	27.20	16.80	86.20	59.20	88.90	30.00	22.10	38.60	9.00	51.10	17.70	4.20	105.00	45.90	133.00	567.00
DI-14	12.80	202.90	245.00	10.00	101.00	8.00	25.60	16.10	111.20	53.30	116.10	27.00	22.30	41.90	8.00	52.20	13.70	3.20	111.00	69.30	147.00	534.50
DI-15	12.80	200.00	323.70	13.00	109.00	13.00	25.90	14.20	165.10	49.50	120.60	35.00	20.40	37.90	10.00	70.20	16.10	3.40	120.00	63.20	191.00	486.40
DI-16'	13.00	230.00	175.00	10.00	110.00	11.00	24.30	16.90	83.90	54.60	83.10	26.00	20.10	44.50	8.00	53.20	14.70	3.70	151.00	55.40	128.00	623.90
DI-16	20.80	211.70	207.00	11.00	118.00	11.00	26.00	18.10	90.30	52.80	96.50	30.00	20.70	45.10	8.00	51.80	15.40	3.60	152.00	60.20	153.00	571.10
DI-17'	56.30	175.20	198.00	9.00	125.00	14.00	25.20	14.50	95.10	45.00	84.50	28.00	19.90	40.70	8.00	48.00	12.10	2.80	158.00	44.50	122.00	459.40
DI-17	13.00	191.10	795.00	17.00	117.00	9.00	25.10	14.70	321.60	49.50	398.60	41.00	21.40	41.40	9.00	52.00	16.20	3.40	151.00	206.10	278.00	488.50
DI-18'	17.30	200.20	508.00	17.00	114.00	8.00	19.70	17.40	207.10	42.80	263.60	38.00	16.70	44.10	9.00	46.10	14.40	3.00	168.00	181.50	280.00	528.70
DI-18	11.70	221.30	1168.00	19.00	124.00	8.00	20.30	18.50	474.50	44.10	593.80	43.00	17.90	48.00	9.00	49.40	15.30	3.40	179.00	326.70	376.00	608.50
DI-19'	14.00	217.30	1318.00	19.00	141.00	10.00	25.00	16.40	519.00	46.00	675.80	47.00	21.50	53.00	10.00	51.90	17.10	3.30	222.00	359.60	406.00	485.80
DI-19	14.30	194.10	1419.00	19.00	155.00	11.00	25.70	17.30	577.20	44.80	707.60	48.00	20.80	50.90	11.00	49.20	17.40	3.30	226.00	360.80	388.00	530.40
DI-20	31.30	232.80	649.00	14.00	131.00	9.00	24.30	15.50	322.40	48.50	298.00	36.00	25.20	49.50	10.00	55.10	13.30	2.90	290.00	260.70	207.00	518.50
DI-21	35.20	231.70	655.80	11.00	199.00	10.00	23.40	25.00	254.70	48.20	289.50	37.00	21.30	58.10	11.00	49.50	16.80	4.00	379.00	157.40	168.00	783.70
DI-22	7.90	383.90	172.20	6.00	103.00	6.00	15.40	24.80	83.60	32.80	73.20	16.00	12.50	49.70	6.00	63.00	11.90	3.40	98.00	37.10	110.00	911.00
DI-23	14.50	354.50	312.60	12.00	90.00	6.00	15.00	23.80	143.20	31.70	135.80	24.00	16.00	54.30	7.00	60.70	14.90	4.10	87.00	69.30	237.00	827.90
DI-24	5.20	352.00	254.10	11.00	84.00	5.00	14.50	21.00	112.10	29.70	111.60	22.00	11.40	53.00	7.00	59.20	13.30	2.60	81.00	53.00	254.00	757.00
DI-25	4.40	330.80	209.50	10.00	87.00	5.00	14.20	19.20	100.70	28.00	92.40	23.00	11.60	51.40	7.00	56.50	12.50	3.00	82.00	46.00	265.00	697.40
DI-26	5.70	341.10	314.10	14.00	78.00	5.00	12.90	19.60	131.80	26.60	144.90	28.00	10.40	48.10	8.00	55.00	13.00	3.70	68.00	66.00	233.00	713.30
DI-27	7.20	369.50	227.90	9.00	85.00	5.00	14.30	18.10	95.70	27.80	100.20	19.00	13.40	51.30	6.00	59.70	10.20	2.50	78.00	43.80	142.00	663.80
DI-28	6.40	346.50	261.70	10.00	78.00	6.00	11.80	20.80	107.80	26.60	113.90	18.00	10.30	46.40	7.00	57.90	12.40	3.10	84.00	50.50	121.00	815.50
DI-29	6.40	327.00	285.80	10.00	79.00	6.00	13.50	17.50	114.10	26.90	120.90	19.00	11.40	47.90	6.00	55.30	11.10	3.00	84.00	46.30	104.00	667.60
DI-30	5.20	332.20	194.10	8.00	159.00	6.00	13.90	16.90	76.40	27.50	80.40	16.00	10.50	43.80	6.00	52.50	10.40	2.50	87.00	30.20	51.00	624.20
DI-31	6.30	363.70	100.80	5.00	80.00	5.00	12.40	22.20	48.00	26.90	44.20	12.00	10.80	40.80	7.00	52.80	10.80	3.10	92.00	22.20	41.00	833.80
DI-32	5.70	367.20	105.20	6.00	84.00	7.00	12.20	34.70	57.40	30.70	43.30	14.00	11.50	34.60	7.00	49.90	13.30	3.60	109.00	24.60	38.00	1273.60
DI-33	7.40	335.40	115.70	8.00	89.00	7.00	12.50	25.40	51.90	29.20	48.90	15.00	13.20	33.20	11.00	51.00	14.80	3.70	98.00	24.00	37.00	1007.40

ANNEX VI: BULK MINERALOGICAL RAW DATA FROM TONDE AREA

Samples	Phyllosilicate	Quartz	K-feldspar	Na-plagioclase	Pyrite	Hematite	Goethite	Undosed
DA-1	69.02	18.86	0.00	0.00	1.88	0.00	6.57	3.67
DA-3	72.33	17.82	0.00	0.00	1.49	0.00	5.15	3.21
DA-6	79.72	11.99	0.00	0.00	1.30	0.00	5.59	1.40
DA-8	42.03	48.94	0.00	0.00	1.11	0.00	3.73	4.19
DA-10	72.19	18.77	0.00	0.00	1.63	0.00	5.47	1.93
DA-12	60.12	29.08	0.00	0.00	0.81	0.00	7.24	2.74
DA-14	76.45	16.77	0.00	0.00	2.14	0.00	0.60	4.04
DA-15	63.89	25.68	0.00	0.00	1.47	0.00	4.60	4.37
DA-17	71.86	18.89	0.00	0.00	1.61	0.00	5.88	1.75
DA-18	18.40	75.33	0.88	0.00	0.00	0.00	2.42	2.97
DA-21	77.29	13.53	0.00	0.00	1.35	0.00	5.38	2.46
DA-23	79.33	10.03	0.00	0.00	1.20	0.00	3.93	5.50
DA-25	70.83	17.20	1.12	0.00	1.22	0.00	4.08	5.55
DA-26	75.49	17.87	0.00	0.00	1.12	0.00	3.66	1.86
DA-28	78.00	14.26	0.00	0.00	1.48	0.00	5.75	0.51
DA-29	70.13	20.83	0.00	0.00	1.84	0.00	3.74	3.46
DA-31	75.34	16.00	0.00	0.00	0.94	0.00	4.13	3.59
DA-32	67.95	19.51	0.00	0.00	3.92	0.00	4.62	4.00
DA-34	73.03	14.89	0.00	0.00	3.68	0.00	5.70	2.70
DA-36	70.43	17.89	0.00	0.00	3.75	0.00	3.64	4.28
DA-38	68.09	15.98	0.00	0.00	4.17	0.00	3.16	8.61
DA-39	67.43	25.58	0.00	0.00	0.98	0.00	4.78	1.24
DA-40	47.25	46.03	0.00	0.00	0.84	0.00	3.16	2.72
DA-41	69.11	23.98	0.00	0.00	0.81	0.00	5.42	0.68
DA-42	46.12	45.85	0.00	0.00	0.00	0.00	4.50	3.53
DA-43	49.03	43.03	0.00	0.00	0.00	0.00	4.95	2.99
DA-44	55.23	34.94	0.00	0.00	1.10	0.00	5.18	3.55
DA-46	57.04	36.99	0.00	0.00	0.75	0.00	4.24	0.98
DA-47	32.83	60.22	0.00	0.00	0.00	0.00	5.41	1.54
DA-48	32.51	62.10	0.00	0.00	0.00	0.00	4.15	1.24
DA-49	25.56	72.12	0.00	0.00	0.00	0.00	0.00	2.32
ES201	71.42	23.12	0.00	0.00	0.62	0.00	0.00	4.84
ES202	77.03	15.88	0.00	0.00	0.00	0.00	5.53	1.56
ES204	69.03	18.03	0.00	0.00	1.15	0.00	4.94	6.85
ES205	72.45	16.97	1.06	0.00	0.94	0.00	4.15	4.43
ES207	80.99	7.62	0.00	0.00	1.15	0.00	6.51	3.72
ES208	83.12	6.48	0.00	0.00	1.22	0.00	6.10	3.09
ES209	79.04	10.98	0.00	0.00	1.43	0.00	4.67	3.88
ES210	82.13	9.03	0.00	0.00	0.98	0.00	6.18	1.68
ES212	80.12	7.04	0.00	0.00	2.61	0.00	5.71	4.51
ES213	79.34	6.10	0.00	0.00	1.08	0.00	11.43	2.06
ES214	77.48	7.33	1.52	0.93	0.81	0.00	8.71	3.22
ES215	58.00	26.92	1.13	0.00	0.79	0.00	12.06	1.10